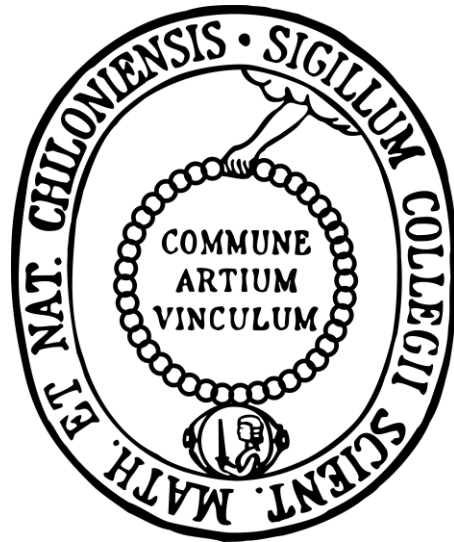


Characterization of photoactivatable Prodrugs of Kinase Inhibitors



Dissertation

zur Erlangung des Doktorgrades
der Mathematisch-Naturwissenschaftlichen Fakultät
der Christian-Albrechts-Universität zu Kiel

vorgelegt von

Boris Pinchuk

Kiel 2017

Dekanin:	Prof. Dr. Natascha Oppelt
Erster Gutachter:	Prof. Dr. Christian Peifer
Zweiter Gutachter:	Prof. Dr. Axel Scheidig
Externer Gutachter:	Prof. Dr. Uwe Knippschild
Tag der mündlichen Prüfung:	12. Mai 2017
Zum Druck genehmigt:	12. Mai 2017

Meinem Vater

Abstract

The approval of imatinib in 2001 marked a milestone in targeted therapy. Protein kinase inhibitors have revolutionized the cancer treatment since then. Progression free survival could be significantly prolonged in many cases. However, tumors often develop resistances during the treatment with kinase inhibitors. As consequence, most patients experience a relapse during initially successful therapy. Systemic adverse side effects are another drawback of kinase inhibitors. Thus, novel approaches in the field of protein kinase inhibitors are urgently required to improve the clinical outcomes.

The present work describes development and characterization of novel photoactivatable prodrugs of several approved small molecule kinase inhibitors. Photoremovable protecting groups were therefore covalently bound to key pharmacophore moieties of active kinase inhibitors. The implementation of a protecting group distinctly diminished the biological activity of protected inhibitors. Directed light irradiation caused photoinduced cleavage of the protecting group. Active kinase inhibitors were released. The concept was successfully verified *in vitro* on approved kinase inhibitor vemurafenib. Spatiotemporal control of the photoinduced release of the active inhibitor could be demonstrated in cellular assays. The approach could be successfully transferred to further kinase inhibitors such as imatinib. However, limitations of the concept were also revealed. In line with this notion, a hitherto undescribed photoinduced conversion of approved inhibitor dabrafenib was demonstrated.

The photoactivatable prodrugs of kinase inhibitors represent a powerful pharmacological tool for profound *in vitro* investigation of protein phosphorylation. However, further development with regard to physicochemical and pharmacokinetic properties is required prior to clinical applications. Novel approaches for targeted reactivation in deeper biological tissues are discussed at the end of the work.

A side project of the present work was the characterization of novel PDGFR β inhibitors. Potent and selective DFG-in and DFG-out inhibitors were compared *in vitro*. In particular, the DFG-out inhibitor **3** exhibited promising cellular activity and might be used for further lead optimization.

Kurzzusammenfassung

Die Zulassung von Imatinib im Jahr 2001 war ein Meilenstein in der Geschichte der gezielten Krebstherapie. Seitdem haben Proteinkinaseinhibitoren die Tumorbehandlung revolutioniert. Das Überleben vieler Krebspatienten wurde signifikant verlängert. Doch leider entwickeln Tumore während der Behandlung mit Kinaseinhibitoren oft Resistenzen, die in den meisten Fällen zu einem Rezidiv führen. Außerdem leiden viele Patienten an systemischen unerwünschten Arzneimittelwirkungen. Neue Konzepte auf dem Feld der Kinaseinhibitoren sind also nötig, um die therapeutische Effizienz und Verträglichkeit zu erhöhen.

Die vorliegende Arbeit beschreibt die Entwicklung und Charakterisierung von neuartigen photoaktivierbaren Prodrugs von mehreren zugelassenen Kinaseinhibitoren. Dafür wurden photoabschaltbare Schutzgruppen kovalent an aktive Kinaseinhibitoren gebunden. Das Einbringen einer Schutzgruppe führte zur pharmakologischen Inaktivierung der Inhibitoren. Durch gezielte Lichtbestrahlung konnte die Schutzgruppe abgespalten werden. Die aktiven Wirkstoffe wurden dadurch freigesetzt. Am Beispiel des zugelassenen Kinaseinhibitors Vemurafenib konnte der Ansatz *in vitro* erfolgreich überprüft werden. Die zeitliche und räumliche Kontrolle der photoinduzierten Aktivierung wurde damit demonstriert. Das Konzept konnte auf weitere Kinaseinhibitoren wie Imatinib erfolgreich übertragen werden. Es wurden aber auch Limitierungen des Ansatzes gezeigt. So wurde eine bis dahin unbekannt photoinduzierte Umwandlung des zugelassenen Kinaseinhibitors Dabrafenib beschrieben.

Die photoaktivierbaren Prodrugs von Kinaseinhibitoren stellen ein wertvolles pharmakologisches Werkzeug dar, um die Proteinphosphorylierung *in vitro* genauer zu untersuchen. Für eine klinische Anwendung ist eine Weiterentwicklung hinsichtlich physikochemischer und pharmakokinetischer Eigenschaften notwendig. Am Ende der Arbeit werden verschiedene Möglichkeiten der gezielten Aktivierung in tieferem Gewebe diskutiert.

Im Rahmen eines Nebenprojekts wurden in dieser Arbeit potente und selektive PDGFR β -Inhibitoren charakterisiert. Dabei wurden DFG-in und DFG-out Inhibitoren verglichen. Besonders der DFG-out Inhibitor **3** zeigte eine vielversprechende zelluläre Aktivität und sollte für eine weitere Optimierung verwendet werden.

Table of Contents

1	Introduction.....	1
1.1	Protein Kinases	1
1.1.1	Protein phosphorylation	1
1.1.2	Kinases in the human genome	3
1.1.3	Kinases as pharmacological targets	5
1.1.4	Kinase domain structure	6
1.2	Protein Kinase Inhibitors.....	11
1.2.1	Progress in the development of potent and selective kinase inhibitors	11
1.2.2	Classification of protein kinase inhibitors	13
1.2.3	Comparison of DFG-in and DFG-out inhibitors	14
1.2.4	Benefits and drawbacks of protein kinase inhibitors in clinical applications	16
1.3	Caged kinase inhibitors.....	19
1.3.1	Regulation of biological processes by light	19
1.3.2	Caging of protein kinase inhibitors	23
1.3.3	Photoremovable protecting groups.....	24
1.3.4	o-nitrobenzyl derivatives as photoremovable protecting groups	27
2	Scope.....	29
3	Results and Discussion	33
3.1	Photoactivatable Prodrugs of Antimelanoma Agent Vemurafenib.....	35
3.1.1	Additional data measured following publication of the article “Photoactivatable Prodrugs of Antimelanoma Agent Vemurafenib”	84
3.2	Design, Synthesis, and Characterization of a Photoactivatable Caged Prodrug of Imatinib.....	87
3.3	Photoactivatable Caged Prodrugs of VEGFR-2 Kinase Inhibitors	113
3.4	Photoinduced Conversion of Antimelanoma Agent Dabrafenib to a Novel Fluorescent BRAF ^{V600E} Inhibitor	139

3.5	Marine derived hamacanthins as lead for the development of novel PDGFR β protein kinase inhibitors	171
3.6	Optimization of potent DFG-in inhibitors of platelet derived growth factor receptor β (PDGF-R β) guided by water thermodynamics	189
3.7	From Type I to Type II: Design, Synthesis, and Characterization of Potent Pyrazin-2-ones as DFG-Out Inhibitors of PDGFR β	245
4	Summary	277
4.1	Photoactivatable prodrugs of kinase inhibitors	277
4.2	Novel PDGFR β inhibitors	282
5	Prospects	283
5.1	Photoactivatable prodrugs of smKIs.....	283
5.1.1	<i>In vivo</i> testing of photoactivatable prodrugs of vemurafenib	283
5.1.2	Approaches to overcome the limited penetration depth of light	286
5.1.3	Concluding remarks.....	296
5.2	PDGFR β inhibitors.....	297
6	References	299
7	Appendix	329
7.1	List of Abbreviations	329
7.2	List of Figures	333
	Curriculum Vitae	337
	Erklärung	339
	Danksagung	343

1 Introduction

1.1 Protein Kinases

1.1.1 Protein phosphorylation

The first description of a phosphorylated protein dates back to the beginning of the 20th century. In 1932, a phosphorylated serine was identified in vitellin, a protein from the egg yolk.¹ Twenty years later, in 1954, the first enzymatic phosphorylation of proteins was shown at the example of phosphorylated casein.² Edwin Krebs and Edmond Fisher revealed that phosphorylation of glycogen phosphorylase *b* is necessary for its activation the following year.³ It was the first proof that protein phosphorylation alters target protein activity. Back in those days, Krebs and Fisher could not even imagine that they brought to light one of the most fundamental regulatory mechanisms in living cells.⁴ However, both scientists were awarded the Nobel Prize in Physiology and Medicine for their research in 1992. Today, it is generally accepted that “protein phosphorylation regulates most aspects of cell life, whereas abnormal phosphorylation is a cause or consequence of disease”.⁵

Protein phosphorylation is a post-translational modification of proteins. Thereby, a phosphate group is covalently bound to an amino acid residue. Nucleoside triphosphates, mostly ATP, serve as phosphate donors. The γ -phosphate group from ATP is transferred to the target protein. The transferases that catalyze this reaction are called protein kinases. Protein phosphorylation is a reversible modification. The enzymes that reverse the reaction are protein phosphatases. Phosphatases cleave the covalent bond of phosphomonoesters and remove the phosphate groups from proteins.

Introduction of a negatively charged phosphate group can have dramatic effects on the function and activity of the affected protein. One possible consequence of the phosphorylation is the structural rearrangement of the target.⁶⁻⁹ Furthermore, phosphorylated amino acid residues often function as specific binding sites for other proteins.^{8,10} Different phosphoresidue binding domains have been identified. For example,

phosphorylated tyrosines are specifically recognized by the Src homology 2 (SH2) domains.^{11,12} 14-3-3 proteins bind to phosphorylated serine^{13,14} and Forkhead-associated (FHA) domains dock to phosphothreonine.¹⁵ Protein phosphorylation often constitutes a starting point for downstream protein interactions. Generally, phosphorylation might affect physico-chemical properties, dynamics, subcellular localization, function, and activity of the modified protein.^{8,9}

The importance of the post-translational modification is underlined by the fact that the majority of proteins in a human cell are phosphorylated at least during mitosis.¹⁶ Protein phosphorylation plays a crucial role in almost all cellular processes.^{17,4} Apart from the regulation of intracellular signal transduction, protein phosphorylation is important for intercellular communication in the majority of physiological processes.¹⁸ Meanwhile, there are more than two hundred thousand scientific articles listed by PubMed that deal with this topic (last updated on January 2017). It is obvious that such a key process like protein phosphorylation should be precisely regulated. Otherwise, severe consequences for the affected cells and the whole organism may occur.

1.1.2 Kinases in the human genome

The entirety of kinases in a genome is called kinome. The human kinome was fully complemented by Gerard Manning and co-workers in 2002.¹⁸ 518 protein kinases encoded in the human genome were revealed. This constitutes almost 2% of protein coding genes in human.¹⁸ Protein kinases thereby belong to one of the largest protein families.^{18, 19} Biological significance of protein kinases is reflected by evolutionary conservation of these enzymes. Thus, for instance, 80% of protein kinases in *C. elegans* have homologs in the human kinome.²⁰ The common eukaryotic protein kinase catalytic domain is highly conserved.^{20, 21}

Protein kinases can be classified due to the acceptor amino acid of the substrate protein. According to this approach, five groups can be distinguished: serine/threonine protein kinases, tyrosine protein kinases, histidine protein kinases, cysteine protein kinases, and aspartyl/glutamyl protein kinases.²² The vast majority of protein kinases in eukaryotes are either serine/threonine or tyrosine kinases.²¹ However, there are also so-called “dual-specificity protein kinases” that can phosphorylate both tyrosine and serine/threonine residues.^{23, 24}

Another approach is to classify the eukaryotic kinases by sequence similarities in their catalytic domains.¹⁸ Seven major groups can be differentiated: AGC, CAMK, CMGC, CK1, STE, TKL, and TK kinases.²⁵ Moreover, several families of atypical kinases were identified. These enzymes have catalytic activity but lack sequence similarity to the conserved protein kinase domain.¹⁸ Phylogenetic relations between human protein kinases can be visualized on the human kinome tree (Figure 1).¹⁸

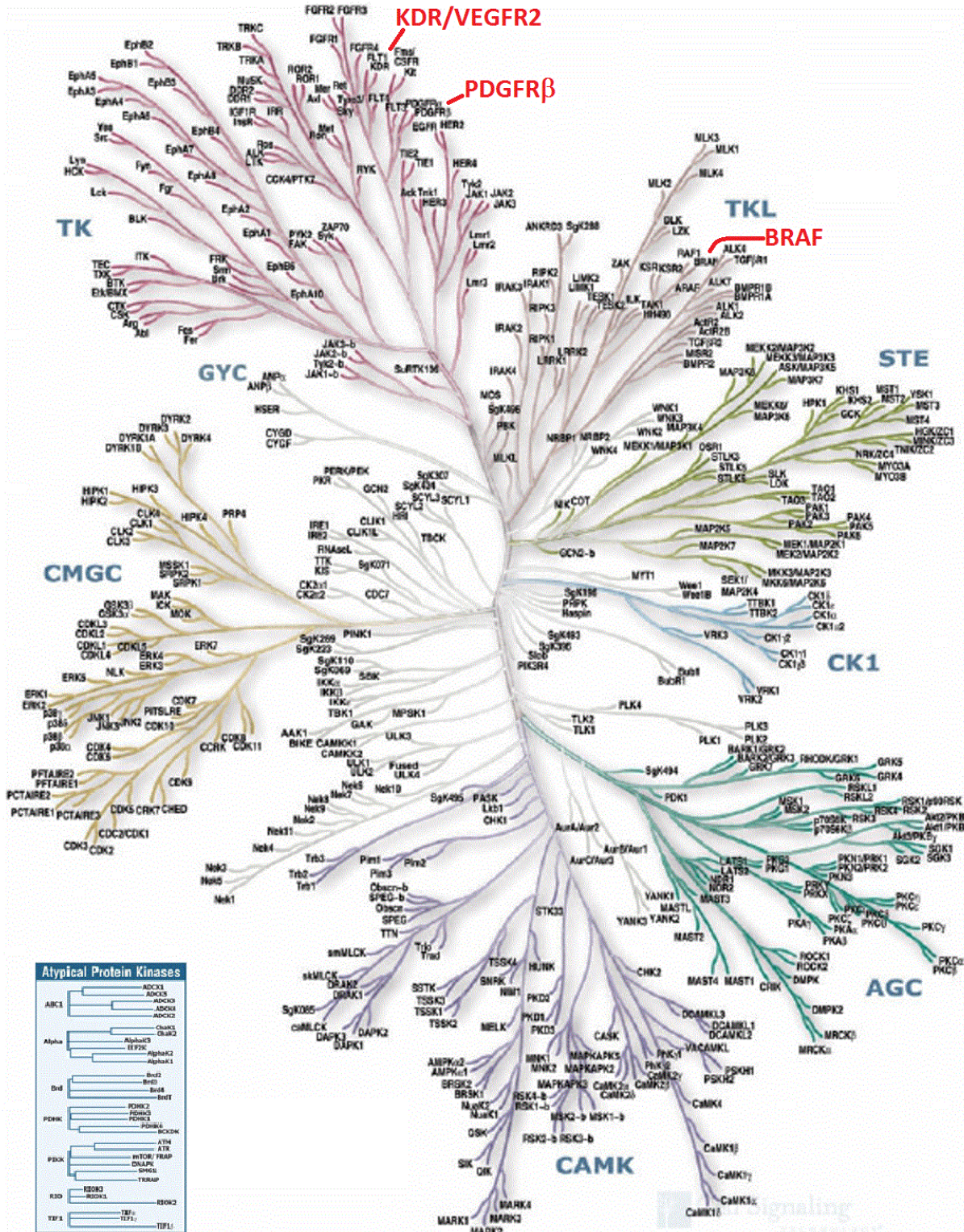


Figure 1: Phylogenetic tree of the human kinome. Seven major protein kinase groups can be distinguished: TKL, STE, CK1, AGC, CAMK, CMGC and TK. Kinases discussed more in this work are labeled with bold red letters. The phylogenetic tree is adapted from cell signaling technology.²⁶

1.1.3 Kinases as pharmacological targets

Due to the crucial role of protein phosphorylation for the regulation of cellular processes, protein kinases became one of the most important drug targets in the twenty-first century.^{5, 27–29} Some studies predict that kinases account for the major part of the “druggable” genome.³⁰

The main indication for targeting protein kinases are oncological malignancies nowadays. The initial link between dysregulation of kinase function and cancer development was established by the end of the 1970s.^{10, 28} Back then, it was demonstrated that the viral oncogene *v-SRC* possessed tyrosine kinase activity.^{31, 32} Meanwhile, significance of kinase signaling is demonstrated for a variety of cancer diseases.^{5, 33–35} Moreover, dependence of some cancer cells on mutated or overexpressed kinases could be proved. This phenomenon was called “oncogene addiction”.³⁶ This dependence³⁷ applies both for serine/threonine³⁷ and tyrosine kinases.³⁸

The findings described above led to a novel approach of inhibiting mutated or overexpressed kinases in the hope of selective cancer treatment. This was the birth of the “targeted” cancer therapy. The idea is to target only the mutated malignant tumours but not all proliferating cells as it is the case in the standard chemotherapy. Fewer side effects and better drug tolerance are expected by this targeted approach.³⁹

Cancer, however, is not the only possible indication for targeting protein kinases. There are several recent rudiments to inhibit kinase signaling for the treatment of inflammatory diseases.²⁷ Tofacitinib, for example, is a JAK inhibitor which was approved 2012 for the therapy of rheumatoid arthritis.⁴⁰ Moreover, directed modulation of protein kinase activity could be used in many other maladies such as diabetes.^{41, 42} Therefore, different kinase inhibitors are undergoing clinical studies in inflammatory, neurodegenerative, cardiovascular, and metabolic diseases.³⁵

1.1.4 Kinase domain structure

For understanding the binding characteristics of different kinase inhibitors, it is necessary to describe the structure of the kinase domain at first.

The vast majority of protein kinases, 478 of 518,⁴³ possess a very conserved catalytic domain. This kinase domain counts about 250 amino acid residues and its structure has already been described in essence in 1991 when the structure of PKA was revealed by crystallography.⁴⁴

The catalytic kinase domain consists of two lobes, the N- and C-termini. Both lobes are connected through a flexible hinge region (Figure 2).

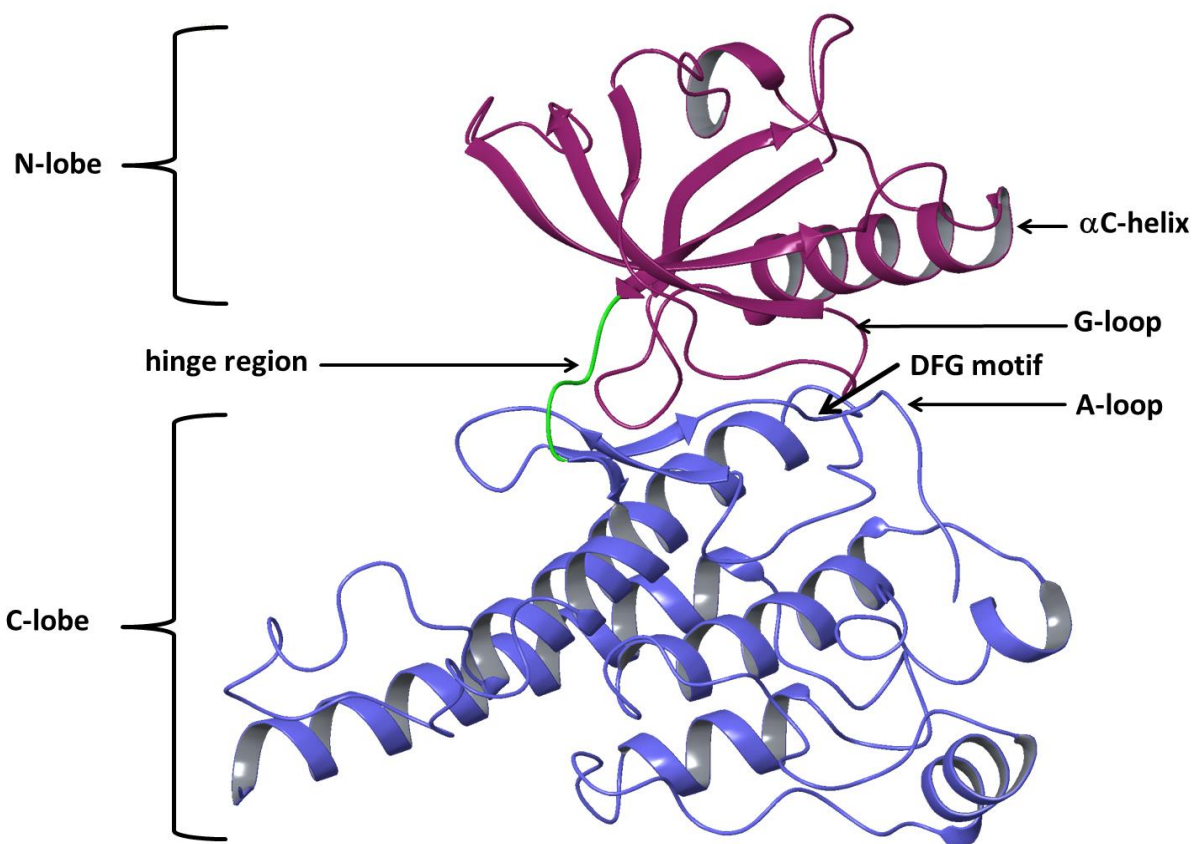


Figure 2: Schematic presentation of the kinase domain of VEGFR-2 (PDB code: 3B8R).⁴⁵ This and subsequent figures showing 3D protein structures were visualized using Maestro 10.4.⁴⁶ The N-terminus is colored purple and the C-terminus is blue. The hinge region is depicted in green.

The N-lobe is mainly composed of five antiparallel β -sheets, the α C-helix and the glycine-rich G-loop. The α C-helix is crucial for the catalytic activity: a conserved glutamate residue in this

helix forms a salt bridge to also conserved lysine (Glu69 and Lys52 in Figure 3). The latter interacts with the phosphate groups of ATP. The G-loop, sometimes also referred to as P-loop, is also important for the interaction with ATP. This loop contains a characteristic glycine rich motif and is highly flexible.²⁸ Simplified, it could be said that the N-lobe is rather responsible for the ATP orientation and thus activation.

The C-lobe (marked blue in Figure 2) consists primarily of α -helices which are connected by numerous loops. One of these loops is the so-called “A-loop”. The A-loop is also referred to as the “activation loop”. This flexible region starts with the conserved amino acid sequence: aspartate, phenylalanine, glycine and is known as the “DFG motif” (Figure 2).^{47, 48} Another conserved region in the A-loop is the “APE motif” which is comprised of alanine, proline, and glutamate.⁴⁹

The hinge region (green in Figure 2) flanks the ATP-binding site situated in the cleft between both lobes. The binding site can be divided into five distinct regions according to the model of Traxler and Furet (Figure 3).⁵⁰ The adenine residue of ATP is located in the adenine pocket (AP) and forms two H-bonds to the hinge region (Asp104 and Met106 in Figure 3). The ribose and phosphate residues are placed in the sugar pocket (SP) and in the phosphate binding region (PBR), accordingly. Adjacent to the AP, two hydrophobic pockets can be highlighted: the hydrophobic pocket I (HP I) that is separated from AP by a “gatekeeper” residue (Gln103 in Figure 3) and the hydrophobic region II (HR II) which is solvent exposed.⁴³ Both hydrophobic pockets are unoccupied by ATP but play a key role in the design of kinase inhibitors.⁵¹ The gatekeeper residue varies between distinct kinases and this can be used for the development of selective inhibitors that address the HP I.⁴⁸ On the other hand, mutations in the gatekeeper residue can cause acquired resistance to kinase inhibitors.^{52, 53}

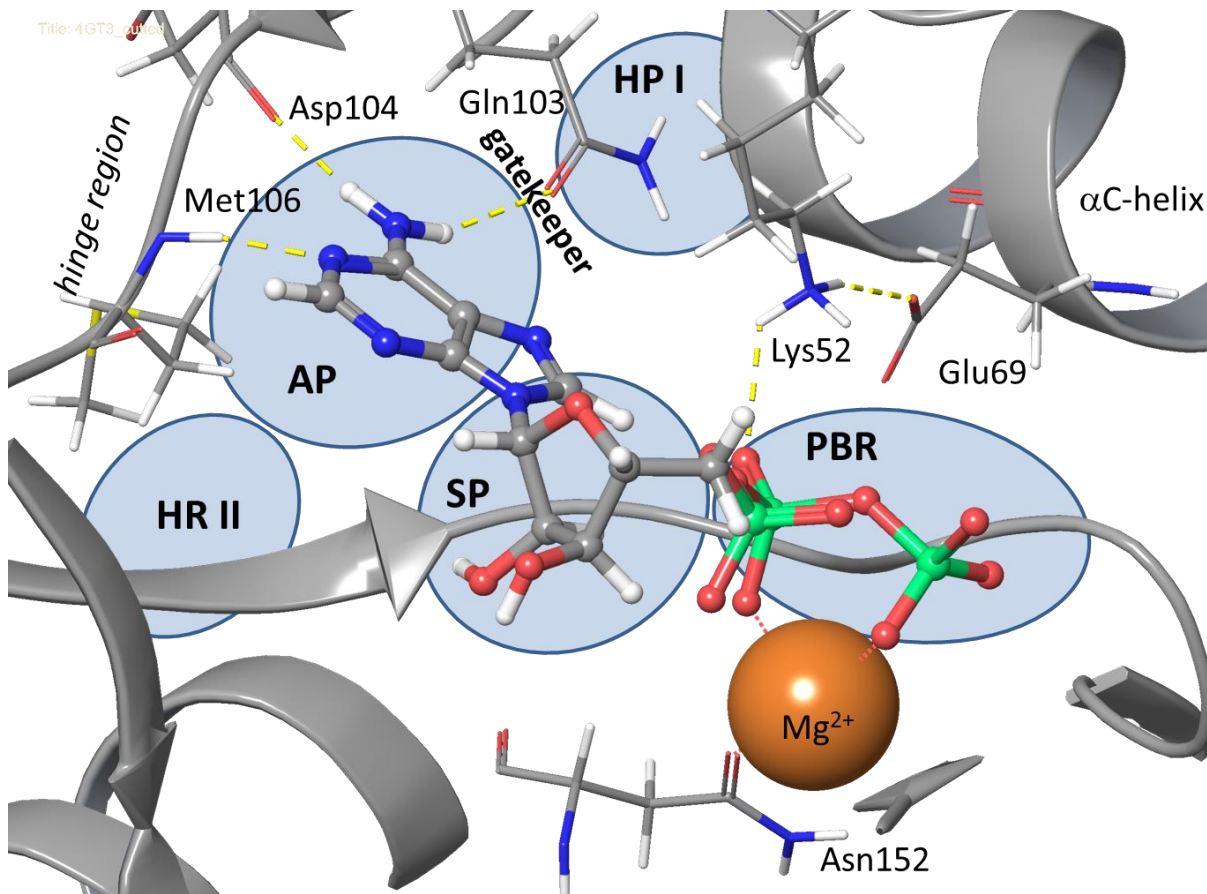


Figure 3: Schematic model of the ATP-binding site in an active kinase. The representation is based on the crystallized structure of ERK2 kinase in complex with ATP (PDB code: 4GT3).⁵⁴ Amino acid residue glutamine 103 (Gln103) was indicated as the gatekeeper in accordance to previous studies.⁵⁵ The pharmacophore model by Traxler and Furet was applied.^{43, 50} Maestro 10.4 was used for visualization.⁴⁶ Only key residues are shown for better clarity. ATP is depicted with ball and sticks. The amino acid residues are represented as thin tubes. H-Bonds are indicated by yellow dashed lines. HR II = hydrophobic region II, AP = adenine pocket, HP I = hydrophobic pocket I, SP = sugar pocket, PBR = phosphate binding region.

The A-loop is inevitable for the catalytic kinase activity. The aspartate in the DFG motif chelates the magnesium ion involved in coordinating ATP.⁴⁹ The same aspartate is also crucial for the transfer of the γ -phosphate from ATP to the target protein.⁵⁶ The activation loop can adopt two different conformations: the DFG-in conformation in the catalytic active state and the DFG-out conformation in inactive-like kinase.²⁸ In the DFG-in conformation the aspartate residue interacts with the magnesium cation, the adjacent phenylalanine points away from the adenine pocket. The ATP-binding site is now accessible for the nucleoside (Figure 4A).⁵⁷ On the contrary, in the DFG-out conformation the phenylalanine residue “flips” into the

catalytic cleft and obstructs access to the ATP-binding site (Figure 4B). In exchange, the so-called “deep” pocket becomes available (red oval in Figure 4B). The switch between DFG-out and DFG-in conformations is crucial for kinase activation and is strictly regulated by different mechanisms, such as phosphorylation of the A-loop.⁵⁸

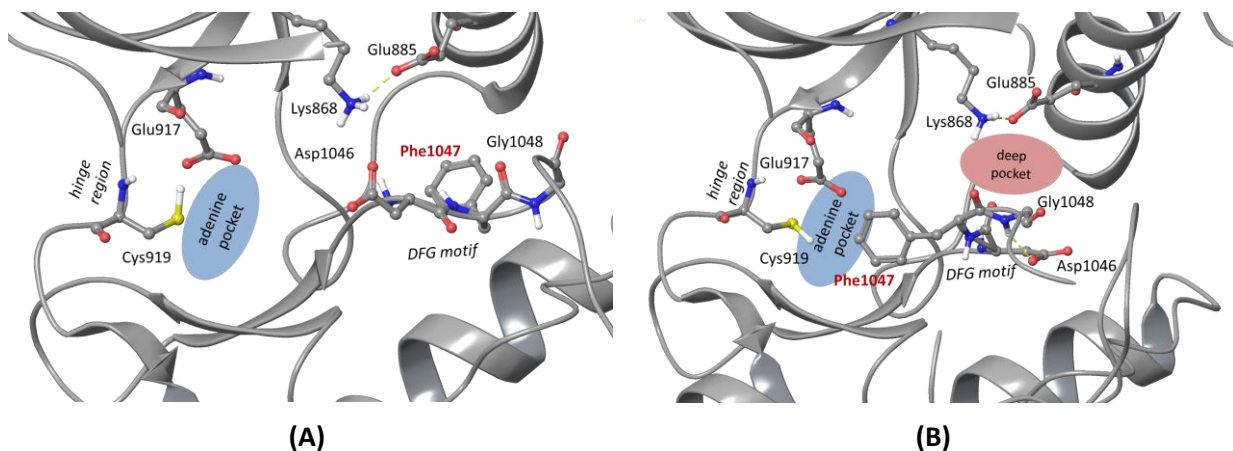


Figure 4: Binding site in the VEGFR-2 kinase domain in different DFG conformations.⁵⁹ The representations were visualized using Maestro 10.4⁴⁶ and are according to the noted PDB codes. (A) DFG-in conformation is shown (PDB code: 3B8R).⁴⁵ The phenylalanine residue Phe1047 blocks the deep pocket. The adenine pocket is exposable for ATP (blue oval). (B) DFG-out conformation is depicted (PDB code: 3EWH).⁶⁰ The phenylalanine residue Phe1047 is now rearranged and blocks access to the adenine pocket for ATP. The deep pocket (red oval) can now be addressed by inhibitors.

Another attribute of the active kinase conformation is the “regulatory spine”.^{28, 35, 61, 62} This spine extends through both kinase lobes, is near-linear arranged, and consists of four hydrophobic residues that interact through H-bonds, CH- π -, and hydrophobic interactions.^{61, 35} Distortion of this linear regulatory spine leads to an inactive enzyme conformation. Furthermore, there is a second characteristic spine in active kinases: the “catalytic spine”.⁶² The latter crosses both lobes and contains the adenine ring from ATP (Figure 5).

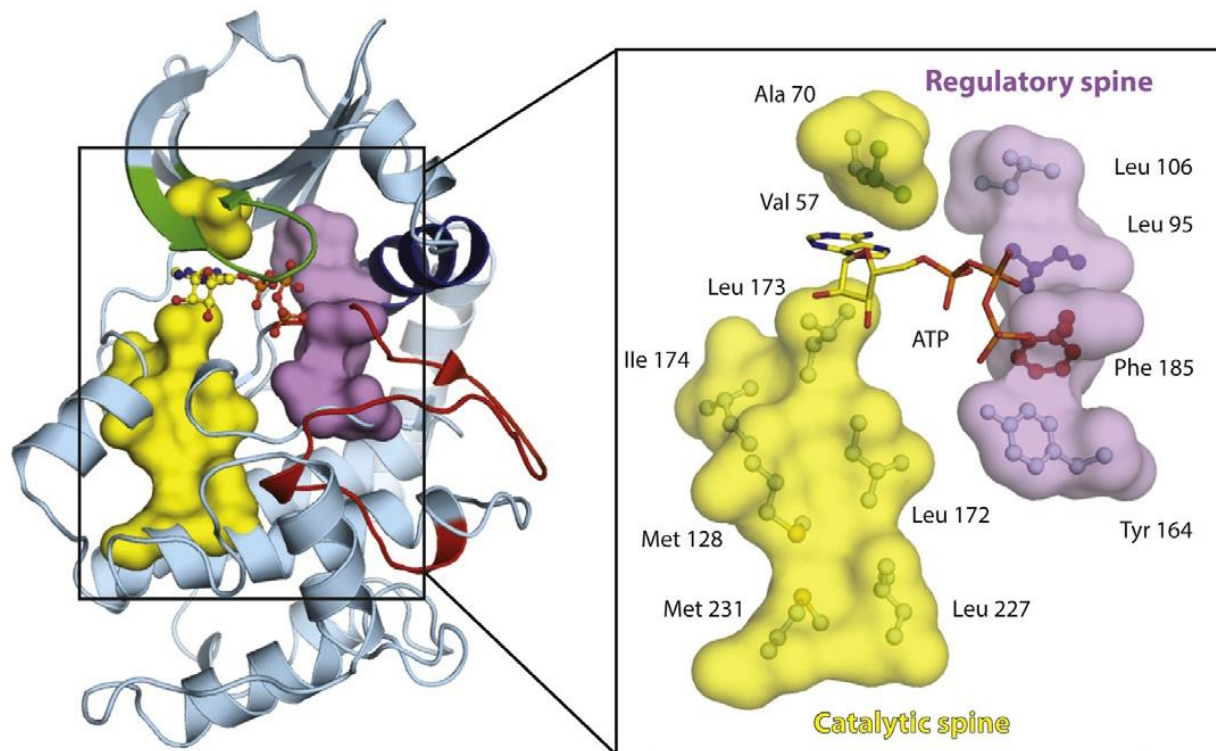


Figure 5: The regulatory (purple) and catalytic (yellow) spines in the active PKA kinase.²⁸ The presentation is in accordance to Kornev *et al.*⁶² and is based on the PDB code: 1ATP.⁶³ Disruption of these spines drives the inactive kinase conformation.

1.2 Protein Kinase Inhibitors

1.2.1 Progress in the development of potent and selective kinase inhibitors

In virtue of clear evidence for the significance of protein phosphorylation in pathogenesis (compare Chapters 1.1.1 and 1.1.3) there has been a great aspiration to develop potent and selective kinase inhibitors since 1970s. The first described protein kinase inhibitors were isoquinolinesulfonamides developed in 1984.^{5, 64} Two years later, in 1986, the antifungal compound staurosporine was discovered as a nanomolar inhibitor of PKC.^{65, 66} The problem about the first kinase inhibitors was their lack of selectivity. The highly conserved ATP binding pocket and high intracellular ATP concentrations in the millimolar range led to the assumption that the development of selective and potent protein kinase inhibitors would be an impossible task.^{5, 39} However, this hypothesis could be impressively disproved by the end of 1980s.

In 1988, first potent inhibitors of tyrosine kinase EGFR have been developed. These compounds exposed significant selectivity over serine/threonine kinases and some other tyrosine kinases such as the insulin receptor.⁶⁷ The first clinically approved protein kinase inhibitor was rapamycin in 1999.⁶⁸ Rapamycin is produced by a soil bacterium *Streptomyces hygroscopicus* and had originally been identified as an antifungal compound back in 1970s.⁶⁹ Some twenty years later, it was revealed that the intracellular target of rapamycin is a serine/threonine kinase. This kinase was then called “mammalian target of rapamycin, mTOR”.⁷⁰ Rapamycin, also known as sirolimus, is still used as immunosuppressive agent for prevention of organ transplant rejections. The trade name of rapamycin is Rapamune®.⁷¹

Motivated by the success of rapamycin many research programs were launched for the rational design of potent protein kinase inhibitors. A new milestone in this development was the approval of imatinib, trade name Gleevec®, in 2001. Imatinib is a potent inhibitor of the tyrosine kinase BCR-ABL, an oncogenic fusion protein caused by the Philadelphia chromosome.^{72, 73} Imatinib exhibits antiproliferative effects on the BCR-ABL positive cancer

cells and is approved for the treatment of chronic myeloid leukemia (CML) and several other malignancies.⁷⁴

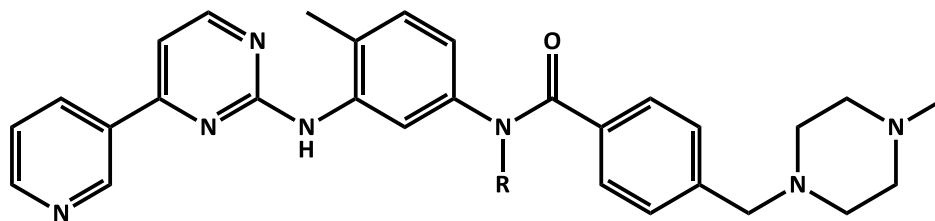


Figure 6: Chemical structure of imatinib, the first approved kinase inhibitor for cancer treatment.

Today, 35 different small-molecule kinase inhibitors are approved for clinical usage, as by October 2016.³⁵ The majority of these drugs are anticancer agents. There are only few exceptions: fasudil, a potent ROCK inhibitor, has been approved in Japan for the treatment of cardiovascular diseases.⁷⁵ Tofacitinib, an inhibitor of JAK tyrosine kinase, was approved for the therapy of rheumatoid arthritis in 2012.⁷⁶ Another example of a kinase inhibitor with an indication outside of oncology is nintedanib which was approved 2014 for the treatment of idiopathic pulmonary fibrosis.⁷⁷ However, a lot of other indications are in focus of kinase inhibitor research. Protein kinase inhibitors are in development for the treatment of inflammatory, autoimmune, and neurodegenerative diseases, for instance.^{27, 78}

The clinical significance of kinase inhibitors is underscored by a great number of these agents currently being in clinical trials.³⁵ Furthermore, kinase inhibition is considered to be the predominant mode of action of experimental agents at least in cancer research.⁷⁹

1.2.2 Classification of protein kinase inhibitors

Protein kinase inhibitors can be categorized into different types according to their binding mode in the target protein. Several classification systems have been proposed. In general, three major strategies targeting protein kinases can be highlighted: kinase inhibitors that bind to the active DFG-in kinase conformation (type I), inhibitors that target the inactive DFG-out state (type II), and the allosteric inhibitors.^{80, 81}

Recently, a comprehensive system for classification of protein kinase inhibitors has been suggested by Roskoski.⁸² Six different inhibitor types are distinguished. The classification is based on the structural properties of the correspondent enzyme inhibitor complexes and will be used in the present work.

Type I inhibitors bind to the active kinase state. The DFG motif is in the in-conformation and the regulatory spine is linearly arranged (compare chapter 1.1.4 for structural details of kinase domain). Type I½ inhibitors target also the DFG-in conformation, but the regulatory spine is distorted now. Therefore, inhibitors of types I and I½ are also called “DFG-in inhibitors”. Type II inhibitors bind the inactive DFG-out conformation and can be declared as “DFG-out inhibitors”. Both, DFG-in and DFG-out inhibitors are ATP-competitive because they target the ATP-binding pocket of the enzymes. Type III inhibitors are allosteric and bind next to the ATP site. Type IV inhibitors are allosteric inhibitors too, but target regions distal from the catalytic cleft. Allosteric inhibitors are considered to be more selective than the compounds that target directly the ATP-binding site.⁸³ Inhibitors that span two regions of the kinase domain are labelled as Type V inhibitors. Type VI inhibitors bind covalently to the target kinase and are irreversible, on the contrary to the Type I-V inhibitors.⁸²

The majority of the approved protein kinase inhibitors are the DFG-in inhibitors, such as the BRAF^{V600E} inhibitors vemurafenib and dabrafenib.^{81, 84} The most prominent example for a DFG-out inhibitor is imatinib. Trametinib is an example of an allosteric kinase inhibitor of type III.⁸² Type VI inhibitors form a covalent bond to cysteine residue in the target kinase via Michael addition. Examples for approved covalent inhibitors are ibrutinib and afatinib, both tyrosine kinase inhibitors.

1.2.3 Comparison of DFG-in and DFG-out inhibitors

As mentioned above both DFG-in and DFG-out inhibitors target the ATP-binding pocket in the catalytic cleft of kinases.³⁵ DFG-in inhibitors use heterocyclic systems to occupy the adenine pocket and form H-bonds to the hinge region^{57,80} (compare Figure 3). Due to the high conservation of adenine pocket, the less conserved adjacent hydrophobic pocket I (HP I) and the hydrophobic region II (HR II) should be addressed to increase selectivity. Especially the gatekeeper amino acid plays an important role for the design of DFG-in inhibitors.

DFG-out inhibitors address additionally to the adenine pocket also the deep pocket and the adjacent regions HP I and HR II. The deep pocket is accessible only in the DFG-out kinase conformation (compare Figure 4). DFG-out inhibitors are often larger than their DFG-in counterparts.

DFG-out kinase conformations are structurally more diverse than DFG-in states.⁸¹ Moreover, the deep pocket is far less conserved compared with the ATP-binding pocket offering specific interaction points for the design of selective inhibitors.^{85,86} Therefore, DFG-out inhibitors are in general considered to be more selective than Type I or Type I½ inhibitors.^{83,85,87-90} However, there are some reports about promiscuousness of DFG-out inhibitors.⁸⁴ Imatinib, for example, binds as DFG-out inhibitor not only the ABL kinase domain but also other tyrosine kinases: c-Kit and PDGFR. Summarizing, targeting the DFG-out conformation by Type II inhibitors does not guarantee high selectivity *per se*.⁸¹ Furthermore, there are several demonstrated examples of selective DFG-in inhibitors.⁹¹⁻⁹³ In conclusion, the unique structural properties of the respective target kinase should be utilized for the design of highly selective protein kinase inhibitors.⁸¹

Beside the selectivity, other pharmacological properties of kinase inhibitors should be taken in consideration when comparing DFG-in and DFG-out inhibitors. All DFG-in inhibitors must compete with high intracellular ATP concentrations in the millimolar range which can contribute to unfavorable loss of potency *in vivo*. In contrast to some former references,⁸⁷ nowadays, DFG-out inhibitors are considered to be ATP-competitive too, since inactive DFG-out kinases can still bind ATP.^{82,35} Nevertheless, kinases have different K_M values for ATP

depending on whether they are in active conformation or not.⁹⁴ The cellular potency of a Type II inhibitor depends therefore on the kinase K_M value in the inactive state.³⁵

The physiological response to a drug *in vivo* depends not only on its selectivity but also on the amount of inhibitor bound to the target enzyme over time. DFG-out inhibitors have been repeatedly reported to have extended target residence time and this might be beneficial for pharmacological applications.^{83,95}

Another important issue to consider when comparing DFG-in and -out inhibitors are different physiological effects that can be obtained by their application.⁸⁴ An example is the inhibition of the BRAF serine/threonine kinase. Mutations in BRAF kinase domain are found in a variety of cancers.⁹⁶ The BRAF^{V600E} mutation determines a constitutively active kinase allowing activation of MEK/ERK signaling in tumor cells in the absence of any extracellular stimuli.⁹⁷ This gain-of-function mutation stabilizes the active DFG-in conformation.⁹⁸ On the contrary, the wild-type BRAF adopts the DFG-out conformation in the absence of extracellular signals.⁹⁸ This discrepancy in conformational states is exploited by selective BRAF^{V600E} inhibitors vemurafenib and dabrafenib.⁹⁹⁻¹⁰¹ Both vemurafenib and dabrafenib are DFG-in inhibitors. On the contrary, type II inhibitors, e.g. sorafenib, bind to the DFG-out conformation of BRAF kinase and exhibit no selectivity towards the V600E-mutant.¹⁰² Therefore, DFG-in inhibitors appear to be more preferable for targeting the BRAF^{V600E} oncogenic kinase. In summary, every individual (patho)physiological situation should be carefully examined to decide which type of inhibitor is more advantageous for the special circumstances.⁸⁴

1.2.4 Benefits and drawbacks of protein kinase inhibitors in clinical applications

Undoubtedly, protein kinase inhibitors revolutionized cancer treatment over the last fifteen years. Small molecule kinase inhibitors (smKIs) are ranked among so-called “targeted therapy”.^{103–105} In contrast to conventional chemotherapy which combats all rapidly proliferating cells in an organism, kinase inhibitors take effect by specifically targeting particular cellular processes involved in the pathogenesis. The approach of inhibiting oncogenic kinases for therapeutic applications was impressively proved by imatinib treatment of CML. Enormous efforts to develop novel potent kinase inhibitors culminated in the approval of more than 30 substances by the end of 2016. This is a remarkable achievement in the history of pharmaceutical research.⁴⁸ Today, protein kinase inhibitors are widely used in the treatment of a variety of tumors and display a significant clinical advantage for affected patients compared to prior therapies in many cases.¹⁰⁵ Imatinib treatment, for instance, produces a durable response with a survival rate over 85% for eight years.¹⁰⁶

However, apart from all progress and achievements in the development of protein kinase inhibitors a lot of remaining problems should be addressed. Even though kinase inhibitors are generally less toxic than highly dosed chemotherapy, therapy with smKIs can cause severe side effects.^{107–109} For example, cardiac- and skin-related toxicities are common for many kinase inhibitors.³⁵ Often, undesired adverse effects can be attributed to off-target interactions due to poor selectivity of applied inhibitors. Nevertheless, even inhibition of the desired target kinase can lead to compound toxicology. The cardiotoxicity of imatinib, for example, is caused by inhibition of the ABL kinase which is also important for appropriate cardiomyocyte function.¹¹⁰

The most important drawback in therapy with kinase inhibitors is probably the development of resistances.^{35, 48, 81, 105} For instance, most patients with melanoma who initially respond to vemurafenib treatment relapse within a year.^{98, 111, 112} Many different mechanisms for the manifestation of acquired resistance to smKI treatment are explicitly reviewed.^{35, 48, 105} It is not within the framework of the present thesis to reveal these mechanisms in greater detail.

Roughly, a distinction can be made between the “on-target” resistances such as point mutations of the gatekeeper residue or amplifications of the targeted kinase, and the “off-target” resistances such as upregulation of downstream or parallel signaling pathways and modulation of cellular metabolism or efflux of the inhibitor.^{57, 105, 113–115} The cancer cells become tolerant to kinase inhibitors due to selection pressure. This evolution is based on the high genomic instability of tumors.^{116, 117}

Rational strategy to overcome acquired therapeutic resistance remains one of the most important challenges for future development of smKIs. Therefore, precise understanding of resistance mechanisms in each individual patient appears to be a necessary prerequisite for further progress. In this context, genomic screening of resistant tumor samples is important for the personalized therapy.

Today, several different approaches are utilized to combat acquired resistances. When dealing with “on-target” mutations it is rational to develop second-line inhibitors that still target the mutated kinase. For example, two second-generation BCR-ABL inhibitors, dasatinib and nilotinib, are available for the treatment of imatinib-resistant CML patients.¹¹⁸ Resistances caused by reactivation of downstream or parallel signaling cascades might be tackled by a combination of two or even more inhibitors. The combination therapy with BRAF^{V600E} inhibitor dabrafenib and MEK inhibitor trametinib delays the occurrence of drug resistance in the melanoma treatment compared with the single agent treatment.¹¹⁹ Unfortunately, the majority of patients acquire resistances even to these second-line therapies.¹²⁰ An interesting approach is the intermittent dosing of kinase inhibitors to forestall the arising of resistances.¹²¹ This strategy is based on the notion that resistant cancer cells might be drug-dependent.¹²² Some ongoing clinical studies are investigating possible benefits of intermittent dosing schedules.^{123, 124}

Besides preventing resistances, efforts for minimization of side effects are required. Increasing the selectivity of administered kinase inhibitors appears to be the method of choice to minimize undesired toxicology. Highly selective inhibitors would be valuable tools to elucidate certain functions of a particular kinase *in vitro*. Moreover, selective inhibitors should be used when integrating different compounds in combination therapies. However, it has

become clear that absolute selectivity is not necessarily required for successful clinical application.⁴⁸ The maybe most prolific inhibitor hitherto, imatinib, is quite promiscuous and targets apart from BCR-ABL some other tyrosine kinases such as PDGFR and KIT.¹²⁵ There are several other examples where multitarget selectivity might be more suitable for cancer treatment.^{35, 48} Nevertheless selectivity profiling should be a must prior to clinical applications. Therefore, efficient kinase selectivity assays over the whole kinome are required. Particularly, novel assays for allosteric inhibition are needed.^{57, 86}

Another shortage that should be improved is the fact that the majority of developed kinase inhibitors target only a small subset of the kinome.⁴⁸ More kinases and their role in pathogenesis should be better explored. This might lead to a greater variety of kinase inhibitors approved for many more applications additional to oncology.

1.3 Caged kinase inhibitors

1.3.1 Regulation of biological processes by light

Exact spatiotemporal control of biological processes is of great significance both for basic research and clinical applications. Light represents an ideal external trigger that can be precisely adjusted in terms of intensity, temporal and local resolution.¹²⁶ It offers numerous advantages for the regulation of biological processes:^{126–130} Light is non-invasive and exhibits great orthogonality toward most chemical and biological systems. By means of modern light sources, such as lasers or LEDs, important characteristics like wavelength, intensity, resolution and duration of illumination can be accurately regulated.¹³⁰

The idea to exploit the positive characteristics of light for clinical applications is not new. First medical applications were developed by the end of 1970s as the PUVA therapy had been approved. PUVA stands for “psoralen and ultraviolet A” and is used for the treatment of skin diseases such as psoriasis, vitiligo and eczema.^{131, 132} Thereby, psoralen is applied to sensitize the skin prior to irradiation.

Another example of a successful application of light in medicine is the photodynamic therapy (PDT).^{133–135} In PDT photosensitizers are utilized to generate singlet oxygen ($^1\text{O}_2$) in living tissue when irradiated with light.^{127, 136} Singlet oxygen is a reactive oxygen species (ROS) which is cell toxic. PDT is used for the treatment of cancer and infectious diseases.^{137–139}

Both PUVA and PDT do not affect selective molecular targets but cause nonspecifically damage in irradiated tissue. However, several novel approaches to apply light more selectively have been developed during the past three decades. Today, three major principles for the regulation of biological process with light can be distinguished:¹⁴⁰ Irreversible photo(de)activation, reversible photoswitching and optogenetics.

Irreversible photoactivation exploits so called “caged compounds”. The term “caging” was coined by Kaplan *et al.* who attached photoremovable protecting groups to ATP and utilized this “caged ATP” to study the Na^+/K^+ pump in 1978.¹⁴¹ Today, the term “caged” is established for “biologically active compound that has been inactivated with a photolabile protecting

group” (PPG).¹²⁶ Synonyms to “caged” are “photoactivatable” and “light-triggered”.¹⁴⁰ When irradiated by light with appropriate wavelength and intensity the photolabile group is cleaved and the active molecule is released. The process of uncaging is irreversible. The mechanism of irreversible photoactivation is shown schematically in Figure 7.

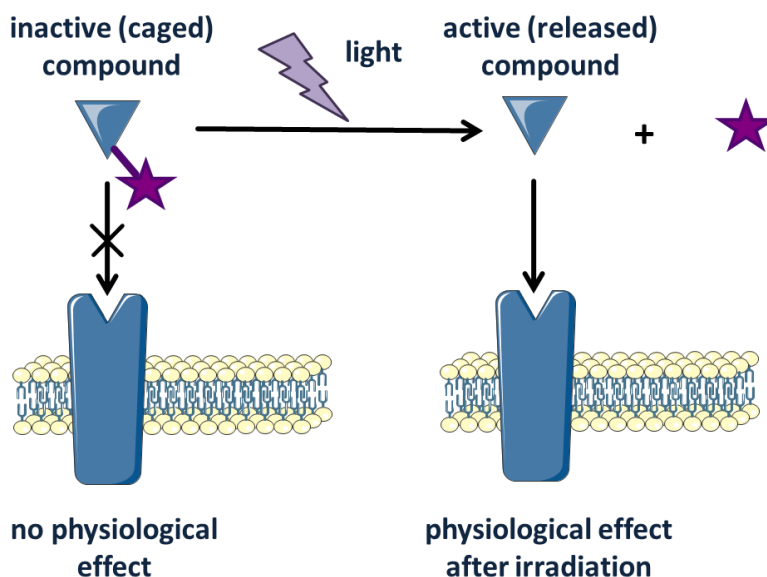


Figure 7: Schematic representation of irreversible photoactivation (uncaging). A photoremovable protecting group (PPG, purple star in the figure) is covalently bound to a compound (blue triangle). As a consequence, the compound is caged and inactive. After irradiation with light at appropriate wavelength the PPG is cleaved and the released active compound can bind to its target. Thus, biological effects can be induced upon irradiation. The activation is irreversible. Some graphical elements used in the visualization such as membrane and receptor were adopted from Servier Medical Art.¹⁴²

The irreversibility of uncaging is an inherent disadvantage of the concept. Another drawback of irreversible photoactivation is the formation of a by-product: the cleavage product of the PPG.^{126, 130} This by-product can exhibit undesired biological effects. Moreover, the cleaved PPG might interfere with the photoreaction by absorbance of used light. However, caging approach offers some advantages too: because of the irreversibility, there is no steady state and excellent off/on ratios can be achieved.¹³⁰ Furthermore, insertion of a PPG can completely abolish the biological effect of a compound. The possible toxicity of the cleaved PPG might also be useful in terms of fighting tumor tissue synergistically.

Reversible photoswitching utilizes the principle of photochromism: Two different forms of a chemical species can be reversibly transformed into each other by the absorption of electromagnetic radiation.¹⁴³ For biological applications a photoswitchable element is usually inserted into the molecular structure of a bioactive compound.¹²⁷ An inactive substance can be shifted to the active isomer by means of light irradiation. The reaction can be inverted by illumination at a different wavelength.^{126, 127, 130, 140, 144} The concept enables a dynamic control of a biological effect that can be reversibly turned on and off. The mechanism of the reversible photoswitching is schematically depicted in Figure 8.

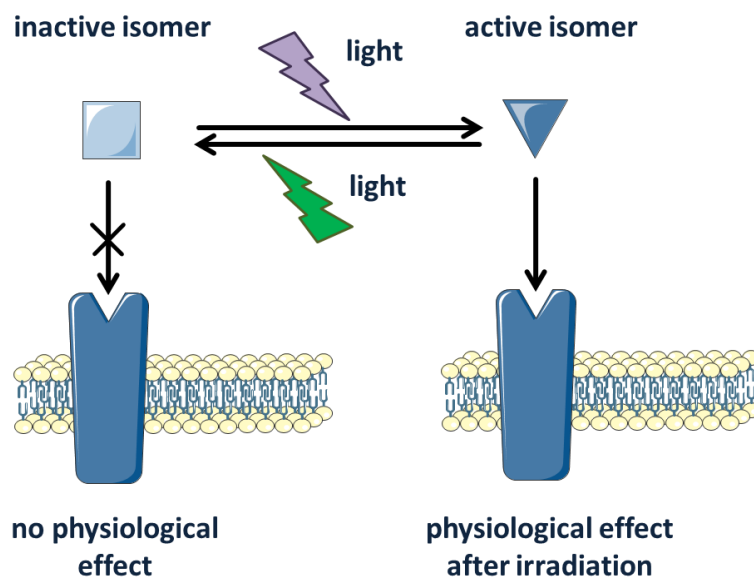


Figure 8: Schematic representation of reversible photoswitching.¹³⁰ An inactive compound (blue square) can be reversibly switched to its active isomer (dark blue triangle) that can interact with its biological target. The activation is reversible. The backward reaction can be induced by irradiation at a different wavelength. Some graphical elements used in the visualization were adopted from Servier Medical Art.¹⁴²

The reversibility and the absence of any by-products are undeniable advantages of photoswitching in comparison with the photoactivation of caged compounds described above. However, occurrence of steady states where both isomers are present can be a non-negligible intricacy of photoswitching.¹²⁶ Therefore, high off/on rates are difficult to achieve and biological effects are often not completely switched off by irradiation of active compounds.^{126, 140, 145–147}

Optogenetics is the combination of optical and genetic methods to achieve dynamic control over biological events in specific cells or tissues.^{148, 149} The method relies on the expression of genetically encoded photo sensor proteins. Most commonly, the photosensitive proteins belong to the rhodopsin family. The function of photoresponsive proteins can be changed upon irradiation and a biological effect can be induced, compare Figure 9.

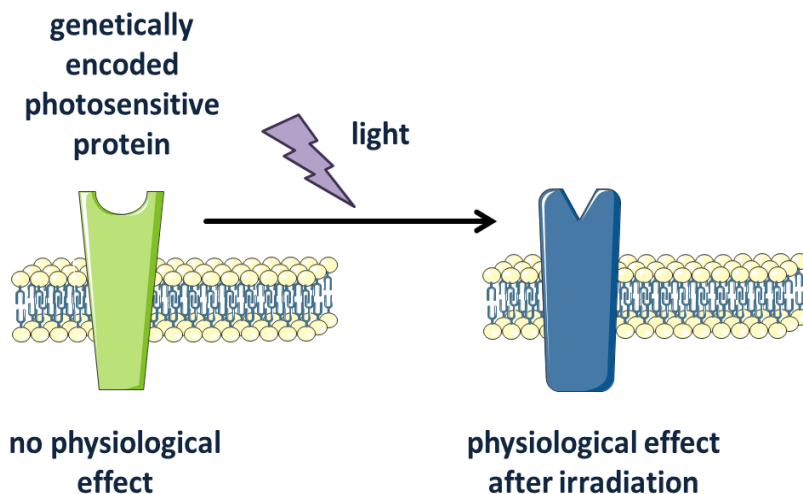


Figure 9: Schematic representation of optogenetics.¹³⁰ A genetically modified, photoresponsive protein, mostly an ion channel can be activated by light to evoke a biological effect. Some graphical elements used in the visualization were adopted from Servier Medical Art.¹⁴²

Optogenetics offers unique tools to investigate basic physiological processes, such as depolarization of neurons,¹⁵⁰ dynamics in neural circuits¹⁵¹ or even sleeping behavior of model organisms.¹⁵² Optogenetics was decorated as “Nature method of the year 2010”.¹⁵³ However, apart from its advantages for fundamental research, necessity of genetic manipulation makes this approach unsuitable for medical applications.¹²⁷

Within the framework of this work it is impossible to mention all current examples for successful implication of light in addressing fundamental biological questions. There are a lot of comprehensive reviews dealing with this topic.^{126–130, 154} Exclusively the concept of kinase inhibitor caging will be discussed in more detail in the present work.

1.3.2 Caging of protein kinase inhibitors

The drawbacks of protein kinase inhibitors described in the chapter 1.2.4 explain the search for novel approaches in the field of smKIs. Major goals are minimization of systemic side effects of kinase inhibitors and prevention of resistances. Spatiotemporal control of kinase inhibitor activity might be a valuable strategy to achieve these objectives. Photoactivatable caged protein kinase inhibitors enable a precise local control of the inhibitory activity. On the supposition that an inactive caged kinase inhibitor shows good bioavailability and is well distributed within entire organism, site directed reactivation by light irradiation could possibly spare non-irradiated tissues from undesired side effects. Furthermore, a sharp increase of the active inhibitor concentration in the target tissue might be achieved by irradiation.¹²⁸ Therefore, it might be possible to confront malignant cells with abruptly high concentrations of an inhibiting agent. These elevated concentrations would not be feasible on the basis of systemic administration due to adverse effects. In other words, photoactivatable kinase inhibitors could possibly enable locally restricted high-dosage cancer therapy. Moreover, the temporal control of inhibitor release might present a possibility for a potent intermittent therapy which could be favorable in prevention of resistances.^{155, 122, 121} Eventually, caged protein kinase inhibitors offer a valuable tool for studying cellular kinase functions and signaling pathways.

The idea to use caged compounds as a technique for investigating biological processes *in vitro* is anything but new. As mentioned above first caged ATP has already been utilized in 1978.¹⁴¹ Since then, different photoactivatable compounds have been described such as caged neurotransmitters, second messengers and phospholipids.¹⁵⁶⁻¹⁶⁰ The caging concept has been utilized for examination of cellular signaling^{161, 162} or investigation of embryonal development.¹⁶³⁻¹⁶⁶ The first described photoactivatable protein kinase inhibitor was a modified peptide-based inhibitor of PKA.^{167, 162} However, despite the significance of protein phosphorylation for cellular processes, only a few caged smKIs have been reported so far.^{165, 166} Moreover, to the best of my knowledge, there were no reports about caging of approved kinase inhibitors at the time of the beginning of my doctoral studies.

1.3.3 Photoremovable protecting groups

The caging concept utilizes photoremovable protecting groups (PPG). Several requirements should be fulfilled for biological applications.^{140, 160, 168} PPGs should be stable as well as soluble under physiological conditions.¹⁴⁰ They should be easy to introduce and rapidly cleaved upon light irradiation. The introduction of a PPG should ideally eradicate the biological activity of compounds to be protected. Large molar extinction coefficients ϵ and high quantum yields Φ of caged compounds are favorable for fast uncaging.¹⁴⁰ The photoinduced reaction should be clean and quantitative.¹⁶⁰ The active compound should be transparent at the wavelength used for decaging to avoid decomposition. The cleavage products of the PPG should also be transparent at the irradiation wavelength to avoid competitive absorption of light.^{168, 160} Furthermore, the photochemical by-products should not be toxic.^{160, 140} However, the last characteristic is not indisputable. The toxicity of the photoinduced by-products could also be advantageous. For example, cytotoxic by-products might be used synergistically with released active kinase inhibitors to fight irradiated cancer cells. Another important criterion for the selection of a PPG is the wavelength required for the photoinduced cleavage. Generally, high energetic irradiation with wavelengths under 300 nm should be avoided because of presumable tissue damage.¹⁶⁰ Irradiation within the bio-optical window (650 – 850 nm)^{169–171} might be most suitable to avoid undesirable absorption by endogenous chromophores, such as hemoglobin.^{172, 173} Penetration depth of wavelengths under 650 nm is quite low, compare Figure 10. Therefore, PPGs that can be cleaved with red or near-infrared irradiation (NIR) should be most favorable for usage in biological settings.

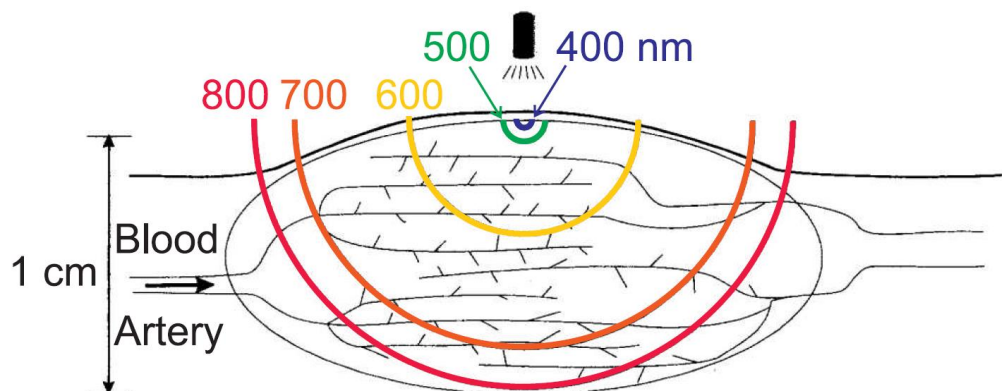
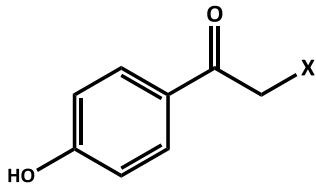
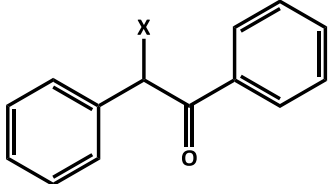
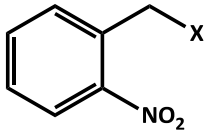
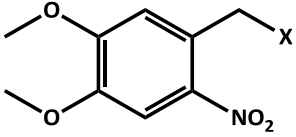
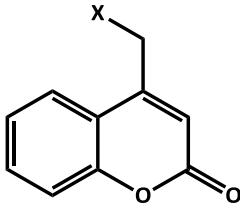
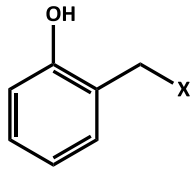
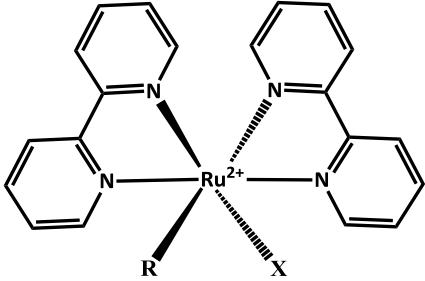
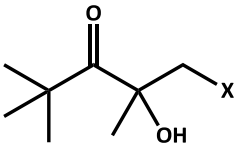
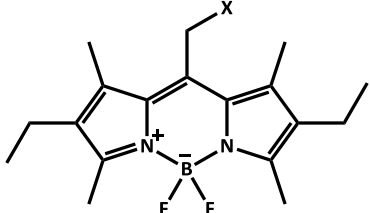


Figure 10: The penetration depth of different light wavelengths into biological tissue.^{172, 173}

To this day, a variety of highly diverse PPGs have been described.^{140, 160, 168, 174, 175} According to Klan *et al.* six different classes of PPGs can be distinguished.^{160, 176} Examples for main categories of photoremovable protecting groups can be found in Table 1.

However, there is no PPG that would perfectly fulfill all characteristics described above.^{160, 168} The choice of a particular protecting group should be guided by current experimental settings and requirements.

Table 1: Non-comprehensive overview of PPGs.^{160, 176, 177} "X" denotes the compounds released upon irradiation.

Category of PPG	Examples of PPG
Arylcarbonylmethyl groups	<div style="display: flex; justify-content: space-around; align-items: center;"> <div style="text-align: center;">  <p><i>p</i>-hydroxyphenacyl</p> </div> <div style="text-align: center;">  <p>benzoin</p> </div> </div>
Nitroaryl groups	<div style="display: flex; justify-content: space-around; align-items: center;"> <div style="text-align: center;">  <p><i>o</i>-nitrobenzyl</p> </div> <div style="text-align: center;">  <p>4,5-dimethoxy-2-nitrobenzyl (DMNB) = 6-nitroveratryl (NV)</p> </div> </div>
Coumarin-4-ylmethyl groups	<div style="text-align: center;">  <p>coumarin-4-ylmethyl</p> </div>
Arylmethyl groups	<div style="text-align: center;">  <p><i>o</i>-hydroxyarylmethyl</p> </div>
Metal-containing groups	<div style="text-align: center;">  <p>metal-containing groups</p> </div>
Miscellaneous groups	<div style="display: flex; justify-content: space-around; align-items: center;"> <div style="text-align: center;">  <p>pivaloyl</p> </div> <div style="text-align: center;">  <p>BODIPY</p> </div> </div>

1.3.4 *o*-nitrobenzyl derivatives as photoremovable protecting groups

In course of the present work the *o*-nitrobenzyl derivatives have been utilized as PPGs for caging of active kinase inhibitors. Due to their stability and easy chemical accessibility, these protecting groups have been the most commonly used groups for photocaging concept.¹⁷⁸ Originally, the *o*-nitrobenzyl derivatives were applied as protecting groups in organic synthesis.¹⁷⁹ The first scientific work with caged compounds utilized these groups already.¹⁴¹ Many derivatives of *o*-nitroaryl groups with different physicochemical properties have been described for various applications.^{165, 166, 180–183} Today, a lot of reagents caged with nitroaryl groups are commercially available.¹⁸⁴

The mechanism of the photoinduced cleavage of a *o*-nitrobenzyl PPG has extensively been investigated.^{178, 185, 186} A reaction schema including hydrogen transfer from the *o*-alkyl position to the nitro group, formation of an *aci*-nitro tautomer and subsequent cyclization to a benzisoxazolol derivative is widely accepted.^{160, 176} In the last step the benzisoxazolol derivative is deprotonated and the PPG is released as *o*-nitrosobenzyl derivative. The deprotection mechanism of a *o*-nitrobenzyl group is schematically shown in Figure 11.

Several parameters determine the reaction rate of the photoinduced deprotection: The caged compound “X”, the substitution pattern of the nitrobenzylic ring, the solvent and its pH.^{168, 178, 181} The released nitroso by-product, cleavage product of the PPG, is cell toxic.¹⁶⁸ Nevertheless, this toxicity could be used for some application as has already been discussed above.

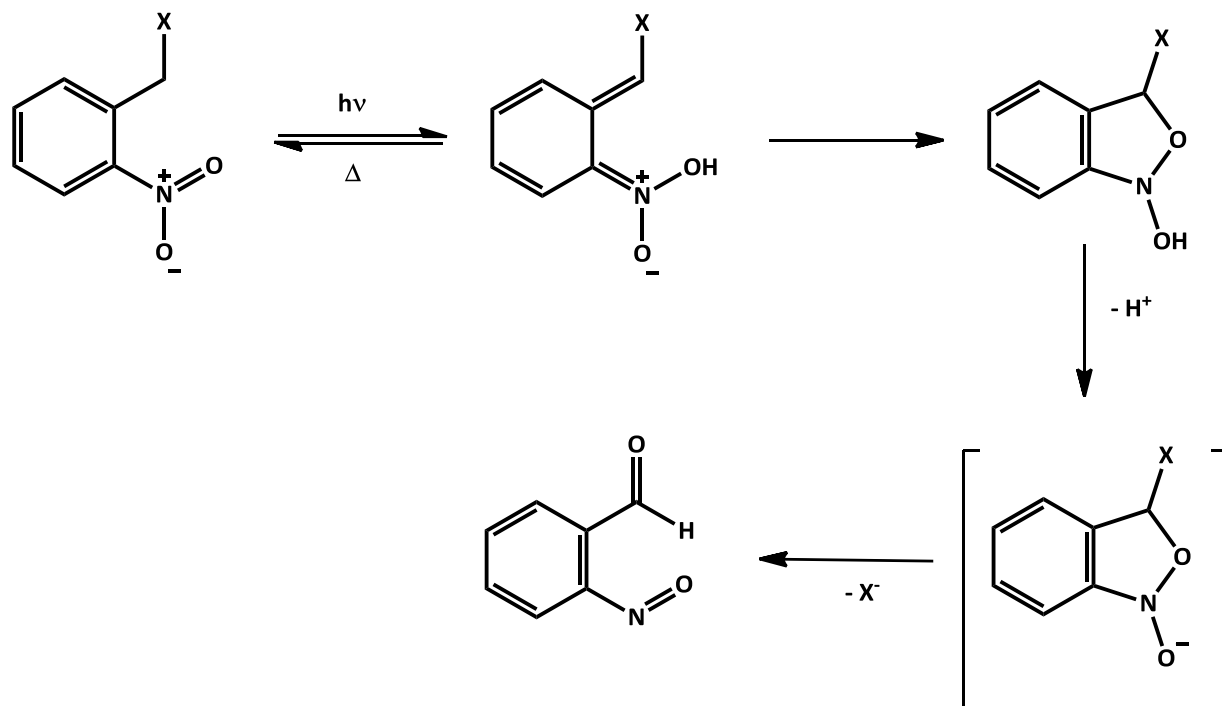


Figure 11: Schematic representation of release mechanism of *o*-nitrobenzyl caged compounds.^{176, 178, 185, 186} “X” stands for the released compound.

To increase the wavelength necessary for the photoinduced cleavage of an *o*-nitrobenzyl PPG, the nitroaryl ring can be substituted with methoxy groups.¹⁸⁷ The 4,5-dimethoxy-2-nitrobenzyl (DMNB) group can be released upon irradiation at about 350 nm (for chemical structure see Table 1). This PPG was utilized in the present work for caging the active smKIs.

2 Scope

The current thesis is devoted to two topics. The main focus of the work was on the biological characterization of novel photoactivatable “caged” prodrugs of protein kinase inhibitors. The aim of this project was to develop caged prodrugs of approved protein kinase inhibitors and to evince their applicability as valuable pharmaceutical tools *in vitro*. It was supposed that light irradiation of caged inhibitors enables a spatiotemporal control over kinase inhibition. To prove this hypothesis, extensive biological characterization of photoactivatable compounds should have been performed. For this purpose, novel assay techniques including custom-made light sources had to be evaluated.

Design and characterization of photoactivatable protein kinase inhibitors was conducted following the workflow shown in Figure 12.

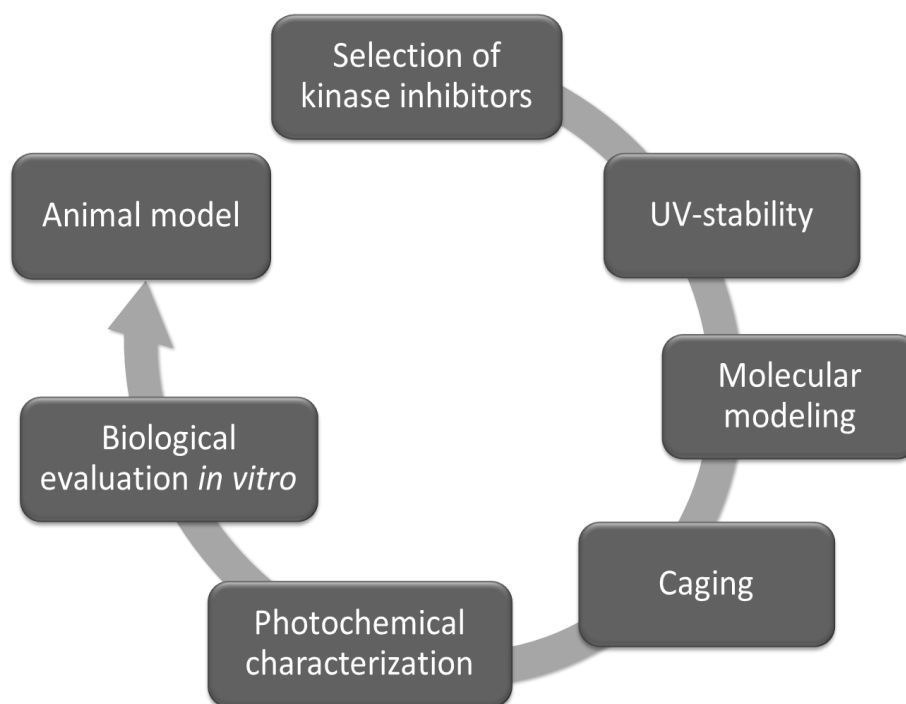


Figure 12: Workflow for the caging of protein kinase inhibitors.¹⁷⁶

Starting point was the selection of active inhibitors with validated molecular targets. Several potent protein kinase inhibitors including approved agents such as imatinib,^{188, 189} vemurafenib,^{99, 100} and dabrafenib¹⁰¹ have been chosen as model compounds. Furthermore,

3,4-diarylmaleimides^{190, 191} as VEGFR-2 inhibitors have been investigated for their applicability to this technique. VEGFR-2 (vascular endothelial growth factor receptor) is a receptor tyrosine kinase (RTK) and plays an important role in the regulation of angiogenesis.¹⁹²

An essential prerequisite for the caging concept is UV-stability of the parent compound. This stability was to be verified for all of the deployed inhibitors. Photostable smKIs were to be examined for possible pharmacophore sites. Molecular modeling was used to predict key interactions between inhibitors and corresponding target kinases.

Caged kinase inhibitors were to be synthesized by coupling the active compounds with an appropriate PPG. Thereby, previously determined key pharmacophore sites were to be addressed. In order to identify an optimal wavelength for irreversible cleavage of the coupled PPG, photochemical characterization of caged inhibitors had to be performed. It was assumed that a rapid release of the parent inhibitor upon irradiation is necessary for successful biological applications. To describe the kinetics of the photoinduced release, irradiation studies of caged inhibitors in different solvents had to be conducted.

Subsequent biological characterization of caged smKIs *in vitro* had two objectives. The first aim was to demonstrate the loss of cellular activity of caged inhibitors. The second goal was the proof of principle: it should be demonstrated that the irradiation at an appropriate wavelength could reactivate the respective kinase inhibitors. The photoinduced release of the parent compound should be controlled both temporally and locally. Several *in vitro* test systems such as proliferation assays, western blot analyses and immunostaining were utilized for validation of this spatiotemporal steering. Moreover, these assays had to be optimized for both dark conditions and directed irradiation.

Furthermore, additional questions not depicted in the workflow (Figure 12) were to be addressed. First, possible cellular toxicity of the cleaved PPG should be investigated. Second, the interference of the applied UV light with the test assays was to be examined. The ultimate aim of the whole project was a launch of animal models for testing the caged inhibitors. However, it should be said that *in vivo* characterization was not the focus of the present work.

Application of the caging concept on smKIs is a multidisciplinary approach. The main focus of my research in this work was the biological characterization of protein kinase inhibitors. The synthesis of the caged compounds was performed by my kind colleagues: Dr. Rebecca Horbert (vemurafenib^{176, 193} and maleimide^{176, 194} projects) and Dr. Melanie Zindler (imatinib project¹⁹⁵). Thorsten von Drathen contributed to chemical analysis in the dabrafenib project.^{196, 197}

The second topic the current work deals with is the characterization of novel DFG-in and DFG-out PDGFR β inhibitors. PDGFR stands for platelet-derived growth factor receptor and is also a RTK. PDGFR exhibits a significant importance for several cellular transduction pathways regulating cellular proliferation, differentiation and tumor progression.^{198, 199} Both RTKs VEGFR-2 and PDGFR β are numbered among the major targets for development of effective inhibitors in oncology.²⁰⁰ Potent DFG-in and DFG-out inhibitors of PDGFR β with the same chemotype were to be developed and characterized *in vitro*. Pyrazine-2-one scaffold derived from marine hamacanthins served as a lead structure. Structure-activity relationships (SAR) of different pyrazine-2(1H)-one derivatives were to be examined.²⁰¹ Further hit optimization was to be performed applying molecular modeling studies such as prediction of water thermodynamics.²⁰² The ultimate aim of the project was the comparison of potent DFG-in and DFG-out inhibitors with the same chemotype (Figure 13) regarding their selectivity and potency in cellular assays.²⁰³ The chemical basis for the biological characterization was laid by previous works of Dr. Joachim Schlosser²⁰⁴ and Dr. Eugen Bethke (born Johannes).²⁰⁵

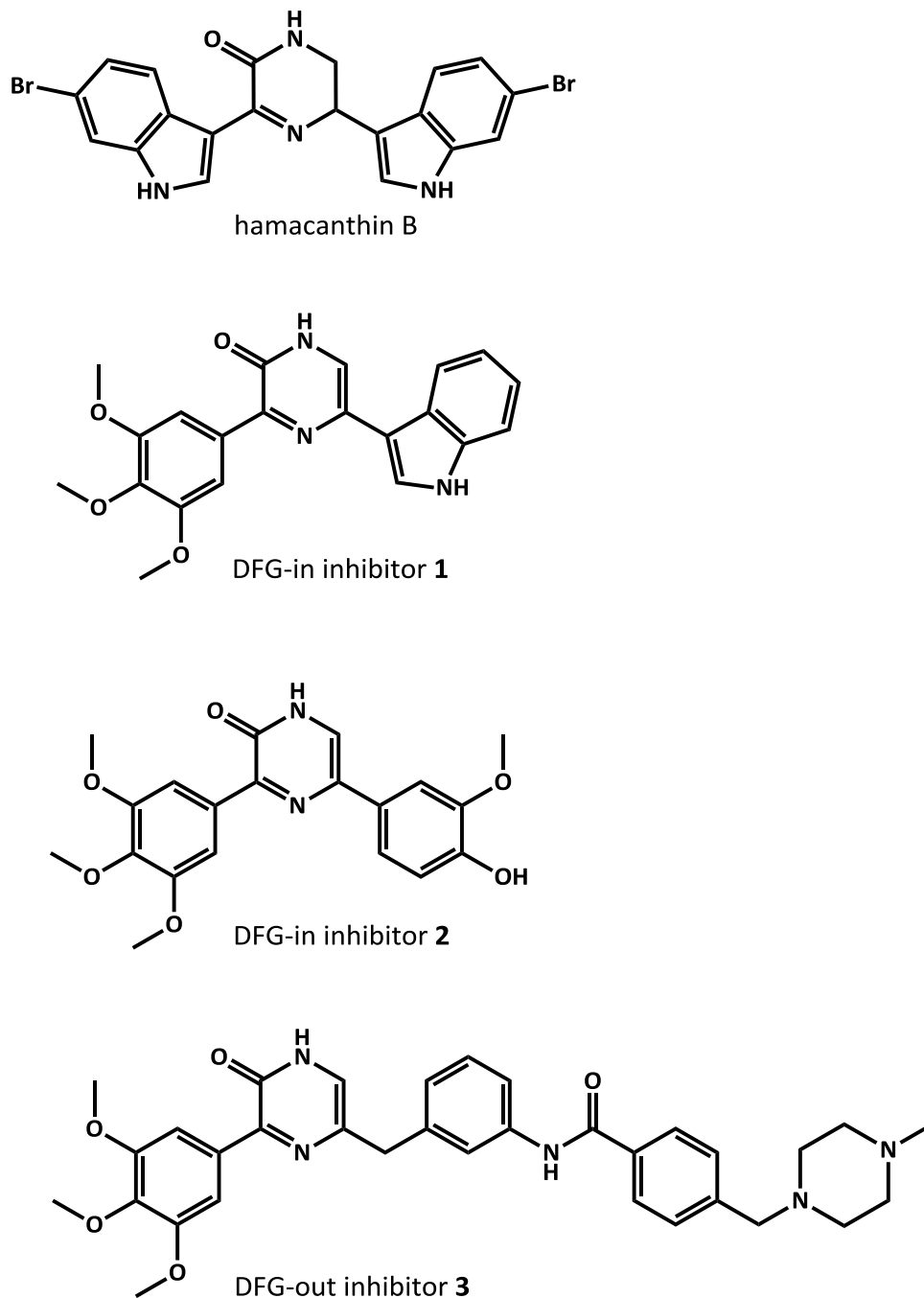


Figure 13: Hamacanthin B as lead for the development of PDGFR β inhibitors with pyrazine-2(1H)-one scaffold. Comparison between DFG-in inhibitors **1** and **2** and DFG out inhibitor **3** was one of the aims in the present thesis.

3 Results and Discussion

The current work is a cumulative dissertation. The thesis consists of seven peer-reviewed scientific papers that were prepared during my PhD work. Each publication is shortly introduced and then reproduced as published in corresponding journals. Supplementary information (SI) for each paper is included. Furthermore, some additional data not included in publication is provided after the corresponding paper (as is the case with photoactivatable prodrugs of vemurafenib).

The first four papers address the topic of photoactivatable “caged” protein kinase inhibitors. The last three publications deal with the development of potent DFG-in and DFG-out PDGFR β inhibitors.

3.1 Photoactivatable Prodrugs of Antimelanoma Agent Vemurafenib

Rebecca Horbert,[§] Boris Pinchuk,[§] Paul Davies, Dario Alessi, and Christian Peifer

[§]Rebecca Horbert and Boris Pinchuk contributed equally to this work.

ACS Chem. Biol. **2015**, *10*, 2099–2107.

<http://pubs.acs.org/doi/full/10.1021/acscchembio.5b00174>

(The article is licensed under the terms of the ACS AuthorChoice license)

Vemurafenib was the first approved drug for personalized therapy of BRAF^{V600} mutated cancers.⁹⁸ Since its approval for melanoma therapy in 2011, vemurafenib has shown impressive clinical results regarding tumor regression and prolonged survival rates.^{111, 112, 206} Unfortunately, most patients develop vemurafenib resistance which cause rapid relapse after only several months of therapy.^{207–209} Furthermore, patients often suffer from side effects during the treatment.^{210, 211}

In the following paper¹⁹³ novel photoactivatable prodrugs of vemurafenib were described. The caged compounds were designed, synthesized and characterized both photochemically and *in vitro*. The workflow for the caging of protein kinase inhibitors (Figure 12) could be successfully applied up to animal models. After verification of the UV-stability of vemurafenib, several caged derivatives of the inhibitor were synthesized. Therefore, the DMNB group was utilized as a PPG. The caged compounds were proved to be inactive in several *in vitro* assays such as kinase assays, western blot analysis, and cell proliferation assays. Photochemical characterization revealed an optimal wavelength for deprotection. Release of active vemurafenib upon irradiation could be impressively proved in all used cellular assays. Different pharmacophore sites of vemurafenib were compared in terms of their applicability for caging. Furthermore, cellular toxicity of the cleaved PPG could be measured. This study was the first proof of principle that photoactivatable prodrugs of approved smKIs can be applied as useful pharmacological tools.

Dr. Rebecca Horbert synthesized the caged compounds. I performed the characterization *in vitro* such as western blot analysis and cell proliferation assays and wrote the half manuscript.

Photoactivatable Prodrugs of Antimelanoma Agent Vemurafenib

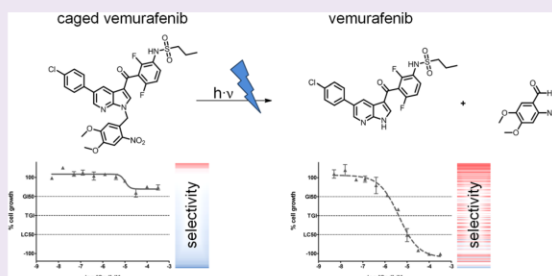
Rebecca Horbert,^{†,§} Boris Pinchuk,^{†,§} Paul Davies,[‡] Dario Alessi,[‡] and Christian Peifer^{*,†}

[†]Pharmaceutical Chemistry, Christian Albrechts University, Gutenbergstraße 76, 24118 Kiel, Germany

[‡]MRC Protein Phosphorylation and Ubiquitylation Unit, College of Life Sciences, University of Dundee, Dow Street, Dundee DD1 5EH, U.K.

Supporting Information

ABSTRACT: In this study, we report on novel photoactivatable caged prodrugs of vemurafenib. This kinase inhibitor was the first approved drug for the personalized treatment of BRAF-mutated melanoma and showed impressive results in clinical studies. However, the occurrence of severe side effects and drug resistance illustrates the urgent need for innovative therapeutic approaches. To conquer these limitations, we implemented photoremovable protecting groups into vemurafenib. In general, this caging concept provides spatial and temporal control over the activation of molecules triggered by ultraviolet light. Thus, higher inhibitor concentrations in tumor tissues might be reached with less systemic effects. Our study describes the first development of caged vemurafenib prodrugs useful as pharmacological tools. We investigated their photochemical characteristics and photoactivation. *In vitro* evaluation proved the intended loss-of-function and the light-dependent recovery of efficacy in kinase and cellular assays. The reported vemurafenib photo prodrugs represent a powerful biological tool for novel pharmacological approaches in cancer research.



Protein kinase inhibitors have been successfully established in cancer treatment over the past 15 years. However, the occurrence of therapy-limiting side effects as well as only temporary efficacy illustrates the urgent need for novel therapeutic approaches.¹ Innovative concepts that are able to reduce adverse events and prolong duration of efficacy by overcoming tumor resistance would be of significant benefit.

Hence, we aimed to develop photoactivatable kinase inhibitor prodrugs. These so-called caged compounds can be activated by irradiation with ultraviolet (UV) light. The implementation of photoremovable protecting groups (PPGs) provides spatial and temporal control over the release of molecules. Therefore, higher drug concentrations can be reached in the area of interest, sparing other compartments.² This approach might enable higher drug concentrations in cancer-afflicted tissues, resulting in a faster, more efficient regression with fewer side effects. Light might be applied on superficial tumors precautionarily after surgical removal or by the use of optical fibers. Beyond novel therapeutic applications, our photo prodrugs could serve as experimental tools, e.g., for kinetic or mechanistic studies. By irradiation with a short laser impulse, the drug might be quickly released in certain tissues or organism compartments.

The photo prodrug concept is essentially based on the blockade of a pharmacophoric group. The PPG is therefore attached to the drug molecule by a covalent bond. This bond then has to be cleaved by radiant energy, releasing the parent bioactive compound. *o*-Nitrobenzyl derivatives have been widely used as PPGs in various biological applications. The first

and most prominent example is certainly the photorelease of caged adenosine triphosphate (ATP) by Kaplan and co-workers in 1978.³ Since then, intensive research has been carried out concerning various classes of protecting groups and evaluation of their photocharacteristics.²

While the caging concept has been successfully applied on various bioagents,^{4–6} there are only a few reports on photoprotected kinase inhibitors. For instance, Morckel et al. used a photoactivatable small-molecule Rho kinase inhibitor.⁷ This tool compound was used to uncover molecular mechanisms of embryonic development in *Xenopus laevis* by targeting specific regions of the living embryo.⁷ In addition, small molecular equivalents of Src kinase have been caged⁸ as well as peptidic PKA inhibitors.⁹ Furthermore, light-regulated protein kinase C peptide-based sensors¹⁰ and tyrosine kinase reporters¹¹ have been described.

In our study, we focused on BRAF^{V600E} inhibitor vemurafenib (1, Zelboraf, Plexxikon/Roche). This serine/threonine kinase inhibitor shows excellent UV stability at 365 nm and is readily chemically accessible regarding the caging concept. Vemurafenib was the first personalized drug for the therapy of BRAF mutant cancer. It received approval for the treatment of metastatic melanoma with BRAF^{V600} mutation in the United States and Europe in 2011 and 2012, respectively.¹² Introduction of vemurafenib into melanoma therapy showed

Received: March 12, 2015

Accepted: June 10, 2015

Published: June 10, 2015

impressive clinical results.^{13–15} However, despite outstanding tumor regressions and distinctive improvements in survival, vemurafenib cannot cure metastatic melanoma. Moreover, the massive dosage of up to 960 mg daily leads to a high incidence of severe adverse events such as arthralgia (joint pain), skin rash, and the development of squamous cell carcinoma.^{14,16,17} Furthermore, most patients suffer from lethal relapse due to drug resistance developed after only a few months of therapy.^{18–22}

Here, we report on the design, synthesis, and biological evaluation of photoactivatable prodrugs of vemurafenib. First, molecular modeling revealed promising pharmacophoric groups to be protected by PPGs. After showing the UV stability of vemurafenib at 365 nm, caged prodrugs were synthesized. In the next step, these prodrugs were photochemically characterized. This included assignment of an optimal wavelength for deprotection and investigation of photoinduced release of vemurafenib. Subsequently, determination of BRAF^{V600E} K_d values and a broad kinase selectivity profile for these compounds proved the intended loss-of-function by photoprotection. Finally, recovery of vemurafenib efficacy by UV irradiation in cells could be demonstrated within proliferation assays as well as by western blot analysis.

With the presented vemurafenib photo prodrugs in hand, we have created a powerful biological tool for novel pharmacological approaches in cancer research.

RESULTS AND DISCUSSION

Molecular Modeling. We first examined ligand–protein interactions of vemurafenib in the active site of BRAF^{V600E} by molecular modeling. In order to design effectless vemurafenib prodrugs, it was necessary to define key pharmacophoric moieties of this kinase inhibitor to be subsequently blocked by PPGs.

In Figure 1A,B, the binding mode of vemurafenib in the ATP pocket of BRAF^{V600E} is shown (PDB code 3OG7;²³ for 2D ligand interaction diagram, see Supporting Information Figure S1). Herein, the type-I ATP-competitive inhibitor vemurafenib²³ is addressing key H-bonds by its 7-azaindole moiety toward the hinge region.²⁴ Furthermore, the sulfonamide NH residue of vemurafenib interacts with backbone amides of another highly conserved amino acid sequence, namely, Asp-Phe-Gly (DFG motif). This DFG motif is located at the beginning of the activation loop (A-loop), which controls substrate access to the active site.²⁵ Hence, both the 7-azaindole and sulfonamide are considered to be suitable pharmacophoric moieties for photoprotection. In line with this notion, modeling PPG-vemurafenib compounds 2 and 4 in the active site of BRAF^{V600E} resulted in significant sterical clashes, indicating nonplausible binding modes (Figure 1C,D). However, we assumed that blocking the central azaindole-NH moiety of vemurafenib's hinge binder would demolish any affinity of the photoprotected prodrugs to every other kinase as well since all type I and II inhibitors use this interaction.²⁴ On the other hand, prodrugs with a PPG attached to the sulfonamide residue might still show some affinity to kinases featuring a flexible binding pocket in this peripheral area. In general, based on slight molecular differences in the kinase architecture involving shape and size of hydrophobic pockets, many tailor-made examples of highly active and selective kinase inhibitors have been developed.^{1,26}

Motivated by the modeling data, we synthesized both NH-photoprotected vemurafenib analogues and compared their

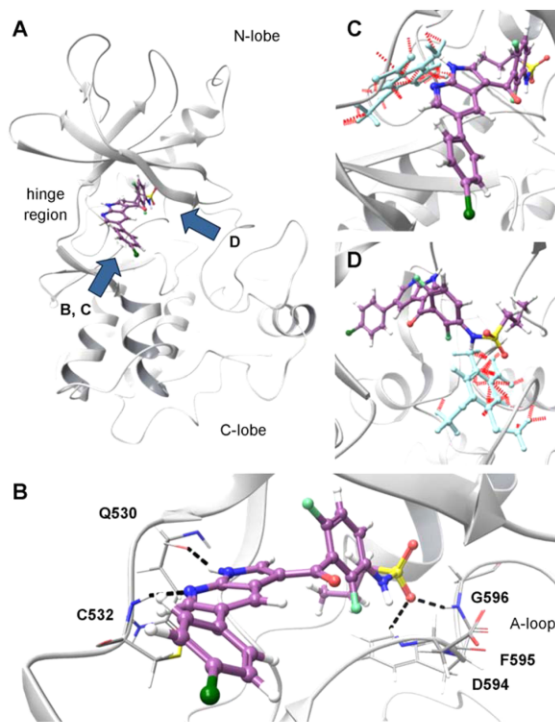


Figure 1. Binding mode of vemurafenib and determination of photoprotection sites. (A) The X-ray defined crystal structure of vemurafenib bound to the active site of BRAF^{V600E} (PDB code 3OG7) is shown. Arrows indicate the perspective of the enlarged views in (B), (C), and (D). N- and C-lobe of the kinase are connected via the flexible hinge region. The ATP pocket is located in the cleft between these two subdomains, occupied by vemurafenib. (B) Detailed view of the interactions between vemurafenib and the ATP pocket. Hydrogen bonds between the ligand and the protein backbone are indicated by black dotted lines. The azaindole moiety addresses the hinge region by two key H-bonds. Access to the active site is controlled by the activation loop (A-loop), starting with the conserved amino acid sequence Asp-Phe-Gly (DFG motif). The sulfonamide residue of the ligand binds to this motif via two H-bonds. Superposition of vemurafenib with azaindole caged prodrug 2 and sulfonamide caged prodrug 4 is illustrated in (C) and (D), respectively. Red dashed lines represent sterical clashes between the PPG (photoremovable protecting group) and the target protein.

anticipated *in vitro* nonefficacy against the target enzyme BRAF^{V600E} and within a broad kinase panel to assess their specificity.

UV Stability of Vemurafenib. In general, reactivation of photoprotected prodrugs requires the parent compound's stability at the used wavelength of irradiated light. Otherwise, the drug molecule would be degraded immediately after its release or even before the bond to the PPG is cleaved. We next examined the UV stability of vemurafenib at 365 nm. For this purpose, we used a light-emitting diode (LED) reactor with a wavelength of 365 nm (5.4 W; for technical information, see Supporting Information Figures S4 and S5) to irradiate a 10 μ M solution of the compound in PBS buffer containing 10% DMSO. HPLC and LC-MS analysis were used for content determination. Under these conditions, vemurafenib showed excellent stability over a period of 20 min (see Supporting

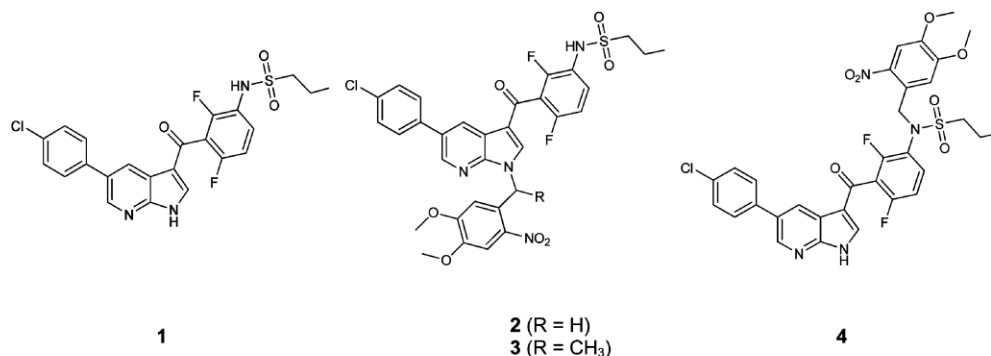


Figure 2. Chemical structures of vemurafenib and caged prodrugs. The chemical structures of vemurafenib (1), azaindole caged derivatives 2 and 3, and sulfonamide caged 4 are shown.

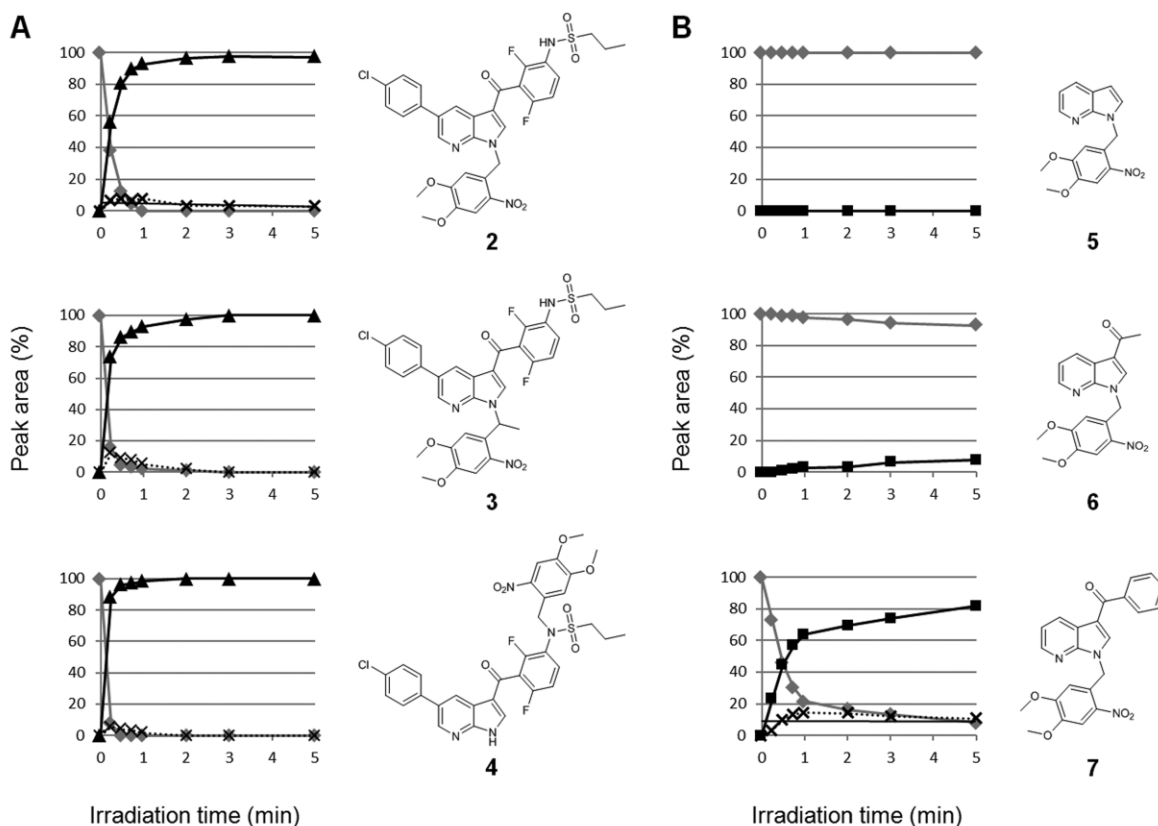


Figure 3. Photoactivation of vemurafenib prodrugs and azaindole derivatives. Uncaging was examined for photoprotected vemurafenib derivatives (A) and azaindole analogues (B). Ten micromolar compound solutions in PBS buffer containing 10% DMSO were irradiated at 365 nm (5.4 W) for 5 min and analyzed by HPLC and LC-MS. The amount of caged probe (diamonds) is plotted against released vemurafenib (triangles, A) or the corresponding azaindole analogue (squares, B), respectively. The formation of a cyclic benzisoxazolidine intermediate could be observed (crosses) and is discussed in Supporting Information Figure S10a. Photoactivation of the compounds in 1 mM DMSO solution is shown in Supporting Information Figure S10b.

Information Figures S2 and S3; for UV/vis absorption spectra of all compounds, see Supporting Information Figure S9).

Synthesis of Caged Prodrugs. Investigation of the binding mode revealed that both NH moieties within the vemurafenib structure should be suitable for the caging concept. Therefore, these functions were protected by PPGs

via nucleophilic substitution. We introduced two related *o*-nitrobenzyl PPGs into the vemurafenib molecule, namely, the 4,5-dimethoxy-2-nitrobenzyl (DMNB) and 4,5-dimethoxy-2-nitrophenylethyl (DMNPE) moieties (Figure 2).

Both azaindole (2) and sulfonamide (4) DMNB photo-protected vemurafenib prodrugs could be synthesized (for

details, see Supporting Information Figure S6 and Supporting Information section 4). These two compounds enabled a comparison to be made between the different protection sites concerning their photorelease characteristics and their biological evaluation, respectively. Through irradiation, the DMNB group produces a nitroso-benzaldehyde, whereas a less toxic ketone is released by the DMNPE moiety.² Therefore, the DMNPE azaindole caged vemurafenib (**3**) was synthesized as well. It is noteworthy that due to sterical hindrance at the sulfonamide only the azaindole DMNPE protected derivative was obtained (as discussed in Supporting Information Figures S7 and S8).

These photo prodrugs were subjected to further photochemical and biological evaluation.

Photochemical Characterization of Caged Prodrugs.

In the following step, we investigated the photorelease kinetics of **2**, **3**, and **4**. For the prodrug concept, it is essential for the parent compound to be released rapidly and quantitatively upon irradiation. Wavelengths shorter than 300 nm might damage tissues or proteins. For the photorelease experiments, we used an LED reactor with an emission at 365 nm to irradiate 10 μ M solutions of the compounds in PBS buffer containing 10% DMSO (for technical information, see Supporting Information Figure S4 and S5; for the experiment in pure DMSO, see Supporting Information Figure S10b). This wavelength has been described for the cleavage of the inserted PPGs, both DMNB and DMNPE.²

The results of photoinduced release of vemurafenib by our photo prodrugs are presented in Figure 3A. Upon irradiation, sulfonamide protected derivative **4** showed the fastest cleavage of the PPG. After 30 s, more than 90% of vemurafenib was released. Azaindole protected **2** and **3** were comparable to each other in their photocharacteristics. More than 90% of vemurafenib was released within 1 min. In the literature, DMNPE is reported to have a higher quantum yield compared to that of DMNB.² However, the assumption that **3** would show faster releasing characteristics than **2** could not be confirmed in our study. According to LC-MS and NMR studies, the formation of a cyclic benzisoxazolidine intermediate could be observed (for details, see Supporting Information Figure S10a).

In order to investigate the minimal structural requirement for the photoreaction, we investigated the vemurafenib scaffold in more detail. In general, N-heterocycles are rarely described leaving groups in photochemistry. We therefore synthesized several azaindole analogues and characterized their photochemical behavior. As illustrated in Figure 3B, caged 7-azaindole **5** was perfectly stable against UV irradiation and did not show any conversion. Photoprotected 3-acetyl-7-azaindole **6** could be uncaged but at a slow reaction rate. However, 3-benzoyl-7-azaindole **7** offered slightly slower photorelease characteristics compared to those of the vemurafenib prodrugs. This motif, therefore, can be considered to be the essential fragment for suitable photorelease of the N-heterocycle in this system.

In conclusion, both NH photoprotection sites within the investigated prodrugs proved to be suitable for rapid and quantitative photorelease. The next question addressed was whether the protection of the NH moieties in vemurafenib would actually diminish the effect on BRAF^{V600E} and also suppress the antiproliferative effect in cells.

Kinase Assays. We therefore determined the binding affinity of caged and uncaged compounds toward BRAF^{V600E} in

a commercially available assay (for details, see Supporting Information). The BRAF^{V600E} K_d values were measured as follows: 10 nM for vemurafenib, 440 nM for **2**, 77 nM for **3**, and 79 nM for **4**, respectively. In line with the modeling data, the caged compounds exhibited a lower binding affinity toward BRAF^{V600E} in comparison to that for vemurafenib. The lowest binding affinity was found for azaindole protected compound **2**. This is strong evidence that protection of the azaindole moiety forestalls the inhibitor–enzyme interaction. Surprisingly, compounds **3** and **4** still show unexpected binding toward BRAF^{V600E}, although their affinities are significantly less than that of vemurafenib. The determined affinities can be explained by minute quantities of unprotected active compound in the samples and/or instability of caged compounds resulting in the release of vemurafenib under the assay conditions.

Subsequently, a selectivity profile over 140 kinases for vemurafenib, **2**, and **4** was performed. The results are presented in a heat map in Figure 4 (for the complete data set, see Supporting Information Table S1). Apparently, vemurafenib at

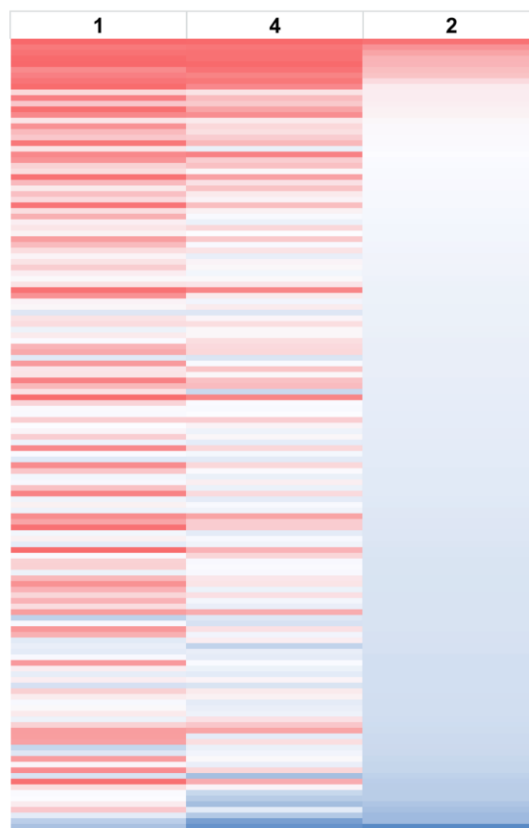


Figure 4. Kinase selectivity profiling of vemurafenib and caged prodrugs. The inhibitory effect of active vemurafenib (**1**) and caged derivatives **2** and **4** was tested in a panel of 140 kinases. The residual activity of kinases was measured after incubation with 10 μ M of each compound. The data is portrayed as a heat map of the mean activity of assay duplicates. The color code refers to the residual kinase activity ranging from red (low residual activity) to blue (high residual activity). Apparently, **2** inhibits significantly less kinases than does vemurafenib and **4**.

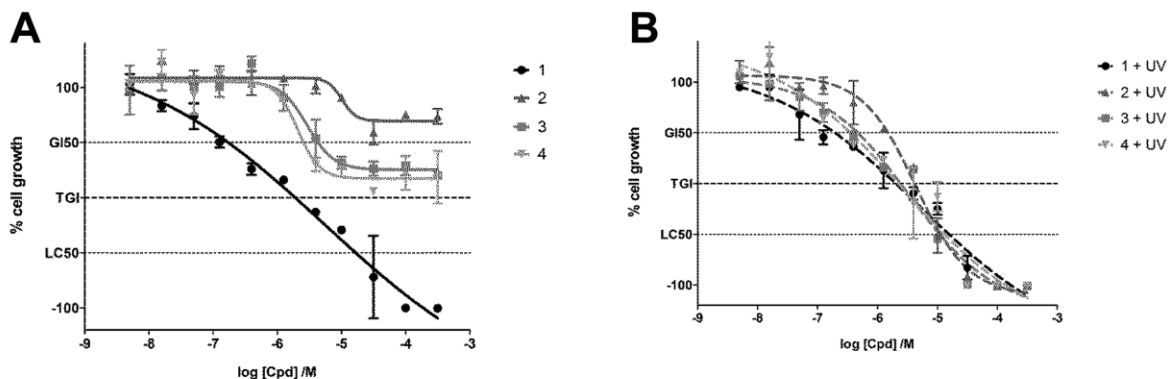


Figure 5. Activation of caged prodrugs in cell proliferation assays. The recovery of vemurafenib's efficacy by UV irradiation was demonstrated using SKMel13 cells. (A) Dose–response curves of vemurafenib (1) and caged prodrugs 2, 3, and 4 were determined without UV irradiation. Cell growth was measured 48 h after incubation with the compounds. Vemurafenib clearly shows cytotoxic effects at concentrations above $1 \mu\text{M}$. The caged derivatives do not exhibit cytotoxic activity: the TGI mark is not reached even at high concentrations. (B) Cells were incubated for 1 h with the compounds and then irradiated at 365 nm (1.8 W) for 5 min. Cell growth was determined 48 h after incubation with the compounds. After irradiation, the caged derivatives show similar dose–response curves as that of active vemurafenib. GI_{50} = 50% growth inhibition; TGI = total growth inhibition; LC_{50} = 50% lethal concentration; $n = 4$. Error bars represent standard deviation.

$10 \mu\text{M}$ potentially inhibits several other kinases besides $\text{BRAF}^{\text{V600E}}$. Altogether, there are 32 kinases whose activities are reduced to less than 30% under the test conditions. The most affected kinases are BRK, MAP4K5, and DDR2. This data clearly indicates that vemurafenib is not highly selective at the tested concentrations in biochemical assays.

Sulfonamide caged compound 4 reduces the activity of 13 kinases to less than 30%. Its inhibitory potency against nontarget kinases is diminished in comparison to that of vemurafenib. However, some nonspecific interactions are still observable. Regarding this data, it can be assumed that protection of the sulfonamide residue prevents binding to $\text{BRAF}^{\text{V600E}}$ but is still not sufficient enough to completely suppress inhibition of other kinases.

In contrast, azaindole protected compound 2 inhibits only two kinases: MAP4K5 (7% residual activity) and RIPK2 (26% residual activity). These findings are in line with the initial assumption that blockade of the hinge binder, the azaindole moiety, would annihilate the affinity to kinases in general more effectively than the protection of the sulfonamide residue.

Cellular Assays. On the basis of the biochemical data, we supposed that the caged derivatives 2, 3, and 4 should show considerably less activity in cellular assays compared to that of vemurafenib. To prove this hypothesis, we investigated the antiproliferative activity of the four compounds in cellular growth assays using the melanoma cell line SKMel13, which carries the $\text{BRAF}^{\text{V600E}}$ mutation.²⁷ Dose–response curves for the nonirradiated compounds were measured (Figure 5A).

Vemurafenib shows potent cytotoxic activity (GI_{50} value $0.17 \mu\text{M}$). This finding corresponds with previous studies, that revealed a strong inhibition of V600E-positive melanoma cells by vemurafenib.^{28–30} In contrast, caged 2, 3, and 4 exhibit no cell toxicity toward the melanoma cells in the nanomolar range (Figure 5A). Cytostatic effects occur at considerably higher concentrations (GI_{50} values: $4.3 \mu\text{M}$ for 3 and $2.6 \mu\text{M}$ for 4). Compound 2 does not show cell growth inhibition at all. Similar results could be reproduced with other V600E-positive melanoma cell lines: SKMel28, M14, and UACC62 (data shown in Supporting Information Table S2). Again, the marginal cytostatic effects of the caged probes at higher

concentrations could be caused by minute impurities of unprotected vemurafenib or by off-target effects of the compounds.

Next, we examined whether the inhibitory potency of the photoprotected compounds in cells could be restored upon UV irradiation. The cell growth assays described above were performed by irradiating the cells with UV light at 365 nm (1.8 W, 5 min) with and without compound incubation. The dose–response curves are presented in Figure 5B. In this assay, the UV irradiation at the applied dosage is well-tolerated by the cells. After UV irradiation, 2, 3, and 4 show antiproliferative activity comparable to that of unprotected vemurafenib (GI_{50} values: $0.19 \mu\text{M}$ for vemurafenib, $1.5 \mu\text{M}$ for 2, $0.46 \mu\text{M}$ for 3, and $0.35 \mu\text{M}$ for 4; Figure 5B). The slightly reduced activity in comparison to that of vemurafenib might be explained by incomplete photorelease under the described conditions.

Summarizing the results of the proliferative cell assays, it can be postulated that the irradiation of the caged compounds restores the potent activity of vemurafenib.

Having demonstrated the photoactivation of vemurafenib from its caged prodrugs, we investigated the effect of the cleaved PPG moieties on cellular growth. Caged 2, 3, and 4 were not suitable to answer this question because of the intrinsic toxicity of the uncaged vemurafenib after irradiation. We therefore used two model compounds: Boc protected L-alanine (Boc-Ala) and its DMNB photoprotected derivative (Boc-Ala-DMNB), as we considered Boc-Ala to be nontoxic (Supporting Information Figure S11). At first, the effect of UV-light-unexposed compounds on proliferation of the SKMel13 cells was measured. Both protected amino acid derivatives did not show any antiproliferative effects even at high concentrations. The same experiment was repeated implementing UV irradiation (365 nm, 1.8 W). Irradiated Boc-Ala is still neither cytotoxic nor cytostatic. In contrast, Boc-Ala-DMNB exhibits distinct antiproliferative activity after irradiation at concentrations above $10 \mu\text{M}$ ($\text{GI}_{50} = 34.4 \mu\text{M}$). Therefore, it can be assumed that the measured cell toxicity is caused by the cleaved DMNB. However, the concentration at which the PPG shows toxicity ($10 \mu\text{M}$) is approximately 100-fold higher than the

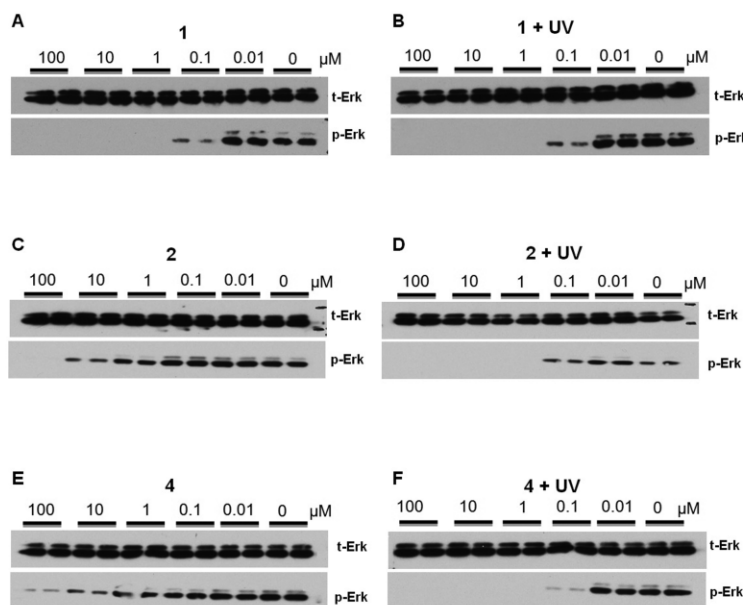


Figure 6. Activation of inhibitory effect of caged prodrugs on BRAF^{V600E} signaling *in vitro*. SKMel13 cells were treated for 1 h at 37 °C with the indicated concentrations of vemurafenib (1) and caged prodrugs 2 and 4. Subsequently, cells were lysed and immunoblotted. (A, C, E) Cells were incubated with the corresponding compound without irradiation. (B, D, F) Cells were incubated with the corresponding compound for 1 h, irradiated at 365 nm (1.8 W) for 5 min, and after a further 1 h of incubation, lysed and immunoblotted. The experiments were carried out in duplicates. t-Erk = total Erk; p-Erk = phosphorylated Erk. For compound 3, see Supporting Information Figure S12. For phosphorylation of Akt, see Supporting Information Figures S13 and S14.

efficacious concentration of the released vemurafenib (0.17 μM).

Western Blots. In order to investigate the impact of vemurafenib and its caged derivatives on BRAF^{V600E} signaling, we performed western blot analysis, including the phosphorylation of ERK as a readout downstream of BRAF. The results for vemurafenib, 2, and 4 are shown in Figure 6 (for 3, see Supporting Information Figure S12).

Initially, ERK phosphorylation in SKMel13 cells was investigated after incubation with nonirradiated compounds. Total ERK was used as a loading control. As reported for a BRAF inhibitor,^{23,28–30} vemurafenib displays dose-dependent pERK inhibition at concentrations higher than 0.01 μM . The phosphorylation of ERK is completely blocked at concentrations above 0.1 μM .

According to the biochemical data, the caged compounds reveal significantly less inhibition of ERK phosphorylation. Even at a concentration of 10 μM , there are detectable signals of pERK. Consecutively, ERK phosphorylation in cells was surveyed after incubation with compounds and subsequent UV irradiation. No alteration in pERK inhibition by vemurafenib could be determined with or without irradiation. This demonstrates that the amount of phosphorylated ERK is not dependent on UV irradiation under the described conditions.

After UV irradiation, 2, 3, and 4 exhibit the same inhibitory potency on pERK as that of active vemurafenib. The complete suppression of ERK phosphorylation could be demonstrated at concentrations above 0.1 μM . Dose dependency correlates with that of vemurafenib.

This indicates that the inhibitory efficacy of vemurafenib on BRAF^{V600E} signaling can be completely reactivated upon irradiation of the caged derivatives with UV light.

Both vemurafenib and its caged compounds exhibit no effect on the phosphorylation of Akt independent from UV irradiation (see Supporting Information Figures S13 and S14).

Conclusions. In this article, we describe the design, synthesis, and photochemical and *in vitro* characterization of novel caged prodrugs of the kinase inhibitor vemurafenib. Molecular modeling studies predicted the obviation of inhibitory potency after insertion of a PPG into vemurafenib. After UV stability of vemurafenib and photoactivation of the caged inhibitors had been confirmed, the compounds were tested in different *in vitro* assays.

In kinase binding assays, selectivity profiling, cellular assays, and western blot analysis, we demonstrated that the insertion of a PPG significantly diminishes the inhibitory efficacy and promiscuity of vemurafenib. In particular, azaindole protected compound 2 revealed hardly measurable activities even at high concentrations, both in biochemical and cellular assays. The nonspecific interactions toward off-target kinases could be drastically reduced by protecting the hinge binder, the azaindole moiety. Finally, we could clearly demonstrate that UV irradiation (365 nm) of caged prodrugs can completely restore the inhibitory potency of vemurafenib in proliferative and signal transduction assays. The cellular growth assays indicated that the applied UV dosage is well-tolerated by the melanoma cells.

There are already some examples of caged kinase inhibitors described in the literature.^{7,31} However, the herein presented caged compounds are, to the best of our knowledge, the first

photoactivatable derivatives of an approved small-molecule kinase inhibitor. Caged kinase inhibitors offer an exciting option for novel therapeutic applications. By targeted irradiation, it might be possible to release high concentrations of an active compound in a precisely controlled way in only appropriate sites afflicted by disease. With this approach of locally restricted activation, it is conceivable that systemic side effects can be prevented and the incidence of acquired resistances, reduced. For instance, the paradoxical stimulation of ERK phosphorylation by vemurafenib in wild-type BRAF cells¹² could presumably be reduced by a caged inhibitor.

Actually, our study is complementary to application of UV light for medical/therapeutic purposes. For instance, the psoralen plus UV-A (PUVA) therapy has been applied in dermatology since the 1970s.³² The fact that UV light can be carcinogenic is commonly known because of its DNA damaging effects, but this is only in the case of UVC and UVB radiation. In contrast, UVA irradiation (wavelengths above 320 nm) does not affect the genetic material and is therefore not harmful at low limited dosage.³³ The implementation of light for release of therapeutically active substances may be restricted due to low tissue penetration. Several solutions for this problem are possible: The required light could be transmitted to the site of interest via optical fibers or endoscopic probes. Moreover, in selected cases, adjacent areas could be illuminated during the surgery.

Besides the *o*-nitrobenzyl derivatives implemented in this study, a variety of PPGs are described in the literature.^{2,6,34} By varying the PPG, the required wavelength can be adapted. The deepest permeation into biological tissue can be achieved by wavelengths within the biological optical window. Wavelengths around 800 nm should best meet this challenge.³⁵ Hence, two-photon excitation could be used, supposing that the caged compound is sensitive to two-photon excitation.⁵

For future therapeutic applications, biological effects of the cleaved PPG and the cyclic benzisoxazolidine intermediate should be thoroughly explored. UV irradiation of the herein utilized *o*-nitrobenzyl PPGs generates supposedly toxic nitroso compounds. In the presented cellular proliferation assays, the released 4,5-dimethoxy-2-nitroso-benzaldehyde (the cleaved DMNB) showed intrinsic toxicity only at concentrations above 10 μ M. This might not be critical because the caged compounds could be applied at much lower concentrations. The caged vemurafenib derivatives exhibit antiproliferative effects already at concentrations around 0.1 μ M. Therefore, there might still be a wide therapeutic window for possible applications. Due to its short half-life, the biological effect of the cyclic intermediate could not be explored in the described assays. Further investigations in cellular assays and animal studies could reveal the effects of cleaved PPGs on biological tissue more thoroughly.

In conclusion, we created novel caged derivatives of the approved kinase inhibitor vemurafenib and proved that these prodrugs can be photoactivated *in vitro*. Our straightforward workflow implemented (1) determination of suitable pharmacophore moieties by modeling, (2) testing the UV stability of the active inhibitor, (3) synthesis of caged prodrugs, (4) characterizing their photoactivation, and (5) evaluating their photoactivation *in vitro*. This rational approach can be used for the generation of other photoactivatable (kinase) inhibitors as well based on different precursors and caged by various PPGs. Additionally, caged kinase inhibitors represent a powerful biochemical tool for studying the kinetics and regulation of

phosphorylation processes in signal transduction cascades. These events can be precisely triggered by a short laser impulse. On the other hand, caged kinase inhibitors create new possibilities for therapeutic applications. Profound research regarding the stability, bioavailability, and toxicity of the caged kinase inhibitors is required to ensure their medical applicability. Further cellular and animal studies are planned to address these questions.

■ ASSOCIATED CONTENT

5 Supporting Information

Figure S1: 2D ligand interaction diagram of vemurafenib in BRAF^{V600E}. Figure S2: Calibration curves of vemurafenib for HPLC analysis. Figure S3: UV stability of vemurafenib. Figure S4: UV sources. Figure S5: Technical setup and emission characteristics of the utilized UV sources. Figure S6: Synthesis of caged prodrugs. Figure S7: Modeled structures of proposed atropisomers of sulfonamide DMNPE protected vemurafenib. Figure S8: Chromatographic separation of DMNPE protected vemurafenib derivatives. Figure S9: UV/vis absorption spectra of key compounds. Figure S10: Photorelease of vemurafenib by caged prodrug 3 and cyclic benzisoxazolidine intermediate formation, photoactivation of vemurafenib prodrugs and azaindole derivatives, and stability of vemurafenib prodrugs in cellular growth medium. Figure S11: Effect of the photo-released PPG on the cell proliferation of SKMel13 cells. Figure S12: Effect of compound 3 on the phosphorylation of ERK in SKMel13 cells. Figure S13: Effect of vemurafenib (1) and caged compounds 2 and 4 on the phosphorylation of Akt in SKMel13 cells. Figure S14: Effect of compound 3 on the phosphorylation of Akt in SKMel13 cells. Figure S15: Binding affinity curves of vemurafenib (1) and prodrugs 2, 3, and 4 toward BRAF^{V600E}. Table S1: Kinase profiling of vemurafenib (1) and prodrugs 2 and 4. Table S2: Cytotoxic activity of vemurafenib (1) and prodrug 2 without and with UV irradiation toward BRAF^{V600E}-positive melanoma cell lines. Methods, chemical synthesis, and compound characterization. The Supporting Information is available free of charge on the ACS Publications website at DOI: 10.1021/acscchembio.5b00174.

■ AUTHOR INFORMATION

Corresponding Author

*E-mail: cpeifer@pharmazie.uni-kiel.de.

Author Contributions

§R.H. and B.P. contributed equally to this work.

Notes

The authors declare no competing financial interest.

■ ACKNOWLEDGMENTS

We thank T. Behrendt, A. Döbber, U. Girreser, and M. Schütt for excellent technical and analytical assistance at the Institute of Pharmacy in Kiel, Germany. We gratefully acknowledge the help of D. Schollmeyer, Institute for Organic Chemistry in Mainz, Germany, for X-ray analysis of compounds. Furthermore, we thank K. Dissanayaka from the MRC Protein Phosphorylation Unit at University of Dundee, Scotland, UK, for providing us with SKMel13 cells. We wish to thank the staff at the National Centre for Protein Kinase Profiling in Dundee for undertaking kinase specificity screening. Financial support by DFG (German Research Society) grant PE 1605/2-1 is greatly acknowledged.

REFERENCES

- (1) Levitzki, A. (2013) Tyrosine kinase inhibitors: views of selectivity, sensitivity, and clinical performance. *Annu. Rev. Pharmacol. Toxicol.* 53, 161–185.
- (2) Klán, P., Solomek, T., Bochet, C. G., Blanc, A., Givens, R., Rubina, M., Popik, V., Kostikov, A., and Wirz, J. (2013) Photo-removable protecting groups in chemistry and biology: reaction mechanisms and efficacy. *Chem. Rev.* 113, 119–191.
- (3) Kaplan, J. H., Forbush, B., and Hoffman, J. F. (1978) Rapid photolytic release of adenosine 5'-triphosphate from a protected analog: utilization by the sodium:potassium pump of human red blood cell ghosts. *Biochemistry* 17, 1929–1935.
- (4) Velema, W. A., Szymanski, W., and Feringa, B. L. (2014) Photopharmacology: beyond proof of principle. *J. Am. Chem. Soc.* 136, 2178–2191.
- (5) Ellis-Davies, G. C. R. (2007) Caged compounds: photorelease technology for control of cellular chemistry and physiology. *Nat. Methods* 4, 619–628.
- (6) Mayer, G., and Heckel, A. (2006) Biologically active molecules with a "light switch". *Angew. Chem., Int. Ed.* 45, 4900–4921.
- (7) Morckel, A. R., Lusic, H., Farzana, L., Yoder, J. A., Deiters, A., and Nascone-Yoder, N. M. (2012) A photoactivatable small-molecule inhibitor for light-controlled spatiotemporal regulation of Rho kinase in live embryos. *Development* 139, 437–442.
- (8) Li, H., Hah, J.-M., and Lawrence, D. S. (2008) Light-mediated liberation of enzymatic activity: "small molecule" caged protein equivalents. *J. Am. Chem. Soc.* 130, 10474–10475.
- (9) Curley, K., and Lawrence, D. S. (1999) Caged regulators of signaling pathways. *Pharmacol. Ther.* 82, 347–354.
- (10) Veldhuyzen, W. F., Nguyen, Q., McMaster, G., and Lawrence, D. S. (2003) A light-activated probe of intracellular protein kinase activity. *J. Am. Chem. Soc.* 125, 13358–13359.
- (11) Wang, Q., Dai, Z., Cahill, S. M., Blumenstein, M., and Lawrence, D. S. (2006) Light-regulated sampling of protein tyrosine kinase activity. *J. Am. Chem. Soc.* 128, 14016–14017.
- (12) Bollag, G., Tsai, J., Zhang, J., Zhang, C., Ibrahim, P., Nolop, K., and Hirth, P. (2012) Vemurafenib: the first drug approved for BRAF-mutant cancer. *Nat. Rev. Drug Discovery* 11, 873–886.
- (13) Flaherty, K. T., Puzanov, I., Kim, K. B., Ribas, A., McArthur, G. A., Sosman, J. A., O'Dwyer, P. J., Lee, R. J., Grippo, J. F., Nolop, K., and Chapman, P. B. (2010) Inhibition of mutated, activated BRAF in metastatic melanoma. *N. Engl. J. Med.* 363, 809–819.
- (14) Chapman, P. B., Hauschild, A., Robert, C., Haanen, J. B., Ascierto, P., Larkin, J., Dummer, R., Garbe, C., Testori, A., Majo, M., Hogg, D., Lorigan, P., Lebbe, C., Jouary, T., Schadendorf, D., Ribas, A., O'Day, S. J., Sosman, J. A., Kirkwood, J. M., Eggermont, A. M. M., Dreno, B., Nolop, K., Li, J., Nelson, B., Hou, J., Lee, R. J., Flaherty, K. T., and McArthur, G. A. (2011) Improved survival with vemurafenib in melanoma with BRAF V600E mutation. *N. Engl. J. Med.* 364, 2507–2516.
- (15) Sosman, J. A., Kim, K. B., Schuchter, L., Gonzalez, R., Pavlick, A. C., Weber, J. S., McArthur, G. A., Hutson, T. E., Moschos, S. J., Flaherty, K. T., Hersey, P., Kefford, R., Lawrence, D., Puzanov, I., Lewis, K. D., Amaravadi, R. K., Chmielowski, B., Lawrence, H. J., Shyr, Y., Ye, F., Li, J., Nolop, K. B., Lee, R. J., Joe, A. K., and Ribas, A. (2012) Survival in BRAF V600-mutant advanced melanoma treated with vemurafenib. *N. Engl. J. Med.* 366, 707–714.
- (16) Jang, S., and Atkins, M. B. (2014) Treatment of BRAF-mutant melanoma: the role of vemurafenib and other therapies. *Clin. Pharmacol. Ther.* 95, 24–31.
- (17) Swaika, A., Crozier, J. A., and Joseph, R. W. (2014) Vemurafenib: an evidence-based review of its clinical utility in the treatment of metastatic melanoma. *Drug Des., Dev. Ther.* 8, 775–787.
- (18) Shi, H., Moriceau, G., Kong, X., Lee, M.-K., Lee, H., Koya, R. C., Ng, C., Chodon, T., Scolyer, R. A., Dahlman, K. B., Sosman, J. A., Kefford, R. F., Long, G. V., Nelson, S. F., Ribas, A., and Lo, R. S. (2012) Melanoma whole-exome sequencing identifies (V600E)B-RAF amplification-mediated acquired B-RAF inhibitor resistance. *Nat. Commun.* 3, 724–740.
- (19) Poulidakos, P. I., Persaud, Y., Janakiraman, M., Kong, X., Ng, C., Moriceau, G., Shi, H., Atefi, M., Titz, B., Gabay, M. T., Salton, M., Dahlman, K. B., Tadi, M., Wargo, J. A., Flaherty, K. T., Kelley, M. C., Misteli, T., Chapman, P. B., Sosman, J. A., Graeber, T. G., Ribas, A., Lo, R. S., Rosen, N., and Solit, D. B. (2011) RAF inhibitor resistance is mediated by dimerization of aberrantly spliced BRAF(V600E). *Nature* 480, 387–390.
- (20) Johannessen, C. M., Boehm, J. S., Kim, S. Y., Thomas, S. R., Wardwell, L., Johnson, L. A., Emery, C. M., Stransky, N., Cogdill, A. P., Barretina, J., Caponigro, G., Hieronymus, H., Murray, R. R., Salehi-Ashtiani, K., Hill, D. E., Vidal, M., Zhao, J. J., Yang, X., Alkan, O., Kim, S., Harris, J. L., Wilson, C. J., Myer, V. E., Finan, P. M., Root, D. E., Roberts, T. M., Golub, T., Flaherty, K. T., Dummer, R., Weber, B. L., Sellers, W. R., Schlegel, R., Wargo, J. A., Hahn, W. C., and Garraway, L. A. (2010) COT drives resistance to RAF inhibition through MAP kinase pathway reactivation. *Nature* 468, 968–972.
- (21) Shi, H., Kong, X., Ribas, A., and Lo, R. S. (2011) Combinatorial treatments that overcome PDGFR β -driven resistance of melanoma cells to V600E-BRAF inhibition. *Cancer Res.* 71, 5067–5074.
- (22) Villanueva, J., Vultur, A., Lee, J. T., Somasundaram, R., Fukunaga-Kalabis, M., Cipolla, A. K., Wubbenhorst, B., Xu, X., Gimotty, P. A., Kee, D., Santiago-Walker, A. E., Letrero, R., D'Andrea, K., Pushparajan, A., Hyden, J. E., Brown, K. D., Lacerre, S., McArthur, G. A., Sosman, J. A., Nathanson, K. L., and Herlyn, M. (2010) Acquired resistance to BRAF inhibitors mediated by a RAF kinase switch in melanoma can be overcome by cotargeting MEK and IGF-1R/PI3K. *Cancer Cell* 18, 683–695.
- (23) Bollag, G., Hirth, P., Tsai, J., Zhang, J., Ibrahim, P. N., Cho, H., Spevak, W., Zhang, C., Zhang, Y., Habets, G., Burton, E. A., Wong, B., Tsang, G., West, B. L., Powell, B., Shelloe, R., Marimuthu, A., Nguyen, H., Zhang, K. Y. J., Artis, D. R., Schlessinger, J., Su, F., Higgins, B., Iyer, R., D'Andrea, K., Koehler, A., Stumm, M., Lin, P. S., Lee, R. J., Grippo, J., Puzanov, I., Kim, K. B., Ribas, A., McArthur, G. A., Sosman, J. A., Chapman, P. B., Flaherty, K. T., Xu, X., Nathanson, K. L., and Nolop, K. (2010) Clinical efficacy of a RAF inhibitor needs broad target blockade in BRAF-mutant melanoma. *Nature* 467, 596–599.
- (24) Dar, A. C., and Shokat, K. M. (2011) The evolution of protein kinase inhibitors from antagonists to agonists of cellular signaling. *Annu. Rev. Biochem.* 80, 769–795.
- (25) Rabiller, M., Getlik, M., Klüter, S., Richters, A., Tüchtmann, S., Simard, J. R., and Rauh, D. (2010) Proteus in the world of proteins: conformational changes in protein kinases. *Arch. Pharm. (Weinheim, Ger.)* 343, 193–206.
- (26) Collins, L., and Workman, P. (2006) Design and development of signal transduction inhibitors for cancer treatment: experience and challenges with kinase targets. *Curr. Signal Transduction Ther.* 1, 13–23.
- (27) Dissanayake, K., Toth, R., Blakey, J., Olsson, O., Campbell, D. G., Prescott, A. R., and MacKintosh, C. (2011) ERK/p90(RSK)/14-3-3 signalling has an impact on expression of PEA3 Ets transcription factors via the transcriptional repressor capicúa. *Biochem. J.* 433, 515–525.
- (28) Yang, H., Higgins, B., Kolinsky, K., Packman, K., Go, Z., Iyer, R., Kolis, S., Zhao, S., Lee, R., Grippo, J. F., Schostack, K., Simcox, M. E., Heimbrook, D., Bollag, D., and Su, F. (2010) RG7204 (PLX4032), a selective BRAFV600E inhibitor, displays potent antitumor activity in preclinical melanoma models. *Cancer Res.* 70, 5518–5527.
- (29) Lee, J. T., Li, L., Brafford, P. A., van den Eijnden, M., Halloran, M. B., Sproesser, K., Haass, N. K., Smalley, K. S. M., Tsai, J., Bollag, G., and Herlyn, M. (2010) PLX4032, a potent inhibitor of the B-Raf V600E oncogene, selectively inhibits V600E-positive melanomas. *Pigm. Cell Melanoma Res.* 23, 820–827.
- (30) Søndergaard, J. N., Nazarian, R., Wang, Q., Guo, D., Hsueh, T., Mok, S., Sazegar, H., MacConail, L. E., Barretina, J. G., Kehoe, S. M., Attar, N., von Eeuw, E., Zuckerman, J. E., Chmielowski, B., Comin-Anduix, B., Koya, R. C., Mischel, P. S., Lo, R. S., and Ribas, A. (2010) Differential sensitivity of melanoma cell lines with BRAFV600E mutation to the specific Raf inhibitor PLX4032. *J. Trans. Med.* 8, 39.

- (31) Wood, J. S., Koszelak, M., Liu, J., and Lawrence, D. S. (1998) A caged protein kinase inhibitor. *J. Am. Chem. Soc.* *120*, 7145–7146.
- (32) Morison, W. L., Parrish, J. A., and Fitzpatrick, T. B. (1978) Controlled study of PUVA and adjunctive topical therapy in the management of psoriasis. *Br. J. Dermatol.* *98*, 125–132.
- (33) Matsumura, Y., and Ananthaswamy, H. N. (2004) Toxic effects of ultraviolet radiation on the skin. *Toxicol. Appl. Pharmacol.* *195*, 298–308.
- (34) Pelliccioli, A. P., and Wirz, J. (2002) Photoremovable protecting groups: reaction mechanisms and applications. *Photochem. Photobiol. Sci.* *1*, 441–458.
- (35) Byrnes, K. R., Waynant, R. W., Ilev, I. K., Wu, X., Barna, L., Smith, K., Heckert, R., Gerst, H., and Anders, J. J. (2005) Light promotes regeneration and functional recovery and alters the immune response after spinal cord injury. *Lasers Surg. Med.* *36*, 171–185.

Supplementary Information for Paper

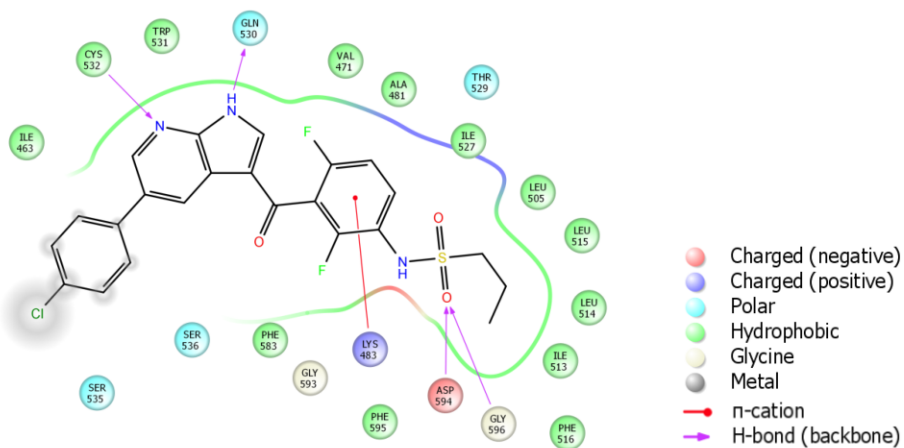
Photoactivatable prodrugs of anti-melanoma agent vemurafenib

Rebecca Horbert, Boris Pinchuk, Paul Davies, Dario Alessi, and Christian Peifer

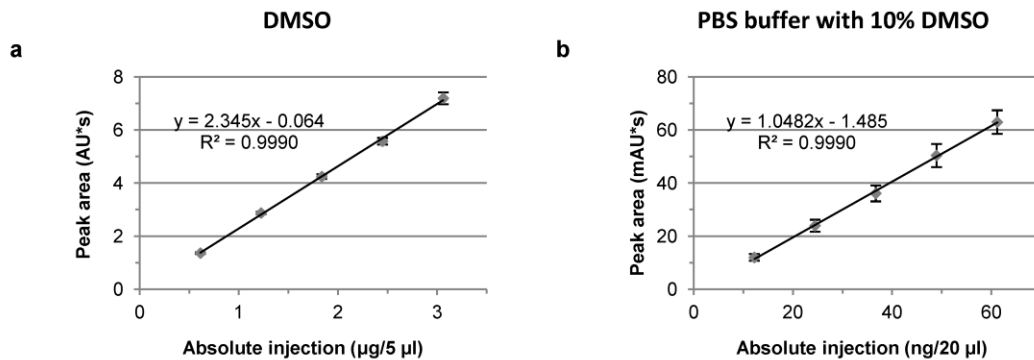
Content

1. Supplementary Figures
2. Supplementary Tables
3. Methods, Chemical synthesis and Compound Characterization
4. Supplementary References

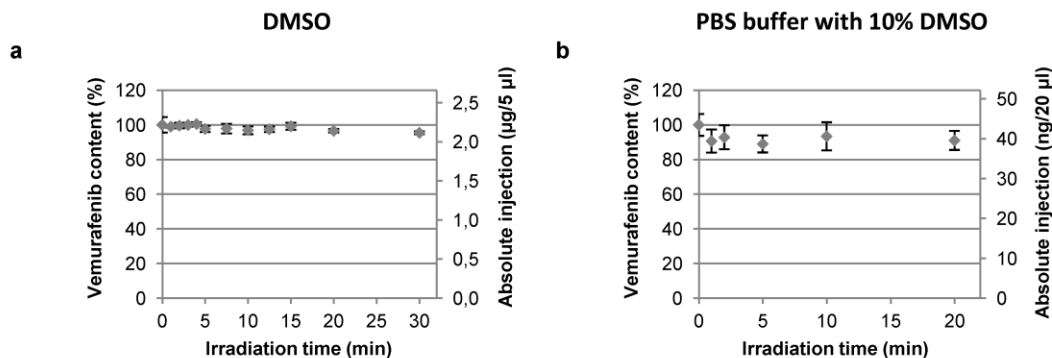
1. Supplementary Figures



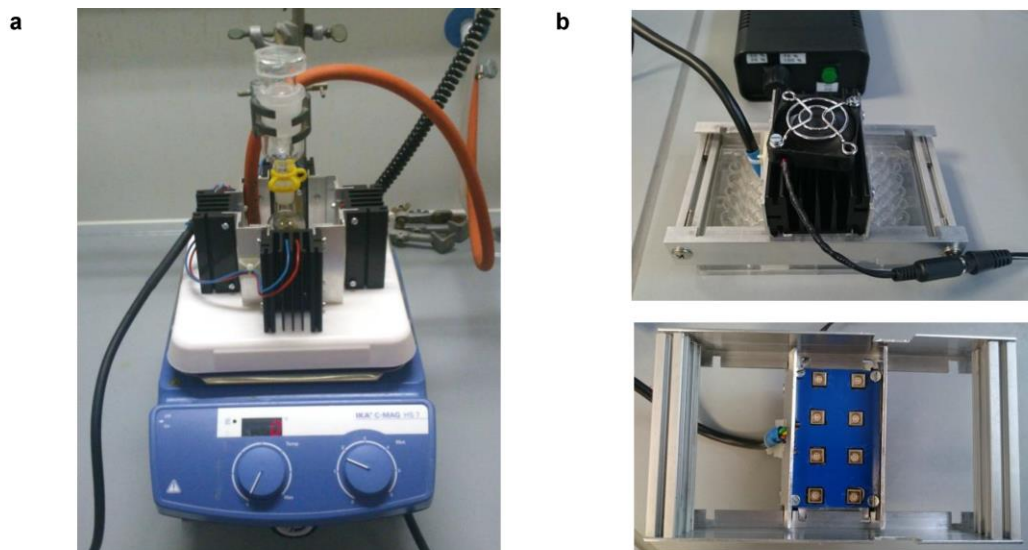
Supplementary Figure 1 | 2D ligand interaction diagram of vemurafenib in BRAF^{V600E}. H-bond interactions to the protein backbone (amino acids CYS 532, GLN 530, ASP 594 and GLY 596) are shown.



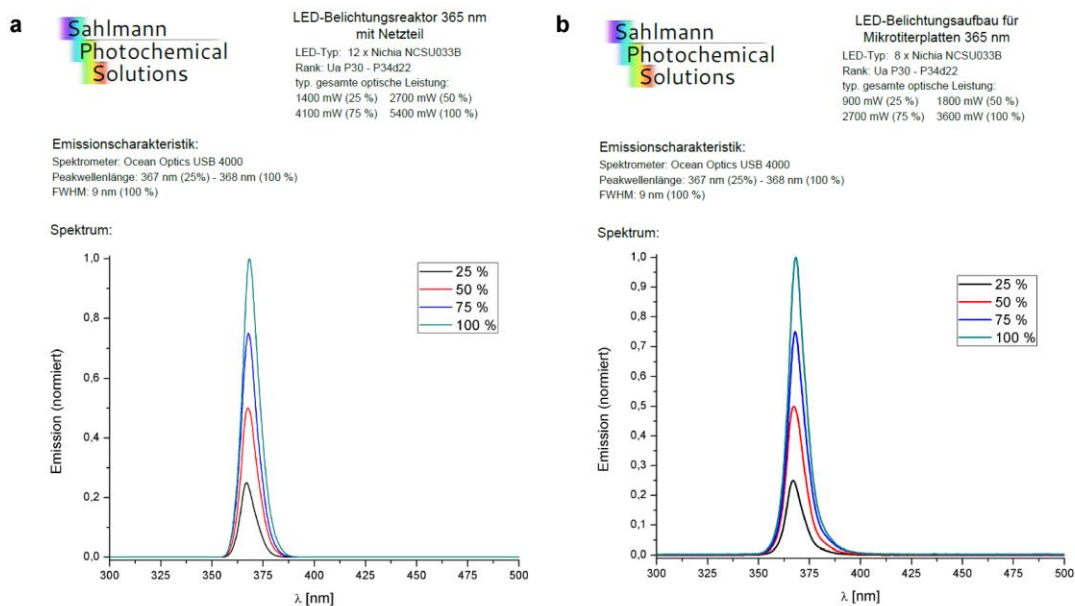
Supplementary Figure 2 | Calibration curves of vemurafenib for HPLC analysis. (a) 25, 50, 75, 100 and 125 μl of 10 mM vemurafenib stock solution in DMSO were diluted to 1 ml with methanol. The absolute injection in μg for an injection volume of 5 μl against the integrated peak area in AU*s is shown. (b) 125, 250, 375, 500 and 625 μl of 0.01 mM vemurafenib stock solution in PBS buffer with 10% DMSO were diluted to 1 ml with PBS buffer resp. methanol. The absolute injection in ng for an injection volume of 20 μl against the integrated peak area in mAU*s is shown. The stock solution was prepared in triplicate and each probe was measured twice ($n = 6$).



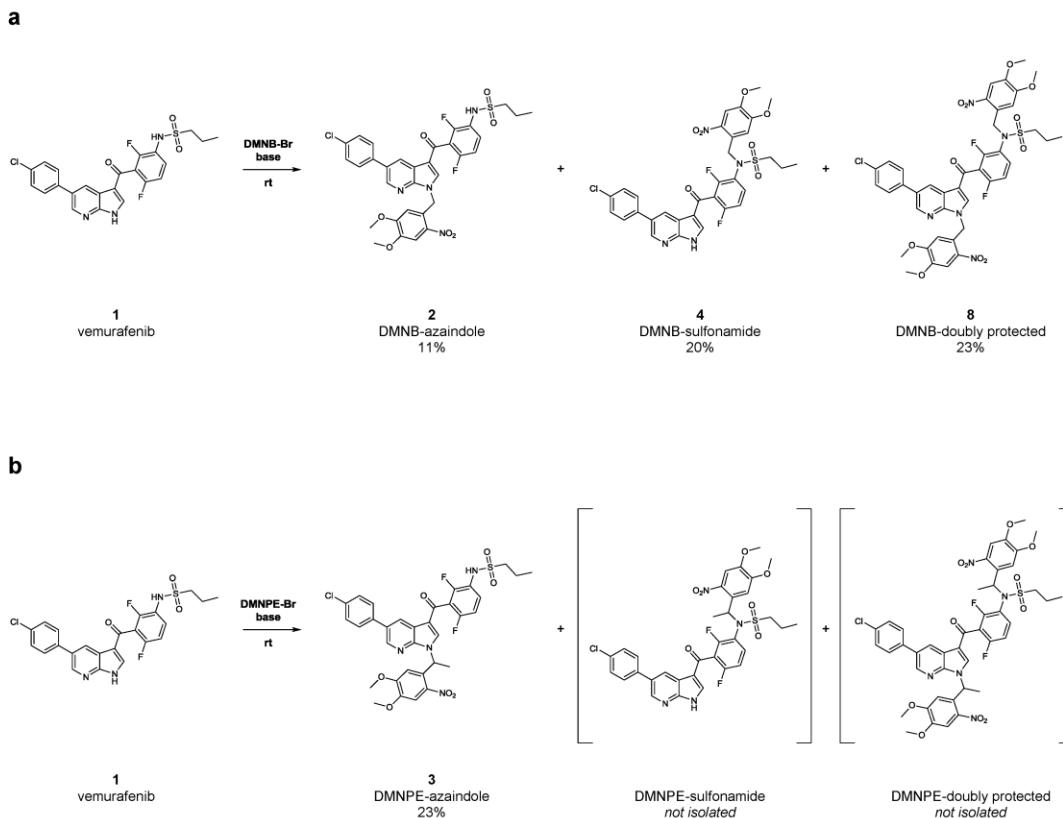
Supplementary Figure 3 | UV stability of vemurafenib. (a) 2 ml of a 10 mM vemurafenib solution in DMSO were irradiated at 365 nm (LED source, 5.4 W) while stirring and air cooling. 100 μl of the irradiated stock solution were diluted to 1 ml with methanol and analyzed in duplicate by HPLC. (b) 2 ml of a 0.01 mM vemurafenib solution in PBS buffer with 10% DMSO were irradiated at 365 nm (LED source, 5.4 W) while stirring and air cooling. 500 μl of the irradiated stock solution were diluted to 1 ml with methanol and analyzed in duplicate by HPLC. Vemurafenib shows an excellent UV stability over a period of 30 resp. 20 min of irradiation at the described experimental conditions.



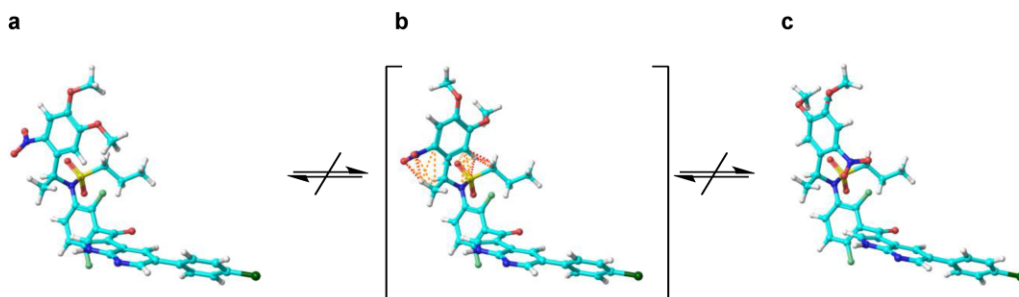
Supplementary Figure 4 | UV sources. (a) LED reactor used for irradiation of solutions in round bottom flasks. (b) LED device for the irradiation of 96-well microtitre plates. Eight LEDs (365 nm) irradiate four rows of wells (32 wells) at once. Accordingly three irradiation cycles are needed for the entire plate. See Supplementary Figure 5 for Technical setup and emission characteristics.



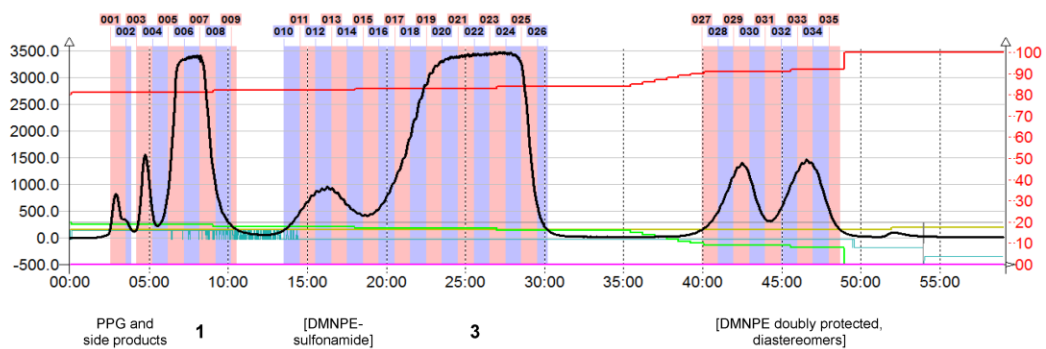
Supplementary Figure 5 | Technical setup and emission characteristics of the utilized UV sources. (a) LED reactor used for irradiation of solutions in round bottom flasks. The reactor consists of 12 LEDs with an emission maximum at a wavelength of 365 nm. The intensity can be adjusted to four levels (25, 50, 75 and 100%). The corresponding optical power in mW is shown. (b) LED device for irradiation of 96-well microtitre plates. There are also four intensity levels available.



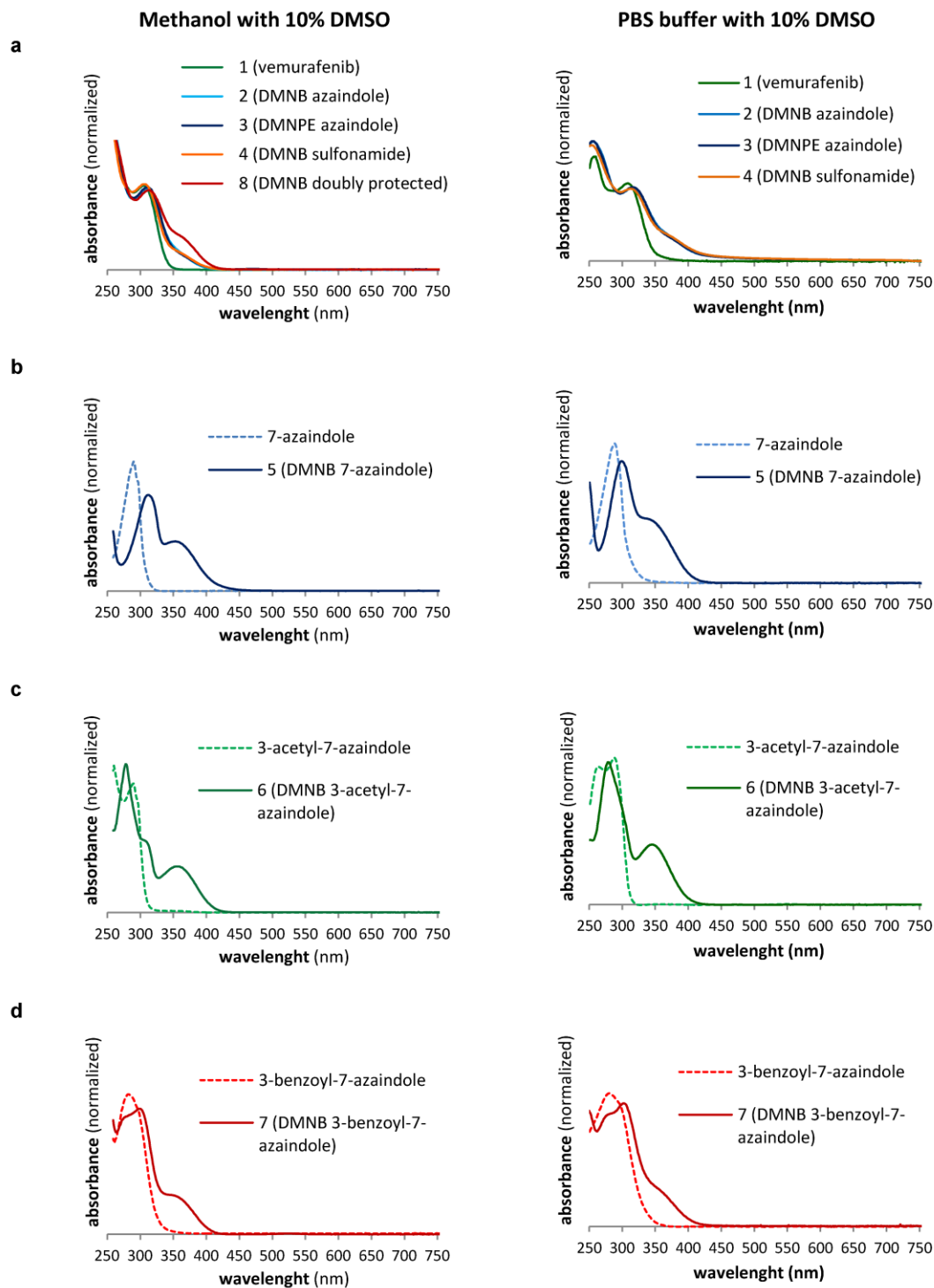
Supplementary Figure 6 | Synthesis of caged prodrugs. Vemurafenib, base and the respective PPG were stirred in DMF at rt yielding caged vemurafenib prodrugs as specified below. (a) The use of 4,5-dimethoxy-2-nitrobenzyl (DMNB) bromide yielded caged prodrugs **2**, **4**, and **8**. These compounds could be isolated by flash chromatography and were fully characterized. Further details can be found in Supplementary Note: Chemical synthesis and Characterization. (b) A comparable reaction was performed using 4,5-dimethoxy-2-nitrophenethyl (DMNPE) bromide. The main product of this reaction was the azaindole-protected compound **3** which was purified by flash chromatography and fully characterized. For further details, see Supplementary Note: Chemical synthesis and Characterization. Side products were formed to small quantities and could not be isolated. LC-MS analysis indicates that sulfonamide- and doubly-protected derivatives were formed analogous to the reaction above. Preliminary NMR analysis suggests that DMNPE-sulfonamide protection results in the formation of two atropisomers (data not shown) which is discussed in Supplementary Figure 7. Due to the presence of two chiral centers in the DMNPE-doubly protected derivative, diastereomers were presumably formed. This hypothesis is supported by preliminary NMR studies (data not shown) and different chromatographical behavior (Supplementary Fig. 8).



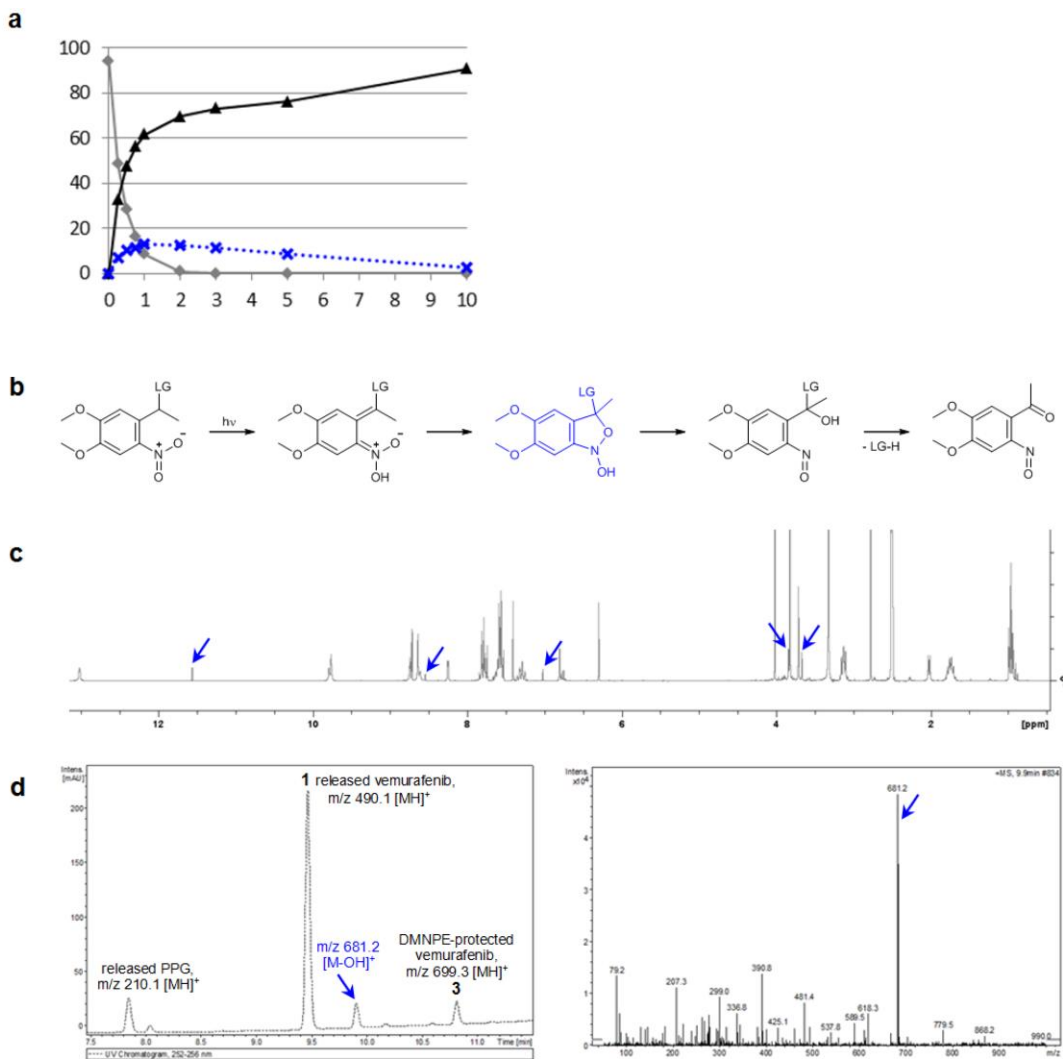
Supplementary Figure 7 | Modeled structures of proposed atropisomers of sulfonamide DMNPE-protected vemurafenib. Due to steric hindrance, DMNPE protection of vemurafenib's sulfonamide supposedly resulted in the formation of two atropisomers shown in (a) and (c). Sterical clashes in the theoretical transition structure can be calculated (b), which would hinder the rotation of the aromatic ring of the PPG. The formation of two stable atropisomers can therefore be assumed. This hypothesis is supported by NMR and LC-MS studies (data not shown).



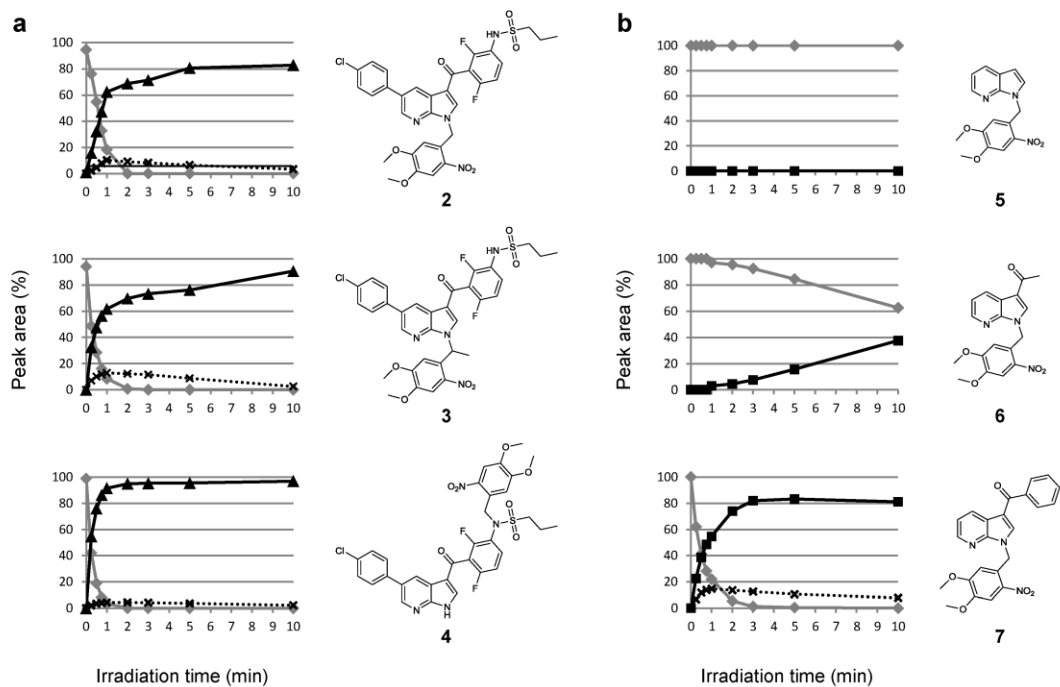
Supplementary Figure 8 | Chromatographic separation of DMNPE-protected vemurafenib derivatives. In the reaction of vemurafenib (**1**) with 4,5-dimethoxy-2-nitrophenethyl (DMNPE) bromide a complex product mixture is generated. This figure shows the chromatographic separation of these products on a C18 reversed phase column. The mobile phase was a gradient of water and methanol. Compound **3**, the DMNPE-azaindole prodrug, was formed as the main product in this reaction (Supplementary Fig. 6). It could be purified and was fully characterized. For further details, see Supplementary Note: Chemical synthesis and Characterization. Vemurafenib was not entirely converted as well as remains of the PPG which can be assigned in the chromatogram. LC-MS and NMR analysis support the hypothesis that DMNPE-sulfonamide and doubly protected derivatives are also formed (data not shown). The formation of doubly protected diastereomers with slightly different chromatographic behavior is discussed in Supplementary Figure 6.



Supplementary Figure 9 | UV/Vis absorption spectra of key compounds. (a) UV/Vis absorption spectra of vemurafenib (1) and its caged prodrugs 2, 3, 4, and 8 in MeOH/DMSO resp. PBS buffer with 10% DMSO. (b) UV/Vis absorption spectra of 7-azaindole and its caged analogue 5. (c) UV/Vis absorption spectra of 3-acetyl-7-azaindole and its caged analogue 6. (d) UV/Vis absorption spectra of 3-benzoyl-7-azaindole and its caged analogue 7. Introduction of the DMNB or DMNPE protecting group into the parent compound's molecular structure leads to increased light absorption between 350 and 400 nm. Within this range the parent compounds do not show absorption. 365 nm can therefore be considered the optimal wavelength for deprotection.



Supplementary Figure 10a | Photorelease of vemurafenib by caged prodrug **3 and cyclic benzisoxazolidine intermediate formation.** (a) A 1 mM solution of compound **3** in DMSO was irradiated at 365 nm (5.4 W) for 10 min and analyzed by HPLC. The amount of caged probe (diamonds) and released, unprotected vemurafenib (triangles) was analyzed time dependently. Additionally the formation of an intermediate could be observed (blue crosses). After 1 min its content reached up to 13% of the peak area as a maximum, before it was slowly degraded again. (b) The proposed cleavage mechanism¹ of the DMNPE protecting group is presented. We hypothesize that the cyclic benzisoxazolidine intermediate (blue structural formula) is detected by the HPLC analysis shown above. In the dark the intermediate was stable for several hours, which allowed further analysis. (c) In the mixed NMR spectrum of a 90 sec irradiated probe the datasets of caged/uncaged vemurafenib and the cleaved PPG can be recognized. Besides, there are additional peaks (integral 0.1) that belong to the intermediate (blue arrows). The sharp singlet of an exchangeable proton with a significant downfield shift of 11.6 ppm supposedly belongs to the N-OH group. (d, left) In the chromatogram of the LC-MS analysis the caged prodrug **3**, uncaged vemurafenib and the cleaved PPG can be identified. The intermediate shows a shorter retention time compared to **3** indicating a more polar structure. (d, right) For the intermediate the corresponding MS spectrum revealed signal of m/z 681. We hypothesize that a hydroxide ion is eliminated by the cyclic benzisoxazolidine during electrospray ionization. Furthermore, the ring opening of the benzisoxazolidine is reported to be the rate-determining step of this reaction² which would explain an accumulation of this intermediate.



Supplementary Figure 10b | Photoactivation of vemurafenib prodrugs and azaindole derivatives. Uncaging was examined for photo-protected vemurafenib derivatives (a) and azaindole analogues (b). 1 mM compound solutions in DMSO were irradiated at 365 nm (5.4 W) for ten minutes and analyzed by HPLC and LC-MS. The amount of caged probe (diamonds) is plotted against released vemurafenib (triangles, a) or the corresponding azaindole analogue (squares, b), respectively. The formation of a cyclic benzisoxazolidine intermediate could be observed (crosses) and is discussed in SI Figure 10a.

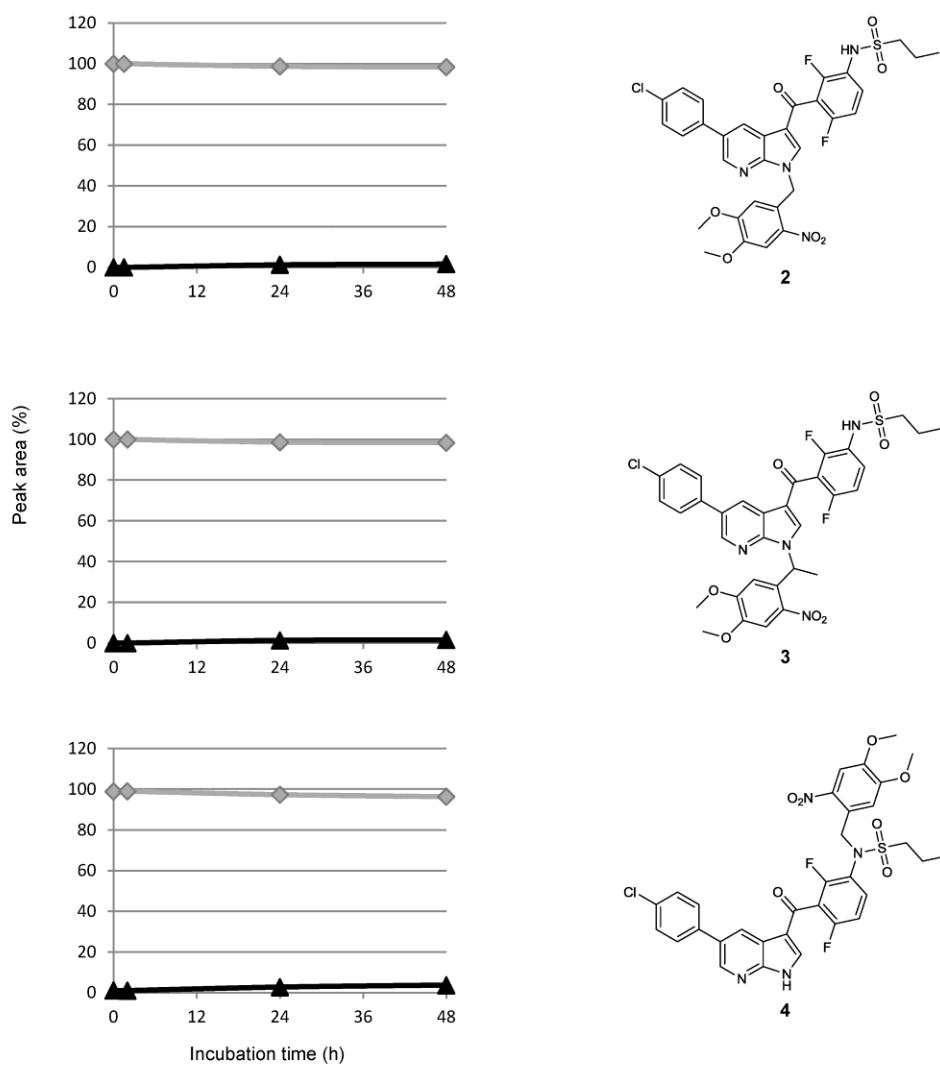


Figure 10c | Stability of vemurafenib prodrugs in cellular growth medium. 0.01 mM compound solutions in DMEM medium with 2 mM L-Glutamine, 1 mM Sodium Pyruvate and 10% DMSO were incubated in a 5% CO₂ humidified atmosphere at 37 °C for 48 h and analyzed by HPLC. The amount of caged probe (diamonds) is plotted against released vemurafenib (triangles). All three prodrugs proved to be stable in the cellular growth medium under the described conditions.

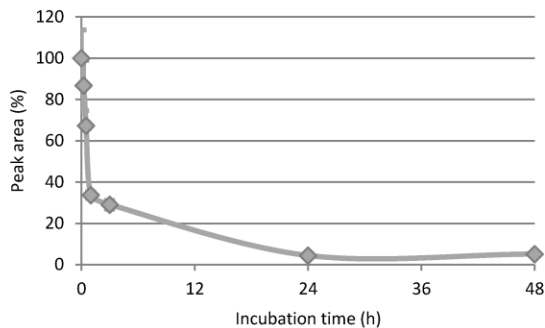
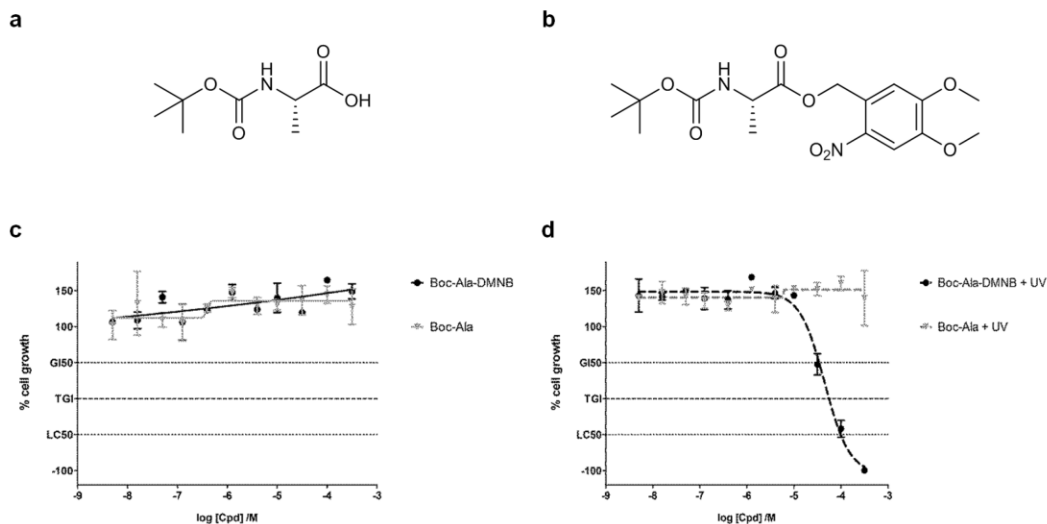
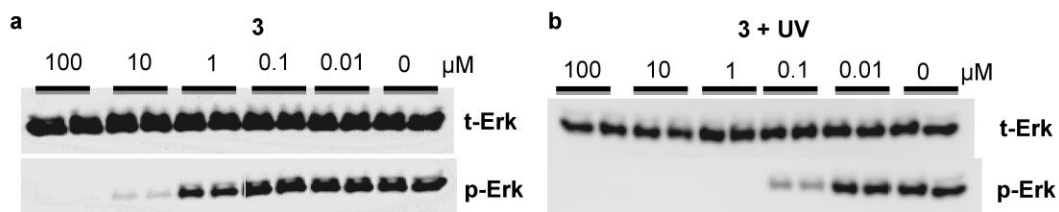


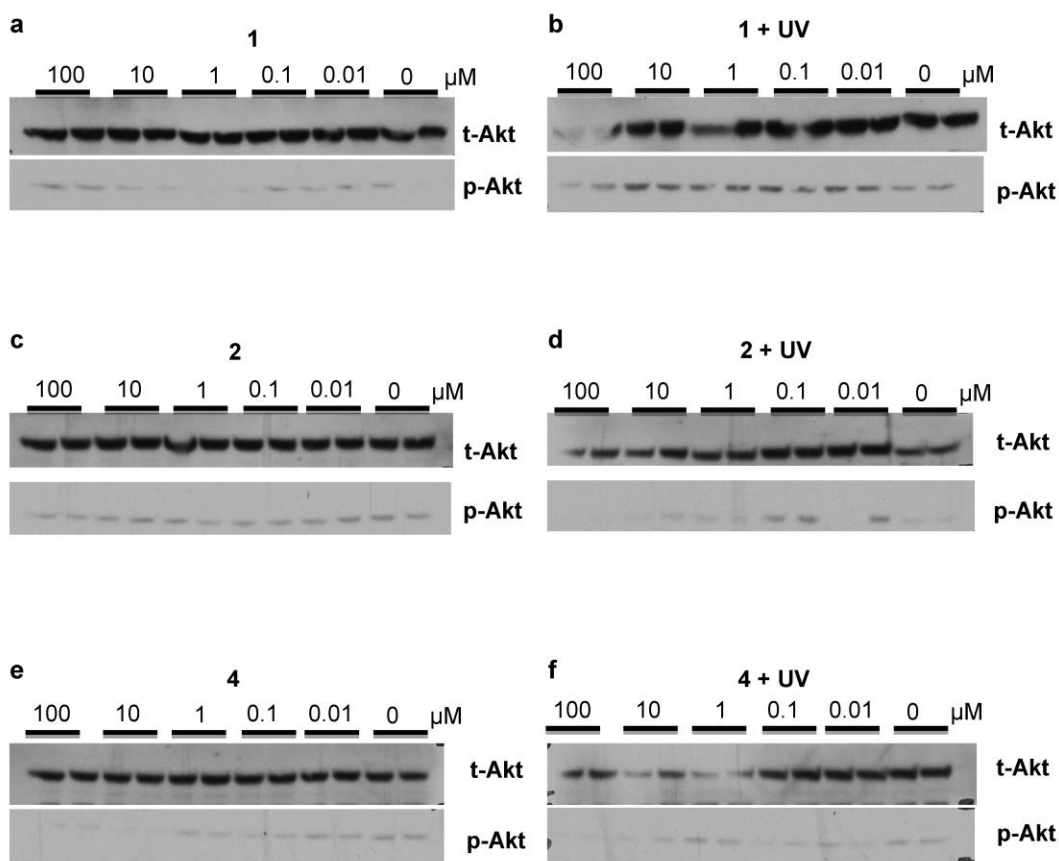
Figure 10d | Cellular uptake of the prodrug 2. SKMe128 cells were incubated with **2** at a concentration of 20 μM for 48 h, and the amount of the compound in the medium was determined by HPLC analysis. The amount of caged probe in the growth medium is plotted against the incubation time. Within 24 h the cellular uptake of the prodrug **2** is close to 100%. After incubation with the caged compound the cells were lysed and the lysates analyzed by LC/MS for **2** and potential metabolites. The applied amount of **2** could be completely retrieved. No metabolites could be detected.



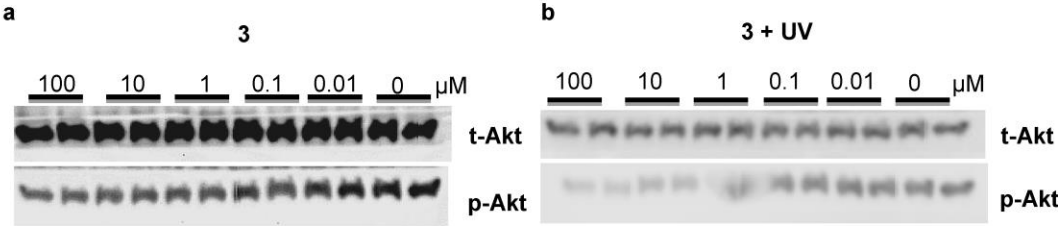
Supplementary Figure 11 | Effect of the photo released PPG on the cell proliferation of SKMe13 cells. (a) Chemical structure of the BOC-protected L-alanine = Boc-Ala. (b) Chemical structure of the DMNB-protected Boc-Ala = Boc-Ala-DMNB. (c) Dose-response-curves of the Boc-Ala and Boc-Ala-DMNB in cell viability assay using the SKMe13 cell line without UV irradiation. Cell growth was determined after 48 h incubation with the compounds. Both compounds do not show any anti-proliferative effects on SKMe13 cells. (d) Dose-response curves of the Boc-Ala and Boc-Ala-DMNB in the same assay as in (c) with UV irradiation. Cells were incubated with compounds for 1 h and then irradiated at 365 nm (1.8 W) for 5 min. Cell growth was determined after 48 h. Herein, the Boc-Ala-DMNB exhibits anti-proliferative efficacy in concentrations above 10 μM providing evidence for the cytotoxicity of the cleaved PPG at higher concentrations. GI50 = 50% growth inhibition; TGI = total growth inhibition; LC50 = 50% lethal concentration; the dose response curves were fitted using the 4-parameter logistic fit option of GraphPad Prism 5; n = 2 and error bars represent standard deviation.



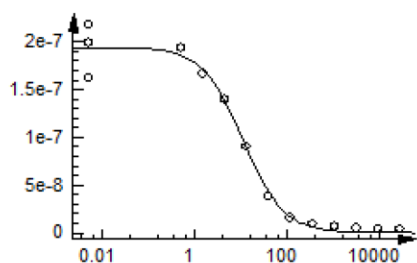
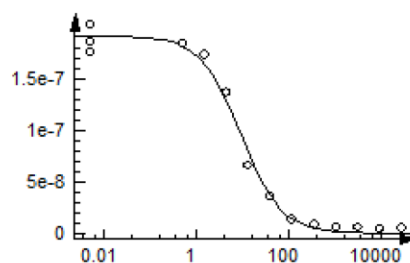
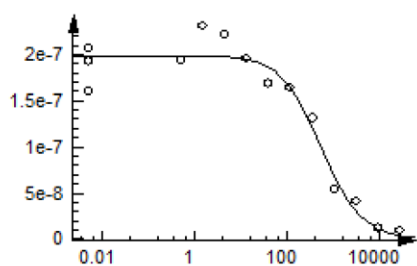
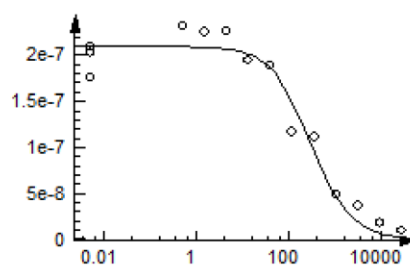
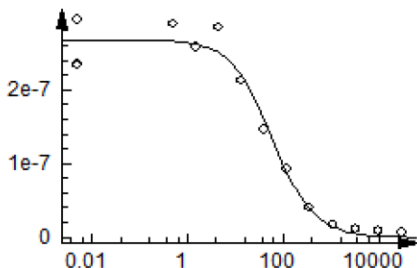
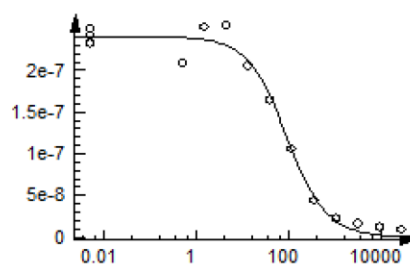
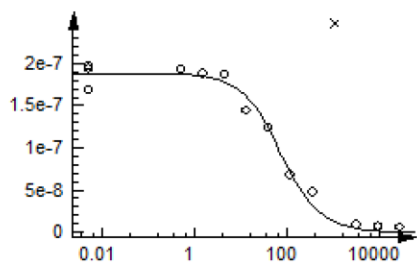
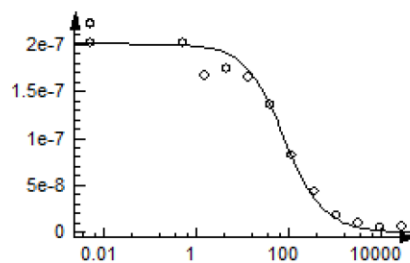
Supplementary Figure 12 | Effect of the compound 3 on the phosphorylation of ERK in the SKMe13 cells. The cells were treated with the indicated concentrations of (3) for 1 h at 37 °C. Cells were lysed and lysates immunoblotted with the indicated antibodies. (a) The cells were incubated with 3 without the irradiation. (b) The cells were incubated with 3 for 1 h, and then irradiated at 365 nm (1.8 W) for 5 min and after further 1 h incubation lysed and immunoblotted.



Supplementary Figure 13 | Effect of vemurafenib (1) and caged compounds 2 and 4 on the phosphorylation of Akt in SKMe13 cells. The cells were treated with the indicated concentrations of the compounds for 1 h at 37 °C, lysed and lysates immunoblotted with the indicated antibodies (see Supporting Information). (a), (c), (e) The cells were incubated with the compound without irradiation. (b), (d), (f) Cells were incubated with the compounds for 1 h, then irradiated at 365 nm (1.8 W) for 5 min. After further 1 h incubation cells were lysed and immunoblotted.



Supplementary Figure 14 | Effect of the compound 3 on the phosphorylation of Akt in the SKMel13 cells. The cells were treated with the indicated concentrations of 3 for 1 h at 37 °C, lysed and lysates immunoblotted with the indicated antibodies. (a) Cells were incubated with 3 without irradiation. (b) Cells were incubated with 3 for 1 h, then irradiated at 365 nm (1.8 W) for 5 min. After further 1 h incubation cells were lysed and immunoblotted.

Compound 1, Replicate 1, $K_d = 11$ nMCompound 1, Replicate , $K_d = 9.4$ nMCompound 2, Replicate 1, $K_d = 570$ nMCompound 2, Replicate 2, $K_d = 310$ nMCompound 3, Replicate 1, $K_d = 60$ nMCompound 3, Replicate 2, $K_d = 94$ nMCompound 4, Replicate 1, $K_d = 76$ nMCompound 4, Replicate 2, $K_d = 82$ nM

Supplementary Figure 15 | Binding affinity curves of vemurafenib (1) and prodrugs 2, 3, and 4 towards BRAF^{V600E}. Measurements were performed at DiscoverRx (San Diego, CA, USA). The amount of the unbound DNA tagged kinase was measured by the qPCR (Signal in a.u., y-axis) and plotted against the corresponding compound concentration in nM in log₁₀ scale (x-axis).

2. Supplementary Tables

Supplementary Table 1| Kinase Profiling of vemurafenib (1) and prodrugs 2 and 4. The inhibitory effect of active vemurafenib and the caged derivatives 2 and 4 was tested on the panel of 140 kinases. The residual activity of kinases was measured after incubation with 10 μ M of each compound. The data is portrayed as mean percentage activity and standard deviation of assay duplicates.

	1		4		2	
MAP4K5	1	0	2	1	7	1
RIPK2	11	9	9	1	26	13
GCK	7	3	6	3	36	21
DDR2	1	0	6	1	45	2
BRK	1	0	2	1	46	4
TrkA	21	7	7	3	51	8
MST2	15	12	16	0	54	14
MLK1	8	8	10	0	68	2
MAP4K3	3	0	20	0	79	4
BRSK2	67	17	73	2	79	5
BTK	14	1	50	1	79	6
DYRK2	57	8	58	12	80	4
Aurora B	5	1	36	8	82	10
CSK	20	15	22	1	82	1
PLK1	74	6	77	10	85	0
MKK2	26	8	67	2	86	5
TTK	57	6	60	5	86	1
MKK1	49	7	71	5	86	8
EIF2AK3	9	1	48	0	87	4
MKK6	74	5	98	16	88	17
CAMK1	20	0	15	2	88	6
MINK1	27	7	61	21	89	1
TSSK1	63	14	53	4	89	4
p38a MAPK	70	27	85	13	90	0
PDGFRA	7	2	34	1	90	3
ROCK 2	49	3	72	6	90	10
AMPK (hum)	77	5	54	9	90	10
DYRK3	53	1	77	2	91	5
JNK3	68	7	83	13	91	1
TESK1	8	1	51	2	91	17
ERK5	70	2	81	16	92	5
MST4	43	4	90	13	92	5
PINK	80	10	96	6	92	3
MARK4	74	10	66	10	93	1
LKB1	82	1	88	17	93	7
IKKe	32	1	57	2	93	3
OSR1	50	0	90	4	94	2
MAPKAP-K3	70	14	73	3	94	2
PDK1	83	14	98	30	94	6
SGK1	73	4	83	0	94	11
JNK2	61	24	85	1	94	15
MARK2	80	1	93	17	95	0
MAPKAP-K2	86	7	86	6	95	3
PRK2	73	11	75	3	96	2
VEG-FR	7	3	19	5	96	6
HER4	25	2	78	3	96	2
STK33	83	5	93	6	96	7
BRSK1	84	0	78	12	97	8
CK2	104	1	104	7	97	1
MEKK1	73	11	84	1	97	2

SmMLCK	69	15	70	1	97	4
PKBa	96	7	84	5	97	9
WNK1	78	13	85	8	98	7
RSK1	88	0	70	5	98	6
Aurora A	46	9	68	12	98	14
MNK2	39	3	67	7	98	4
PKA	102	1	106	9	98	12
SIK3	30	1	90	8	98	22
PIM3	75	2	55	4	99	4
MARK1	74	5	84	5	99	20
ERK8	15	1	53	4	99	2
MNK1	48	7	50	11	99	7
EPH-B4	72	5	115	18	99	6
YES1	3	0	18	6	99	14
PIM1	65	4	89	1	100	15
PIM2	87	3	89	6	100	11
ASK1	89	17	88	5	100	24
MSK1	61	3	61	0	100	0
IKKb	88	1	83	4	100	13
ERK2	84	8	95	19	101	9
DYRK1A	61	7	84	6	101	4
HIPK3	95	9	100	1	101	1
SIK2	20	2	66	15	101	21
TTBK1	89	6	92	9	101	0
ERK1	103	13	102	19	102	5
NEK2a	22	5	67	2	102	2
ULK2	56	3	87	6	102	15
EPH-A4	93	19	98	13	102	1
PRAK	90	14	80	7	102	10
PAK4	53	16	97	7	103	5
IGF-1R	16	1	68	5	103	6
HIPK1	95	13	101	0	103	13
TLK1	81	0	89	9	103	4
DAPK1	95	11	95	11	104	6
IR	22	5	36	2	104	4
IRR	36	7	60	8	104	12
MLK3	6	1	60	16	104	2
CAMKKb	93	2	101	3	105	2
SRPK1	81	3	91	0	105	5
CK1δ	100	7	95	7	106	13
Src	3	1	45	9	106	8
CHK2	87	6	66	11	106	8
IRAK1	63	2	90	7	107	2
MST3	62	1	87	2	107	2
TBK1	96	3	90	5	107	3
MPSK1	48	9	76	8	107	5
TAK1	25	0	74	4	107	1
TGFBR1	45	2	96	28	107	8
HIPK2	66	4	71	4	107	2
TAO1	45	7	92	10	107	7
ULK1	69	5	98	10	108	5
GSK3b	32	4	41	8	108	3
p38g MAPK	121	3	104	12	108	6
EF2K	90	10	108	14	108	1
FGF-R1	29	5	72	9	108	4
SYK	43	4	93	0	108	23
MELK	103	1	80	28	108	11
p38d MAPK	99	13	120	36	109	4
PKCa	101	2	98	5	109	12

PHK	90	7	101	3	110	5
NUAK1	30	5	89	5	111	6
CDK9-Cyclin T1	80	8	96	8	111	1
PKBb	99	12	102	6	111	3
S6K1	80	13	83	2	111	13
CK1γ2	109	10	107	14	111	20
JNK1	62	43	77	3	111	8
RSK2	79	3	82	20	111	1
EPH-A2	91	3	101	9	112	10
MARK3	86	7	98	3	112	5
TIE2	77	2	95	11	112	6
EPH-B3	96	8	73	5	112	0
CDK2-Cyclin A	63	3	57	4	113	6
JAK2	32	11	36	2	113	2
PAK2	32	6	101	15	114	11
ABL	35	9	70	5	114	15
NEK6	117	7	97	2	115	11
PKCy	104	15	94	16	115	6
p38b MAPK	32	1	86	7	117	6
ZAP70	84	6	98	0	118	5
CLK2	22	1	65	13	118	7
TTBK2	108	13	136	30	121	4
Lck	6	0	41	4	123	1
PKD1	70	8	84	5	124	8
PAK6	87	2	117	21	124	5
IRAK4	88	2	125	11	125	3
PAK5	78	3	137	2	130	14
EPH-B2	57	2	102	6	134	2
PKCz	101	1	128	27	139	6
CHK1	123	3	160	18	139	1
EPH-B1	133	9	170	18	177	32

Supplementary Table 2| Cytotoxic activity of vemurafenib (1) and prodrug 2 without and after UV irradiation towards BRAF^{V600E}-positive melanoma cell lines. For the experiments without UV irradiation the cells were incubated 48 h with the compounds. For the irradiation experiments cells were incubated for 1 h with the compounds and then irradiated at 365 nm (1.8 W) for five minutes. Cell growth was measured 48 h after incubation with the compounds. For dose-response studies, 11 different concentrations of compounds were tested in duplicates. GI50 and TGI-values were calculated after sigmoidal fitting using the 4-parameter logistic fit option of GraphPad Prism 5. GI50 = 50% growth inhibition; TGI = total growth inhibition; n.r. = value not reached because of low compound activity; average values of two independent experiments are determined.

cell line	GI50 values / μM				TGI values / μM			
	1	1 (5 min, 365 nm)	2	2 (5 min, 365 nm)	1	1 (5 min, 365 nm)	2	2 (5 min, 365 nm)
M14	0.06	0.04	1.36	0.04	0.99	0.65	n.r.	0.65
UACC62	0.03	0.01	1.06	0.04	0.42	0.19	n.r.	0.35
SKMel28	0.75	0.05	451	0.99	3.35	0.72	n.r.	1.89
SKMel13	0.17	0.19	n.r.	1.50	1.90	2.01	n.r.	4.15

3. Methods, Chemical synthesis and Compound Characterization

Molecular modeling of vemurafenib and caged prodrugs.

Visualization was performed by Maestro, version 9.7, Schrödinger, LLC, New York, NY, 2014. The crystal structure (pdb 3OG7) was processed by the Protein Preparation Wizard; Epik version 2.7, Schrödinger, LLC, New York, NY, 2013; Impact version 6.2, Schrödinger, LLC, New York, NY, 2014; Prime version 3.4, Schrödinger, LLC, New York, NY, 2014. Default settings were used. Missing side chains and loops were filled in with Prime. Furthermore selenomethionines were converted to methionines. Water molecules and the second non inhibitor binding protein chain were deleted.

Inhibitor moieties accessible to photo-protection (N-heterocycle and sulfonamide) were modeled regarding their interactions within the ATP binding pocket of BRAF^{V600E}. Steric hindrance due to introduction of the PPG was determined by flexible ligand alignment and calculation of ligand-protein contacts. Ugly contacts with a contact cutoff ratio < 0.5 were indicated by red dashed lines. The cutoff ratio was calculated by Maestro based on the following formula:

$$C = D12 / (R1+R2)$$

where D12 is the distance between atomic centers 1 and 2, and R1 and R2 are the radii of atomic centers 1 and 2. C increases monotonically for each contact type, that is C(ugly) < C(bad) < C(good).

Reagents and solvents for synthesis and analytics.

All reagents and solvents were obtained from commercial sources. The solvents were not dried and used as received. The synthetic procedures were not performed under special nitrogen or argon atmosphere. Reagents were purchased from abcr GmbH, Fisher Scientific GmbH/Acros, Sigma-Aldrich Chemie or VWR International GmbH.

UV stability in DMSO via HPLC analysis.

Vemurafenib was dissolved in DMSO at 10 mM and irradiated at 365 nm (LED source: 12x Nichia NCSU033B, Sahlmann Photochemical Solutions, 100%, 5.4 W) up to 30 min. The solution was stirred and cooled with compressed air flow during illumination. HPLC probes were 1:10 diluted with methanol. Hence 5 µl injection volume of an 1 mM HPLC probe equates an absolute injection of 2.45 µg (see Supplementary Figure 2, calibration curve). A Hewlett Packard 1050 Series with an Agilent ZORBAX® Eclipse XDB-C8, 5 µm (4.6 mm × 150 mm) column was used. Mobile phase (flow rate 1.5 ml/min) was a gradient mixture of KH₂PO₄ buffer (0.01 M, pH 2.3) and methanol over a runtime of 16 min. The detection wavelength was 254 nm. Additional to HPLC analysis LC-MS was used to confirm compound identity.

UV stability in PBS buffer with 10% DMSO via HPLC analysis.

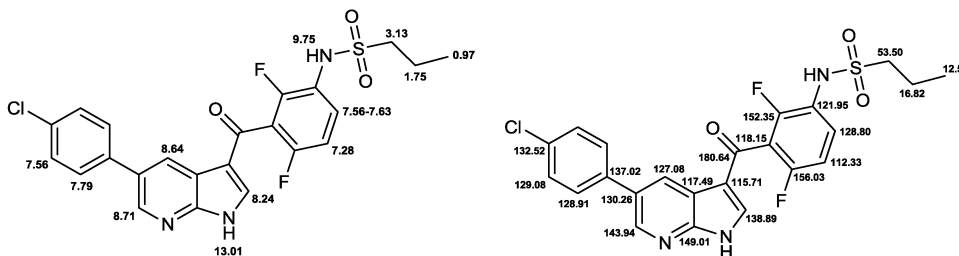
Vemurafenib was dissolved in PBS buffer with 10% DMSO at 0.01 mM and irradiated at 365 nm (LED source: 12x Nichia NCSU033B, Sahlmann Photochemical Solutions, 100%, 5.4 W) up to 20 min. The solution was stirred and cooled with compressed air flow during illumination. HPLC probes were 1:1 diluted with methanol. Hence 20 μ l injection volume of an 0.005 mM HPLC probe equates an absolute injection of 49 ng (see Supplementary Figure 2, calibration curve). A Hewlett Packard 1050 Series with a Phenomenex Kinetex™ C8, 5 μ m (4.6 mm \times 150 mm) column was used. Mobile phase (flow rate 1.5 ml/min) was a gradient mixture of KH_2PO_4 buffer (0.01 M, pH 2.3) and methanol over a runtime of 14 min. The detection wavelength was 254 nm. Additional to HPLC analysis LC-MS was used to confirm compound identity.

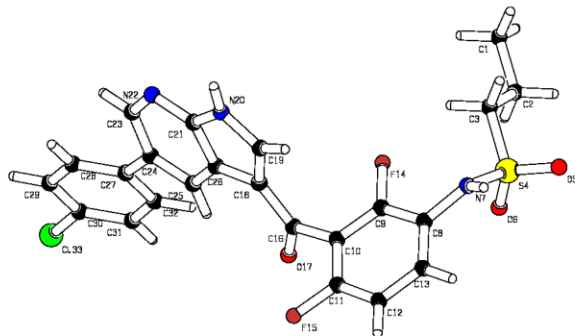
Isolation of vemurafenib, synthesis of photoactivatable vemurafenib prodrugs

The PPG was introduced into the vemurafenib molecule *via* nucleophilic substitution on nitrogen moieties of vemurafenib adapting a protocol by Lin *et al.*³ Through this reaction singly and doubly protected vemurafenib analogues were formed and subsequently separated by flash chromatography (Supplementary Fig. 6 and Supplementary Note: Chemical synthesis and Characterization).

N-(3-(5-(4-chlorophenyl)-1H-pyrrolo[2,3-b]pyridine-3-carbonyl)-2,4-difluorophenyl)propane-1-sulfonamide, INN: vemurafenib (1)

A tablet of Zelboraf® was pestled and mixed with Merck silica gel 60 (15-40 μ m). Extraction with dichloromethane and ethyl acetate was performed using a LaFlash system (VWR) and yielded 228 mg (95%) as white needle-shaped crystals. Purity (HPLC) > 98%; mp: 270.8 °C; ¹H NMR (300 MHz, DMSO-d₆): δ 0.97 (t, ³J = 7.4 Hz, 3H), 1.75 (tq, ³J = 7.7 Hz, ³J = 7.4 Hz, 2H), 3.13 (t, ³J = 7.7 Hz, 2H), 7.28 (ddd, ³J = 8.8 Hz, ³J_{HF} = 8.8 Hz, ⁵J_{HF} = 1.4 Hz, 1H), 7.56 (d, ³J = 8.6 Hz, 2H), 7.54-7.63 (m, 1H), 7.79 (d, ³J = 8.6 Hz, 2H), 8.24 (s, 1H), 8.64 (d, ⁴J = 1.7 Hz, 1H), 8.71 (d, ⁴J = 2.3 Hz, 1H), 9.75 (bs, 1H), 13.01 (bs, 1H); ¹³C NMR (75 MHz, DMSO-d₆): δ 12.59, 16.82, 53.50, 112.33 (dd, ²J_{CF} = 22.5 Hz, ⁴J_{CF} = 3.7 Hz), 115.71, 117.49, 118.15 (dd, ²J_{CF} = 24.6 Hz, ²J_{CF} = 22.4 Hz), 121.95 (dd, ²J_{CF} = 13.6 Hz, ⁴J_{CF} = 3.7 Hz), 127.08, 128.80 (dd, ³J_{CF} = 10.0 Hz, ³J_{CF} = 1.6 Hz), 128.91, 129.08, 130.26, 132.52, 137.02, 138.89, 143.94, 149.01, 152.35 (dd, ¹J_{CF} = 249.5 Hz, ³J_{CF} = 8.5 Hz), 156.03 (dd, ¹J_{CF} = 246.5 Hz, ³J_{CF} = 7.0 Hz), 180.64; ¹⁹F NMR (282 MHz, DMSO-d₆): δ -122.00, -116.74; LC-MS (ESI): *m/z* (rel. Intens.) 490.1 (100.0%), 492.0 (39.1%), 491.0 (26.3%), 493.0 (10.7%) [MH]⁺.

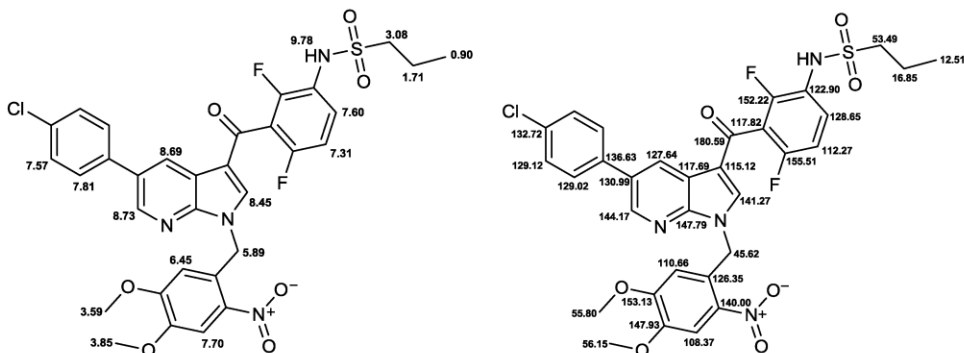


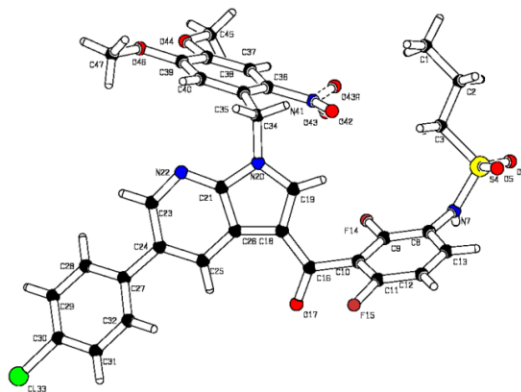


Molecular structure determined by X-ray crystallography. Cambridge Crystallographic Data Centre deposition number: CCDC 1044606. Data accessible via <http://www.ccdc.cam.ac.uk>.

N-(3-(5-(4-chlorophenyl)-1-(4,5-dimethoxy-2-nitrobenzyl)-1H-pyrrolo[2,3-b]pyridine-3-carbonyl)-2,4-difluorophenyl)propane-1-sulfonamide (2)

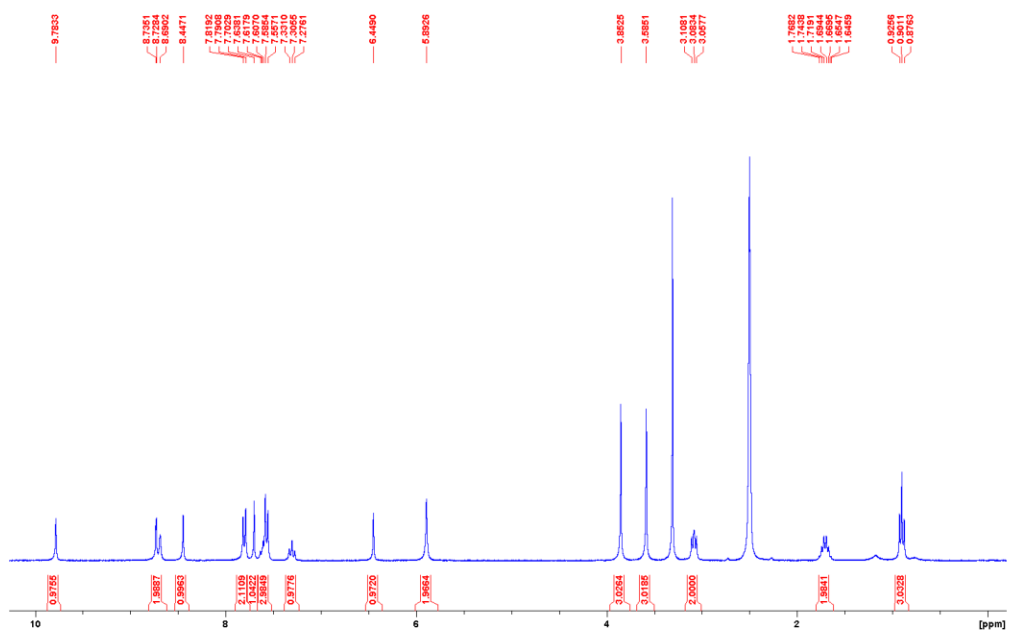
0.25 mmol (122 mg) vemurafenib, 0.25 mmol (69 mg) 4,5-dimethoxy-2-nitrobenzyl bromide and 1.25 mmol (173 mg) K_2CO_3 were dissolved in 10 ml DMF. The reaction mixture was stirred for one hour at rt. After evaporation the yellowish oil was redissolved in ethyl acetate, washed with brine and dried over Na_2SO_4 . The crude product was purified by flash silica gel chromatography with a gradient of petroleum ether and ethyl acetate to yield 0.026 mmol (18 mg, 11%) of a yellowish solid. Purity (HPLC) > 98%; mp: 199.9 °C; 1H NMR (300 MHz, DMSO- d_6): δ 0.90 (t, $^3J = 7.4$ Hz, 3H), 1.71 (tq, $^3J = 7.5$ Hz, $^3J = 7.4$ Hz, 2H), 3.08 (t, $^3J = 7.5$ Hz, 2H), 3.59 (s, 3H), 3.85 (s, 3H), 5.89 (s, 2H), 6.45 (s, 1H), 7.31 (ddd, $^3J_{HF} = 9.0$ Hz, $^3J = 8.7$ Hz, $^5J_{HF} = 1.6$ Hz, 1H), 7.57 (d, $^3J = 8.5$ Hz, 2H), 7.60 (dd, $^3J = 8.7$ Hz, $^4J_{HF} = 6.1$ Hz, 1H), 7.70 (s, 1H), 7.81 (d, $^3J = 8.5$ Hz, 2H), 8.45 (s, 1H), 8.69 (bs, 1H), 8.73 (d, $^4J = 2.0$ Hz, 1H), 9.78 (bs, 1H); ^{13}C NMR (75 MHz, DMSO- d_6): δ 12.51, 16.85, 45.62, 53.49, 55.80, 56.15, 108.37, 110.66, 112.27 (d, $^2J_{CF} = 22.7$ Hz), 115.12, 117.69, 117.82 (t, $^2J_{CF} = 23.5$ Hz), 122.90 (d, $^2J_{CF} = 15.5$ Hz), 126.35, 127.64, 128.65 (d, $^3J_{CF} = 8.1$ Hz), 129.02, 129.12, 130.99, 132.72, 136.63, 140.00, 141.27, 144.17, 147.79, 147.93, 152.22 (dd, $^1J_{CF} = 252.6$ Hz, $^3J_{CF} = 8.4$ Hz), 153.13, 155.51 (dd, $^1J_{CF} = 251.1$ Hz, $^3J_{CF} = 6.8$ Hz), 180.59; ^{19}F NMR (282 MHz, DMSO- d_6): δ -122.16, -116.71; LC-MS (ESI): m/z (rel. Intens.) 685.2 (100.0%), 687.0 (50.7%), 686.2 (47.3%), 688.1 (25.8%) $[MH]^+$.

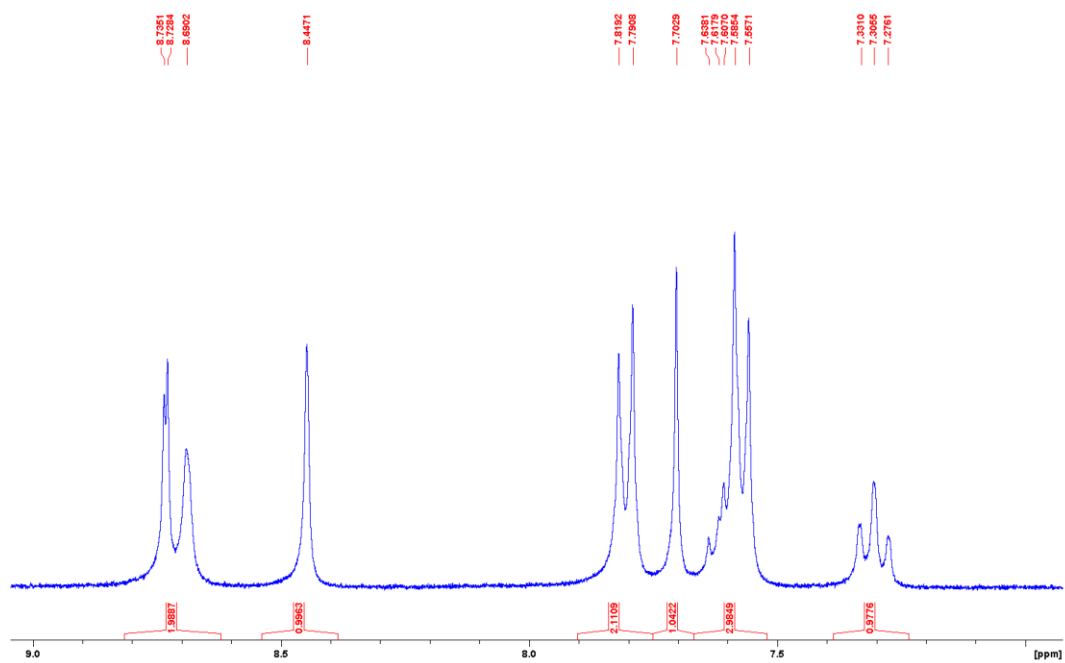




Molecular structure determined by X-ray crystallography. CCDC number: 1044607. Data accessible via <http://www.ccdc.cam.ac.uk>.

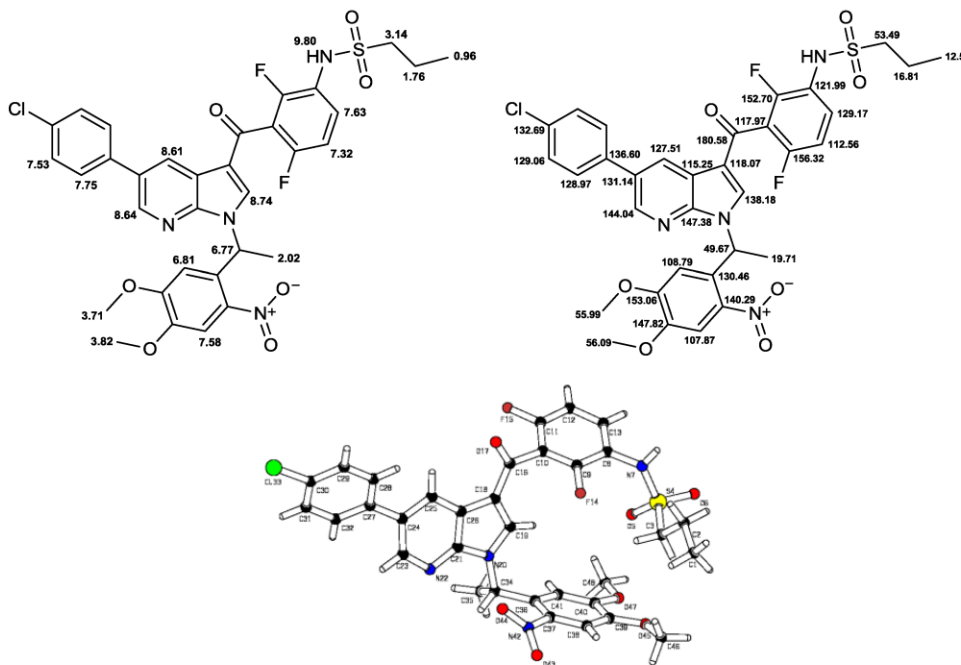
¹H NMR





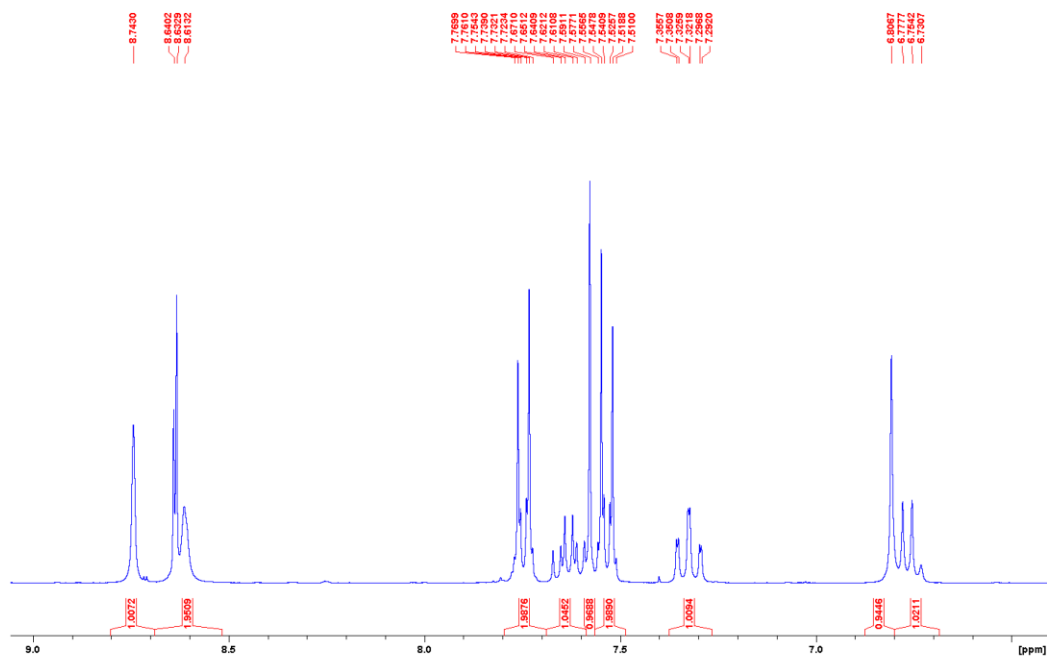
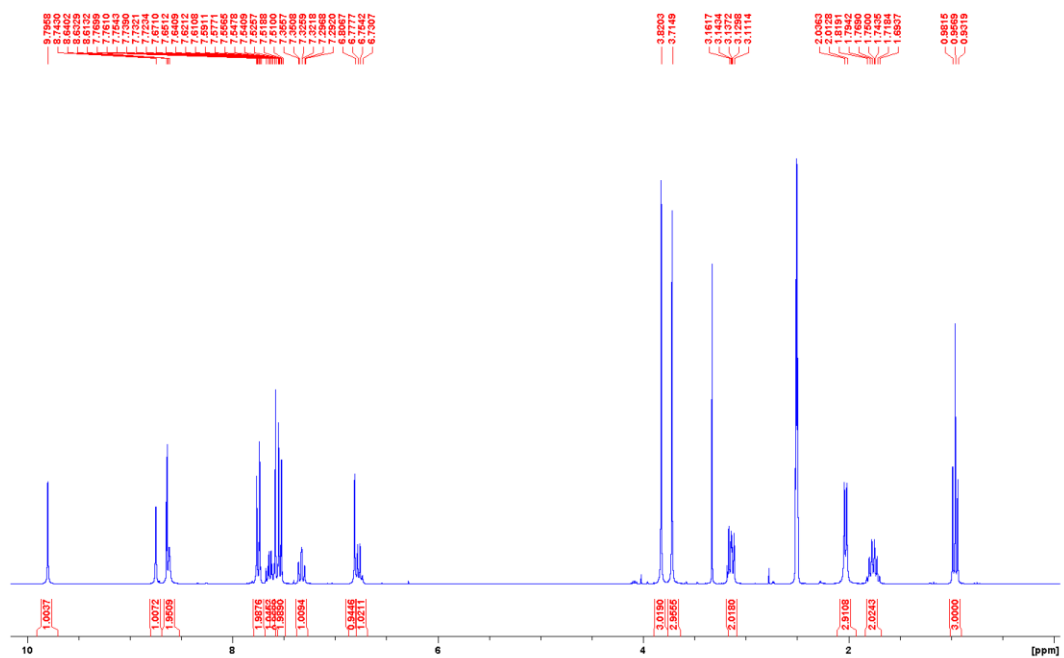
N-(3-(5-(4-chlorophenyl)-1-(1-(4,5-dimethoxy-2-nitrophenyl)ethyl)-1H-pyrrolo[2,3-b]pyridine-3-carbonyl)-2,4-difluorophenyl)propane-1-sulfonamide (3)

For the substitution of the hydroxyl function 1.0 mmol (230 mg) 1-(4,5-dimethoxy-2-nitrophenyl)ethanol was dissolved in 8 ml dichloromethane and 3.0 mmol (0.28 ml) PBr_3 , diluted with 1 ml dichloromethane, was added dropwise at 0 °C. After stirring 30 min at 0 °C and another 15 min at rt the reaction mixture was washed with brine, dried over Na_2SO_4 , filtered and used after evaporation without further purification. The formed 1-(1-bromoethyl)-4,5-dimethoxy-2-nitrobenzene was dissolved in 15 ml DMF. 0.6 mmol (295 mg) vemurafenib and 2.4 mmol (330 mg) K_2CO_3 were added and stirred over night at rt. After evaporation the yellowish oil was redissolved in ethyl acetate, washed with brine and dried over Na_2SO_4 . Flash silica gel chromatography with a gradient of petroleum ether and ethyl acetate yielded 0.14 mmol (98 mg, 23%) of a yellowish solid. Purity (HPLC) > 98%; mp: 217.6 °C; ^1H NMR (300 MHz, DMSO-d_6): δ 0.96 (t, $^3J = 7.5$ Hz, 3H), 1.71 (tq, $^3J = 7.6$ Hz, $^3J = 7.5$ Hz, 2H), 2.02 (d, $^3J = 7.1$ Hz, 3H), 3.14 (t, $^3J = 7.6$ Hz, 2H), 3.71 (s, 3H), 3.82 (s, 3H), 6.77 (q, $^3J = 7.1$ Hz, 1H), 6.81 (s, 1H), 7.32 (ddd, $^3J = 8.9$ Hz, $^3J_{\text{HF}} = 8.8$ Hz, $^5J_{\text{HF}} = 1.5$ Hz, 1H), 7.53 (d, $^3J = 8.8$ Hz, 2H), 7.58 (s, 1H), 7.63 (ddd, $^3J = 8.9$ Hz, $^4J_{\text{HF}} = 5.9$ Hz, $^4J_{\text{HF}} = 5.9$ Hz, 1H), 7.75 (d, $^3J = 8.8$ Hz, 2H), 8.61 (bs, 1H), 8.64 (d, $^6J = 2.2$ Hz, 1H), 8.74 (s, 1H), 9.80 (bs, 1H); ^{13}C NMR (75 MHz, DMSO-d_6): δ 12.59, 16.81, 19.71, 49.67, 53.49, 55.99, 56.09, 107.87, 108.79, 112.56 (dd, $^3J_{\text{CF}} = 22.8$ Hz, $^5J_{\text{CF}} = 2.8$ Hz), 115.25, 117.97 (dd, $^2J_{\text{CF}} = 24.2$ Hz, $^2J_{\text{CF}} = 21.9$ Hz), 118.07, 121.99 (dd, $^2J_{\text{CF}} = 13.5$ Hz, $^4J_{\text{CF}} = 3.4$ Hz), 127.51, 128.97, 129.06, 129.17 (d, $^4J_{\text{CF}} = 0.2$ Hz), 130.46, 131.14, 132.69, 136.60, 138.18, 140.29, 144.04, 147.38, 147.82, 152.70 (dd, $^1J_{\text{CF}} = 250.2$ Hz, $^3J_{\text{CF}} = 8.4$ Hz), 153.06, 156.32 (dd, $^1J_{\text{CF}} = 247.2$ Hz, $^3J_{\text{CF}} = 6.6$ Hz), 180.58; ^{19}F NMR (282 MHz, DMSO-d_6): δ -121.45, -116.50; LC-MS (ESI): m/z (rel. Intens.) 699.2 (100.0%), 700.3 (25.6%), 701.2 (47.8%), 702.2 (30.9%) $[\text{MH}]^+$.



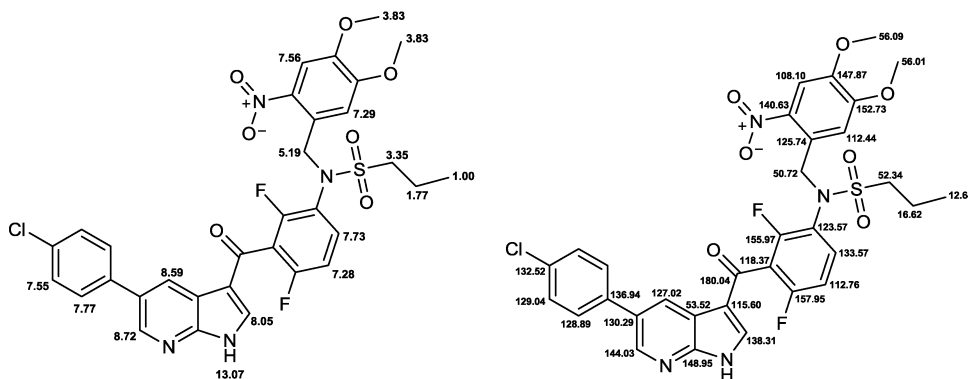
Molecular structure determined by X-ray crystallography. CCDC number: 1044608. Data accessible via <http://www.ccdc.cam.ac.uk>.

¹H NMR

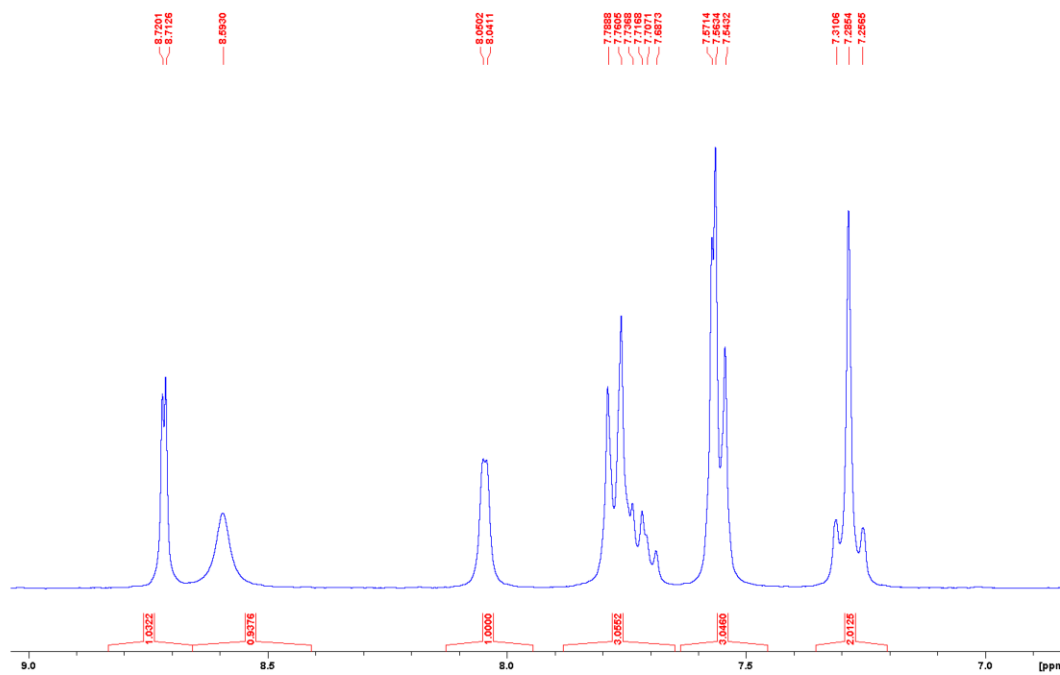
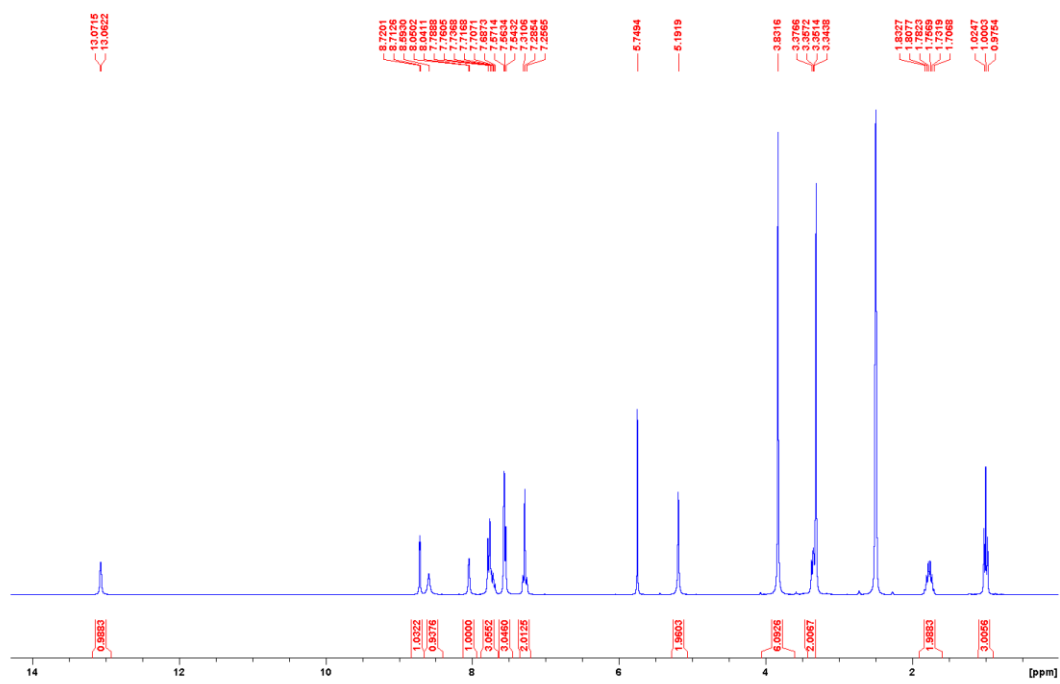


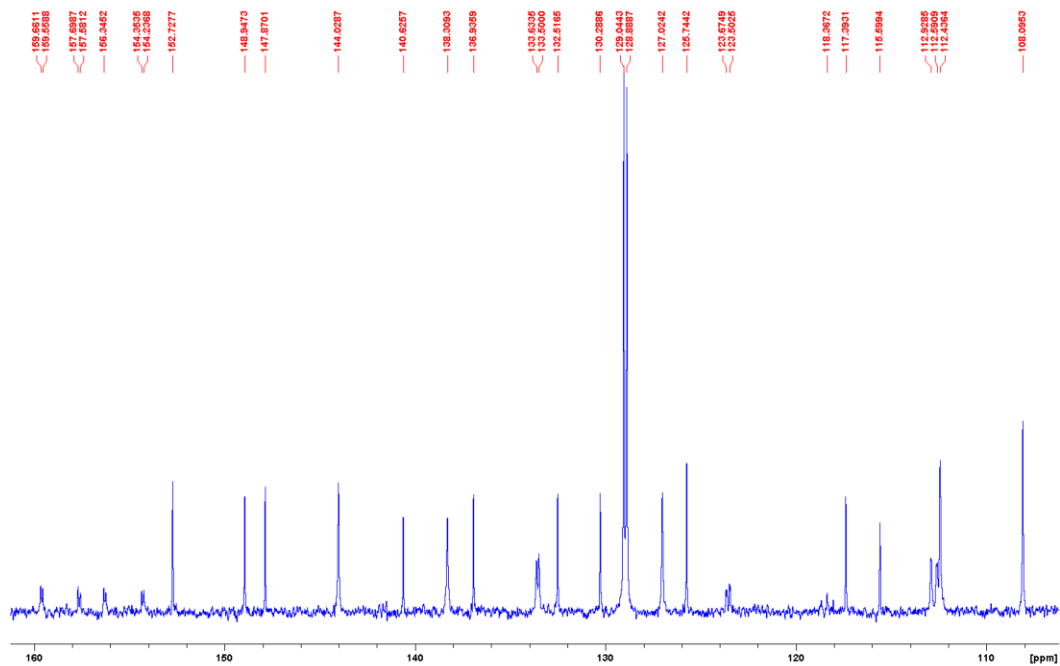
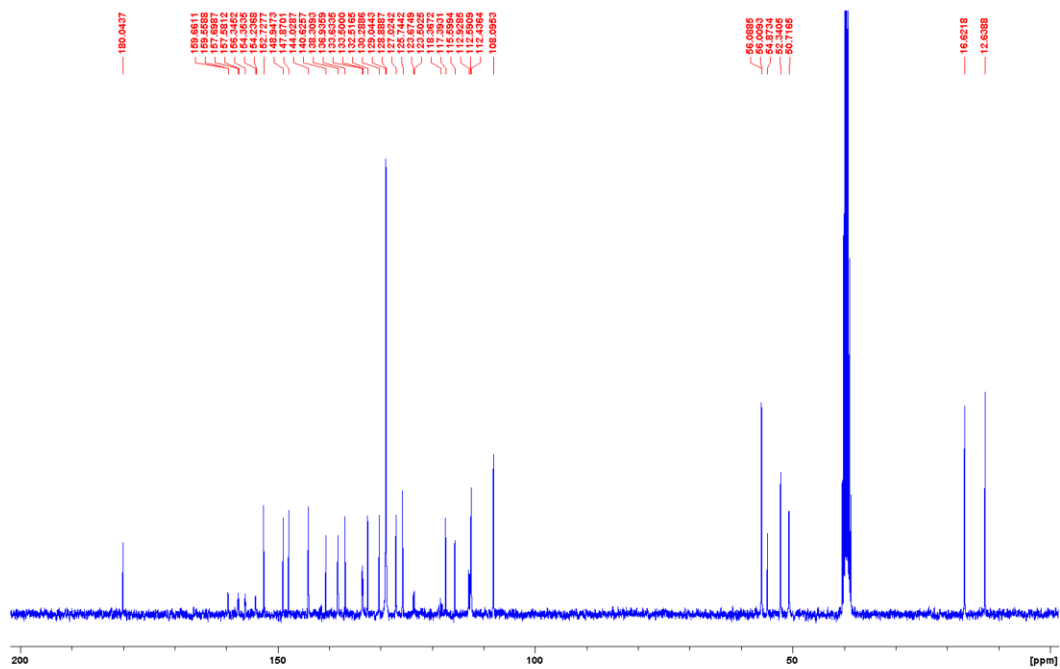
N-(3-(5-(4-chlorophenyl)-1H-pyrrolo[2,3-b]pyridine-3-carbonyl)-2,4-difluorophenyl)-N-(4,5-dimethoxy-2-nitrobenzyl)propane-1-sulfonamide (4)

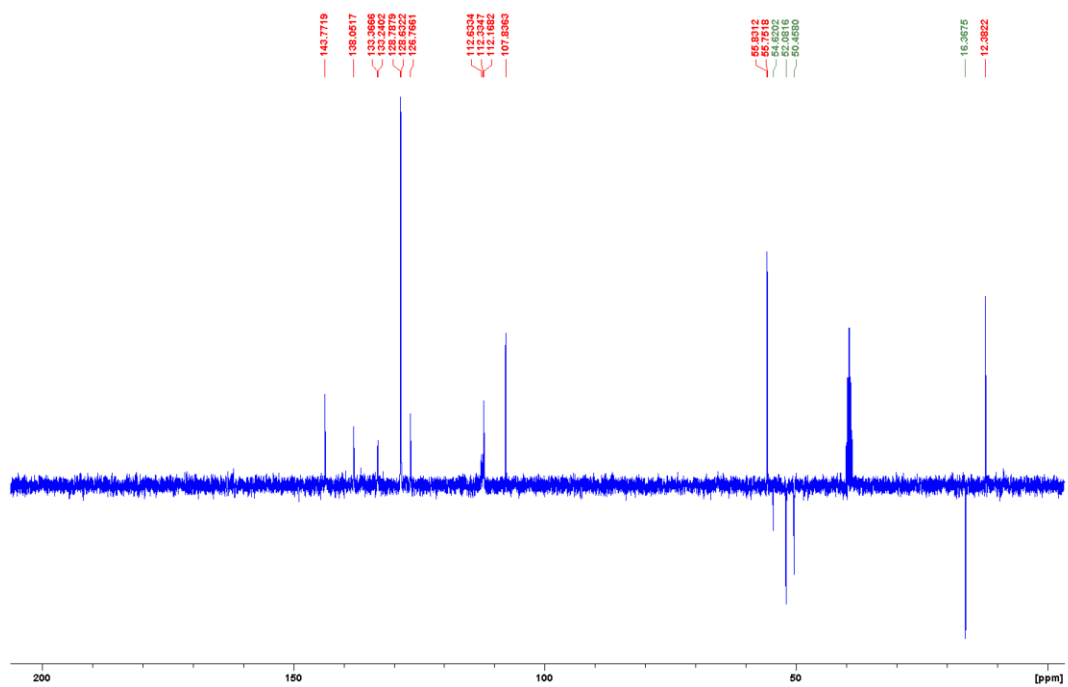
0.5 mmol (245 mg) vemurafenib and 0.7 mmol (179 mg) 4,5-dimethoxy-2-nitrobenzyl bromide were dissolved in 15 ml DMF. An amount of 2.0 mmol (0.34 ml) N,N-diisopropylethylamine (Hunig's base) was diluted with DMF to 5 ml and added dropwise over 30 min. The mixture was stirred over night at rt. After evaporation the yellowish oil was redissolved in ethyl acetate, washed with brine and dried over Na₂SO₄. Flash silica gel chromatography with a gradient of petroleum ether and ethyl acetate yielded 0.1 mmol (67 mg, 20%) of a yellowish solid. Purity (HPLC) > 98%; mp: 237.0 °C; ¹H NMR (300 MHz, DMSO-d₆): δ 1.00 (t, ³J = 7.4 Hz, 3H), 1.77 (tq, ³J = 7.5 Hz, ³J = 7.4 Hz, 2H), 3.35 (t, ³J = 7.5 Hz, 2H), 3.83 (s, 6H), 5.19 (s, 2H), 7.28 (dd, ³J = 8.4 Hz, ³J_{HF} = 8.1 Hz, 1H), 7.29 (s, 1H), 7.55 (d, ³J = 8.5 Hz, 2H), 7.56 (s, 1H), 7.73 (ddd, ³J = 8.4 Hz, ⁴J_{HF} = 6.0 Hz, ⁴J_{HF} = 6.0 Hz, 1H), 7.77 (d, ³J = 8.5 Hz, 2H), 8.05 (d, ³J = 2.7, 1H), 8.59 (bs, 1H), 8.72 (d, ⁴J = 2.3 Hz, 1H), 13.07 (d, ³J = 2.7, 1H); ¹³C NMR (75 MHz, DMSO-d₆): δ 12.64, 16.62, 50.72, 52.34, 56.01, 56.09, 108.10, 112.44, 112.767 (dd, ²J_{CF} = 22.9 Hz, ⁴J_{CF} = 2.6 Hz), 115.60, 117.39, 118.377 (dd, ²J_{CF} = 23.6 Hz, ²J_{CF} = 22.8 Hz), 123.577 (dd, ²J_{CF} = 12.9 Hz, ⁴J_{CF} = 3.5 Hz), 125.74, 127.02, 128.89, 129.04, 130.29, 132.52, 133.57 (d, ³J_{CF} = 10.1 Hz), 136.94, 138.31, 140.63, 144.03, 147.87, 148.95, 152.73, 155.977 (dd, ¹J_{CF} = 252.4 Hz, ³J_{CF} = 8.8 Hz), 157.95 (dd, ¹J_{CF} = 250.3 Hz, ³J_{CF} = 7.7 Hz), 180.04; ¹⁹F NMR (282 MHz, DMSO-d₆): δ -116.33, -112.15; LC-MS (ESI): *m/z* (rel. Intens.) 685.2 (100.0%), 686.3 (45.2%), 687.2 (35.3%), 688.3 (15.7%) [MH]⁺. HRMS (EI): *m/z* calculated 684.1257, found 684.1264



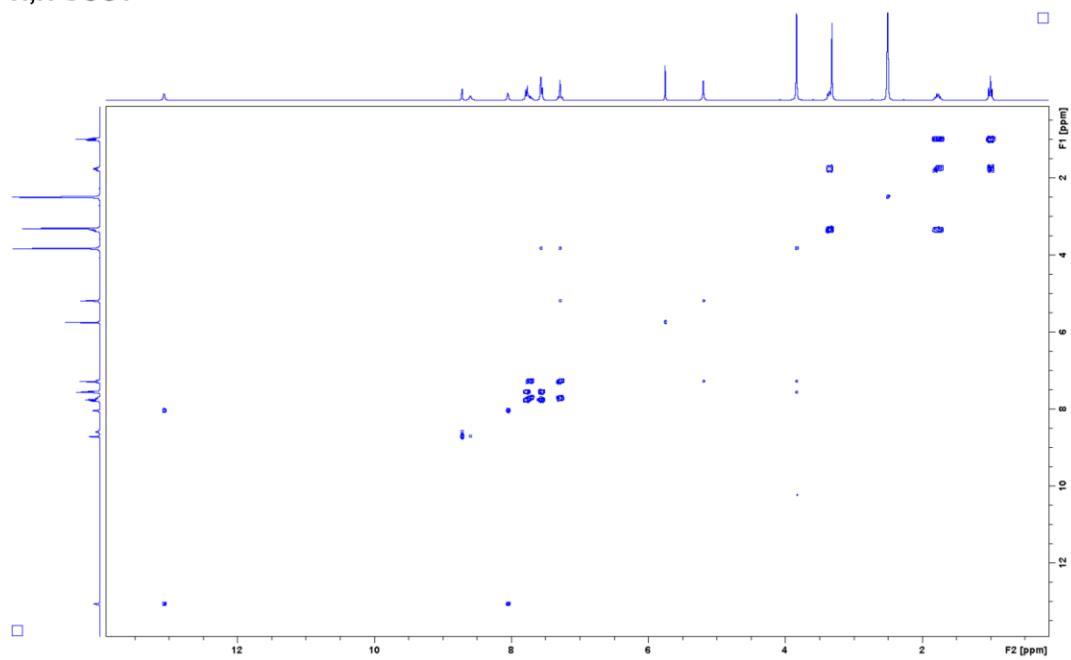
¹H NMR



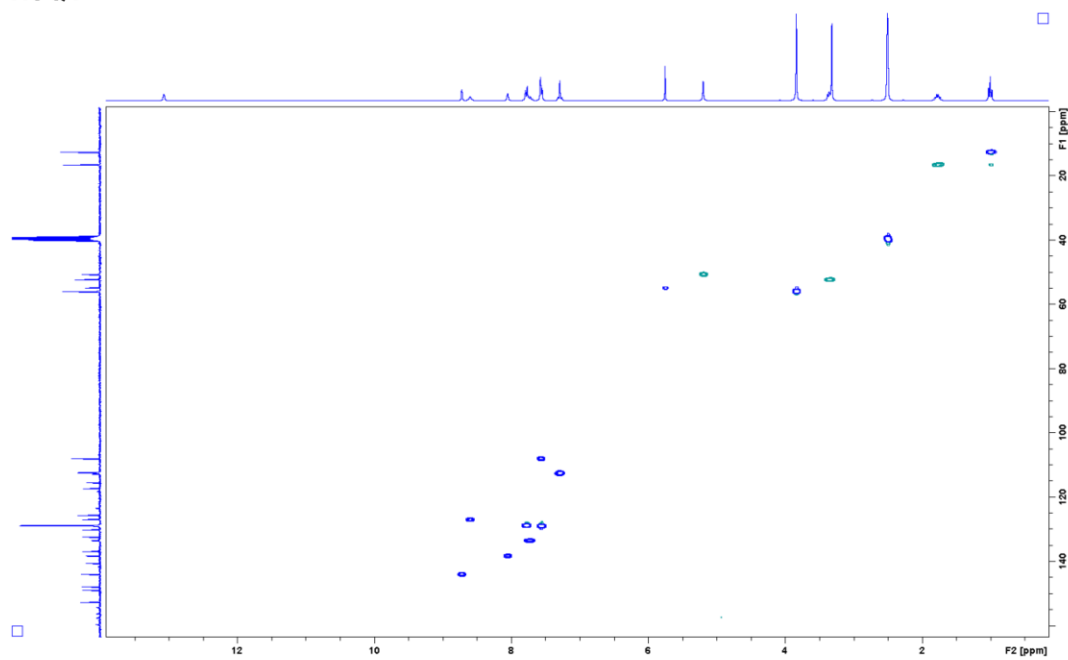
^{13}C NMR (udeft)

^{13}C NMR (dept135)

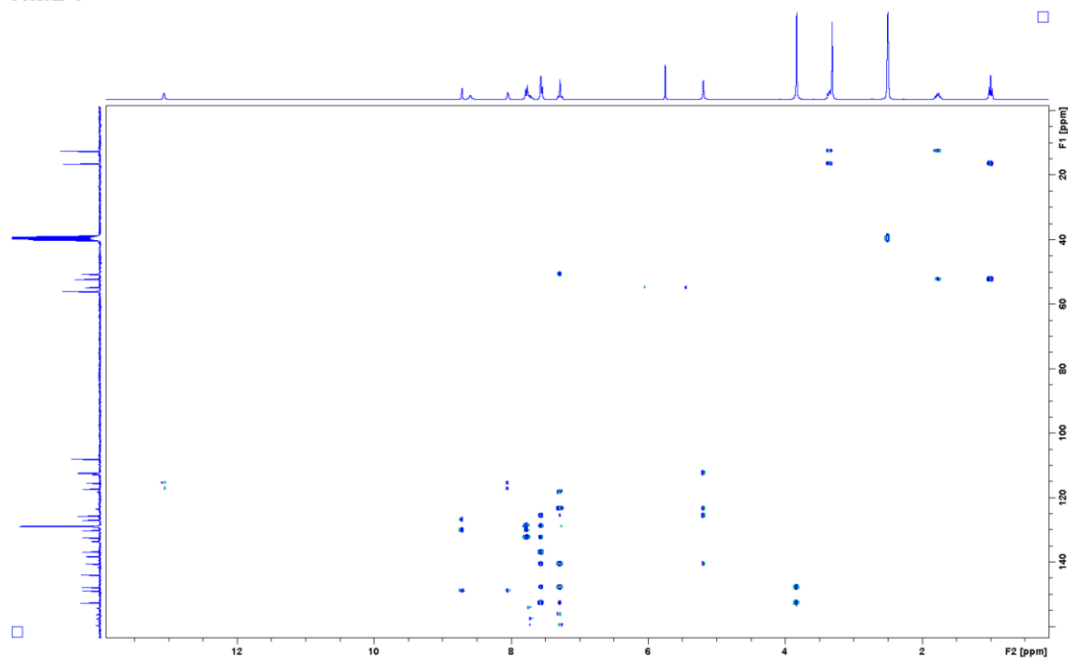
H,H COSY

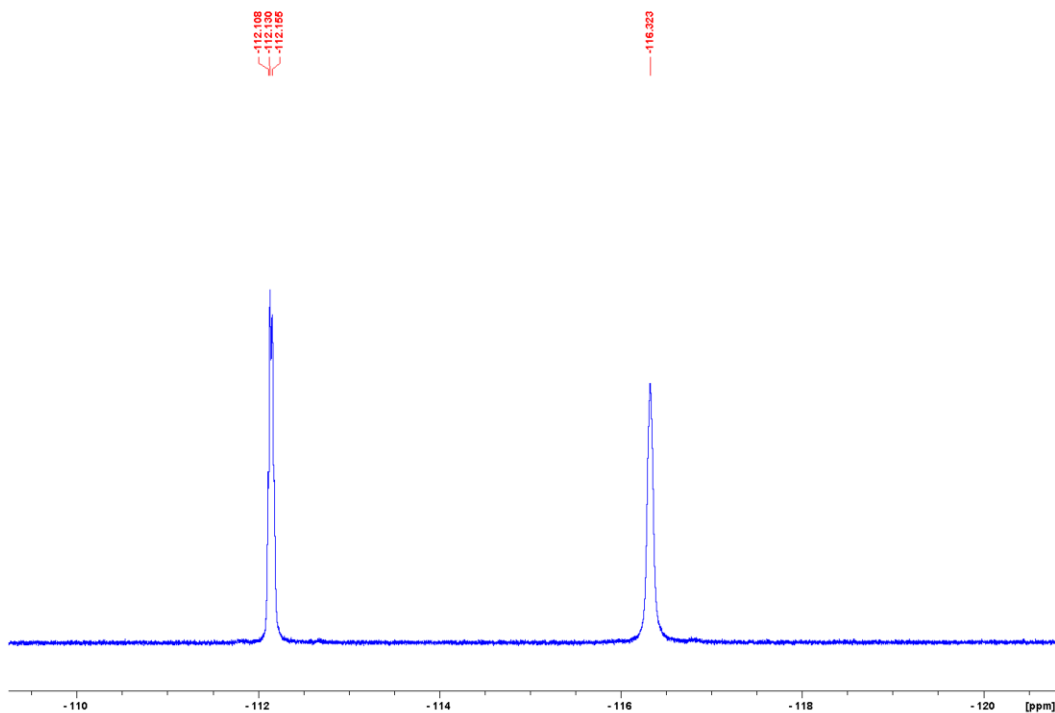


HSQC

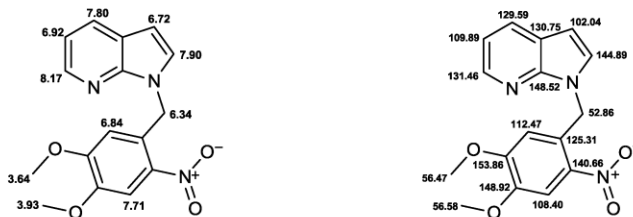


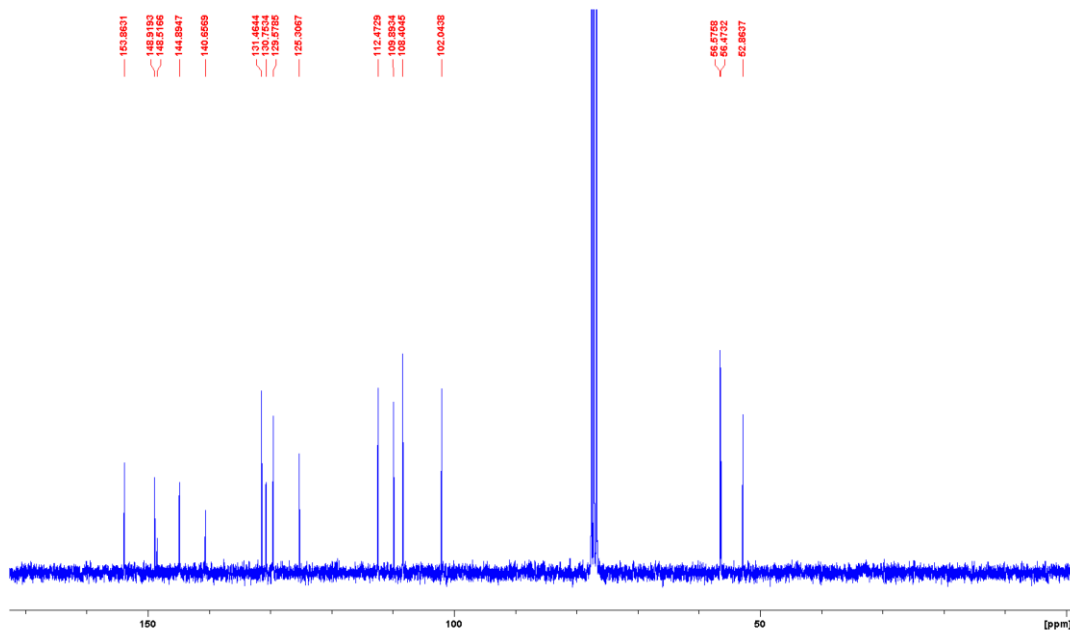
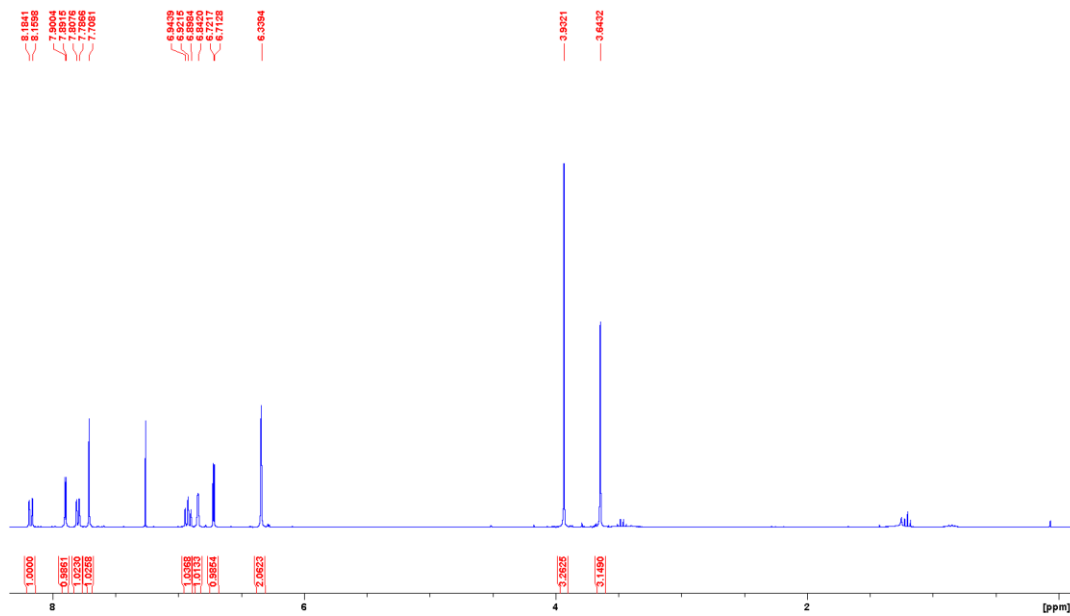
HMBC



^{19}F NMR**1-(4,5-dimethoxy-2-nitrobenzyl)-1H-pyrrolo[2,3-b]pyridine (5)**

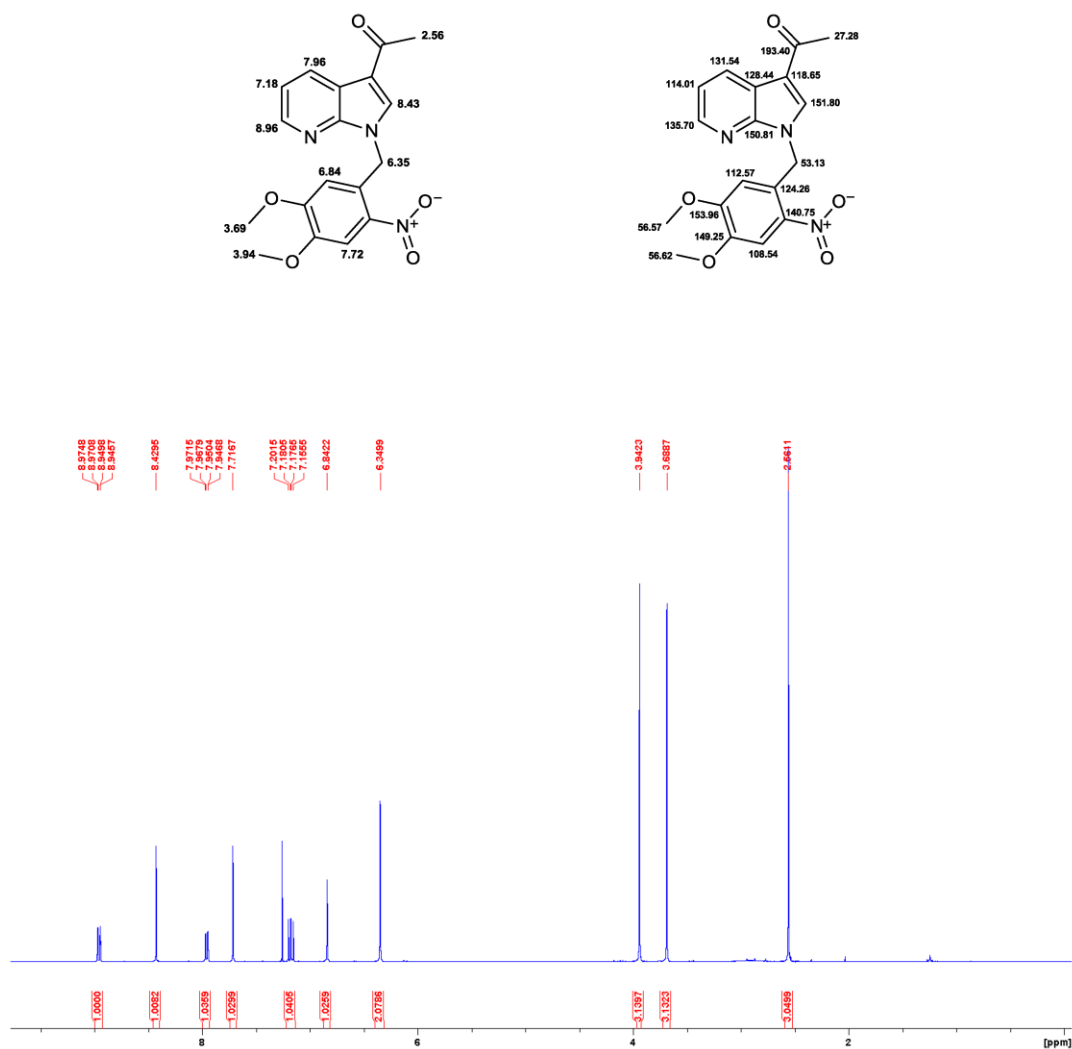
0.5 mmol (60 mg) 7-azaindole, 0.75 mmol (207 mg) 4,5-dimethoxy-2-nitrobenzyl bromide and 2.0 mmol (150 mg) Li_2CO_3 were dissolved in 20 ml DMF and stirred over night at rt. After evaporation the semisolid crude product was stirred with ice water and the aqueous phase poured out subsequently. This procedure was repeated twice. The remainder was dissolved in ethyl acetate, dried over Na_2SO_4 , filtered and reduced to a bright yellow solid (0.32 mmol, 100 mg, 64%). Purity (HPLC) > 98%; mp: 120.5 °C; ^1H NMR (300 MHz, CDCl_3): δ 3.64 (s, 3H), 3.93 (s, 3H), 6.34 (s, 2H), 6.72 (d, $^4J = 2.7$ Hz, 1 H), 6.84 (bs, 1H), 6.92 (t, $^3J = 6.8$ Hz, 1H), 7.71 (s, 1H), 7.80 (d, $^3J = 6.3$ Hz, 1H), 7.90 (d, $^3J = 2.7$ Hz, 1H), 8.17 (d, $^3J = 7.3$ Hz, 1H); ^{13}C NMR (75 MHz, CDCl_3): δ 52.86, 56.47, 56.58, 102.04, 108.40, 109.89, 112.47, 125.31, 129.59, 130.75, 131.46, 140.66, 144.89, 148.52, 148.92, 153.86; LC-MS (ESI): m/z (rel. Intens.) 514.1 (100.0%), 315.1 (15.9%) $[\text{MH}]^+$.

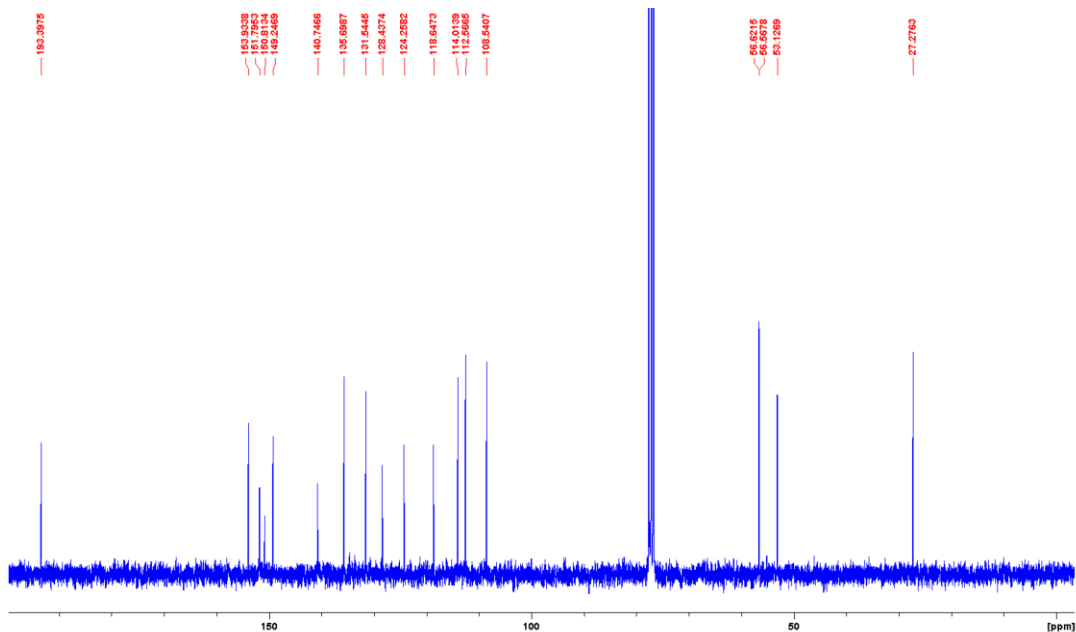




1-(1-(4,5-dimethoxy-2-nitrobenzyl)-1H-pyrrolo[2,3-b]pyridin-3-yl)ethanone (6)

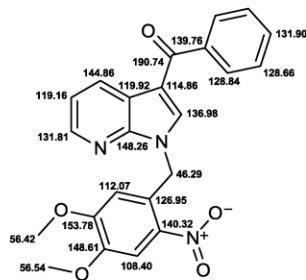
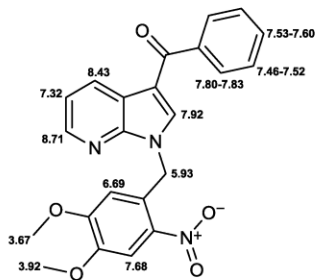
1.0 mmol (160 mg) 3-acetyl-7-azaindole, 1.5 mmol (414 mg) 4,5-dimethoxy-2-nitrobenzyl bromide and 4.0 mmol (300 mg) Li_2CO_3 were dissolved in 40 ml DMF and stirred over night at rt. After evaporation the crude product was washed with 20 ml ice water. The remainder was dissolved in dichloromethane, dried over Na_2SO_4 , filtered and reduced to a pale yellow solid (0.47 mmol, 167 mg, 47%). Purity (HPLC) > 98%; mp: 202.4 °C; ^1H NMR (300 MHz, CDCl_3): δ 2.56 (s, 3H), 3.69 (s, 3H), 3.94 (s, 3H), 6.35 (s, 2H), 6.84 (s, 1H), 7.18 (dd, $^3J = 7.5$ Hz, $^3J = 6.3$ Hz, 1H), 7.72 (s, 1H), 7.96 (dd, $^3J = 6.3$ Hz, $^4J = 1.1$ Hz, 1H), 8.43 (s, 1H), 8.96 (dd, $^3J = 7.5$ Hz, $^4J = 1.1$ Hz, 1H); ^{13}C NMR (75 MHz, CDCl_3): δ 27.28, 53.13, 56.57, 56.62, 108.54, 112.57, 114.01, 118.65, 124.26, 128.44, 131.54, 135.70, 140.75, 149.25, 150.81, 151.80, 153.93, 193.40; LC-MS (ESI): m/z (rel. Intens.) 356.1 (100.0%), 357.0 (27.6%), 358.1 (9.5%) $[\text{MH}]^+$.

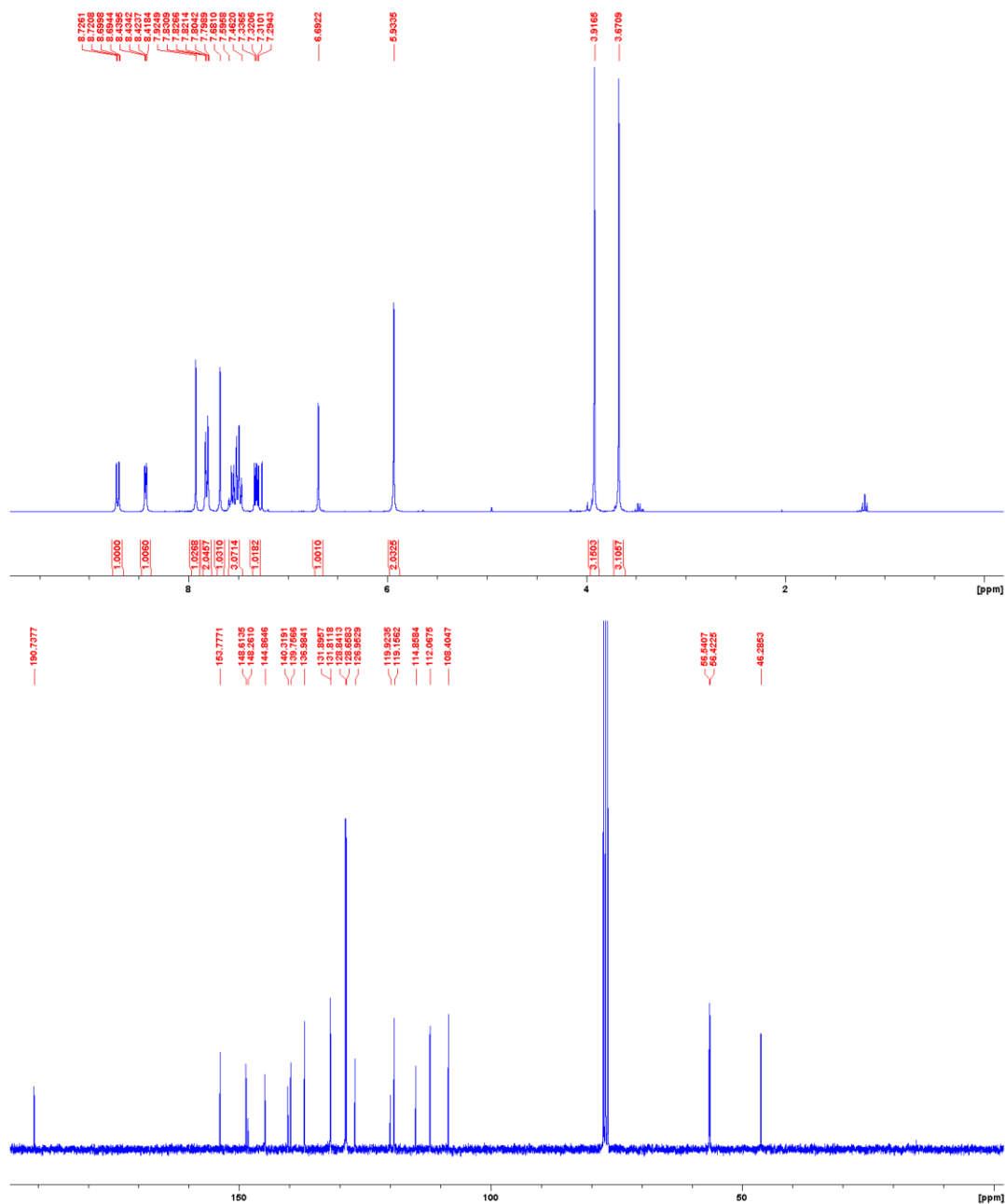




(1-(4,5-dimethoxy-2-nitrobenzyl)-1H-pyrrolo[2,3-b]pyridin-3-yl)(phenyl)methanone (7)

0.5 mmol (111 mg) 3-benzoyl-7-azaindole, 0.75 mmol (207 mg) 4,5-dimethoxy-2-nitrobenzyl bromide and 2.0 mmol (150 mg) Li_2CO_3 were dissolved in 15 ml DMF and stirred for 72 hours at rt. After evaporation the crude product was washed with 20 ml ice water. The remainder was dissolved in dichloromethane, dried over Na_2SO_4 , filtered and reduced to a pale yellow solid (0.21 mmol, 171 mg, 41%). Purity (HPLC) > 98%; mp: 162.1 °C; ^1H NMR (300 MHz, CDCl_3): δ 3.67 (s, 3H), 3.92 (s, 3H), 5.93 (s, 2H), 6.69 (s, 1H), 7.32 (dd, $^3J = 7.9$ Hz, $^3J = 4.8$ Hz, 1H), 7.46-7.52 (m, 2H), 7.53-7.60 (m, 1H), 7.68 (s, 1H), 7.80-7.83 (m, 2H), 7.92 (s, 1H), 8.43 (dd, $^3J = 4.7$ Hz, $^4J = 1.6$ Hz, 1H), 8.71 (dd, $^3J = 7.9$ Hz, $^4J = 1.6$ Hz, 1H); ^{13}C NMR (75 MHz, CDCl_3): δ 46.29, 56.42, 56.54, 108.40, 112.07, 114.86, 119.16, 119.92, 126.95, 128.66, 128.84, 131.81, 131.90, 136.98, 139.76, 140.32, 144.86, 148.26, 148.61, 153.78, 190.74; LC-MS (ESI): m/z (rel. Intens.) 418.4 (100.0%), 419.3 (18.6%) $[\text{MH}]^+$.

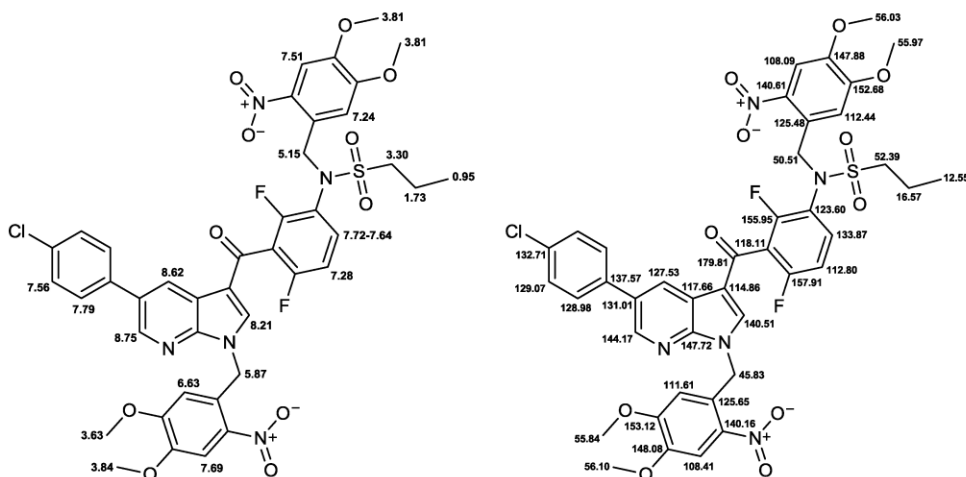




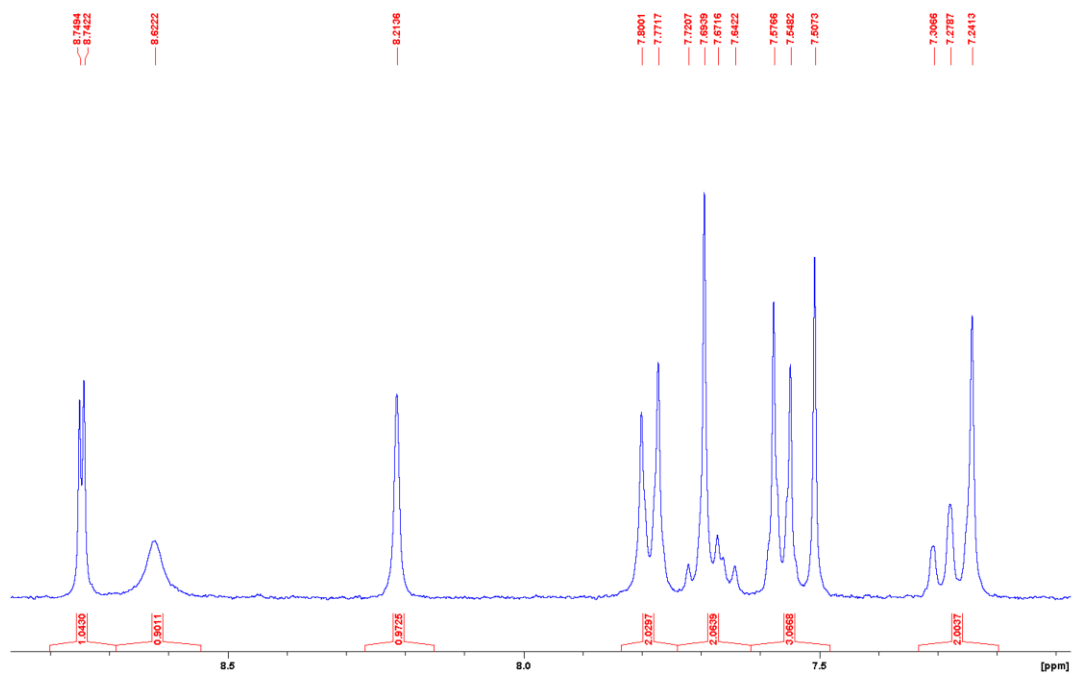
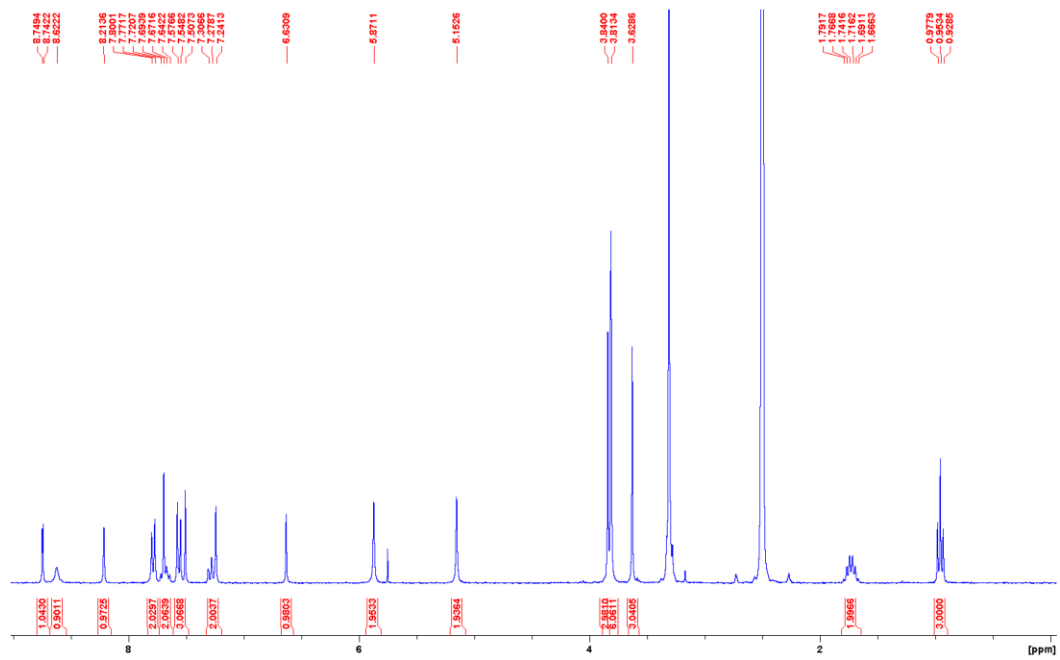
N-(3-(5-(4-chlorophenyl)-1-(4,5-dimethoxy-2-nitrobenzyl)-1H-pyrrolo[2,3-b]pyridine-3-carbonyl)-2,4-difluorophenyl)-N-(4,5-dimethoxy-2-nitrobenzyl)propane-1-sulfonamide (8)

0.5 mmol (245 mg) vemurafenib and 0.7 mmol (179 mg) 4,5-dimethoxy-2-nitrobenzyl bromide were dissolved in 15 ml DMF. An amount of 2.0 mmol (0.34 ml) N,N-

diisopropylethylamine (Hunig's base) was diluted with DMF to 5 ml and added dropwise over 30 min. The mixture was stirred over night at rt. After evaporation the yellowish oil was redissolved in ethyl acetate, washed with brine and dried over Na_2SO_4 . Flash silica gel chromatography with a gradient of petroleum ether and ethyl acetate yielded 0.1 mmol (100 mg, 23%) of a yellowish solid. Purity (HPLC) > 98%; mp: 253.7 °C; ^1H NMR (300 MHz, DMSO-d₆): δ 0.95 (t, $^3J = 7.4$ Hz, 3H), 1.73 (tq, $^3J = 7.5$ Hz, $^3J = 7.4$ Hz, 2H), 3.30 (t, $J = 7.5$ Hz, 2H), 3.63 (s, 3H), 3.81 (s, 6H), 3.84 (s, 3H), 5.15 (s, 2H), 5.87 (s, 2H), 6.63 (s, 1H), 7.24 (s, 1H), 7.28 (dd, $^3J = 8.4$ Hz, $^3J_{\text{HF}} = 8.4$ Hz, 1H), 7.51 (s, 1H), 7.56 (d, $^3J = 8.5$ Hz, 2H), 7.72-7.64 (m, 1H), 7.69 (s, 1H), 7.79 (d, $^3J = 8.5$ Hz, 2H), 8.21 (s, 1H), 8.62 (bs, 1H), 8.75 (d, $^4J = 2.2$ Hz, 1H); ^{13}C NMR (75 MHz, DMSO-d₆): δ 12.55, 16.57, 45.83, 50.51, 52.39, 55.84, 55.97, 56.03, 56.10, 108.09, 108.41, 111.61, 112.44, 112.80 (dd, $^2J_{\text{CF}} = 22.1$ Hz, $^4J_{\text{CF}} = 3.3$ Hz), 114.86, 117.66, 118.11 (dd, $^2J_{\text{CF}} = 26.1$ Hz, $^2J_{\text{CF}} = 23.2$ Hz), 123.60 (dd, $^2J_{\text{CF}} = 11.9$ Hz, $^4J_{\text{CF}} = 3.0$ Hz), 125.48, 125.65, 127.53, 128.98, 129.07, 131.01, 132.71, 133.87 (d, $^3J_{\text{CF}} = 10.2$ Hz), 136.57, 140.16, 140.51, 140.61, 144.17, 147.72, 147.88, 148.08, 152.68, 153.12, 155.95 (dd, $^1J_{\text{CF}} = 251.7$ Hz, $^3J_{\text{CF}} = 7.3$ Hz), 157.91 (dd, $^1J_{\text{CF}} = 250.7$ Hz, $^3J_{\text{CF}} = 7.0$ Hz), 179.81; ^{19}F NMR (282 MHz, DMSO-d₆): δ -111.99, -112.15; LC-MS (ESI): m/z (rel. Intens.) 880.2 (100.0%), 882.3 (30.3%), 881.2 (24.2%) $[\text{MH}]^+$.



¹H NMR



Synthesis of caged amino acids.

The DMNB and *tert*-butyloxycarbonyl (Boc) protected L-alanine (Boc-Ala-DMNB) was synthesized as described in⁴. A solution of BOC protected L-alanine (Boc-Ala) in toluene was treated with 4,5-dimethoxy-2-nitrobenzyl bromide in the presence of DBU and stirred at 80 °C for one hour. The crude product was filtered, washed with brine, dried over Na₂SO₄ and purified by flash silica gel chromatography.

Test compound purity via HPLC analysis.

HPLC analysis was performed on a Hewlett Packard 1050 Series with a Phenomenex Kinetex™ C8, 5 μm (4.6 mm × 150 mm) column. Injection volume of the methanolic compound solution was 20 μl. As mobile phase (flow rate 1.5 ml/min) served a gradient of KH₂PO₄ buffer (0.01 M, pH 2.3) and methanol over 14 min. The detection wavelength was 254 nm. All key compounds submitted to biological assays were proven by this method to show ≥ 98% purity.

NMR.

¹H, ¹³C and ¹⁹F NMR spectra were recorded on a Bruker Avance III 300 instrument at 300 K with a multinuclear probe head using the manufacturer's pulse programs. Spectra were referenced to internal DMSO-*d*₆/CHCl₃ (¹H NMR: δ 2.50/7.26 ppm), internal DMSO-*d*₆/CDCl₃ (¹³C NMR: δ 39.5/77.2 ppm) *resp.* external CFC₃ (¹⁹F NMR: δ 0.0 ppm). The following NMR abbreviations are used: b (broad), s (singlet), d (doublet), t (triplet), m (unresolved multiplet). NMR assignments were determined by analysis of multidimensional spectra (H,H COSY, HSQC, HMBC). Images of ¹H NMR spectral data is provided for all key compounds (see Supplementary Note: Chemical synthesis and Characterization). Exemplary, twodimensional spectral data is provided for **4**.

LC-MS.

Samples were chromatographically separated utilizing an Agilent 1100 HPLC system consisting of a thermostated autosampler, diode array detection, and an Agilent ZORBAX® Eclipse XDB-C8, 5 μm (4.6 mm × 150 mm). Elution was achieved with a solvent gradient system of water and acetonitrile, with 0.1% of acetic acid and a flow rate of 1 ml/min. The eluent flow was splitted to the mass spectrometer.

Mass spectrometry was carried out using a Bruker Esquire ~LC instrument with electrospray ionization operating in the positive ion mode. Following parameters were used: drying gas nitrogen 8 l/min, nebulizer 35 psi, dry gas heating 350 °C, HV capillary 4000 V, HV EndPlate offset -500 V.

UV/Vis absorption spectra.

Spectra were recorded on UV/Vis spectrophotometer Varian Cary® 50 Scan, Agilent Technologies. UV/VIS absorbance was measured in methanol (compounds **1-4**) *resp.* DMSO (compounds **5-8**) as well as in PBS buffer with 10% DMSO. Compounds were diluted until peak absorbance was in a range of 0.6 to 0.8. Subsequently, graphs were normalized on

basis of area under the curve between 260 and 320 nm. Compound **8** was not soluble in the aqueous medium.

Photoactivation experiments.

For the photoactivation experiments compounds were dissolved in DMSO (1 mM) resp. in PBS buffer with 10% DMSO (0.01 mM). The solutions were irradiated at 365 nm (LED source: 12x Nichia NCSU033B, Sahlmann Photochemical Solutions, 100%, 5.4 W) up to 10 minutes. The solutions were stirred and cooled by compressed air flow during illumination. After 0.25, 0.5, 0.75, 1, 2, 3, 5 and 10 min of irradiation samples were taken. Subsequently, HPLC probes were 1:5 resp 1:1 diluted with methanol. Injection volume was 20 μ l (compounds **2-4**) resp. 30 μ l (compounds **5-7**). A Hewlett Packard 1050 Series with a Phenomenex Kinetex™ C8, 5 μ m (4.6 mm \times 150 mm) column was used. Mobile phase was a gradient mixture of KH₂PO₄ buffer (0.01 M, pH 2.3) and methanol over a runtime of 14 min. The detection wavelength was 254 nm (compounds **2-4**) resp. 300 nm (compounds **5-7**). Additional to HPLC retention time LC-MS was used to confirm identity.

Determination of the binding constants (Kds).

Binding affinities of vemurafenib, **2**, **3**, and **4** towards BRAF^{V600E} were measured in the KdELECTSM assay at DiscoverX (San Diego, CA, USA). KINOMEscan™ is a competition binding assay that quantitatively measures the ability of a compound to compete with an immobilized active-site directed ligand⁵. Binding constants (Kd values) were calculated from duplicate 11-point dose-response curves. The highest tested compound concentration was 30 μ M. The 3-fold serial dilution of each tested inhibitor was prepared in 100% DMSO. The final DMSO concentration in the assay was 1%. All determined dose-response curves are shown in Supplementary Figure 15.

Kinase profiling.

Vemurafenib and caged compounds **2** and **4** were screened against 140 kinases in the Premier Screen at the International Center for Kinase Profiling at the University of Dundee, Scotland. The used method was a radioactive filter binding assay using ³³P ATP, for details see references ^{6,7}. The substances were dissolved in DMSO at a tested concentration of 10 μ M. The mean percentage residual kinase activity and standard deviations of assay duplicates were determined. The complete dataset is shown in Supplementary Table 1.

Cell culture and proliferative assays.

SKMel13 cells were kindly provided by K. Dissanayake from the MRC Protein Phosphorylation Unit, College of Life Sciences, Dundee. SKMel28 cells were purchased from CLS Cell Lines Service GmbH. M14 and UACC62 cells were kindly provided by European Screening Port. SKMel28 cells were grown in DMEM medium with 2 mM L-Glutamine, 1 mM Sodium Pyruvate and 10% FCS. Other cells were grown in RPMI 1640 Glutamax with 10% FCS. All cells were incubated in a 5% CO₂ humidified atmosphere at 37 °C. For proliferation experiments, the cells were grown in cell flasks until approximately 90% confluency and then seeded to give 7000 cells in 100 μ l per well into 96-well CulturePlates™ (PerkinElmer,

Waltham, US). In addition to the test plates, one plate was prepared for reference measurement at day zero. All plates were incubated for 24 h at 37 °C in a humidified atmosphere with 5% CO₂. Compounds that were dissolved in 100% DMSO (v/v) were added to the test plates. The final DMSO concentration in the assay was 0.5% (v/v). Viability of the cells in the day zero control plates were determined on the same day without adding any compounds. For viability measurement the Resazurin assay was used. The shift in the fluorescence signal was measured at the LS55 Fluorescence spectrometer (PerkinElmer, Waltham, US). Test plates were incubated for further 48 h and cell viability was defined as just described. Measured raw data was converted into percent of cell growth by using the high control (0.5% DMSO (v/v) without compound) and the day zero control. For dose-response studies, 11 different concentrations of compounds were tested in duplicates. IC₅₀ values were calculated using the 4-parameter logistic fit option of GraphPad Prism 5.

Western blot analysis.

Cells were treated with the indicated concentrations of vemurafenib, **2**, **3**, and **4** for 1 h at 37 °C. The same experiments were repeated with irradiation. The compounds were irradiated at 365 nm (1.8 W) for five minutes, 30 min after addition to the cells. Cells were lysed and lysates immunoblotted with the indicated antibodies. The lysis buffer contained both phosphatase and protease inhibitors. Similar results were obtained in duplicate experiments.

Primary antibodies:

- p44/42 MAPK (Erk1/2) (137F5) rabbit m-ab (t-Erk) Ref: #4695S Cell signaling technology
- P-p44/42 MAPK (T202/Y204) (197G2) rabbit m-ab (p-Erk) Ref: #4377S Cell signaling technology
- P-Akt (T308) (244F9) rabbit mAb Ref: #4056S Cell signalling technology
- Anti-PKB alpha S742B 1st Bleed (t-Akt), 1 x 0,05 mg; 0,28 mg/ml (courtesy by the lab of Prof. Dario Alessi, MRC, Dundee, Scotland)

Secondary antibodies:

- Anti-rabbit IgG, HRP-linked Antibody Ref: #7074P2 Cell signalling technology
- Rabbit anti-sheep, HRP-linked Antibody (courtesy by the lab of Prof. Dario Alessi, MRC, Dundee, Scotland)

4. Supplementary References

1. Gaplovsky, M. *et al.* Photochemical reaction mechanisms of 2-nitrobenzyl compounds: 2-Nitrobenzyl alcohols form 2-nitroso hydrates by dual proton transfer, *Photochem. Photobiol. Sci.* **4**, 33 (2005).
2. Klán, P. *et al.* Photoremovable Protecting Groups in Chemistry and Biology: Reaction Mechanisms and Efficacy, *Chem. Rev.* **113**, 119–191 (2013).
3. Lin, W. *et al.* A Model for Light-Triggered Porphyrin Anticancer Prodrugs Based on ano-Nitrobenzyl Photolabile Group, *Eur. J. Org. Chem.* **2008**, 793–796 (2008).

4. Aoshima, H. Tanaka, D. & Kamimura, A. Synthesis of Photolabile Caged Amino Acids for Measuring Amino Acid Transporters, *Bioscience, Biotechnology and Biochemistry* **56**, 1086–1089 (2014).
5. Fabian, M. A. *et al.* A small molecule-kinase interaction map for clinical kinase inhibitors, *Nature Biotech.* **23**, 329–336 (2005).
6. Hastie, C. J. McLauchlan, H. J. & Cohen, P. Assay of protein kinases using radiolabeled ATP: a protocol, *Nature Protocols* **1**, 968–971 (2006).
7. Bain, J. *et al.* The selectivity of protein kinase inhibitors: a further update, *Biochem. J.* **408**, 297–315 (2007).

3.1.1 Additional data measured following publication of the article “Photoactivatable Prodrugs of Antimelanoma Agent Vemurafenib”

Release of active vemurafenib from its caged prodrugs was proved to be precisely controlled by UV irradiation in the paper “Photoactivatable Prodrugs of Antimelanoma Agent Vemurafenib”. The inhibitory activity was measured only upon irradiation of caged compounds. However, no local resolution of photoinduced release was demonstrated.

To prove that activity of vemurafenib can be restored spatially, immunofluorescence experiments were performed. SKMel13 melanoma cells which carry the BRAF^{V600E} mutation²¹² were used. The cells were seeded to give 16,000 cells in 50 μ l per well into a 96-half-well plate (#675986, Greiner Bio-One GmbH, Kremsmünster, Austria). The plate was incubated for 48 h at 37 °C in a humidified atmosphere with 5% CO₂. Vemurafenib and its photoactivatable prodrug **4** (compare Figure 14 for chemical structures) were dissolved in cell medium and added to the cells to give the end concentrations of 1 and 5 μ M, respectively.

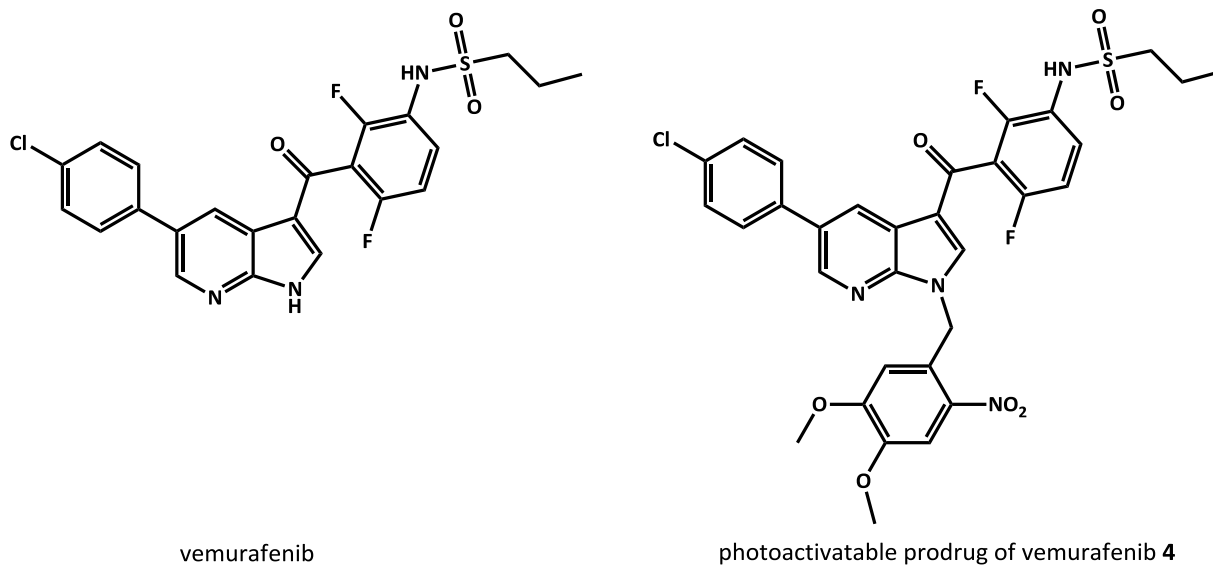


Figure 14: Chemical structures of vemurafenib and its photoactivatable prodrug 4. The caged compound **4** corresponds to the caged prodrug **2** in the article “Photoactivatable Prodrugs of Antimelanoma Agent Vemurafenib”.¹⁹³

The cells were incubated with the compounds for 1 h at 37 °C and were then fixed with 4% paraformaldehyde, washed with DPBS, and permeabilized with ice cold methanol. Afterwards

the cells were blocked with 5% goat serum and stained with phospho-Erk rabbit mAb (#4370, New England Biolabs GmbH, Frankfurt am Main, Germany). The primary Ab was diluted 1:500 in Ab dilution buffer (DPBS with 0.3% Triton X-100 and 1% BSA) prior to use. After incubating with primary Ab overnight at 4 °C, the cells were washed with DPBS and treated with secondary anti-rabbit Ab. The secondary Ab was conjugated with the fluorescent dye Alexa Fluor® 594 (#8889, New England Biolabs GmbH, Frankfurt am Main, Germany). The anti-rabbit Ab was diluted 1:1000 in Ab dilution buffer prior to use. After 2 h incubation at 37 °C in the dark, the cells were washed with DPBS and the fluorescence images were taken at the ImageXpress® Micro XL (Molecular Devices, Sunnyvale CA, USA). The magnification was 10x. Texas red filter set was used for the visualization. The results of this staining without UV irradiation are shown in Figure 15.

As previously described in the publication,¹⁹³ active vemurafenib blocks the constitutively active BRAF^{V600E} kinase. This inhibition causes the reduction of phosphorylated ERK in the cells. Therefore, active vemurafenib reduces the signal of phospho-ERK (also compare the western blot analysis in the paper).¹⁹³ On the contrary, the caged prodrug of vemurafenib **4** should not be active in the dark and should not block the phosphorylation of ERK. This could be verified by the immunofluorescence assay (Figure 15). Only vemurafenib diminishes the red signal of phosphorylated ERK. By contrast, the caged prodrug is inactive.

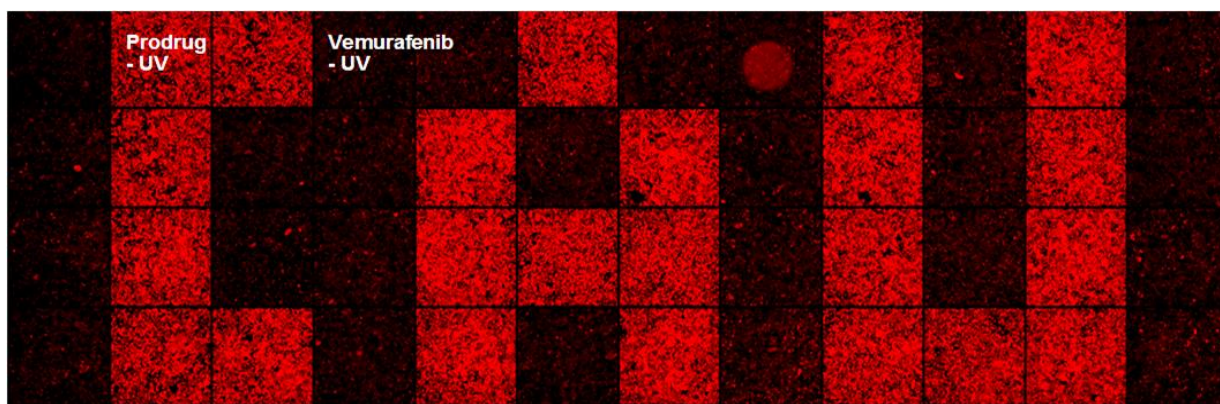


Figure 15: Phospho-ERK staining of melanoma SKMel13 cells after incubation with vemurafenib and the photoactivatable prodrug **4.** The top four rows of a 96-well-plate with treated cells are shown. The phosphorylated ERK is immunostained with a combination of primary and secondary Ab. The latter one is conjugated to a red fluorescent dye. The experiment was performed in dark without UV irradiation.

A variation of the immunofluorescence experiment described above was performed. Herein, the SKMel28 cells in four bottom rows of the same 96-well-plate were treated with prodrug **4** and DMSO as control. On the contrary to top rows, the bottom rows were now irradiated at 365 nm with 0.9 W for five minutes. Apart from that, the same protocol as for the not irradiated wells was applied. The results of this experiment are shown in Figure 16.

First, it could be demonstrated that the applied irradiation alone did not reduce the phosphorylation of ERK. Thus, the irradiated cells treated with DMSO still exhibited strong red signal of phospho-ERK (Figure 16). Furthermore, it was shown that the caged prodrug **4** could be spatially reactivated by irradiation. The caged compound inhibited the phosphorylation of ERK only where irradiated, compare Figures 15 and 16.

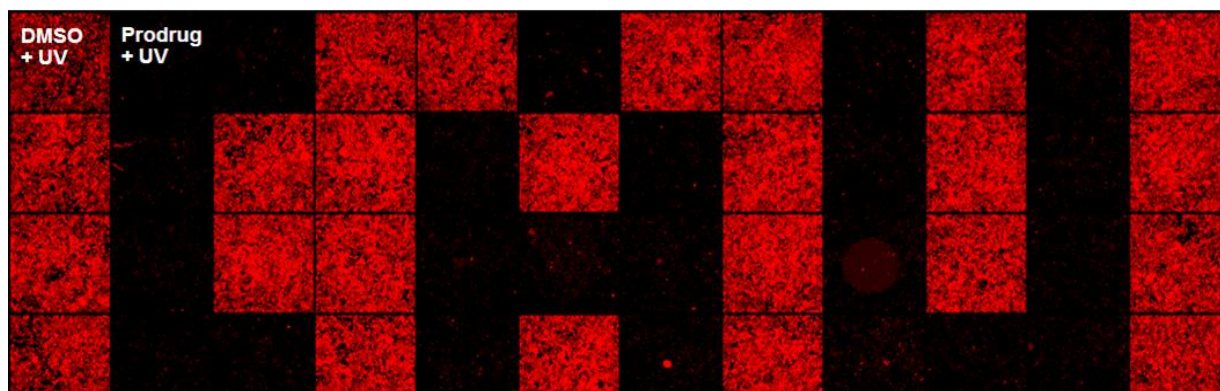


Figure 16: Phospho-ERK staining of melanoma SKMel13 cells after incubation with DMSO and the photoactivatable prodrug **4 of vemurafenib.** The bottom four rows of the same 96-well-plate as in Figure 15 are shown. These rows were irradiated at 365 nm with 0.9 W for five minutes. The phosphorylated ERK is immunostained with a combination of a primary and a secondary Ab. The latter one is conjugated to a red fluorescent dye.

The demonstrated immunofluorescence experiments proved the possibility of local control of action of protein kinase inhibitors *in vitro*. The photocaged inhibitors can be precisely reactivated by spatial resolution of applied irradiation.

3.2 Design, Synthesis, and Characterization of a Photoactivatable Caged Prodrug of Imatinib

Melanie Zindler, Boris Pinchuk, Christian Renn, Rebecca Horbert, Alexander Döbber, and Christian Peifer

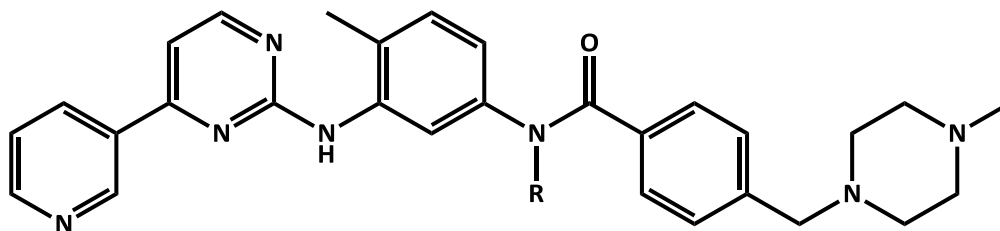
ChemMedChem **2015**, *10*, 1335 – 1338.

DOI: 10.1002/cmdc.201500163

Imatinib (Figure 6) was the first rationally developed protein kinase inhibitor.⁵ The inhibitor targets the ABL kinase and was originally approved for the therapy of Philadelphia chromosome positive CML in 2001.^{188, 189} Afterwards, it was discovered that besides ABL imatinib also potently inhibits other tyrosine kinases such as c-Kit and PDGFR.²¹³ Therefore, the agent was also approved for the treatment of further cancers including Philadelphia chromosome positive ALL²¹⁴ and gastrointestinal tumors (GIST).²¹⁵

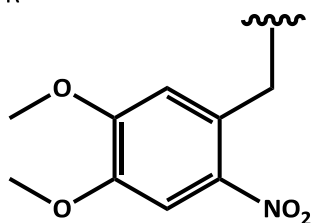
In the following paper¹⁹⁵ a photoactivatable prodrug of imatinib was described. The goal was to develop a pharmacological tool that could be highly useful for studying multiple signaling pathways affected by imatinib. Molecular modeling studies were applied to identify suitable pharmacophore sites in imatinib for attaching a PPG. Two possible positions were determined: the NH functions of the amide in the benzanilide and of the *N*-arylpyrimidine-2-amine. The amide function was utilized in the published paper. Two different PPGs were attached to this moiety: the DMNB group and the coumarin-4-ylmethyl group (compare Table 1). Therefore, two different photoactivatable derivatives of imatinib, compounds **5** and **6**, were yielded: (Figure 17).

Both caged compounds were photochemically characterized. It became obvious that the coumaryl-4-methyl protected derivative **6** was not eligible for biological applications due to very slow photoinduced release of imatinib. On the contrary, the DMNB-protected derivative **5** was successfully utilized as a photoactivatable prodrug of imatinib in a kinase assay.



compound 5:

R =



compound 6:

R =

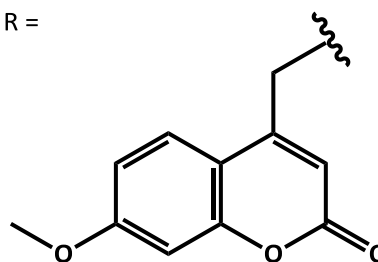


Figure 17: Chemical structures of photoactivatable prodrugs of imatinib.¹⁹⁵ DMNB- caged imatinib derivative **5** and coumarin-4-ylmethyl caged derivative **6** correspond to the compounds **2** and **3** in the article “Design, Synthesis, and Characterization of a Photoactivatable Caged Prodrug of Imatinib”, respectively.¹⁹⁵

Dr. Melanie Zindler synthesized the caged derivatives of imatinib. I performed the kinase assays together with Christian Renn who was my Master student at that time.

Design, Synthesis, and Characterization of a Photoactivatable Caged Prodrug of Imatinib

Melanie Zindler, Boris Pinchuk, Christian Renn, Rebecca Horbert, Alexander Döbber, and Christian Peifer*^[a]

Imatinib is the first protein kinase inhibitor approved for clinical use and is a seminal drug for the concept of targeted therapy. Herein we report on the design, synthesis, photokinetic properties, and in vitro enzymatic evaluation of a photoactivatable caged prodrug of imatinib. This approach allows spatial and temporal control over the activation of imatinib triggered by ultraviolet light. The successful application of the photoactivation concept to this significant kinase inhibitor provides further evidence for the caging technique as a feasible approach in the kinase field. The presented photoactivatable imatinib prodrug will be highly useful as a pharmacological tool to study the impact of imatinib toward biological systems in greater detail.

Since the introduction of the tyrosine kinase inhibitor imatinib^[1] (Gleevec/Glivec) into the market in 2001, protein kinase inhibitors have been successfully established mainly in targeted/personalized therapeutic approaches against cancer.^[2] Originally, the prototypical type-II inhibitor^[3] imatinib was approved for the therapy of Philadelphia chromosome-positive chronic myelogenous leukemia (Ph⁺-CML).^[4] In this way, at the molecular level the drug targets the Abelson murine leukemia viral oncogene homolog 1 (ABL1).^[5] In addition to ABL1, it was discovered that imatinib also potently inhibits further tyrosine kinases involved in malignancies including c-KIT and platelet-derived growth factor receptor (PDGF-R).^[6] Therefore, imatinib has become an option for the treatment of multiple cancers including gastrointestinal tumors (GIST).^[7,8] Along with the fact that significant progress has been made in cancer therapy, imatinib has also been used in countless experimental in vitro and in vivo studies.^[9–12] Considering the prominent role of this multi-kinase inhibitor in signal-transduction analysis, it would be beneficial to develop a photoactivatable imatinib prodrug.

Therefore, we aimed to provide a so-called caged compound that can be activated by irradiation with ultraviolet (UV) light.^[13] In general, the implementation of a photoremovable protecting group (PPG)^[14] provides spatial and temporal control over the release of a bioactive molecule.^[15] As consequence, significant concentrations of the bioactive compound


can be generated at a defined time point in an irradiated area of interest.^[16,17] The caged prodrug concept is essentially based on covalently blocking a pharmacophore moiety by a PPG, rendering the compound biologically inactive.^[18] For this purpose *o*-nitrobenzyl^[19] and coumarylmethyl^[20] derivatives have been widely used, among others, as PPGs in various biological applications.^[21–23] There are currently only few reports on photoactivatable kinase inhibitors. These include a caged small-molecule Rho kinase inhibitor,^[24] equivalents of Src kinase,^[21] and peptidic PKA inhibitors.^[25] Recently, a study about photo-switchable RET kinase inhibitors was published.^[26]

In this study, we set out to design, synthesize, and characterize a photoactivatable derivative of imatinib. First, by using molecular modeling we sought to define a suitable pharmacophoric position in imatinib to covalently attach the PPG. For this purpose we docked the type-II binder imatinib into the active site of our in-house PDGF-R β homology model in the DFG-out conformation.^[27] We also chose this receptor tyrosine kinase, as imatinib potently blocks PDGF-R β (IC₅₀ = 0.1 μ M),^[28] and an enzymatic PDGF-R β assay has been established by our research group to test the compounds.^[27,29]

The modeled ligand interaction diagram of imatinib in the ATP binding pocket of PDGF-R β revealed two prominent positions to covalently attach a PPG (Figure 1). Namely, the NH functions of the amide in the benzanilide and the *N*-arylpyrimidine-2-amine moiety both address key hydrogen bonds to PDGF-R β . Moreover, the tight ligand–protein complex suggested no steric tolerance at these positions within the binding pocket. In line with this notion, modeling of both *N*-*o*-nitrobenzyl-substituted imatinib derivatives in the active site of PDGF-R β did not result in plausible binding modes (not shown).

To determine if one of these NH positions in imatinib would be chemically suitable for subsequent PPG photocleavage, we first synthesized an imatinib fragment bound to 4,5-dimethoxy-2-nitrobenzyl (compound 1, Figure 2; the *N*-[(2-nitrophenyl)methyl]-*N*-phenylpyrimidin-2-amine fragment will be investigated in due course of this project). Next, a 1 mM DMSO solution of 1 was subjected to irradiation (see the Supporting Information for UV spectrum and details). We found that photo-induced cleavage of compound 1 at $\lambda = 365$ nm (5.4 W) resulted in rapid and nearly quantitative cleavage under these conditions, yielding the parent benzanilide fragment (and the leaving group 4,5-dimethoxy-2-nitrosobenzaldehyde based on MS analysis, not shown) within 5 min (Figure 3). We therefore subsequently focused on the amide NH function in imatinib to attach the PPG.

[a] Dr. M. Zindler, B. Pinchuk, C. Renn, R. Horbert, A. Döbber, Prof. Dr. C. Peifer
Christian Albrechts University of Kiel
Institute of Pharmacy, Gutenbergstr. 76, 24118 Kiel (Germany)
E-mail: cpeifer@pharmazie.uni-kiel.de

 Supporting information for this article is available on the WWW under
<http://dx.doi.org/10.1002/cmdc.201500163>.

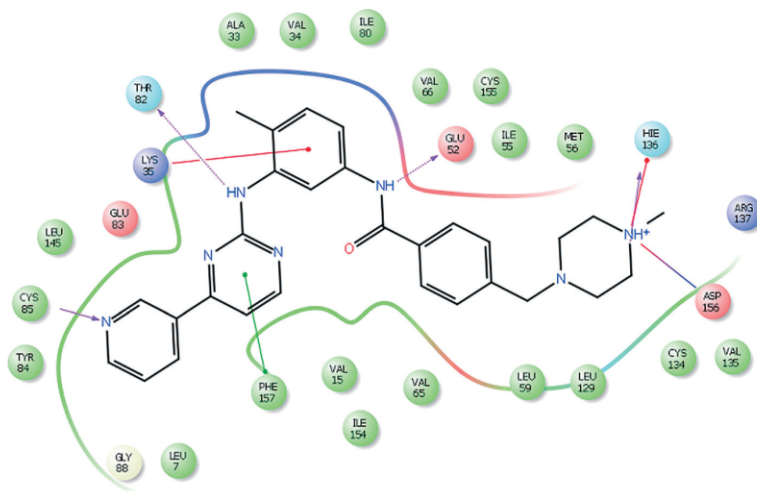


Figure 1. Modeled ligand interaction diagram of imatinib in the active site of a PDGF-R β homology model in the DFG-out conformation. Key ligand–protein interactions are shown. The binding mode of imatinib in the closely related kinase c-Src (PDB ID: 2OIQ)^[20] is highly similar (not shown).

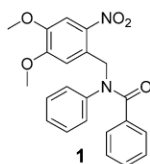


Figure 2. Photoactivatable imatinib fragment **1**. The compound contains the benzamide scaffold of imatinib which is caged at the amide with the 4,5-dimethoxy-2-nitrobenzyl (DMNB) moiety.

Motivated by these results, we designed two differently PPG-caged prodrugs at the amide function of imatinib that bears the 4,5-dimethoxy-2-nitrobenzyl (DMNB, **2**) and coumarylmethyl moieties (**3**), respectively (Figure 4). Both PPGs have been reported to be suitable for caged prodrug applications in biological settings.^[22]

We aimed to develop a straightforward synthetic strategy for the preparation of the planned caged prodrugs. Initially, our attempts toward base-catalyzed S_N reactions

directly with imatinib and 1-(bromomethyl)-4,5-dimethoxy-2-nitrobenzene were unsuccessful, as only the imatinib–piperazine *N*-DMNB alkylated product could be isolated (which was stable under irradiation; see Supporting Information). However, an S_N reaction using the core scaffold of imatinib 4-methyl-*N*3-[4-(3-pyridyl)pyrimidin-2-yl]benzene-1,3-diamine **4** with the benzyl-brominated PPG reagents DMNB-Br or coumarylbromomethyl yielded compounds **5a** and **5b**, respectively (Scheme 1). In turn, introduction of the 4-[(4-methylpiperazin-1-yl)methyl]benzamide side chain in the final step yielded both PPG-protected compounds **2** and **3**, respectively (Scheme 1).

With these caged prodrugs of imatinib in hand, we next evalu-

ated their photochemical properties. Based on the UV/Vis spectra of the compounds, we irradiated 1 mM solutions of **2** and **3** in DMSO for 12 min with light at a wavelength of 365 nm. Under these conditions, photocleavage of **3** was very poor, yielding only ~10% of imatinib (Supporting Information). In contrast, **2** was efficiently photocleaved within 10 min to produce imatinib (Figure 5) along with the leaving group 4,5-dimethoxy-2-nitrosobenzaldehyde as determined by MS analysis (not shown).

We next characterized the biological activity of imatinib and caged prodrug **2** in an enzymatic PDGF-R β assay without and with UV irradiation at $\lambda = 365$ nm. In this assay imatinib was found to potently inhibit PDGF-R β (IC₅₀ = 0.059 μ M); this is in good agreement with the reported value (IC₅₀ = 0.1 μ M).^[28] In line with our modeling data, caged compound **2** was signifi-

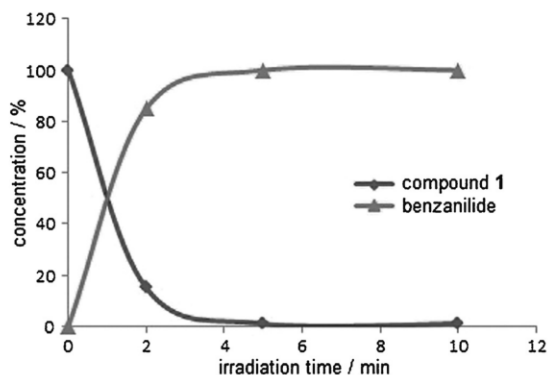


Figure 3. Time-dependent photoinduced cleavage of caged imatinib fragment **1** to yield benzanilide upon irradiation with UV light ($\lambda = 365$ nm, 5.4 W).

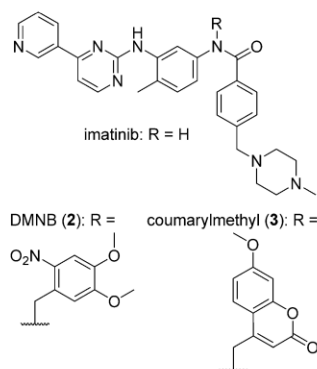
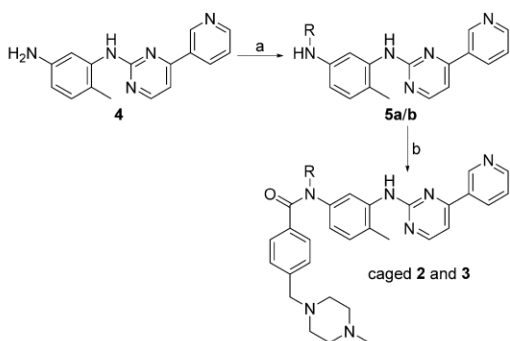


Figure 4. Chemical structures of imatinib and designed photoactivatable caged prodrugs **2** and **3**.



Scheme 1. Synthesis of caged imatinib derivatives **2** (R = DMNB) and **3** (R = coumarylmethyl). Reagents and conditions: a) DMNB-Br (for **5a**), 4-(bromomethyl)-7-methoxychromen-2-one (coumarylbromomethyl) (for **5b**), Li_2CO_3 , DMF; b) 4-[(4-methylpiperazin-1-yl)methyl]benzoyl chloride, pyridine, 0°C → RT. Full synthetic details are provided in the Supporting Information.

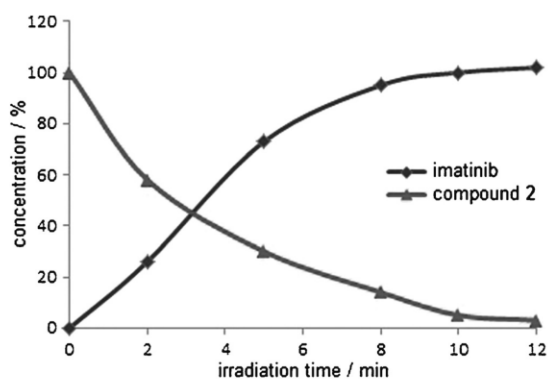


Figure 5. Time-dependent photoinduced cleavage of caged imatinib prodrug **2** upon irradiation with UV light ($\lambda = 365\text{ nm}$, 5.4 W). After 5 min irradiation, 70% of **3** was cleaved to produce imatinib.

cantly less biologically active without UV irradiation (**2** PDGF-R β IC₅₀ = 5.8 μM). In contrast, testing **2** in the assay irradiated at $\lambda = 365\text{ nm}$ (5.4 W) for 10 min revealed an inhibition of PDGF-R β (IC₅₀ = 0.089 μM) similar to that of native imatinib (Figure 6). Notably, the residual biological activity of caged prodrug **2** results from minor impurities of uncaged imatinib in the sample (~1% based on HPLC analysis). Thus, at total compound concentrations > 10 μM in the assay, the inhibitory effects on PDGF-R β cannot be differentiated. However, their difference regarding blockage of PDGF-R β is still significant in the range of typical in vitro assay concentrations (0.01–1 μM).

In conclusion, we have demonstrated that a caged prodrug of the kinase inhibitor imatinib could be successfully generated and characterized. Compound **2** was photoactivated by UV light at a wavelength of 365 nm within 10 min in an in vitro PDGF-R β assay to restore the biological activity of the parent imatinib. In contrast to imatinib, **1** can be almost quantitatively uncaged within 3 min. This indicates a significant influence of the leaving group (active inhibitor) toward the uncaging pro-

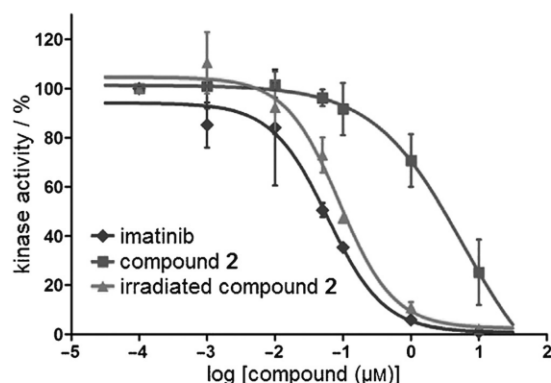


Figure 6. Biological activity of imatinib and caged prodrug **2** in an in vitro PDGF-R β assay without and with irradiation at $\lambda = 365\text{ nm}$ (5.4 W) for 10 min (\pm SD, $n = 3$, see Supporting Information for details).

cess. Thus, we will investigate further PPG systems in order to optimize the uncaging of imatinib. Our study further validates the powerful caging technique in the kinase field and provides a valuable pharmacological tool to study the biological effects of imatinib in novel settings and in greater detail. Finally, our approach holds great promise for future applications involving other kinase inhibitors as well.

Experimental Section

All modeling was performed on a DELL 8 core system. For preparation, visualization, and building the 3D structures, Maestro (version 10.0.013, release 2014-4, Schrödinger LLC, New York, NY, USA) was used.

Synthesis of *N*-(4,5-dimethoxy-2-nitrobenzyl)-*N*-(4-methyl-3-((4-(pyridine-3-yl)pyrimidine-2-yl)amino)phenyl)-4-((4-methylpiperazin-1-yl)methyl)benzamide (2): Compound **5a** (330 mg, 700 μmol) was dissolved in dry pyridine (20 mL). The reaction mixture was cooled to 0°C , and 4-[(4-methylpiperazin-1-yl)methyl]benzoyl chloride (288 mg, 1.00 mmol) was added in portions under a nitrogen atmosphere. The solution was stirred for 3 h at room temperature, and H_2O (100 mL) was added. The mixture was extracted with EtOAc ($3 \times 100\text{ mL}$), and the combined organic layers were dried over anhydrous Na_2SO_4 . The solvent was removed under vacuum, and the residue was purified by flash chromatography (SiO_2 , reversed phase, MeOH/ H_2O) to give compound **2** as a pale-yellow solid (40 mg, yield: 8%). $^1\text{H NMR}$ (300 MHz, $[\text{D}_2\text{O}]/\text{DMSO}$): $\delta = 2.09$ (s, 3H, pip- CH_3), 2.14 (s, 3H, CH_3), 2.21 (mc, 8H, pip-H-2,3,5,6), 3.33 (s, 2H, pip- CH_2), 3.74 (s, 3H, OCH_3), 3.82 (s, 3H, OCH_3), 5.38 (bs, 2H, CH_2), 6.79 (dd, 1H, $^3J = 8.1\text{ Hz}$, $^4J = 2.1\text{ Hz}$, ph-H-6), 7.03 (s, 1H, nitrobenz-H-6), 7.05 (d, 1H, $^3J = 8.1\text{ Hz}$, ph-H-5), 7.13 (d, 2H, $^3J = 8.2\text{ Hz}$, benz-H-3,5), 7.34 (d, 2H, $^3J = 8.2\text{ Hz}$, benz-H-2,6), 7.44 (d, 1H, $^3J = 5.2\text{ Hz}$, pyrim-H-5), 7.49 (ddd, 1H, $^3J = 8.0\text{ Hz}$, $^3J = 4.0\text{ Hz}$, pyr-H-5), 7.61 (s, 1H, nitrobenz-H-3), 7.62 (d, 1H, $^4J = 2.0\text{ Hz}$, ph-H-2), 8.36 (td, 1H, $^3J = 8.0\text{ Hz}$, $^4J = 2.0\text{ Hz}$, pyr-H-4), 8.44 (d, 1H, $^3J = 5.2\text{ Hz}$, pyrim-H-6), 8.69 (d, 1H, $^4J = 4.0\text{ Hz}$, pyr-H-6), 8.80 (s, 1H, pyrim-NH), 9.23 ppm (d, 1H, $^4J = 1.7\text{ Hz}$, pyr-H-2); $^{13}\text{C NMR}$ (75.5 MHz, $[\text{D}_2\text{O}]/\text{DMSO}$): $\delta = 17.5$ (q, CH_3), 45.6 (q, pip- CH_3), 50.6 (t, CH_2), 52.3, 54.6 (d, pip-C-2,3,5,6), 55.8, 55.9 (q, OCH_3), 61.4 (t, pip- CH_2), 107.9 (d, pyrim-C-5), 108.2 (d, nitrobenz-C-3), 110.5 (d, nitrobenz-C-6),



122.5 (d, ph-C-2), 122.9 (d, ph-C-6), 123.7 (d, pyr-C-5), 127.3 (s, nitrobenz-C-2), 128.1 (d, benz-C-3,5), 128.3 (d, benz-C-2,6), 129.5 (s, ph-C-1), 130.5 (d, ph-C-5), 131.9 (s, pyr-C-3), 134.1 (d, pyr-C-4), 134.3 (s, benz-C-4), 138.3 (s, ph-C-4), 139.9 (s, ph-C-3), 140.3 (s, benz-C-1), 140.7 (s, nitrobenz-C-1), 147.3 (s, nitrobenz-C-5), 148.0 (d, pyr-C-2), 151.4 (d, pyr-C-6), 152.9 (s, nitrobenz-C-4), 159.2 (d, pyrim-H-6), 160.6 (s, pyrim-C-4), 161.5 (s, pyrim-C-2), 169.9 ppm (s, C=O); IR (ATR): $\bar{\nu}$ = 2836 (C–H), 1643 (C=O), 1574, 1330 (NO₂), 795 cm⁻¹ (arom); MS (ESI, MeOH): m/z (%) = 689.1 (100) [M + H]⁺. Further experimental details can be found in the Supporting Information.

Acknowledgements

This research project was supported by the German Research Society (DFG) grant PE 1605/2-1. We thank Dr. Ulrich Girreser and Martin Schütt (Institute of Pharmacy in Kiel, Germany) for excellent technical and analytical assistance.

Keywords: caged prodrugs · imatinib · inhibitors · kinases · PDGF-R β · photoactivation

- [1] K. K. Parmar, R. S. King, *Cancer Pract.* **2001**, *9*, 263–265.
- [2] S. J. Baker, E. P. Reddy, *Mt. Sinai J. Med.* **2010**, *77*, 573–586.
- [3] A. C. Dar, K. M. Shokat, *Annu. Rev. Biochem.* **2011**, *80*, 769–795.
- [4] H. M. Kantarjian, M. Talpaz, *Semin. Oncol.* **2001**, *28*, 9–18.
- [5] A. Virgili, M. Koptyra, Y. Dasgupta, E. Glodkowska-Mrowka, T. Stoklosa, E. P. Nacheva, T. Skorski, *Cancer Res.* **2011**, *71*, 5381–5386.
- [6] M. Baccarani, D. Cillonì, M. Rondoni, E. Ottaviani, F. Messa, S. Merante, M. Tiribelli, F. Buccisano, N. Testoni, E. Gottardi, A. de Vivo, E. Giugliano, I. Iacobucci, S. Paolini, S. Soverini, G. Rosti, F. Rancati, C. Astolfi, F. Pane, G. Saglio, G. Martinelli, *Hematol. J.* **2007**, *92*, 1173–1179.
- [7] a) J. Dorn, H. Spatz, M. Schmieder, T. F. Barth, A. Blatz, D. Henne-Bruns, U. Knippschild, K. Kramer, *BMC Cancer* **2010**, *10*, 350; b) K. Søreide, O. M. Sandvik, J. A. Søreide, E. Gudlaugsson, K. Mangseth, H. K. Haugland, *Clin. Transl. Oncol.* **2012**, *14*, 619–629.
- [8] K. Adekola, M. Agulnik, *Curr. Oncol. Rep.* **2012**, *14*, 327–332.
- [9] R. Capdeville, E. Buchdunger, J. Zimmermann, A. Matter, *Nat. Rev. Drug Discovery* **2002**, *1*, 493–502.

- [10] R. Steri, J. Achenbach, D. Steinhilber, M. Schubert-Zsilavec, E. Proschak, *Biochem. Pharmacol.* **2012**, *83*, 1674–1681.
- [11] P. La Rosée, M. W. Deininger, *Semin. Hematol.* **2010**, *47*, 335–343.
- [12] A. C. Dar, M. S. Lopez, K. M. Shokat, *Chem. Biol.* **2008**, *15*, 1015–1022.
- [13] W. A. Velema, W. Szymanski, B. L. Feringa, *J. Am. Chem. Soc.* **2014**, *136*, 2178–2191.
- [14] G. C. Ellis-Davies, *Nat. Methods* **2007**, *4*, 619–628.
- [15] H. M. Lee, D. R. Larson, D. S. Lawrence, *ACS Chem. Biol.* **2009**, *4*, 409–427.
- [16] G. Mayer, A. Heckel, *Angew. Chem. Int. Ed.* **2006**, *45*, 4900–4921; *Angew. Chem.* **2006**, *118*, 5020–5042.
- [17] C. Brieke, F. Rohrbach, A. Gottschalk, G. Mayer, A. Heckel, *Angew. Chem. Int. Ed.* **2012**, *51*, 8446–8476; *Angew. Chem.* **2012**, *124*, 8572–8604.
- [18] P. Klán, T. Šolomek, C. G. Bochet, A. Blanc, R. Givens, M. Rubina, V. Popik, A. Kostikov, J. Wirz, *Chem. Rev.* **2013**, *113*, 119–191.
- [19] A. Deiters, *Curr. Opin. Chem. Biol.* **2009**, *13*, 678–686.
- [20] R. S. Givens, M. Rubina, J. Wirz, *Photochem. Photobiol. Sci.* **2012**, *11*, 472–488.
- [21] H. Li, J.-M. Hah, D. S. Lawrence, *J. Am. Chem. Soc.* **2008**, *130*, 10474–10475.
- [22] G. Dormán, G. D. Prestwich, *Trends Biotechnol.* **2000**, *18*, 64–77.
- [23] D. Geissler, W. Kresse, B. Wiesner, J. Bendig, H. Kettnermann, V. Hagen, *Chembiochem* **2003**, *4*, 162–170.
- [24] A. R. Morckel, H. Lusic, L. Farzana, J. A. Yoder, A. Deiters, N. M. Nascone-Yoder, *Development* **2012**, *139*, 437–442.
- [25] K. Curley, D. S. Lawrence, *Pharmacol. Ther.* **1999**, *82*, 347–354.
- [26] R. Ferreira, J. R. Nilsson, C. Solano, J. Andréasson, M. Gröthli, *Sci. Rep.* **2015**, *5*, 9769.
- [27] R. Horbert, B. Pinchuk, E. Johannes, J. Schlosser, D. Schmidt, D. Cappel, F. Totzke, C. Schachtele, C. Peifer, *J. Med. Chem.* **2015**, *58*, 170–182.
- [28] C. Sourbier, C. J. Ricketts, S. Matsumoto, D. R. Crooks, P. J. Liao, P. Z. Mannes, Y. Yang, M. H. Wei, G. Srivastava, S. Ghosh, V. Chen, C. D. Vocke, M. Merino, R. Srinivasan, M. C. Krishna, J. B. Mitchell, A. M. Pendergast, T. A. Rouault, L. Neckers, W. M. Linehan, *Cancer Cell* **2014**, *26*, 840–850.
- [29] B. Pinchuk, E. Johannes, S. Gul, J. Schlosser, C. Schachtele, F. Totzke, C. Peifer, *Mar. Drugs* **2013**, *11*, 3209–3223.
- [30] M. A. Seeliger, B. Nagar, F. Frank, X. Cao, M. N. Henderson, J. Kuriyan, *Structure* **2007**, *15*, 299–311.

Received: April 13, 2015

Published online on June 15, 2015



Supporting Information

Design, Synthesis, and Characterization of a Photoactivatable Caged Prodrug of Imatinib

Melanie Zindler, Boris Pinchuk, Christian Renn, Rebecca Horbert, Alexander Döbber, and
Christian Peifer^{*[a]}

cmdc_201500163_sm_miscellaneous_information.pdf

Supporting Information

Design, synthesis and characterization of a photoactivatable caged prodrug of imatinib

Melanie Zindler, Boris Pinchuk, Christian Renn, Rebecca Horbert, Alexander Döbber, and Christian Peifer. University of Kiel, Institute of Pharmacy, Gutenbergstr. 76, D-24118 Kiel.

Table of contents

General chemistry	1
Procedures and analytical data for compounds 1 - 7	3
UV-vis spectra of compounds.....	16
Kinetic studies of compound 3	18
Biological evaluation.....	19
UV sources for photochemical experiments	19

General chemistry

^1H (300 MHz) and ^{13}C (75 MHz) NMR were recorded on a Bruker Avance III 300 spectrometer (Rheinstetten, Germany) at 300 K with a multinuclear probe head using the manufacturer's pulse programs. The data are reported as follows: chemical shifts in ppm from Me_4Si (TMS) as external standard, multiplicity and coupling constant (Hz). NMR spectra were obtained on a ^1H (300 MHz) and ^{13}C spectra (75 MHz) were referenced either to TMS or to internal DMSO-d_5 (^1H NMR δ 2.50) and internal DMSO-d_6 (^{13}C NMR δ 39.5) or internal CHCl_3 (^1H -NMR δ 7.26) and internal CDCl_3 (^{13}C -NMR δ 77.0). All coupling constants (J values) are quoted in Hz. The following

NMR abbreviations are used: b (broad), s (singlet), d (doublet), t (triplet), m (unresolved multiplet). The labelling scheme of structures to correlate NMR signals can be found in Supporting Information.

Mass spectra of the compounds were recorded after chromatographic separation. Mixtures were separated with an Agilent 1100 HPLC system (Waldbronn, Germany) consisting of a thermostated autosampler, diode array detection and an Agilent Zorbax Eclipse XDB-C8 column (150 × 4.6 mm, 5 µm particle size). Elution was achieved with a solvent gradient system of water and acetonitrile, with 0.1 % of acetic acid and a flow rate of 1 ml/min. The eluent flow was splitted to the mass spectrometer.

Mass spectra with nominal resolution were recorded with an Esquire ~LC mass spectrometer (Bruker Daltonik, Bremen, Germany), with electrospray ionization operating in the positive ion mode, with the following parameters: drying gas nitrogen 8 l/min, nebulizer 35 psi, dry gas heating 350 °C, HV capillary 4000 V, HV EndPlate offset -500 V. GC/MS was performed on a HP6890 Series System. EI-mass spectra were recorded on a Varian MAT 311A (70 eV). HRMS spectra were recorded on a MAT-95 (Finnigan).

Infrared spectra were recorded with a Spectrum 100 FT-IR spectrometer (PerkinElmer, United States).

Ultraviolet-visible spectra were recorded with a Cary 50 Scan UV-Visible spectrophotometer (Varian Deutschland GmbH, Darmstadt, Germany) in methanol (HPLC grade) as solvent.

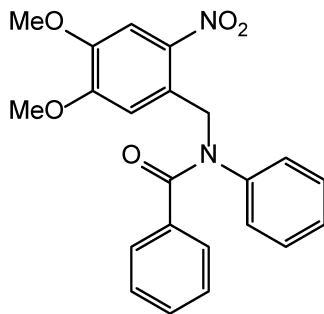
Where appropriate, column chromatography was performed for crude precursors with Merck silica gel 60 (0.063-0.200 mm) or Acros organics silica gel (0.060-0.200 mm; pore diameter ca. 60 nm). Column chromatography for test compounds was performed using a LaFlash system (VWR) with Merck silica gel 60 (0.015-0.040 mm)

or RP8 columns. The progress of the reactions was monitored by thin-layer chromatography (TLC) performed with Merck silica gel 60 F-245 plates. Where necessary, reactions were carried out in a nitrogen atmosphere using 4 Å molecular sieves. All reagents and solvents were obtained from commercial sources and used as received (THF was used after distillation over K/benzophenone). Reagents were purchased from Sigma-Aldrich Chemie, Steinheim, Germany; Lancaster Synthesis, Mühlheim, Germany or Acros, Nidderau, Germany.

HPLC analysis was performed on a Hewlett-Packard HP 1090 Series II using a Thermo Betasil C8 (150 x 4.6 mm 5µM) column (mobile phase flow 1.5 ml/min, gradient KH₂PO₄ buffer pH 2.3/methanol, UV-detection 230/254 nm). All key compounds submitted to biological assays were proven by this method to show ≥ 98 % purity.

Procedures and analytical data for compounds 1 - 7

Preparation of *N*-(4, 5-dimethoxy-2-nitrobenzyl)-*N*-phenyl-benzamide (1)



Compound **6** (172 mg, 600 µmol) was dissolved in dry pyridine (20 mL). The reaction mixture was cooled to 0 °C and benzoyl chloride (140 mg, 1.00 mmol) was added in portions under nitrogen atmosphere. The solution was stirred for 1 h at room

temperature and water (100 mL) was added. The mixture was extracted with ethyl acetate (3x100 mL) and the combined organic layers were dried over anhydrous sodium sulfate. The solvent was removed in vacuum and the residue was purified by flash chromatography (silica gel, petroleum ether/ethyl acetate) to give compound **1** as a yellow solid (174 mg, yield: 74%).

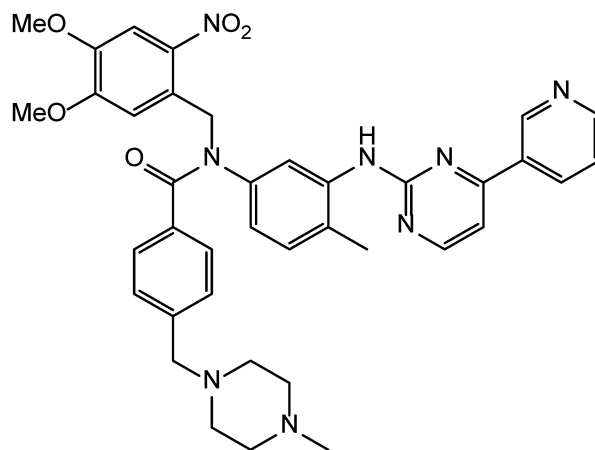
¹H-NMR (300 MHz, DMSO-d₆): δ = 3.83 (s, 6 H, -OCH₃), 5.40 (s, 2 H, -CH₂), 7.06 (s, 1 H, nitrobenz-*H*-6), 7.13 (m_c, 3 H, ph-*H*-3,4,5), 7.17 – 7.20 (m, 2 H, ph-*H*-2,6), 7.22 – 7.29 (m, 3 H, benz-*H*-3,4,5), 7.31 – 7.34 (m, 2 H, benz-*H*-2,6), 7.59 (s, 1 H, nitrobenz-*H*-3) ppm.

¹³C-NMR (75.5 MHz, DMSO-d₆): δ = 50.1 (t, -CH₂), 50.1, 56.0 (q, -OCH₃), 108.1 (d, nitrobenz-*C*-3), 110.9 (d, nitrobenz-*C*-6), 126.7 (d, ph-*C*-4), 126.9 (s, nitrobenz-*C*-2), 127.5 (d, ph-*C*-3,5), 127.8 (d, benz-*C*-3,5), 128.2 (d, benz-*C*-2,6), 129.0 (d, ph-*C*-2,6), 129.6 (d, benz-*C*-4), 135.8 (s, benz-*C*-1), 140.5 (s, nitrobenz-*C*-1), 142.6 (s, ph-*C*-1), 147.4 (s, nitrobenz-*C*-5), 152.8 (s, nitrobenz-*C*-4), 170.0 (s, -C=O) ppm.

IR (ATR): $\tilde{\nu}$ = 3051 (N-H), 1688 (C=O), 1579, 1331 (-NO₂), 792 (arom.) cm⁻¹.

MS (ESI, MeOH): *m/z* (%) = 393.1 (100) [M+H]⁺, 196.1 (12) [C₉H₁₀O₄N].

Preparation of *N*-(4, 5-dimethoxy-2-nitrobenzyl)-*N*-(4-methyl-3-((4-(pyridine-3-yl)pyrimidine-2-yl)amino)phenyl)-4-((4-methylpiperazin-1-yl)methyl)-benzamide (2)



Compound **5a** (330 mg, 700 μmol) was dissolved in dry pyridine (20 mL). The reaction mixture was cooled to 0 °C and 4-[(4-methylpiperazin-1-yl)-methyl]-benzoyl chloride (288 mg, 1.00 mmol) was added in portions under nitrogen atmosphere. The solution was stirred for 3 h at room temperature and water (100 mL) was added. The mixture was extracted with ethyl acetate (3x100 mL) and the combined organic layers were dried over anhydrous sodium sulfate. The solvent was removed in vacuum and the residue was purified by flash chromatography (SiO_2 reversed phase, MeOH/water) to give compound **2** as a yellow solid (40 mg, yield: 8%).

$^1\text{H-NMR}$ (300 MHz, DMSO-d_6): δ = 2.09 (s, 3 H, pip- CH_3), 2.14 (s, 3 H, CH_3), 2.21 (m_c , 8 H, pip- $H_{2,3,5,6}$), 3.33 (s, 2H, pip- CH_2), 3.74 (s, 3 H, $-\text{OCH}_3$), 3.82 (s, 3 H, $-\text{OCH}_3$), 5.38 (bs, 2 H, $-\text{CH}_2$), 6.79 (dd, 1 H, $^3J = 8.1$ Hz, $^4J = 2.1$ Hz, ph- H_6), 7.03 (s, 1 H, nitrobenz- H_6), 7.05 (d, 1 H, $^3J = 8.1$ Hz, ph- H_5), 7.13 (d, 2 H, $^3J = 8.2$ Hz,

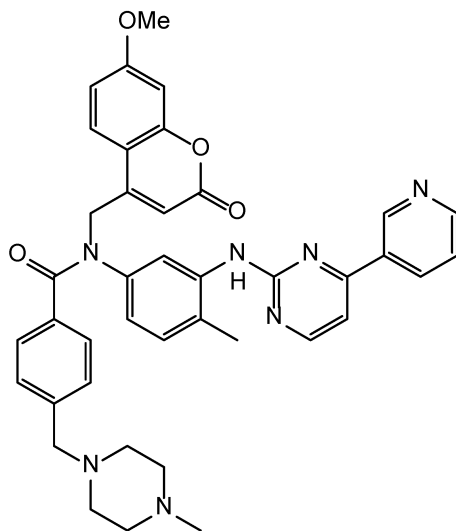
benz-*H*-3,5), 7.34 (d, 2 H, $^3J = 8.2$ Hz, benz-*H*-2,6), 7.44 (d, 1 H, $^3J = 5.2$ Hz, pyrim-*H*-5), 7.49 (ddd, 1 H, $^3J = 8.0$ Hz, $^3J = 4.0$ Hz, pyr-*H*-5), 7.61 (s, 1 H, nitrobenz-*H*-3), 7.62 (d, 1 H, $^4J = 2.0$ Hz, ph-*H*-2), 8.36 (td, 1 H, $^3J = 8.0$ Hz, $^4J = 2.0$ Hz, pyr-*H*-4), 8.44 (d, 1 H, $^3J = 5.1$ Hz, pyrim-*H*-6), 8.69 (d, 1 H, $^4J = 4.0$ Hz, pyr-*H*-6), 8.80 (s, 1 H, pyrim-NH), 9.23 (d, 1 H, $^4J = 1.7$ Hz, pyr-*H*-2) ppm.

$^{13}\text{C-NMR}$ (75.5 MHz, DMSO- d_6): $\delta = 17.5$ (q, CH₃), 45.6 (q, pip-CH₃), 50.6 (t, -CH₂), 52.3, 54.6 (d, pip-C-2,3,5,6), 55.8, 55.9 (q, -OCH₃), 61.4 (t, pip-CH₂), 107.9 (d, pyrim-C-5), 108.2 (d, nitrobenz-C-3), 110.5 (d, nitrobenz-C-6), 122.5 (d, ph-C-2), 122.9 (d, ph-C-6), 123.7 (d, pyr-C-5), 127.3 (s, nitrobenz-C-2), 128.1 (d, benz-C-3,5), 128.3 (d, benz-C-2,6), 129.5 (s, ph-C-1), 130.5 (d, ph-C-5), 131.9 (s, pyr-C-3), 134.1 (d, pyr-C-4), 134.3 (s, benz-C-4), 138.3 (s, ph-C-4), 139.9 (s, ph-C-3), 140.3 (s, benz-C-1), 140.7 (s, nitrobenz-C-1), 147.3 (s, nitrobenz-C-5), 148.0 (d, pyr-C-2), 151.4 (d, pyr-C-6), 152.9 (s, nitrobenz-C-4), 159.2 (d, pyrim-*H*-6), 160.6 (s, pyrim-C-4), 161.5 (s, pyrim-C-2), 169.9 (s, -C=O) ppm.

IR (ATR): $\tilde{\nu} = 2836$ (C-H), 1643 (C=O), 1574, 1330 (-NO₂), 795 (arom.) cm⁻¹.

MS (ESI, MeOH): m/z (%) = 689.1 (100) [M+H]⁺.

Preparation of *N*-((7-methoxy-2-oxo-2*H*-chromen-4-yl)methyl)-*N*-(4-methyl-3-((4-(pyridine-3-yl)pyrimidine-2-yl)amino)phenyl)-3-((4-methylpiperazin-1-yl)methyl)-benzamide (3)



Compound **5b** (186 mg, 400 μmol) was dissolved in dry pyridine (20 mL). The reaction mixture was cooled to 0 °C and 4-[(4-methylpiperazin-1-yl)-methyl]-benzoyl chloride (194 mg, 600 μmol) was added in portions under nitrogen atmosphere. The solution was stirred for 3 h at room temperature and water (100 mL) was added. The mixture was extracted with ethyl acetate (3x100 mL) and the combined organic layers were dried over anhydrous sodium sulfate. The solvent was removed in vacuum and the residue was purified by flash chromatography (SiO_2 reversed phase, MeOH/water) to give compound **3** as a yellow solid (30 mg, yield: 11%).

$^1\text{H-NMR}$ (300 MHz, DMSO-d_6): δ = 2.07 (s, 3 H, pip- CH_3), 2.11 (s, 3 H, CH_3), 2.23 (m_c, 8 H, pip-*H*-2,3,5,6), 3.85 (s, 3 H, $-\text{OCH}_3$), 4.49 (d, 2 H, 3J = 5.4 Hz, $-\text{CH}_2$), 6.17 (d, 1 H, 3J = 5.4 Hz, $-\text{CH}_2\text{NH}$), 6.19 (bs, 1 H, cum-*H*-3), 6.38 (dd, 1 H, 3J = 8.1 Hz,

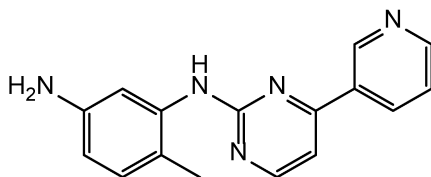
$^4J = 2.4$ Hz, ph-*H*-6), 6.86 (d, 1 H, $^4J = 2.4$ Hz, ph-*H*-2), 6.93 (dd, 1 H, $^3J = 8.1$ Hz, $^4J = 2.4$ Hz, ph-*H*-5), 6.95 (d, 1 H, $^3J = 8.8$ Hz, cum-*H*-5), 7.01 (d, 1 H, $^4J = 2.4$ Hz, cum-*H*-8), 7.35 (d, 1 H, $^3J = 5.2$ Hz, pyrim-*H*-5), 7.52 (ddd, 1 H, $^3J = 8.0$ Hz, $^3J = 4.8$ Hz, pyr-*H*-5), 7.80 (d, 1 H, $^3J = 8.8$ Hz, cum-*H*-6), 8.38 (td, 1 H, $^3J = 8.0$ Hz, $^4J = 2.3$ Hz, pyr-*H*-4), 8.42 (d, 1 H, $^3J = 5.2$ Hz, pyrim-*H*-6), 8.65 (dd, 1 H, $^3J = 4.8$ Hz, $^4J = 1.7$ Hz, pyr-*H*-6), 8.72 (s, 1 H, pyrim-NH), 9.24 (d, 1 H, $^4J = 2.3$ Hz, pyr-*H*-2) ppm.

$^{13}\text{C-NMR}$ (75.5 MHz, DMSO- d_6): $\delta = 17.2$ (q, CH₃), 45.6 (s, pip-CH₃), 43.4 (t, -CH₂), 52.5, 54.9 (d, pip-C -2,3,5,6), 55.9 (q, -OCH₃), 62.8 (d, pip-CH₂), 100.8 (d, cum-C-8), 107.2 (d, pyrim-C-5), 108.7 (d, cum-C-3), 108.9 (d, ph-C-6), 109.3 (d, ph-C-2), 111.4 (s, cum-C-10), 112.1 (d, cum-C-5), 120.1 (s, ph-C-1), 123.7 (d, pyr-C-5), 125.7 (d, cum-CC-6), 130.5 (d, ph-C-5), 132.2 (s, pyr-C-3), 134.1 (d, pyr-C-4), 138.2 (s, ph-C-4), 146.3 (s, ph-C-3), 148.0 (d, pyr-C-2), 151.3 (d, pyr-C-6), 154.5 (s, cum-C-9), 154.9 (s, cum-C-4), 159.2 (d, pyrim-C-6), 160.4 (s, cum-C-2), 161.1 (s, pyrim-C-2), 161.4 (s, pyrim-C-4), 162.3 (s, cum-C-7) ppm.

IR (ATR): $\tilde{\nu} = 3344$ (N-H), 1704 (C=O), 797 (arom.) cm^{-1} .

MS (ESI, MeOH): m/z (%) = 482.7 (52) [M+H]⁺, 342.0 (100) [C₂₀H₁₆N₅O].

Preparation of 6-Methyl-N-[4-(pyridine-3-yl)-pyrimidine-2-yl]-benzene-1,3-diamine (4)



Imatinib (1.77 g, 3.00 mmol) was diluted in concentrated HCl (30 mL) and concentrated CH₃COOH (30 mL). The reaction mixture was refluxed for 8 h and then stirred at room temperature overnight. To the solution water (100 mL) and 50% NaOH solution (50 mL) were added. The mixture was extracted with ethyl acetate (3x100 mL). The combined organic layer was dried over anhydrous sodium sulfate, and the organic solvent was removed under vacuum. The residue was diluted in CH₂Cl₂ and filtered over bas. Al₂O₃. The solvent was removed under vacuum to afford the desired compound **4** as a white solid (804 mg, yield: 97%).

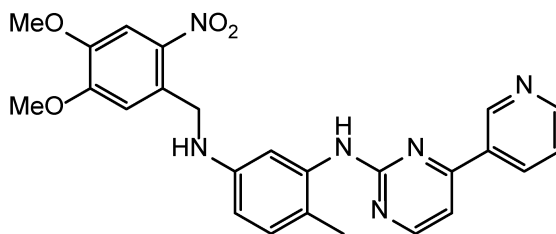
¹H-NMR (300 MHz, DMSO-d₆): δ = 2.06 (s, 3 H, CH₃), 4.84 (s, 2 H, NH₂), 6.33 (dd, 1 H, ³J = 8.0 Hz, ⁴J = 2.3 Hz, ph-H-4), 6.79 (d, 1 H, ⁴J = 2.3 Hz, ph-H-2), 6.86 (d, 1 H, ³J = 8.0 Hz, ph-H-5), 7.35 (d, 1 H, ³J = 5.2 Hz, pyrim-H-5), 7.53 (ddd, 1 H, ³J = 8.0 Hz, ³J = 4.8 Hz, pyr-H-5), 8.40 (td, 1 H, ³J = 8.0 Hz, ⁴J = 1.7 Hz, pyr-H-4), 8.46 (d, 1 H, ³J = 5.2 Hz, pyrim-H-6), 8.67 (s, 1 H, pyrim-NH), 8.68 (dd, 1 H, ³J = 4.8 Hz, ⁴J = 1.7 Hz, pyr-H-6), 9.24 (d, 1 H, ⁴J = 1.7 Hz, pyr-H-2) ppm.

¹³C-NMR (75.5 MHz, DMSO-d₆): δ = 17.2 (q, CH₃), 107.0 (d, pyrim-C-5), 110.9 (d, ph-C-4), 111.0 (d, ph-C-2), 119.2 (s, ph-C-3), 123.7 (d, pyr-C-5), 130.3 (d, pyr-C-6), 132.2 (s, pyrim-C-4), 134.2 (d, pyr-C-4), 137.9 (s, pyr-C-3), 146.7 (s, ph-C-6), 148.0

(d, pyr-*H*-2), 151.2 (d, pyr-*C*-6), 159.3 (d, pyrim-*C*-6), 161.2 (s, pyrim-*C*-2), 161.4 (s, ph-*C*-1) ppm.

MS (ESI, MeOH): m/z (%) = 278.4 (100) [M+H]⁺.

Preparation of *N*¹-(4, 5-dimethoxy-2-nitrobenzyl)-4-methyl-*N*³-(4-(pyridine-3-yl)-pyrimidine-2-yl)benzene-1,3-diamine (5a)



Compound **4** (693 mg, 2.50 mmol), lithium carbonate (738 mg, 10.0 mmol) and 4, 5-dimethoxy-2-nitrobenzyl bromide (690 mg, 2.50 mmol) were dissolved in DMF (50 mL). The mixture was stirred at room temperature overnight. The solvent was removed in vacuum and the residue was dissolved in ethyl acetate (200 mL) and water (100 mL). The organic layer was washed with brine (2x100 mL) and water (2x100 mL) and dried over anhydrous sodium sulfate. The solvent was removed in vacuum and the residue was purified by flash chromatography (silica gel, petroleum ether/ethyl acetate) to give compound **5a** as a light yellow solid (820 mg, yield: 69 %).

¹H-NMR (300 MHz, DMSO-*d*₆): δ = 2.06 (s, 3 H, CH₃), 3.73 (s, 3 H, -OCH₃), 3.83 (s, 3 H, -OCH₃), 4.56 (bs, 2 H, -CH₂), 6.12 (bs, 1 H, -CH₂NH), 6.33 (dd, 1 H, ³*J* = 8.0 Hz, ⁴*J* = 2.3 Hz, ph-*H*-6), 6.82 (d, 1 H, ⁴*J* = 2.3 Hz, ph-*H*-2), 6.91 (d, 1 H, ³*J* = 8.0 Hz, ph-*H*-5), 7.22 (s, 1 H, nitrobenz-*H*-6), 7.36 (d, 1 H, ³*J* = 5.2 Hz, pyrim-*H*-5), 7.52 (ddd,

10

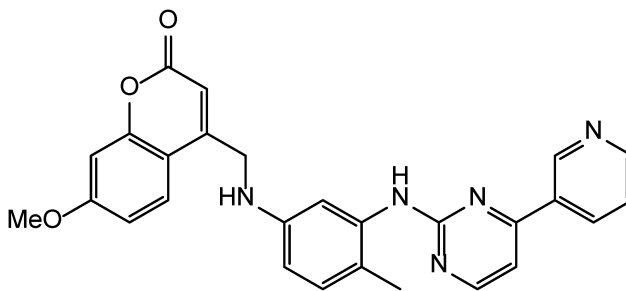
1 H, $^3J = 8.0$ Hz, $^3J = 4.8$ Hz, pyr-*H*-5), 7.64 (s, 1 H, nitrobenz-*H*-3), 8.37 (td, 1 H, $^3J = 8.0$ Hz, $^4J = 1.7$ Hz, pyr-*H*-4), 8.42 (d, 1 H, $^3J = 5.1$ Hz, pyrim-*H*-6), 8.68 (dd, 1 H, $^3J = 3.2$ Hz, $^4J = 1.7$ Hz, pyr-*H*-6), 8.70 (s, 1 H, pyrim-NH), 9.23 (d, 1 H, $^4J = 1.7$ Hz, pyr-*H*-2) ppm.

$^{13}\text{C-NMR}$ (75.5 MHz, DMSO- d_6): $\delta = 17.2$ (q, CH₃), 44.7 (t, -CH₂), 55.8, 55.9 (q, -OCH₃), 107.2 (d, pyrim-C-5), 108.2 (d, nitrobenz-C-3), 109.2 (d, ph-C-6), 109.5 (d, ph-C-2), 111.4 (d, nitrobenz-C-6), 120.1 (s, ph-C-1), 123.7 (d, pyr-C-5), 130.4 (d, ph-C-5), 131.1 (s, nitrobenz-C-1), 132.2 (s, pyr-C-3), 134.2 (d, pyr-C-4), 138.1 (s, ph-C-4), 146.7 (s, ph-C-3), 140.6 (s, nitrobenz-C-2), 147.1 (s, nitrobenz-C-5), 148.0 (s, pyr-C-2), 151.3 (d, pyr-C-6), 153.0 (s, nitrobenz-C-4), 159.2 (d, pyrim-C-6), 161.2 (s, pyrim-C-2), 161.4 (s, pyrim-C-4) ppm.

IR (ATR): $\tilde{\nu} = 3292$ (N-H), 1671 (C=O), 1576, 1330 (-NO₂), 791 (arom.) cm⁻¹.

HR/MS (EI, MeOH): m/z berechnet = 472.1859, m/z gefunden = 472.1852.

Preparation of 7-Methoxy-4-[[[4-methyl-3-((4-(pyridine-3-yl)-pyrimidine-2-yl)-amino)phenyl]-amino]methyl]-2H-chromen-2-on (5b)



Compound **4** (277 mg, 1.00 mmol), lithium carbonate (295 mg, 4.00 mmol) and 4-(bromomethyl)-7-methoxycoumarin (269 mg, 1.00 mmol) were dissolved in DMF (20 mL). The mixture was stirred at room temperature overnight. The solvent was

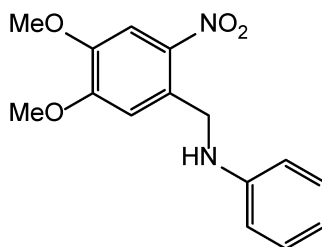
removed in vacuum and the residue was dissolved in ethyl acetate (200 mL) and water (100 mL). The organic layer was washed with brine (2x100 mL) and water (2x100 mL) and dried over anhydrous sodium sulfate. The solvent was removed in vacuum and the residue was purified by flash chromatography (SiO₂ reversed phase, MeOH/water) to give compound **5b** as a light yellow solid (227 mg, yield: 49 %).

¹H-NMR (300 MHz, DMSO-d₆): δ = 2.08 (s, 3 H, CH₃), 3.85 (s, 3 H, -OCH₃), 4.49 (d, 2 H, ³J = 5.4 Hz, -CH₂), 6.17 (d, 1 H, ³J = 5.4 Hz, -CH₂NH), 6.19 (bs, 1 H, cum-H-3), 6.38 (dd, 1 H, ³J = 8.1 Hz, ⁴J = 2.4 Hz, ph-H-6), 6.86 (d, 1 H, ⁴J = 2.4 Hz, ph-H-2), 6.93 (dd, 1 H, ³J = 8.1 Hz, ⁴J = 2.4 Hz, ph-H-5), 6.95 (d, 1 H, ³J = 8.8 Hz, cum-H-5), 7.01 (d, 1 H, ⁴J = 2.4 Hz, cum-H-8), 7.35 (d, 1 H, ³J = 5.2 Hz, pyrim-H-5), 7.52 (ddd, 1 H, ³J = 8.0 Hz, ³J = 4.8 Hz, pyr-H-5), 7.80 (d, 1 H, ³J = 8.8 Hz, cum-H-6), 8.38 (td, 1 H, ³J = 8.0 Hz, ⁴J = 2.3 Hz, pyr-H-4), 8.42 (d, 1 H, ³J = 5.2 Hz, pyrim-H-6), 8.65 (dd, 1 H, ³J = 4.8 Hz, ⁴J = 1.7 Hz, pyr-H-6), 8.72 (s, 1 H, pyrim-NH), 9.24 (d, 1 H, ⁴J = 2.3 Hz, pyr-H-2) ppm.

¹³C-NMR (75.5 MHz, DMSO-d₆): δ = 17.2 (q, CH₃), 43.4 (t, -CH₂), 55.9 (q, -OCH₃), 100.8 (d, cum-C-8), 107.2 (d, pyrim-C-5), 108.7 (d, cum-C-3), 108.9 (d, ph-C-6), 109.3 (d, ph-C-2), 111.4 (s, cum-C-10), 112.1 (d, cum-C-5), 120.1 (s, ph-C-1), 123.7 (d, pyr-C-5), 125.7 (d, cum-CC-6), 130.5 (d, ph-C-5), 132.2 (s, pyr-C-3), 134.1 (d, pyr-C-4), 138.2 (s, ph-C-4), 146.3 (s, ph-C-3), 148.0 (d, pyr-C-2), 151.3 (d, pyr-C-6), 154.5 (s, cum-C-9), 154.9 (s, cum-C-4), 159.2 (d, pyrim-C-6), 160.4 (s, cum-C-2), 161.1 (s, pyrim-C-2), 161.4 (s, pyrim-C-4), 162.3 (s, cum-C-7) ppm.

IR (ATR): $\tilde{\nu}$ = 3344 (N-H), 1707 (C=O), 796 (arom.) cm⁻¹.

MS (ESI, MeOH): m/z (%) = 466.4 (100) [M+H]⁺.

Preparation of *N*-(4, 5-dimethoxy-2-nitrobenzyl)-benzamine (6)

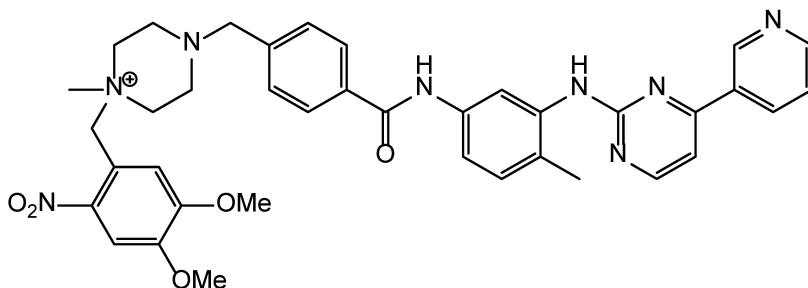
Freshly distilled aniline (203 mg, 2.18 mmol), lithium carbonate (590 mg, 8.00 mmol) and 4, 5-dimethoxybenzyl bromide (602 mg, 2.18 mmol) were dissolved in DMF (20 mL). The mixture was stirred at room temperature overnight. The solvent was removed in vacuum and the residue dissolved in ethyl acetate (200 mL) and water (50 mL). The organic layer was washed with brine (2x100 mL) and water (2x100 mL) and dried over anhydrous sodium sulfate. The solvent was removed in vacuum and the residue purified by flash chromatography (silica gel, petroleum ether/ethyl acetate) to give compound **6** as a white solid (517 mg, yield: 82%).

¹H-NMR (300 MHz, DMSO-d₆): δ = 3.83 (s, 6 H, -OCH₃), 5.40 (s, 2 H, -CH₂), 6.12 (bs, 1 H, -CH₂NH), 7.06 (s, 1 H, nitrobenz-*H*-6), 7.22 – 7.29 (m, 3 H, benz-*H*-3,4,5), 7.31 – 7.34 (m, 2 H, benz-*H*-2,6), 7.59 (s, 1 H, nitro-benz-*H*-3) ppm.

¹³C-NMR (75.5 MHz, DMSO-d₆): δ = 50.1 (t, -CH₂), 50.1, 56.0 (q, -OCH₃), 108.1 (d, nitrobenz-*C*-3), 110.9 (d, nitrobenz-*C*-6), 126.9 (s, nitrobenz-*C*-2), 127.8 (d, benz-*C*-3,5), 128.2 (d, benz-*C*-2,6), 129.6 (d, benz-*C*-4), 135.8 (s, benz-*C*-1), 140.5 (s, nitrobenz-*C*-1), 147.4 (s, nitrobenz-*C*-5), 152.8 (s, nitrobenz-*C*-4) ppm.

MS (ESI, MeOH): *m/z* (%) = 289.1 (100) [M+H]⁺, 196.1 (12%) [C₉H₁₀O₄N].

Preparation of 1-(4,5-dimethoxy-2-nitrobenzyl)-4-{4-[(4-methyl-3-((4-(pyridine-3-yl)pyrimidine-2-yl)amino)phenyl)carbamoyl]benzyl}-piperazine-1-ium (7)



Imatinib free base (247 mg, 500 μmol), lithium carbonate (148 mg, 2.00 mmol) and 4, 5-dimethoxy-2-nitrobenzyl bromide (138 mg, 500 μmol) were dissolved in DMF (30 mL). The mixture was stirred at room temperature overnight. The solvent was removed in vacuum and the residue was dissolved in ethyl acetate (100 mL) and water (50 mL). The organic layer was washed with brine (2x50 mL) and water (2x50 mL) and dried over anhydrous sodium sulfate. The solvent was removed in vacuum and the residue was purified by flash chromatography (silica gel, dichloromethane/MeOH) to give compound **7** as a yellow solid (43 mg, yield: 12%).

$^1\text{H-NMR}$ (300 MHz, DMSO-d_6): δ = 2.22 (s, 3 H, ph- CH_3), 2.65 – 2.88 (m, 4 H, pip- $\text{H}_{2,6}$), 2.94 (s, 3H, pip- CH_3), 3.41 – 3.59 (m, 4 H, pip- $\text{H}_{3,5}$), 3.70 (s, 2 H, CH_2 -benz), 3.92 (s, 3 H, $-\text{OCH}_3$), 3.93 (s, 3 H, $-\text{OCH}_3$), 5.03 (s, 2 H, nitro-benz- CH_2), 7.21 (d, 1 H, 3J = 8.7 Hz, ph- H_{5}), 7.43 (d, 1 H, 3J = 5.2 Hz, pyrim- H_{4}), 7.41 (s, 1 H, nitro-benz- H_{6}), 7.45 (d, 2 H, 3J = 8.3 Hz, benz- $\text{H}_{3,5}$), 7.48 (dd, 1 H, 3J = 8.7 Hz, 4J = 2.1 Hz, ph- H_{6}), 7.51 (ddd, 1 H, 3J = 8.0 Hz, 3J = 4.7 Hz, pyr- H_{5}), 7.75 (s, 1 H, nitro-benz- H_{3}), 7.95 (d, 2 H, 3J = 8.3 Hz, benz- $\text{H}_{2,6}$), 8.08 (d, 1 H, 4J = 2.1 Hz, ph- H_{2}), 8.47

(ddd, 1 H, $^3J = 8.0$ Hz, $^4J = 2.3$ Hz, $^4J = 1.7$ Hz, pyr-*H*-6), 8.51 (d, 1 H, $^3J = 5.2$ Hz, pyrim-*H*-5), 8.68 (dd, 1 H, $^3J = 4.7$ Hz, $^4J = 1.6$ Hz, pyr-*H*-4), 8.97 (s, 1 H, ph-NH), 9.27 (d, 1 H, $^4J = 1.6$ Hz, pyr-*H*-2), 10.17 (s, 1 H, -CONH) ppm.

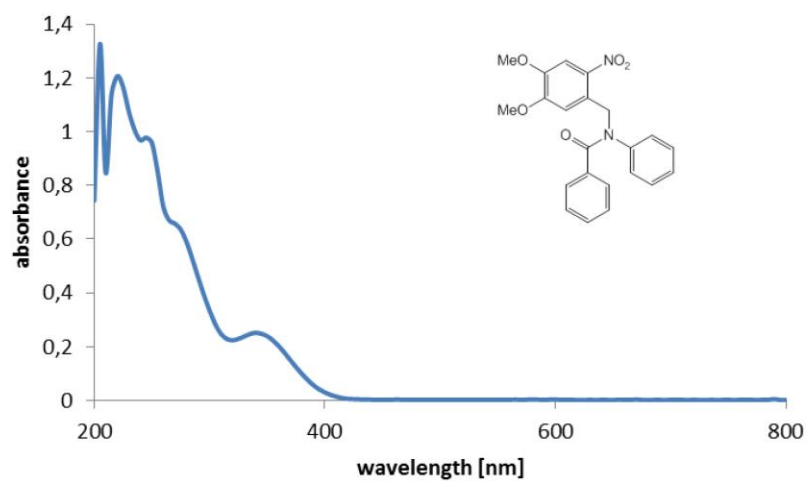
$^{13}\text{C-NMR}$ (75.5 MHz, DMSO- d_6): $\delta = 17.6$ (q, ph- CH_3), 45.6 (d, pip-C-2,6), 43.5 (q, pip- CH_3), 56.3, 56.6 (s, nitro-benz-C-4,5), 59.5 (d, pip-C-3,5), 60.0 (t, CH_2 -benz), 63.8 (t, nitro-benz- CH_2), 107.5 (d, pyrim-C-4), 109.1 (d, nitro-benz-C-3), 114.6 (s, nitro-benz-C-1), 116.8 (d, ph-C-6), 117.3 (d, ph-C-2), 118.1 (d, nitro-benz-C-6), 123.7 (d, pyr-C-5), 127.8 (d, benz-C-2,6), 127.7 (s, ph-C-3), 128.6 (d, benz-C-3,5), 130.0 (d, ph-C-5), 132.2 (s, pyr-C-3), 134.0 (s, benz-C-4), 134.4 (d, pyr-C-6), 137.0 (s, ph-C-1), 137.8 (s, ph-C-4), 141.0 (s, benz-C-1), 143.5 (s, nitro-benz-C-2), 148.2 (d, pyr-C-2), 149.8 (s, nitro-benz-C-4), 151.3 (d, pyr-C-4), 152.1 (s, nitro-benz-C-5), 159.4 (d, pyrim-C-5), 161.1 (s, pyrim-C-3), 161.5 (s, pyrim-C-1), 165.0 (s, C=O) ppm.

IR (ATR): $\tilde{\nu} = 3366$ (N-H), 1651 (C=O), 1524, 1325 ($-\text{NO}_2$), 798 (arom.) cm^{-1} .

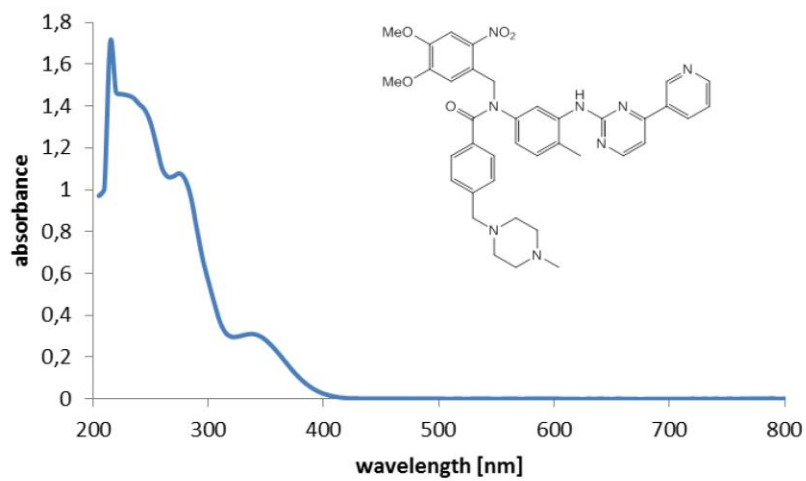
MS (ESI, MeOH): m/z (%) = 689.4 (100) [M].

UV-vis spectra of compounds

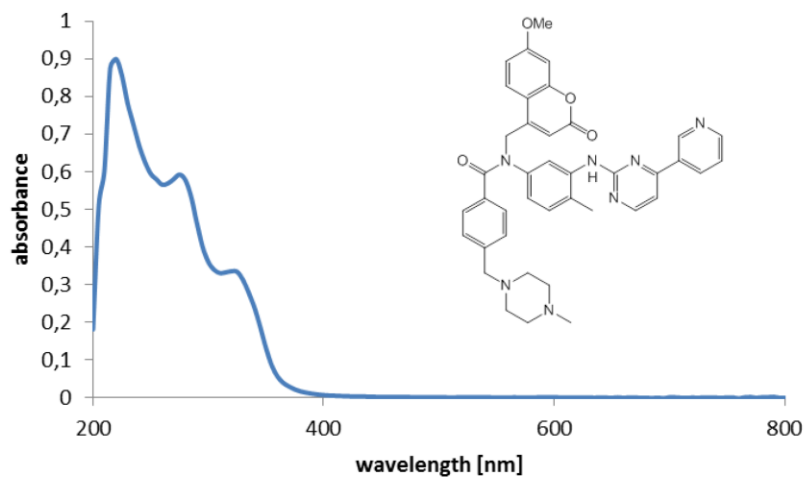
UV-vis spectrum of compound 1



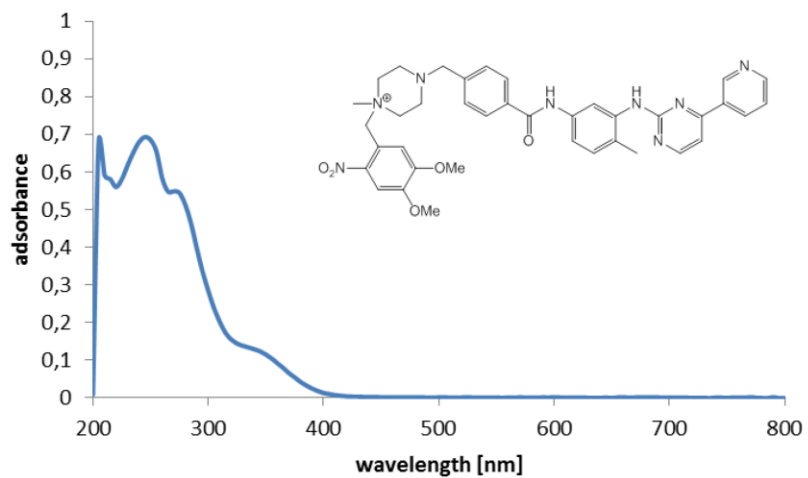
UV-vis spectrum of compound 2



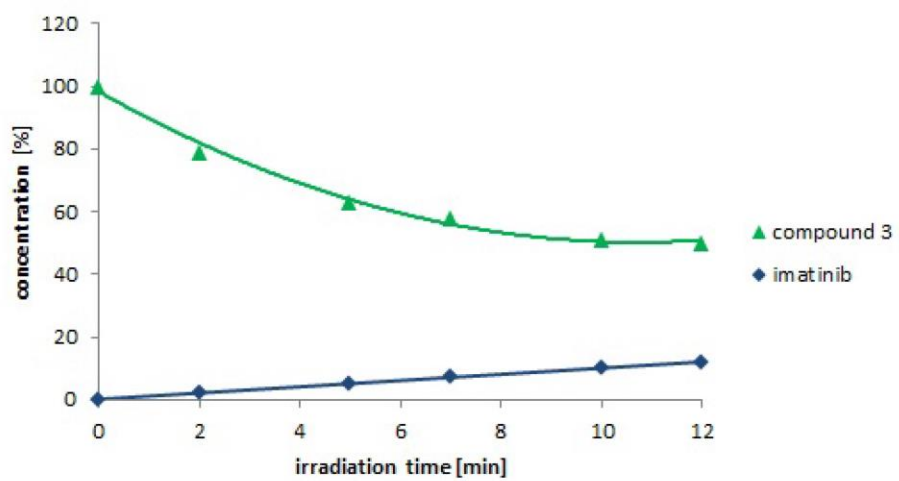
UV-vis spectrum of compound 3



UV-vis spectrum of compound 6



Kinetic studies of compound 3

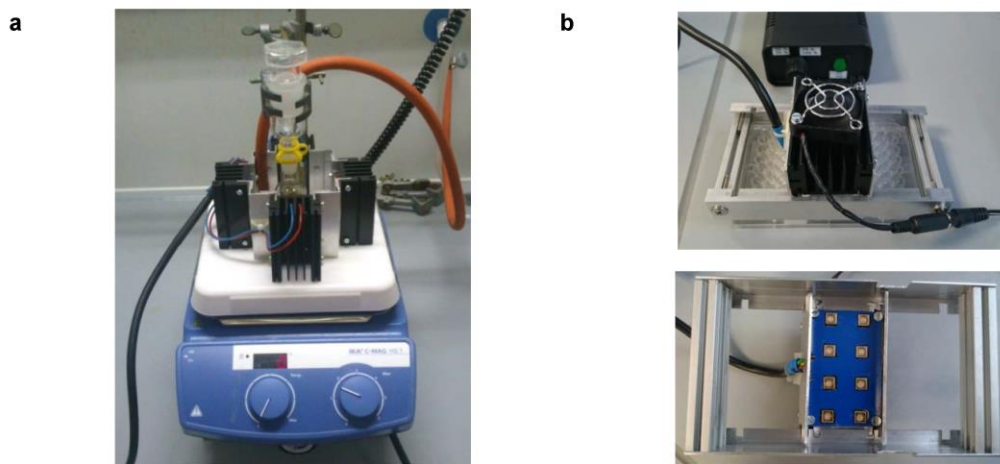


Time dependent photo induced cleavage of caged imatinib prodrug **3** upon irradiation with UV light (365 nm, 5.4 W).

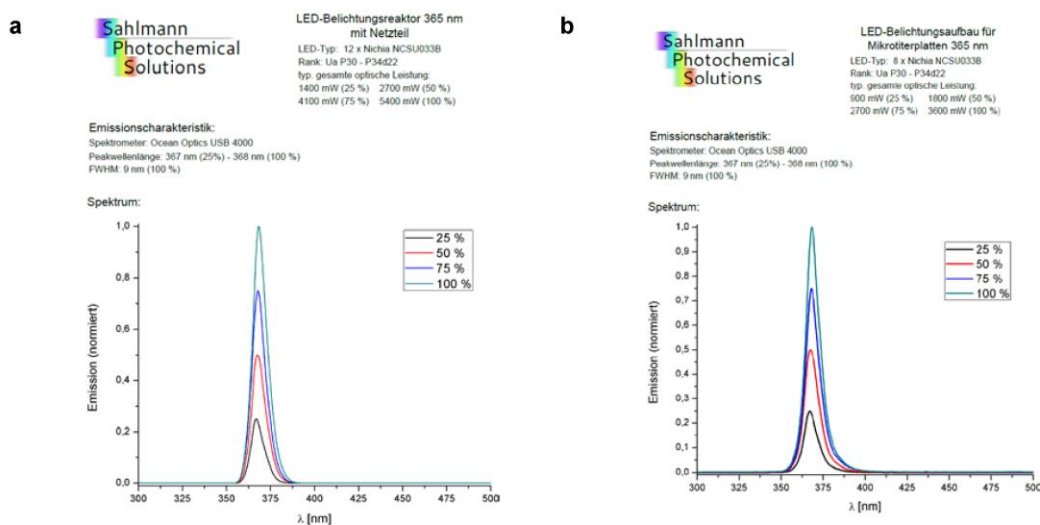
Biological evaluation

All inhibitor solutions were prepared freshly in DMSO prior to each experiment and used immediately. The PDGF-R β Kinase Enzyme System ADP-GloTM Kinase assay from *Promega* was used to determine biological activity of test compounds.

UV sources for photochemical experiments



UV sources. (a) LED reactor used for irradiation of solutions in round bottom flasks. (b) LED device for the irradiation of 96-well microtitre plates. Eight LEDs (365 nm) irradiate four rows of wells (32 wells) at once. Accordingly three irradiation cycles are needed for the entire plate.



Technical setup and emission characteristics of the utilized UV sources. (a) LED reactor used for irradiation of solutions in round bottom flasks. The reactor consists of 12 LEDs with an emission maximum at a wavelength of 365 nm. The intensity can be adjusted to four levels (25, 50, 75 and 100%). The corresponding optical power in mW is shown. (b) LED device for irradiation of 96-well microtitre plates. There are also four intensity levels available.

3.3 Photoactivatable Caged Prodrugs of VEGFR-2 Kinase Inhibitors

Boris Pinchuk, Rebecca Horbert, Alexander Döbber, Lydia Kuhl and Christian Peifer

Molecules **2016**, *21*(5), 570.

DOI: 10.3390/molecules21050570

The vascular endothelial growth factor receptor 2 (VEGFR-2) is a key mediator of angiogenesis.¹⁹² This tyrosine kinase plays an important role in tumor growth and intraocular diseases and is therefore a significant drug target.^{216–218} Today, nine smKIs of VEGFR-2 are approved for the therapy of various cancers.²¹⁹ However, VEGFR-2-inhibitors are often promiscuous and show significant off-target effects.³⁵ Thus, novel inhibitors and approaches for VEGFR-2 research are still highly demanded.

3,4-Diarylmaleimids were reported to be potent inhibitors of VEGFR-2.^{190, 191} In the following paper photoactivatable prodrugs of VEGFR-2 inhibitors **7** and **8** (Figure 18) were reported. The goal was to apply the photocaging technique on potent VEGFR-2 inhibitors and thereby to enable spatiotemporal control of VEGFR-2 kinase activity. To best of our knowledge the referred compounds were the first caged VEGFR-2 inhibitors reported so far.

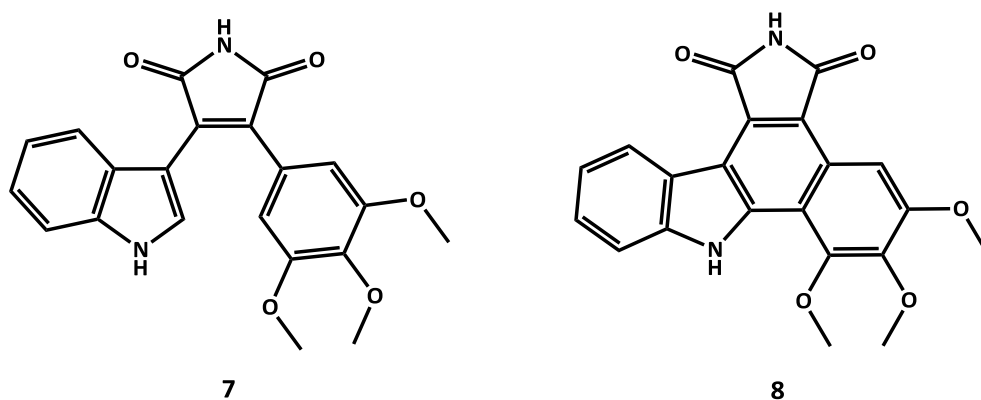


Figure 18: Chemical structures of examined VEGFR-2 inhibitors.^{190, 191, 194} 3,4-diarylmaleimide **7** and carbazole **8** correspond to the compounds **1** and **3** in the article “Photoactivatable Caged Prodrugs of VEGFR-2 Kinase Inhibitors”, respectively.¹⁹⁴

The typical workflow for caging protein kinase inhibitors (Figure 12) was applied. The DMNB group was utilized as PPG. Two caged derivatives **9** and **10** were yielded (Figure 19).

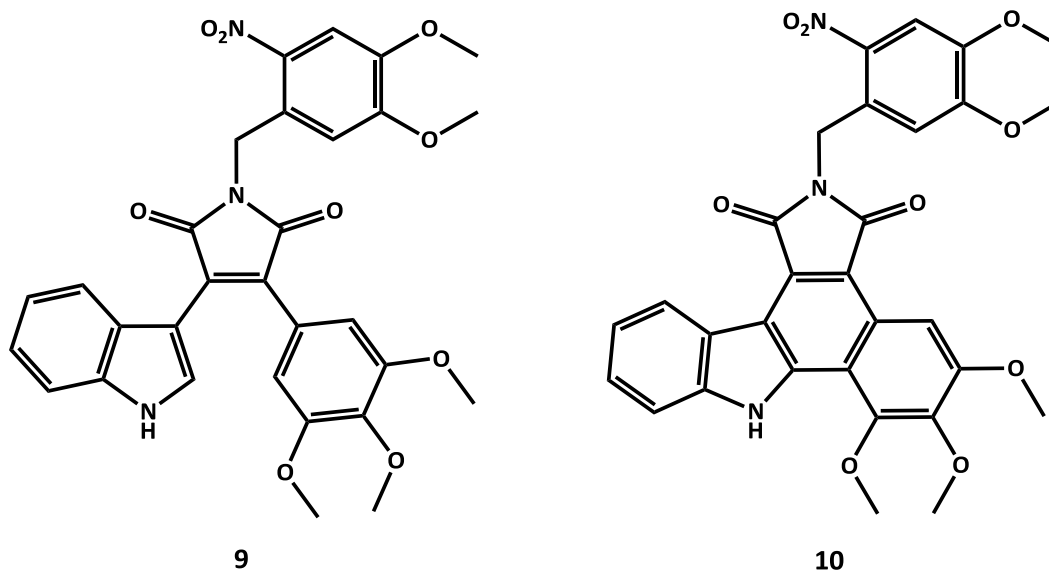


Figure 19: Chemical structures of photoactivatable VEGFR-2 inhibitors.¹⁹⁴ Caged 3,4-diarylmaleimide **9** and caged carbazole **10** correspond to the compounds **4** and **5** in the article “Photoactivatable Caged Prodrugs of VEGFR-2 Kinase Inhibitors”, respectively.¹⁹⁴

The loss-off-function of VEGFR-2 inhibitors due to photoprotection could be demonstrated both in enzymatic and cellular assays. It was observed that the diarylmaleimide **7** is of limited suitability for caging with the DMNB group due to its photoinduced reaction to the respective carbazole **8** at the wavelength used for PPG-cleavage. In contrast to the maleimide, the photoinduced release of active carbazole inhibitor **8** from its caged derivative **10** succeeded fast, clearly and without any observable by-products.¹⁹⁴

The autofluorescence of carbazole **8** and its photoactivatable prodrug **10** was used for examination of cellular bioavailability of the compounds. It was demonstrated that the insertion of the DMNB PPG does not diminish the cellular uptake of the utilized inhibitors.¹⁹⁴

Dr. Rebecca Horbert synthesized the caged compounds. I performed the characterization of all compounds both photochemically and in several *in vitro* assays such as fluorescence microscopy and cell proliferation assays. Furthermore, I wrote the manuscript.



Article

Photoactivatable Caged Prodrugs of VEGFR-2 Kinase Inhibitors

Boris Pinchuk, Rebecca Horbert, Alexander Döbber, Lydia Kuhl and Christian Peifer *

Institute of Pharmacy, University of Kiel, Gutenbergstr. 76, D-24118 Kiel, Germany; bpinchuk@pharmazie.uni-kiel.de (B.P.); rhorbert@pharmazie.uni-kiel.de (R.H.); adoebber@pharmazie.uni-kiel.de (A.D.); lkuhl@pharmazie.uni-kiel.de (L.K.)

* Correspondence: cpeifer@pharmazie.uni-kiel.de; Tel.: +49-431-880-1137

Academic Editor: Wiktor Szymański

Received: 16 March 2016; Accepted: 21 April 2016; Published: 29 April 2016

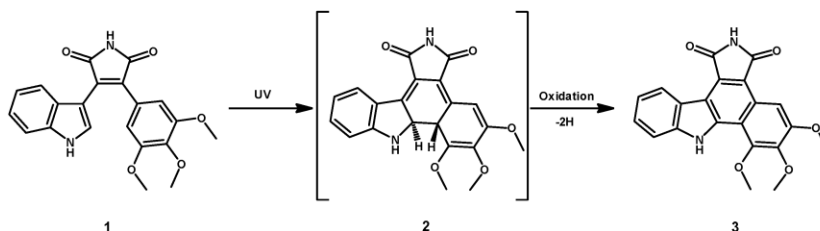
Abstract: In this study, we report on the design, synthesis, photokinetic properties and *in vitro* evaluation of photoactivatable caged prodrugs for the receptor tyrosine kinase VEGFR-2. Highly potent VEGFR-2 inhibitors **1** and **3** were caged by introduction of a photoremovable protecting group (PPG) to yield the caged prodrugs **4** and **5**. As expected, enzymatic and cellular proliferation assays showed dramatically diminished efficacy of caged prodrugs *in vitro*. Upon ultraviolet (UV) irradiation of the prodrugs original inhibitory activity was completely restored and even distinctly reinforced, as was the case for the prodrug **4**. The presented results are a further evidence for caging technique being an interesting approach in the protein kinase field. It could enable spatial and temporal control for the inhibition of VEGFR-2. The described photoactivatable prodrugs might be highly useful as biological probes for studying the VEGFR-2 signal transduction.

Keywords: photoactivatable prodrugs; caging; receptor tyrosine kinase; kinase inhibitors; VEGFR-2; 3,4-diarylmaleimides; photoremovable protecting group (PPG)

1. Introduction

Among protein kinases (PK), receptor tyrosine kinases such as vascular endothelial growth factor receptor (VEGFR) are significant drug targets for the development of clinically effective small molecule kinase inhibitors (smKI) [1–3]. VEGFR-2 plays an important role in the physiological regulation of angiogenesis [4]. This receptor tyrosine kinase is one of the key mediators of pathophysiological formation of blood vessels associated with tumor growth and intraocular neovascular diseases [5–8]. Besides therapeutic antibodies [9], small molecule tyrosine kinase inhibitors (TKIs) targeting VEGFR have been developed for the treatment of various neoplastic diseases [10–15]. Seven VEGFR inhibitors have been approved until 2016 [16]. However, TKI are often promiscuous, showing significant affinity for related tyrosine kinases such as fibroblast growth factor receptor (FGF-R), epidermal growth factor receptor (EGF-R), platelet derived growth factor receptors (PDGFR α/β), c-kit, Src, and for further PK [17,18]. The lack of specificity and off-target effects often limit the therapeutic value of such inhibitors. Besides cancer, VEGFR mediated angiogenesis is also critical in inflammation, wound healing, cardiovascular diseases, psoriasis, rheumatoid arthritis, and macular degeneration [7,19–23]. The impressive number of diseases illustrates the enormous potential for therapeutic agents and for biological probes in VEGFR research or related biological chemistry applications.

In 2006 a novel class of potent VEGFR inhibitors, namely 3,4-diarylmaleimides, was reported by Peifer *et al.* [24,25]. Within this series compound **1** showed the highest potency with an IC₅₀ towards VEGFR-2 of 2.5 nM [24]. The 1,6- π -electrocyclization of **1** followed by subsequent oxidation to carbazole **3** caused by UV-irradiation was also described (Scheme 1) [25].



Scheme 1. Ultraviolet (UV)-induced 1,6- π -electrocyclization of the 3,4-diarylmaleimide **1** followed by oxidation to the carbazole derivative **3** [25]. The intermediate **2** could not be isolated.

Both compounds, **1** and **3**, were found to be potent and specific VEGFR-2 inhibitors with strong anti-angiogenetic activity (VEGFR-2, IC_{50} = 2.5 nM and 62 nM for **1** and **3**, respectively) [25]. In light of the immense significance of VEGFR-2 inhibitors we aimed to develop relevant photoactivatable caged VEGFR-2 prodrugs. An approach using photoremovable protecting groups (PPG) provides spatial and temporal control over the release of a bioactive molecule by irradiation with UV light [26–28]. The bioactive inhibitor can be generated at a defined time point in an irradiated area of interest. Caged VEGFR-2 prodrugs could serve as novel experimental tools, e.g., for kinetic or mechanistic studies. Moreover, caged inhibitors should minimize systemic side effects. This might enable higher dosage of inactive prodrugs. Consequently, controllable irradiation should increase the concentration of the active drug in a cancer-afflicted tissue sharply.

A caged prodrug is typically designed by blocking a crucial pharmacophore moiety of the inhibitor using a PPG. Regarding smKI, this is most effectively done by blocking the hinge binder as this motif is basically used by all type I/II inhibitors [29]. Preventing a smKI from binding to the central hinge region not only renders the compound biologically inactive against the PK of interest but most likely against all other PK as well [30]. The modeled binding modes of **1** and **3** in the ATP binding site of VEGFR-2 were previously described [24]. Key interactions between the ligand and the protein are the H-bonds of the maleimide moiety towards the hinge region as shown in Figure 1.

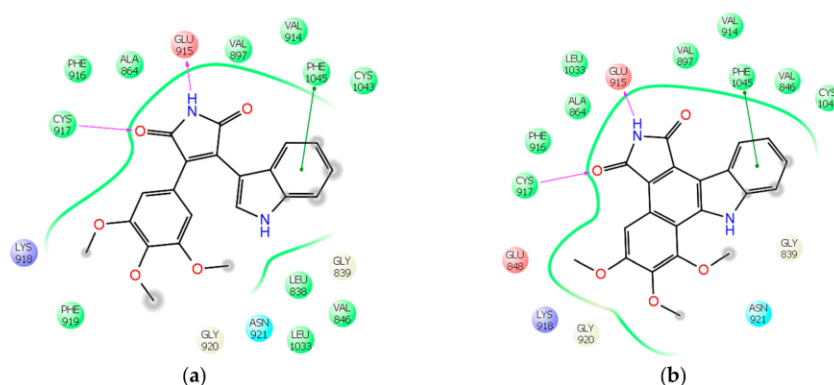


Figure 1. Modeled ligand interaction diagrams of VEGFR-2 inhibitors **1** and **3** in the ATP binding pocket of VEGFR-2 (pdb code 3CJF). Key ligand protein interactions are shown including H-bonds of the maleimide moiety towards Glu915 and Cys917 in the hinge region. (a) Binding mode of **1**; (b) Binding mode of **3**.

Among PPGs, *o*-nitrobenzyl derivatives (*o*-NB) have been successfully used in various biological applications [26,28,31–33]. The 4,5-dimethoxy-2-nitrobenzyl (DMNB) protecting group is a variation of *o*-NB that can be cleaved by irradiation at 365 nm [34]. This wavelength is less energetic compared to 254 nm used for the cleavage of *o*-NB, so extensive cell damage can be avoided [35]. There are some

recent examples for the use of DMNB including photoactivatable protein antigens for controlling the antibody-antigen interactions [36], a caged transmitter for studying neuron–glia interactions [37], and caged abscisic acid used to promote photo-induced protein dimerization [38]. We applied the DMNB caged concept to the key maleimide hinge binding motif of VEGFR-2 inhibitors **1** and **3** by designing compounds **4** and **5**, respectively, in which the relevant hinge binding NH moiety is blocked (Figure 2).

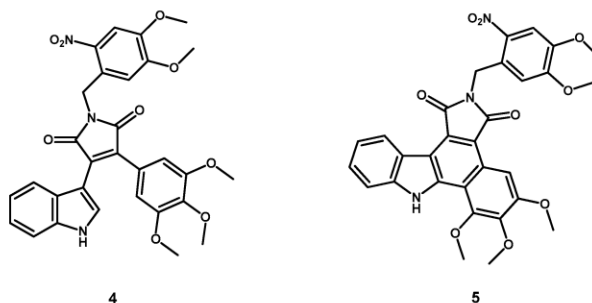


Figure 2. Designed caged compounds **4** and **5** with the 4,5-dimethoxy-2-nitrobenzyl (DMNB) protecting group attached to the maleimide resp. carbazole in order to prevent hinge binding.

Herein, we report on the design, synthesis, photochemical characterization and biological evaluation of the compounds **4** and **5**. These compounds are photoactivatable prodrugs of the previously described VEGFR-2 inhibitors **1** and **3**, respectively. First, molecular modeling studies predicted that blocking the maleimide moiety of the active compounds should diminish the inhibitory efficacy. Having the caged prodrugs synthesized, we next investigated the photoinduced cleavage of PPG and the release of the native inhibitors. The loss-of-function by photoprotection was proven *in vitro* both in enzymatic and in cellular proliferation assays. Finally, reconstitution of the inhibitory activity by UV irradiation has been demonstrated in cellular assays. The here presented photoactivatable prodrugs of VEGFR-2 inhibitors could be used as a novel pharmacological approach in VEGF-signaling research.

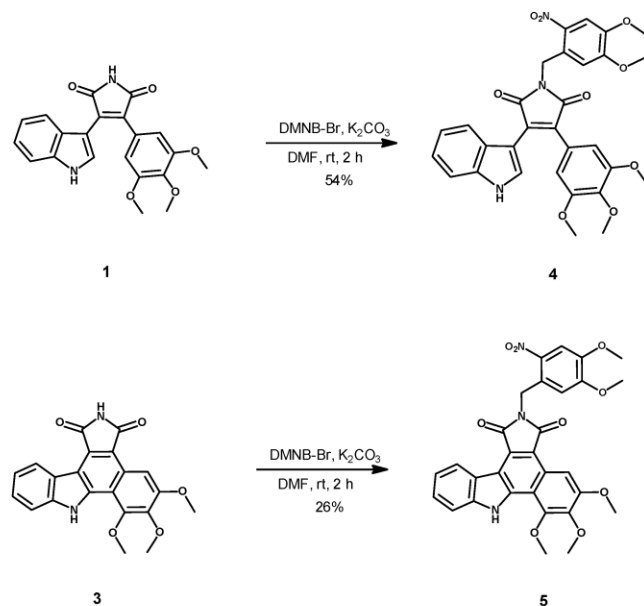
2. Results

2.1. Molecular Modeling

Molecular docking of the active compounds **1** and **3** into the ATP binding site of VEGFR-2 (pdb code 3CJF) revealed the maleimide moiety as the key pharmacophore group for the inhibitors interaction towards the hinge region of the target protein (Figure 1). To prove our prodrug concept we additionally docked caged **4** and **5** into the same pocket. In accordance with our hypothesis, the latter docking experiment did not result in plausible binding modes of the caged compounds in the active site (not shown). The DMNB protecting group prevented key H-bond-interactions to the hinge region. Moreover, the caged compounds did not fit into the binding pocket due to sterical clashes. Motivated by modeling results we synthesized **4** and **5** and subsequently characterized these compounds for their photochemical properties to determine parameters for decaging and potential usability for biological evaluation.

2.2. Synthesis

Compounds **1** and **3** were synthesized by literature procedures [25,39]. The synthesis of the caged compounds **4** and **5** from **1** and **3**, respectively, was found to proceed straightforward in terms of a base catalyzed S_N reaction by deprotonation of the acidic maleimide moiety, and using DMNB-Br as a reactant (Scheme 2).



Scheme 2. Synthesis of 4 and 5 [25,39].

2.3. Photochemical Characterization

Having both active and caged compounds, we investigated their photochemical characteristics. First, we recorded the UV/Vis absorption spectra both for maleimide and carbazole derivatives before and after insertion of the DMNB group, to find an appropriate wavelength for PPG cleavage. The normalized spectra are shown in Figure 3. The raw spectra can be found in the Supplementary Materials (Figure S1).

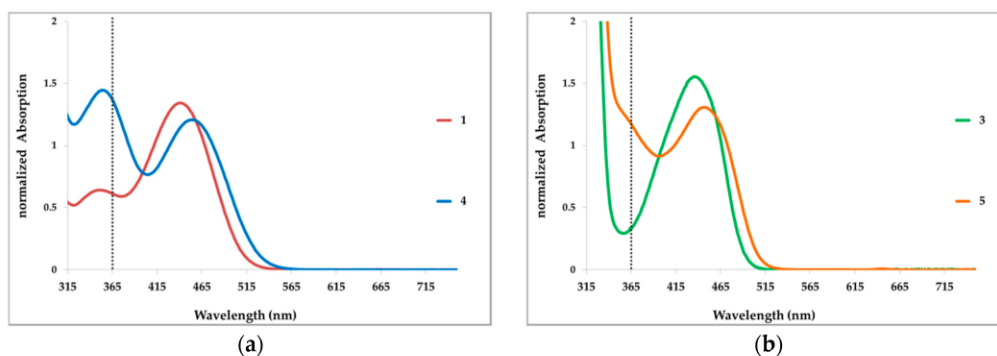


Figure 3. Normalized UV/Vis absorption spectra of compounds in DMSO. (a) UV/Vis absorption spectra of maleimide 1 (red line) and its caged prodrug 4 (blue line); (b) UV/Vis absorption spectra of carbazole 3 (green line) and its caged analogue 5 (orange line). The black dotted line in both diagrams flags 365 nm as the wavelength used for irradiation of caged compounds.

As shown in Figure 3, introduction of the DMNB PPG leads to increased light absorption around 365 nm (black dotted line). This applies for maleimides (Figure 3a) and carbazoles (Figure 3b). The same wavelength was previously described for the cleavage of the inserted DMNB group [27]. Wavelengths shorter than 300 nm are highly energetic and can easily damage biological tissues. 365 nm

can therefore be considered as the optimal wavelength for deprotection. Furthermore, the inserted PPG in **4** and **5** causes a weak bathochromic spectral shift of these compounds. This effect can be explained by an increased electron density due to substitution of the hydrogen at the imide nitrogen by the DMNB protecting group.

In general, one of the preconditions for successful caging approaches is the stability of the parent compounds when irradiated at the wavelength used for PPG cleavage. This stability is crucial, otherwise the actual inhibitor molecule would be degraded immediately after its release from the caged compound. For this reason, we next examined the stability of **1** and **3** towards irradiation at 365 nm. The light-emitting diode (LED) reactor with a wavelength of 365 nm (5.4 W; for technical information, see Supplementary Materials Figures S2 and S3) was used to irradiate 1 mM solutions of **1** and **3** in DMSO (Figure 4). HPLC and LC-MS analysis were used for content determination.

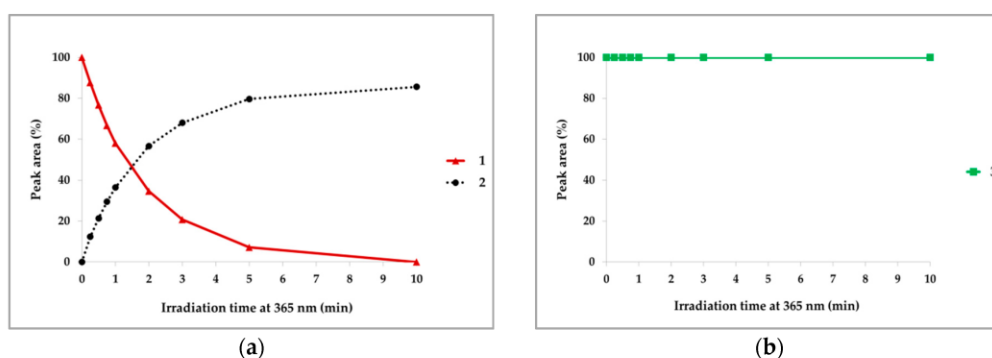


Figure 4. UV stability of the parent VEGFR-2 inhibitors. The compounds were irradiated at 365 nm with 5.4 W for up to 10 min and analyzed time dependently by HPLC. The detection wavelength for the HPLC analysis was 300 nm. The area under the HPLC-peaks is plotted against the irradiation time. (a) Irradiation of 1 mM solution of **1** in DMSO (red line). By progressing irradiation, **1** is converted into the intermediate product **2** (dotted black line); (b) Irradiation of 1 mM solution of **3** in DMSO (green line). **3** is stable under the described UV irradiation.

Irradiation of **1** at 365 nm induced the 1,6- π -electrocyclization of the 3,4-diarylmaleimide **1** to the intermediate **2** as analyzed by LC-MS (also see Scheme 1). Under the used irradiation conditions the subsequent oxidation to carbazole **3** did not occur (Figure 4a). Resulting from its instability at 365 nm, the maleimide **1** is not optimally suitable for the photocaging concept. In contrast, the carbazole **3** is quite stable under irradiation by 365 nm (Supplementary Figure S1b). Based on this data, the carbazole derivative **3** is more eligible for the caging concept than the 3,4-diarylmaleimide **1**.

A further prerequisite for an application of caged prodrugs is a rapid and quantitative release of active parent compounds by irradiation. To examine this, we investigated the uncaging of **4** and **5** induced by irradiation at 365 nm with 5.4 W (Figure 5). Exposure to UV light caused the cleavage of the DMNB PPG from caged compound **4**. Initially released maleimide **1** is converted to the intermediate **2** by proceeding irradiation, which is in line to the previously described instability of **1**, (compare Figure 4a). As expected, carbazole **3** was rapidly released from the caged derivative **5** by irradiating at 365 nm. Due to UV stability of **3** no other by-products could be detected.

Due to the results of photochemical characterization, it can be summarized that the caged carbazole **5** was a suitable candidate for our VEGFR-2 inhibitor caging concept. The straightforward release of parent compound **3** by short UV irradiation and the UV stability of uncaged molecule made the carbazoles interesting for biological evaluation *in vitro*. Although the maleimide **1** does not possess appropriate UV stability, we tested the caged **4** *in vitro* to determine its cellular efficacy too.

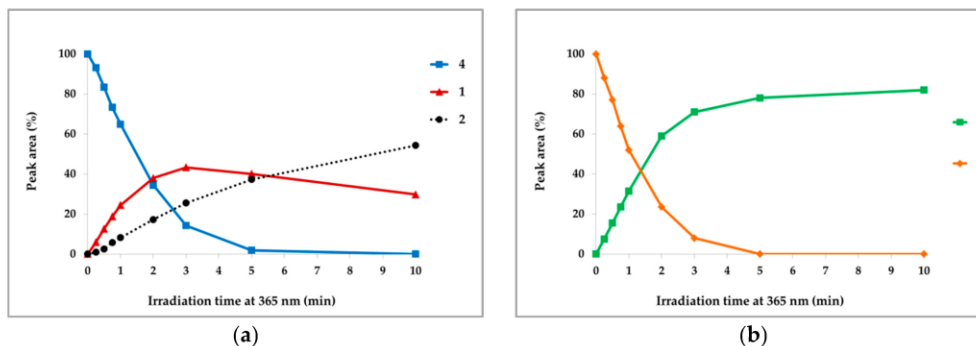


Figure 5. Release of parent VEGFR-2 inhibitors by irradiating their caged prodrugs. The DMNB-protected derivatives were irradiated at 365 nm with 5.4 W for up to 10 min. The uncaging was examined by HPLC and LC-MS analysis. The detection wavelength for the HPLC analysis was 300 nm. The amount of released parent compounds and their caged prodrugs are plotted as areas under HPLC-peaks against irradiation time. (a) Irradiation of 1 mM solution of 4 in DMSO (blue line) yields initially the maleimide 1 (red line). Continuing UV exposure leads to 1,6- π -electrocyclization of 1 to 2 (dotted black line); (b) Irradiation of 1 mM solution of 5 in DMSO (orange line) results in the clean release of carbazole 3 (green line).

2.4. Enzyme Assays

As predicted by molecular modeling, insertion of the protecting group DMNB should diminish the inhibitory activity both of the maleimide 1 and the carbazole 3. To prove this hypothesis, active compounds 1 and 3 and caged prodrugs 4 and 5 were tested in a radiometric kinase assay [40]. The IC_{50} values towards VEGFR-2 were determined (Table 1).

Table 1. Inhibitory activity of parent and caged compounds in a VEGFR-2 kinase assay (ProQinase, Freiburg, Germany) [40]. The IC_{50} values are presented.

Compound	VEGFR-2 IC_{50} (μ M)
1	0.005
3	0.152
4	4.590
5	44.80

The IC_{50} value of 1 is in low nanomolar range ($IC_{50} = 0.005 \mu$ M) and is comparable with the previously determined value [24]. The carbazole derivative 3 is an effective VEGFR-2 inhibitor too, although it is less active than 1 ($IC_{50} = 0.152 \mu$ M). Moreover, the measured IC_{50} values confirm that the caging significantly reduces the compounds activity. The caged compounds have at least a two magnitudes lower efficacy than the active inhibitors. The determined IC_{50} values are 4.59 μ M and 44.8 μ M for 4 and 5, respectively. The minimal residual activity of the caged compounds can be explained by minor impurities of active inhibitors in the samples. To sum up, we verified that the insertion of the DMNB PPG significantly decreases the inhibitory efficacy both of maleimides and of carbazoles.

To compare the active inhibitors 1 and 3, a selectivity profile over 79 kinases was recorded [41,42]. The residual kinase activities are presented as a heatmap (Figure 6, for raw data see Supplementary Table S1). The selectivity profile shows that the diaryl maleimide 1 is more selective than its carbazole derivative 3.

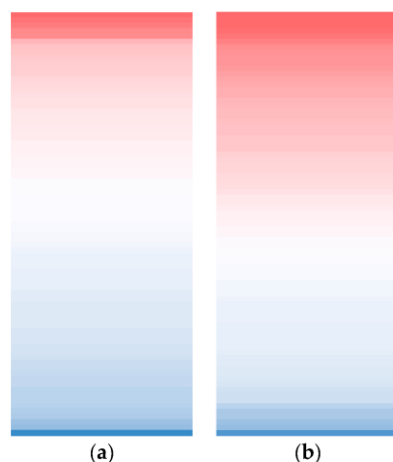


Figure 6. Selectivity profile of active compounds in a panel of 79 kinases. The inhibitory effect was examined at inhibitor's concentration of 0.1 μM by determination of residual kinase activity. The data are presented as a heatmap. The columns have been individually ranked from low (red) to high (blue) residual activity values. The raw data are shown in the Supplementary Table S1. (a) Selectivity profile of **1**; (b) Selectivity profile of **3** (MRC, Dundee, Scotland).

2.5. Cellular Assays

Due to the findings described above, we supposed that the caged molecules **4** and **5** would be considerably less active in cellular assays as well compared to the parent compounds **1** and **3**. To prove this hypothesis, we examined their antiproliferative activity *in vitro*. Growth assays on VEGFR-2 dependent PC-3 cells [43–45] were performed.

Dose-response curves for non-irradiated compounds are shown in Figure 7a. The corresponding GI_{50} values (compounds concentration at which the cellular growth is inhibited by 50%) are shown in Table 2. Compounds **1** and **3** exhibit potent antiproliferative efficacy at concentrations in the low μM range. The GI_{50} value for the maleimide **1** was measured as 6.4 μM . In contrast to **1**, its caged derivative **4** exhibits very marginal antiproliferative activity, even at high concentrations the GI_{50} for **4** was not reached. The carbazole **3** ($\text{GI}_{50} = 0.2 \mu\text{M}$) is more potent in this assay than the maleimide **1**. This increased cytostatic activity could be caused by promiscuity of **3** that inhibits more kinases than **1** and therefore induces higher stress for the exposed cells. This unexpected cellular response to **3** should be examined in greater depth. Once again, the caged derivative **5** was significantly less active ($\text{GI}_{50} = 34.6 \mu\text{M}$) than its parent compound **3**. The low cytostatic activity of the caged compounds at high concentrations might be explained by minor impurities of non-caged parent compounds in the samples.

Dose-response curves for non-irradiated compounds are displayed in After proving the diminished cellular activity of caged compounds, we next explored if their antiproliferative efficacy could be restored by UV irradiation. The cellular growth assays described above were repeated and the compound treated PC-3 cells were exposed to UV light at 365 nm (5 min, 1.1 kW/m^2). The measured dose-response curves are shown in Figure 7b. The corresponding GI_{50} values are listed in Table 2. Previously, control experiments verified that the PC-3 cells tolerate the applied dosage of UV irradiation sufficiently well; the cellular growth is reduced only to 90% by used irradiation (Supplementary Figure S4). The determined dose-response curves demonstrate that 5 min exposure to UV light completely restores the inhibitory activity of the caged compounds. After irradiation, the caged derivatives exhibit comparable or even stronger antiproliferative efficacy compared to that of their not caged parent compounds. The detected GI_{50} value of the irradiated **1** (2.9 μM) is slightly lower than of non-irradiated **1** (6.4 μM). However, a significantly increased inhibitory effect could be detected for the

irradiated caged **4** (GI_{50} value was $0.1 \mu\text{M}$). Interestingly, the caged molecule **4** is about 10-fold more active after UV treatment than its parent maleimide **1**. One of the possible reasons for this increased activity might be a biological effect of the released protecting group. To investigate the effect of the cleaved PPG moiety, we used two model compounds: Boc-protected L-alanine (Boc-Ala) and its DMNB photo protected derivative (DMNB-Boc-Ala), as we considered Boc-Ala to be nontoxic. First, the effect of UV unexposed compounds on proliferation of the PC-3 cells was explored. Both protected amino acid derivatives did not show any antiproliferative effects even at high concentrations (Supplementary Figure S5c). The same experiment was repeated with UV irradiation (365 nm , 5 min , 1.1 kW/m^2). UV exposed Boc-Ala does not have any effect on cellular growth. In contrast, DMNB-Boc-Ala exhibits distinct antiproliferative activity after irradiation at concentrations above $10 \mu\text{M}$ ($GI_{50} = 50.3 \mu\text{M}$) (Supplementary Figure S5d). Therefore, it could be assumed that the antiproliferative activity in this assay is caused by the cleaved DMNB. However, the concentration at which the PPG shows toxicity (above $10 \mu\text{M}$) is approximately 500-fold higher than the efficacious concentration of the irradiated **4**. Thus, it is not only the cleaved PPG that is responsible for dramatically increased activity of UV-exposed **4**. Presumably, the following parameters contribute to the biological efficacy of irradiated **4**: The released active inhibitor **1**, the formation of the intermediate **2** (Figure 5a), the cleaved PPG and, finally, the UV irradiation itself cause the described rise of activity in synergistic manner. After irradiation, the carbazole **3** displayed a similar efficacy to that before UV exposure: GI_{50} value was $0.38 \mu\text{M}$. The activity of its caged derivative **5** was completely restored by irradiation ($GI_{50} = 0.22 \mu\text{M}$).

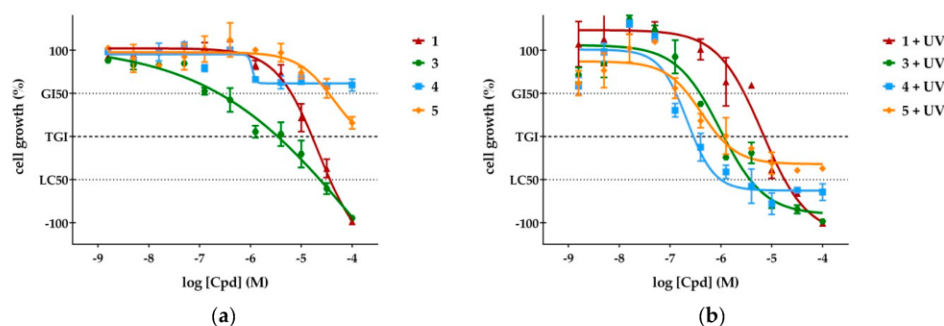


Figure 7. Antiproliferative activity of tested compounds on VEGFR-2 dependent PC-3 cells. (a) Dose-response curves of active inhibitors (**1** and **3**) and their corresponding caged compounds (**4** and **5**) were determined without UV irradiation. Cell growth was measured 48 h after incubation with the compounds. The caged derivatives do not exhibit cytotoxic activity: the TGI mark is not reached even at high concentrations; (b) Cells were incubated for 1 h with the compounds and then irradiated at 365 nm (1.1 kW/m^2) for 5 min. Cell growth was determined 48 h after incubation with the compounds. After irradiation, the caged derivatives show similar (**5**) or even left shifted (**4**) dose-response curves as that of active compounds. GI_{50} = 50% growth inhibition; TGI = total growth inhibition; LC_{50} = 50% lethal concentration; $n = 4$. Error bars represent standard deviation. The effect of UV irradiation on the PC-3 cells is shown in Supplementary Figure S4.

Table 2. Antiproliferative activity of tested compounds in cellular growth assays with PC-3 cells, without and after irradiation at 365 nm (1.1 kW/m^2). The GI_{50} values (50% cellular growth inhibition) are presented. “Not reached”: The tested compound did not inhibit the cell growth to 50%.

Compound	GI_{50} without Irradiation (μM)	GI_{50} after Irradiation (μM)
1	6.4	2.9
3	0.2	0.4
4	not reached	0.1
5	34.6	0.2

Summing up, we demonstrated that the insertion of the DMNB PPG effectively diminishes the activity of the inhibitors **1** and **3**. The antiproliferative efficacy can be restored easily or even reinforced by UV irradiation of the corresponding caged compounds **4** and **5**.

Next, we investigated the cellular bioavailability of the caged prodrugs. For this purpose, we used the autofluorescence of the carbazole **3** and its caged derivative **5**. The emission spectra of both compounds are shown in the Supplementary Figure S6. The fluorescence microscopy was used to explore the uptake of the compounds into the cells. Live PC-3 cells were stained with 10 μ M solutions of **3** or **5**, and then fixed with formalin. Subsequently, the cell nuclei were counterstained with 1 μ g/mL DAPI. As demonstrated by fluorescence microscopy (Figure 8) both carbazoles **3** and **5** are taken up into the cells, but not within the cell nuclei. The insertion of the DMNB PPG does not alter the cellular uptake of the carbazoles (Figure 8b). Due to this data, it can be concluded that the DMNB PPG does not decrease the cell permeability of the inhibitors.

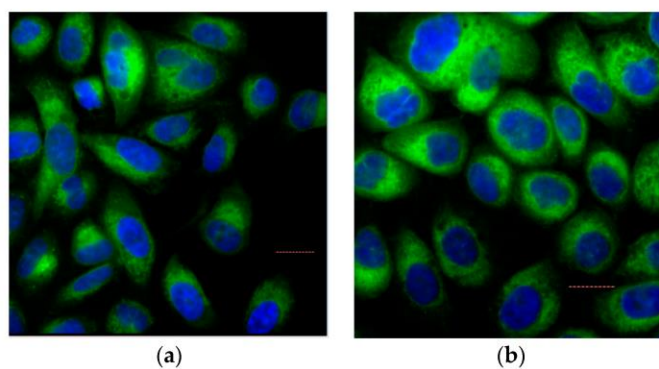


Figure 8. Microscopic images of stained PC-3 cells. The investigated compounds **3** and **5** are shown in green. Both compounds were applied at 10 μ M concentrations. The cell nuclei were counterstained with 1 μ g/mL DAPI and are marked blue. The dashed line represents 20.3 μ m. (a) Staining with carbazole **3**; (b) Staining with caged compound **5**.

3. Discussion

There are examples of photoactivatable kinase inhibitors described in the literature [31,35,46]. The interest in this research field is motivated by exciting options offered by the caging concept in basic research as well as in therapeutic applications. Targeted irradiation enables release of active inhibitors at higher concentrations in a precisely controlled way. Temporally and locally verifiable activation is a powerful pharmacological tool to study the biological effects of inhibiting kinase signaling. Moreover, this caging approach could spare undesirable side effects associated with kinase inhibitor therapy.

Our research group has already evaluated caged derivatives of the approved kinase inhibitors vemurafenib [30] and imatinib [47] *in vitro*. To the best of our knowledge, there are no caged VEGFR-2 inhibitors described so far. Therefore, it was our motivation to verify the caging concept on this therapeutically important kinase. In this article, we report on the design, synthesis, photochemical and *in vitro* characterization of previously published VEGFR-2 inhibitors **1** and **3** [24,25]. By usage of DMNB as the PPG, we synthesized caged derivatives **4** and **5**. These novel photoactivatable prodrugs of VEGFR-2 inhibitors can be used in a variety of experiments investigating the VEGF-signaling. Irradiation of the caged maleimide **4** did not result in a clean release of the parent inhibitor **1** but yielded a mixture of **1** and **2**. The intermediate **2** could not be isolated but it could have some unexplored biological effects *in situ* due to its oxidation to **3**. Another interesting result was the increased antiproliferative activity of **4** after irradiation. The cytotoxic activity of **4** after UV exposure was 10-fold higher in cellular assays compared to its parent compound **1**. This observation cannot be explained

separately whether by the formation of intermediate **2** nor by the cleaved PPG. The anticipated formation of **2** alone is unlikely to cause this gain of activity, because it was not observed during irradiation of **1** under the same experimental conditions. By usage of model compounds it could be demonstrated that the cleaved DMNB group exhibit antiproliferative activity only in concentrations above 10 μM . Presumably, there are some synergistic effects of the released inhibitor, the generated intermediate, the cleaved PPG and the UV irradiation that cause the increased efficacy of irradiated **4**. On the one hand, this increased activity could promote the usage of **4** as a research tool for VEGF-signaling. On the other hand, the distinct gain of antiproliferative efficacy towards cancer cells can be very interesting for possible medicinal applications. In contrast to maleimides, the photoinduced release of active carbazole **3** from its caged derivative **5** succeeded clearly, fast, and without formation of observable byproducts. The insertion of the DMNB group did not prevent the cellular uptake of the carbazole. Therefore, caged carbazole **5** provides a photoactivatable VEGFR-2 inhibitor that can be used as a valuable tool for studying VEGF-signaling.

The implementation of DMNB caged kinase inhibitors in therapeutically relevant approaches might be restricted due to necessity of UV light for the release of active compounds. Although UVA irradiation (wavelengths above 320 nm) causes less direct DNA damage than UVB or UVC exposure [48], high dosage of UVA is toxic and can lead to oxidative stress, photoaging, and immunosuppression [48,49]. Another restriction for a medical application of caged prodrugs is the poor penetration of UV light into biological tissues. Only depths of about 100 μm can be reached [50]. There are several possible solutions to overcome the poor penetration: optical fibers or endoscopic probes can transmit the required light to the site of action. Moreover, nearby areas could be irradiated during surgery.

One option to dispense with UV light is the usage of protecting groups that are cleavable by the visible light irradiation. Some current examples of these groups are BODIPY derived PPGs and thiocoumarins. BODIPY-based protecting groups can be removed with green wavelengths above 500 nm [51]. Irradiation with cyan light can cleave thionated coumarins [52]. The application of visible light for uncaging would enable nontoxic release of active compounds in deeper tissue layers. The best permeation through biological tissues can be achieved within the biological optical window by wavelengths around 800 nm [53]. Hence, two-photon excitation is an interesting approach, even though it requires special equipment like fs-pulsed lasers [54]. It remains to be seen if these novel developments would allow a medical application of the caged compounds.

4. Materials and Methods

4.1. Molecular Modeling

Molecular modeling was performed on a DELL 8 core system. For visualization Maestro, version 9.7, Schrödinger, LLC, (New York, NY, USA, 2014) was used. Protein crystal structures were prepared prior to docking by the Protein Preparation Wizard [55] utilizing the following programs: Epik, version 2.7, 2014 [56]; Prime, version 2.4, 2014 [57]. Thus, the X-ray crystal structure refinement process included addition of hydrogen atoms, optimization of hydrogen bonds, and removal of atomic clashes. Default settings were used. Missing side chains and loops were filled in with Prime. Furthermore, selenomethionines were converted to methionines and water molecules were deleted.

Additionally, ligands were prepared in order to create energetically minimized 3D geometries and assign proper bond orders (MacroModel, version 10.3, 2014 [58]). Accessible tautomer and ionization states were calculated prior to screening (LigPrep, version 2.9, 2014 [59]). To generate bioactive conformers a conformational search method was used (ConfGen, version 2.7, 2014 [60]). Receptor grid generation was performed by Glide, version 6.2, 2014 [61]. For ligand docking and screening the Glide SP workflow was used. Energetically minimized ligand conformations were docked into the active site of the protein; possible binding poses were determined and subsequently ranked based on their calculated binding affinities.

4.2. Chemistry

All reagents and solvents were obtained from commercial sources and used as received (THF was used after distillation over K/benzophenone). Reagents were purchased from abcr GmbH (Karlsruhe, Germany), Fisher Scientific GmbH/Acros (Schwerte, Germany), Sigma-Aldrich Chemie (Hamburg, Germany) or VWR International GmbH (Hannover, Germany).

Where appropriate, column chromatography was performed for crude precursors with Merck (Darmstadt, Germany) silica gel 60 (0.063–0.200 mm) or Acros Organics silica gel (0.060–0.200 mm; pore diameter *ca.* 60 nm). Column chromatography was performed on a LaFlash system (VWR) using silica gel columns (PF-30SIHP, 30 μ m, 40 g, puriFlash) or RP18 columns (PF-15C18HP, 15 μ m, 55 g, puriFlash). The crude product was loaded on Merck silica gel 60 (15–40 μ m). The progress of reactions was monitored by thin-layer chromatography (TLC) utilizing silica gel polyester sheets (SIL G/UV254, 0.2 mm, Polygram[®], Macherey-Nagel GmbH (Düren, Germany)).

High-performance liquid chromatography (HPLC) analyses were performed on a 1050 Series system (Hewlett Packard, Ratingen, Germany). As column an Agilent ZORBAX[®] Eclipse XDB-C8, 5 μ m (4.6 mm \times 150 mm) was used. Injection volume of the compound solutions was 20 μ L. As mobile phase (flow rate 1.5 mL/min) served a gradient of KH₂PO₄ buffer (10 mM, pH 2.3) and methanol over 14 min. The detection wavelength was adapted to the according UV/vis absorption spectra. All key compounds submitted to biological assays were proven by this method to show \geq 98% purity.

Melting points were determined on a SMP3 apparatus (Stuart Scientific, Staffordshire, UK) and are uncorrected. ¹H- (300 MHz) and ¹³C- (75 MHz) NMR were recorded on an Avance III 300 spectrometer (Bruker, Rheinstetten, Germany) at 300 K with a multinuclear probe head using the manufacturer's pulse programs. The data are reported as follows: chemical shifts in ppm from Me₄Si (TMS) as external standard, multiplicity and coupling constant (Hz). NMR spectra were obtained on a ¹H (300 MHz) and ¹³C spectra (75 MHz) were referenced either to TMS or to internal DMSO-*d*₅ (¹H-NMR δ 2.50) and internal DMSO-*d*₆ (¹³C-NMR δ 39.5) or internal CHCl₃ (¹H-NMR δ 7.26) and internal CDCl₃ (¹³C-NMR δ 77.0). All coupling constants (*J* values) are quoted in Hz. The following NMR abbreviations are used: b (broad), s (singlet), d (doublet), t (triplet), m (unresolved multiplet). The labeling scheme of structures to correlate NMR signals is included in the data.

LC-MS samples were chromatographically separated utilizing a 1100 HPLC system (Agilent, Waldbronn, Germany) consisting of a thermostated autosampler, diode array detection, and an Agilent ZORBAX[®] Eclipse XDB-C8, 5 μ m (4.6 mm \times 150 mm). Elution was achieved with a solvent gradient system of water and acetonitrile, with 0.1% of acetic acid and a flow rate of 1 mL/min. The eluent flow was splitted to the mass spectrometer. Mass spectrometry was carried out using a Bruker Esquire-LC instrument (Bruker Daltonik, Bremen, Germany), with electrospray ionization (ESI) operating in the positive ion mode. Following parameters were used: drying gas nitrogen 8 L/min, nebulizer 35 psi, dry gas heating 350 °C, HV capillary 4000 V, HV EndPlate offset –500 V. For full experimental details of the synthesis and characterization of described compounds see Chemical Synthesis and Characterization.

4.3. Chemical Synthesis and Characterization

4.3.1. 3-(1*H*-Indol-3-yl)-4-(3,4,5-trimethoxyphenyl)-1*H*-pyrrole-2,5-dione (1)

2-(3,4,5-Trimethoxyphenyl)acetamide (10 mmol, 2.25 g) was dissolved in dry THF (30 mL) under nitrogen atmosphere and the reaction mixture was cooled to 0 °C. Ethyl 2-(1*H*-indol-3-yl)-2-oxoacetate (13 mmol, 2.82 g) dissolved in dry THF (40 mL) was added dropwise. Afterwards, potassium *tert*-butoxide solution (1M in THF, 40 mmol, 40 mL) was added. Subsequently, the deep purple reaction mixture was stirred for 6 h at room temperature. Quenching of the reaction with saturated ammonium chloride solution (40 mL) changed the color to orange. After addition of ethyl acetate (50 mL), the solution was stirred for another 15 min. After filtration, the organic layer was washed with brine, dried over Na₂SO₄ and evacuated. The crude product was purified by flash silica gel chromatography with a gradient of petroleum ether and ethyl acetate to give an orange solid (5.9 mmol, 2.25 g, 59%).

$C_{21}H_{18}N_2O_2$ (M_r 378.38, Figure 9). Purity (HPLC) > 98%; m.p. 243 °C; 1H -NMR (DMSO- d_6): δ 3.38 (s, 6H), 3.67 (s, 3H), 6.37 (d, $^3J = 8.0$ Hz, 1H), 6.74 (s, 2H), 6.76 (t, $^3J = 7.9$ Hz, 1H), 7.09 (t, $^3J = 7.6$ Hz, 1H), 7.45 (d, $^3J = 8.0$ Hz, 1H), 7.98 (d, $^3J = 1.7$ Hz, 1H), 11.03 (s, 1H), 11.89 (bs, 1H); ^{13}C -NMR (DMSO- d_6): δ 55.5, 60.1, 104.2, 107.6, 112.1, 119.6, 121.5, 122.0, 123.7, 125.5, 128.2, 131.2, 131.8, 136.4, 138.1, 152.2, 172.2, 172.5; LC-MS (ESI): m/z 379 [MH] $^+$.

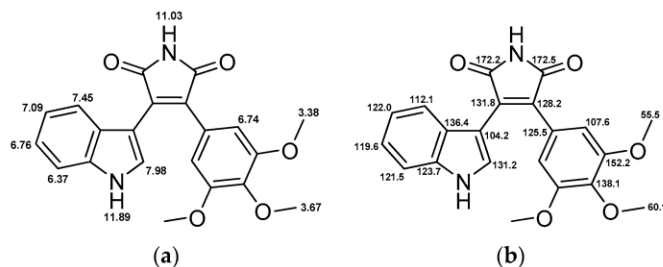


Figure 9. Chemical structure of **1** and relevant NMR shifts for (a) 1H -NMR; and (b) ^{13}C -NMR.

4.3.2. 5,6,7-Trimethoxybenzo[*a*]pyrrolo[3,4-*c*]carbazole-1,3(2*H*,8*H*)-dione (**3**)

3-(1*H*-Indol-3-yl)-4-(3,4,5-trimethoxyphenyl)-1*H*-pyrrole-2,5-dione (**1**, 0.3 mmol, 114 mg) was dissolved in DMSO (20 mL) and irradiated with an LED reactor at 365 nm (5.4 W) for 30 min. Ethyl acetate (100 mL) was added and washed thoroughly with water, dried over Na_2SO_4 and concentrated. Purification by flash silica gel chromatography with a gradient of petroleum ether and ethyl acetate afforded an orange solid (0.03 mmol, 12 mg, 11%). $C_{21}H_{16}N_2O_5$ (M_r 376.36, Figure 10). Purity (HPLC) >98%; m.p. 275 °C; 1H -NMR (DMSO- d_6): δ 3.95 (s, 3H), 3.97 (s, 3H), 4.19 (s, 3H), 7.32 (t, $^3J = 7.6$, 1H), 7.50 (t, $^3J = 7.6$, 1H), 7.88 (d, $^3J = 8.1$, 1H), 8.23 (s, 1H), 8.89 (d, $^3J = 7.8$, 1H), 11.03 (s, 1H), 11.84 (s, 1H); ^{13}C -NMR (DMSO- d_6): δ 55.8, 60.9, 61.6, 100.0, 111.6, 112.5, 113.2, 116.9, 120.4, 120.4, 123.5, 123.9, 126.0, 127.7, 138.4, 139.9, 141.3, 148.5, 154.5, 170.4, 171.6; LC-MS (ESI): m/z 377 [MH] $^+$.

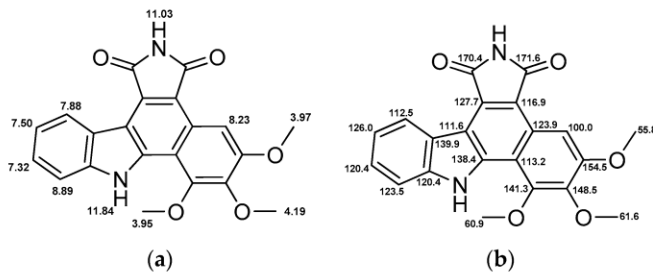


Figure 10. Chemical structure of **3** and relevant NMR shifts for (a) 1H -NMR; and (b) ^{13}C -NMR.

4.3.3. 1-(4,5-Dimethoxy-2-nitrobenzyl)-3-(1*H*-indol-3-yl)-4-(3,4,5-trimethoxyphenyl)-1*H*-pyrrole-2,5-dione (**4**)

3-(1*H*-Indol-3-yl)-4-(3,4,5-trimethoxyphenyl)-1*H*-pyrrole-2,5-dione (**1**, 0.5 mmol, 189 mg) and K_2CO_3 (1 mmol, 138 mg) were dissolved in dry DMF (15 mL). 4,5-dimethoxy-2-nitrobenzyl bromide (0.5 mmol, 138 mg) was dissolved in dry DMF (2 mL) and added dropwise to the reaction mixture. After stirring at room temperature for 2 h, the solvent was evaporated and the crude product was redissolved in ethyl acetate, washed with brine, dried over Na_2SO_4 and concentrated. Purification by flash silica gel chromatography with a gradient of petroleum ether and ethyl acetate afforded an orange solid (0.27 mmol, 155 mg, 54%). $C_{30}H_{27}N_3O_9$ (M_r 573.55, Figure 11). Purity (HPLC) >98%; m.p. 205 °C; 1H -NMR (DMSO- d_6): δ 3.38 (s, 6H), 3.68 (s, 3H), 3.84 (s, 3H), 3.87 (s, 3H), 5.08 (s, 2H), 6.38 (d, $^3J = 8.1$ Hz, 1H), 6.77 (s, 2H), 6.78 (t, $^3J = 7.3$ Hz, 1H), 6.95 (s, 1H), 7.11 (t, $^3J = 7.5$ Hz, 1H), 7.46 (d, $^3J = 8.0$ Hz, 1H),

7.66 (s, 1H), 8.04 (d, $^3J = 2.6$ Hz, 1H), 11.96 (s, 1H); ^{13}C -NMR (DMSO- d_6): δ 38.5, 55.5, 56.1, 56.2, 60.1, 104.3, 107.6, 108.2, 111.3, 112.2, 119.8, 121.7, 122.2, 123.6, 125.3, 126.2, 127.3, 131.5, 131.7, 136.5, 138.2, 140.5, 147.8, 152.2, 153.0, 170.8, 170.9; LC-MS (ESI): m/z 574 [MH] $^+$.

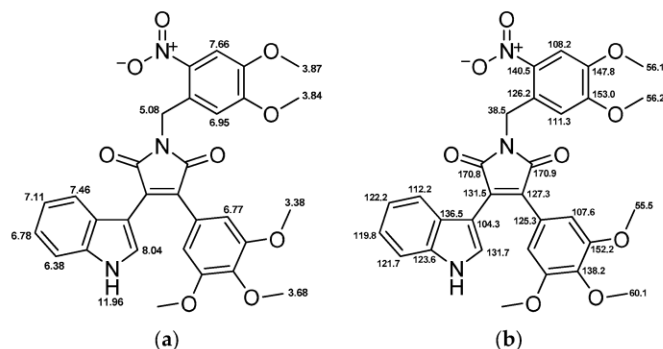


Figure 11. Chemical structure of 4 and relevant NMR shifts for (a) ^1H -NMR; and (b) ^{13}C -NMR.

4.3.4. 2-(4,5-Dimethoxy-2-nitrobenzyl)-5,6,7-trimethoxybenzo[*a*]pyrrolo[3,4-*c*]carbazole-1,3(2*H*,8*H*)-dione (5)

5,6,7-Trimethoxybenzo[*a*]pyrrolo[3,4-*c*]carbazole-1,3(2*H*,8*H*)-dione (3, 0.13 mmol, 28 mg) and K_2CO_3 (0.38 mmol, 52 mg) were dissolved in dry DMF (5 mL). 4,5-Dimethoxy-2-nitrobenzyl bromide (0.13 mmol, 33 mg) was dissolved in dry DMF (2 mL) and added dropwise to the reaction mixture. After stirring at room temperature for 2 h, the solvent was evaporated and the crude product redissolved in ethyl acetate, washed with brine, dried over Na_2SO_4 and concentrated. Recrystallization from ethyl acetate gave an orange solid (0.03 mmol, 19 mg, 26%). $\text{C}_{30}\text{H}_{25}\text{N}_3\text{O}_9$ (M_r 571.53, Figure 12). Purity (HPLC) >98%; m.p. 283 °C; ^1H -NMR (DMSO- d_6): δ 3.71 (s, 3H), 3.86 (s, 3H), 3.97 (s, 3H), 4.21 (s, 3H), 5.15 (s, 2H), 6.96 (s, 1H), 7.33 (t, $^3J = 7.4$ Hz, 1H), 7.52 (t, $^3J = 7.4$ Hz, 1H), 7.68 (s, 1H), 7.90 (d, $^3J = 7.6$ Hz, 1H), 8.23 (s, 1H), 8.87 (d, $^3J = 7.6$ Hz, 1H), 11.88 (s, 1H); ^{13}C -NMR (DMSO- d_6): δ 38.0, 55.8, 56.1, 60.9, 61.6, 100.0, 108.3, 111.0, 111.8, 112.6, 113.1, 115.9, 120.2, 120.6, 123.4, 123.9, 126.2, 126.5, 126.7, 138.5, 139.9, 140.4, 141.5, 147.7, 148.5, 153.1, 154.8, 168.8, 169.8; LC-MS (ESI): m/z 571 [MH] $^+$.

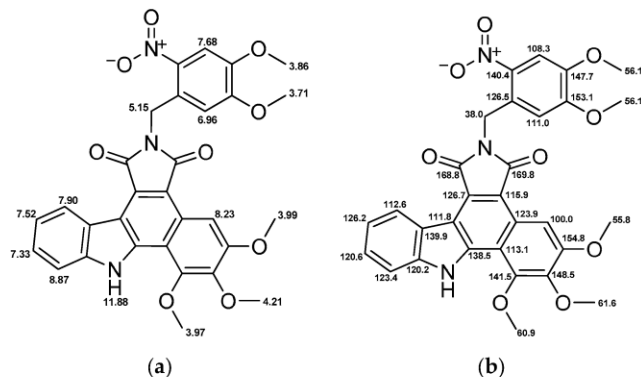


Figure 12. Chemical structure of 5 and relevant NMR shifts for (a) ^1H -NMR; and (b) ^{13}C -NMR.

4.3.5. 2-(3,4,5-Trimethoxyphenyl)acetamide (7)

2-(3,4,5-Trimethoxyphenyl)acetic acid (20 mmol, 4.6 g) was dissolved in anhydrous THF (30 mL). After addition of thionyl chloride (40 mmol, 3 mL) and a catalytic amount of DMF, the reaction mixture was heated to 40 °C until gas formation was completed (30 min). Subsequently, the solvent

and excessive thionyl chloride were removed under reduced pressure. This step was repeated after addition of THF (10 mL). The remaining brown oil was dissolved in DCM (50 mL) and cooled to 0 °C. Next, ammonia solution (25%, 10 mL) was added to the mixture and stirred for 1 h at room temperature. After addition of hydrochloric acid (1m, 20 mL), the organic layer was washed with brine and dried over Na₂SO₄. Evacuation and recrystallization from ethanol afforded grey needles (16.8 mmol, 3.86 g, 84%). C₁₁H₁₅NO₄ (M_r 225.24, Figure 13). Purity (HPLC) >98%; m.p. 124 °C; ¹H-NMR (CDCl₃): δ 3.50 (s, 2H), 3.82 (s, 3H), 3.84 (s, 6H), 5.53 (bs, 1H), 5.79 (bs, 1H), 6.47 (s, 2H); ¹³C-NMR (CDCl₃): δ 43.8, 56.3, 61.0, 106.5, 130.6, 137.4, 153.7, 173.6; LC-MS (ESI): *m/z* 226 [MH]⁺.

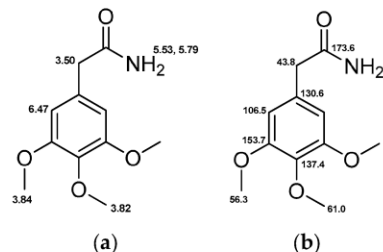


Figure 13. Chemical structure of 7 and relevant NMR shifts for (a) ¹H-NMR; and (b) ¹³C-NMR.

4.3.6. Ethyl 2-(1*H*-indol-3-yl)-2-oxoacetate (10)

Indole (40 mmol, 4.8 g) was dissolved in dry DCM (70 mL) under nitrogen atmosphere and stirred at 0 °C. After dropwise addition of diethylaluminium chloride solution (1m in hexane, 60 mmol, 60 mL), the reaction mixture was stirred for 30 min at 0 °C. Subsequently, ethyl oxalyl chloride (60 mmol, 6.8 mL) was added dropwise followed by stirring for further 3 h. In the next step, ice was carefully added to the reaction mixture for hydrolysis. The organic layer was washed with saturated ammonium chloride solution and brine, dried over Na₂SO₄ and concentrated. Purification by flash silica gel chromatography with a gradient of petroleum ether and ethyl acetate afforded light-pink needles (21.9 mmol, 4.75 g, 55%). C₁₂H₁₁NO₃ (M_r 217.22, Figure 14). Purity (HPLC) >98%; m.p. 186 °C; ¹H-NMR (CDCl₃): δ 1.34 (t, ³J = 7.1 Hz, 3H), 4.36 (q, ³J = 7.1, 2H), 7.24–7.33 (m, 2H), 7.53–7.58 (m, 1H), 8.14–8.19 (m, 1H), 8.42 (d, ³J = 3.3, 1H), 12.38 (bs, 1H); ¹³C-NMR (CDCl₃): δ 13.9, 61.6, 112.4, 112.7, 121.1, 122.8, 123.8, 125.5, 136.7, 138.2, 163.6, 179.1; LC-MS (ESI): *m/z* 218 [MH]⁺.

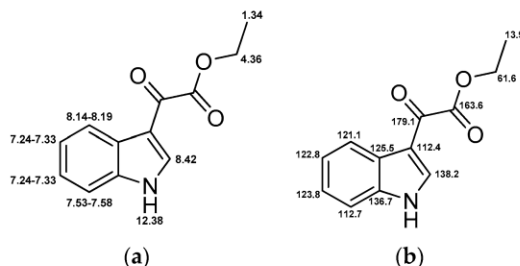


Figure 14. Chemical structure of 10 and relevant NMR shifts for (a) ¹H-NMR; and (b) ¹³C-NMR.

4.4. Photochemical Characterization

4.4.1. UV/Vis Absorption Spectra

Spectra were recorded on UV/Vis spectrophotometer Varian Cary[®] 50 Scan (Agilent Technologies). UV/Vis absorbance was measured in DMSO. Concentration of compounds was 0.1 mM. Subsequently, graphs were normalized on basis of area under the curve between 415 nm and 520 nm.

4.4.2. Fluorescence Emission Spectra

Spectra were recorded on LS55 Fluorescence spectrometer (Perkin Elmer, Waltham, MA, USA). The excitation and emission slits were set to 5 nm. The fluorescence was measured in DMSO. Concentration of compounds was 0.5 mM. The emission spectrum of carbazole **3** was recorded at constant excitation with 480 nm. Caged carbazole **5** was excited at 500 nm.

4.4.3. UV Stability

Compounds **1** and **3** were dissolved in DMSO (1 mM) and irradiated at 365 nm (LED source: 12× Nichia NCSU033B, Sahlmann Photochemical Solutions, Bad Segeberg, Germany, 100%, 5.4 W) up to 10 min. Aliquots were diluted 1:10 with methanol and analyzed by HPLC. Additional to HPLC analysis LC-MS was used to confirm compound identity.

4.4.4. Photoactivation

Compounds **4** and **5** were dissolved in DMSO (1 mM) and the solutions were irradiated at 365 nm (LED source: 12× Nichia NCSU033B, Sahlmann Photochemical Solutions, 100%, 5.4 W) up to 10 min. After 0.25, 0.5, 0.75, 1, 2, 3, 5 and 10 min of irradiation samples were taken. Aliquots were diluted 1:5 with methanol and subsequently analyzed by HPLC. Additional to retention time LC-MS was used to proof identity.

4.5. Kinase Assays

4.5.1. Determination of IC₅₀ Values

The VEGFR-2 IC₅₀ profile for **1**, **3**, **4** and **5** was determined using VEGFR-2 protein kinase by a radiometric ³³PanQinase[®] assay [40]. IC₅₀ values were measured by testing 10 semi-log concentrations of each compound in the range from 1 × 10⁻⁴ M to 3 × 10⁻⁹ M, for single samples. Prior to testing, the compounds were dissolved to prepare 1 × 10⁻² M stock solutions in 100% DMSO. The final DMSO concentration in the reaction cocktails was 1% in all cases. Analyses were performed by ProQinase (Freiburg, Germany).

4.5.2. Kinase Profiling

Compounds **1** and **3** were screened against 79 kinases. The used method was a radioactive filter binding assay using ³³P ATP, for details see references [41,42]. The substances were dissolved in DMSO at tested concentration of 0.1 μM. The mean percentage residual kinase activity and standard deviations of assay duplicates were determined. Analyses were performed by the International Center for Kinase Profiling at the University of Dundee, UK.

4.6. Cellular Assays

4.6.1. Cell Culture

PC-3 cells were purchased from CLS Cell Lines Service GmbH (Eppelheim, Germany). The cells were grown in DMEM:Hams F12 (1:1) medium with 5% FCS. PC-3 cells were incubated in a 5% CO₂ humidified atmosphere at 37 °C.

4.6.2. Proliferation Assays

The cells were grown in cell flasks until approximately 90% confluence and then seeded to give 13000 cells in 100 μL per well into 96-well CulturePlates[™] (Perkin Elmer). In addition to the test plates, one plate was prepared for reference measurement at day zero. All plates were incubated for 24 h at 37 °C in a humidified atmosphere with 5% CO₂. Compounds **1**, **3**, **4**, and **5** were dissolved in 100% DMSO (*v/v*) and added to the test plates. The final DMSO concentration in the assay was 0.5% (*v/v*).

Viability of the cells in the day zero control plates were determined on the same day without adding any compounds. For viability measurement the resazurin assay was used. The shift in the fluorescence signal was measured at the LS55 Fluorescence spectrometer (Perkin Elmer). For the photoactivation experiments the test plates were irradiated at 365 nm for 5 min (LED source: 8× Nichia NCSU033B, Sahlmann Photochemical Solutions, 50%, 1.1 kW/m²). Test plates were incubated for further 48 h and cell viability was defined as described above. Measured raw data was converted into percent of cell growth by using the high control (0.5% DMSO (*v/v*) without compound) and the day zero control. For dose-response studies, 11 different concentrations of compounds were tested in duplicates. IC₅₀ values were calculated using the 4-parameter logarithmic fit option of GraphPad Prism 5.

4.6.3. Cell Staining

PC-3 cells were stained with the carbazole **3** and its caged derivative **5**. For this purpose, the cells were seeded to give 15,000 cells in 50 µL per well into 96-well half area microplate (Ref.: 675986, Greiner bio-one, Kremsmünster, Austria). The plate was incubated for 48 h at 37 °C in a humidified atmosphere with 5% CO₂. Compounds **3** and **5** were dissolved in DMEM:Hams F12 (1:1) medium with 5% FCS and added to the cells to give the endconcentration of 10 µM, respectively. The cells were incubated with the compounds for 30 min at 37 °C. After that, the cells were washed twice with PBS and fixed with 3.3% formalin for 15 min. Then the cells were washed twice with PBS again and the cell nuclei were counterstained with 1 µg/mL DAPI in PBS. After 30 min incubation at 37 °C, the cells were washed with PBS and the fluorescence images were taken at the ImageXpress[®] Micro XL (Molecular Devices, Sunnyvale CA, USA). The magnification was 60×. Following filter sets were used for the visualisation of compounds (Table 3).

Table 3. Filter sets used for the cell staining.

Compound	Filter Set	Exciter (nm) (Center/Bandwidth)	Emitter (nm) (Center/Bandwidth)
DAPI	DAPI	377/50	447/60
3	GFP	472/30	520/35
5	YFP	500/24	542/27

Supplementary Materials: Supplementary materials can be accessed at: <http://www.mdpi.com/1420-3049/21/5/570/s1>.

Acknowledgments: This research project was supported by DFG (German Research Society) grant PE 1605/2-1. We thank Ulrich Girreser and Martin Schütt for excellent technical and analytical assistance at the Institute of Pharmacy in Kiel, Germany. We wish to thank the staff at the National Centre for Protein Kinase Profiling in Dundee for undertaking kinase specificity screening.

Author Contributions: B.P., R.H. and C.P. conceived and designed the experiments; R.H. and L.K. performed synthesis and photochemical characterization; B.P. performed the biological evaluation *in vitro*; B.P. and R.H. analyzed the data; A.D. contributed caged amino acids; B.P. wrote the paper.

Conflicts of Interest: The authors declare no competing financial interest.

Abbreviations

DAPI	4',6-diamidino-2-phenylindole
DMNB	4,5-dimethoxy-2-nitrobenzyl
e.g.	for example
HPLC	high performance liquid chromatography
LC	liquid chromatography
MS	mass spectrometry
PBS	phosphate buffered saline

PPG	photoremovable protecting group
resp.	respectively
UV	ultraviolet
VEGF	vascular endothelial growth factor
VEGFR	vascular endothelial growth factor receptor

References

1. Hall, R.D.; Le, T.M.; Haggstrom, D.E.; Gentzler, R.D. Angiogenesis inhibition as a therapeutic strategy in non-small cell lung cancer (NSCLC). *Transl. Lung Cancer Res.* **2015**, *4*, 515–523. [[PubMed](#)]
2. Cella, D.; Beaumont, J.L. Pazopanib in the treatment of advanced renal cell carcinoma. *Ther. Adv. Urol.* **2016**, *8*, 61–69. [[CrossRef](#)] [[PubMed](#)]
3. Awasthi, N.; Schwarz, R.E. Profile of nintedanib in the treatment of solid tumors: The evidence to date. *Onco. Targets Ther.* **2015**, *8*, 3691–3701. [[CrossRef](#)] [[PubMed](#)]
4. Ferrara, N.; Gerber, H.-P.; LeCouter, J. The biology of VEGF and its receptors. *Nat. Med.* **2003**, *9*, 669–676. [[CrossRef](#)] [[PubMed](#)]
5. Huang, H.; Shen, J.; Viores, S.A. Blockade of VEGFR1 and 2 suppresses pathological angiogenesis and vascular leakage in the eye. *PLoS ONE* **2011**, *6*, e21411. [[CrossRef](#)] [[PubMed](#)]
6. Lee, S.H.; Jeong, D.; Han, Y.-S.; Baek, M.J. Pivotal role of vascular endothelial growth factor pathway in tumor angiogenesis. *Ann. Surg. Treat. Res.* **2015**, *89*, 1–8. [[CrossRef](#)] [[PubMed](#)]
7. Shibuya, M. Vascular endothelial growth factor and its receptor system: physiological functions in angiogenesis and pathological roles in various diseases. *J. Biochem.* **2013**, *153*, 13–19. [[CrossRef](#)] [[PubMed](#)]
8. Hartsough, E.J.; Meyer, R.D.; Chitalia, V.; Jiang, Y.; Marquez, V.E.; Zhdanova, I.V.; Weinberg, J.; Costello, C.E.; Rahimi, N. Lysine methylation promotes VEGFR-2 activation and angiogenesis. *Sci. Signal.* **2013**, *6*, ra104. [[CrossRef](#)] [[PubMed](#)]
9. Ferrara, N.; Hillan, K.J.; Novotny, W. Bevacizumab (Avastin), a humanized anti-VEGF monoclonal antibody for cancer therapy. *Biochem. Biophys. Res. Commun.* **2005**, *333*, 328–335. [[CrossRef](#)] [[PubMed](#)]
10. Rolfo, C.; Bronte, G.; Sortino, G.; Papadimitriou, K.; Passiglia, F.; Fiorentino, E.; Marogy, G.; Russo, A.; Peeters, M. The role of targeted therapy for gastrointestinal tumors. *Expert Rev. Gastroenterol. Hepatol.* **2014**, *8*, 875–885. [[CrossRef](#)] [[PubMed](#)]
11. Noonan, S.; Man Wong, K.; Jimeno, A. Nintedanib, a novel triple angiokinase inhibitor for the treatment of non-small cell lung cancer. *Drugs Today* **2015**, *51*, 357–366. [[CrossRef](#)] [[PubMed](#)]
12. Bischoff, J.; Ignatov, A. The Role of Targeted Agents in the Treatment of Metastatic Breast Cancer. *Breast Care* **2010**, *5*, 134–141. [[CrossRef](#)] [[PubMed](#)]
13. Ryan, C.W. Dosing strategies and optimization of targeted therapy in advanced renal cell carcinoma. *J. Oncol. Pharm. Pract.* **2015**. [[CrossRef](#)] [[PubMed](#)]
14. Rutkowski, P.; Stepniak, J. The safety of regorafenib for the treatment of gastrointestinal stromal tumors. *Expert Opin. Drug Saf.* **2016**, *15*, 105–116. [[CrossRef](#)] [[PubMed](#)]
15. Corrado, A.; Ferrari, S.M.; Politti, U.; Mazzi, V.; Miccoli, M.; Materazzi, G.; Antonelli, A.; Ulisse, S.; Fallahi, P.; Miccoli, P. Aggressive thyroid cancer: targeted therapy with sorafenib. *Min. Endocrinol.* **2015**, in press.
16. Wu, P.; Nielsen, T.E.; Clausen, M.H. FDA-approved small-molecule kinase inhibitors. *Trends Pharmacol. Sci.* **2015**, *36*, 422–439. [[CrossRef](#)] [[PubMed](#)]
17. Rini, B.I.; Small, E.J. Biology and clinical development of vascular endothelial growth factor-targeted therapy in renal cell carcinoma. *J. Clin. Oncol.* **2005**, *23*, 1028–1043. [[CrossRef](#)] [[PubMed](#)]
18. Wu, P.; Nielsen, T.E.; Clausen, M.H. Small-molecule kinase inhibitors: an analysis of FDA-approved drugs. *Drug Discov. Today* **2016**, *21*, 5–10. [[CrossRef](#)] [[PubMed](#)]
19. Marina, M.E.; Roman, I.I.; Constantin, A.-M.; Mihai, C.M.; Tătaru, A.D. VEGF involvement in psoriasis. *Clujul Med.* **2015**, *88*, 247–252. [[CrossRef](#)] [[PubMed](#)]
20. Scott, A.W.; Bressler, S.B. Long-term follow-up of vascular endothelial growth factor inhibitor therapy for neovascular age-related macular degeneration. *Curr. Opin. Ophthalmol.* **2013**, *24*, 190–196. [[CrossRef](#)] [[PubMed](#)]

21. Gao, W.; Sweeney, C.; Walsh, C.; Rooney, P.; McCormick, J.; Veale, D.J.; Fearon, U. Notch signalling pathways mediate synovial angiogenesis in response to vascular endothelial growth factor and angiopoietin 2. *Ann. Rheum. Dis.* **2013**, *72*, 1080–1088. [[CrossRef](#)] [[PubMed](#)]
22. Voelkel, N.F.; Gomez-Arroyo, J. The role of vascular endothelial growth factor in pulmonary arterial hypertension. The angiogenesis paradox. *Am. J. Respir. Cell Mol. Biol.* **2014**, *51*, 474–484. [[CrossRef](#)] [[PubMed](#)]
23. Li, W.; Man, X.-Y.; Chen, J.-Q.; Zhou, J.; Cai, S.-Q.; Zheng, M. Targeting VEGF/VEGFR in the treatment of psoriasis. *Discov. Med.* **2014**, *18*, 97–104. [[PubMed](#)]
24. Peifer, C.; Krasowski, A.; Hämmerle, N.; Kohlbacher, O.; Dannhardt, G.; Totzke, F.; Schächtele, C.; Laufer, S. Profile and molecular modeling of 3-(indole-3-yl)-4-(3,4,5-trimethoxyphenyl)-1H-pyrrole-2,5-dione (**1**) as a highly selective VEGF-R2/3 inhibitor. *J. Med. Chem.* **2006**, *49*, 7549–7553. [[CrossRef](#)] [[PubMed](#)]
25. Peifer, C.; Stoiber, T.; Unger, E.; Totzke, F.; Schächtele, C.; Marmé, D.; Brenk, R.; Klebe, G.; Schollmeyer, D.; Dannhardt, G. Design, synthesis, and biological evaluation of 3,4-diarylmaleimides as angiogenesis inhibitors. *J. Med. Chem.* **2006**, *49*, 1271–1281. [[CrossRef](#)] [[PubMed](#)]
26. Mayer, G.; Heckel, A. Biologically active molecules with a “light switch”. *Angew. Chem. Int. Ed.* **2006**, *45*, 4900–4921. [[CrossRef](#)] [[PubMed](#)]
27. Klán, P.; Šolomek, T.; Bochet, C.G.; Blanc, A.; Givens, R.; Rubina, M.; Popik, V.; Kostikov, A.; Wirz, J. Photoremovable protecting groups in chemistry and biology: Reaction mechanisms and efficacy. *Chem. Rev.* **2013**, *113*, 119–191. [[CrossRef](#)] [[PubMed](#)]
28. Ellis-Davies, G.C.R. Caged compounds: Photorelease technology for control of cellular chemistry and physiology. *Nat. Meth.* **2007**, *4*, 619–628. [[CrossRef](#)] [[PubMed](#)]
29. Zhao, Z.; Wu, H.; Wang, L.; Liu, Y.; Knapp, S.; Liu, Q.; Gray, N.S. Exploration of type II binding mode: A privileged approach for kinase inhibitor focused drug discovery? *ACS Chem. Biol.* **2014**, *9*, 1230–1241. [[CrossRef](#)] [[PubMed](#)]
30. Horbert, R.; Pinchuk, B.; Davies, P.; Alessi, D.; Peifer, C. Photoactivatable Prodrugs of Antimelanoma Agent Vemurafenib. *ACS Chem. Biol.* **2015**, *10*, 2099–2107. [[CrossRef](#)] [[PubMed](#)]
31. Morckel, A.R.; Lusic, H.; Farzana, L.; Yoder, J.A.; Deiters, A.; Nascone-Yoder, N.M. A photoactivatable small-molecule inhibitor for light-controlled spatiotemporal regulation of Rho kinase in live embryos. *Development* **2011**, *139*, 437–442. [[CrossRef](#)] [[PubMed](#)]
32. Kaplan, J.H.; Forbush, B.; Hoffman, J.F. Rapid photolytic release of adenosine 5'-triphosphate from a protected analogue: Utilization by the Na:K pump of human red blood cell ghosts. *Biochemistry* **1978**, *17*, 1929–1935. [[CrossRef](#)] [[PubMed](#)]
33. Corrie, J.E.; Furuta, T.; Givens, R.; Yousef, A.L.; Goeldner, M. Photoremovable Protecting Groups Used for the Caging of Biomolecules. In *Dynamic Studies in Biology: Phototriggers, Photoswitches and Caged Biomolecules*; Goeldner, M., Givens, R., Eds.; Wiley-VCH: Weinheim, Germany, 2005; pp. 1–94.
34. Sadovskii, O.; Jaikaran, A.S.I.; Samanta, S.; Fabian, M.R.; Dowling, R.J.O.; Sonenberg, N.; Woolley, G.A. A collection of caged compounds for probing roles of local translation in neurobiology. *Bioorg. Med. Chem.* **2010**, *18*, 7746–7752. [[CrossRef](#)] [[PubMed](#)]
35. Bliman, D.; Nilsson, J.R.; Kettunen, P.; Andréasson, J.; Grötl, M. A Caged Ret Kinase Inhibitor and its Effect on Motoneuron Development in Zebrafish Embryos. *Sci. Rep.* **2015**, *5*, 13109. [[CrossRef](#)] [[PubMed](#)]
36. Tang, S.; Wan, Z.; Gao, Y.; Zheng, J.-S.; Wang, J.; Si, Y.-Y.; Chen, X.; Qi, H.; Liu, L.; Liu, W. Total chemical synthesis of photoactivatable proteins for light-controlled manipulation of antigen–antibody interactions. *Chem. Sci.* **2016**, *7*, 1891–1895. [[CrossRef](#)]
37. Janett, E.; Bernardinelli, Y.; Müller, D.; Bochet, C.G. Synthesis of FMRFaNV, a Photoreleasable Caged Transmitter Designed to Study Neuron–Glia Interactions in the Central Nervous System. *Bioconjugate Chem.* **2015**, *26*, 2408–2418. [[CrossRef](#)] [[PubMed](#)]
38. Wright, C.W.; Guo, Z.-F.; Liang, F.-S. Light Control of Cellular Processes by Using Photocaged Abscisic Acid. *ChemBioChem* **2015**, *16*, 254–261. [[CrossRef](#)] [[PubMed](#)]
39. Horbert, R. Photoactivatable Kinase Inhibitors. Ph.D. Thesis, Christian-Albrechts-University of Kiel, Kiel, Germany, 2015.
40. *Flash Plate-Based Protein Kinase Assay Protocol (33 PanQinase[®] Assay)*; ProQinase GmbH: Freiburg im Breisgau, Germany, 2012.

41. Hastie, C.J.; McLauchlan, H.J.; Cohen, P. Assay of protein kinases using radiolabeled ATP: A protocol. *Nat. Protoc.* **2006**, *1*, 968–971. [[CrossRef](#)] [[PubMed](#)]
42. Bain, J.; Plater, L.; Elliott, M.; Shpiro, N.; Hastie, C.J.; McLauchlan, H.; Klevernic, I.; Arthur, J.S.C.; Alessi, D.R.; Cohen, P. The selectivity of protein kinase inhibitors: A further update. *Biochem. J.* **2007**, *408*, 297–315. [[CrossRef](#)] [[PubMed](#)]
43. Yi, T.; Yi, Z.; Cho, S.-G.; Luo, J.; Pandey, M.K.; Aggarwal, B.B.; Liu, M. Gambogic acid inhibits angiogenesis and prostate tumor growth by suppressing vascular endothelial growth factor receptor 2 signaling. *Cancer Res.* **2008**, *68*, 1843–1850. [[CrossRef](#)] [[PubMed](#)]
44. Soares, P.; Costa, R.; Froufe, H.J.C.; Calhelha, R.C.; Peixoto, D.; Ferreira, I.C.F.R.; Abreu, R.M.V.; Soares, R.; Queiroz, M.-J.R.P. 1-Aryl-3-[4-(thieno[3,2-*d*]pyrimidin-4-yloxy)phenyl]ureas as VEGFR-2 tyrosine kinase inhibitors: Synthesis, biological evaluation, and molecular modelling studies. *Biomed. Res. Int.* **2013**, *2013*, 154856. [[CrossRef](#)] [[PubMed](#)]
45. Saraswati, S.; Kumar, S.; Alhaider, A.A. α -Santalol inhibits the angiogenesis and growth of human prostate tumor growth by targeting vascular endothelial growth factor receptor 2-mediated AKT/mTOR/P70S6K signaling pathway. *Mol. Cancer* **2013**, *12*, 147. [[CrossRef](#)] [[PubMed](#)]
46. Wood, J.S.; Koszelak, M.; Liu, J.; Lawrence, D.S. A Caged Protein Kinase Inhibitor. *J. Am. Chem. Soc.* **1998**, *1998*, 7145–7146. [[CrossRef](#)]
47. Zindler, M.; Pinchuk, B.; Renn, C.; Horbert, R.; Döbber, A.; Peifer, C. Design, Synthesis, and Characterization of a Photoactivatable Caged Prodrug of Imatinib. *ChemMedChem* **2015**, *10*, 1335–1338. [[CrossRef](#)] [[PubMed](#)]
48. Matsumura, Y.; Ananthaswamy, H.N. Toxic effects of ultraviolet radiation on the skin. *Toxicol. Appl. Pharmacol.* **2004**, *195*, 298–308. [[CrossRef](#)] [[PubMed](#)]
49. D’Orazio, J.; Jarrett, S.; Amaro-Ortiz, A.; Scott, T. UV Radiation and the Skin. *Int. J. Mol. Sci.* **2013**, *14*, 12222–12248. [[CrossRef](#)] [[PubMed](#)]
50. Capinera, J.L. *Encyclopedia of Entomology*, 2nd ed.; Springer: Dordrecht, The Netherlands; London, UK, 2008.
51. Goswami, P.P.; Syed, A.; Beck, C.L.; Albright, T.R.; Mahoney, K.M.; Unash, R.; Smith, E.A.; Winter, A.H. BODIPY-Derived Photoremovable Protecting Groups Unmasked with Green Light. *J. Am. Chem. Soc.* **2015**, *137*, 3783–3786. [[CrossRef](#)] [[PubMed](#)]
52. Fournier, L.; Aujard, I.; le Saux, T.; Maurin, S.; Beaupierre, S.; Baudin, J.-B.; Jullien, L. Coumarinylmethyl Caging Groups with Redshifted Absorption. *Chem. Eur. J.* **2013**, *19*, 17494–17507. [[CrossRef](#)] [[PubMed](#)]
53. Byrnes, K.R.; Waynant, R.W.; Ilev, I.K.; Wu, X.; Barna, L.; Smith, K.; Heckert, R.; Gerst, H.; Anders, J.J. Light promotes regeneration and functional recovery and alters the immune response after spinal cord injury. *Lasers Surg. Med.* **2005**, *36*, 171–185. [[CrossRef](#)] [[PubMed](#)]
54. Bort, G.; Gallavardin, T.; Ogden, D.; Dalko, P.I. From One-Photon to Two-Photon Probes: “Caged” Compounds, Actuators, and Photoswitches. *Angew. Chem. Int. Ed.* **2013**, *52*, 4526–4537. [[CrossRef](#)] [[PubMed](#)]
55. Schrödinger Release 2014-2: Schrödinger Suite 2014-2 Protein Preparation Wizard; Epik, version 2.8; Impact, version 6.3; Prime, version 3.6; Schrödinger, LLC: New York, NY, USA, 2014.
56. Schrödinger Release 2014-1: Epik, version 2.7; Schrödinger, LLC: New York, NY, USA, 2014.
57. Small-Molecule Drug Discovery Suite 2014-2: PrimeX, version 2.4; Schrödinger, LLC: New York, NY, USA, 2014.
58. Schrödinger Release 2014-1: MacroModel, version 10.3; Schrödinger, LLC: New York, NY, USA, 2014.
59. Schrödinger Release 2014-1: LigPrep, version 2.9; Schrödinger, LLC: New York, NY, USA, 2014.
60. Schrödinger Release 2014-1: ConfGen, version 2.7; Schrödinger, LLC: New York, NY, USA, 2014.
61. Small-Molecule Drug Discovery Suite 2014-1: Glide, version 6.2; Schrödinger, LLC: New York, NY, USA, 2014.

Sample Availability: Samples of the compounds **1**, **3**, **4** and **5** are available from the authors.



© 2016 by the authors; licensee MDPI, Basel, Switzerland. This article is an open access article distributed under the terms and conditions of the Creative Commons Attribution (CC-BY) license (<http://creativecommons.org/licenses/by/4.0/>).

Supplementary Materials: Photoactivatable Caged Prodrugs of VEGFR-2 Kinase Inhibitors

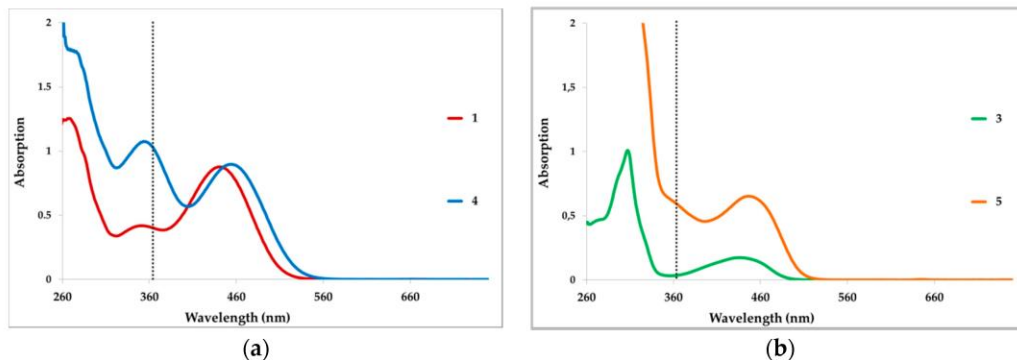


Figure S1. Raw UV/Vis absorption spectra of 0.1 mM compounds in DMSO. (a) UV/Vis absorption spectra of maleimide (1) (red line) and its caged prodrug 4 (blue line). (b) UV/Vis absorption spectra of carbazole (3) (green line) and its caged analogue 5 (orange line). The black dotted line in both diagrams flags 365 nm as the wavelength used for irradiation of caged compounds.

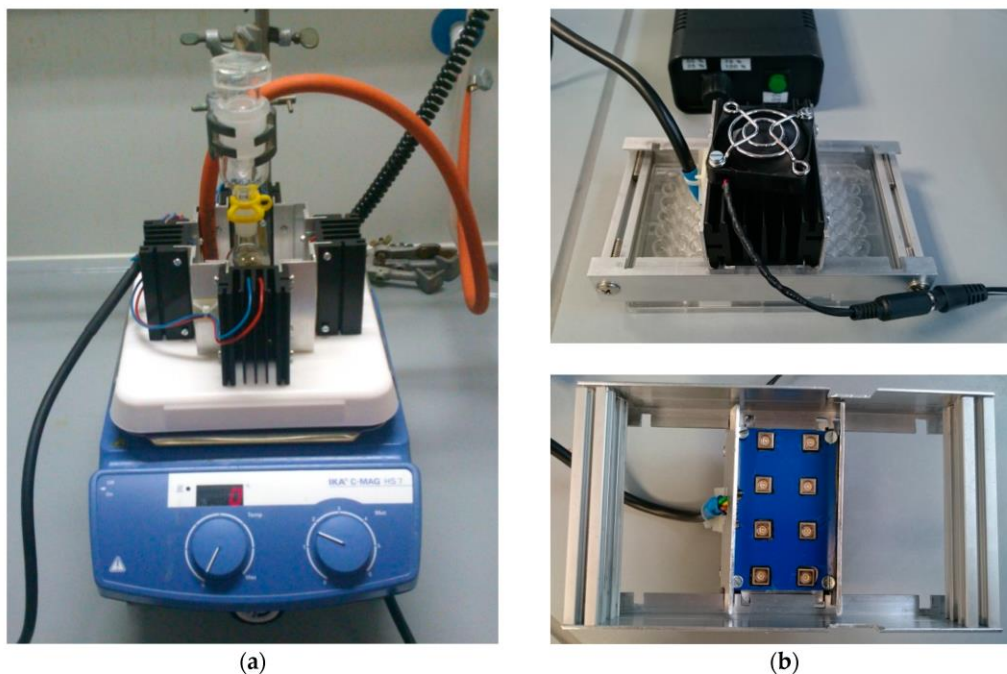


Figure S2. UV sources used for irradiation at 365 nm. (a) LED reactor used for irradiation of solutions in round bottom flasks. (b) LED device for the irradiation of 96-well microtiter plates. Eight LEDs (365 nm) irradiate four rows of wells (32 wells) at once. Accordingly three irradiation cycles are needed for the entire plate. See Figure S3 for Technical setup and emission characteristics.

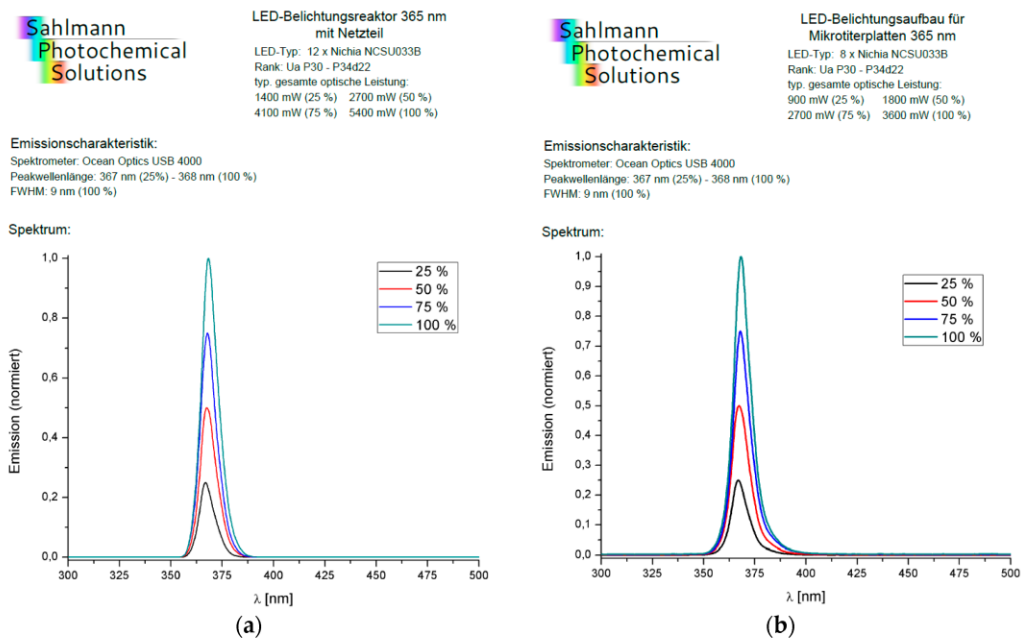


Figure S3. Emission characteristics of the used UV sources. **(a)** LED reactor used for irradiation of solutions in round bottom flasks. The reactor consists of 12 LEDs with an emission maximum at a wavelength of 365 nm. The intensity can be adjusted to four levels (25, 50, 75 and 100%). The corresponding optical power in mW is shown. **(b)** LED device for irradiation of 96-well microtiter plates. There are also four intensity levels available.

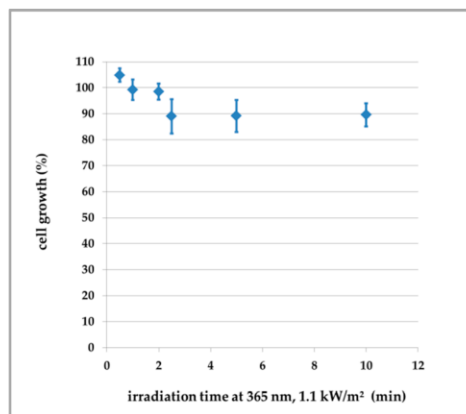


Figure S4. Cell growth of PC-3 cells depending on the irradiation time. Cells were irradiated at 365 nm (1.1 kW/m²) for indicated periods of time. Cell growth was determined after 48 h.

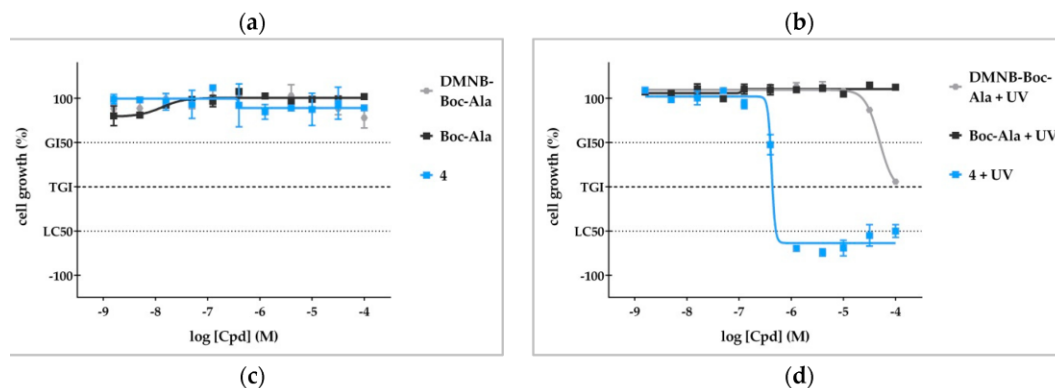


Figure S5. Effect of the photo released PPG on the cell proliferation of PC-3 cells. (a) Chemical structure of the BOC-protected L-alanine = Boc-Ala. (b) Chemical structure of the DMNB-protected Boc-Ala = DMNB-Boc-Ala. (c) Dose-response-curves of the Boc-Ala, DMNB-Boc-Ala and caged compound 4 in cell viability assay using the PC-3 cells without UV irradiation. Cell growth was determined after 48 h incubation with the compounds. The tested compounds do not show any anti-proliferative effects. (d) Dose-response curves of 4, Boc-Ala and DMNB-Boc-Ala in the same assay as in (c) with UV irradiation. Cells were incubated with compounds for 1 h and then irradiated at 365 nm (1.1 kW/m²) for 5 min. Cell growth was determined after 48 h. Herein, the DMNB-Boc-Ala exhibits anti-proliferative efficacy in concentrations above 30 μ M providing evidence for the cytotoxicity of the cleaved PPG at higher concentrations. GI₅₀ = 50% growth inhibition; TGI = total growth inhibition; LC₅₀ = 50% lethal concentration; the dose response curves were fitted using the 4-parameter logistic fit option of GraphPad Prism 5; n = 2 and error bars represent standard deviation.

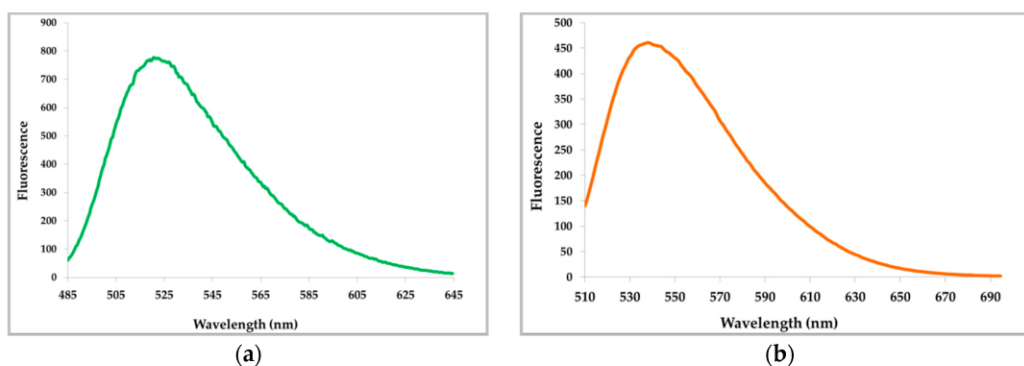


Figure S6. Raw fluorescence emission spectra of 0.5 mM compounds 3 and 5 in DMSO. (a) Fluorescence emission spectrum of carbazole (3); Excitation wavelength: 480 nm. (b) Fluorescence emission spectrum of caged carbazole (5); Excitation wavelength: 500 nm.

Table S1. Kinase profiling of maleimide **1** and carbazole **2**. The inhibitory effect of active compounds was tested on a panel of 79 kinases. The residual activity of kinases was measured after incubation with 0.1 μM of each compound. The data is portrayed as mean percentage activity and standard deviation of assay duplicates. (MRC, Dundee, Scotland).

Kinase	Compound 3	Deviation	Compound 1	Deviation
MKK1	67	5	54	27
ERK1	91	25	100	5
ERK2	93	0	94	5
JNK1	96	5	96	13
JNK2	93	16	78	14
p38a MAPK	78	12	89	0
P38b MAPK	89	17	86	8
p38g MAPK	86	7	91	2
p38s MAPK	90	17	108	0
ERK8	11	1	46	5
RSK1	51	6	96	7
RSK2	62	6	91	1
PDK1	39	1	68	4
PKBa	81	16	66	4
PKBb	91	9	98	2
SGK1	52	15	75	5
S6K1	28	1	65	4
PKA	90	5	93	13
ROCK 2	88	6	97	2
PRK2	52	2	84	4
PKCa	90	14	113	5
PKC zeta	98	2	102	6
PKD1	60	9	100	12
MSK1	55	10	69	1
MNK1	79	4	80	0
MNK2	81	1	90	15
MAPKAP-K2	95	4	94	2
PRAK	85	2	91	7
CAMKKb	49	3	81	3
CAMK1	94	18	107	1
SmMLCK	30	5	60	17
PHK	41	6	73	8
CHK1	34	3	72	0
CHK2	63	2	64	9
GSK3b	5	1	21	2
CDK2-Cyclin A	28	4	59	5
PLK1	49	5	79	9
PLK1 (Okadaic Acid)	83	0	85	2
Aurora B	47	14	84	12
AMPK	75	13	78	8
MARK3	73	3	90	5
BRSK2	66	2	94	8
MELK	55	7	74	13
CK1	78	2	86	5
CK2	91	10	94	9
DYRK1A	26	0	73	2
DYRK2	17	0	57	15

DYRK3	46	5	85	6
NEK2a	91	6	87	1
NEK6	104	9	96	2
IKKb	113	25	102	7
PIM1	5	1	14	1
PIM2	115	12	115	5
PIM3	4	2	5	1
SRPK1	83	5	85	1
MST2	24	2	53	0
EFK2	109	15	104	3
HIPK2	7	1	23	2
PAK4	55	6	75	3
PAK5	84	4	105	1
PAK6	99	2	97	5
Src	86	1	81	0
Lck	91	4	91	2
CSK	99	1	138	8
FGF-R1	92	1	69	9
IRR	41	0	58	1
EPH A2	109	4	104	6
MST4	69	3	94	7
SYK	86	16	85	5
YES1	88	5	84	14
IKKe	63	8	80	3
TBK1	85	7	87	1
IGF1-R	65	4	90	24
VEG-FR	37	2	10	0
BTK	90	1	93	14
IR-HIS	88	15	101	11
EPH-B3	133	4	104	14
TBK1 (DU12569)	73	2	88	5
IKK epsilon (14231)	94	5	85	7

3.4 Photoinduced Conversion of Antimelanoma Agent Dabrafenib to a Novel Fluorescent BRAF^{V600E} Inhibitor

Boris Pinchuk, Thorsten von Drathen, Viktoria Opel, and Christian Peifer

ACS Med. Chem. Lett. **2016**, *7* (10), 962–966.

DOI: 10.1021/acsmchemlett.6b00340

Dabrafenib (Figure 20), trade name “Tafinlar”, was the second approved selective BRAF^{V600E} inhibitor after vemurafenib.^{101, 220} It shows significant clinical benefits for the treatment of BRAF^{V600E} mutated melanoma in comparison to standard chemotherapy.²²¹ Unfortunately, similar to vemurafenib, most patients treated with dabrafenib suffer from relapses due to acquired resistance within several months of the therapy.²²² Even the combination treatment of dabrafenib with an MEK inhibitor trametinib does not lead to a durable response.^{223, 224}

In course of our work on photoactivatable protein kinase inhibitors, we intended to develop photoactivatable prodrugs of dabrafenib. First, we examined the UV stability of the parent inhibitor. To our great surprise, it was found that dabrafenib is not stable to UV irradiation whether in DMSO nor in aqueous solutions. Moreover, even under daylight exposure dabrafenib degraded rapidly in solution.¹⁹⁶ To the best of our knowledge, this photoinduced decomposition was not previously described for the widely applied drug dabrafenib. As key consequence of this finding, any work with dabrafenib solutions should be carried out under light protection.

Furthermore, parallel to photoinduced degradation of dabrafenib, formation of a new compound was observed. This novel substance was isolated and chemically characterized as product of a 6- π -electrocyclization of dabrafenib (Figure 20).

The novel compound **11** was extensively characterized both photochemically and *in vitro*. Antiproliferative activity of **11** was demonstrated on melanoma cells. It was supposed that **11** could be a DNA intercalator, due to its planar aromatic scaffold. However, this hypothesis was disproved by several assays. Further extensive *in vitro* examination including kinase assays,

cell proliferation assays, and measurement of antiproliferative activity in NCI60 cell line screening²²⁵ confirmed that **11** is still a BRAF^{V600E} inhibitor. Compound **11** was determined to be more selective but less potent than dabrafenib. Moreover, it was revealed that **11** exhibits a strong autofluorescence and therefore can be used for cellular staining.

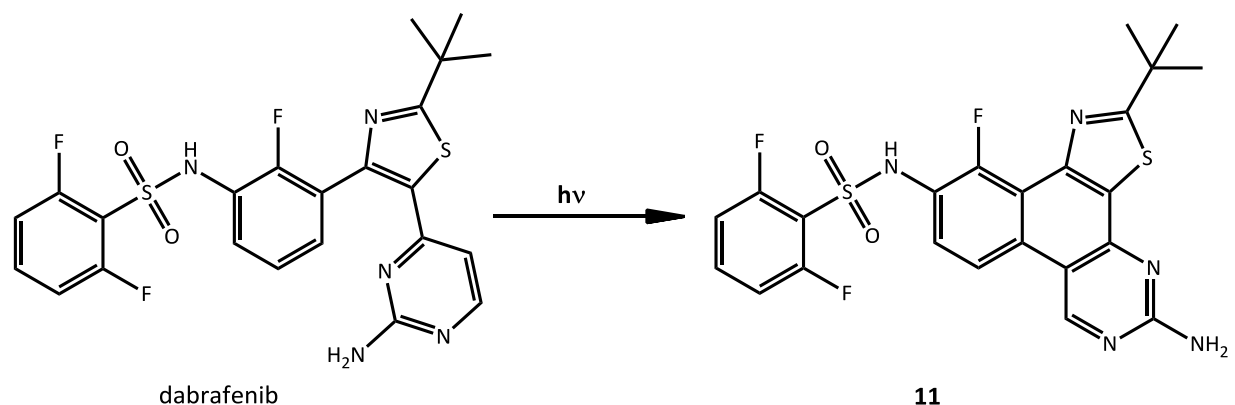


Figure 20: Photoinduced conversion of the approved smKI dabrafenib to the novel inhibitor **11.**¹⁹⁶ Compound **11** corresponds to the derivative **2** in the article “Photoinduced Conversion of Antimelanoma Agent Dabrafenib to a Novel Fluorescent BRAF^{V600E} Inhibitor”.¹⁹⁶

Thorsten von Drathen isolated and chemically characterized compound **11**. Viktoria Opel performed kinetic measurements of photoinduced conversion of dabrafenib to **11**. I supervised the whole project and conducted all *in vitro* studies described in the publication. Moreover, I wrote the manuscript for the publication.

Photoinduced Conversion of Antimelanoma Agent Dabrafenib to a Novel Fluorescent BRAF^{V600E} Inhibitor

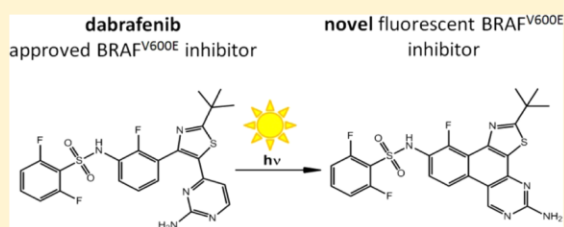
Boris Pinchuk, Thorsten von Drathen, Viktoria Opel, and Christian Peifer*

Institute of Pharmacy, University of Kiel, Gutenbergstr. 76, D-24118 Kiel, Germany

Supporting Information

ABSTRACT: Dabrafenib (Tafinlar) was approved in 2013 by the FDA as a selective single agent treatment for patients with BRAF^{V600E} mutation-positive advanced melanoma. One year later, a combination of dabrafenib and trametinib was used for treatment of BRAF^{V600E/K} mutant metastatic melanoma. In the present study, we report on hitherto not described photosensitivity of dabrafenib both in organic and aqueous media. The half-lives for dabrafenib degradation were determined. Moreover, we revealed photoinduced chemical conversion of dabrafenib to its planar fluorescent derivative dabrafenib_photo 2. This novel compound could be isolated and biologically characterized *in vitro*. Both enzymatic and cellular assays proved that 2 is still a potent BRAF^{V600E} inhibitor. The intracellular formation of 2 from dabrafenib upon ultraviolet irradiation is shown. The herein presented findings should be taken in account when handling dabrafenib both in preclinical research and in clinical applications.

KEYWORDS: Dabrafenib, BRAF^{V600E}, photoinduced conversion, kinase inhibitor, fluorescent probe



Dabrafenib was the second selective BRAF^{V600E} inhibitor after vemurafenib that was approved for the treatment of BRAF^{V600} mutated melanoma.^{1,2} It showed significant clinical benefits compared to alkylating chemotherapeutic agent dacarbazine in clinical studies.³ The median progression free survival (PFS) for patients treated by dabrafenib is about five months. Unfortunately, almost all patients suffer from relapses due to acquired resistance after half a year.⁴ To overcome the resistance development, combined therapy targeting different kinases in the MAPK signaling pathway was proposed. Accordingly, the combination of dabrafenib and trametinib (MEK inhibitor) showed improved clinical efficacy compared to dabrafenib monotherapy in clinical trials.⁵ The median PFS could be increased to 9 months. Based on this data the combination regimen of dabrafenib with trametinib was approved in 2014 by FDA.⁶ Despite superior response rates and longer therapeutic benefits of the combination therapy, most patients still relapse within one year.⁷ Therefore, the acquired resistance and partially severe side effects during the BRAF^{V600E}-inhibitor therapy require further research and developments in the melanoma field.

In the course of our research on photoactivatable kinase inhibitors,^{8–10} we set out to design and synthesize photo-protected prodrugs of dabrafenib. A photostable parent compound is a fundamental requirement for successful caging approach. Thus, to prove the photostability of dabrafenib we irradiated 200 μM solution of the inhibitor in DMSO with 226 W/m^2 ultraviolet light (UV) at 365 nm. To our surprise, dabrafenib was not stable under the described conditions forming a number of decay products. We examined the time

dependency of the photoinduced degradation and performed HPLC measurements of irradiated samples. As shown in Figure 1, the degradation is a first-order reaction with a half-life for dabrafenib of 65.0 s. Interestingly, parallel to decomposition of dabrafenib formation of a major new compound was observed

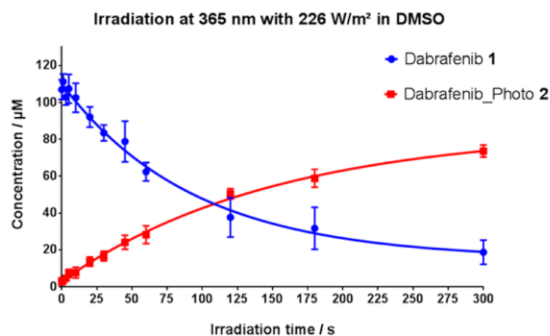


Figure 1. Photoinduced conversion of dabrafenib (1) to “dabrafenib_photo” (2). A 200 μM solution of 1 in DMSO was irradiated at 365 nm with 226 W/m^2 for up to 5 min. The irradiated samples were diluted 1:2 with methanol and analyzed by HPLC. The determined areas under the HPLC peaks were converted to appropriate compound concentrations based on calibration curves (Supplementary Figure S1) ($n = 4$).

Received: August 24, 2016

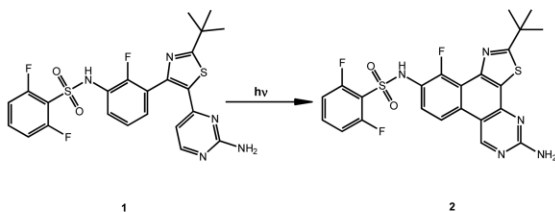
Accepted: September 20, 2016

Published: September 20, 2016

(red line in Figure 1). Accordingly to the experimental setup, we named this substance “dabrafenib_photo” (2).

Next, we isolated compound 2 and characterized it as *N*-(5-amino-2-(*tert*-butyl)-11-fluorobenzo[*f*]thiazolo[4,5-*h*]-quinazolin-10-yl)-2,6-difluorobenzenesulfonamide (Scheme 1).

Scheme 1. Photoinduced Conversion of Dabrafenib (1) to Dabrafenib_photo (2)



Therefore, we postulated the photoinduced conversion of dabrafenib (1) to the novel compound 2 in the sense of a 6- π -photocyclization followed by oxidation as described in Scheme 1.

It is noteworthy to mention that under the conditions used in our experiments the photoinduced conversion of dabrafenib (1) to 2 in DMSO solution is not a quantitative reaction. In line with this notion, small amounts of not further characterized byproducts were detected by HPLC analysis.

As kinase inhibitors were typically used in *in vitro* assays we next investigated whether the photoinduced degradation of dabrafenib (1) and the formation of 2 occurs in aqueous media too. Thus, we repeated the experiment described before but now the dabrafenib solution was prepared in cell culture medium DMEM instead of pure DMSO. When irradiated under the previously described settings the photoreaction (Scheme 1) proceeded only by approximately 10% (Supplementary Figure S2a). However, when the radiation power was increased to 1130 W/m² significant conversion of dabrafenib (1) to 2 could be detected (Supplementary Figure S2b, half-life of the dabrafenib decay was 294 s). A similar photoinduced reaction was also observed in phosphate buffered saline DPBS (Supplementary Figure S3a). Herein, the half-life of dabrafenib in DPBS was 145 s when irradiated with 1130 W/m² at 365 nm. Interestingly, in DMSO dabrafenib decayed significantly more readily than in aqueous solutions: half-life of 1 in DMSO was 19.5 s at 365 nm illumination by 1130 W/m². Moreover, the nascent 2 was not stable in DMSO under this high irradiation power and photolyzed further to several not identified products (Supplementary Figure S3b). The determined values for half-lives in different solutions are summarized in Supplementary Table S1.

Motivated by these results, we became interested in the fate of dabrafenib in aqueous solution under normal lab conditions. Indeed, under daylight exposure dabrafenib reacted relatively fast both in DMSO and in DMEM (Supplementary Figures S4 and S5). Especially in DMSO the degradation proceeded within the range of minutes and the solution became yellowish due to formation of dabrafenib_photo (2). In contrast to the described photoinduced conversion, we found no evidence for thermal decomposition of dabrafenib at 37 °C in the dark (Supplementary Figure S6).

The presented results are highly relevant when handling dabrafenib solutions in the lab. As consequence all dabrafenib solutions should be protected from light exposure. To our best

knowledge the revealed photoinduced degradation of dabrafenib (1) has not been described previously. Interestingly, the CHMP (Committee for Medicinal Products for Human Use) assessment report states “...the drug substance manufactured by the proposed supplier is sufficiently stable...”¹¹

Having the photoconverted product 2 in hand, we wanted to examine the photochemical properties and the biological activities of this novel compound in more detail. Accordingly, we synthesized dabrafenib_photo (2) in larger quantities and characterized it both photochemically and *in vitro*.

Dabrafenib_photo (2) reveals different spectroscopic characteristics than the parent dabrafenib (1). The UV/vis spectra of the compounds show increased absorption of 2 around 400 nm in comparison to 1 (Supplementary Figure S7). The bathochromic shift can be explained by the formation of a pan-aromatic phenanthrene derivative in 2. Interestingly, this conjugated planar ring system causes green fluorescence of 2 when excited by 375 nm (Supplementary Figure S8). Therefore, when incubating cells with dabrafenib_photo 2 its intracellular localization has been analyzed by fluorescence microscopy (see below).

To further examine the biological activity of 2 several approaches were performed. First, we assumed that 2 could be a DNA intercalator due to its planar aromatic structure. However, spectrophotometric investigation (Supplementary Figure S13) and gel electrophoresis analysis (Supplementary Figure S14) have not provided any evidence for an interaction of 2 with DNA.

Based on structural similarity to dabrafenib (1) we supposed that 2 could also be a BraF^{V600E} inhibitor. Molecular modeling studies predicted similar binding modes of both dabrafenib (1) and dabrafenib_photo (2) in the active site of BraF^{V600E}. The calculated 2D ligand interaction diagrams are shown in Figure 2. For the 3D binding modes, see Supplementary Figure S10.

Therefore, our modeling studies support the assumption that 2 is a BRAF^{V600E} inhibitor even though the calculated docking score (Schrödinger Glide) for dabrafenib (−15.7) is higher than for 2 (−11.7).

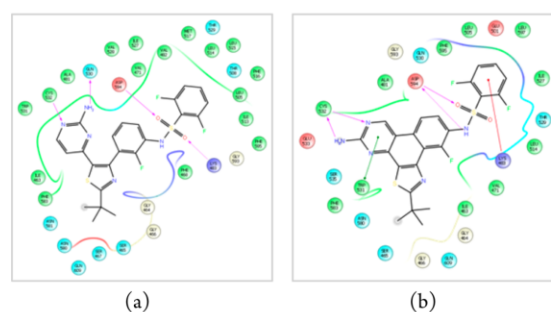


Figure 2. Modeled ligand interaction diagrams of (a) dabrafenib (1) and (b) dabrafenib_photo (2) in the active site of BRAF^{V600E} (pdb 4XV2). Key ligand–protein interactions are shown. H-bonds between the ligand and the protein backbone are indicated by purple arrows. The binding modes of both compounds are closely related: The aminopyrimidine moieties of both compounds address the hinge region of the kinase by two H-bonds. The sulfonamide residues, respectively, bind to the aspartate594 via one (1) or two (2) H-bonds. The difluorophenyl moieties occupy the deeper hydrophobic pocket I, and the *tert*-butyl residues are exposed to the solvent.

To prove our hypothesis, we determined the IC_{50} values of both **1** and **2** toward BRAF^{V600E} (Supplementary Figure S11). In our assay the measured IC_{50} value of **1** was 9.0 nM and was thus comparable to the IC_{50} described in the literature (0.8 nM).^{2,12} The IC_{50} of **2** was 280 nM. Hence, these results are in line with our modeling studies: dabrafenib_photo (**2**) is a BRAF^{V600E} inhibitor although less potent than dabrafenib (**1**).

After proving the inhibitory activity of **2** toward BRAF^{V600E}, we set out to examine the selectivity of this compound. Thus, selectivity profiles of both **1** and **2** were measured in a panel of 321 kinases. The residual kinase activities after incubation with 1 μ M compounds are displayed as TREEspot™ Kinase dendrograms in Figure 3. Herein, it is obvious that **2** inhibits

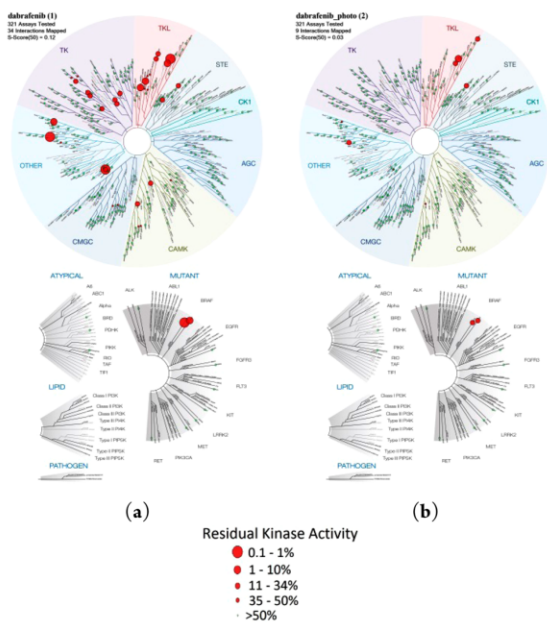


Figure 3. Dendrogram representation of the selectivity profile of compounds **1** (a) and **2** (b) at a concentration of 1 μ M against 321 kinases. The residual kinase activity was determined compared to DMSO control. Images were generated using TREEspot Software Tool, DISCOVERX CORPORATION 2010. The complete raw data are shown in the Supplementary Table S2 (ProQinase, Freiburg, Germany).

significantly less kinases than **1**. Moreover, **2** has also a better selectivity score than **1** (Supplementary Table S2). Therefore, we concluded that the novel inhibitor **2** is more selective for BRAF^{V600E} than dabrafenib.

Next, we examined the cytotoxic activity of **1** and **2** toward BRAF^{V600E}-dependent melanoma cell line SKMEL28.¹³ The cellular growth was measured after 48 h incubation with different concentrations of **1** and **2**. Additionally, the first approved BRAF^{V600E} inhibitor vemurafenib was included as reference. The results of these antiproliferative experiments are shown in Figure 4a.

The cellular growth assays revealed that the novel compound **2** exhibits cytostatic activity on melanoma cells in a concentration range between 10 nM and 30 μ M, while at higher concentrations the effect becomes cytotoxic. The TGI-value, compound concentration at which the cell growth is

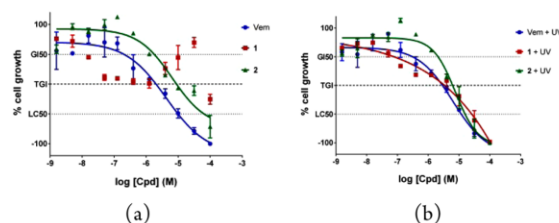


Figure 4. Antiproliferative activity of tested compounds on BRAF^{V600E}-dependent melanoma SKMEL28 cells. (a) Dose–response curves of dabrafenib (**1**), dabrafenib_photo (**2**), and the approved BRAF^{V600E} inhibitor vemurafenib (Vem) without UV irradiation. (b) SKMEL28 cells were incubated for 1 h with the compounds and then irradiated at 365 nm (1.13 kW/m²) for 5 min. Cell growth was determined 48 h after incubation with the compounds. GI₅₀ = 50% growth inhibition; TGI = total growth inhibition; LC₅₀ = 50% lethal concentration; *n* = 4. Error bars represent standard deviation.

completely inhibited, has been determined to be 8.9 μ M for **2**. Consequently, dabrafenib_photo (**2**) can be considered as an antiproliferative agent against BRAF^{V600E}-mutated melanoma cells *in vitro* although less potent than vemurafenib (TGI = 2.0 μ M). Strikingly, the dose–response curve for dabrafenib (**1**) does not show the typical sigmoidal fit. Although **1** exhibits nanomolar cytostatic activity, in a higher concentration range between 1 and 30 μ M the dose–response curve showed reproducibly unusual results with only weak inhibition of cell growth (Figure 4a). This unconventional cellular response at lower micromolar dabrafenib concentrations may indicate a special situation in SKMEL28 cells, e.g., efflux pump-mediated resistance, and should be explored in more detail in future studies.

The proliferation assays described above were repeated with the compound treated SKMEL28 cells exposed to UV light at 365 nm (5 min, 1.13 kW/m²). The determined dose–response curves are shown in Figure 4b. As expected from our former studies,⁸ there is no change in the cellular response to the reference inhibitor vemurafenib caused by irradiation. However, irradiated dabrafenib (**1**) shows a comparable dose–response curve to dabrafenib_photo (**2**) providing strong evidence for the photoinduced intracellular conversion of **1** to **2** *in vitro*.

To further prove our hypothesis of intracellular photo-induced transformation of dabrafenib (**1**) to its derivative **2**, we used the autofluorescence of **2** (Supplementary Figure S8b) and performed fluorescence microscopy experiments. First, the melanoma cells SKMEL28 were incubated with dabrafenib_photo (**2**). The compound passed cellular membrane and could be clearly detected within the cells (Figure 5a). In contrast, dabrafenib (**1**) was not visible under the same fluorescent microscopic conditions (Figure 5b, second column left) because of its different excitation wavelength. Treating cells with dabrafenib (**1**) and exposure to increasing dosage of UV irradiation at 365 nm shows that photoinduced transformation of dabrafenib (**1**) to fluorescent **2** takes place (increasing fluorescence by enduring irradiation, Figure 5b). The control nuclei counterstaining with DAPI did not show any changes upon irradiation.

The combined staining and irradiation experiments displayed in Figure 5 provided strong evidence for the intracellular transformation of dabrafenib (**1**) to the novel compound **2** upon UV light exposure.

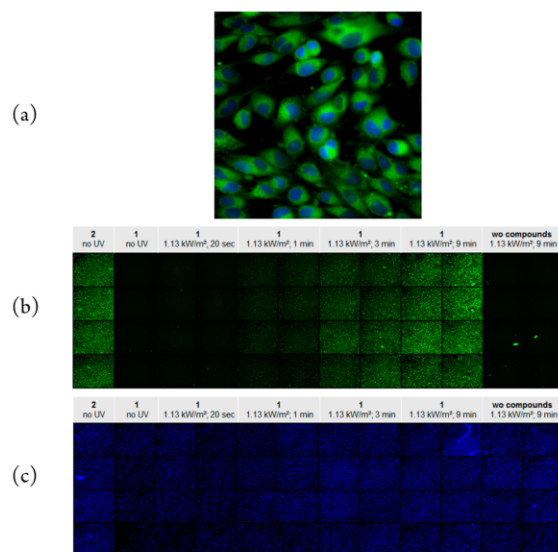


Figure 5. (a) SKMEL28 cells were incubated with dabrafenib_photo (2). The inhibitor was applied at 100 μM concentration and is shown in green. The cell nuclei were counterstained with 1 $\mu\text{g}/\text{mL}$ DAPI and are marked in blue. The microscopic image was taken with 60 \times magnification. (b) SKMEL28 cells were seeded in 48 wells of a 96-well plate. The cells in the first column were incubated with dabrafenib_photo (2) without UV exposure. The cells in the columns 2 to 10 were incubated with dabrafenib (1) and exposed to increasing dosage of UV light at 365 nm (see captions above the columns). The cells in the last two right columns were not incubated with any compound but just irradiated with the highest UV amount. The overview image of the plate consists of single well images taken with 10 \times magnification. (c) The same cell plate from (b). All cell nuclei in the plate were counterstained with 1 $\mu\text{g}/\text{mL}$ DAPI and are marked in blue.

To explore the cellular mechanism of action of dabrafenib_photo (2) in more detail, we sent compound 2 for the NCI 60 cell line screening¹⁴ to the National Cancer Institute (NCI, Rockville, MD, USA). Herein, the cell growth of 59 different cancer cell lines was measured after incubation with 10 μM dabrafenib_photo (2). The determined one-dose mean graph is presented in the [Supplementary Figure S12](#). Furthermore, we evaluated the data using the COMPARE Analysis tool.¹⁵ Shortly, the cellular response to 2 was compared to cellular responses of 100 synthetic compounds in the NCI 60 database. The database compounds were then ranked in the order of similarity compared to dabrafenib_photo (2) assuming compound 2 may possess a similar mechanism of action to the compounds with high correlation coefficient in this ranking.¹⁵ The results of the COMPARE analysis are shown in [Supplementary Table S3](#). Strikingly, the first nine top-ranked entries are all either approved BRAF^{V600E} inhibitors (dabrafenib and vemurafenib “Zelboraf”) or 5-(2-substituted pyrimidin-4-yl)imidazo[2,1-b]thiazole derivatives (NSC: S755437, S755453, S761592, SS761584, S761586) previously described as antiproliferative agents against BRAF^{V600E}-mutated melanoma cell line A375.^{16,13} Thus, the correlation results of the COMPARE analysis are further evidence that the novel compound 2 is an effective BRAF^{V600E} inhibitor *in vitro*.

To summarize, we have revealed the photoinduced transformation of the approved kinase inhibitor dabrafenib (1) to a

novel compound 2. Dabrafenib solutions were evaluated to be instable upon exposure to both ultraviolet and daylight irradiation. This photoinduced degradation should be taken into account when handling dabrafenib solutions. The novel compound 2 was characterized as a BRAF^{V600E} inhibitor *in vitro*. The enhanced autofluorescence of 2 could be used successfully for intracellular imaging of the inhibitor. The improved selectivity profile of 2 compared to dabrafenib (1) could be used as a starting point for development of more selective BRAF^{V600E} inhibitors.

■ ASSOCIATED CONTENT

Supporting Information

The Supporting Information is available free of charge on the ACS Publications website at DOI: 10.1021/acsmchemlett.6b00340.

Molecular modeling studies, chemical procedures, analytical data for the synthesis of 2, irradiation experiments, kinase and cellular assays (PDF)

■ AUTHOR INFORMATION

Corresponding Author

*E-mail: cpeifer@pharmazie.uni-kiel.de. Tel: +49-431-880-1137.

Author Contributions

B.P. and C.P. conceived and designed the experiments. T.v.D. performed synthesis. V.O. performed photochemical characterization. B.P. performed the biological evaluation *in vitro* and wrote the paper.

Funding

This research project was supported by DFG (German Research Society) grant PE 1605/2-1.

Notes

The authors declare no competing financial interest.

■ ACKNOWLEDGMENTS

We thank Ulrich Girreser and Martin Schütt for excellent technical and analytical assistance at the Institute of Pharmacy in Kiel, Germany. We wish to thank the staff at the National Cancer Institute (NCI, Rockville, MD, USA) for NCI 60 profiling of 2. We would like to thank the working group of Prof. Beitz at the Institute of Pharmacy in Kiel for providing us the DNA for gel electrophoresis.

■ ABBREVIATIONS

CHMP, Committee for Medicinal Products for Human Use; DAPI, 4',6-diamidino-2-phenylindole; DMEM, Dulbecco's modified Eagle's medium; DMSO, dimethyl sulfoxide; DPBS, Dulbecco's phosphate buffered saline; FDA, Food and Drug Administration; HPLC, high performance liquid chromatography; LC, liquid chromatography; MS, mass spectrometry; NCI, National Cancer Institute; NSC, National Service Center; PBS, phosphate buffered saline; PFS, progression free; resp, respectively; UV, ultraviolet

■ REFERENCES

- (1) Banzi, M.; De Blasio, S.; Lallas, A.; Longo, C.; Moscarella, E.; Alfano, R.; Argenziano, G. Dabrafenib: a new opportunity for the treatment of BRAF V600-positive melanoma. *OncoTargets Ther.* **2016**, *9*, 2725–2733.
- (2) Rheault, T. R.; Stellwagen, J. C.; Adjabeng, G. M.; Hornberger, K. R.; Petrov, K. G.; Waterson, A. G.; Dickerson, S. H.; Mook, R. A., JR;

Laquerre, S. G.; King, A. J.; Rossanese, O. W.; Arnone, M. R.; Smitheman, K. N.; Kane-Carson, L. S.; Han, C.; Moorthy, G. S.; Moss, K. G.; Uehling, D. E. Discovery of Dabrafenib: A Selective Inhibitor of Raf Kinases with Antitumor Activity against B-Raf-Driven Tumors. *ACS Med. Chem. Lett.* **2013**, *4* (3), 358–362.

(3) Hauschild, A.; Grob, J.-J.; Demidov, L. V.; Jouary, T.; Gutzmer, R.; Millward, M.; Rutkowski, P.; Blank, C. U.; Miller, W. H.; Kaempgen, E.; Martín-Algarra, S.; Karaszewska, B.; Mauch, C.; Chiarion-Sileni, V.; Martin, A.-M.; Swann, S.; Haney, P.; Mirakhur, B.; Guckert, M. E.; Goodman, V.; Chapman, P. B. Dabrafenib in BRAF-mutated metastatic melanoma: A multicentre, open-label, phase 3 randomised controlled trial. *Lancet* **2012**, *380* (9839), 358–365.

(4) Sullivan, R. J.; Flaherty, K. T. Resistance to BRAF-targeted therapy in melanoma. *Eur. J. Cancer* **2013**, *49* (6), 1297–1304.

(5) Long, G. V.; Stroyakovskiy, D.; Gogas, H.; Levchenko, E.; de Braud, F.; Larkin, J.; Garbe, C.; Jouary, T.; Hauschild, A.; Grob, J. J.; Chiarion Sileni, V.; Lebbe, C.; Mandala, M.; Millward, M.; Arance, A.; Bondarenko, I.; Haanen, J. B. A. G.; Hansson, J.; Utikal, J.; Ferraresi, V.; Kovalenko, N.; Mohr, P.; Probachai, V.; Schadendorf, D.; Nathan, P.; Robert, C.; Ribas, A.; DeMarini, D. J.; Irani, J. G.; Casey, M.; Ouellet, D.; Martin, A.-M.; Le, N.; Patel, K.; Flaherty, K. Combined BRAF and MEK inhibition versus BRAF inhibition alone in melanoma. *N. Engl. J. Med.* **2014**, *371* (20), 1877–1888.

(6) Silas Inman. Dabrafenib/Trametinib Combination Approved for Advanced Melanoma. <http://global.onclive.com/web-exclusives/FDA-Approves-First-Ever-Combination-for-Metastatic-Melanoma?p=2#sthash.qg6jAGJX.dpuf>.

(7) Zhu, Z.; Liu, W.; Gotlieb, V. The rapidly evolving therapies for advanced melanoma—Towards immunotherapy, molecular targeted therapy, and beyond. *CR REV ONCOL-HEM* **2016**, *99*, 91–99.

(8) Horbert, R.; Pinchuk, B.; Davies, P.; Alessi, D.; Peifer, C. Photoactivatable Prodrugs of Antimelanoma Agent Vemurafenib. *ACS Chem. Biol.* **2015**, *10* (9), 2099–2107.

(9) Pinchuk, B.; Horbert, R.; Dobber, A.; Kuhl, L.; Peifer, C. Photoactivatable Caged Prodrugs of VEGFR-2 Kinase Inhibitors. *Molecules* **2016**, *21* (5), 570.

(10) Zindler, M.; Pinchuk, B.; Renn, C.; Horbert, R.; Dobber, A.; Peifer, C. Design, Synthesis, and Characterization of a Photoactivatable Caged Prodrug of Imatinib. *ChemMedChem* **2015**, *10* (8), 1335–1338.

(11) Committee for Medicinal Products for Human Use. *CHMP assessment report Tafinlar*. EMA/CHMP/242419/2013/corr 1, 2013.

(12) Laquerre, S.; Arnone, M.; Moss, K.; Yang, J.; Fisher, K.; Kane-Carson, L. S.; Smitheman, K.; Ward, J.; Heidrich, B.; Rheault, T.; Adjabeng, G.; Hornberger, K.; Stellwagen, J.; Waterson, A.; Han, C.; Mook, R. A.; Uehling, D.; King, A. J. Abstract B88: A selective Raf kinase inhibitor induces cell death and tumor regression of human cancer cell lines encoding B-RafV600E mutation. *Mol. Cancer Ther.* **2009**, *8*, B88–B88.

(13) Domingo, E.; Schwartz, S. BRAF (v-raf murine sarcoma viral oncogene homolog B1). *Atlas of Genetics and Cytogenetics in Oncology and Haematology [Online]* **2011**, DOI: 10.4267/2042/38125.

(14) Shoemaker, R. H. The NCI60 human tumour cell line anticancer drug screen. *Nat. Rev. Cancer* **2006**, *6* (10), 813–823.

(15) Paull, K. D.; Hamel, E.; Malspeis, L. COMPARE Introduction. Prediction of Biochemical Mechanism of Action from the In Vitro Antitumor Screen of the National Cancer Institute, 2015. https://dtp.cancer.gov/databases_tools/docs/compare/compare.htm (accessed August 15, 2016).

(16) Park, J.-H.; Oh, C.-H. Synthesis of New 6-(4-Fluorophenyl)-5-(2-substituted pyrimidin-4-yl)imidazo[2,1-b]thiazole Derivatives and their Antiproliferative Activity against Melanoma Cell Line. *Bull. Korean Chem. Soc.* **2010**, *31* (10), 2854–2860.

Supplementary Information for the manuscript

Photoinduced Conversion of Antimelanoma Agent Dabrafenib to a novel fluorescent BRAF^{V600E} Inhibitor

Boris Pinchuk, Thorsten von Drathen, Viktoria Opel, Christian Peifer

Content

1. Supplementary Figures
2. Supplementary Tables
3. Methods
4. Supplementary References

1. Supplementary Figures

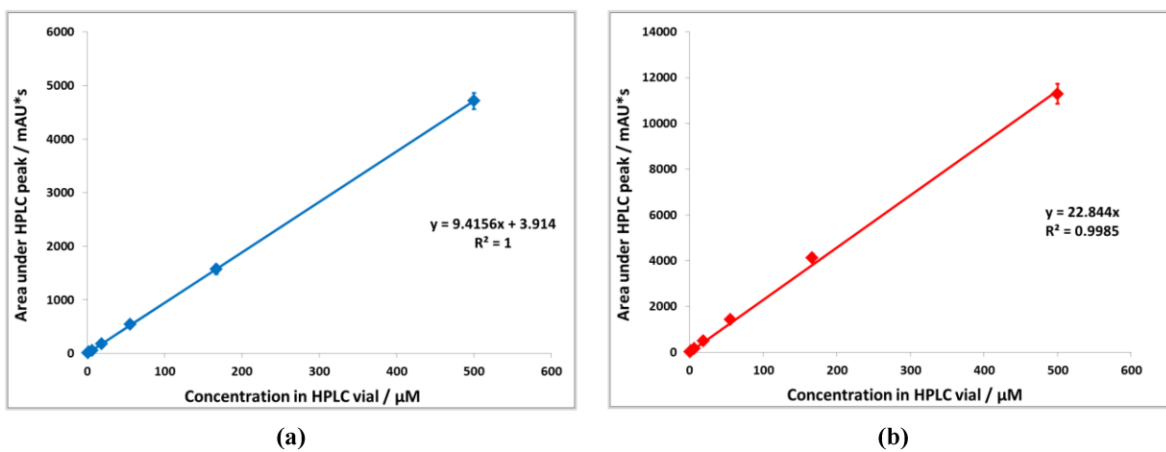


Figure S1. (a) Calibration curves of dabrafenib (1) and (b) dabrafenib_photo (2) for HPLC analysis. Several solutions with different compound concentrations in DMSO were diluted 1:2 with methanol. The integrated peak area in mAU*s is plotted against the sample end concentration in HPLC vials in μM. The stock solutions were prepared in duplicate and each probe was measured twice ($n = 4$).

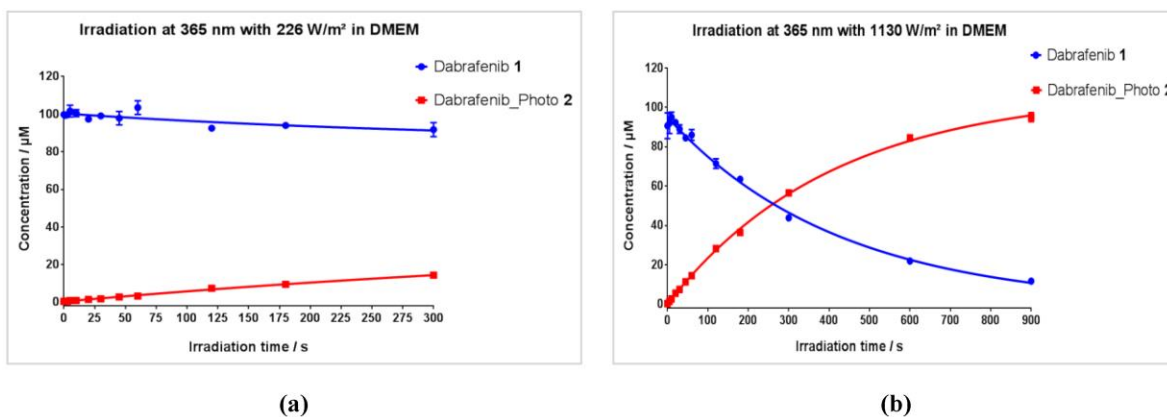


Figure S2. Irradiation of dabrafenib (**1**) in cell culture medium DMEM. **(a)** 200 µM solution of **1** in DMEM was irradiated at 365 nm with 226 W/m² for up to 5 min ($n = 2$). **(b)** 200 µM solution of **1** in DMEM was irradiated at 365 nm with 1130 W/m² for up to 15 min. The irradiated samples were diluted 1:2 with methanol and analyzed by HPLC. The determined areas under the HPLC peaks were converted to appropriate compound's concentrations based on calibration curves (Figure S1) ($n = 4$).

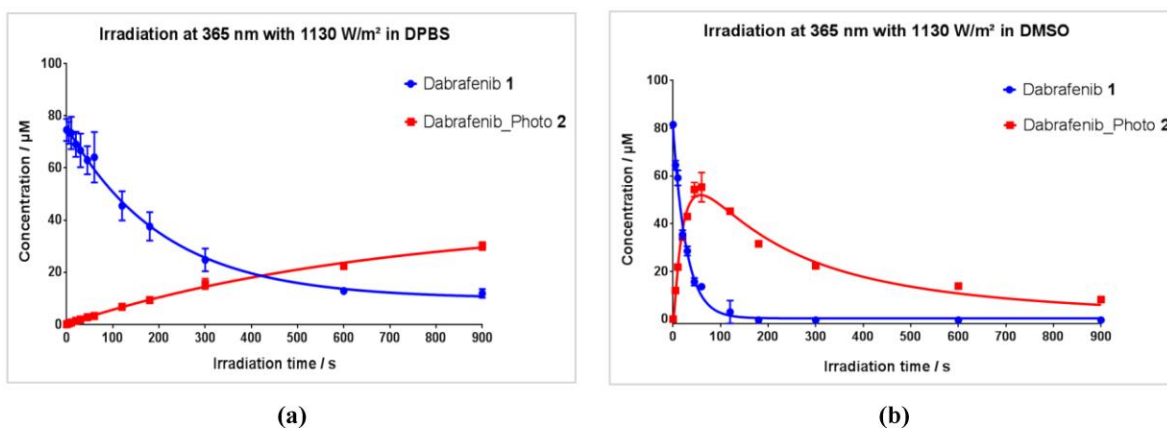


Figure S3. **(a)** 200 µM solution of **1** in phosphate buffered saline DPBS was irradiated at 365 nm with 1130 W/m² for up to 15 min. **(b)** 200 µM solution of **1** in DMSO was irradiated at 365 nm with 1130 W/m² for up to 15 min. The irradiated samples were diluted 1:2 with methanol and analyzed by HPLC. The determined areas under the HPLC peaks were converted to appropriate compound's concentrations based on calibration curves (Figure S1) ($n = 4$).

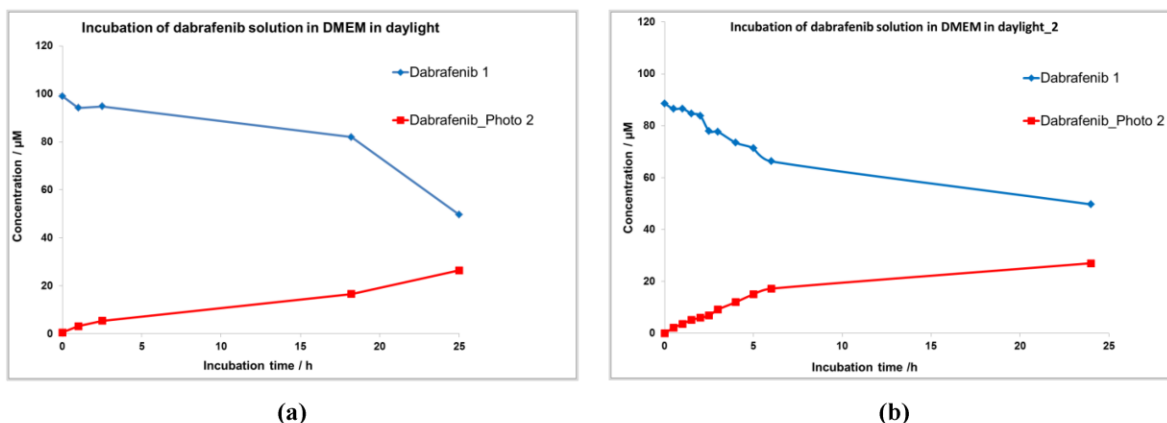


Figure S4. Stability of 200 μM dabrafenib (**1**) in DMEM under daylight exposure. (a) 200 μM solution of **1** in DMEM was incubated for one day at room temperature at a window sill. (b) The experiment was repeated on a sunnier day. The samples were diluted 1:2 with methanol and analyzed by HPLC. The determined areas under the HPLC peaks were converted to appropriate compound's concentrations based on calibration curves (Figure S1).

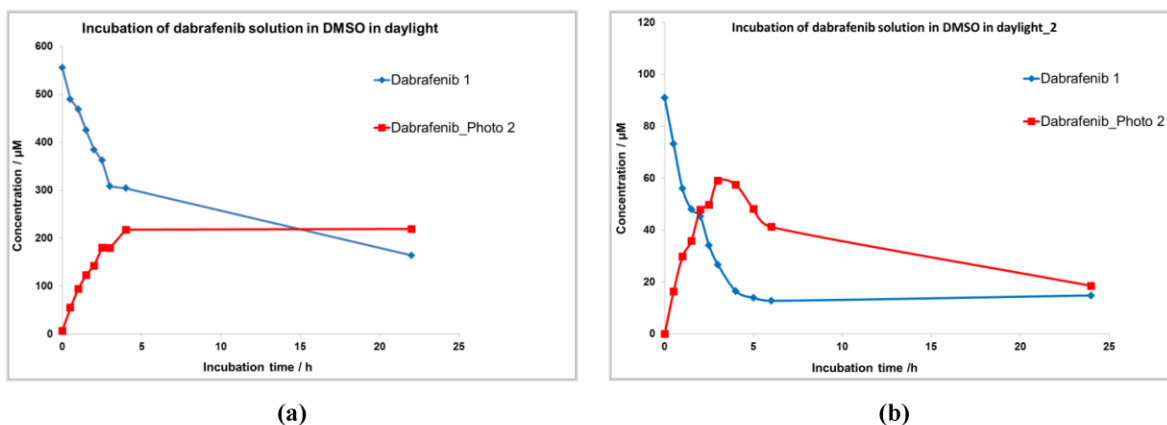


Figure S5. Stability of dabrafenib in DMSO by daylight. (a) 1100 μM solution of **1** in DMSO was incubated at room temperature at a window sill. (b) 200 μM solution of **1** in DMSO was incubated at room temperature at a window sill on a sunnier day than in (a). The samples were diluted 1:2 with methanol and analyzed by HPLC. The determined areas under the HPLC peaks were converted to appropriate compound's concentrations based on calibration curves (Figure S1).

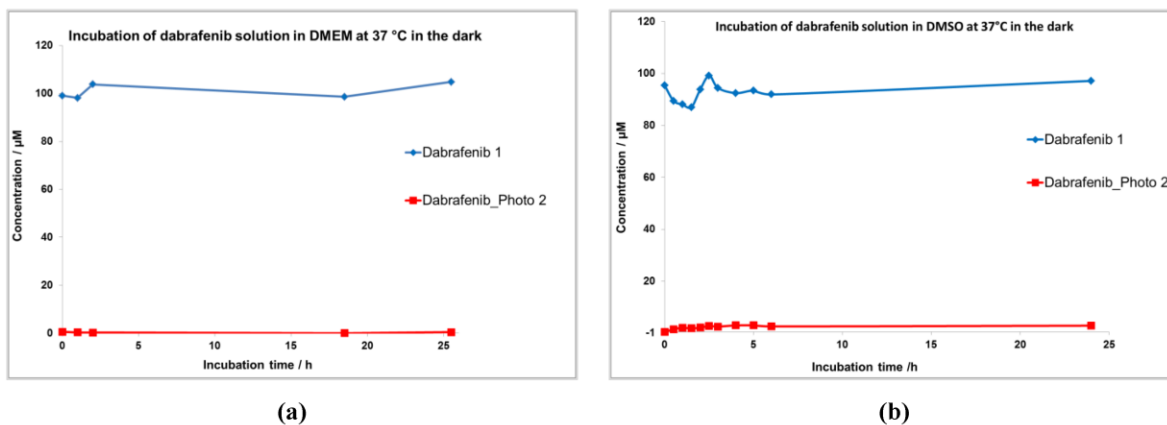


Figure S6. Stability of 200 μM dabrafenib (**1**) at 37 °C in the dark. (a) 200 μM solution of **1** in DMEM was incubated for one day at 37°C in dark incubator (b) The experiment was repeated in DMSO. The samples were diluted 1:2 with methanol and analyzed by HPLC. The determined areas under the HPLC peaks were converted to appropriate compound's concentrations based on calibration curves (Figure S1).

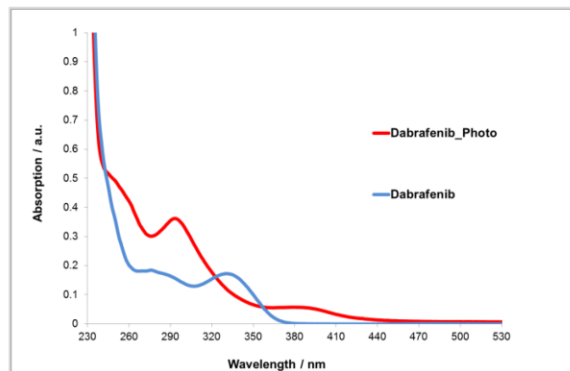


Figure S7. Raw UV/Vis absorption spectra of 20 μM compounds in Tris/EDTA (TE) buffer, pH 7.5.

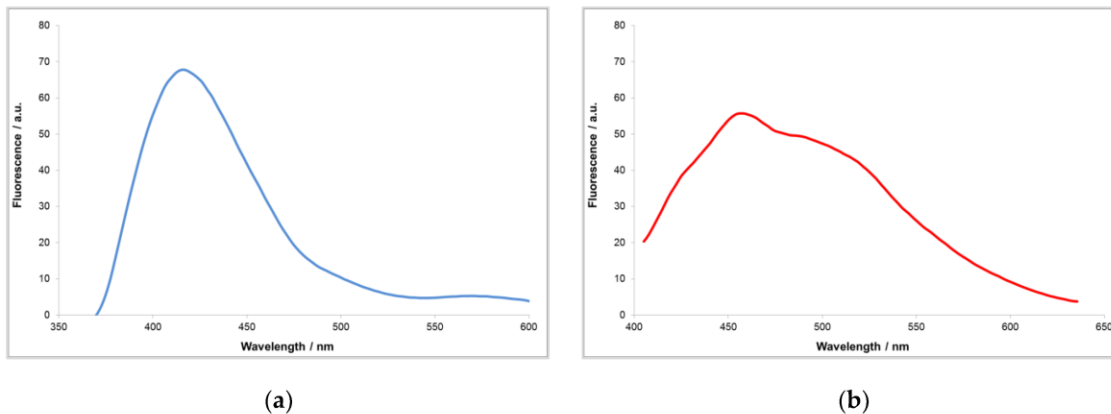


Figure S8. Raw fluorescence emission spectra of 40 μM compounds **1** and **2** in TE buffer, pH 7.5. (a) Fluorescence emission spectrum of dabrafenib (**1**); Excitation wavelength: 330 nm. (b) Fluorescence emission spectrum of dabrafenib_photo (**2**); Excitation wavelength: 375 nm.

Sahlmann
Photochemical
Solutions

LED-Belichtungsaufbau für
Mikrotiterplatten 365 nm - Version: 1 LED / Well
LED-Typ: 16 x Nichia NCSU276A U365
Rank: P35d21-P37
typ. gesamte optische Leistung:
16x 750 mW = 12000 mW (100 %)

Emissionscharakteristik:
Spektrometer: Ocean Optics USB 4000
Peakwellenlänge: 369 nm (100 %)
FWHM: 10 nm (100 %)

Spektrum:

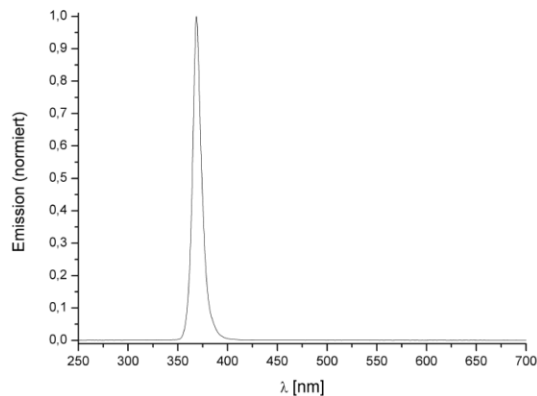


Figure S9. Emission characteristics of the used UV source for irradiation of 96-well microtiter plates. The device consists of 16 equal LEDs with an emission maximum at a wavelength of 369 nm. The added optical power is 12 W at 100%. The intensity can be adjusted in 1% steps. Each LED can be exactly positioned above one well of a 96-well plate. Therefore, 16 wells in two columns can be simultaneously irradiated.

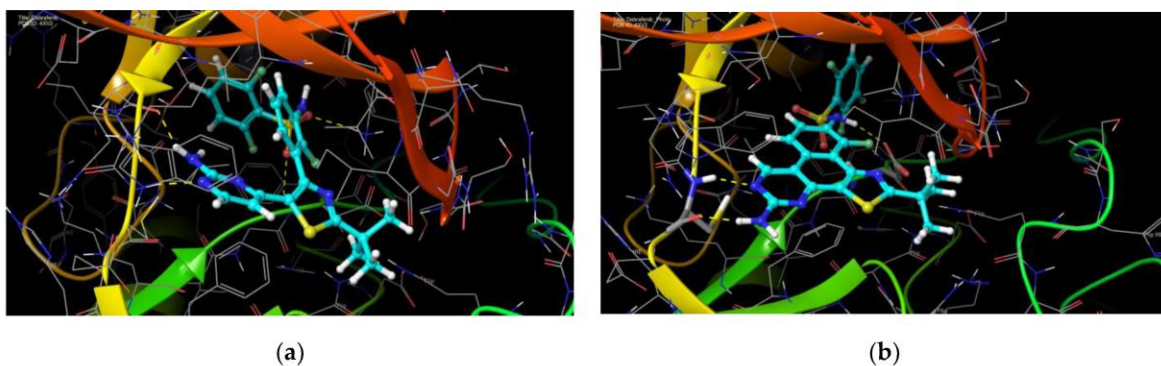


Figure S10. Modelled binding modes of dabrafenib (1) (a) and dabrafenib_photo (2) (b) in the active site of BRAF^{V600E} (pdb: 4XV2). The carbons of the inhibitors are displayed cyan. The H-Bonds between the ligands and the protein are shown as yellow dashed lines.

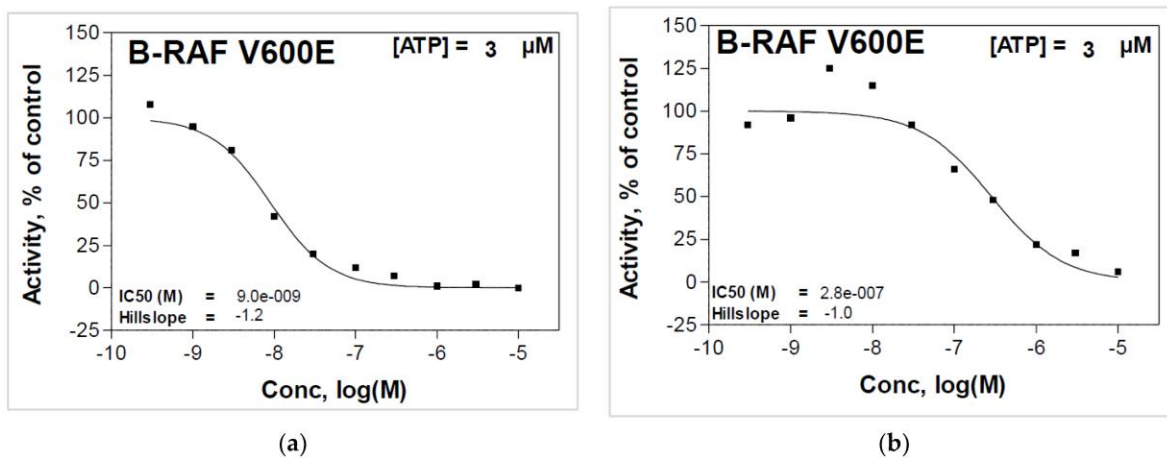


Figure S11. Determination of IC_{50} values towards BRAF^{V600E}. (a) Dose-response curve of dabrafenib (1). (b) Dose-response curve of dabrafenib_photo (2). The kinase assays were performed by ProQinase (Freiburg, Germany).

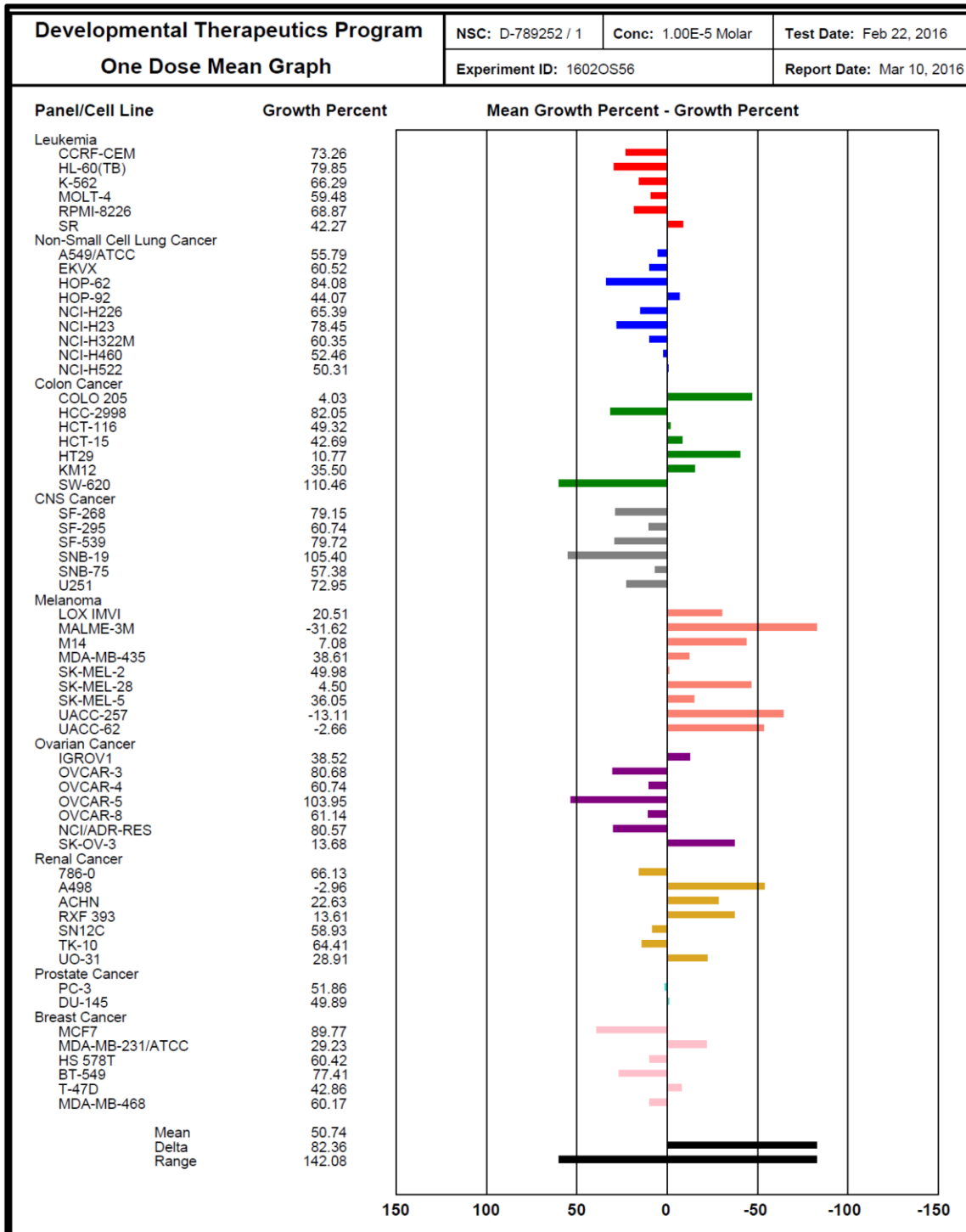


Figure S12. One Dose Mean Graph: Mean cellular growth after incubating of 59 cancer cell lines with 10 μ M dabrafenib_photo (2). The experiments were performed by NCI (National Cancer Institute, Rockville, MD, USA).

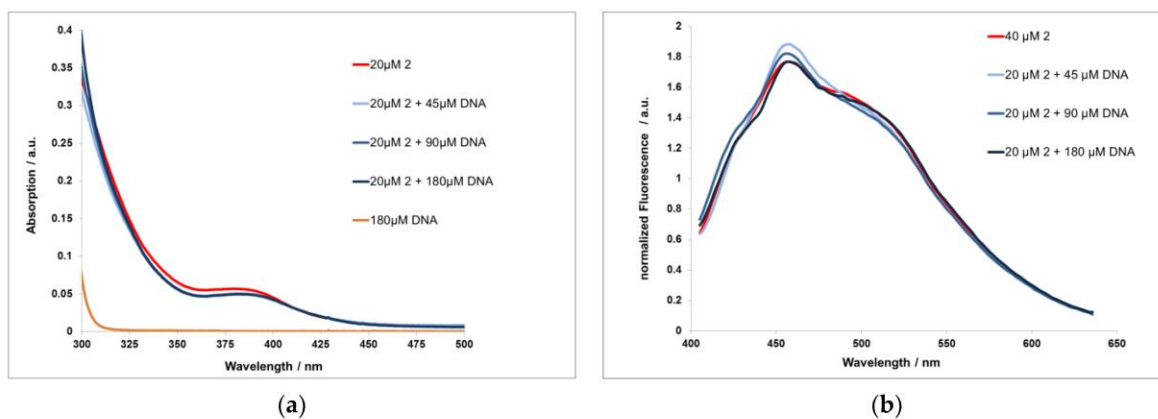


Figure S13. (a) Raw UV/Vis absorption spectra of **2** (20 μM) incubated with increasing concentration of calf thymus DNA in Tris/EDTA (TE) buffer, pH 7.5 (n=3). (b) Normalized fluorescence emission spectra of compound **2** incubated with increasing concentration of calf thymus DNA in TE buffer, pH 7.5. Excitation wavelength: 375 nm (n=3). Neither the absorption spectra of **2** nor the fluorescence spectra show any significant changes due to DNA addition. Accordingly, there is no evidence for DNA interaction with **2**.

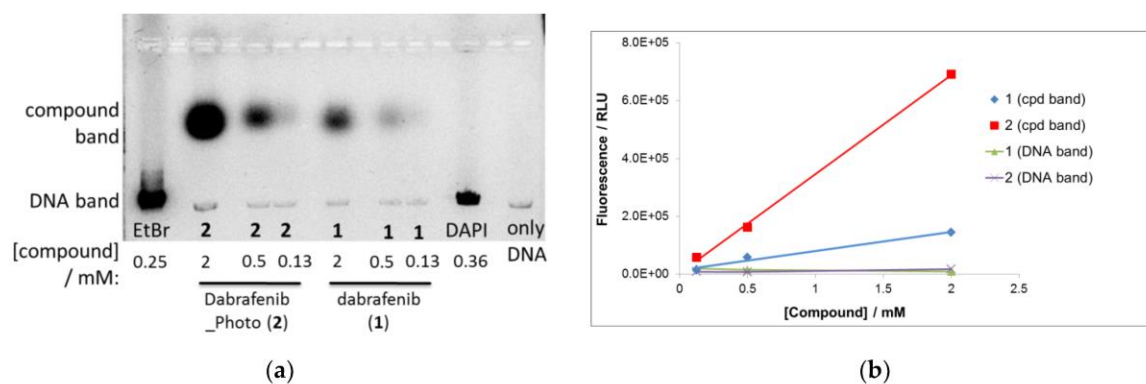


Figure S14. (a) Agarose gel electrophoresis of a PCR product (DNA) preincubated with different concentrations of **1** and **2**. The DNA was stained with two reference dyes: ethidium bromide (EtBr) and DAPI. For the negative control only the PCR product was used (only DNA). Two different bands have been detected: the “compound band” and the “DNA band”. It is clearly to see that the compounds **1** and **2** show different running behavior than the DNA. (b) The fluorescence intensity of individual spots in the compound (cpd) and DNA bands was quantified for **1** and **2**. The intensities are plotted against the compound concentration. The intensity of the spots in the compound band is linear to the compound’s concentration. The intensity of the DNA band is in the range of the negative control. There is no evidence for DNA staining by the compounds.

2. Supplementary Tables

Table S1. Half-live periods for photoinduced decay of 200 μM dabrafenib **1** in different solvents, when irradiated by UV light at 365 nm with 1130 W/m^2 .

Solvent	DMSO	DPBS	DMEM
Half-live / s	19.5	145	294

Table S2. Kinase profiling of dabrafenib (**1**) and dabrafenib_photo (**2**). The inhibitory effect of active compounds was tested on a panel of 321 kinases. The residual activity of kinases was measured after incubation with 1 μM of each compound. The data is portrayed as mean percentage residual activity. (ProQinase, Freiburg, Germany).

Kinase	Kinase Family*	Dabrafenib_photo (2)	Dabrafenib (1)
ABL1	TK	93	94
ABL2	TK	99	77
ACK1	TK	75	29
ACV-R1	TKL	79	47
ACV-R1B	TKL	84	22
ACV-R2A	TKL	74	9
ACV-R2B	TKL	88	46
ACV-RL1	TKL	87	75
AKT1 aa106-480	AGC	88	94
AKT2 aa107-481	AGC	114	91
AKT3 aa106-479	AGC	89	80
ALK (GST-HIS-tag)	TK	104	105
AMPK-alpha1 aa1-550	CAMK	81	49
ARK5	CAMK	95	101
ASK1	STE	104	98
Aurora-A	OTHER	103	102
Aurora-B	OTHER	90	81
Aurora-C	OTHER	104	92
AXL	TK	100	75
BLK	TK	52	29
BMPR1A	TKL	96	48
BMX	TK	87	75
B-RAF V600E	TKL	27	1
B-RAF	TKL	27	5
BRK	TK	104	26
BRSK1	CAMK	102	105
BRSK2	CAMK	88	50
BTK	TK	75	96
BUB1B	OTHER	89	101
CAMK1D	CAMK	97	116
CAMK2A	CAMK	80	81
CAMK2B	CAMK	83	78
CAMK2D	CAMK	96	97
CAMK2G	CAMK	118	102

CAMK4	CAMK	94	91
CAMKK1	OTHER	88	95
CAMKK2	OTHER	107	113
CDC42BPA	AGC	82	88
CDC42BPB	AGC	100	98
CDC7/ASK	OTHER	95	92
CDK1/CycA2	CMGC	100	84
CDK1/CycB1	CMGC	89	89
CDK1/CycE1	CMGC	83	57
CDK19/CycC	CMGC	98	94
CDK2/CycA2	CMGC	70	72
CDK2/CycE1	CMGC	93	90
CDK3/CycC	CMGC	97	86
CDK3/CycE1	CMGC	98	103
CDK4/CycD1	CMGC	88	97
CDK4/CycD3	CMGC	100	119
CDK5/p25NCK	CMGC	101	98
CDK5/p35NCK	CMGC	77	82
CDK6/CycD1	CMGC	113	104
CDK6/CycD3		97	74
CDK7/CycH/MAT1	CMGC	123	109
CDK8/CycC	CMGC	100	109
CDK9/CycK	CMGC	93	98
CDK9/CycT1	CMGC	102	106
CHK1	CAMK	94	100
CHK2	CAMK	72	103
CK1-alpha1	CK1	86	94
CK1-delta	CK1	79	81
CK1-epsilon	CK1	84	89
CK1-gamma1	CK1	63	96
CK1-gamma2	CK1	104	101
CK1-gamma3	CK1	86	91
CK2-alpha1	OTHER	88	85
CK2-alpha2	OTHER	94	84
CLK1	CMGC	91	89
CLK2	CMGC	90	98
CLK3	CMGC	82	74
CLK4	CMGC	81	74
COT	STE	93	85
CSF1-R	TK	109	109
CSK	TK	87	34
DAPK1	CAMK	79	75
DAPK2	CAMK	81	92
DAPK3	CAMK	58	54
DCAMKL2	CAMK	90	77
DDR2	TK	69	14
DMPK	AGC	95	103
DNA-PK	ATYP	94	92
DYRK1A	CMGC	88	90

DYRK1B	CMGC	106	98
DYRK2	CMGC	94	98
DYRK3	CMGC	83	91
DYRK4	CMGC	92	38
EEF2K	ATYPICAL	88	93
EGF-R	TK	104	119
EIF2AK2	OTHER	93	95
EIF2AK3	OTHER	47	4
EPHA1	TK	94	81
EPHA2	TK	109	133
EPHA3	TK	92	91
EPHA4	TK	99	97
EPHA5	TK	109	116
EPHA6	TK	99	72
EPHA7	TK	96	102
EPHA8	TK	95	105
EPHB1	TK	76	94
EPHB2	TK	91	94
EPHB3	TK	93	92
EPHB4	TK	93	97
ERBB2	TK	109	96
ERBB4	TK	80	91
ERK1	CMGC	84	92
ERK2	CMGC	99	88
ERK5	CMGC	80	74
ERK7	CMGC	81	80
FAK aa2-1052	TK	99	89
FER	TK	111	94
FES	TK	93	88
FGF-R1	TK	90	89
FGF-R2	TK	91	92
FGF-R3	TK	91	118
FGF-R4	TK	104	93
FGR	TK	91	60
FLT3	TK	104	117
FRK	TK	103	111
FYN	TK	97	36
GRK2	AGC	90	95
GRK3	AGC	96	86
GRK4	AGC	70	59
GRK5	AGC	84	85
GRK6	AGC	76	79
GRK7	AGC	81	76
GSG2	OTHER	118	147
GSK3-alpha	CMGC	88	97
GSK3-beta	CMGC	91	97
HCK	TK	82	91
HIPK1	CMGC	81	87
HIPK2	CMGC	80	80

HIPK3	CMGC	96	99
HIPK4	CMGC	82	37
HRI	OTHER	69	16
IGF1-R	TK	100	81
IKK-alpha	OTHER	88	97
IKK-beta	OTHER	79	94
IKK-epsilon	OTHER	90	97
INS-R	TK	112	108
INSR-R	TK	107	103
IRAK1	TKL	90	84
IRAK4 (untagged)	TKL	90	103
ITK	TK	94	109
JAK1 aa850-1154	TK	90	84
JAK2	TK	85	90
JAK3	TK	100	115
JNK1	CMGC	75	89
JNK2	CMGC	95	105
JNK3	CMGC	70	118
KIT	TK	95	94
LCK	TK	80	38
LIMK1	TKL	100	98
LIMK2	TKL	92	87
LRRK2	TKL	93	102
LTK	TK	90	93
LYN	TK	87	51
MAP3K1	STE	90	84
MAP3K10	STE	102	91
MAP3K11	STE	22	55
MAP3K7/MAP3K7IP1	STE	86	76
MAP3K9	STE	66	70
MAP4K2	STE	114	115
MAP4K4	STE	95	95
MAP4K5	STE	87	90
MAPKAPK2	CAMK	69	69
MAPKAPK3	CAMK	93	92
MAPKAPK5	CAMK	83	37
MARK1	CAMK	90	90
MARK2	CAMK	92	94
MARK3	CAMK	99	96
MARK4	CAMK	88	84
MATK	TK	101	90
MEK1	STE	79	94
MEK2	STE	92	91
MEK5	STE	80	90
MEKK2	STE	83	57
MEKK3	STE	117	96
MELK	CAMK	41	27
MERTK	TK	124	115
MET	TK	90	89

MINK1	STE	90	100
MKK4	STE	81	87
MKK6 S207D/T211D**	STE	70	96
MKK7	STE	83	78
MKNK1	CAMK	117	128
MKNK2	CAMK	98	63
MLK4	TKL	90	92
MST1	STE	86	105
MST2	STE	89	94
MST3	STE	28	14
MST4	STE	98	103
mTOR	ATYPICAL	103	99
MUSK	TK	80	113
MYLK	CAMK	87	74
MYLK2	CAMK	113	112
MYLK3	CAMK	93	100
NEK1	OTHER	92	63
NEK11	OTHER	60	1
NEK2	OTHER	103	83
NEK3	OTHER	118	85
NEK4	OTHER	96	92
NEK6	OTHER	96	99
NEK7	OTHER	27	42
NEK9	OTHER	96	106
NIK	STE	104	100
NLK	CMGC	91	78
p38-alpha	CMGC	96	111
p38-beta	CMGC	101	104
p38-delta	CMGC	91	85
p38-gamma	CMGC	100	102
PAK1	STE	93	91
PAK2	STE	102	88
PAK3	STE	87	87
PAK4	STE	86	68
PAK6	STE	89	79
PAK7	STE	77	78
PASK	CAMK	99	98
PBK	OTHER	92	99
PCTAIRE1/CycY	CMGC	87	53
PDGFR-alpha	TK	97	103
PDGFR-beta	TK	105	93
PDK1	AGC	82	94
PHKG1	CAMK	98	97
PHKG2	CAMK	92	88
PIM1	CAMK	108	109
PIM2	CAMK	81	77
PIM3	CAMK	105	100
PKA	AGC	104	95
PKC-alpha	AGC	107	100

PKC-beta1	AGC	94	99
PKC-beta2	AGC	75	84
PKC-delta	AGC	100	119
PKC-epsilon	AGC	133	132
PKC-eta	AGC	78	90
PKC-gamma	AGC	103	102
PKC-iota	AGC	91	100
PKC-mu	AGC	93	33
PKC-nu	AGC	98	100
PKC-theta	AGC	115	120
PKC-zeta	AGC	107	109
PKMYT1	OTHER	84	88
PLK1	OTHER	101	99
PLK3	OTHER	91	91
PRK1	AGC	102	101
PRK2	AGC	91	78
PRKD2	CAMK	79	30
PRKG1	AGC	99	96
PRKG2	AGC	102	102
PRKX	AGC	82	77
PYK2	TK	91	109
RAF1 Y340D/Y341D (untagged)**	TKL	9	1
RET	TK	69	81
RIPK2	TKL	70	5
RIPK5	TKL	83	82
ROCK1	AGC	98	104
ROCK2	AGC	100	103
RON	TK	116	104
ROS	TK	109	96
RPS6KA1	AGC	107	90
RPS6KA2	AGC	84	81
RPS6KA3	AGC	90	77
RPS6KA4	AGC	84	86
RPS6KA5	AGC	95	97
RPS6KA6	AGC	97	98
S6K	AGC	87	75
S6K-beta	AGC	90	98
SAK	OTHER	44	6
SGK1	AGC	87	75
SGK2	AGC	91	101
SGK3	AGC	89	97
SIK1	CAMK	90	98
SIK2	CAMK	101	98
SIK3	CAMK	98	60
SLK	STE	95	90
SNARK	CAMK	81	90
SNK	OTHER	91	94
SRC (GST-HIS-tag)	TK	89	68
SRMS	TK	70	10

SRPK1	CMGC	99	105
SRPK2	CMGC	108	111
STK17A	CAMK	80	91
STK23	CAMK	97	105
STK25	STE	57	51
STK33	CAMK	82	76
STK39	STE	92	81
SYK aa1-635	TK	95	111
TAOK2	STE	84	35
TAOK3	STE	87	91
TBK1	OTHER	95	88
TEC	TK	87	87
TGFB-R1	TKL	102	22
TGFB-R2	TKL	81	42
TIE2	TK	79	58
TLK1	AGC	92	108
TLK2	AGC	109	96
TNK1	TK	82	19
TRK-A	TK	54	78
TRK-B	TK	65	100
TRK-C	TK	82	93
TSF1	OTHER	93	105
TSK2	CAMK	95	86
TSSK1	CAMK	88	84
TTBK1	CK1	79	89
TTBK2	CK1	104	104
TTK	OTHER	90	92
TXK	TK	71	88
TYK2	TK	92	96
TYRO3	TK	91	90
VEGF-R1	TK	111	84
VEGF-R2	TK	95	82
VEGF-R3	TK	76	94
VRK1	CK1	82	77
VRK2	CK1	116	103
WEE1	OTHER	87	91
WNK1	OTHER	103	98
WNK2	OTHER	101	103
WNK3	OTHER	91	89
YES	TK	124	105
ZAK	TKL	103	101
ZAP70	TK	95	92
Selectivity Score (portion of kinases with < 50 % residual activity):		0.030	0.093

*Classification of protein kinase families (Manning et al. Science 6 December 2002: Vol. 298 no. 5600 pp. 1912-1934):

AGC: containing PKA, PKG and PKC families

CAMK: Calcium/Calmoduline-dependent protein kinases

CK1: Casein kinase 1 -like

CMGC: containing CDK, MAPK ,GSK3 and CLK families

TK: Tyrosine Kinase

TKL: Tyrosine Kinase-like

STE: Homologs of Yeast Sterile 7, Sterile 11, Sterile 20 Kinases

** Constitutively active kinase

Table S3. COMPARE Analyses of cellular response to dabrafenib_photo 2 (NSC:S789252) and to 100 synthetic compounds from the NCI database. The synthetic compounds are ranked in the order of similarity of cellular response to the response to 2. NSC = numeric identifier for substances submitted to NCI for testing. NCI = National Cancer Institute, USA.

Rank	Correlation	Seed Vector ident For Display	Target Vector ident For Display	Target Vector descriptor For Display	Count Common Cell Lines	Seed Standard Deviation	Target Standard Deviation
1	0.812	NSC:S789252	NSC:S755437		58	29.893	0.673
2	0.792	NSC:S789252	NSC:S755453		56	29.992	0.518
3	0.782	NSC:S789252	NSC:S764134	DABRAFENIB MESYLATE	52	29.923	1.361
4	0.763	NSC:S789252	NSC:S761592		57	28.115	0.627
5	0.759	NSC:S789252	NSC:S761592		59	29.885	0.66
6	0.751	NSC:S789252	NSC:S755437		59	29.885	0.662
7	0.747	NSC:S789252	NSC:S761431	ZELBORAF	59	29.885	0.707
8	0.731	NSC:S789252	NSC:S761586		59	29.885	0.686
9	0.731	NSC:S789252	NSC:S761584		59	29.885	0.618
10	0.723	NSC:S789252	NSC:S756457	SB-610251-B	59	29.885	0.33
11	0.713	NSC:S789252	NSC:S755461		56	29.992	0.521
12	0.683	NSC:S789252	NSC:S766143		56	30.357	0.439
13	0.659	NSC:S789252	NSC:S756221	GW405841X	58	30.141	0.2
14	0.655	NSC:S789252	NSC:S756456	SB-590885-AAD	59	29.885	0.813
15	0.645	NSC:S789252	NSC:S756464	SB-682330-A	57	30.37	0.584
16	0.631	NSC:S789252	NSC:S755435		59	29.885	0.408
17	0.629	NSC:S789252	NSC:S756376	GW813360X	59	29.885	0.2
18	0.606	NSC:S789252	NSC:S633406		58	30.115	0.234
19	0.605	NSC:S789252	NSC:S757299	PROCHLORPERAZIN E EDISYLATE (USAN)	51	31.454	0.286
20	0.598	NSC:S789252	NSC:S766538	MMV666069	57	29.816	0.356
21	0.586	NSC:S789252	NSC:S753193		58	28.099	0.303
22	0.583	NSC:S789252	NSC:S706829		56	30.38	0.687
23	0.58	NSC:S789252	NSC:S718507		55	30.557	0.315
24	0.578	NSC:S789252	NSC:S756458	SB-614067-R	59	29.885	0.354
25	0.576	NSC:S789252	NSC:S707477		51	30.005	0.249
26	0.572	NSC:S789252	NSC:S683437		53	30.338	0.273
27	0.571	NSC:S789252	NSC:S654294		41	31.282	0.232
28	0.57	NSC:S789252	NSC:S707469		52	31.027	0.24
29	0.568	NSC:S789252	NSC:S13477		59	29.885	0.311
30	0.564	NSC:S789252	NSC:S46061		57	29.923	0.278
31	0.554	NSC:S789252	NSC:S656082		45	31.046	0.464
32	0.554	NSC:S789252	NSC:S721875		56	30.146	0.251
33	0.549	NSC:S789252	NSC:S760091	MEPARTRICIN (USAN)	56	30.425	0.213
34	0.547	NSC:S789252	NSC:S667672		55	30.127	0.306

35	0.546	NSC:S789252	NSC:S644609		43	32.302	0.265
36	0.546	NSC:S789252	NSC:S683710		51	30.605	0.228
37	0.546	NSC:S789252	NSC:S701104		57	29.523	0.503
38	0.541	NSC:S789252	NSC:S354462	HYPOTHEMYCIN	58	30.115	0.699
39	0.534	NSC:S789252	NSC:S722656	PARTRICIN MORPHOLIDE A	55	30.724	0.138
40	0.532	NSC:S789252	NSC:S71755	CARPHENAZINE MALEATE(USAN)	59	29.885	0.242
41	0.531	NSC:S789252	NSC:S688369		54	29.801	0.172
42	0.529	NSC:S789252	NSC:S757349	THIORIDAZINE HYDROCHLORIDE	54	31.123	0.239
43	0.527	NSC:S789252	NSC:S758434	HYCANTHONE (USAN)	59	29.885	0.159
44	0.524	NSC:S789252	NSC:S756661	CHLORPROMAZINE (USAN)	58	29.856	0.266
45	0.522	NSC:S789252	NSC:S119608		58	30.114	0.348
46	0.519	NSC:S789252	NSC:S78714	CLOTHIXAMIDE MALEATE (USAN)	59	29.885	0.31
47	0.519	NSC:S789252	NSC:S355147		54	28.016	0.087
48	0.518	NSC:S789252	NSC:S665686		58	30.115	0.257
49	0.516	NSC:S789252	NSC:S756685	CLEMASTINE (USAN)	56	30.342	0.276
50	0.513	NSC:S789252	NSC:S628119		47	31.183	0.232
50	-0.4	NSC:S789252	NSC:S685262		57	29.532	0.162
48	-0.403	NSC:S789252	NSC:S647044		46	31.972	0.396
49	-0.403	NSC:S789252	NSC:S643125		44	32.388	0.492
46	-0.404	NSC:S789252	NSC:S665313		55	30.294	0.262
47	-0.404	NSC:S789252	NSC:S127445	ASPERGILLIC ACID, HYDROXY	50	28.137	0.34
45	-0.405	NSC:S789252	NSC:S641210		49	31.493	0.492
43	-0.407	NSC:S789252	NSC:S728318		57	30.358	0.887
44	-0.407	NSC:S789252	NSC:S634232		43	32.393	0.235
42	-0.409	NSC:S789252	NSC:S668840		50	32.06	0.188
40	-0.41	NSC:S789252	NSC:S631542		48	31.81	0.313
41	-0.41	NSC:S789252	NSC:S646609		46	31.873	0.375
39	-0.411	NSC:S789252	NSC:S647753	ANTINEOPLASTIC-D647753	44	29.978	0.724
37	-0.412	NSC:S789252	NSC:S633925		45	31.5	0.204
38	-0.412	NSC:S789252	NSC:S761834		54	30.211	0.419
36	-0.413	NSC:S789252	NSC:S691569		49	30.545	0.2
34	-0.415	NSC:S789252	NSC:S632990	ABRIN A	42	30.615	0.135
35	-0.415	NSC:S789252	NSC:S688323		57	30.378	0.254
33	-0.416	NSC:S789252	NSC:S719179		57	30.365	0.373
31	-0.419	NSC:S789252	NSC:S646606		53	30.615	0.253
32	-0.419	NSC:S789252	NSC:S694493		58	30.115	0.346
29	-0.424	NSC:S789252	NSC:S625735		46	32.265	0.187
30	-0.424	NSC:S789252	NSC:S700429		49	27.741	0.135
27	-0.428	NSC:S789252	NSC:S635453		41	31.813	0.862

28	-0.428	NSC:S789252	NSC:S642397		46	32.034	0.518
26	-0.429	NSC:S789252	NSC:S666607		56	30.553	1.038
25	-0.43	NSC:S789252	NSC:S635536		44	31.276	0.204
24	-0.432	NSC:S789252	NSC:S690741		50	31.672	0.251
23	-0.434	NSC:S789252	NSC:S724628		56	30.628	0.397
22	-0.437	NSC:S789252	NSC:S682690		52	30.295	0.21
21	-0.438	NSC:S789252	NSC:S638643		57	30.361	0.398
20	-0.442	NSC:S789252	NSC:S117181	CYCLOPIAZONIC ACID	42	33.4	0.35
19	-0.443	NSC:S789252	NSC:S651362		45	31.026	0.187
18	-0.445	NSC:S789252	NSC:S654626		41	32.356	0.32
17	-0.451	NSC:S789252	NSC:S642396		46	32.034	0.542
16	-0.454	NSC:S789252	NSC:S635961		44	32.426	0.356
15	-0.459	NSC:S789252	NSC:S642401		46	32.034	0.509
14	-0.46	NSC:S789252	NSC:S345646	OLEASIDE A	55	28.717	0.235
13	-0.467	NSC:S789252	NSC:S642399		46	32.034	0.5
12	-0.482	NSC:S789252	NSC:S646610		43	31.655	0.363
10	-0.484	NSC:S789252	NSC:S743434		58	30.115	0.418
11	-0.484	NSC:S789252	NSC:S646608		46	31.873	0.353
9	-0.485	NSC:S789252	NSC:S642398		46	32.034	0.513
8	-0.486	NSC:S789252	NSC:S646604		52	29.598	0.341
7	-0.488	NSC:S789252	NSC:S653438		58	30.115	0.511
6	-0.495	NSC:S789252	NSC:S642400		46	32.034	0.497
5	-0.505	NSC:S789252	NSC:S627875		46	32.452	0.154
4	-0.508	NSC:S789252	NSC:S645317	SANGUILUTINE PSEUDOBASE	42	30.531	0.435
3	-0.51	NSC:S789252	NSC:S721194		52	27.878	0.164
2	-0.511	NSC:S789252	NSC:S642402		44	32.654	0.52
1	-0.521	NSC:S789252	NSC:S658361		41	30.264	0.426

3. Methods

3.1. Photochemical Characterization

3.1.1. UV/Vis Absorption Spectra

Spectra were recorded on UV/Vis spectrophotometer Varian Cary[®] 50 Scan (Agilent Technologies, CA, USA). UV/Vis absorbance was measured in TE buffer (10 mM Tris, 1 mM EDTA, pH 7.5). Concentration of compounds was 0.02 mM. For the DNA titration experiments 0.04 mM of **2** were mixed 1+1 with 0.36, 0.18 and 0.09 mM calf thymus DNA. The solutions were incubated for two minutes at room temperature. The end concentration of **2** was 0.02 mM.

3.1.2. Fluorescence Emission Spectra

Spectra were recorded on LS55 Fluorescence spectrometer (Perkin Elmer, Waltham, MA, USA). The excitation and emission slits were set to 10 nm. The fluorescence was measured in TE buffer (10 mM Tris, 1 mM EDTA, pH 7.5). Concentration of compounds was 0.04 mM. The emission spectrum of dabrafenib (**1**) was recorded at constant excitation with 330 nm. Dabrafenib_photo (**2**) was excited at 370 nm. For the DNA titration experiments 0.04 mM of **2** were mixed 1+1 with 0.36, 0.18 and 0.09 mM calf thymus DNA. The solutions were incubated for two minutes at room temperature and then excited at 375 nm. The end concentration of **2** was 0.02 mM.

3.1.3. Dabrafenib stability under daylight exposure and in the dark

Compound **1** was dissolved in DMSO (1.1 mM). The solution was placed in a clear glass flask on a windowsill. After particular incubation times samples were taken, diluted 1:2 with methanol and analyzed by HPLC. Additional to HPLC analysis LC-MS was used to confirm compound identity. The same experiment was repeated in DMEM (200 μ M solution of **1**). Moreover, 200 μ M solutions of **1** in DMEM and in DMSO were also incubated at 37 °C in the dark. The samples were measured as described above.

3.1.4. Irradiation of dabrafenib solutions at 365 nm.

Compound **1** was dissolved in DMSO, DPBS and DMEM (200 μ M) and the solutions were irradiated at 365 nm (LED source: 16x Nichia. NCSU276A.U365, Sahlmann Photochemical Solutions, Figure S8) with 1130 W/m² and 226 W/m² for up to 15 min. After determined irradiation times samples were taken. Aliquots were diluted 1:2 with methanol and subsequently analyzed by HPLC. Additional to retention time LC-MS was used to proof the identity.

3.2. Molecular modeling

Molecular modeling was performed on a DELL 4 core system. For visualization Maestro, version 9.7, Schrödinger, LLC, (New York, NY, USA, 2014) was used. Protein crystal structures were prepared prior to docking by the Protein Preparation Wizard (*1*) utilizing the following programs: Epik, version 2.7, 2014 (*2*); Prime, version 2.4, 2014 (*3*). Thus, the X-ray crystal structure refinement process included addition of hydrogen atoms, optimization of hydrogen bonds, and removal of atomic clashes. Default settings were used. Missing side chains and loops were filled in with Prime. Furthermore, selenomethionines were converted to methionines and water molecules were deleted.

Additionally, ligands were prepared in order to create energetically minimized 3D geometries and assign proper bond orders (MacroModel, version 10.3, 2014 (*4*)). Accessible tautomer and ionization states were calculated prior to screening (LigPrep, version 2.9, 2014 (*5*)). To generate bioactive conformers a conformational search method was used (ConfGen, version 2.7, 2014 (*6*)). Receptor grid generation was performed by Glide, version 6.2, 2014 (*7*). For ligand docking the Glide SP workflow was used. Energetically minimized ligand conformations were docked into the active site of the protein; possible binding poses were determined and subsequently ranked based on their calculated binding affinities.

3.3. Kinase Assays

3.3.1. Determination of IC₅₀ values

The BRAF^{V600E} IC₅₀ profile for **1** and **2** was determined using BRAF^{V600E} protein kinase by a radiometric ³³PanQinase[®] assay (8). IC₅₀ values were measured by testing 10 semi-log concentrations of each compound in the range from 1 × 10⁻⁵ M to 3 × 10⁻¹⁰ M, for single samples. Prior to testing, the compounds were dissolved to prepare 1 × 10⁻³ M stock solutions in 100% DMSO. The final DMSO concentration in the reaction cocktails was 1% in all cases. Analyses were performed by ProQinase (Freiburg, Germany).

3.3.2. Kinase profiling

Compounds **1** and **2** were screened against 321 kinases. The used method was radiometric protein kinase assay (³³PanQinase[®] Activity Assay) (8). The substances were dissolved in DMSO at a concentration of 100 μM. The final DMSO concentration in all reaction cocktails (including high and low controls) was 1%. The mean percentage residual kinase activity was determined. Analyses were performed by ProQinase (Freiburg, Germany).

3.4. Cellular Assays

3.4.1. Cell culture

SKMEL28 cells were purchased from CLS Cell Lines Service GmbH (Eppenheim, Germany). The cells were grown in DMEM medium with 2 mM L-Glutamine, 1 mM Sodium Pyruvate and 10%. SKMEL28 cells were incubated in a 5% CO₂ humidified atmosphere at 37 °C.

3.4.2. Proliferation Assays

The cells were grown in cell flasks until approximately 90% confluence and then seeded to give 21000 cells in 100 μl per well into 96-well CulturePlates™ (Perkin Elmer). In addition to the test plates, one plate was prepared for reference measurement at day zero. All plates were incubated for 24 h at 37 °C in a humidified atmosphere with 5% CO₂. Compounds **1**, and **2** were dissolved in 100% DMSO (v/v) and added to the test plates. The final DMSO concentration in the assay was 0.5% (v/v). Viability of the cells in the day zero control plates were determined on the same day without adding any compounds. For viability measurement the resazurin assay was used. The shift in the fluorescence signal was measured at the LS55 Fluorescence spectrometer (Perkin Elmer). For the photoactivation experiments the test plates were irradiated at 365 nm for 5 min (LED source: 16× Nichia NCSU276a, Sahlmann Photochemical Solutions, 5%, 1.13 kW/m²). Test plates were incubated for further 48 h and cell viability was defined as described above. Measured raw data was converted into percent of cell growth by using the high control (0.5% DMSO (v/v) without compound) and the day zero control. For dose-response studies, 11 different concentrations of compounds were tested in duplicates. IC₅₀ values were calculated using the 4-parameter logarithmic fit option of GraphPad Prism 5.

3.4.3. Cell Staining

SKMEL28 cells were stained with the dabrafenib (**1**) and **2**. For this purpose, the cells were seeded to give 15,000 cells in 50 μL per well into 96-well half area microplate (Ref.: 675986, Greiner bio-one, Kremsmünster, Austria). The plate was incubated for 72 h at 37 °C in a humidified atmosphere with 5% CO₂. Compounds **1** and **2** were dissolved in DMEM medium with 10% FCS and added to the cells to give the end concentration of 100 μM, respectively. The cells were incubated with the compounds for 15 min at 37 °C. Where indicated the cells were irradiated at 365 nm with 1.13 kW/m². After that, the cells were washed twice with DPBS and fixed with 3.3% formalin for 20 min. Then the cells were washed twice with DPBS again and the cell nuclei were counterstained with 1 μg/mL DAPI in PBS. After 10 min incubation at 37 °C, the cells were washed with DPBS and the fluorescence images were taken at the ImageXpress[®] Micro XL

(Molecular Devices, Sunnyvale CA, USA). The magnification was 60x and 10x. Following filter sets were used for the visualization of compounds (Table S4).

Table S4. Filter sets used for the cell staining.

Compound	Filter Set	Exciter (nm) (Center/Bandwidth)	Emitter (nm) (Center/Bandwidth)
DAPI	DAPI	377/50	447/60
1, 2	CFP	438/24	483/32

3.5. Agarose gel electrophoresis

The 1% agarose gel was prepared by dissolving 0.5 g agarose in 50 ml of boiling TAE (Tris base, acetic acid and EDTA) buffer. 1 μ l of 10 μ g/ μ l ethidium bromide was added to the hot solution.

4 μ l of a PCR product (DNA, 800 bp, 100 ng/ μ l) were mixed with 1 μ l of **1** and **2** in different concentrations. For two positive controls the same amount of nucleotide was incubated with 1 μ l of ethidium bromide or DAPI (100 ng/ μ l, respectively). After 10 min of incubation at room temperature 1 μ l of loading buffer (TAE buffer with glycerol and Orange G) was added. The samples were then loaded on 1% agarose gel. The gel electrophoresis was run for 30 min at 120 V. The visualization was performed at the Lumi-Imager F1 Workstation (Roche Life Sciences, Mannheim, Germany). The individual lines and bands were analyzed by LumiAnalyst 3.1 Image Analysis Software.

3.6. Chemistry

All reagents and solvents were obtained from commercial sources and used as received. Reagents were purchased from abcr GmbH (Karlsruhe, Germany), Fisher Scientific GmbH/Acros (Schwerte, Germany), Sigma-Aldrich Chemie (Hamburg, Germany) or VWR International GmbH (Hannover, Germany).

Where appropriate, column chromatography was performed for crude precursors with Merck (Darmstadt, Germany) silica gel 60 (0.063–0.200 mm) or Acros Organics silica gel (0.060–0.200 mm; pore diameter ca. 60 nm). Column chromatography was performed on a LaFlash system (VWR) using silica gel columns (PF-30SIHP, 30 μ m, 40 g, puriFlash) or RP18 columns (PF-15C18HP, 15 μ m, 55 g, puriFlash). The crude product was loaded on Merck silica gel 60 (15–40 μ m). The progress of reactions was monitored by thin-layer chromatography (TLC) utilizing silica gel polyester sheets (SIL G/UV254, 0.2 mm, Polygram[®], Macherey-Nagel GmbH, Düren, Germany).

High-performance liquid chromatography (HPLC) analyses were performed on a 1050 Series system (Hewlett Packard, Ratingen, Germany). As column an Agilent ZORBAX[®] Eclipse XDB-C8, 5 μ m (4.6 mm \times 150 mm) was used. Injection volume of the compound solutions was 20 μ L. As mobile phase (flow rate 1.5 mL/min) served a gradient of KH₂PO₄ buffer (10 mM, pH 2.3) and methanol over 14 min. The detection wavelength was adapted to the according UV/vis absorption spectra. All key compounds submitted to biological assays were proven by this method to show \geq 98% purity.

Melting points were determined on a SMP3 apparatus (Stuart Scientific, Staffordshire, UK) and are uncorrected. ¹H- (300 MHz) and ¹³C- (75 MHz) NMR were recorded on an Avance III 300 spectrometer (Bruker, Rheinstetten, Germany) at 300 K with a multinuclear probe head using the manufacturer's pulse programs. The data are reported as follows: chemical shifts in ppm from Me₄Si (TMS) as external standard, multiplicity and coupling constant (Hz). NMR spectra were obtained on a ¹H (300 MHz) and ¹³C spectra (75 MHz) were referenced either to TMS or to internal DMSO-d₅ (¹H-NMR δ 2.50) and internal DMSO-d₆ (¹³C-NMR δ 39.5) or internal CHCl₃ (¹H-NMR δ 7.26) and internal CDCl₃ (¹³C-NMR δ 77.0). All

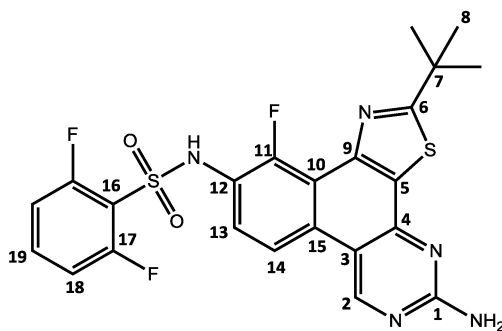
coupling constants (*J* values) are quoted in Hz. The following NMR abbreviations are used: b (broad), s (singlet), d (doublet), t (triplet), m (unresolved multiplet). The labeling scheme of structures to correlate NMR signals is included in the data.

LC-MS samples were chromatographically separated utilizing a 1100 HPLC system (Agilent, Waldbronn, Germany) consisting of a thermostated autosampler, diode array detection, and an Agilent ZORBAX® Eclipse XDB-C8, 5 μm (4.6 mm × 150 mm). Elution was achieved with a solvent gradient system of water and acetonitrile, with 0.1% of acetic acid and a flow rate of 1 mL/min. The eluent flow was splitted to the mass spectrometer. Mass spectrometry was carried out using a Bruker Esquire-LC instrument (Bruker Daltonik, Bremen, Germany), with electrospray ionization (ESI) operating in the positive ion mode. Following parameters were used: drying gas nitrogen 8 L/min, nebulizer 35 psi, dry gas heating 350 °C, HV capillary 4000 V, HV EndPlate offset -500 V

Chemical synthesis and Compound Characterization

N-(5-amino-2-*tert*-butyl)-11-fluorbenzol[*f*]thiazol-[4,5-*h*]-quinazolin-10-yl)-2,6-difluorbenzonsulfonamide

= Dabrafenib_photo (2)



C₂₃H₁₈F₃N₅O₂S₂ (*M_r* = 517.09)

Solution of 5 mg (9.6 μmol) dabrafenib in 2 ml THF was irradiated at 365 nm with 5.4 W for 2 min. This procedure was repeated 18 times at room temperature. The reaction batches were combined. The total initial weight of dabrafenib was 101 mg (190 μmol). The solvent was removed under reduced pressure and the residue was purified by the flash chromatography (SiO₂ reversed phase, MeOH/water gradient 50:50 to 100:0) to give compound **2** as a yellowish solid (36.2 mg, 70.0 μmol, yield: 37%).

¹H-NMR (DMSO-*d*₆, 300 MHz): δ = 1.52 (s, 9 H, *H*-8), 7.28 (m, 2 H, NH₂), 7.28 (ddd, ⁵*J* = 0.4 Hz, ⁴*J* = 1.7 Hz, ³*J* = 8.5 Hz, ³*J* = 8.9 Hz, 2 H, *H*-18), 7.59 (dd, ³*J* = 7.4 Hz, ³*J* = 7.8 Hz, 1 H, *H*-13), 7.71 (tt, ⁴*J* = 6.1 Hz, ³*J* = 8.5 Hz, 1 H, *H*-19), 8.56 (dd, ⁴*J* = 0.9 Hz, ³*J* = 9.3 Hz, 1 H, *H*-14), 9.79 (s, 1 H, *H*-2), 11.01 (s, 1 H, NH) ppm.

¹³C-NMR (DMSO-*d*₆, 300 MHz): δ = 30.4 (s, *C*-8), 38.3 (s, *C*-7), 110.9 (d, ⁴*J*_{CF} = 1.6 Hz, *C*-3), 113.4 (dd, ²*J*_{CF} = 22.7 Hz, ²*J*_{CH} = 3.5 Hz, *C*-18), 114.6 (d, ³*J*_{CF} = 10.3 Hz, *C*-9), 117.4 (d, ²*J*_{CF} = 16.1 Hz, *C*-16), 117.6 (dd, ⁴*J*_{CF} = 0.54 Hz, ²*J*_{CH} = 4.4 Hz, *C*-13), 120.8 (d, ²*J*_{CF} = 12.3 Hz, *C*-10), 125.4 (s, *C*-13), 129.3 (d, ³*J*_{CF} = 3.9 Hz, *C*-15), 130.6 (s, *C*-5), 135.9 (tt, ³*J*_{CF} = 10.9 Hz, ²*J*_{CH} = 3.3 Hz, *C*-19), 148.8 (dd, ²*J*_{CF} = 0.54 Hz, ²*J*_{CH} = 7.2 Hz, *C*-12), 149.2 (s, *C*-4), 150.1 (s, *C*-11), 157.1 160.5 (dd, ³*J*_{FF} = 257.3 Hz, ²*J*_{CF} = 3.61 Hz, *C*-4), 157.9 (s, *C*-2), 162.1 (s, *C*-1), 184.0 (s, *C*-6) ppm.

¹⁵N-HMBC (DMSO-*d*₆, 300 MHz): δ = 9.79/-119.60, 11.01/-268.37 ppm.

¹⁹F-NMR (DMSO-*d*₆, 300 MHz): δ = -121.03 (s, 1 F, *F*-11), -107.18 (m, 2 F, *F*-17) ppm.

HRMS (EI, 205 °C, THF): *m/z* = 517.0849 [M]⁺.

LC-MS (ESI, 70 eV, MeOH): *t_R* = 9.3 min; *m/z* (%) = 518.1 (100) [M+H]⁺.

IR (ATR): $\tilde{\nu}$ = 3490 (N-H), 3176 (arom. C-H), 2926 (C-H₃), 1696 (N=N), 1613 (N-H), 1587, 1522, 1488, 1469 (arom. C=C), 1342 (sulfonamide), 1277, 1240, 1174 (C-F) cm⁻¹.

4. Supplementary References

1. Schrödinger Release 2014-2: Schrödinger Suite 2014-2 Protein Preparation Wizard; Epik version 2.8, Schrödinger, LLC, New York, NY, 2014; Impact version 6.3, Schrödinger, LLC, New York, NY, 2014; Prime version 3.6, Schrödinger, LLC, New York, NY, 2014.
2. Schrödinger Release 2014-1: Epik, version 2.7, Schrödinger, LLC, New York, NY, 2014.
3. Small-Molecule Drug Discovery Suite 2014-2: PrimeX, version 2.4, Schrödinger, LLC, New York, NY, 2014.
4. Schrödinger Release 2014-1: MacroModel, version 10.3, Schrödinger, LLC, New York, NY, 2014.
5. Schrödinger Release 2014-1: LigPrep, version 2.9, Schrödinger, LLC, New York, NY, 2014.
6. Schrödinger Release 2014-1: ConfGen, version 2.7, Schrödinger, LLC, New York, NY, 2014.
7. Small-Molecule Drug Discovery Suite 2014-1: Glide, version 6.2, Schrödinger, LLC, New York, NY, 2014.
8. ProQinase GmbH. FlashPlate-based Protein Kinase Assay Protocol (33 PanQinase® Assay) (accessed February 17, 2016).
9. Hastie, C. J.; McLauchlan, H. J.; Cohen, P. Assay of protein kinases using radiolabeled ATP: a protocol. *Nature protocols* **2006**, *1* (2), 968–971. DOI: 10.1038/nprot.2006.149.
10. Bain, J.; Plater, L.; Elliott, M.; Shpiro, N.; Hastie, C. J.; McLauchlan, H.; Klevernic, I.; Arthur, J. S. C.; Alessi, D. R.; Cohen, P. The selectivity of protein kinase inhibitors: a further update. *The Biochemical journal* **2007**, *408* (3), 297–315. DOI: 10.1042/BJ20070797.

3.5 Marine derived hamacanthins as lead for the development of novel PDGFR β protein kinase inhibitors

Boris Pinchuk, Eugen Johannes, Sheraz Gul, Joachim Schlosser, Christoph Schaechtele, Frank Totzke and Christian Peifer

Mar. Drugs **2013**, *11*, 3209-3223.

DOI: 10.3390/md11093209

Hamacanthins are deep-sea sponge derived bisindole alkaloids showing a dihydropyrazinone ring system (Figure 21).^{226, 227} Cis-3,4-dihydrohamacanthin B was reported to be a potent and selective inhibitor of pyruvate kinase in multidrug resistant bacteria such as MRSA.²²⁸ Moreover, protein kinase inhibitors with the 2(1*H*)-pyrazinone scaffold were described.²²⁹ Based on these findings, we assumed that the hamacanthine core could be a suitable lead structure for the design of smKIs. Therefore, we set out to develop potent VEGFR-2 inhibitors with the pyrazinone scaffold.²⁰¹

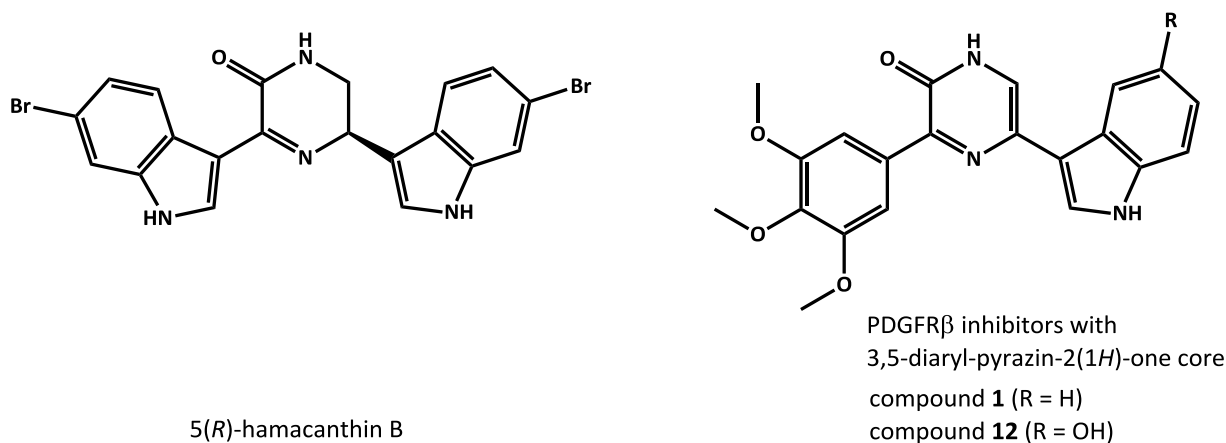


Figure 21: Chemical structures of marine derived hamacanthin B²²⁷ and designed PDGFR β inhibitors with pyrazine-2(1*H*)-one core.²⁰¹ Compounds **1** and **12** correspond to the compounds **5** and **8** in the paper “Marine derived hamacanthins as lead for the development of novel PDGFR β protein kinase inhibitors”, respectively.

Molecular modelling studies suggested that hamacanthin derivatives possessing the flat 3,5-diaryl-pyrazin-2(1*H*)-one core should optimally occupy the ATP binding pocket of VEGFR-2 and several derivatives were reported in the following paper.²⁰¹ Small SAR studies were performed to identify suitable aryl substituents in 3- and 5-positions of the pyrazin-2(1*H*)-one. Thereby, a novel microwave-mediated ring closure strategy was utilized for synthesis of new compounds.²³⁰ The IC₅₀ values of the synthesized inhibitors were determined in a panel of protein kinases. Herein, compounds **1** and **12** (Figure 21) were identified as VEGFR-2 inhibitors. These inhibitors exhibited even stronger potency toward the PDGFR β kinase. Cellular antiproliferative assays confirmed the cytotoxic activity of **1** and **12** against PDGFR β dependent cancer cell lines. Therefore, hamacanthin-derived pyrazin-2(1*H*)-ones were used as hit-to-leads for further development of highly potent and selective PDGFR β -inhibitors.

Dr. Eugen Bethke (born Johannes) synthesized all compounds to be tested and performed the molecular modeling studies. I evaluated all compounds in cellular assays.

Mar. Drugs **2013**, *11*, 3209-3223; doi:10.3390/md11093209

OPEN ACCESS

marine drugs

ISSN 1660-3397

www.mdpi.com/journal/marinedrugs

Article

Marine Derived Hamacanthins as Lead for the Development of Novel PDGFR β Protein Kinase Inhibitors

Boris Pinchuk ^{1,2}, Eugen Johannes ¹, Sheraz Gul ², Joachim Schlosser ¹, Christoph Schaechtele ³, Frank Totzke ³ and Christian Peifer ^{1,*}

¹ Institute of Pharmacy, University of Kiel, Gutenbergstraße 76, Kiel D-24118, Germany; E-Mails: bpinchuk@pharmazie.uni-kiel.de (B.P.); ejohannes@pharmazie.uni-kiel.de (E.J.); jschlosser@pharmazie.uni-kiel.de (J.S.)

² European ScreeningPort GmbH, Schnackenburgallee 114, Hamburg D-22525, Germany; E-Mail: sheraz.gul@screeningport.com

³ ProQinase GmbH, Breisacherstraße 117, Freiburg D-79106, Germany; E-Mails: c.schaechtele@proqinase.com (C.S.); f.totzke@proqinase.com (F.T.)

* Author to whom correspondence should be addressed; E-Mail: cpeifer@pharmazie.uni-kiel.de; Tel.: +49-431-880-1137; Fax +49-431-880-1352.

Received: 7 June 2013; in revised form: 1 August 2013 / Accepted: 8 August 2013 /

Published: 26 August 2013

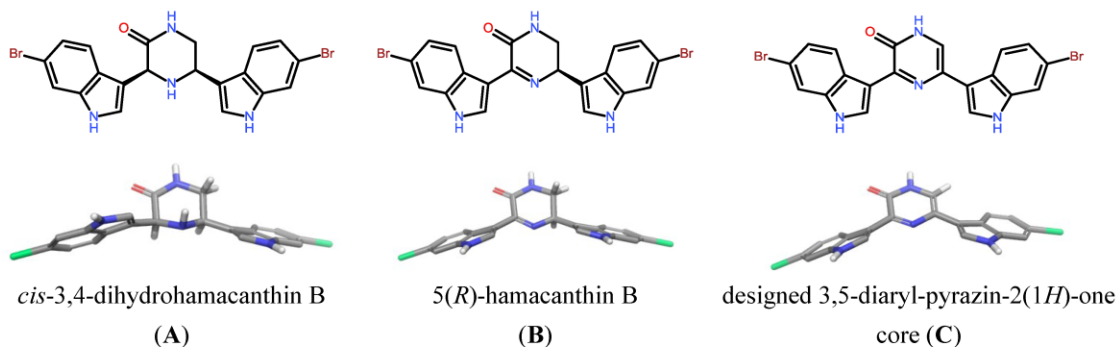
Abstract: In this study, we report on pyrazin-2(1*H*)-ones as lead for the development of potent adenosine triphosphate (ATP) competitive protein kinase inhibitors with implications as anti-cancer drugs. Initially, we identified the pyrazin-2(1*H*)-one scaffold from hamacanthins (deep sea marine sponge alkaloids) by Molecular Modeling studies as core binding motif in the ATP pocket of receptor tyrosine kinases (RTK), which are validated drug targets for the treatment of various neoplastic diseases. Structure-based design studies on a human RTK member PDGFR (platelet-derived growth factor receptor) suggested a straight forward lead optimization strategy. Accordingly, we focused on a Medicinal Chemistry project to develop pyrazin-2(1*H*)-ones as optimized PDGFR binders. In order to reveal Structure-Activity-Relationships (SAR), we established a flexible synthetic route via microwave mediated ring closure to asymmetric 3,5-substituted pyrazin-2(1*H*)-ones and produced a set of novel compounds. Herein, we identified highly potent PDGFR binders with IC₅₀ values in an enzymatic assay below μ M range, and possessing significant activity against PDGFR dependent cancer cells. Thus, marine hamacanthin-derived pyrazin-2(1*H*)-ones showing interesting properties as lead for their further development towards potent PDGFR-inhibitors.

Keywords: marine sponge derived hamacanthins; pyrazin-2(1*H*)-ones; receptor tyrosine kinases; PDGFR inhibitors; anti-cancer activity

1. Introduction

Marine-derived bioactive compounds and their novel chemical scaffolds have been shown to be attractive starting points for drug discovery programs [1–3]. In this regard, we became interested in the marine alkaloid family of hamacanthins [4–6]. In the course of our work to develop ATP-competitive receptor tyrosine kinase (RTK) inhibitors with anti-cancer activity [7–10], we focused on the deep-sea sponge derived bis-indole alkaloids possessing a 3,5-bis-indole-piperazin-2-one and 3,5-bis-indole-3,4-dihydropyrazin-2(1*H*)-one scaffold, respectively (Figure 1) [4,5,11,12]. Recently, *cis*-3,4-dihydro hamacanthin B was reported to be a potent bacterial methicillin-resistant *Staphylococcus* protein kinase (PK) inhibitor (MRSA-PK inhibitor) with an IC₅₀ value of 0.016 μM and significant selectivity over human protein kinase isoforms [13]. Furthermore, the 2(1*H*)-pyrazinone scaffold is present as core moiety in PK inhibitors [14]. Among human PK are validated drug targets in oncology; over-activated RTK including VEGFR, PDGFR and c-kit are considered to be major targets for the development of clinically effective inhibitors [15–17]. In line with this notion, many anti-cancer compounds that are advanced into the clinic show (group-) selectivity towards VEGFR, FGFR, EGFR, PDGFRα/β, c-kit, and Flt-3 [18]. Since all PKs from the kinome use ATP as a cofactor for the phosphorylation of proteins in signal transduction pathways, they share a highly conserved ATP binding pocket that is the molecular binding site of most PK inhibitors [19]. Thus, small molecular differences in amino acid identities adjacent to the ATP pocket provide selectivity filters for specific inhibitors [20]. Therefore, we hypothesize that the hamacanthin-core could serve as a suitable scaffold for the design of specific PK inhibitors.

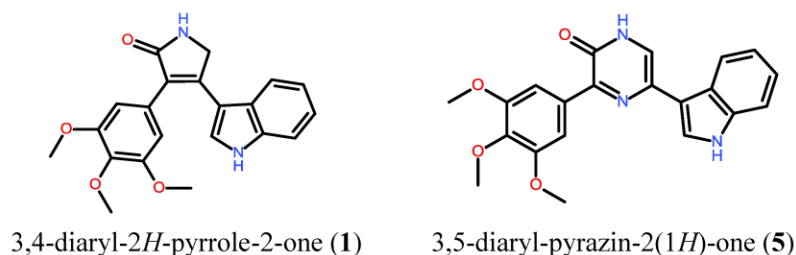
Figure 1. Chemical 2D-representation and energy minimized (Schrödinger Suite 2011: MacroModel, version 9.9, Schrödinger, LLC, New York, NY, 2012) 3D-structures of hamacanthin family members, and 3,5-bis(6-bromo-1*H*-indol-3-yl)-1*H*-pyrazin-2-one as the concept of this study. The compounds formally show different oxidation status of the piperazine-2-one core with significant impact to 3,5-diaryl-conformational parameters.



Our molecular modeling and docking approaches for the ATP binding pocket of the RTK VEGF-R2 suggests that only the 3,5-diaryl-pyrazin-2(1*H*)-one core (Figure 1C) is capable of occupying the narrow ATP active site of this RTK. Furthermore, the pyrazin-2(1*H*)-one core was reported to be a key binding motif to PK [14]. In contrast, neither the 3,5-bis-indole-piperazin-2-one nor the 3,5-bis-indole-3,4-dihydropyrazin-2(1*H*)-one core of hamacanthins produced plausible docking poses. The lack of reasonable binding modes in our modeling studies is mainly due to the chiral center(s) of the core scaffold positioning the 3,5-bis-indole-moieties out of the piperazin-2-one ring-plane, and the 5-indole moiety out of the 5,6-dihydropyrazin-2(1*H*)-one ring plane, respectively (Figure 1A,B). Our observation is in line with the notion that *cis*-3,4-dihydrohamacanthin B was reported to be an allosteric MRSA-PK inhibitor that addresses a tetrameric interface region of the PK-protein, and was not determined by X-ray analysis as ligand binding to the ATP site [4].

In this study, we designed the aryl-substitution pattern of the 6-membered 3,5-diaryl-pyrazin-2(1*H*)-one (compound **5**) based on the corresponding 5-membered 3,4-diaryl-2*H*-pyrrole-2-one (compound **1**, Figure 2), a potent inhibitor developed in a former project showing strong activity against the RTK VEGF-R2/3 ($IC_{50} = 0.03 \mu\text{M}$) and with good efficacy in cellular assays [9].

Figure 2. Structures of the reported potent VEGF-R2/3 inhibitor, compound **1** and the newly designed and synthesized compound **5** of this study showing comparable decoration patterns of the aryl moieties.



2. Results and Discussion

2.1. Synthesis of Designed Compound **5**

In order to confirm the hypothesis that the pyrazin-2(1*H*)-ones are suitable scaffolds for PK inhibitor development, we synthesized compound **5** that involved a modified microwave-mediated ring closure strategy (Figure 3) [12]. In summary, glyoxylic acid **2** was activated by carbonyldiimidazole (CDI) and coupled with tryptamine to produce compound **3**, which upon DDQ-oxidation yielded compound **4**. Ring closure in the final step to produce the targeted pyrazin-2(1*H*)-one compound **5** was straightforward and involved an optimized microwave-mediated reaction using ammonium acetate as the nitrogen source.

2.2. Biological Evaluation: Activity against PKs

Interestingly, in a preliminary screen [21] involving 24 therapeutically relevant PK targets, compound **5** inhibited VEGF-R2/3 in the low μM range, and most potently inhibited PDGFR β with an

IC₅₀ of 0.5 μM. Moreover, compound **5** was shown to exhibit promising selectivity over the other PK enzymes tested as part of the panel (Table 1). Thus, in order to further enhance potency of this lead compound towards the PDGFRβ drug target [22] we used a structure-based optimization approach. As no X-ray structure of the PK domain of PDGFR was available in the public domain, we generated a homology model of PDGFRβ based on the highly related RTK VEGF-R2 as template structure (pdb code 2p2h [23] using Schrödinger Prime, version 3.1, Schrödinger, LLC, New York, NY, USA, 2012).

Figure 3. Synthesis of designed compound **5** by microwave mediated ring closure strategy. Reagents and conditions: (a) 1. CDI, dichloromethane 2. tryptamine; (b) DDQ, THF; (c) NH₄Ac, HAc, microwave heating for 5 min.

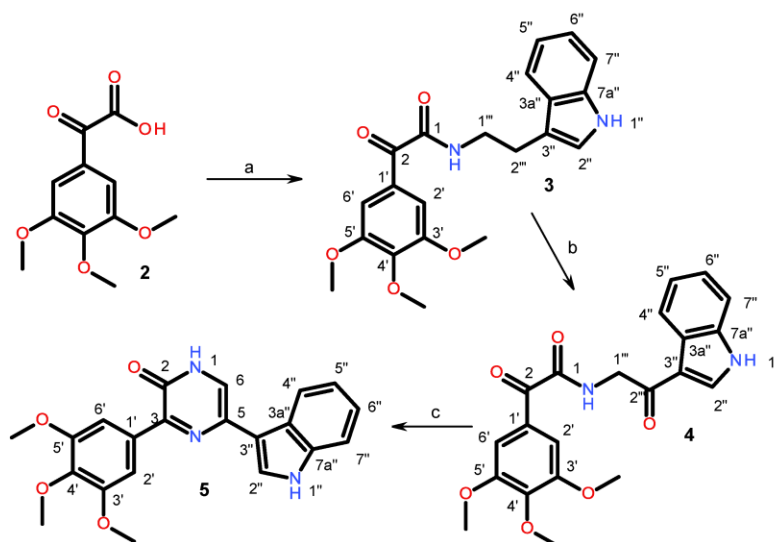


Table 1. IC₅₀ values (μM) of compounds **1** and **5** in a panel [21] of 24 therapeutically relevant PK targets (- indicates no significant PK inhibition was observed at a compound concentration of 100 μM).

Protein kinase	IC ₅₀ (μM) for Compound 1	IC ₅₀ (μM) for Compound 5
AKT1	-	-
ARK5	16	-
Aurora-A	46	-
Aurora-B	66	-
B-RAF-VE	-	-
CDK2/CycA	66	-
CDK4/CycD1	56	-
COT	32	-
EGFR	23	-
EPHB4	53	-
ERBB2	51	-
FAK	9	-
IGF1R	22	-
SRC	14	-

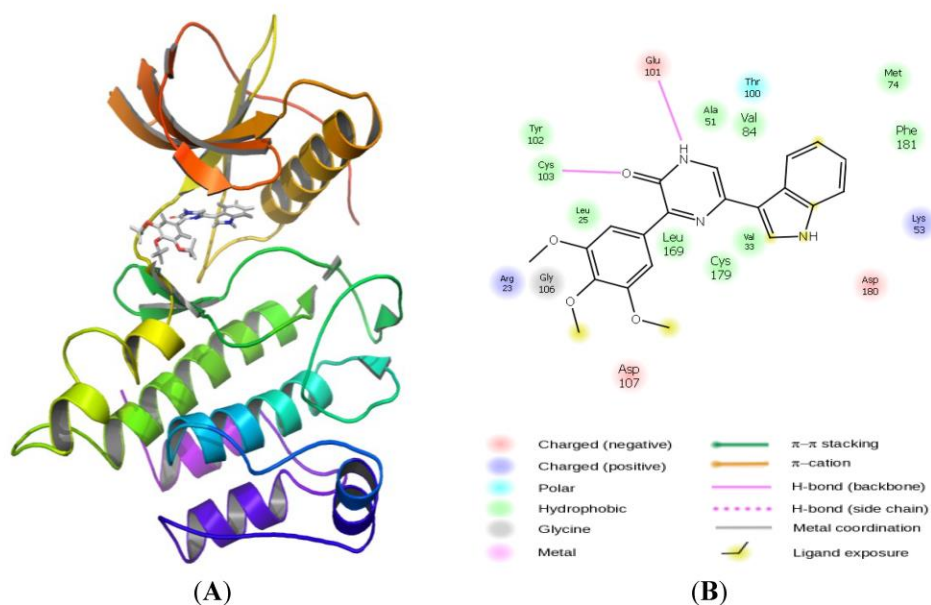
Table 1. Cont.

VEGF-R2	0.031	4
VEGF-R3	0.037	5
FLT3	61	36
INSR	43	-
MET	60	-
PDGFR β	11	0.5
PLK1	-	-
SAK	10	-
TIE2	5	-
CK2a1	-	-

2.3. Molecular Modeling

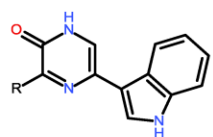
Docking compound **5** into the ATP binding site of our homology model of PDGFR β revealed an interesting and reasonable binding mode (Figure 4, details of the methodology can be found in Section 3.2). The key features of the interaction of compound **5** include the hydrogen bonds formed with the backbone carbonyl of Glu101 and to the amine of Cys103 in the hinge region of the PK, respectively. The indole ring is located in the hydrophobic pocket I whereas the trimethoxyphenyl moiety is located in the solvent exposed hydrophobic region II (in accord with a type-I PK inhibitor [24]).

Figure 4. (A) Homology model of PDGFR β based on template structure of VEGF-R2 (pdb code 2p2h [23]) and modeled binding mode of compound **5** in the ATP pocket. (B) Ligand-interaction diagram of compound **5** in the ATP binding site of the PDGFR β homology model. Key amino acid residues and hydrogen bonds are shown (see legend).



Having demonstrated a rational binding mode for compound **5** in the active site of PDGFR β , we subsequently aimed to optimize this compound by performing a virtual screen against a focused set of compounds, with particular focus upon varying the indole at the pyrazin-2(1*H*)-one 5' position, as the pyrazin-2(1*H*)-one 3'-(3,4,5-trimethoxyphenyl) moiety had already been shown to be required in order to inhibit PDGFR β (Figure 5 [9,25]).

Figure 5. Aryl variation of the pyrazin-2(1*H*)-one 3'-position and PDGFR β IC₅₀ values (μ M) of compounds **5–7**.



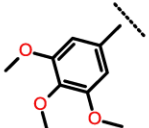
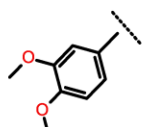
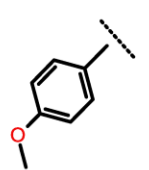
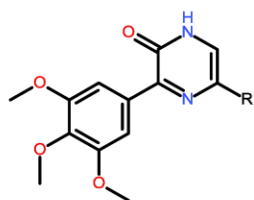
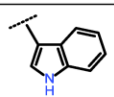
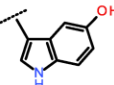
#cpd	R	PDGFR β IC ₅₀ (μ M)
5		0.5
6		1.5
7		19

Figure 6. 5'-OH-Indole variation and PDGFR β -IC₅₀ values (μ M) of compounds **5** and **8**.



#cpd	R	PDGFR β IC ₅₀ (μ M)
5		0.5
8		0.3

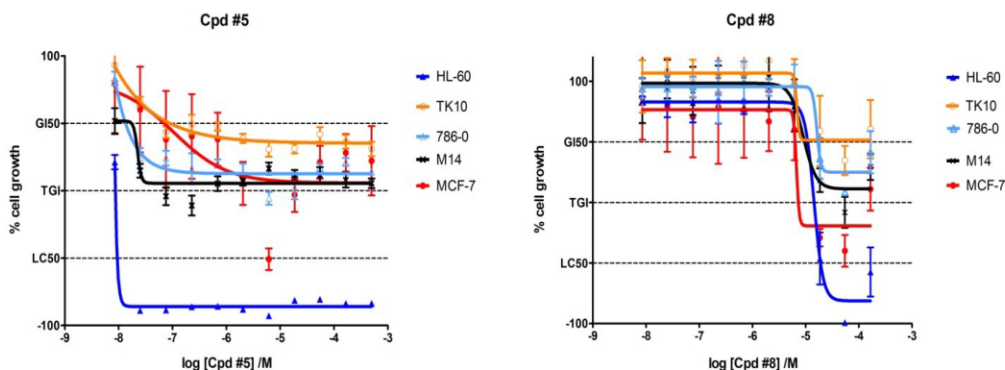
Thus, the indole moiety originally present in the pyrazin-2(1*H*)-one 5'-position was systematically varied by synthetically feasible decoration patterns yielding a set of virtual compounds. The subsequent ligand preparation, docking and scoring campaign using Schrödinger Glide SP (Suite 2012 Glide version 5.8, Schrödinger, LLC, New York, NY, USA) produced a list with compound **8** as the one that was predicted to inhibit PDGFR β most potently (Figure 6). The general binding mode of compound **8** is comparable to the binding pose of compound **5** with the pyrazin-2(1*H*)-one core addressing H-bonds to Glu101 and Cys103 (Figure 4), but with the indole-5'OH situated in the hydrophobic pocket II addressing an additional H-bond to the backbone amide-carbonyl oxygen of Val84.

In accordance with our modeling, compound **8** showed slightly enhanced potency against PDGFR β in the PDGFR β assay (IC₅₀ value = 0.3 μ M, Figure 6).

2.4. Biological Activity in Cancer Cell Lines of Compounds **5** and **8**

In order to determine the cytotoxic profiles of compounds **5** and **8**, they were evaluated in cell viability assays (Figure 7) including HL-60, a human myeloblastic leukemia cell line, as it has been shown that the proliferation and differentiation of these cells depend upon PDGFR-signalling [26]. Cells were treated with compounds **5** and **8** and after 48 h incubation, their viability was determined. The compounds exhibited a differentiated cytotoxic profile. Both compounds were shown to be cytotoxic against HL-60 cells such that compound **5** was associated with an IC₅₀ value of 0.026 μ M and exhibited a significantly stronger anti-proliferative effect than compound **8** that had an IC₅₀ value of 30 μ M. This is in sharp contrast to the data from isolated PDGFR β assay and may be due to limited cellular bioavailability of **8**. Interestingly, the other cells tested were significantly less affected. This is in line with the notion that HL-60 cells depend on PDGFR-signaling [26]. However, in our ongoing studies we are currently investigating further molecular details of the reported selectivity of compound **5** against HL-60 cells.

Figure 7. Determination of cytotoxic profiles of compounds **5** and **8** in cell viability assays using HL-60, TK 10, 786-0, M 14, and MCF-7 cell lines.



Mar. Drugs 2013, 11

3216

3. Experimental Section

3.1. Chemistry and Synthesis of Test Compounds

^1H (300 MHz) and ^{13}C (75 MHz) NMR were recorded on a Bruker Avance III 300 spectrometer (Rheinstetten, Germany) at 300 K with a multinuclear probe head using the manufacturer's pulse programs. The data are reported as follows: chemical shift in ppm from Me_4Si (TMS) as external standard, multiplicity and coupling constant (Hz). NMR spectra were obtained on a ^1H (300 MHz) and ^{13}C spectra (75 MHz) were referenced either to TMS or to internal DMSO-d_5 (^1H NMR δ 2.50) and internal DMSO-d_6 (^{13}C NMR δ 39.5) or internal CHCl_3 (^1H NMR δ 7.26) and internal CDCl_3 (^{13}C NMR δ 77.0). All coupling constants (J values) are quoted in Hz. The following NMR abbreviations are used: br (broad), s (singlet), d (doublet), t (triplet), m (unresolved multiplet). The labelling scheme of structures to correlate NMR signals can be found in Supporting Information.

Mass spectra of the compounds were recorded after chromatographic separation. Mixtures were separated with an Agilent 1100 HPLC system (Waldbronn; Germany) consisting of a thermostated autosampler, diode array detection and an Agilent Zorbax Eclipse XDB-C8 column (150 \times 4.6 mm, 5 μm particle size). Elution was achieved with a solvent gradient system of water and acetonitrile, with 0.1% of acetic acid and a flow rate of 1 mL/min. The eluent flow was splitted to the mass spectrometer.

Mass spectra with nominal resolution were recorded with an Esquire \sim LC mass spectrometer (Bruker Daltonik, Bremen, Germany), with electrospray ionization operating in the positive ion mode, with the following parameters: drying gas nitrogen 8 L/min, nebulizer 35 psi, dry gas heating 350 $^\circ\text{C}$, HV capillary 4000 V, HV EndPlate offset -500 V. GC/MS was performed on a HP6890 Series System. EI-Mass spectra were recorded on a Varian MAT 311A (70 eV). HRMS spectra were recorded on a MAT-95 (Finnigan).

Melting points/decomposition temperatures were determined on a Büchi apparatus according to Dr. Tottoli and are uncorrected.

Where appropriate, column chromatography was performed for crude precursors with Merck silica gel 60 (0.063–0.200 mm) or Acros organics silica gel (0.060–0.200 mm; pore diameter *ca.* 60 nm). Column chromatography for test compounds was performed using a La-Flash-System (VWR) with Merck silica gel 60 (0.015–0.040 mm) or RP8 columns. The progress of the reactions was monitored by thin-layer chromatography (TLC) performed with Merck silica gel 60 F-245 plates. Where necessary, reactions were carried out in a nitrogen atmosphere using 4Å molecular sieves. All reagents and solvents were obtained from commercial sources and used as received (THF was used after distillation over K/benzophenone). Reagents were purchased from Sigma-Aldrich Chemie, Steinheim, Germany; Lancaster Synthesis, Mühlheim, Germany or Acros, Nidderau, Germany.

HPLC analysis was performed on a Hewlett-Packard HP 1090 Series II using a Thermo Betasil C8 (150 \times 4.6, 5 μm) column (mobile phase flow 1.5 mL/min, gradient KH_2PO_4 buffer pH 2.3/methanol, UV-detection 230/254 nm). All key compounds were proven by this method to show $\geq 98\%$ purity.

3.1.1. Synthesis of Compound 3

CDI (1.1 equivalent) was added to a solution of 1 equivalent 2-oxo-2-(3,4,5-trimethoxyphenyl)acetic acid (**2**) in *N*-methylpyrrolidone and reacted at room temperature for 1 h. Then, tryptamine (1 equiv)

Mar. Drugs 2013, 11

3217

was added and the mixture was stirred overnight. Then, water was added to quench the reaction and the mixture was extracted three times with EtOAc. The combined organic phase was evaporated under reduced pressure and the residue purified by flash silica gel chromatography to afford *N*-[2-(1*H*-indol-3-yl)ethyl]-2-oxo-2-(3,4,5-trimethoxyphenyl)acetamide (**3**). Yield: (2.2 g, 91%); mp 119 °C; ¹H NMR (300 MHz, DMSO-*d*₆) δ: 2.98 (t, *J* = 7.3 Hz, 2H, CH₂-2'''), 3.57 (dt, *J* = 7.1, 6.1 Hz, 2H, CH₂-1'''), 3.77 (s, 9H, 3 OMe), 6.98 (t, *J* = 6.9 Hz, 1H, H-5''), 7.07 (t, *J* = 7.0 Hz, 1H, H-6''), 7.20 (d, *J* = 2.3 Hz, 1H, H-2''), 7.28 (s, 2H, H-2',6'), 7.34 (d, *J* = 8.0 Hz, 1H, H-7''), 7.57 (d, *J* = 7.7 Hz, 1H, H-4''), 8.99 (t, *J* = 5.75 Hz, 1H, CONH), 10.82 (s, 1H, NH-1''); ¹³C NMR (75 MHz, DMSO-*d*₆) δ: 24.8 (CH₂-2'''), 39.1 (CH₂-1'''), 56.0 (2',5'-OMe), 60.3 (4'-OMe), 107.3 (CH-2',6'), 111.3 (CH-7''), 111.4 (C_q-3''), 118.2 (CH-5'',4''), 120.9 (CH-6''), 122.7 (CH-2''), 127.1 (C_q-3a''), 128.0 (C_q-1'), 136.2 (C_q-7a''), 143.1 (C_q-4'), 152.8 (C_q-3',5'), 164.6 (CO-1), 188.9 (CO-2); LC-MS *m/z* 383 [M + H]⁺.

3.1.2. Synthesis of Compound 4

To a solution of **3** in THF/H₂O (9:1) at 0 °C, DDQ (1.5 equiv. dissolved in THF) was added dropwise and stirred for 1 h. Then the solvent was evaporated to dryness. To the residual mixture, methanol was added. The precipitate was filtered off and washed with H₂O and methanol to afford *N*-[2-(1*H*-indol-3-yl)-2-oxo-ethyl]-2-oxo-2-(3,4,5-trimethoxyphenyl)acetamide (**4**). Yield: (363 mg, 58%); mp 201 °C; ¹H NMR (300 MHz, DMSO-*d*₆) δ: 3.80 (s, 3H, OMe), 3.93 (s, 6H, 2 OMe), 4.69 (d, *J* = 6.0 Hz, 2H, CH₂-1''), 7.23 (m, 2H, H-5'',6''), 7.51 (m, 1H, H-7''), 7.57 (s, 2H, H-2',6'), 8.16 (m, 1H, H-4''), 8.51 (d, *J* = 3.15 Hz, 1H, H-2''), 9.21 (t, *J* = 5.9 Hz, 1H, CONH), 12.08 (s, 1H, NH-1''); ¹³C NMR (75 MHz, DMSO-*d*₆) δ: 45.4 (CH₂-1'''), 56.1 (2',5'-OMe), 60.3(4'-OMe), 107.5 (CH-2',6'), 112.2 (CH-7''), 113.8 (C_q-3''), 121.0 (CH-4''), 122.0, 122.9 (CH-5'',6''), 125.4 (C_q-3a''), 128.2 (C_q-1'), 133.9 (CH-2''), 136.4 (C_q-7a''), 143.1 (C_q-4'), 152.9 (C_q-3',5'), 166.3 (CO-1), 189.1 (CO-2), 189.7 (CO-2''); LC-MS *m/z* 397 [M + H]⁺.

General procedure for pyrazinone ring closure using microwave synthesis (compounds **5**, **6** and **8a**) [27].

A microwave vial (5 mL) was equipped with ammonium acetate (10 equiv) and a solution of diketone **4** [27] (1 equiv) in acetic acid (3 mL). The vial was sealed and stirred at 160 °C for 4 min in a microwave synthesizer (CEM Discover). The reaction vessel was cooled to rt when H₂O was added to precipitate the pyrazinone, which was filtered off. The pyrazinone was purified by preparative HPLC (RP-phase) to afford the test compound ≥98% purity.

3.1.3. Synthesis of Compound 5

By using the general procedure for pyrazinone ring closure we obtained 5-(1*H*-indole-3-yl)-3-(3,4,5-trimethoxyphenyl)pyrazin-2(1*H*)-one (**5**). Yield after final purification: (31 mg, 11%); mp 293 °C; ¹H NMR (300 MHz, DMSO-*d*₆) δ: 3.76 (s, 3H, OMe), 3.88 (s, 6H, 2 OMe), 7.12 (m, 2H, H-5'',6''), 7.44 (m, 1H, H-7''), 7.90 (s, 1H, H-6), 7.92 (d, *J* = 2.6 Hz, 1H, H-2''), 8.01 (s, 2H, H-2',6'), 8.30 (d, *J* = 7.4 Hz, 1H, H-4''), 11.34 (s, 1H, NH-1''), 12.53 (s, 1H, NH-1); ¹³C NMR (75 MHz, DMSO-*d*₆) δ: 55.8 (2',5'-OMe), 60.1 (4'-OMe), 106.0(CH-2',6'), 111.8 (C_q-7'') 112.1(C_q-3''), 119.4, 120.4, 121.5 (CH-4'',5'',6''), 123.1 (CH-2'',6), 124.8 (C_q-3a''), 131.9 (C_q-1',7a''), 136.7 (C_q-3,5), 138.9 (C_q-4'), 152.3

Mar. Drugs 2013, 11

3218

(C_q-3',5'), 154.1 (CO-2); LC-MS *m/z* 378 [M + H]⁺. HRMS: *m/z* calculated for [M]⁺ C₂₁H₁₉N₃O₄: 377.1375; found 377.1363.

3.1.4. Synthesis of Compound 6

By using general procedure for pyrazinone ring closure, 3-(3,4-dimethoxyphenyl)-5-(1*H*-indol-3-yl)-1*H*-pyrazin-2-one (**6**) was synthesized from *N*-[2-(1*H*-indole-3-yl)-2-oxoethyl]-2-(3,4-dimethoxyphenyl)-2-oxoacetamide [27]. Yield: (50 mg, 51%); mp 259 °C; ¹H NMR (300 MHz, DMSO-*d*₆) δ: 3.84 (s, 3H, OMe), 3.87 (s, 3H, OMe), 7.12 (m, 3H, H-3',5'',6''), 7.44 (d, *J* = 7.4 Hz, 1H, H-7''), 7.81 (s, 1H, H-6), 7.90 (d, *J* = 2.6 Hz, 1H, H-2''), 8.18 (d, *J* = 1.9 Hz, 1H, H-6'), 8.25 (d, *J* = 7.7 Hz, 1H, H-4''), 8.30 (dd, *J* = 8.6, 1.9 Hz, 1H, H-2'), 11.34 (s, 1H, NH-1''), 12.40 (s b, 1H, NH-1); ¹³C NMR (75 MHz, DMSO-*d*₆) δ: 55.3, 55.5 (2 OMe), 110.9 (CH-3'), 111.4 (CH-6''), 111.8 (CH-7''), 112.3 (C_q-3''), 119.4 (CH-6'), 120.4 (CH-4''), 121.4 (CH-5''), 122.1 (CH-2''), 123.1 (CH-2'',6), 124.8 (C_q-3a''), 129.3 (C_q-1'), 136.7 (C_q-7a''), 148.1 (C_q-3'',5'',5'), 150.2 (C_q-4'), 154.1 (CO-2); LC-MS *m/z* 348 [M + H]⁺. HRMS: *m/z* calculated for [M]⁺ C₂₀H₁₇N₃O₃: 347.1270; found: 347.1254.

3.1.5. Synthesis of Compound 7

By using general procedure for pyrazinone ring closure, 3-(4-methoxyphenyl)-5-(1*H*-indol-3-yl)-1*H*-pyrazin-2-one (**7**) was synthesized from *N*-[2-(1*H*-indole-3-yl)-2-oxoethyl]-2-(4-methoxyphenyl)-2-oxoacetamide [27]. Yield: (200 mg, 58%); mp 232 °C; ¹H NMR (300 MHz, DMSO-*d*₆) δ: 3.84 (s, 3H, OMe), 7.06 (d, *J* = 9.1 Hz, 2H, H-3',5'), 7.10-7.18 (m, 2H, H-5'',6''), 7.43 (d, *J* = 7.1 Hz, 1H, H-7''), 7.78 (s, 1H, H-6), 7.88 (d, *J* = 2.6 Hz, 1H, H-2''), 8.15 (d, *J* = 7.2 Hz, 1H, H-4''), 8.50 (d, *J* = 9.0 Hz, 2H, H-2',6'), 11.34 (s, 1H, NH-1''), 12.42 (s, 1H, NH-2); ¹³C NMR (75 MHz, DMSO-*d*₆) δ: 55.2 (OMe), 111.7 (CH-7''), 112.3 (C_q-3''), 113.4 (CH-3',5'), 119.5 (CH-6''), 120.2 (CH-7''), 121.4 (CH-5''), 123.2 (CH-2'',6), 124.7 (C_q-3a',5), 129.1 (C_q-1'), 130.0 (CH-2',6'), 136.7 (C_q-3,7a''), 154.2 (CO-2), 160.3 (C_q-4'); LC-MS *m/z* 318 [M + H]⁺. HRMS: *m/z* calculated for [M]⁺ C₁₉H₁₅N₃O₂: 317.1164; found: 317.1175.

3.1.6. Synthesis of Compound 8a

By using general procedure for pyrazinone ring closure 5-(5-benzyloxy-1*H*-indol-3-yl)-3-(3,4,5-trimethoxyphenyl)-1*H*-pyrazin-2-one, compound **8a** was synthesized from *N*-[2-(5-benzyloxy-1*H*-indol-3-yl)-2-oxo-ethyl]-2-oxo-2-(3,4,5-trimethoxyphenyl)acetamide [27]. Yield: (220 mg, 76%); mp 231 °C; ¹H NMR (300 MHz, DMSO-*d*₆) δ: 3.73 (s, 3H, OMe), 3.81 (s, 6H, 2 OMe), 5.09 (s, 2H, CH₂), 6.93 (dd, *J* = 8.8, 2.40 Hz, 1H, H-6''), 7.32-7.46 (m, 6H, H-7'', 5 H-Bn), 7.88 (s, 1H, H-6), 7.90 (d, *J* = 2.5 Hz, 2H, H-2'',4''), 7.97 (s, 2H, H-2',6'), 11.22 (d, *J* = 2.5 Hz, 1H, NH-1''), 12.36 (s, 1H, NH-1); ¹³C NMR (75 MHz, DMSO-*d*₆) δ: 55.9 (2 OMe), 60.1 (OMe), 70.3 (CH₂), 105.4 (CH-4''), 106.2 (CH-2',6'), 111.1 (CH-6''), 111.7 (C_q-3''), 112.1 (CH-7''), 124.0 (CH-2'',6), 125.3 (C_q-3a''), 127.7, 127.7, 128.3 (5 CH-Bn), 132.0 (C_q-7a''), 132.2 (C_q-1',3a''), 137.6 (C_q-3,5), 139.0 (C_q-4'), 152.3 (C_q-3',5'), 152.8 (C_q-5''), 154.1 (CO-2); LC-MS *m/z* 484 [M + H]⁺. HRMS: *m/z* calculated for [M]⁺ C₂₈H₂₅N₃O₅: 483.1794; found: 483.1776.

3.1.7. Synthesis of Compound 8

A microwave vial (5 mL) was equipped with compound **8a** (100 mg), cyclohexene (90 mg), Pd/C 10% (20 mg) and methanol (1.5 mL). The vial was sealed and stirred 10 min at 100 °C in a microwave synthesizer. The solution was filtered and cooled to room temperature to form a precipitate which was filtered and washed with methanol and Et₂O to afford 5-(5-hydroxy-1*H*-indole-3-yl)-3-(3,4,5-trimethoxyphenyl)pyrazin-2(1*H*)-one, compound **8**. Yield: (52 mg, 64%); mp 340 °C; ¹H NMR (300 MHz, DMSO-*d*₆) δ: 3.76 (s, 3H, OMe), 3.88 (s, 6H, 2 OMe), 6.68 (dd, *J* = 8.7, 2.33 Hz, 1H, H-6''), 7.23 (d, *J* = 8.6 Hz, 1H, H-7''), 7.64 (d, *J* = 2.2 Hz, 1H, H-4''), 7.79 (s, 1H, H-6), 7.80 (d, *J* = 2.7 Hz, 1H, H-2''), 8.00 (s, 2H, H-2',6'), 8.67 (s, 1H, OH), 11.05 (d, *J* = 2.4 Hz, 1H, NH-1''), 12.47 (s, 1H, NH-1); ¹³C NMR (75 MHz, DMSO-*d*₆) δ: 55.7 (2 OMe), 60.1 (OMe), 104.7 (CH-4''), 106.0 (CH-2',6'), 111.3 (C_q-3''), 111.8, 111.9 (CH-6'',7''), 123.5 (CH-2'',6), 125.7 (C_q-4''), 131.9 (C_q-1'',7a''), 132.8 (C_q-3a''), 138.8 (C_q-4''), 151.2 (COH-5''), 152.3 (C_q-3',5'), 154.0 (CO-2); LC-MS *m/z* 394 [M + H]⁺.

3.2. Molecular Modeling

All modeling was performed on a DELL 8 core system. For visualization and building the structures Maestro (version 9.3) from Schrödinger (Schrödinger, LLC, New York, NY, USA, 2012) was used (VEGF-R2 pdb code 2p2h, [23]). The illustrations of modeling were generated by Maestro. For compound docking and screening the Schrödinger "Glide SP" workflow was used [28]. The goal of the Glide methodology is to semiquantitatively rank the ability of candidate ligands to bind to a specified conformation of the protein receptor. Prior to determining binding poses of ligands energetically minimized compound conformations were generated, docked into the active site and subsequently ranked based on their calculated binding affinity.

3.3. Biological Evaluation

All inhibitor solutions were prepared freshly in DMSO prior to each experiment and used immediately.

3.3.1. Selectivity Profiling of Compounds by IC₅₀ Values Using 24 Protein Kinases

Recombinant protein kinases. The inhibitory profile of compounds was determined using the following 24 protein kinases (GenBankAcc.No. available on <http://www.proqinase.com/pages/science> [29]): AKT1, ARK5, Aurora-A, Aurora-B, B-Raf-VE, CDK2/CycA, CDK4/CycD1, CK2-A1, EGF-R, EPHB4, ERBB2, FAK, IGF1-R, SRC, VEGF-R2, VEGF-R3, FLT3, INS-R, MET, PDGFRβ, PLK1, SAK, TIE2 and COT. All protein kinases were expressed using human cDNAs in Sf9 insect cells as recombinant GST-fusion proteins or His-tagged proteins by means of the baculovirus expression system. Kinases were purified by affinity chromatography using either GSH-agarose (Sigma) or Ni-NTA-agarose (Qiagen). The purity and identity of each kinase was determined by SDS-PAGE/silver staining and western blot analysis using specific antibodies.

Protein kinase Assay. A proprietary protein kinase assay (³³PanQinase[®] Activity Assay) was used for measuring the kinase activity of the 24 protein kinases. All protein kinase assays were performed in 96-well FlashPlates[™] (Perkin Elmer/NEN, Boston, MA, USA) in a 50 μL reaction volumes. Assays for all enzymes were performed in a solution containing 60 mM HEPES-NaOH, pH 7.5, 3 mM MgCl₂,

Mar. Drugs 2013, 11

3220

3 mM MnCl₂, 3 μM Na-orthovanadate, 1.2 mM DTT, 50 μg/mL PEG20000, 1 μM [γ -³³P]-ATP (approx. 5 × 10⁵ cpm per well), recombinant protein kinase (50–400 ng). Depending upon the kinase being assayed, appropriate substrates were used and were as follows (substrates shown in parentheses): AKT1 (GSK3/14-27), ARK5 (autophosphorylation), Aurora-A, Aurora-B (Tetra(LRRWSLG)), B-Raf-VE (MEK1 KM), CDK2/CycA (histone H1), CDK4/CycD1 (Rb-CTF), CK2-A1 (Casein), EGF-R, EPHB4, ERBB2, FAK, IGF1-R, SRC, VEGF-R2, VEGF-R3 (poly(Glu,Tyr) 4:1), FLT3, INS-R, MET, PDGFR β (poly(Ala,Glu,Lys,Tyr) 6:2:5:1), PLK1 (Casein), SAK (autophosphorylation), TIE2 (poly(Glu,Tyr) 4:1), COT (autophosphorylation). The IC₅₀ values were measured by testing 10 concentrations of compounds by single sampling. The final DMSO concentration in the assay was 1% (v/v). The data were fitted using the 4-parameter logistic fit option of GraphPad Prism 5.

3.3.2. Cell Culture and Proliferative Assays using HL-60, TK 10, 786-0, M 14, and MCF-7 Cells

The cells were grown in RPMI 1640 Glutamax with 10% FCS, 100 μg/mL streptomycin and 100 U/mL Penicillin G and incubated in a 5% CO₂ humidified atmosphere at 37 °C. For proliferation experiments, cells were seeded in 20 μL pro well into 384-well Greiner 384 CellStar[®] plates (Greiner Bio-One I. AG, Kremsmünster, AT). In addition to the test plates, one plate was prepared for the reference measurement at day zero. All plates were incubated for 24 h at 37 °C in a humidified atmosphere with 5% CO₂. Compounds **5** and **8** that were dissolved in 100% DMSO (v/v) were added to test plates using the Echo 550[®] Liquid Handler (Labcyte Inc., Sunnyvale, UK). The final DMSO concentration in the assay was 0.5% v/v. The viability of the cells in the day zero control plates were determined on the same day without adding any compounds. The CellTiter-Glo[®] Viability Assay was used to determine the viability of cells using the standard protocol for this assay (Promega Corp., Madison, WI, USA). The luminescence signal was measured at the EnSpire[®] Multimode Plate Reader (PerkinElmer, Waltham, MA, USA). Test plates were incubated for further 48 h and the cell viability was defined as just described. Measured raw data were converted into percent of cell growth by using the high control (0.5% DMSO v/v without compound) and the day zero control. For dose-response studies, 11 different concentrations of compounds were tested in quadruplicates. The IC₅₀ values were calculated using the 4-parameter logistic fit option of GraphPad Prism 5.

4. Conclusions

In this study, we developed pyrazin-2(1*H*)-ones as potent and PDGFR β inhibitors based on marine derived hamacanthins. Modeling studies showed the core moiety of hamacanthins to bind in the ATP binding pocket of RTK and suggested a straightforward strategy towards potent PDGFR β binders. For subsequent optimization of hamacanthin derivatives as PDGFR β inhibitors, a flexible synthetic route via microwave-mediated ring closure to asymmetric 3,5-substituted pyrazin-2(1*H*)-ones was established and a set of novel compounds was produced. Herein, we identified highly potent PDGFR β binders with IC₅₀ values in an enzymatic assay below μM range with compound **5** possessing significant activity against PDGFR dependent cancer cells. Thus, marine hamacanthin-derived pyrazin-2(1*H*)-ones showed interesting properties as lead for the further development of highly potent and selective PDGFR β -inhibitors.

Mar. Drugs **2013**, *11*

3221

Acknowledgments

We thank Martin Schütt for excellent technical assistance during synthesis at the Institute of Pharmacy, Kiel and Janina Rahlff for excellent cell culture assistance at the European ScreeningPort GmbH, Hamburg.

Conflicts of Interest

The authors declare no conflict of interest.

References

1. Haefner, B. Drugs from the deep: Marine natural products as drug candidates. *Drug Discov. Today* **2003**, *8*, 536–544.
2. Gupta, L.; Talwar, A.; Chauhan, P.M. Bis and tris indole alkaloids from marine organisms: New leads for drug discovery. *Curr. Med. Chem.* **2007**, *14*, 1789–1803.
3. Skropeta, D.; Pastro, N.; Zivanovic, A. Kinase inhibitors from marine sponges. *Mar. Drugs* **2011**, *9*, 2131–2154.
4. Kouko, T.; Matsumura, K.; Kawasaki, T. Total synthesis of marine bisindole alkaloids, (+)-hamacanthins A, B and (–)-antipode of *cis*-dihydrohamacanthin B. *Tetrahedron* **2005**, *61*, 2309–2318.
5. Bao, B.; Sun, Q.; Yao, X.; Hong, J.; Lee, C.-O.; Cho, H.Y.; Jung, J.H. Bisindole alkaloids of the topsentin and hamacanthin classes from a marine sponge *Spongisorites* sp. *J. Nat. Prod.* **2007**, *70*, 2–8.
6. Casapullo, A.; Bifulco, G.; Bruno, I.; Riccio, R. New bisindole alkaloids of the topsentin and hamacanthin classes from the Mediterranean marine sponge *Rhaphisia lacazei*. *J. Nat. Prod.* **2000**, *63*, 447–451.
7. Peifer, C.; Bühler, S.; Hauser, D.; Kinkel, K.; Totzke, F.; Schaechtele, C.; Laufer, S. Design, synthesis and characterization of N9/N7-substituted 6-aminopurines as VEGF-R and EGF-R inhibitors. *Eur. J. Med. Chem.* **2009**, *44*, 1788–1793.
8. Peifer, C.; Kinkel, K.; Abadleh, M.; Schollmeyer, D.; Laufer, S. From five- to six-membered rings: 3,4-diarylquinolinone as lead for novel p38MAP kinase inhibitors. *J. Med. Chem.* **2007**, *50*, 1213–1221.
9. Peifer, C.; Krasowski, A.; Hämmerle, N.; Kohlbacher, O.; Dannhardt, G.; Totzke, F.; Schaechtele, C.; Laufer, S. Profile and molecular modeling of 3-(indole-3-yl)-4-(3,4,5-trimethoxyphenyl)-1*H*-pyrrole-2,5-dione(1) as a highly selective VEGF-R2/3 inhibitor. *J. Med. Chem.* **2006**, *49*, 7549–7553.
10. Peifer, C.; Selig, R.; Kinkel, K.; Ott, D.; Totzke, F.; Schaechtele, C.; Heidenreich, R.; Röcken, M.; Schollmeyer, D.; Laufer, S. Design, synthesis, and biological evaluation of novel 3-aryl-4-(1*H*-indole-3-yl)-1,5-dihydro-2*H*-pyrrole-2-ones as vascular endothelial growth factor receptor (VEGF-R) inhibitors. *J. Med. Chem.* **2008**, *51*, 3814–3824.
11. Jiang, B.; Yang, C.G.; Wang, J. Enantioselective synthesis for the (–)-antipode of the pyrazinone marine alkaloid, hamacanthin A. *J. Org. Chem.* **2001**, *66*, 4865–4869.

Mar. Drugs **2013**, *11*

3222

12. Miyake, F.Y.; Yakushijin, K.; Horne, D.A. Synthesis of marine sponge bisindole alkaloids dihydrohamacanthins. *Org. Lett.* **2002**, *4*, 941–943.
13. Zoraghi, R.; Worrall, L.; See, R.H.; Strangman, W.; Popplewell, W.L.; Gong, H.; Samaai, T.; Swayze, R.D.; Kaur, S.; Vuckovic, M.; *et al.* Methicillin-resistant *Staphylococcus aureus* (MRSA) pyruvate kinase as a target for bis-indole alkaloids with antibacterial activities. *J. Biol. Chem.* **2011**, *286*, 44716–44725.
14. Caldwell, J.J.; Veillard, N.; Collins, I. Design and synthesis of 2(1*H*)-pyrazinones as inhibitors of protein kinases. *Tetrahedron* **2012**, *68*, 9713–9728.
15. Dar, A.C.; Shokat, K.M. The evolution of protein kinase inhibitors from antagonists to agonists of cellular signaling. *Ann. Rev. Biochem.* **2011**, *80*, 769–795.
16. Appelmann, I.; Liersch, R.; Kessler, T.; Mesters, R.; Berdel, W. Angiogenesis inhibition in cancer therapy: Platelet-derived growth factor (PDGF) and vascular endothelial growth factor (VEGF) and their receptors: Biological functions and role in malignancy. *Recent Results Cancer Res.* **2010**, *180*, 51–81.
17. Koch, S.; Tugues, S.; Li, X.; Gualandi, L.; Claesson-Welsh, L. Signal transduction by vascular endothelial growth factor receptors. *Biochem. J.* **2011**, *437*, 169–183.
18. Zhou, Y.; Chen, Y.; Tong, L.; Xie, H.; Wen, W.; Zhang, J.; Xi, Y.; Shen, Y.; Geng, M.; Wang, Y.; *et al.* AL3810, a multi-tyrosine kinase inhibitor, exhibits potent anti-angiogenic and anti-tumour activity via targeting VEGFR, FGFR and PDGFR. *J. Cell. Mol. Med.* **2012**, *16*, 2321–2330.
19. Noble, M.E.M.; Endicott, J.A.; Johnson, L.N. Protein kinase inhibitors: Insights into drug design from structure. *Science* **2004**, *303*, 1800–1805.
20. Norman, R.A.; Toader, D.; Ferguson, A.D. Structural approaches to obtain kinase selectivity. *Trends Pharmacol. Sci.* **2012**, *33*, 273–278.
21. Sachsenmaier, C.; Schachtele, C. Integrated technology platform protein kinases for drug development in oncology. *Biotechniques* **2002**, *33*, S101–S106.
22. Heldin, C.H.; Westermark, B. Mechanism of action and *in vivo* role of platelet-derived growth factor. *Physiol. Rev.* **1999**, *79*, 1283–1316.
23. Hodous, B.L.; Geuns-Meyer, S.; Hughes, P.; Albrecht, B.; Bellon, S.; Bready, J.; Caenepeel, S.; Cee, V.; Chaffee, S.; Coxon, A.; *et al.* Evolution of a highly selective and potent 2-(pyridin-2-yl)-1,3,5-triazine tie-2 kinase inhibitor. *J. Med. Chem.* **2007**, *50*, 611–626.
24. Garuti, L.; Roberti, M.; Bottegoni, G. Non-ATP competitive protein kinase inhibitors. *Curr. Med. Chem.* **2010**, *17*, 2804–2821.
25. Peifer, C.; Stoiber, T.; Unger, E.; Totzke, F.; Schachtele, C.; Marmé, D.; Brenk, R.; Klebe, G.; Schollmeyer, D.; Dannhardt, G. Design, synthesis, and biological evaluation of 3,4-diarylmaleimides as angiogenesis inhibitors. *J. Med. Chem.* **2006**, *49*, 1271–1281.
26. Reiterer, G.; Yen, A. Platelet-derived growth factor receptor regulates myeloid and monocytic differentiation of HL-60 cells. *Cancer Res.* **2007**, *67*, 7765–7772.
27. Johannes, E.; Horbert, R.; Schlosser, J.; Schmidt, D.; Peifer, C. Effective synthesis of 3,5-diaryl-(1*H*)-pyrazin-2-ones via microwave mediated ring closure. *Tetrahedron Lett.* **2013**, *54*, 4067–4072.

Mar. Drugs **2013**, *11*

3223

28. Halgren, T.A.; Murphy, R.B.; Friesner, R.A.; Beard, H.S.; Frye, L.L.; Pollard, W.T.; Banks, J.L. Glide: A new approach for rapid, accurate docking and scoring. 2. Enrichment factors in database screening. *J. Med. Chem.* **2004**, *47*, 1750–1759.
29. ProQinase Targeting Cancer. Available online: <http://www.proqinase.com> (accessed on 19 August 2013).

© 2013 by the authors; licensee MDPI, Basel, Switzerland. This article is an open access article distributed under the terms and conditions of the Creative Commons Attribution license (<http://creativecommons.org/licenses/by/3.0/>).

3.6 Optimization of potent DFG-in inhibitors of platelet derived growth factor receptor β (PDGF-R β) guided by water thermodynamics

Rebecca Horbert,^{||} Boris Pinchuk,^{||} Eugen Johannes, Joachim Schlosser, Dorian Schmidt, Daniel Cappel, Frank Totzke, Christoph Schächtele, and Christian Peifer

^{||}Rebecca Horbert and Boris Pinchuk contributed equally to this work.

J. Med. Chem. **2015**, *58*, 170–182.

<http://pubs.acs.org/doi/full/10.1021/jm500373x>

(The article is licensed under the terms of the ACS AuthorChoice license)

The following paper describes the development of potent DFG-in PDGFR β inhibitors based on pyrazin-2(1*H*)-one compounds reported in the previous article.²⁰¹ Molecular modeling studies combined with extensive SAR examination were performed. For inhibitor optimization hydration sites in the binding pocket of PDGFR β were calculated. The displacement of water molecules from a hydrophobic binding pocket which can significantly affect the ligand affinity was previously described.²³¹ WaterMap technology^{232, 233} was used to predict thermodynamic characteristics of solvent molecules to be displaced. The same technology had already been applied by other research groups for design of selective kinase inhibitors.²³⁴

Utilization of WaterMap technology led to design of potent inhibitors of PDGFR β .²⁰² The key hydration sites in the kinase ATP binding pocket were either displaced or replaced by designed ligand moieties. The most potent inhibitor, compound **2** (Figure 22), exhibited an IC₅₀ value of 20 nM toward PDGFR β and showed a reasonable selectivity in a panel of 300 wild-type kinases.

However, the promising characteristics of **2** in enzyme assays could not be fully translated into cellular activity. The inhibitor showed only modest inhibition of cancer cell growth as demonstrated by cellular proliferation assays. In line with this notion, compound **2** barely

inhibited the PDGFR β signalling in cells as shown by western blot analysis. The non-effective cellular activity of the designed inhibitor might be explained by the compound's limited cellular bioavailability as measured by cellular uptake experiments. Further optimization of this compounds series regarding the improvement of ADME properties is therefore essential.

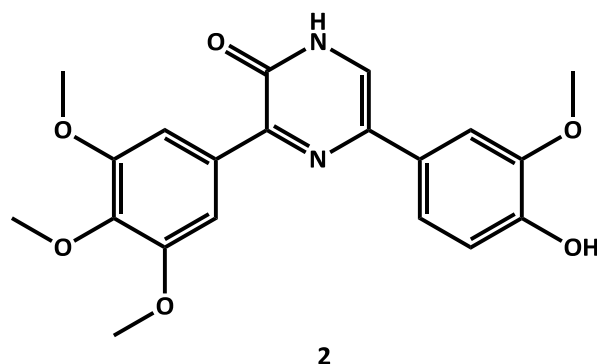


Figure 22: Chemical structure of compound 2, a novel potent DFG-in inhibitor of PDGFR β . Compound 2 corresponds to compound 38 in the article "Optimization of potent DFG-in inhibitors of platelet derived growth factor receptor β (PDGF-R β) guided by water thermodynamics".²⁰²

Nevertheless, rational design of the compound 2 was a clear proof for the usefulness of molecular modeling studies including the WaterMap technology for the development and optimization of potent protein kinase inhibitors.

Dr. Rebecca Horbert performed molecular modelling studies. Dr. Daniel Cappel utilized the WaterMap technology. Dr. Eugen Bethke (born Johannes) and Dr. Joachim Schlosser synthesized the novel compounds. I performed the *in vitro* characterization of all compounds, including cellular proliferation, western blots and cellular uptake experiments.

Optimization of Potent *DFG-in* Inhibitors of Platelet Derived Growth Factor Receptor β (PDGF-R β) Guided by Water Thermodynamics

Rebecca Horbert,^{†,||} Boris Pinchuk,^{†,||} Eugen Johannes,[†] Joachim Schlosser,[†] Dorian Schmidt,[†] Daniel Cappel,[‡] Frank Totzke,[§] Christoph Schächtele,[§] and Christian Peifer^{*,†}

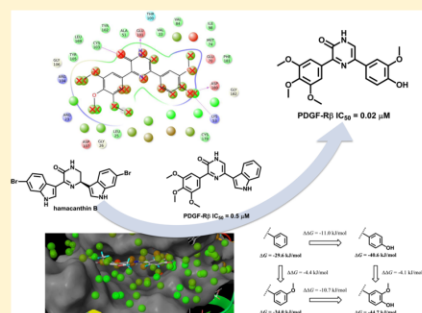
[†]Institute of Pharmacy, Christian-Albrechts-University of Kiel, Gutenbergstraße 76, D-24116 Kiel, Germany

[‡]Schrödinger GmbH, Dynamostraße 13, D-68165 Mannheim, Germany

[§]ProQinase GmbH, Breisacherstraße 117, D-79106 Freiburg, Germany

Supporting Information

ABSTRACT: In this study we report on the hit optimization of substituted 3,5-diaryl-pyrazin-2(1*H*)-ones toward potent and effective platelet-derived growth factor receptor (PDGF-R) β -inhibitors. Originally, the 3,5-diaryl-pyrazin-2-one core was derived from the marine sponge alkaloid family of hamacanthins. In our first series compound **2** was discovered as a promising hit showing strong activity against PDGF-R β in the kinase assay ($IC_{50} = 0.5 \mu\text{M}$). Furthermore, **2** was shown to be selective for PDGF-R β in a panel of 24 therapeutically relevant protein kinases. Molecular modeling studies on a PDGF-R β homology model using prediction of water thermodynamics suggested an optimization strategy for the 3,5-diaryl-pyrazin-2-ones as *DFG-in* binders by using a phenolic OH function to replace a structural water molecule in the ATP binding site. Indeed, we identified compound **38** as a highly potent inhibitor with an IC_{50} value of $0.02 \mu\text{M}$ in a PDGF-R β enzymatic assay also showing activity against PDGF-R dependent cancer cells.



INTRODUCTION

In our ongoing study to develop ATP-competitive receptor tyrosine kinase (RTK) inhibitors with anticancer activity, we focused on the hamacanthin B family of deep-sea sponge derived bis-indole alkaloids possessing a 3,5-bisindole-3,4-dihydropyrazin(1*H*)-2-one scaffold.¹ In line with this notion, *cis*-3,4-dihydropyrazin(1*H*)-2-one hamacanthin B was reported to be a potent bacterial methicillin-resistant *Staphylococcus* protein kinase inhibitor (MRSA-PK inhibitor) with an IC_{50} value of $0.016 \mu\text{M}$ and possessing significant selectivity over human protein kinase isoforms.² Moreover, substituted (1*H*)-pyrazin-2-ones have been investigated as human protein kinase (PK) inhibitors showing this moiety to be suitable as a core scaffold for PK inhibitor design.³ Among human PKs in oncology, overactivated RTK including VEGFR, PDGF-R, and c-kit are considered to be major targets for the development of clinically effective inhibitors.⁴ Thus, many anticancer compounds that are advanced into the clinic show (group-) selectivity toward VEGF-R, FGF-R, EGF-R, PDGF-R, c-kit, and Flt-3 (Chart 1).⁵ Furthermore, inhibitors addressing a single PK with high selectivity are of significant interest. A recent study reported about the development of imidazo[1,2- α]pyridines with potent PDGF-R activity and oral bioavailability.⁶

Therefore, we designed the aryl-substitution patterns of the 6-membered 3,5-diaryl-pyrazin-2(1*H*)-one **2**¹ based on the corresponding 5-membered 3,4-diaryl-2*H*-pyrrole-2-one (com-

pound **1**, Chart 2), a potent inhibitor of VEGF-R2/3 ($IC_{50} = 0.03 \mu\text{M}$) with good efficacy in cellular assays.⁷

RESULTS AND DISCUSSION

Chemistry. The test compounds reported in this study were synthesized by our flexible synthetic platform to produce targeted 3,5-diaryl-pyrazin-2(1*H*)-ones (VI, Scheme 1).⁸ As key intermediates for the final ring closure, the open-chained diketoamides (V) were accessible via two different routes. On the one hand, arylglyoxylic acid (I) was activated by carbonyldiimidazole (CDI) and coupled with the α -ketoamine moiety (II) to produce the open-chained diketoamide (V). On the other hand, CDI mediated coupling of arylglyoxylic acid (I) and amine (III) gave amide (IV), which yielded ketoamide (V) upon DDQ-oxidation. Microwave-mediated ring closure in the final step by using the open-chained diketoamide (V) and ammonium acetate as nitrogen source yielded the desired 3,5-diaryl-pyrazin-2(1*H*)-ones (VI).

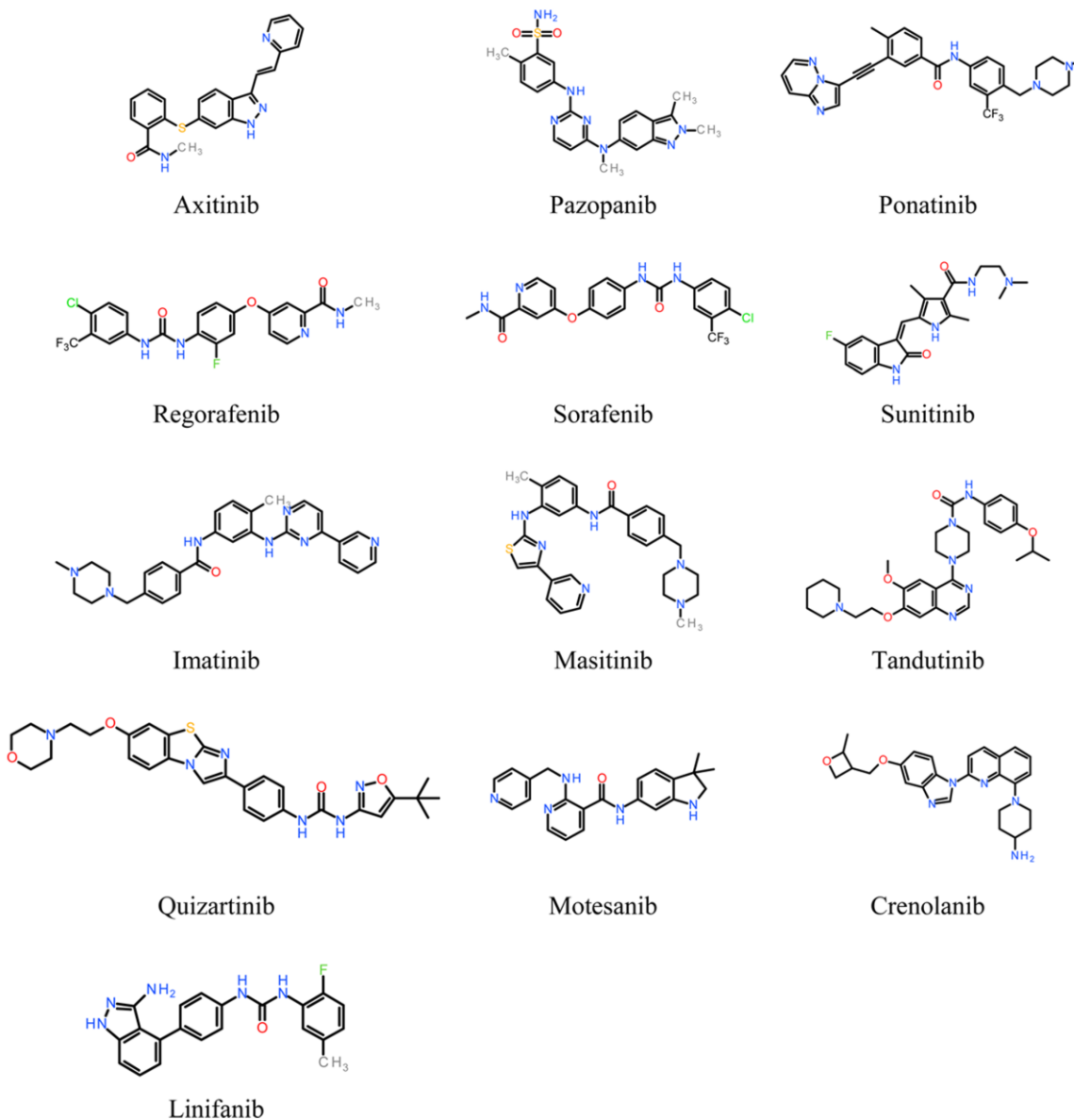
Molecular Modeling and Binding Mode. In a preliminary *in vitro* screening involving 24 therapeutically relevant PK, compound **2** was actually determined to potently inhibit PDGF-R β with an IC_{50} of $0.5 \mu\text{M}$.¹ Moreover, compound **2** was shown to be selective over the other PK enzymes tested in

Special Issue: New Frontiers in Kinases

Received: March 10, 2014

Published: July 9, 2014

Chart 1. Selection of Small Molecule Kinase Inhibitors (smKI, Approved or in Clinical Phases) Targeting PDGF-R (among Other PKs)

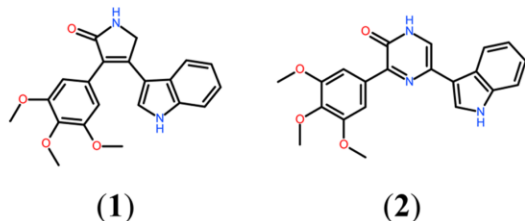


this panel (VEGF-R2 IC_{50} = 4 μ M, VEGF-R3 IC_{50} = 5 μ M, FLT3 IC_{50} = 36 μ M; IC_{50} -values >100 μ M: AKT1, ARK5, Aurora-A/B, B-RAF-VE, CDK2/CycA, CDK4/CycD1, COT, EGFR, EPHB4, ERBB2, FAK, IGF1R, SRC, INSR, MET, PLK1, SAK, TIE2, and CK2a1). Thus, we aimed to further enhance the potency of this hit compound toward PDGF-R β by using a homology model/docking approach since no X-ray structure of the PDGF-R PK domain is available in the public domain. Besides, the vast majority of ATP-competitive inhibitors can be categorized in type I or type II binders.⁹ That is, binding two different conformations of the ATP site, namely, the “*DFG-in*” (type I) and “*DFG-out*” (type II)

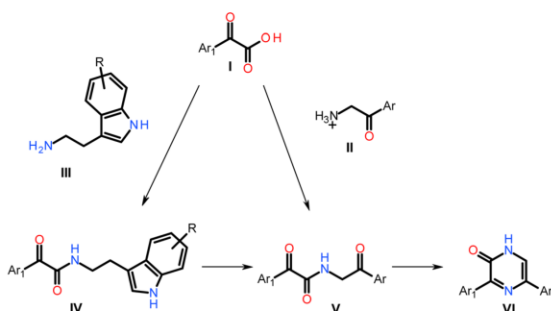
conformation. In order to address the question to which PDGF-R β -conformation compound 2 is likely to bind, we compared the molecular structure of 2 to a VEGF-R2-*DFG-in*-ligand (type I inhibitor pyridinyl-triazine, pdb 2p2h¹⁰) and to a prototypical *DFG-out* binder (type II inhibitor imatinib, pdb 2hyy¹¹), respectively (Figure 1).

The binding pose overlay of the inhibitor structures in Figure 1 (shown as bound to the ATP binding pocket) suggests that compound 2 represents most likely a *DFG-in* binder. First, compared to the VEGF-R2-type-I pyridinyl-triazine inhibitor, compound 2 is matching well in terms of molecular shape. Furthermore, docked compound 2 is also occupying a

Chart 2. Chemical Structures of the Potent 3,4-Diaryl-2H-pyrrole-2-one VEGF-R2/3 Inhibitor 1 and 3,5-Diaryl-pyrazin-2(1H)-one 2 of This Study Showing Comparable Decoration Patterns of the Aryl Moieties



Scheme 1. General Preparation Scheme of 3,5-Diaryl-pyrazin-2(1H)-ones (VI)^a



^aThe ketoamides (V) were prepared in two different routes, either via CDI mediated coupling of arylglyoxylic acid (I) and α -ketoamines (II) or via CDI mediated coupling of arylglyoxylic acid (I) and indolethylamines (III) to produce 2-oxo-2-phenylacetamides (IV), which yielded the corresponding (V) upon DDQ-oxidation. Final compounds (VI) were prepared in a microwave reaction using ammonium acetate as nitrogen source (method d). For clarity, the test compounds were numbered consecutively (2–39). Analytical data for all relevant compounds is available in Supporting Information.

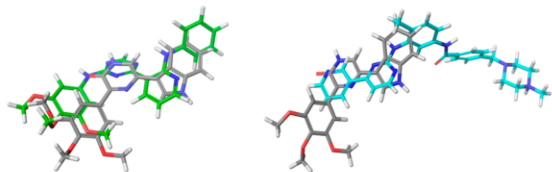


Figure 1. Left: Overlay of modeled docking pose of **2** (gray color) as oriented in the ATP binding pocket of VEGF-R2 and crystallographically determined binding mode of *DFG-in*/type I VEGF-R2 inhibitor 4-(2-anilinopyridin-3-yl)-*N*-(3,4,5-trimethoxyphenyl)-1,3,5-triazin-2-amine (green color, pdb 2p2h). Right: Superposition of docking pose of **2** (gray color) and *DFG-out*/type II inhibitor imatinib (light blue color, pdb 2hyy).

comparable space in the VEGF-R2 binding pocket. Second, the deep pocket binding part of the well-established *DFG-out*/type II-binder imatinib, namely, the 4-[(4-methylpiperazin-1-yl)-methyl]benzamide moiety, is not present in **2** (Figure 1, right). Third, docking of compound **2** into PK structures related to PDGF-R β possessing *DFG-out* conformations (Abl-kinase, pdb 2hyy;¹¹ VEGF-R2, pdb 3vhk⁹ and 1t46;¹² c-src, pdb 3f3w¹³) revealed predicted binding poses in the ATP site not consistent with the originally present type II inhibitors. In contrast,

plausible *DFG-in* binding modes were successfully calculated by docking experiments with **2** modeled in several *DFG-in* ATP-binding pockets (not shown) possessing significant sequence similarity to PDGF-R β (VEGF-R2, pdb 2p2h,¹⁰ 3cjg,¹⁴ and 3c7q;¹⁵ fms, pdb 3lcd¹⁶). Therefore, on the basis of the highly related RTK VEGF-R2 we generated two PDGF-R β homology models, namely, using VEGF-R2 template structures in the *DFG-in* (pdb 2p2h¹⁰) and *DFG-out* conformation (pdb 1t46¹²), respectively. However, because only the *DFG-in* homology model proved to predict reasonable binding poses for **2** in the ATP binding pocket, this structure was used for further modeling studies in this project (Figure 2, pdb 2p2h; Schrödinger Prime,¹⁷ version 3.2, Schrödinger, LLC, New York, NY, USA, 2013).

In order to validate the modeled hinge-binding mode of **2** in the ATP site of our PDGF-R β *DFG-in* homology model (Figure 2), we first synthesized and evaluated compounds **3** and **4** for their potency against PDGF-R β (Chart 3). Accordingly to our docking results the introduction of the 6-methyl group at the 3,5-diaryl-pyrazin-2(1H)-one core (compound **3**) is blocking the inhibitor's dual H-bond interactions to the hinge region (Glu101/Cys103) and thus killing the biological activity of **3**.

Likewise, compared to compound **2**, the lactam-regioisomeric structure **4** should be able to address an H-bond only to Glu101 but not be able to accept the H-bond from Cys103 thus showing reduced biological activity. In fact, the biological activities of **3** and **4** are in line with the proposed binding mode demonstrating a valid modeled pose of **2** in the active site of PDGF-R β . Motivated by the *in vitro* confirmation of our *DFG-in* homology model based binding mode, we retained the 3,5-diaryl-pyrazin-2(1H)-one core and next focused on the 3-aryl moiety.

Optimization of the 3-Aryl Substitution Pattern.

According to the calculated binding mode the 3-aryl part of **2** is situated in the HRII which opens to the solvent (Figure 2). To further investigate the structure–activity relationships (SARs) and to optimize the 3-aryl system we used a straightforward docking/scoring approach. Although no direct ligand–protein interactions are involved in this area, our molecular docking campaign showed slight differences in the predicted binding affinities for variations of the methoxy-aryl substitution. As a result, compound **2** was top-ranked followed by **5**, **15**, and **7** (series 1, Table 1). For compounds **8** and **9** bearing an *ortho*-methoxy substitution (causing a 1H-pyrazin-2-one/3-aryl dihedral angle of almost 90°), no binding mode was predicted in the narrow ATP pocket. Further 3-aryl variations of **2** showed no significant docking scores. Hence, derived from the modeling approach we synthesized a selection of compounds (**5**–**15** showing systematic variations of the 1H-pyrazin-2-one-3-aryl moiety, series 1, Table 1), which were subsequently tested against PDGF-R β . Actually the docking/scoring results were reflected by the *in vitro* testing data. In accordance with the data of this series the 3-(3,4,5-trimethoxyphenyl) moiety in **2** was determined to be optimal: decreasing the number of methoxy groups (**5** and **6**) as well as positional changes of the aryl-methoxy groups (**7**, **8**, and **9**) resulted in diminished ligand affinity. Also, compared to hit compound **2**, the biological activity in this series could not be increased by introducing other moieties into the 3-aryl system such as morpholine (**12**), 4-fluor (**13**), 4-ethyl, or indole (**15**).

Optimization of the 5-Aryl Substitution Pattern.

Therefore, we retained the 3-(3,4,5-trimethoxyphenyl)-1H-

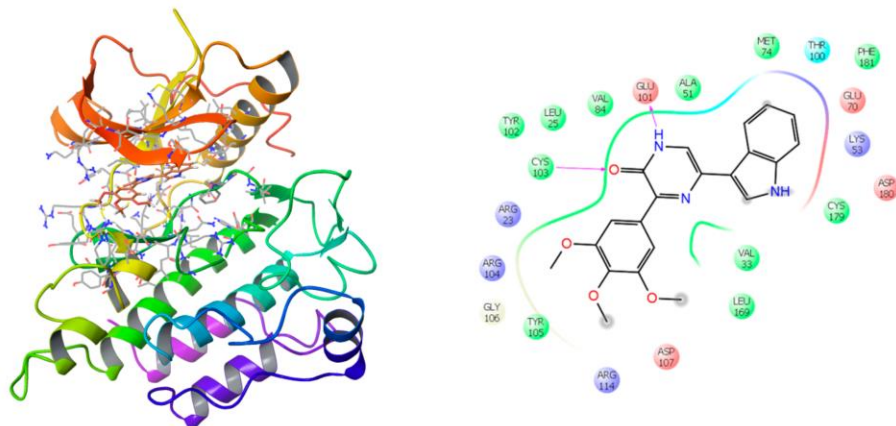
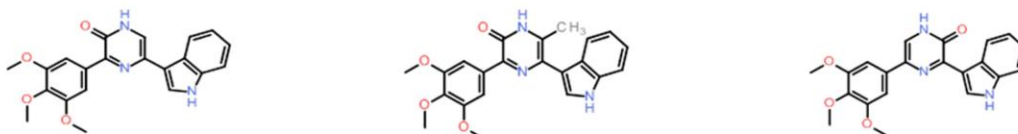


Figure 2. Left: *DFG-in* homology model of the PDGF- $R\beta$ kinase domain based on the template structure of crystallographically determined VEGF-R2 (pdb 2p2h) and modeled binding mode of hit compound **2** (brown color) in the ATP binding pocket. Right: Ligand interaction diagram of modeled binding mode of **2** in the ATP binding pocket of the PDGF- $R\beta$ PK domain. Key amino acid residues and ligand-active site interactions are shown. The central pyrazin-2(1*H*)-one core is involved in a dual H-bond interaction to the hinge region residues Glu101 and Cys103. The pyrazin-2(1*H*)-one 3-(3,4,5-trimethoxy) part is situated in the hydrophobic region II (HRII), whereas the pyrazin-2(1*H*)-one-5-(indole-3yl) part is occupying the hydrophobic pocket I (HPI).

Chart 3. Chemical Structures and Biological Activity against PDGF- $R\beta$ (*in Vitro* Kinase Assay) of Key 3,5-Diaryl-pyrazin-2(1*H*)-ones **2, **3**, and **4** to Confirm the Calculated Hinge-Binding Motif of **2** in the Homology-Modeled ATP Binding Pocket of the PDGF- $R\beta$ PK**



(2) PDGF- $R\beta$ $IC_{50} = 0.5 \mu M$ **(3)** PDGF- $R\beta$ $IC_{50} > 100 \mu M$ **(4)** PDGF- $R\beta$ $IC_{50} = 12 \mu M$

Table 1. Series 1: SAR Data of Variations of Hit Compound **2 (PDGF- $R\beta$ $IC_{50} = 0.5 \mu M$) Regarding the Pyrazin-2(1*H*)-one-3-aryl Substitution Pattern; Biological Activity Was Determined for Each Compound against PDGF- $R\beta$ in an *in Vitro* Kinase Assay**

#	R	PDGF- $R\beta$ IC_{50} [μM]	#	R	PDGF- $R\beta$ IC_{50} [μM]
2		0.5	10		5
5		1.5	11		13
6		19	12		13
7		4	13		12
8		> 100	14		32
9		> 100	15		2

pyrazin-2-one system, and for further optimization of **2** we next concentrated on variations of the 5-indole moiety, which is situated in the buried HPI (Figure 2). We first generated a focused virtual set of substituted 5-indole variations of compound **2** and performed docking experiments using the PDGF- $R\beta$ homology model structure (Schrödinger GlideSP,¹⁸ version 5.9, Schrödinger, LLC, New York, NY, USA, 2013). From the top-ranked docking hits (Figure 3) we prepared 14 synthetically accessible compounds and tested those for their biological activity against PDGF- $R\beta$ (series 2, Table 2).

In line with the calculated modeling data compounds, **16**, **24**, and **27** were indeed determined to show good activity against PDGF- $R\beta$ (Table 2). The naphthyl moiety of **24** (IC_{50} PDGF- $R\beta$ = 1 μM) is filling the HPI, whereas the 5'-hydroxyindole in **16** (IC_{50} PDGF- $R\beta$ = 0.3 μM) is addressing an additional H-bond to the gatekeeper residue Thr100 (Figure 3). Only the biological activity against PDGF- $R\beta$ of compound **16** (showing the 5'-hydroxyindole decoration) was determined to be in the sub- μM range (as was the parent compound **2**). However, the flat *in vitro* SARs for further compounds of this 1*H*-pyrazin-2-one-5-aryl series 2 (**17–29**, see Table 2) poorly matches the docking/scoring of the compounds. In contrast to the good correlation of predicted ligand–protein interactions of our PDGF- $R\beta$ homology model with the SAR (series 1), so far these results may indicate a structural misarrangement regarding the HPI in our model. However, the inconsistency

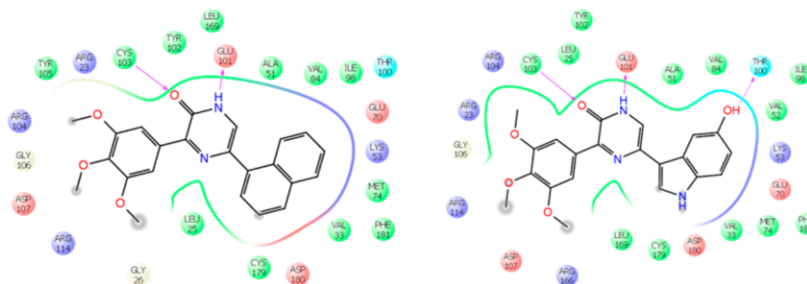


Figure 3. Ligand interaction diagram of top-ranked compounds **24** (left) and **16** (right) in the ATP binding site of the PDGF-R β homology model. Key amino acid residues and ligand–active site interactions are shown. GlideSP ranking of the compounds (top-down): **24**, **16**, **27**, **29**, **18**, **28**, **22**, **21**, **20**, **19**, **2**, **17**, **16**, **25**, and **23**.

Table 2. Series 2: SAR Data of Variations of Hit Compound 2 (PDGF-R β IC₅₀ = 0.5 μ M) Regarding the Pyrazin-2(1H)-one-5-aryl Substitution Pattern

#	R	PDGF-R β IC ₅₀ [μ M]	#	R	PDGF-R β IC ₅₀ [μ M]
16		0.3	23		26
17		1	24		1
18		14	25		8
19		56	26		2
20		2	27		1
21		9	28		2
22		3	29		7

of the modeling/*in vitro* SAR correlation for this pocket could refer to particular parameters triggering ligand affinity, which are not sufficiently implemented in the applied docking/scoring process.

WaterMap Calculations. Namely, this phenomenon may be explained by the thermodynamic contribution of displacing water molecules, predominantly in hydrophobic binding pockets. It is considered to be a key factor for ligand affinity (“hydrophobic effect”).¹⁹ In order to investigate if entropic critically water molecules in the ATP binding pocket of PDGF-R β could be predictable parameters for the optimization of 3,5-diaryl-pyrazin-2(1H)-ones in our project, we calculated hydration sites in the PDGF-R β homology model apo-structure by using the WaterMap technology^{17,18} (Figure 4). The WaterMap method combines calculations for molecular dynamics, solvent clustering, and statistical thermodynamics to assess the enthalpy, entropy, and free energy of water “hydration sites”. Moreover, WaterMap has been successfully applied to study parameters driving selectivity for ligands in the ATP pocket of protein kinases.²⁰ Having the WaterMap results for the PDGF-R β homology model apo structure in hand, we designed a set of 5-phenyl variations of the 3-(3,4,5-

trimethoxyphenyl)-1H-pyrazin-2-one scaffold (compounds **30–38**, series 3, Table 3). Herein, the concept of the 5-phenyl decoration was based on the idea to investigate SARs in terms of the displacement of hydration sites. In turn, all compounds of this project were docked into the ATP pocket of our PDGF-R β homology model. As an outcome, compound **38** was calculated to be the top hit of this docking campaign. Strikingly, the predicted high affinity of **38** was confirmed by the *in vitro* assay (**38** IC₅₀ PDGF-R β = 0.02 μ M, Table 3) demonstrating this compound to be the most potent inhibitor of all three series. The docking pose actually shows that the majority of key hydration sites calculated by WaterMap were displaced by the inhibitor (Figure 4). In detail, the 3-(3,4,5-trimethoxyphenyl) moiety displaces all relevant hydration sites in the HRII. In the hinge region two of the most unstable hydration sites (colored in red) are displaced by the lactam moiety of the 1H-pyrazin-2-one core. This approach also offers a strong structural explanation for the comparable high affinity of this lactam-regioisomer (also see **2** versus **4**, Chart 3). Most notably, within the HPI the 4'-phenolic OH of **38** is not only displacing an unstable hydration site (colored in light red) but this OH group is also replacing a stable water molecule (colored in green), positioning the OH function in an H-bond network between Lys53 and Asp180 (Figure 4). This water replacement should be unfavorable in terms of entropy but can be compensated by enthalpy summing up to a total decrease of Gibbs free energy (ΔG). In addition, the vicinal 3'-methoxy group of **38** displaces two unstable hydration sites in the rear HPI. However, two hydration sites imbedded by Val33, Val84, Ile98, and Met74 were not yet affected by the present inhibitors. Hence, the displacement of these water molecules will be the subject of our ongoing inhibitor optimization strategy.

Considering the displacement of hydration sites (Figures 4 and 5; for complete data, see Supporting Information), a differentiated analysis regarding the contribution of various functional groups at the phenyl moiety toward ligand affinity can be discussed²¹ based on the SAR data of series 3 (Table 3). The phenolic-4'-OH is essential for potent ligand affinity toward PDGF-R β as compounds **35** and **38** show IC₅₀ values in the sub- μ M range. In contrast, compounds having 4'-methoxy (**30** and **37**) or 4'-chloro (**32**) substitutions were determined to be significantly less active. Interestingly, the phenyl-3'-substituted compounds **31** (3-methoxy, IC₅₀ PDGF-R β = 1.4 μ M) and **33** (3-chloro, IC₅₀ PDGF-R β = 0.8 μ M) are moderate binders. This may be due to displacement of the two hydration sites #8 and #83 with unfavorable ΔG (see Figure 5 and Supporting Information) at the rear pocket while leaving the

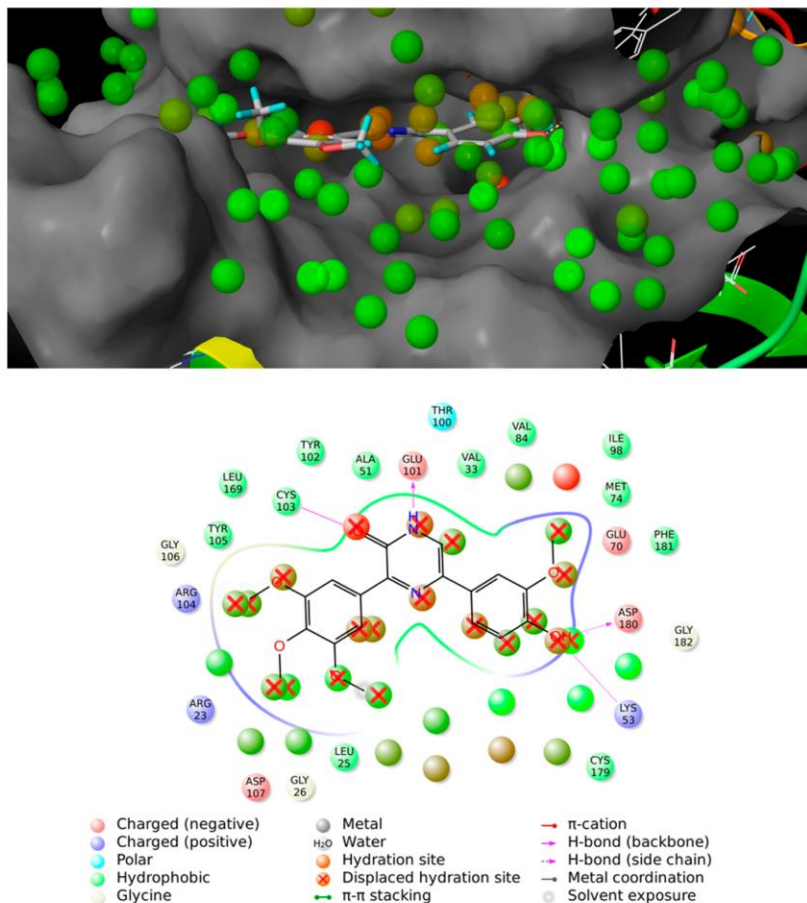


Figure 4. Top: Docking pose of **38** (PDGF-R β IC₅₀ = 0.02 μ M) in the ATP binding pocket of the PDGF-R β PK homology model domain showing the molecular surface (docking by Glide) and overlay of hydration sites (colored spheres; for color code, see below) calculated by WaterMap. Bottom: Ligand–protein interaction diagram of **38** in the ATP binding pocket of the PDGF-R β homology model. Key hydration sites from WaterMap calculations on the PDGF-R β homology model apo-structure are superimposed to illustrate the displacement of hydration sites by the inhibitor. Hydration sites shown as red spheres represent “unstable” water molecules. Their displacement results in an increase of environmental entropy (“hydrophobic effect”). Green spheres symbolize “stable” water molecules, which should not be displaced by an inhibitor in terms of unfavorable enthalpic effects.

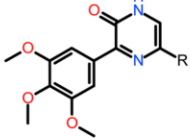
structural water #13 between Lys53 and Asp180 in place (with favorable ΔG). The phenyl-2'-substituted compounds **34** (2-chloro, IC₅₀ PDGF-R β = 5 μ M) and **36** (phenolic-2-OH, IC₅₀ PDGF-R β = 2 μ M) also showing moderate affinity indicate steric space at this part of the binding site (hydration site #34). Thus, the 2'-phenyl position of this series may be suitable for further ligand optimization regarding interactions to the HPI.

On the basis of the PDGF-R β IC₅₀ values of compounds **31**, **35**, **38**, and **39**, we quantified the relative contribution of the 3'-methoxy and the 4'-hydroxyphenyl substituents toward the experimental ΔG of these inhibitors. The values of ΔG are based on the calculation²¹ of $\Delta G = -RT \cdot \ln IC_{50}$ (Figure 5). Within this set of compounds the 4'-hydroxy moiety contributes approximately -11 kJ/mol to the actual free binding enthalpy, while the 3'-methoxy moiety (~ -4.3 kJ/mol) adds 3-fold less value to ΔG . In this regard, the WaterMap calculations are in good accordance: the 4'-hydroxy moiety is replacing the hydration site #13 for which an entropic term of

15.5 kJ/mol has been calculated. The 3'-methoxy moiety is displacing hydration site #83 with a calculated $-T\Delta S$ of 4.8 kJ/mol (indicating the methoxy-oxygen to partly compensates the hydration site oxygen). In addition to the SAR discussed above, these numbers further highlight the importance of the phenyl 4'-hydroxy moiety in terms of replacing a structural water molecule.

The most potent PDGF-R β -inhibitors of the 1*H*-pyrazin-2-ones were tested against the closely related PK VEGF-R2 and c-kit (Table 4). Herein, compound **38** showed only moderate 10-fold selectivity for PDGF-R β over VEGF-R2 and c-kit suggesting comparable *DFG-in* binding modes in these kinases, which is in line with the findings of Furet et al.²² In their study it is shown that PK having a cysteine residue in the *DFG*-minus-1-position favor *DFG-in* binding of ligands that can form a sulfur–aromatic interaction to this cysteine. In fact, in the binding mode of the ligands in our PDGF-R β model this is the case for Cys179 (D180-F181-G182, also see LID Figure 2, right, and Figure 4, bottom) explaining why in addition to

Table 3. Series 3: SAR Data of Variations of Hit Compound 2 (PDGF-R β IC₅₀ = 0.5 μ M) Regarding the Pyrazin-2(1H)-one-5-phenyl Substitution Pattern^a



#	R	PDGF-R β IC ₅₀ [μ M]	#	R	PDGF-R β IC ₅₀ [μ M]
30		22	35		0.1
31		1.4	36		2
32		31	37		19
33		0.8	38		0.02
34		5	39		8

^aThe design of the phenyl decoration was based on joined WaterMap/Glide docking calculations. The biological activity against PDGF-R β of compound **38** (PDGF-R β IC₅₀ = 0.02 μ M) showing the phenyl-3'-methoxy-4'-hydroxy decoration could be significantly improved compared to the parent hit compound **2**.

PDGF-R β these compounds also potently inhibit VEGF-R2 and c-kit (and Flt3, see Table 4 and Figure 6).

Table 4. Biological Activity of Selected Compounds against PDGF-R β and the Closely Related PK VEGF-R2 and c-kit (Activated Kinase Assays, for Details See Experimental Section)

#	PDGF-R β	VEGF-R2	c-kit
	IC ₅₀ (μ M)	IC ₅₀ (μ M)	IC ₅₀ (μ M)
2	0.5	2.3	0.9
16	0.3	1.0	2.7
31	1.4	23	7.4
33	0.8	56	2.4
35	0.1	2.2	0.4
38	0.02	0.2	0.2

Furthermore, compound **38** was profiled for selectivity at a concentration of 1 μ M in a panel of 300 wild-type kinases. Herein, **38** most potently inhibited PDGF-R β (residual activity = 1%) but also blocked further PKs, albeit to a lesser extent (Figure 6, also see Supporting Information). However, compound **38** could be shown to be a promising hit with reasonable selectivity for further optimization toward an effective PDGF-R β inhibitor for clinical use.

Cellular Assays. Furthermore, we evaluated a selection of potent inhibitors of this project for their cytotoxic profiles using five different cell lines including HL-60, a human myeloblastic leukemia cell line (Figure 7). It has been shown that the proliferation and differentiation particularly of the HL-60 cells depend upon PDGF-R signaling.²³ Cells were treated with the

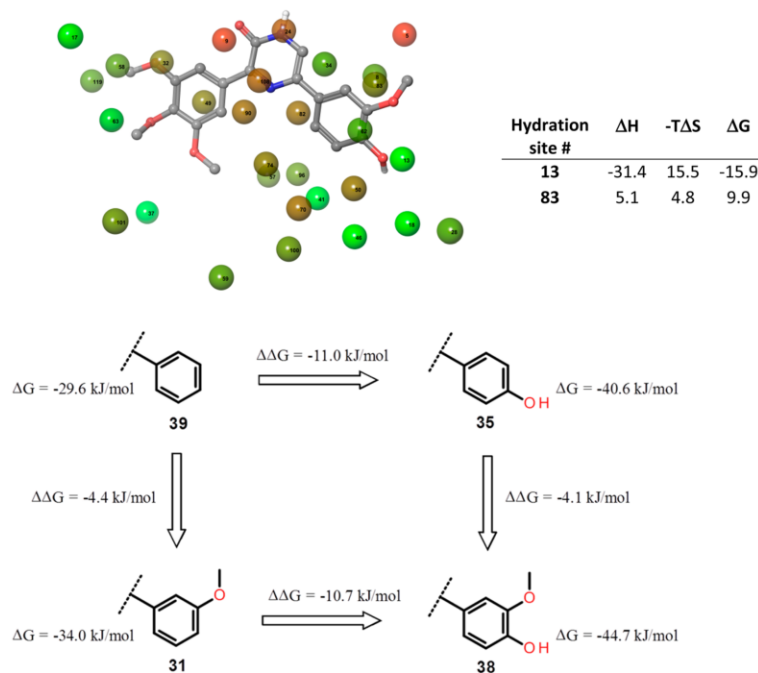


Figure 5. Top: Overlay of **38** (only polar hydrogens shown) and selected WaterMap hydration sites (within 5 Å of the ligand and $\Delta G > 4.2$ kJ/mol or < -4.2 kJ/mol) in the PDGF-R β homology model apo-structure. The hydration sites are numbered consecutively and are colored based on their respective ΔG values in kJ/mol from red/unstable to green/stable. For the key hydration sites #13 and #83, calculated ΔG , enthalpies, and entropies (in kJ/mol) with respect to bulk solvent are shown (complete data for all hydration sites can be found in the Supporting Information). Below: Experimentally determined relative contribution of 3'-methoxy and 4'-hydroxy phenyl-substituents to ΔG of the inhibitors **31** (IC₅₀ = 1.4 μ M), **35** (IC₅₀ = 0.1 μ M), **38** (IC₅₀ = 0.02 μ M), and **39** (IC₅₀ = 8 μ M) against PDGF-R β .

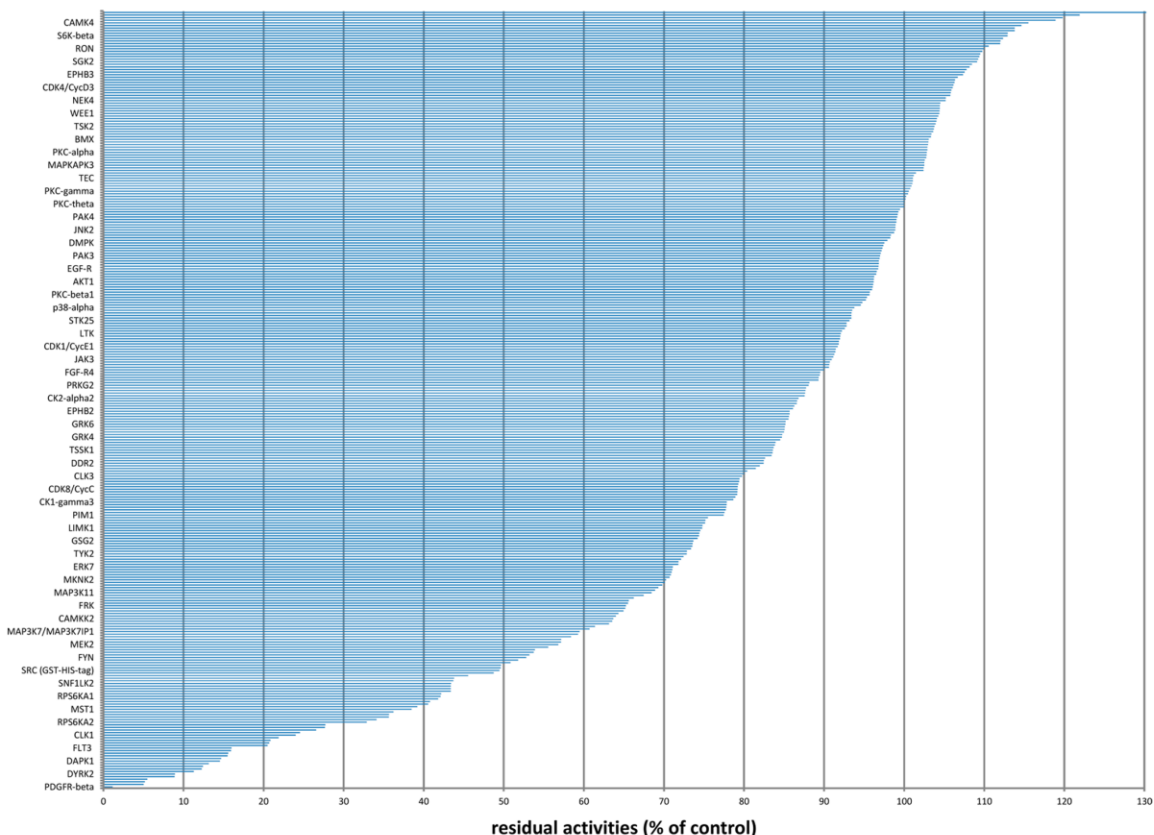


Figure 6. Graphical representation of the selectivity profile of compound **38** at a concentration of $1 \mu\text{M}$ against 300 wild-type protein kinases (mean of duplicate measurements). For clarity of representation, not all PK are shown at the y-axis (for full details see Supporting Information). PKs showing residual activity less than 50%: PDGF-R β (1%), RET (5%), HIPK4 (5%), CLK4 (5%), RIPK2 (9%), DYRK2 (9%), ACV-R2B (11%), LRRK2 (12%), CLK2 (12%), ACV-R1 (13%), DAPK1 (15%), MELK (15%), RPS6KA6 (16%), ACV-RL1 (16%), DYRK1B (16%), FLT3 (16%), DYRK3 (20%), VEGF-R2 (21%), DAPK3 (21%), PIM3 (22%), CLK1 (24%), DAPK2 (25%), RPS6KA3 (27%), CSF1-R (28%), TGF β -R2 (28%), RPS6KA2 (33%), HIPK2 (34%), TRK-C (36%), MST2 (36%), FGR (36%), MST1 (38%), FGF-R2 (39%), ARK5 (41%), VEGF-R3 (41%), KIT (42%), RPS6KA1 (42%), HIPK1 (42%), BLK (43%), DYRK1A (43%), IRAK4 (43%), SNF1LK2 (43%), TRK-A (44%), MERTK (44%), ITK (46%), CDK5/p35NCK (49%), SRC (49%), DYRK4 (50%), and TRK-B (50%). For assay details and abbreviations also visit www.proqinase.com.

test compounds and their viability was determined after 48 h incubation. All test compounds were shown to be cytotoxic against HL-60 cells. Interestingly, the other cells tested were significantly less affected by treatment of **2**, which is in line with the notion that HL-60 cells depend on PDGF-R signaling. Compound **2** was determined to have an IC_{50} value of $0.026 \mu\text{M}$ against HL-60 cells¹ and exhibited a significantly stronger antiproliferative effect than **38** that had an IC_{50} value of $3.2 \mu\text{M}$ in this assay. However, even if **38** showed to be most potent against HL-60 cells within the other cell lines tested in this project, the reduced cellular efficacy of **38** compared to **2** is in sharp contrast to the data from isolated PDGF-R β assay (Table 4). This may be due to inferior ADME properties such as limited cellular bioavailability, unspecific protein binding, or a metabolic inactivation particularly of the key phenolic-OH moiety of **38**. Thus, in order to estimate the cellular uptake of **38**, an assay was performed using Caco-2 cells²⁵ (Figure 8).

The data shows that compound **38** is slowly penetrating into the cells reaching a maximum intracellular concentration of approximately 40% after 60 min of incubation time. The

cellular uptake is paralleled by a decrease of **38** in the assay medium. However, although this data provides evidence for a moderate cellular bioavailability of **38**, the total recovery of the inhibitor (in both portions, medium and intracellular) was determined to be approximately 70%. As discussed above this may be due to unfavorable ADME properties of **38** such as nonspecific protein binding and metabolization.

Effect of Compound 38 on the Signal Transduction in U87 Cells. In order to analyze the effect of **38** on the PDGF signal transduction, a Western blot experiment was performed using U87 cells. Herein, the phosphorylation of Akt and ERK upon PDGF BB stimulation in the absence and presence of **38** was determined in a concentration-dependent manner (Figure 9). In this experiment **38** was able to decrease significantly the phosphorylation of AKT at a concentration of $3 \mu\text{M}$. Furthermore, the ERK phosphorylation was less affected as expected for an inhibitor blocking PDGF-R signaling.²⁶

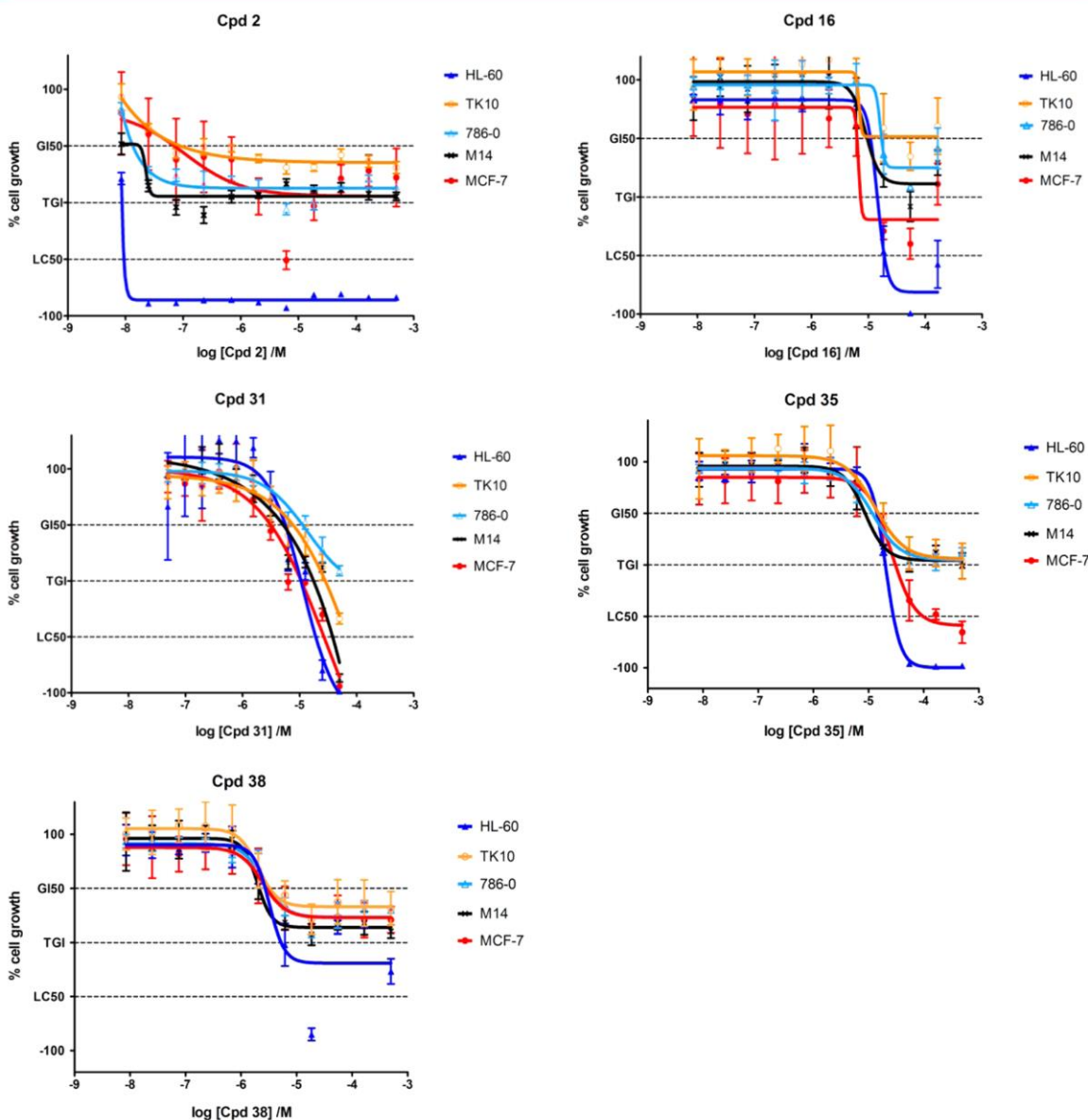


Figure 7. Determination of cytotoxic profiles of compounds 2, 16, 31, 35, and 38 in cell viability assays using HL-60, TK10, 786-0, M14, and MCF-7 cell lines.

CONCLUSIONS

In this article we demonstrate the successful optimization of 3,5-diaryl-pyrazin-2(1*H*)-ones as potent PDGF- $R\beta$ inhibitors. SARs for three pyrazin-2(1*H*)-ones series showing variable 3,5-aryl substitution patterns have been investigated. The 3,4,5-trimethoxy system at the 3-aryl position proved to be optimal and was therefore retained for further optimization. This moiety is situated in the HRII where the molecular modeling correlated accurately with the biological data. However, standard docking/scoring only insufficiently reflected the impact of the “hydrophobic effect” in the HPI where the 5-aryl system is located. The thermodynamic contribution of

displacing water molecules from key hydration sites could be calculated by the WaterMap technology. This approach led to the design of compounds featuring both displacement and replacement of key hydration sites. Herein, the gain in ligand affinity can be explained by the displacement of key hydration sites of the 3,5-diaryl-pyrazin-2(1*H*)-one core scaffold. Moreover, the replacement of a structural water molecule in the active site by the 4'-phenolic OH group of 38 in combination with the displacement of two further unstable hydration sites by the vicinal 3'-methoxy moiety of 38 essentially contributes to the ligand's affinity. This resulted in a 25-fold increase of the IC_{50} value for 38 (PDGF- $R\beta$): $IC_{50} = 0.02 \mu\text{M}$ compared to the

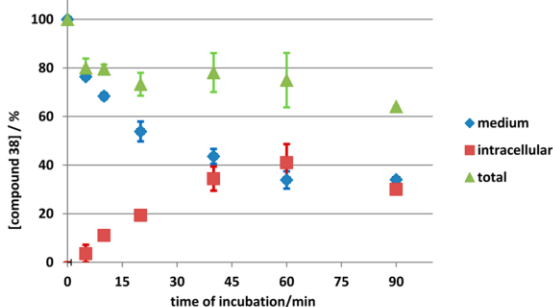


Figure 8. Measurement of the cellular uptake of **38** using a Caco-2 model. Cells were incubated with **38** at a concentration of 50 μM for 90 min, and the amount of **38** in the medium as well as the intracellular portion of **38** was determined by HPLC analysis (a control experiment using propranolol was performed; for further details see Supporting Information).

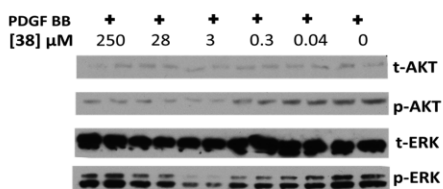


Figure 9. Effect of **38** on the signaling in U87 cells. The cells were treated with the indicated concentrations of **38** for 60 min at 37 $^{\circ}\text{C}$ and stimulated with 10 ng/mL PDGF BB for 10 min. Cells were lysed and lysates immunoblotted with the indicated antibodies (for details see Supporting Information). Similar results were obtained in duplicate experiments.

hit compound **2** (PDGF-R β : IC_{50} = 0.5 μM). A selectivity profile in a panel of 300 PKs was determined for **38** showing the compound to most potently block PDGF-R β activity. However, the promising activity of **38** in the kinase assay did not fully translate into potent efficacy in cellular assays as analyzed by Western blot. The moderate cellular efficacy of **38** may be due to the compound's limited ADME properties such as inferior cellular bioavailability based on poor permeability or the susceptibility to metabolic degradation particularly of the phenolic hydroxy moiety. Further hit-to-lead development of this compound series toward potent PDGF-R β inhibitors is therefore essential.

EXPERIMENTAL SECTION

^1H (300 MHz) and ^{13}C (75 MHz) NMR were recorded on a Bruker Avance III 300 spectrometer (Rheinstetten, Germany) at 300 K with a multinuclear probe head using the manufacturer's pulse programs. The data are reported as follows: chemical shifts in ppm from Me_4Si (TMS) as external standard, multiplicity, and coupling constant (Hz). NMR spectra were obtained, and ^1H (300 MHz) and ^{13}C spectra (75 MHz) were referenced either to TMS or to internal $\text{DMSO}-d_6$ (^1H NMR δ 2.50) and internal $\text{DMSO}-d_6$ (^{13}C NMR δ 39.5) or internal CHCl_3 (^1H NMR δ 7.26) and internal CDCl_3 (^{13}C NMR δ 77.0). All coupling constants (J values) are quoted in Hz. The following NMR abbreviations are used: b (broad), s (singlet), d (doublet), t (triplet), and m (unresolved multiplet). The labeling scheme of structures to correlate NMR signals can be found in Supporting Information.

Mass spectra of the compounds were recorded after chromatographic separation. Mixtures were separated with an Agilent 1100 HPLC system (Waldbronn, Germany) consisting of a thermostated

autosampler, diode array detection, and an Agilent Zorbax Eclipse XDB-C8 column (150 \times 4.6 mm, 5 μm particle size). Elution was achieved with a solvent gradient system of water and acetonitrile, with 0.1% of acetic acid and a flow rate of 1 mL/min. The eluent flow was splitted to the mass spectrometer.

Mass spectra with nominal resolution were recorded with an Esquire $\sim\text{LC}$ mass spectrometer (Bruker Daltonik, Bremen, Germany), with electrospray ionization operating in the positive ion mode, with the following parameters: drying gas nitrogen 8 l/min, nebulizer 35 psi, dry gas heating 350 $^{\circ}\text{C}$, HV capillary 4000 V, and HV end plate offset -500 V. GC/MS was performed on a HP6890 Series System. EI-mass spectra were recorded on a Varian MAT 311A (70 eV). HRMS spectra were recorded on a MAT-95 (Finnigan).

Where appropriate, column chromatography was performed for crude precursors with Merck silica gel 60 (0.063–0.200 mm) or Acros organics silica gel (0.060–0.200 mm; pore diameter ca. 60 nm). Column chromatography for test compounds was performed using a LaFlash system (VWR) with Merck silica gel 60 (0.015–0.040 mm) or RP8 columns. The progress of the reactions was monitored by thin-layer chromatography (TLC) performed with Merck silica gel 60 F-245 plates. Where necessary, reactions were carried out in a nitrogen atmosphere using 4 \AA molecular sieves. All reagents and solvents were obtained from commercial sources and used as received (THF was used after distillation over K/benzophenone). Reagents were purchased from Sigma-Aldrich Chemie, Steinheim, Germany; Lancaster Synthesis, M \ddot{u} hlheim, Germany; or Acros, Nidderau, Germany.

HPLC analysis was performed on a Hewlett-Packard HP 1090 Series II using a Thermo Betasil C8 (150 \times 4.6 mm 5 μM) column (mobile phase flow 1.5 mL/min, gradient KH_2PO_4 buffer pH 2.3/methanol, UV-detection 230/254 nm). All key compounds submitted to biological assays were proven by this method to show $\geq 98\%$ purity.

Synthesis of Compounds. Synthesis of arylglyoxylic acids (I, Scheme 1) was achieved by SeO_2 -mediated oxidation of the respective acetophenone in pyridine.²⁴ The α -ketoamines (II, Scheme 1) were prepared either by Del \acute{e} pine reaction from acetophenones²⁷ or by using aryl acids as starting material.²⁸ The open-chained diketamides (V, Scheme 1) were synthesized via two different routes: (a) by CDI-mediated coupling of arylglyoxylic acids I and aryl α -ketoamines II or (b) by CDI-mediated coupling⁷ of arylglyoxylic acids I and indole derivatives III to yield indole-amides IV. Subsequent DDQ oxidation¹ of the indole side-chain in IV yielded indole-diketamides V. All test compounds were synthesized in the final step accordingly to the general microwave mediated method using ammonium acetate as nitrogen source:¹ a microwave vial (5 mL) was equipped with ammonium acetate (10 equiv) and a solution of open-chained diketamide V (1 equiv) in 3 mL acetic acid (total volume). The vial was sealed and stirred at 160 $^{\circ}\text{C}$ for 4 min in a microwave synthesizer (CEM Discover). The reaction vessel was cooled to rt when H_2O was added to precipitate the raw pyrazinone, which was filtered off and purified by preparative HPLC (RP-phase) to afford the test compound in $\geq 98\%$ purity.

The experimental procedures for the preparation of compounds **5**, **6**, **8**, **12**, **13**, **15**, and **31** are reported in our recent study.⁷ The experimental procedure for the preparation of compounds **2** and **16** are reported in the literature.¹ The analytical data for the other compounds of this article (**3b/3c/3**, **4a/4**, **7b/7c/7**, **9b/9c/9**, **10b/10c/10**, **11b/11c/11**, **14b/14c/14**, **17b/17c/17**, **18a/18**, **19a/19**, **20b/20c/20**, **21a/21**, **22a/22**, **23a/23**, **24a/24**, **25a/25**, **26a/26**, **27a/27**, **28a/28**, **29a/29**, **30a/30**, **32a/32**, **33a/33**, **34a/34**, **35a/35**, **36a/36**, **37a/37**, **38a/38**, and **39a/39**) can be found in the Supporting Information. X-ray data for compounds **24** (CCDC number: 986158) and **29a** (CCDC number: 986159) is also given in the Supporting Information.

Molecular Modeling. All modeling was performed on a DELL 8 core system. For preparation, visualization and building the 3D structures Maestro (version 9.3) from Schrödinger (Schrödinger, LLC, New York, NY, 2013) was used. The illustrations of modeling were generated by Maestro. For compound docking and screening the Schrödinger "Glide SP" workflow was used.¹⁸ The goal of the Glide

methodology is to semiquantitatively rank the ability of candidate ligands to bind to a specified conformation of the protein receptor.²⁹ Prior to determining binding poses of ligands, energetically minimized compound conformations were generated, docked into the active site, and subsequently ranked based on their calculated binding affinity. The homology model for PDGF-R β was performed using the Prime workflow,^{16,30} primary sequence data of PDGF-R β (<http://www.uniprot.org/uniprot/P09619>), and the VEGF-R2 template structures in the DFG-in- (pdb 2p2h) and DFG-out-conformation (pdb 1t46), respectively.

WaterMap computes water properties (location, occupancy, enthalpy, entropy, and free energy) through a combination of molecular dynamics, solvent clustering, and statistical thermodynamic analysis. First, a 2 ns explicit-solvent molecular dynamics simulation of the protein with the ligand removed is run in order to sample the configurations of water molecules in the binding site. The coordinates of the protein are restrained with a 5.0 kcal/mol/Å² harmonic potential applied to the initial positions of the heavy atoms, which ensures convergence of the water sampling around the protein conformation of interest. Waters from approximately 2000 equally spaced frames from the molecular dynamics simulation are then spatially clustered to form localized hydration sites, and the thermodynamic properties of those sites are computed. The enthalpy is computed as the average nonbonded molecular mechanics interaction energies of the waters in the hydration site with the rest of the system. The entropy is computed by numerically integrating a local expansion of spatial and orientational correlation functions, as described in the inhomogeneous solvation theory work by Lazaridis.³¹ The relevant solvation thermodynamic quantities for the ligand are computed based on the amount of overlap with the hydration sites.

Biological Evaluation. All inhibitor solutions were prepared freshly in DMSO prior to each experiment and used immediately.

Determination of IC₅₀ Values of Compounds. Recombinant Protein Kinases. The inhibitory profile of compounds was determined using the following 24 protein kinases (GenBankAcc. No. available on <http://www.proqinase.com/pages/science>): AKT1, ARK5, Aurora-A, Aurora-B, B-Raf-VE, CDK2/CycA, CDK4/CycD1, CK2-A1, EGF-R, EPHB4, ERBB2, FAK, IGF1-R, SRC, VEGF-R2, VEGF-R3, FLT3, INS-R, MET, PDGF-R β , PLK1, SAK, TIE2, and COT. All protein kinases were expressed using human cDNAs in Sf9 insect cells as recombinant GST-fusion proteins or His-tagged proteins by means of the baculovirus expression system. Kinases were purified by affinity chromatography using either GSH-agarose (Sigma) or Ni-NTH-agarose (Qiagen). The purity and identity of each kinase was determined by SDS-PAGE/silver staining and Western blot analysis using specific antibodies.

Protein Kinase Assay. A proprietary protein kinase assay (³³PanQinase Activity Assay) was used for measuring the kinase activity of the 24 protein kinases. All protein kinase assays were performed in 96-well FlashPlates™ (PerkinElmer/NEN, Boston, MA, USA) in 50 μ L reaction volumes. Assays for all enzymes were performed in a solution containing 60 mM HEPES-NaOH, pH 7.5, 3 mM MgCl₂, 3 mM MnCl₂, 3 μ M Na-orthovanadate, 1.2 mM DTT, 50 μ g/mL PEG20000, 1 μ M [γ -³³P]-ATP (approximately 5 \times 10⁵ cpm per well), and recombinant protein kinase (50–400 ng). Depending upon the kinase being assayed, appropriate substrates were used and were as follows (substrates shown in parentheses): AKT1 (GSK3/14–27), ARK5 (autophosphorylation), Aurora-A, Aurora-B (Tetra-(LRRWSLG)), B-Raf-V600E (MEK1 KM), CDK2/CycA (histone H1), CDK4/CycD1 (Rb-CTF), CK2-A1 (casein), EGF-R, EPHB4, ERBB2, FAK, IGF1-R, SRC, VEGF-R2, VEGF-R3 (poly(Glu,Tyr) 4:1), FLT3, INS-R, MET, PDGF-R β (poly(Ala,Glu,Lys,Tyr) 6:2:5:1), PLK1 (casein), SAK (autophosphorylation), TIE2 (poly(Glu,Tyr) 4:1), and COT (autophosphorylation). The IC₅₀ values were measured by testing 10 concentrations of compounds in singlicate. The final DMSO concentration in the assay was 1% (v/v). The data were fitted using the 4-parameter logistic fit option of GraphPad Prism 5.

Cell Culture and Proliferative Assays Using HL-60, TK 10, 786-0, M14, and MCF-7 cells. The cells were grown in RPMI 1640

Glutamax with 10% FCS, 100 μ g/mL streptomycin, and 100 U/mL penicillin G and incubated in a 5% CO₂ humidified atmosphere at 37 °C. For proliferation experiments, cells were seeded in 20 μ L pro well into 384-well Greiner 384 CellStar plates (Greiner Bio-One I. AG, Kremsmünster, AT). In addition to the test plates, one plate was prepared for the reference measurement at day zero. All plates were incubated for 24 h at 37 °C in a humidified atmosphere with 5% CO₂. Compounds that were dissolved in 100% DMSO (v/v) were added to test plates using the Echo 550 Liquid Handler (Labcyte Inc., Sunnyvale, UK). The final DMSO concentration in the assay was 0.5% (v/v). The viability of the cells in the day zero control plates were determined on the same day without adding any compounds. The CellTiter-Glo Viability Assay was used to determine the viability of cells using the standard protocol for this assay (Promega Corp., Madison, US). The luminescence signal was measured at the EnSpire Multimode Plate Reader (PerkinElmer, Waltham, US). Test plates were incubated for further 48 h, and the cell viability was defined as just described. Measured raw data were converted into percent of cell growth by using the high control (0.5% DMSO (v/v) without compound) and the day zero control. For dose–response studies, 11 different concentrations of compounds were tested in quadruplicates. The IC₅₀ values were calculated using the 4-parameter logistic fit option of GraphPad Prism 5.

■ ASSOCIATED CONTENT

■ Supporting Information

Details of WaterMap calculation, spectroscopic details, IR data, purity and X-ray analysis of compounds, selectivity profile of 38, measurement of intracellular uptake, and Western blot analysis. This material is available free of charge via the Internet at <http://pubs.acs.org>.

■ AUTHOR INFORMATION

■ Corresponding Author

*(C.P.) Tel: 0049 431 880 1137. Fax: 0049 431 880 1352. E-mail: cpeifer@pharmazie.uni-kiel.de.

■ Author Contributions

U.R.H. and B.P. contributed equally to this work. The manuscript was written through contributions of all authors. All authors have given approval to the final version of the manuscript.

■ Notes

The authors declare no competing financial interest.

■ ACKNOWLEDGMENTS

We thank Martin Schütt and Dr. Ulrich Girreser for excellent technical and analytical assistance at the Institute of Pharmacy in Kiel, Germany. We gratefully acknowledge the help of Dr. Dieter Schollmeyer, University of Mainz, Institute for Organic Chemistry, Germany, for X-ray analysis of compounds. Financial support by DFG grant (PE 1605/2-1) is greatly acknowledged.

■ ABBREVIATIONS USED

ADME, adsorption, distribution, metabolism, excretion; AKT1, v-akt murine thymoma viral oncogene homologue 1 (PKB); ARK5, AMPK-related protein kinase 5 (NUAK1); aurora, aurora kinase; B-RAF, v-raf murine sarcoma viral oncogene homologue B1; CDI, carbonyldiimidazole; CDK, cyclin-dependent kinase; COT, mitogen-activated protein kinase kinase kinase 8 (MAP3K8); DDQ, 2,3-dichloro-5,6-dicyano-1,4-benzoquinone; DFG-in/out, sequence motif of aspartic acid-phenylalanine-glycine of a loop in the PK domain; DMSO, dimethyl sulfoxide; EGF-R, epidermal growth factor receptor;

EPHB, EPH receptor B; FAK, focal adhesion kinase; FLT3, fms-related tyrosine kinase 3; HPI, hydrophobic pocket I; HRIL, hydrophobic region II; IGF1-R, insulin-like growth factor 1 receptor; INS-R, insulin receptor; MET, met proto-oncogene (hepatocyte growth factor receptor); PDGF-R, platelet-derived growth factor receptor; PK, protein kinase; PLK1, polo-like kinase 1; RTK, receptor tyrosine kinase; SAK, serine/threonine-protein kinase (PLK4); smKI, small molecule kinase inhibitor; SRC, v-src sarcoma (Schmidt–Ruppin A-2) viral oncogene homologue; TIE2, tunica interna endothelial cell kinase; VEGF-R, vascular endothelial growth factor receptor

REFERENCES

- (1) Pinchuk, B.; Johannes, E.; Gul, S.; Schlosser, J.; Schachtele, C.; Totzke, F.; Peifer, C. Marine derived hamacanthins as lead for the development of novel PDGF-Rbeta protein kinase inhibitors. *Marine Drugs* **2013**, *11*, 3209–23.
- (2) Zoraghi, R.; Worrall, L.; See, R. H.; Strangman, W.; Popplewell, W. L.; Gong, H. S.; Samaai, T.; Swayze, R. D.; Kaur, S.; Vuckovic, M.; Finlay, B. B.; Brunham, R. C.; McMaster, W. R.; Davies-Coleman, M. T.; Strynadka, N. C.; Andersen, R. J.; Reiner, N. E. Methicillin-resistant *Staphylococcus aureus* (MRSA) pyruvate kinase as a target for bis-indole alkaloids with antibacterial activities. *J. Biol. Chem.* **2011**, *286*, 44716–44725.
- (3) Caldwell, J. J.; Veillard, N.; Collins, I. Design and synthesis of 2(1H)-pyrazinones as inhibitors of protein kinases. *Tetrahedron* **2012**, *68*, 9713–9728.
- (4) Ibrahim, N.; Yu, Y.; Walsh, W. R.; Yang, J. L. Molecular targeted therapies for cancer: sorafenib mono-therapy and its combination with other therapies. *Oncology Rep.* **2012**, *27*, 1303–11.
- (5) Hicken, E. J.; Marmsater, F. P.; Munson, M. C.; Schlachter, S. T.; Robinson, J. E.; Allen, S.; Burgess, L. E.; DeLisle, R. K.; Rizzi, J. P.; Topalov, G. T.; Zhao, Q.; Hicks, J. M.; Kallan, N. C.; Tarlton, E.; Allen, A.; Callejo, M.; Cox, A.; Rana, S.; Klopfenstein, N.; Woessner, R.; Lyssikatos, J. P. Discovery of a novel class of imidazo[1,2-a]pyridines with potent PDGFR activity and oral bioavailability. *Med. Chem. Lett.* **2014**, *5*, 78–83.
- (6) (a) Fabbro, D.; Cowan-Jacob, S. W.; Mobitz, H.; Martiny-Baron, G. Targeting cancer with small-molecular-weight kinase inhibitors. *Methods Mol. Biol.* **2012**, *795*, 1–34. (b) Jänne, P. A.; Gray, N.; Jeff Settleman, J. Chemical structures and known kinase targets for clinically approved kinase inhibitors. *Nat. Rev. Drug Discovery* **2009**, *8*, 709–723. (c) <http://www.nlm.nih.gov/cgi>.
- (7) Peifer, C.; Selig, R.; Kinkel, K.; Ott, D.; Totzke, F.; Schachtele, C.; Heidenreich, R.; Rocken, M.; Schollmeyer, D.; Laufer, S. Design, synthesis, and biological evaluation of novel 3-aryl-4-(1H-indole-3-yl)-1,5-dihydro-2H-pyrrole-2-ones as vascular endothelial growth factor receptor (VEGF-R) inhibitors. *J. Med. Chem.* **2008**, *51*, 3814–24.
- (8) Johannes, E.; Horbert, R.; Schlosser, J.; Schmidt, D.; Peifer, C. Effective synthesis of 3,5-diaryl-(1H)-pyrazin-2-ones via microwave mediated ring closure. *Tetrahedron Lett.* **2013**, *54*, 4067–4072.
- (9) (a) Dar, A. C.; Shokat, K. M. The evolution of protein kinase inhibitors from antagonists to agonists of cellular signaling. *Annu. Rev. Biochem.* **2011**, *80*, 769–795. (b) Iwata, H.; Oki, H.; Okada, K.; Takagi, T.; Tawada, M.; Miyazaki, Y.; Imamura, S.; Hori, A.; Lawson, J. D.; Hixon, M. S.; Kimura, H.; Miki, H. A back-to-front fragment-based drug design search strategy targeting the DFG-out pocket of protein tyrosine kinases. *ACS Med. Chem. Lett.* **2012**, *3*, 342–346.
- (10) Hodous, B. L.; Geuns-Meyer, S. D.; Hughes, P. E.; Albrecht, B. K.; Bellon, S.; Bready, J.; Caenepeel, S.; Cee, V. J.; Chaffee, S. C.; Coxon, A.; Emery, M.; Fretland, J.; Gallant, P.; Gu, Y.; Hoffman, D.; Johnson, R. E.; Kendall, R.; Kim, J. L.; Long, A. M.; Morrison, M.; Olivieri, P. R.; Patel, V. F.; Polverino, A.; Rose, P.; Tempest, P.; Wang, L.; Whittington, D. A.; Zhao, H. L. Evolution of a highly selective and potent 2-(pyridin-2-yl)-1,3,5-triazine tie-2 kinase inhibitor. *J. Med. Chem.* **2007**, *50*, 611–626.
- (11) Cowan-Jacob, S. W.; Fendrich, G.; Floersheimer, A.; Furet, P.; Liebetanz, J.; Rummel, G.; Rheinberger, P.; Centeleghe, M.; Fabbro, D.; Manley, P. W. Structural biology contributions to the discovery of drugs to treat chronic myelogenous leukaemia. *Acta Crystallogr., Sect. D: Biol. Crystallogr.* **2007**, *63*, 80–93.
- (12) Mol, C. D.; Dougan, D. R.; Schneider, T. R.; Skene, R. J.; Kraus, M. L.; Scheibe, D. N.; Snell, G. P.; Zou, H.; Sang, B. C.; Wilson, K. P. Structural basis for the autoinhibition and STI-571 inhibition of c-KIT tyrosine kinase. *J. Biol. Chem.* **2004**, *279*, 31655–63.
- (13) Getlik, M.; Grutter, C.; Simard, J. R.; Kluter, S.; Rabiller, M.; Rode, H. B.; Robubi, A.; Rauh, D. Hybrid compound design to overcome the gatekeeper T338M mutation in cSrc. *J. Med. Chem.* **2009**, *52*, 3915–3926.
- (14) Harris, P. A.; Bloor, A.; Cheung, M.; Kumar, R.; Crosby, R. M.; Davis-Ward, R. G.; Epperly, A. H.; Hinkle, K. W.; Hunter, R. N., III; Johnson, J. H.; Knick, V. B.; Laudeman, C. P.; Luttrell, D. K.; Mook, R. A.; Nolte, R. T.; Rudolph, S. K.; Szewczyk, J. R.; Truesdale, A. T.; Veal, J. M.; Wang, L.; Stafford, J. A. Discovery of 5-[[4-[(2,3-dimethyl-2H-indazol-6-yl)methylamino]-2-pyrimidinyl]amino]-2-methyl-benzene-sulfonamide (Pazopanib), a novel and potent vascular endothelial growth factor receptor inhibitor. *J. Med. Chem.* **2008**, *51*, 4632–40.
- (15) Hilberg, F.; Roth, G. J.; Krssak, M.; Kautschitsch, S.; Sommergruber, W.; Tontsch-Grunt, U.; Garin-Chesa, P.; Bader, G.; Zoepfel, A.; Quant, J.; Heckel, A.; Rettig, W. J. BIBF 1120: triple angiokinase inhibitor with sustained receptor blockade and good antitumor efficacy. *Cancer Res.* **2008**, *68*, 4774–82.
- (16) Meyers, M. J.; Pelc, M.; Kamtekar, S.; Day, J.; Poda, G. I.; Hall, M. K.; Michener, M. L.; Reitz, B. A.; Mathis, K. J.; Pierce, B. S.; Parikh, M. D.; Mischke, D. A.; Long, S. A.; Parlow, J. J.; Anderson, D. R.; Thorarensen, A. Structure-based drug design enables conversion of a DFG-in binding CSF-1R kinase inhibitor to a DFG-out binding mode. *Bioorg. Med. Chem. Lett.* **2010**, *20*, 1543–7.
- (17) (a) Jacobson, M. P.; Kaminski, G. A.; Friesner, R. A.; Rapp, C. S. Force field validation using protein side chain prediction. *J. Phys. Chem. B* **2002**, *106*, 11673–11680. (b) Jacobson, M. P.; Pincus, D. L.; Rapp, C. S.; Day, T. J. F.; Honig, B.; Shaw, D. E.; Friesner, R. A. A hierarchical approach to all-atom protein loop prediction. *Proteins: Struct., Funct., Bioinf.* **2004**, *55*, 351–367.
- (18) Friesner, R. A.; Banks, J. L.; Murphy, R. B.; Halgren, T. A.; Klicic, J. J.; Mainz, D. T.; Repasky, M. P.; Knoll, E. H.; Shelley, M.; Perry, J. K.; Shaw, D. E.; Francis, P.; Shenkin, P. S. Glide: A new approach for rapid, accurate docking and scoring. 1. Method and assessment of docking accuracy. *J. Med. Chem.* **2004**, *47*, 1739–1749.
- (19) (a) Abel, R.; Young, T.; Farid, R.; Berne, B. J.; Friesner, R. A. Role of the active-site solvent in the thermodynamics of factor Xa ligand binding. *J. Am. Chem. Soc.* **2008**, *130*, 2817–2831. (b) Young, T.; Abel, R.; Kim, B.; Berne, B. J.; Friesner, R. A. Motifs for molecular recognition exploiting hydrophobic enclosure in protein-ligand binding. *Proc. Natl. Acad. Sci. U.S.A.* **2007**, *104*, 808–13. (c) Haider, K.; Huggins, D. J. Combining solvent thermodynamic profiles with functionality maps of the Hsp90 binding site to predict the displacement of water molecules. *J. Chem. Inf. Modeling* **2013**, *53*, 2571–86. (d) Snyder, P. W.; et al. Mechanism of the hydrophobic effect in the biomolecular recognition of arylsulfonamides by carbonic anhydrase. *Proc. Natl. Acad. Sci. U.S.A.* **2011**, *108*, 17889–17894. (e) Breiten, B.; et al. Water networks contribute to enthalpy/entropy compensation in protein-ligand binding. *J. Am. Chem. Soc.* **2013**, *135*, 15579–15584.
- (20) (a) Robinson, D. D.; Sherman, W.; Farid, R. Understanding kinase selectivity through energetic analysis of binding site waters. *ChemMedChem* **2010**, *5*, 618–27. (b) Myriantopoulos, V.; Kritsanida, M.; Gaboriaud-Kolar, N.; Magiatis, P.; Ferandin, Y.; Durieu, E.; Lozach, O.; Cappel, D.; Soundararajan, M.; Filippakopoulos, P.; Sherman, W.; Knapp, S.; Meijer, L.; Mikros, E.; Skaltsounis, A. L. Novel inverse binding mode of indirubin derivatives yields improved selectivity for DYRK kinases. *ACS Med. Chem. Lett.* **2013**, *4*, 22–26.
- (21) Abad-Zapatero, C. Ligand efficiency indices for effective drug discovery. *Expert Opin. Drug Discovery* **2007**, *2*, 469–88.
- (22) Furet, P.; Bold, G.; Meyer, T.; Roessel, J.; Guagnano, V. Aromatic interactions with phenylalanine 691 and cysteine 828: a concept for FMS-like tyrosine kinase-3 inhibition. Application to the

discovery of a new class of potential antileukemia agents. *J. Med. Chem.* **2006**, *49*, 4451–4454.

(23) Reiterer, G.; Yen, A. Platelet-derived growth factor receptor regulates myeloid and monocytic differentiation of HL-60 cells. *Cancer Res.* **2007**, *67*, 7765–72.

(24) Riley, H. L. Oxidation Activity of Selenium Dioxide. *Nature* **1947**, *159*, 571–572.

(25) (a) Schwering, U. Dissertation, University of Kiel; http://macau.uni-kiel.de/receive/dissertation_diss_00005345. (b) Fogh, J.; Fogh, J. M.; Orfeo, T. One hundred and twenty-seven cultured human tumor cell lines producing tumors in nude mice. *J. Natl. Cancer Inst.* **1977**, *59*, 221–226.

(26) Servidei, T.; Riccardi, A.; Sanguinetti, M.; Dominici, C.; Riccardi, R. Increased sensitivity to the platelet-derived growth factor (PDGF) receptor inhibitor STI571 in chemoresistant glioma cells is associated with enhanced PDGF-BB-mediated signaling and STI571-induced Akt inactivation. *J. Cell. Physiol.* **2006**, *208*, 220–228.

(27) Delepine, M. Sur l'hexaméthylène-amines; seld d'ammmonium; action des acides; production d'amines primaires. *C. R. Hebd. Seances Acad. Sci.* **1895**, *120*, 501–502.

(28) Suzuki, M.; Iwasaki, T.; Miyoshi, M.; Okumura, K.; Matsumoto, K. Synthesis of amino-acids and related compounds. New convenient syntheses of alpha-C-acylamino acids and alpha-amino ketones. *J. Org. Chem.* **1973**, *38*, 3571–3575.

(29) Halgren, T. A.; Murphy, R. B.; Friesner, R. A.; Beard, H. S.; Frye, L. L.; Pollard, W. T.; Banks, J. L. Glide: A new approach for rapid, accurate docking and scoring. 2. Enrichment factors in database screening. *J. Med. Chem.* **2004**, *47*, 1750–1759.

(30) Jacobson, M. P.; Friesner, R. A.; Xiang, Z. X.; Honig, B. On the role of the crystal environment in determining protein side-chain conformations. *J. Mol. Biol.* **2002**, *320*, 597–608.

(31) (a) Lazaridis, T. Inhomogeneous fluid approach to solvation thermodynamics. 1. Theory. *J. Phys. Chem. B* **1998**, *102*, 3531–3541. (b) Lazaridis, T. Inhomogeneous fluid approach to solvation thermodynamics. 2. Applications to simple fluids. *J. Phys. Chem. B* **1998**, *102*, 3542–3550.

Supporting Information for Paper:

Optimization of potent DFG-in inhibitors of Platelet Derived Growth Factor Receptor β (PDGF-R β) guided by water thermodynamics

Rebecca Horbert^{§‡}, Boris Pinchuk^{§‡}, Eugen Johannes[§], Joachim Schlosser[§], Dorian Schmidt[§], Daniel Cappel^{}, Frank Totzke[♦], Christoph Schächtele[♦], and Christian Peifer^{§*}.*

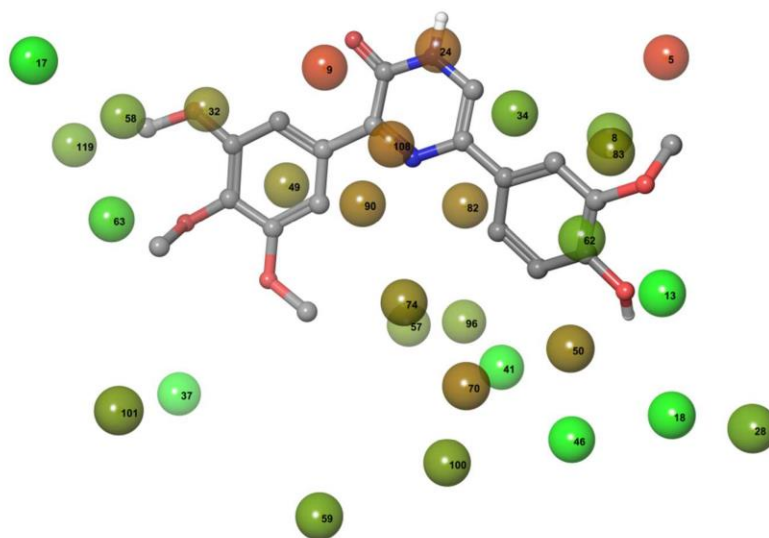
[§]Institute of Pharmacy, Christian-Albrechts-University of Kiel, Gutenbergstraße 76, D-24116
Kiel, Germany

^{*}Schrödinger GmbH, Dynamostraße 13, D-68165 Mannheim, Germany

[♦]ProQinase GmbH, Breisacherstraße 117, D-79106 Freiburg, Germany

[‡]These authors contributed equally.

WaterMap results



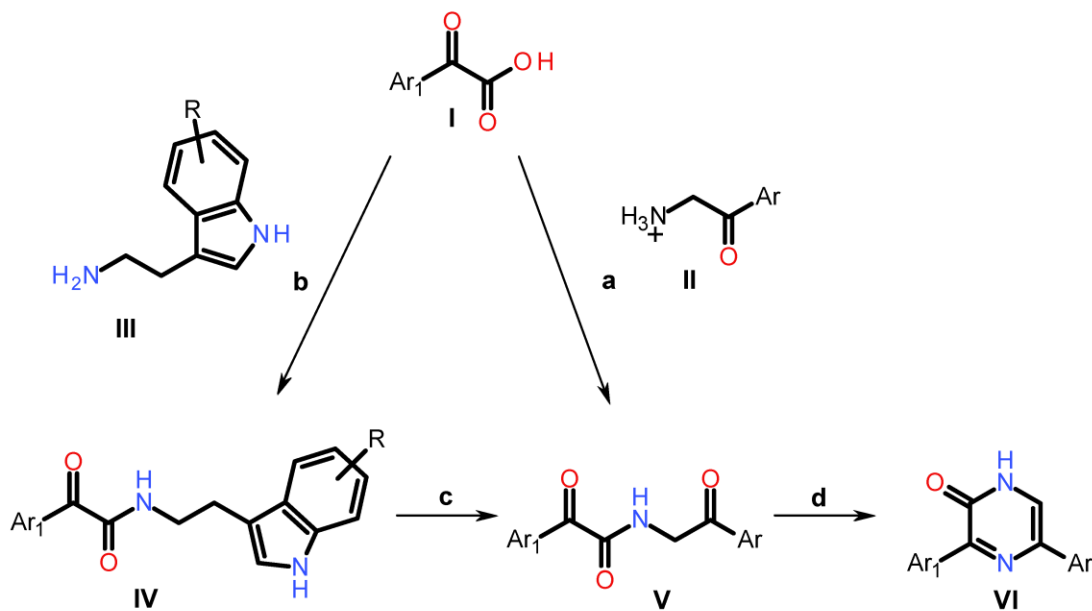
#	ΔH	$-T\Delta S$	ΔG
5	7.8	18.0	25.8
8	-10.5	15.9	5.5
9	8.9	15.2	24.1
13	-31.4	15.5	-15.9
17	-27.4	14.5	-12.9
18	-21.7	12.1	-9.5
24	3.7	13.5	17.2
28	-5.3	10.0	4.7
32	0.5	10.0	10.6
34	-5.0	9.3	4.4
37	-32.9	12.2	-20.7
41	-17.9	8.2	-9.7
46	-18.2	7.8	-10.4
49	4.5	6.6	11.0
50	5.6	7.0	12.6
57	0.0	6.7	6.7
58	-1.1	6.4	5.3
59	-0.6	6.2	5.6
62	-1.8	5.9	4.2
63	-10.2	5.6	-4.6
70	8.5	5.4	13.9
74	6.7	4.9	11.6
82	9.3	4.4	13.7
83	5.1	4.8	9.9
90	10.2	4.0	14.1
96	2.6	3.9	6.5
100	3.6	3.5	7.2
101	3.8	3.8	7.6
108	12.3	3.8	16.2
119	1.3	3.4	4.8

Overlay of **38** and selected WaterMap hydration sites (within 5 Å of the ligand and $\Delta G > 4.2$ kJ/mol or < -4.2 kJ/mol) in the PDGF-R β homology model apo-structure. The hydration sites are numbered consecutively and are colored based on their respective ΔG values in kJ/mol from red/unstable to green/stable. For all hydration sites calculated ΔG , enthalpies ΔH and entropies ΔTS (in kJ/mol) with respect to bulk solvent are shown. The 1*H*-pyrazin-2-one-5-phenyl moiety occupies the HPI (right site) with the 4'-phenolic OH involved in H-bond interactions between Lys53 and Asp180 while the vicinal 3'-methoxy group is situated at the rear end of this binding

pocket. Key hydration sites from WaterMap calculations on the PDGF-R β homology model apo-structure are superimposed to illustrate the displacement of hydration sites by the inhibitor. Hydration sites shown as red spheres represent “unstable” water molecules. Their displacement results in an increase of environmental entropy (“hydrophobic effect”). Green spheres symbolize “stable” water molecules which should not be displaced by an inhibitor in terms of unfavorable entropic effects. However, replacing “stable” structural hydration sites may result in a decrease of ΔG by forming enthalpic favorable ligand-protein interactions.

Experimental details chemical part

The general preparation method of 3,5-diaryl-pyrazin-2(1*H*)-ones (VI) is shown in the scheme below. As precursor for the final pyrazin-2(1*H*)-one ring closure open chained ketoamides (V) were prepared via two different routes, dependent on the availability of starting material: either via CDI mediated coupling of arylglyoxylic acid (I) and α -ketoamines (II) (method a) or via CDI mediated coupling of arylglyoxylic acid (I) and indolethylamines (III) (method b) to produce N-[2-(1*H*-indol-3-yl)ethyl]-2-oxo-2-phenyl-acetamides (IV) which yielded the corresponding ketoamides (V) upon DDQ-oxidation (method c). In the final step targeted 3,5-diaryl-pyrazin-2(1*H*)-ones (VI) were prepared in a microwave reaction using ammonium acetate as nitrogen source (method d). For clarity, in this paper the 3,5-diaryl-pyrazin-2(1*H*)-one test compounds were numbered consecutively (**2 - 39**). Their relevant precursor materials were labeled by a, b, or c, respectively, to indicate the synthetic method of preparation described above (e.g. **3b**, **3c**).



Analytical data for compounds:

3b/3c/3, 4a/4, 7b/7c/7, 9b/9c/9, 10b/10c/10, 11b/11c/11, 14b/14c/14, 17b/17c/17, 18a/18, 19a/19, 20b/20c/20, 21a/21, 22a/22, 23a/23, 24a/24, 25a/25, 26a/26, 27a/27, 28a/28, 29a/29, 30a/30, 32a/32, 33a/33, 34a/34, 35a/35, 36a/36, 37a/37, 38a/38, 39a/39

N-(1-(1*H*-Indol-3-yl)propan-2-yl)-2-(3,4,5-trimethoxyphenyl)-2-oxoacetamide (**3b**). ¹H-NMR (300 MHz): (DMSO-*d*₆) δ in ppm: 1.19 (d, 3 H, *J* = 6.57 Hz), 2.89 (m, 2 H), 3.73 (s, 6 H), 3.76 (s, 3 H), 4.28 (m, 1 H), 7.00 (m, 2 H), 7.17 (s, 2 H), 7.32 (d, 1 H, *J* = 7.71 Hz), 7.59 (d, 1 H, *J* = 7.71 Hz), 8.86 (d, 1 H, *J* = 8.20 Hz) 10.80 (s, 1 H); ¹³C-NMR (75 MHz): (DMSO-*d*₆) δ in ppm: 20.13, 31.62, 45.48, 55.93, 60.26, 107.01, 111.17, 111.28, 118.23, 118.35, 120.84, 123.19, 127.36, 128.00, 136.14, 143.04, 152.79, 164.38, 189.33; IR (cm⁻¹): 3391, 3283, 1664, 1645,

1580, 1500, 1455, 1415, 1328, 1240, 1165, 1126, 1000, 808, 771, 754, 727, 705. LC-MS: 21.9 min, m/z 396 $[M]^+$ $C_{22}H_{24}N_2O_5$ (M_r 396.44). MP: 128 °C. Yield: 180 mg (79 %).

N-[2-(1*H*-Indol-3-yl)-1-methyl-2-oxo-ethyl]-2-oxo-2-(3,4,5-trimethoxyphenyl)acetamide (**3c**).

1H -NMR (300 MHz): ($CDCl_3$) δ in ppm: 1.60 (d, 2 H, $J = 7.07$ Hz), 3.89 (s, 6 H), 3.94 (s, 3 H), 5.39 (dq, 1 H, $J = 7.24, 7.07$ Hz), 7.31 (m, 2 H), 7.42 (m, 1 H), 7.71 (s, 2 H), 8.01 (d, 1 H, $J = 2.27$ Hz), 8.09 (d, 1 H, $J = 7.83$ Hz), 8.36 (m, 1 H), 9.06 (bs, 1 H); ^{13}C -NMR (75 MHz): ($CDCl_3$) δ in ppm: 20.08, 50.88, 56.26, 60.99, 108.74, 111.62, 114.74, 122.33, 123.16, 124.23, 125.65, 128.27, 131.93, 136.44, 144.02, 152.85, 161.71, 185.57, 192.52; IR (cm^{-1}): 3301, 1682, 1663, 1646, 1624, 1582, 1518, 1502, 1456, 1415, 1336, 1248, 1233, 1163, 1124, 1094, 982, 897, 859. LC-MS: 7.7 min, m/z 411,1 $[MH]^+$ $C_{22}H_{22}N_2O_6$ (M_r 410.15). MP: 193 °C. Yield: 74 mg (48 %).

5-(1*H*-Indol-3-yl)-6-methyl-3-(3,4,5-trimethoxyphenyl)-1*H*-pyrazin-2-one (**3**). 1H -NMR

(300 MHz): ($DMSO-d_6$) δ in ppm: 2.44 (s, 3 H), 3.73 (s, 3 H), 3.82 (s, 6 H), 7.10 (m, 2 H), 7.44 (d, 1 H, $J = 7.83$ Hz), 7.58 (s, 1 H), 8.00 (s, 2 H), 8.06 (d, 1 H, $J = 8.08$ Hz), 11.33 (s, 1 H), 12.55 (bs, 1 H); ^{13}C -NMR (75 MHz): ($DMSO-d_6$) δ in ppm: 17.15, 55.71, 60.08, 105.59, 111.59, 111.96, 119.07, 120.51, 121.48, 124.48, 126.50, 131.99, 136.03, 138.57, 152.28, 154.47; IR (cm^{-1}): 3288, 1637, 1579, 1541, 1505, 1452, 1413, 1385, 1326, 1224, 1167, 1119, 1035, 1009, 986, 864, 768, 744, 724. LC-MS: 6.6 min, m/z 392.2 $[MH]^+$ $C_{22}H_{21}N_3O_4$ (M_r 391.42) HRMS: m/z calculated 352.1423; found 352.1412. MP: 287 °C. Yield: 20 mg (30 %).

N-(2-(3,4,5-Trimethoxyphenyl)-2-oxoethyl)-2-(1*H*-indol-3-yl)-2-oxoacetamide (**4a**). 1H -NMR

(300 MHz): ($DMSO-d_6$) δ in ppm: 3.75 (s, 3 H), 3.88 (s, 6 H), 4.78 (d, 2 H, $J = 5.81$ Hz), 7.30

(m, 4 H), 7.55 (m, 1 H), 8.25 (m, 1 H), 8.78 (s, 1 H), 8.98 (t, 1 H, $J = 5.81$ Hz), 12.24 (s, 1 H); ^{13}C -NMR (75 MHz): (DMSO- d_6) δ in ppm: 46.39, 56.52, 60.55, 105.89, 112.61, 112.96, 121.66, 122.99, 123.87, 126.48, 130.45, 136.66, 138.94, 153.26, 164.22, 182.03, 193.69 IR (cm^{-1}): 3342, 1667, 1612, 1583, 1493, 1453, 1409, 1354, 1314, 1232, 1121, 1098, 1009, 893, 808, 747, 703. LC-MS: 7.3 min, m/z 397.0 $[\text{MH}]^+$ $\text{C}_{21}\text{H}_{20}\text{N}_2\text{O}_6$ (M_r 396.39). MP: 250 °C. Yield: 250 mg (45 %).

3-(1*H*-Indol-3-yl)-5-(3,4,5-trimethoxyphenyl)-1*H*-pyrazin-2-one (**4**). ^1H -NMR (300 MHz): (DMSO- d_6) δ in ppm: 3.72 (s, 3 H), 3.93 (s, 6 H), 7.19 (m, 2 H), 7.38 (s, 2 H), 7.52 (m, 1 H), 7.89 (m, 1 H), 8.83 (m, 2 H), 11.66 (s, 1 H), 12.41 (bs, 1 H); ^{13}C -NMR (75 MHz): (DMSO- d_6) δ in ppm: 56.16, 60.45, 102.33, 112.18, 112.33, 118.41, 120.90, 122.64, 126.26, 131.27, 131.82, 132.93, 136.67, 137.13, 150.17, 153.55, 153.70, 154.50 IR (cm^{-1}): 3324, 1653, 1615, 1583, 1532, 1504, 1428, 1419, 1237, 1222, 1124, 1113, 989, 967, 855, 819, 730, 708, 672. LC-MS: 7.1 min, m/z 378.2 $[\text{MH}]^+$ $\text{C}_{21}\text{H}_{19}\text{N}_3\text{O}_4$ (M_r 377.39) HRMS: m/z calculated 377.1375; found 377.1367. MP: 316 °C. Yield: 140 mg (68 %).

N-[2-(1*H*-Indol-3-yl)ethyl]-2-(3,5-dimethoxyphenyl)-2-oxoacetamide (**7b**). ^1H -NMR (300 MHz): (DMSO- d_6) δ in ppm: 2.94 (t, 2 H, $J = 7.20$ Hz), 3.53 (dt, 2 H, $J = 7.20, 5.68$ Hz), 3.77 (s, 6 H), 6.84 (m, 1 H), 6.91–7.12 (m, 4 H), 7.18 (m, 1 H), 7.33 (d, 1 H, $J = 7.96$ Hz), 7.57 (d, 1 H, $J = 7.71$ Hz), 9.03 (t, 1 H, $J = 5.68$ Hz), 10.84 (s, 1 H); ^{13}C -NMR (75 MHz): (DMSO- d_6) δ in ppm: 25.15, 55.92, 106.73, 107.68, 111.69, 111.73, 118.62, 121.31, 123.09, 127.50, 135.09, 136.60, 160.75, 160.93, 165.00, 190.26 IR (cm^{-1}): 1657, 1591, 1520, 1454, 1425, 1300, 1204, 1154, 1061, 846, 673. GC-MS: 17.4 min, m/z 352 $[\text{M}]^+$ $\text{C}_{20}\text{H}_{20}\text{N}_2\text{O}_4$ (M_r 353.38). MP: 90 °C. Yield: 1.1 g (73 %).

2-(3,5-Dimethoxyphenyl)-N-[2-(1*H*-indol-3-yl)-2-oxo-ethyl]-2-oxo-acetamide (**7c**). ¹H-NMR (300 MHz): (DMSO-d₆) δ in ppm: 3.85 (s, 6 H), 4.68 (d, 2 H, J = 5.81 Hz), 6.87 (s, 1 H), 7.28 (m, 3 H), 7.48 (m, 1 H), 8.15 (m, 1 H), 8.50 (s, 1 H), 9.24 (t, 1 H, J = 5.81 Hz), 12.08 (s, 1 H); ¹³C-NMR (75 MHz): (DMSO-d₆) δ in ppm: 45.78, 56.00, 107.16, 107.79, 112.60, 123.33, 125.70, 134.27, 135.26, 136.80, 161.02, 166.27, 189.34, 190.72; IR (cm⁻¹): 3253, 1692, 1661, 1649, 1634, 1593, 1521, 1456, 1430, 1355, 1313, 1286, 1210, 1155, 1064, 1027, 925, 844, 753, 743, 679. MS (EI): m/z 337.1 [M]⁺ C₂₀H₁₈N₂O₅ (M_r 366.37). MP: 183 °C. Yield: 0.5 g (44 %).

3-(3,5-Dimethoxyphenyl)-5-(1*H*-indol-3-yl)-1*H*-pyrazin-2-one (**7**). ¹H-NMR (300 MHz): (DMSO-d₆) δ in ppm: 3.83 (s, 6 H), 6.61 (s, 1 H), 7.11 (m, 2 H), 7.43 (d, 1 H, J = 7.45 Hz), 7.75 (m, 2 H), 7.92 (m, 2 H), 8.25 (d, 1 H, J = 8.08 Hz), 11.38 (s, 1 H); ¹³C-NMR (75 MHz): (DMSO-d₆) δ in ppm: 55.01, 101.45, 106.47, 111.86, 112.15, 119.55, 120.39, 121.52, 123.27, 124.82, 136.75, 138.33, 154.20, 160.05; IR (cm⁻¹): 3381, 2971, 1738, 1656, 1639, 1599, 1455, 1423, 1366, 1353, 1229, 1217, 1205, 1152, 1064, 824, 743, 701, 688. HRMS: m/z calculated 347.1270; found 347.1247 C₂₀H₁₇N₃O₃ (M_r 347.37). MP: 183 °C. Yield: 35 mg (15 %).

N-[2-(1*H*-Indol-3-yl)ethyl]-2-oxo-2-(2,3,4-trimethoxyphenyl)acetamide (**9b**). ¹H-NMR (300 MHz): (DMSO-d₆) δ in ppm: 2.94 (t, 2 H, J = 7.45 Hz), 3.49 (dt, 2 H, J = 7.45, 5.81 Hz), 3.74 (s, 3 H), 3.77 (s, 3 H), 3.88 (s, 1 H), 7.02 (m, 3 H), 7.21 (m, 1 H), 7.34 (d, 1 H, J = 7.96 Hz), 7.44 (m, 1 H), 7.57 (d, 1 H, J = 7.33 Hz), 8.69 (t, 1 H, J = 5.81 Hz), 10.84 (s, 1 H); ¹³C-NMR (75 MHz): (DMSO-d₆) δ in ppm: 25.33, 39.57, 56.61, 60.70, 61.70, 108.44, 111.72, 111.84, 118.55, 118.63, 121.29, 121.76, 123.13, 126.19, 127.51, 136.60, 141.55, 154.56, 158.86, 166.83,

190.50 IR (cm⁻¹): 3274, 1659, 1617, 1632, 1586, 1560, 1459, 1411, 1336, 1288, 1255, 1207, 1104, 1081, 1008, 883, 854, 818, 798, 751, 700; LC-MS: 7.2 min, m/z 405,1 [MNa]⁺ C₂₁H₂₂N₂O₅ (M_r 382.41). MP: 238 °C. Yield: 495 mg (78 %).

N-[2-(1*H*-Indol-3-yl)-2-oxo-ethyl]-2-oxo-2-(2,3,4-trimethoxyphenyl)acetamide (**9c**). ¹H-NMR (300 MHz): (DMSO-d₆) δ in ppm: 3.74 (s, 3 H), 3.80 (s, 3 H), 3.88 (s, 3 H), 4.62 (d, 2 H, J = 5.43 Hz), 6.98 (d, 1 H, J = 8.84 Hz), 7.22 (m, 2 H), 7.51 (m, 2 H), 8.19 (m, 1 H), 8.50 (d, 1 H, J = 1.89 Hz), 8.89 (t, 1 H, J = 5.43 Hz), 12.06 (s, s H); ¹³C-NMR (75 MHz): (DMSO-d₆) δ in ppm: 45.37, 56.25, 60.35, 61.37, 107.97, 112.17, 114.00, 121.14, 121.41, 121.88, 122.91, 125.39, 126.15, 133.84, 136.41, 141.25, 154.24, 158.47, 166.44, 189.32, 189.74; IR (cm⁻¹): 3221, 3121, 1681, 1671, 1642, 1614, 1590, 156, 1531, 1446, 1435, 1411, 1288, 1255, 1242, 1207, 1166, 1098, 1060, 1008, 972, 936, 928, 792, 760, 737, 701; LC-MS: 7.7 min, m/z 397,1 [MH]⁺ C₂₁H₂₀N₂O₆ (M_r 396.39). MP: 204 °C. Yield: 345 mg (74 %).

5-(1*H*-Indol-3-yl)-3-(2,3,4-trimethoxyphenyl)-1*H*-pyrazin-2-one (**9**). ¹H-NMR (300 MHz): (DMSO-d₆) δ in ppm: 3.77 (s, 3 H), 3.81 (s, 3 H), 3.86 (s, 3 H), 6.89 (d, 1 H, J = 8.59 Hz), 7.07 (m, 2 H), 7.40 (d, 1 H, J = 7.96 Hz), 7.78 (d, 1 H, J = 2.54 Hz), 7.85 (s, 1 H), 8.03 (d, 1 H, J = 7.71 Hz), 11.32 (s, 1 H), 12.15 (bs, 1 H); ¹³C-NMR (75 MHz): (DMSO-d₆) δ in ppm: 55.94, 60.21, 60.85, 107.43, 111.67, 112.18, 119.38, 120.37, 121.38, 123.14, 124.38, 124.64, 124.71, 136.66, 141.46, 151.70, 154.05, 154.32; IR (cm⁻¹): 3243, 1655, 1614, 1598, 1412, 1317, 1271, 1214, 1119, 1095, 1075, 1030, 1010, 992, 802, 762, 740, 687. LC-MS: 6.6 min, m/z 378.2 [MH]⁺ C₂₁H₁₉N₃O₄ (M_r 377.39) HRMS: m/z calculated 377.1375; found 377.1361. MP: 204 °C. Yield: 345 mg (74 %).

N-(2-(1*H*-Indol-3-yl)ethyl)-2-(4-ethoxy-3-methoxyphenyl)-2-oxoacetamide (**10b**). ¹H-NMR (300 MHz): (DMSO-*d*₆) δ in ppm: 1.36 (t, 3 H, J = 6.88 Hz), 2.95 (t, 2 H, J = 7.07 Hz), 3.54 (dt, 2 H, J = 7.07, 5.68 Hz), 3.78 (s, 3 H), 4.12 (q, 2 H, J = 6.88 Hz), 7.03 (m, 3 H), 7.19 (s, 1 H), 7.35 (d, 1 H, J = 7.83 Hz), 7.53 (m, 3 H), 8.92 (t, 1 H, J = 5.68 Hz), 10.84 (s, 1 H); ¹³C-NMR (75 MHz): (DMSO-*d*₆) δ in ppm: 14.44, 24.80, 55.43, 64.11, 110.77, 111.34, 111.38, 111.57, 118.26, 120.93, 122.79, 125.91, 127.17, 136.23, 148.77, 153.49, 165.21, 188.93; IR (cm⁻¹): 3407, 3299, 1668, 1643, 1595, 1513, 1458, 1419, 1343, 1271, 1258, 1240, 1176, 1143, 1021, 792, 766, 753, 730, 672. GC-MS: 21.9 min, m/z 366 [M]⁺ C₂₁H₂₂N₂O₄ (M_r 366.41). MP: 139 °C. Yield: 250 mg (76 %).

2-(4-Ethoxy-3-methoxy-phenyl)-N-[2-(1*H*-indol-3-yl)-2-oxo-ethyl]-2-oxo-acetamide (**10c**). ¹H-NMR (300 MHz): (DMSO-*d*₆) δ in ppm: 1.37 (t, 3 H, J = 6.76 Hz), 3.89 (s, 3 H), 4.15 (q, 2 H, J = 6.76 Hz), 4.67 (d, 2 H, J = 5.81 Hz), 7.19 (m, 3 H), 7.50 (m, 1 H), 7.69 (d, 1 H, J = 1.64 Hz), 7.83 (d, 1 H, J = 8.46 Hz), 8.19 (m, 1 H), 8.52 (d, 1 H, J = 2.40 Hz), 9.14 (t, 1 H, J = 5.81 Hz), 12.07 (s, 1 H); ¹³C-NMR (75 MHz): (DMSO-*d*₆) δ in ppm: 14.48, 45.43, 55.52, 64.16, 111.55, 111.81, 112.23, 113.90, 121.11, 121.93, 122.95, 125.36, 125.58, 125.67, 133.84, 136.44, 148.78, 153.59, 166.16, 189.10; IR (cm⁻¹): 3365, 1674, 1648, 1592, 1511, 1466, 1433, 1417, 1391, 1309, 1264, 1245, 1141, 1116, 1033, 1016, 943, 883, 795, 776, 736, 664. LC-MS: 7.5 min, m/z 381.1 [MH]⁺ C₂₁H₂₀N₂O₅ (M_r 380.39). MP: 201 °C. Yield: 165 mg (55 %).

3-(4-Ethoxy-3-methoxy-phenyl)-5-(1*H*-indol-3-yl)-1*H*-pyrazin-2-one (**10**). ¹H-NMR (300 MHz): (DMSO-*d*₆) δ in ppm: 1.37 (t, 3 H, J = 6.78 Hz), 3.87 (s, 3 H), 4.10 (q, 2 H, J = 6.78 Hz), 7.10

(m, 3 H), 7.43 (d, 1 H, $J = 8.08$ Hz), 7.80 (s, 1 H), 7.89 (s, 1 H), 8.17 (s, 1 H), 8.26 (m, 2 H), 11.34 (s, 1 H), 12.43 (bs, 1 H); ^{13}C -NMR (75 MHz): (DMSO- d_6) δ in ppm: 14.69, 55.20, 63.64, 111.47, 111.77, 111.80, 112.27, 119.41, 120.37, 121.41, 122.06, 123.08, 124.78, 129.15, 136.70, 148.20, 149.38, 154.14; IR (cm^{-1}): 3378, 1636, 1618, 1602, 1505, 1452, 1420, 1392, 1273, 1226, 1140, 1117, 1032, 832, 805, 783, 744. LC-MS: 7.7 min, m/z 362.3 $[\text{MH}]^+$ $\text{C}_{21}\text{H}_{19}\text{N}_3\text{O}_3$ (M_r 361.39) HRMS: m/z calculated 361.1426; found 361.1409. MP: 212 °C. Yield: 10 mg (11 %).

N-(2-(1*H*-Indol-3-yl)ethyl)-2-(1,3-benzodioxol-5-yl)-2-oxoacetamide (**11b**). ^1H -NMR (300 MHz): (DMSO- d_6) δ in ppm: 2.93 (t, 2 H, $J = 7.20$ Hz), 3.52 (dt, 2 H, $J = 7.20, 5.68$ Hz), 6.17 (s, 2 H), 7.02 (m, 3 H), 7.18 (d, 1 H, $J = 2.27$ Hz), 7.35 (m, 2 H), 7.49 (dd, 1 H, $J = 8.21, 1.77$ Hz), 7.57 (d, 1 H, $J = 7.20$ Hz), 8.94 (t, 1 H, $J = 5.68$ Hz), 10.83 (s, 1 H); ^{13}C -NMR (75 MHz): (DMSO- d_6) δ in ppm: 25.15, 39.54, 102.71, 108.24, 108.60, 111.72, 118.63, 121.30, 123.21, 127.52, 127.79, 128.05, 136.59, 148.34, 153.00, 165.36, 188.92; IR (cm^{-1}): 3345, 1651, 1615, 1597, 1554, 1497, 1448, 1421, 1311, 1250, 1116, 1035, 916, 827, 766. GC-MS: 17.0 min, m/z 336 $[\text{M}]^+$ $\text{C}_{19}\text{H}_{16}\text{N}_2\text{O}_4$ (M_r 336.34). MP: 79 °C. Yield: 2.2 g (79 %).

2-(1,3-Benzodioxol-5-yl)-N-[2-(1*H*-indol-3-yl)-2-oxo-ethyl]-2-oxo-acetamide (**11c**). ^1H -NMR (300 MHz): (DMSO- d_6) δ in ppm: 4.65 (d, 2 H, $J = 5.81$ Hz), 6.22 (s, 2 H), 7.21 (m, 3 H), 7.54 (m, 2 H), 7.84 (d, 1 H, $J = 8.59$ Hz), 8.19 (m, 1 H), 8.51 (s, 1 H), 9.15 (t, 1 H, $J = 5.81$ Hz), 12.07 (s, 1 H); ^{13}C -NMR (75 MHz): (DMSO- d_6) δ in ppm: 45.80, 102.75, 108.64, 108.80, 112.58, 114.23, 121.50, 122.28, 123.31, 125.68, 127.94, 134.22, 136.79, 148.36, 153.14, 166.16, 188.56, 189.34; IR (cm^{-1}): 3405, 3289, 1691, 1649, 1630, 1616, 1599, 1505, 1483, 1446, 1434, 1316,

1283, 1262, 1245, 1163, 1145, 1088, 1039, 940, 878, 796, 735, 714. MS (EI): m/z 350.1 $[M]^+$
 $C_{19}H_{14}N_2O_5$ (M_r 350.32). MP: 257 °C. Yield: 2.4 g (89 %).

3-(1,3-Benzodioxol-5-yl)-5-(1*H*-indol-3-yl)-1*H*-pyrazin-2-one (**11**). 1H -NMR (300 MHz): (DMSO- d_6) δ in ppm: 6.11 (s, 2 H), 7.09 (m, 3 H), 7.43 (d, 1 H, $J = 7.33$ Hz), 7.80 (s, 1 H), 7.89 (d, 1 H, $J = 1.52$ Hz), 8.02 (s, 1 H), 8.11 (d, 1 H, $J = 7.33$ Hz), 8.22 (d, 1 H, $J = 8.46$ Hz), 11.36 (s, 1 H), 12.48 (bs, 1 H); ^{13}C -NMR (75 MHz): (DMSO- d_6) δ in ppm: 101.60, 108.16, 108.50, 112.17, 112.60, 119.92, 120.47, 121.80, 123.70, 123.75, 125.00, 131.06, 137.09, 147.44, 148.68, 154.47; IR (cm^{-1}): 3398, 1971, 1739, 1441, 1366, 1260, 1228, 1217, 1037, 928, 915, 874, 812, 751, 662. LC-MS: 7.1 min, m/z 331.1 $[MH]^+$ $C_{19}H_{13}N_3O_3$ (M_r 331.32) HRMS: m/z calculated 331.0957; found 331.0970. MP: 253 °C. Yield: 50 mg (13 %).

N-(2-(1*H*-Indol-3-yl)ethyl)-2-(4-ethylphenyl)-2-oxoacetamide (**14b**). 1H -NMR (300 MHz): (DMSO- d_6) δ in ppm: 1.18 (t, 3 H, $J = 7.52$ Hz), 2.68 (q, 2 H, $J = 7.52$ Hz), 2.97 (t, 2 H, $J = 6.82$ Hz), 3.55 (m, 2 H), 7.04 (m, 2 H), 7.20 (s, 1 H), 7.37 (m, 3 H), 7.59 (d, 1 H, $J = 7.58$ Hz), 7.82 (d, 2 H, $J = 8.08$ Hz), 8.96 (m, 1 H), 10.84 (s, 1 H); ^{13}C NMR (75 MHz): (DMSO- d_6) δ in ppm: 15.02, 24.79, 28.30, 39.15, 111.35, 118.25, 120.92, 122.83, 127.17, 128.21, 129.97, 130.70, 136.25, 151.10, 165.04, 190.10; IR (cm^{-1}): 3047, 2972, 1674, 1662, 1635, 1603, 1457, 1346, 1318, 1227, 1181, 110, 1072, 789, 758, 738. GC-MS: m/z 320 $[M]^+$ $C_{20}H_{20}N_2O_2$ (M_r 320.39). MP: 116 °C. Yield: 600 mg (88 %).

2-(4-Ethylphenyl)-N-[2-(1*H*-indol-3-yl)-2-oxo-ethyl]-2-oxo-acetamide (**14c**). 1H -NMR (300 MHz): (DMSO- d_6) δ in ppm: 1.22 (t, 3 H, $J = 7.52$ Hz), 2.71 (q, 2 H, $J = 7.52$ Hz), 4.68 (d,

2 H, $J = 5.81$ Hz), 7.23 (m, 2 H), 7.47 (m, 3 H), 8.05 (d, 2 H, $J = 7.96$ Hz), 8.20 (m, 1 H), 8.50 (d, 1 H, $J = 2.53$ Hz), 9.17 (t, 1 H, $J = 5.81$ Hz), 12.06 (s, 1 H); ^{13}C -NMR (75 MHz): (DMSO- d_6) δ in ppm: 15.05, 28.32, 45.39, 112.19, 113.89, 121.13, 121.88, 122.90, 125.31, 128.29, 130.13, 130.83, 133.79, 136.42, 151.29, 165.65, 188.90, 189.99; IR (cm^{-1}): 3380, 1685, 1659, 1635, 1618, 1602, 1530, 1492, 1444, 1434, 1412, 1315, 1270, 1246, 1151, 1110, 1092, 937, 856, 741, 701. LC-MS: 8.4 min, m/z 335.1 $[\text{MH}]^+$ $\text{C}_{20}\text{H}_{18}\text{N}_2\text{O}_3$ (M_r 334.37). MP: 217 °C. Yield: 240 mg (38 %).

3-(4-Ethylphenyl)-5-(1*H*-indol-3-yl)-1*H*-pyrazin-2-one (**14**). ^1H -NMR (300 MHz): (DMSO- d_6) δ in ppm: 1.23 (t, 3 H, $J = 7.45$ Hz), 2.67 (q, 2 H, $J = 7.45$ Hz), 7.12 (m, 2 H), 7.34 (d, 2 H, $J = 8.08$ Hz), 7.43 (d, 1 H, $J = 7.83$ Hz), 7.84 (s, 1 H), 7.89 (s, 1 H), 8.17 (d, 1 H, $J = 7.83$ Hz), 8.38 (d, 2 H, $J = 8.08$ Hz), 11.35 (s, 1 H), 12.44 (bs, 1 H); ^{13}C -NMR (75 MHz): (DMSO- d_6) δ in ppm: 15.43, 28.05, 111.74, 112.25, 119.54, 120.29, 121.42, 123.27, 124.71, 127.36, 128.46, 134.08, 136.71, 145.16, 154.20; IR (cm^{-1}): 3421, 1636, 1606, 155, 1426, 1288, 1231, 1087, 1043, 1018, 984, 967, 881, 843, 819, 740, 714. LC-MS: 7.8 min, m/z 316.2 $[\text{MH}]^+$ $\text{C}_{20}\text{H}_{17}\text{N}_3\text{O}$ (M_r 315.37) HRMS: m/z calculated 315.1371; found 315.1355. MP: 267 °C. Yield: 5 mg (5 %)

N-[2-(5-Methyl-1*H*-indol-3-yl)ethyl]-2-(3,4,5-trimethoxyphenyl)-2-oxoacetamide (**17b**). ^1H -NMR (300 MHz): (DMSO- d_6) δ in ppm: 2.34 (s, 3 H), 2.92 (t, 2 H, $J = 7.20$ Hz), 3.53 (dt, 2 H, $J = 7.20, 5.68$ Hz), 3.76 (s, 9 H), 6.87 (m, 1 H), 7.23 (m, 6 H), 8.99 (t, 1 H, $J = 5.68$ Hz), 10.68 (s, 1 H); ^{13}C -NMR (75 MHz): (DMSO- d_6) δ in ppm: 21.22, 24.80, 39.19, 55.98, 60.26, 107.25, 110.91, 111.04, 117.86, 122.54, 122.75, 125.29, 126.62, 127.40, 128.01, 128.18, 128.88, 134.62, 143.10, 152.76, 164.59, 188.92; IR (cm^{-1}): 3369, 3283, 1675, 1655, 1636, 1578, 1501, 1414,

1334, 1160, 1127, 996, 876. GC-MS: m/z 396 $[M]^+$ $C_{22}H_{24}N_2O_5$ (M_r 396.44). MP: 97 °C. Yield: 400 mg (97 %).

N-[2-(5-Methyl-1*H*-Indol-3-yl)-2-oxoethyl]-2-(3,4,5-trimethoxyphenyl)-2-oxoacetamide (**17c**).

1H -NMR (300 MHz): (DMSO- d_6) δ in ppm: 2.40 (s, 3 H), 3.79 (s, 3 H), 3.91 (s, 6 H), 4.65 (d, 2 H, $J = 5.68$ Hz), 7.05 (d, 1 H, $J = 8.21$ Hz), 7.37 (d, 1 H, $J = 8.21$ Hz), 7.55 (s, 2 H), 7.94 (s, 1 H), 8.43 (d, 1 H, $J = 2.53$ Hz), 9.18 (t, 1 H, $J = 5.68$ Hz), 11.95 (s, 1 H); ^{13}C -NMR (75 MHz): (DMSO- d_6) δ in ppm: 21.34, 45.41, 56.07, 60.26, 107.49, 111.83, 113.45, 120.76, 124.37, 125.62, 128.14, 130.73, 133.77, 134.71, 143.11, 152.90, 166.16, 188.97, 189.62; IR (cm^{-1}): 3332, 1692, 1650, 1625, 1588, 1545, 1526, 1416, 1335, 1323, 1162, 1122, 990, 799, 765, 724. LC-MS: 7.8 min, m/z 411,1 $[MH]^+$ $C_{22}H_{22}N_2O_6$ (M_r 410.42). MP: 208 °C. Yield: 240 mg (77 %).

5-(5-Methyl-1*H*-indol-3-yl)-3-(3,4,5-trimethoxyphenyl)pyrazin-2(1*H*)-one (**17**). 1H -NMR

(300 MHz): (DMSO- d_6) δ in ppm: 2.39 (s, 3 H), 3.75 (s, 3 H), 3.89 (s, 6 H), 6.96 (d, 1 H, $J = 8.08$ Hz), 7.30 (d, 1 H, $J = 8.08$ Hz), 7.85 (m, 2 H), 8.00 (s, 1 H), 8.08 (s, 1 H), 11.21 (s, 1 H), 12.52 (bs, 1 H); ^{13}C -NMR (75 MHz): (DMSO- d_6) δ in ppm: 21.38, 55.76, 60.11, 105.97, 111.41, 111.61, 119.98, 123.08, 123.28, 125.07, 127.87, 131.92, 135.10, 138.89, 152.29, 154.10; IR (cm^{-1}): 3354, 1634, 1600, 1579, 1539, 1499, 1456, 1411, 1327, 1216, 1169, 1120, 987, 868, 843, 784, 768. LC-MS: 6.8 min, m/z 392.3 $[MH]^+$ $C_{22}H_{21}N_3O_4$ (M_r 391.42) HRMS: m/z calculated 391.1532; found 391.1514. MP: 304 °C. Yield: 16 mg (17 %).

N-[2-(1-Methylindol-3-yl)-2-oxo-ethyl]-2-oxo-2-(3,4,5-trimethoxyphenyl)acetamide (**18a**). 1H -

NMR (300 MHz): (DMSO- d_6) δ in ppm: 3.79 (s, 3 H), 3.89 (s, 3 H), 3.93 (s, 6 H), 4.65 (d, 2 H, J

= 5.31 Hz), 7.28 (m, 2 H), 7.57 (m, 3 H), 8.15 (d, 1 H, $J = 7.58$ Hz), 8.53 (s, 1 H), 9.22 (t, 1 H, $J = 5.31$ Hz); ^{13}C -NMR (75 MHz): (DMSO- d_6) δ in ppm: 33.26, 45.33, 56.11, 60.28, 107.46, 110.76, 112.68, 121.12, 122.32, 123.01, 125.75, 128.14, 137.10, 143.12, 152.94, 166.25, 188.57, 189.72; IR (cm^{-1}): 3294, 1670, 1614, 1578, 1527, 1466, 1416, 1375, 1339, 1162, 1126, 1083, 995, 912, 860, 753, 726. LC-MS: 7.9 min, m/z 411.1 $[\text{MH}]^+$ $\text{C}_{22}\text{H}_{22}\text{N}_2\text{O}_6$ (M_r 410.42). MP: 165 °C. Yield: 80 mg (13 %).

5-(1-Methylindol-3-yl)-3-(3,4,5-trimethoxyphenyl)-1*H*-pyrazin-2-one (18). ^1H -NMR (300 MHz): (DMSO- d_6) δ in ppm: 3.75 (s, 3 H), 3.84 (s, 3 H), 3.87 (s, 6 H), 7.17 (m, 2 H), 7.49 (d, 1 H, $J = 8.08$ Hz), 7.83 (s, 1 H), 7.90 (s, 1 H), 7.97 (s, 2 H), 8.27 (d, 1 H, $J = 7.83$ Hz), 12.58 (bs, 1 H); ^{13}C -NMR (75 MHz): (DMSO- d_6) δ in ppm: 32.65, 55.78, 60.10, 106.02, 110.09, 111.24, 119.63, 120.56, 121.57, 125.09, 127.36, 131.83, 137.10, 138.93, 152.29, 154.07 IR (cm^{-1}): 1638, 1615, 1579, 1504, 1464, 1412, 1383, 1337, 1319, 1232, 1220, 1123, 998, 868, 811, 765, 735. LC-MS: 7.2 min, m/z 392.2 $[\text{MH}]^+$ $\text{C}_{22}\text{H}_{21}\text{N}_3\text{O}_4$ (M_r 391.42) HRMS: m/z calculated 391.1532; found 391.1516. MP: 226 °C. Yield: 12 mg (18 %).

N-[2-(6-Fluoro-1*H*-indol-3-yl)-2-oxo-ethyl]-2-oxo-2-(3,4,5-trimethoxyphenyl)acetamide (19a). ^1H -NMR (300 MHz): (DMSO- d_6) δ in ppm: 2.93 (t, 2 H, $J = 7.14$ Hz), 5.54 (dt, 2 H, $J = 7.14$, 5.68 Hz), 3.77 (s, 9 H), 6.82 (m, 1 H), 7.10 (m, 1 H), 7.23 (m, 3 H), 7.54 (dd, 1 H, $J = 8.72$, 5.56 Hz), 8.99 (t, 1 H, $J = 5.68$ Hz), 10.91 (s, 1 H); ^{13}C -NMR (75 MHz): (DMSO- d_6) δ in ppm: 24.67, 39.06, 55.98, 60.26, 97.25 ($^2J_{\text{CF}} = 25.3$ Hz), 106.70 ($^2J_{\text{CF}} = 24.2$ Hz), 107.26, 111.70, 119.21 ($^3J_{\text{CF}} = 10.3$ Hz), 123.27 ($^4J_{\text{CF}} = 2.9$ Hz), 124.05, 127.98, 136.01 ($^3J_{\text{CF}} = 12.7$ Hz), 143.12, 152.75, 158.84 ($^1J_{\text{CF}} = 232.2$ Hz), 164.57, 188.87; IR (cm^{-1}): 3354, 1661, 1646, 1580, 1502,

1454, 1412, 1333, 1232, 1159, 1122, 1089, 991, 951, 803, 755. GC-MS: m/z 400 $[M]^+$
 $C_{21}H_{21}FN_2O_5$ (M_r 400.10). MP: 140 °C. Yield: 330 mg (79 %).

5-(6-Fluoro-1*H*-indol-3-yl)-3-(3,4,5-trimethoxyphenyl)-1*H*-pyrazin-2-one (**19**). 1H -NMR (300 MHz): (DMSO- d_6) δ in ppm: 3.79 (s, 3 H), 3.92 (s, 6 H), 4.68 (d, 2 H, $J = 5.94$ Hz), 7.08 (dd, 1 H, $J = 9.82, 8.72, 2.34$ Hz), 7.30 (dd, 1 H, $J = 9.66, 2.34$ Hz), 7.55 (s, 2 H), 8.12 (dd, 1 H, $J = 8.72, 5.68$ Hz), 8.52 (d, 1 H, $J = 3.03$ Hz), 9.23 (t, 1 H, $J = 5.94$ Hz), 12.13 (s, 1 H); ^{13}C -NMR (75 MHz): (DMSO- d_6) δ in ppm: 45.38, 56.10, 60.28, 98.52 ($^2J_{CF} = 25.6$ Hz), 107.45, 110.33 ($^2J_{CF} = 23.8$ Hz), 113.80, 122.04, 122.12 ($^3J_{CF} = 10.3$ Hz), 128.13, 134.62 ($^4J_{CF} = 2.3$ Hz), 136.51 ($^3J_{CF} = 12.6$ Hz), 152.95, 159.32 ($^1J_{CF} = 235.5$ Hz), 166.24, 189.22, 189.69; IR (cm^{-1}): 3308, 1694, 1643, 1623, 1575, 1501, 1414, 1340, 1320, 1288, 1227, 1126, 1107, 1092, 993, 949, 936, 834, 815, 760. LC-MS: 7.7 min, m/z 415.1 $[MH]^+$ $C_{21}H_{19}FN_2O_6$ (M_r 414.38). MP: 216 °C. Yield: 225 mg (72 %).

N-[2-(6-Methoxy-1*H*-indol-3-yl)ethyl]-2-(3,4,5-trimethoxyphenyl)-2-oxoacetamide (**20b**). 1H -NMR (300 MHz): (DMSO- d_6) δ in ppm: 2.91 (t, 2 H, $J = 7.20$ Hz), 3.53 (dt, 2 H, $J = 7.20, 5.68$ Hz), 3.73 (s, 3 H), 3.77 (s, 9 H), 6.63 (dd, 1 H, $J = 8.55, 2.18$ Hz), 7.05 (d, 1 H, $J = 1.77$ Hz), 7.27 (s, 2 H), 7.47 (d, 1 H, $J = 8.55$ Hz), 8.98 (t, 1 H, $J = 5.68$ Hz), 10.62 (s, 1 H); ^{13}C -NMR (75 MHz): (DMSO- d_6) δ in ppm: 24.88, 39.17, 55.14, 56.00, 60.28, 94.46, 107.27, 108.50, 111.41, 118.82, 121.22, 121.60, 128.03, 136.95, 143.12, 152.78, 155.54, 164.59, 188.93 IR (cm^{-1}): 1653, 1628, 1579, 1500, 1453, 1413, 1333, 1233, 1158, 1121, 1026, 994, 803. GC-MS: m/z 412 $[M]^+$ $C_{22}H_{24}N_2O_6$ (M_r 412.44). MP: 80 °C. Yield: 400 mg (93 %).

N-[2-(6-Methoxy-1*H*-indol-3-yl)-2-oxo-ethyl]-2-oxo-2-(3,4,5-trimethoxyphenyl)acetamide

(**20c**). ¹H-NMR (300 MHz): (DMSO-*d*₆) δ in ppm: 3.79 (s, 6 H), 3.91 (s, 6 H), 4.64 (d, 2 H, J = 5.68 Hz), 6.85 (d, 1 H, J = 8.72 Hz), 6.97 (s, 1 H), 7.55 (s, 2 H), 7.98 (d, 1 H, J = 8.72 Hz), 8.36 (d, 1 H, J = 2.53 Hz), 9.18 (t, 1 H, J = 5.68 Hz), 11.86 (s, 1 H); ¹³C-NMR (75 MHz): (DMSO-*d*₆) δ in ppm: 45.26, 55.18, 56.09, 60.25, 95.25, 107.46, 111.74, 113.89, 119.29, 121.59, 128.12, 132.85, 137.31, 143.11, 152.91, 156.41, 166.19, 188.96, 189.68; IR (cm⁻¹): 3420, 3254, 1682, 1646, 1622, 1571, 1534, 1499, 1452, 1440, 1408, 1341, 1300, 1221, 1165, 1149, 1111, 1092, 1001, 948, 818. LC-MS: 7.4 min, m/z 427.1 [MH]⁺ C₂₂H₂₂N₂O₇ (Mr 426.42). MP: 212 °C. Yield: 174 mg (56 %).

5-(6-Methoxy-1*H*-indol-3-yl)-3-(3,4,5-trimethoxyphenyl)-1*H*-pyrazin-2-one (**20**). ¹H-NMR (300 MHz): (DMSO-*d*₆) δ in ppm: 3.73 (s, 3 H), 3.78 (s, 3 H), 3.87 (s, 6 H), 6.74 (d, 1 H, J = 8.72 Hz), 6.91 (s, 1 H), 7.78 (s, 1 H), 7.86 (s, 1 H), 7.97 (s, 2 H), 8.15 (d, 1 H, J = 8.72 Hz), 11.13 (s, 1 H), 12.51 (bs, 1 H); ¹³C-NMR (75 MHz): (DMSO-*d*₆) δ in ppm: 55.12, 55.76, 60.11, 94.59, 105.93, 109.71, 112.12, 119.18, 121.71, 122.37, 131.92, 132.34, 137.49, 138.86, 146.94, 152.30, 154.11, 155.66; IR (cm⁻¹): 3370, 1644, 1617, 1583, 1505, 1460, 1412, 1339, 1326, 1293, 1224, 1128, 1031, 1013, 1000, 867, 804, 771. HRMS: m/z calculated 407.1481; found 407.1477 C₂₂H₂₁N₃O₅ (Mr 407.42). MP: 250 °C. Yield: 20 mg (21 %).

Methyl-3-[2-[[2-oxo-2-(3,4,5-trimethoxyphenyl)acetyl]amino]acetyl]-1*H*-indole-6-carboxylate

(**21a**). ¹H-NMR (300 MHz): (DMSO-*d*₆) δ in ppm: 3.79 (s, 3 H), 3.87 (s, 3 H), 3.92 (s, 6 H), 4.71 (d, 2 H, J = 5.90 Hz), 7.54 (s, 2 H), 7.83 (dd, 1 H, J = 8.42, 1.49 Hz), 8.13 (dd, 1 H, J = 1.49, 0.66 Hz), 8.22 (dd, 1 H, J = 8.42, 0.66 Hz), 8.71 (s, 1 H), 9.24 (t, 1 H, J = 5.90 Hz), 12.43 (bs, 1

H); ^{13}C -NMR (75 MHz): (DMSO- d_6) δ in ppm: 45.62, 51.99, 56.12, 60.29, 107.46, 113.98, 120.89, 122.60, 124.09, 128.13, 128.97, 135.87, 136.82, 143.14, 152.94, 166.24, 166.67, 189.34, 189.64; IR (cm^{-1}): 3302, 3104, 2948, 1711, 1654, 1623, 1582, 1503, 1413, 1339, 1297, 1277, 1211, 1122, 1080, 987, 920, 771, 745 731. LC-MS: 7.4 min, m/z 455.0 $[\text{MH}]^+$ $\text{C}_{23}\text{H}_{22}\text{N}_2\text{O}_8$ (M_r 454.43). MP: 212 °C. Yield: 160 mg (38 %).

Methyl-3-[6-oxo-5-(3,4,5-trimethoxyphenyl)-1*H*-pyrazin-3-yl]-1*H*-indole-6-carboxylate (**21**).

^1H -NMR (300 MHz): (DMSO- d_6) δ in ppm: 3.75 (s, 3 H), 3.86 (s, 3 H), 3.88 (s, 6 H), 7.69 (dd, 1 H, $J = 8.59, 1.65$ Hz), 7.93 (s, 1 H), 7.99 (s, 2 H), 8.10 (dd, 1 H, $J = 1.65, 0.66$ Hz), 8.17 (d, 1 H, $J = 2.64$ Hz), 8.38 (d, 1 H, $J = 8.59$ Hz) 11.76 (d, 1 H, $J = 2.64$ Hz), 12.56 (bs, 1 H)M; ^{13}C -NMR (75 MHz): (DMSO- d_6) δ in ppm: 51.81, 55.77, 60.12, 105.98, 112.72, 113.82, 119.96, 120.29, 122.46, 122.84, 126.86, 128.22, 131.21, 131.78, 135.97, 138.97, 147.36, 152.32, 154.22, 167.09; IR (cm^{-1}): 3315, 1708, 1688, 1636, 1623, 1502, 1440, 1413, 1331, 1282, 1215, 1119, 1109, 987, 768, 740, 712. LC-MS: 8.0 min, m/z 436.3 $[\text{MH}]^+$ $\text{C}_{23}\text{H}_{21}\text{N}_3\text{O}_6$ (M_r 435.43). MP: 298 °C (decomposition). Yield: 76 mg (57 %).

N-[2-(Benzofuran-3-yl)-2-oxo-ethyl]-2-oxo-2-(3,4,5-trimethoxyphenyl)acetamide (**22a**).

^1H -NMR (300 MHz): (DMSO- d_6) δ in ppm: 3.80 (s, 3 H), 3.92 (s, 6 H), 4.74 (d, 2 H, $J = 5.56$ Hz), 7.44 (m, 2 H), 7.51 (s, 2 H), 7.74 (d, 1 H, $J = 7.58$ Hz), 8.08 (d, 1 H, $J = 7.58$ Hz), 9.15 (s, 1 H), 9.34 (t, 1 H, $J = 5.56$ Hz); ^{13}C -NMR (75 MHz): (DMSO- d_6) δ in ppm: 46.33, 56.08, 60.28, 107.39, 111.81, 119.00, 121.79, 123.65, 124.76, 125.83, 127.99, 143.20, 152.92, 153.76, 154.70, 166.15, 189.33, 190.35; IR (cm^{-1}): 1675, 1642, 1584, 1560, 1551, 1504, 1454, 1417, 1338, 1287,

1259, 1236, 1195, 1169, 1127, 1082, 995, 925, 761. LC-MS: 8.2 min, m/z 398.1 $[\text{MH}]^+$
 $\text{C}_{21}\text{H}_{19}\text{NO}_7$ (M_r 397.38). MP: 195 °C. Yield: 231 mg (82 %).

5-(Benzofuran-3-yl)-3-(3,4,5-trimethoxyphenyl)-1*H*-pyrazin-2-one (**22**). $^1\text{H-NMR}$ (300 MHz): (DMSO- d_6) δ in ppm: 3.75 (s, 3 H), 3.87 (s, 6 H), 7.37 (m, 2 H), 7.65 (d, 1 H, $J = 8.08$ Hz), 7.95 (s, 2 H), 8.00 (s, 1 H), 8.27 (d, 1 H, $J = 7.07$ Hz), 8.52 (s, 1 H), 12.76 (bs, 1 H); $^{13}\text{C-NMR}$ (75 MHz): (DMSO- d_6) δ in ppm: 55.79, 60.12, 106.03, 111.63, 118.04, 121.64, 123.15, 124.02, 124.73, 125.17, 127.06, 131.40, 139.19, 142.49, 148.68, 152.33, 154.55, 155.10; IR (cm^{-1}): 3367, 1639, 1615, 1582, 1505, 1460, 1447, 1412, 1339, 1231, 1124, 1093, 1002, 857, 740. HRMS: m/z calculated 378.1215; found 378.1207 $\text{C}_{21}\text{H}_{18}\text{N}_2\text{O}_5$ (M_r 378.38). MP: 214 °C. Yield: 31 mg (33 %).

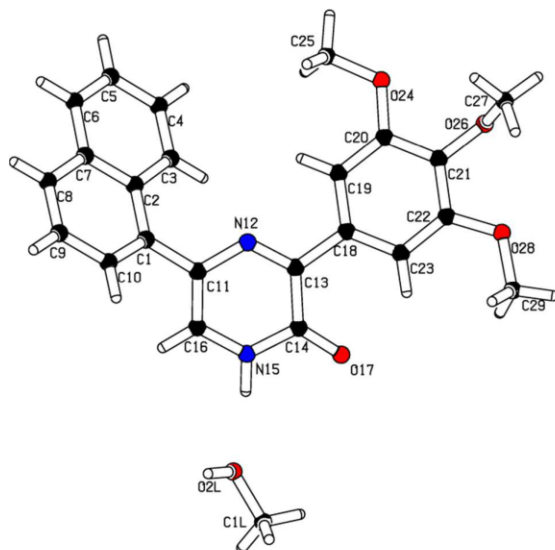
N-[2-(Quinolin-3-yl)-2-oxoethyl]-2-(3,4,5-trimethoxyphenyl)-2-oxoacetamide (**23a**). $^1\text{H-NMR}$ (300 MHz): (DMSO- d_6) δ in ppm: 3.80 (s, 3 H), 3.89 (s, 6 H), 5.01 (d, 2 H, $J = 5.56$ Hz), 7.49 (s, 2 H), 7.75 (m, 1 H), 7.94 (m, 1 H), 8.12 (m, 1 H), 8.19 (m, 1 H), 9.18 (m, 1 H), 9.38 (m, 2 H); $^{13}\text{C-NMR}$ (75 MHz): (DMSO- d_6) δ in ppm: 46.03, 56.16, 60.31, 107.43, 126.47, 127.21, 127.73, 128.01, 128.85, 129.83, 132.41, 137.69, 143.29, 148.45, 149.25, 152.95, 166.09, 189.26, 194.11; IR (cm^{-1}): 3390, 1689, 1674, 1652, 1616, 1576, 1499, 1413, 1331, 1315, 1232, 1164, 1123, 994, 955, 980, 789, 756, 728. LC-MS: 7.3 min, m/z 409.3 $[\text{MH}]^+$ $\text{C}_{22}\text{H}_{20}\text{N}_2\text{O}_6$ (M_r 408.40). MP: 211 °C. Yield: 240 mg (47 %).

5-(3-Quinolyl)-3-(3,4,5-trimethoxyphenyl)-1*H*-pyrazin-2-one (**23**). $^1\text{H-NMR}$ (300 MHz): (DMSO- d_6) δ in ppm: 3.75 (s, 3 H), 3.88 (s, 6 H), 7.62 (m, 1 H), 7.74 (m, 1 H), 7.93 (s, 2 H),

8.03 (m, 2 H), 8.30 (s, 1 H), 8.85 (s, 1 H), 9.53 (s, 1 H), 12.90 (s, 1 H); ^{13}C -NMR (75 MHz): (DMSO- d_6) δ in ppm: 55.90, 60.10, 106.36, 124.35, 126.96, 127.52, 128.38, 128.63, 128.96, 129.26, 130.39, 131.21, 139.42, 146.72, 147.87, 152.30, 154.75; IR (cm^{-1}): 1643, 1634, 1608, 1583, 1505, 1469, 1411, 1340, 1311, 1250, 1228, 1197, 1180, 1124, 1008, 913, 866, 853, 7822, 769, 749, 702. LC-MS: 6.3 min, m/z 390.1 $[\text{MH}]^+$ $\text{C}_{22}\text{H}_{19}\text{N}_3\text{O}_4$ (M_r 389.40) HRMS: m/z calculated 189.1375; found 189.1369. MP: 242 °C. Yield: 19 mg (20 %).

N-[2-(1-Naphthyl)-2-oxo-ethyl]-2-oxo-2-(3,4,5-trimethoxyphenyl)acetamide (**24a**). ^1H -NMR (300 MHz): (DMSO- d_6) δ in ppm: 3.80 (s, 3 H), 3.89 (s, 6 H), 4.86 (d, 2 H, $J = 5.68$ Hz), 7.52 (m, 3 H), 7.63 (m, 3 H), 8.03 (m, 1 H), 8.20 (m, 2 H), 8.55 (m, 1 H), 9.45 (t, 1 H, $J = 5.68$ Hz); ^{13}C -NMR (75 MHz): (DMSO- d_6) δ in ppm: 56.06, 60.30, 107.40, 124.80, 125.04, 126.54, 127.99, 128.06, 128.30, 128.60, 129.50, 133.00, 133.48, 143.21, 152.94, 1666.19, 189.33, 198.55; IR (cm^{-1}): 3378, 2939, 1690, 1678, 1668, 1652, 1578, 1498, 1452, 1414, 1337, 1317, 1224, 1167, 1126, 1091, 990, 940, 875, 801, 774, 766. MS (EI): m/z 407.0 $[\text{M}]^+$ $\text{C}_{23}\text{H}_{21}\text{NO}_6$ (M_r 407.42). MP: 124 °C. Yield: 200 mg (32 %).

5-(1-Naphthyl)-3-(3,4,5-trimethoxyphenyl)-1*H*-pyrazin-2-one (**24**). ^1H -NMR (300 MHz): (DMSO- d_6) δ in ppm: 3.72 (s, 3 H), 3.77 (s, 6 H), 7.59 (m, 4 H), 7.72 (s, 1 H), 7.87 (s, 2 H), 7.98 (m, 2 H), 8.28 (m, 1 H), 12.78 (bs, 1 H); ^{13}C -NMR (75 MHz): (DMSO- d_6) δ in ppm: 55.79, 60.12, 106.15, 125.50, 125.61, 126.00, 126.18, 126.83, 128.32, 128.40, 130.90, 131.46, 133.28, 133.69, 134.16, 139.18, 148.33, 152.28, 154.51; IR (cm^{-1}): 2934, 1653, 1579, 1503, 1465, 1411, 1337, 1228, 1176, 1124, 990, 864, 810, 782, 770, 678. HRMS: m/z calculated 388.1423; found 388.1420 $\text{C}_{23}\text{H}_{20}\text{N}_2\text{O}_4$ (M_r 388.42). MP: 200 °C. Yield: 20 mg (21 %).



ORTEP of molecular structure of compound **24** (containing methanol) determined by Xray crystallography showing the atom numbering scheme. CambridgeCrystallographic Data Centre (CCDC) number: 986158

N-[2-(2-Naphthyl)-2-oxo-ethyl]-2-oxo-2-(3,4,5-trimethoxyphenyl)acetamide (**25a**). $^1\text{H-NMR}$ (300 MHz): (DMSO- d_6) δ in ppm: 3.79 (s, 3 H), 3.90 (s, 6 H), 4.99 (d, 2 H, $J = 5.31$ Hz), 7.51 (s, 2 H), 7.68 (m, 2 H), 8.04 (m, 3 H), 8.15 (d, 1 H, $J = 7.83$ Hz), 8.81 (s, 1 H), 9.34 (t, 1 H, $J = 5.31$ Hz); $^{13}\text{C-NMR}$ (75 MHz): (DMSO- d_6) δ in ppm: 45.84, 56.13, 60.28, 107.43, 123.32, 127.06, 127.71, 128.05, 128.46, 128.87, 129.59, 130.03, 132.01, 132.10, 135.25, 143.22, 152.93, 166.09, 189.37, 194.39; IR (cm^{-1}): 3268, 1691, 1677, 1638, 1588, 1469, 1417, 1338, 1256, 1168, 1121, 1013, 999, 856, 822, 759, 739. LC-MS: 8.7 min, m/z 408.1 $[\text{MH}]^+$ $\text{C}_{23}\text{H}_{21}\text{NO}_6$ (M_r 407.42). MP: 125 °C. Yield: 130 mg (43 %).

5-(2-Naphthyl)-3-(3,4,5-trimethoxyphenyl)-1*H*-pyrazin-2-one (**25**). $^1\text{H-NMR}$ (300 MHz): (DMSO- d_6) δ in ppm: 3.75 (s, 3 H), 3.88 (s, 6 H), 7.50 (m, 2 H), 7.95 (m, 5 H), 8.15 (m, 2 H),

8.52 (s, 1 H), 12.80 (bs, 1 H); ^{13}C -NMR (75 MHz): (DMSO- d_6) δ in ppm: 55.89, 60.11, 106.31, 122.95, 123.05, 123.62, 125.93, 126.36, 127.49, 128.20, 128.24, 131.20, 131.46, 132.29, 133.18, 133.39, 139.30, 148.95, 152.29, 154.72; IR (cm^{-1}): 1643, 1626, 1578, 1500, 1451, 1409, 1335, 1233, 1223, 1121, 1002, 869, 844, 810, 772, 747. LC-MS: 7.9 min, m/z 389.2 $[\text{MH}]^+$ $\text{C}_{23}\text{H}_{20}\text{N}_2\text{O}_4$ (M_r 388.42) HRMS: m/z calculated 388.1423; found 388.1426. MP: 235 °C. Yield: 37 mg (39 %).

N-[2-(3-Furyl)-2-oxo-ethyl]-2-oxo-2-(3,4,5-trimethoxyphenyl)acetamide (**26a**). ^1H -NMR (300 MHz): (DMSO- d_6) δ in ppm: 3.79 (s, 3 H), 3.87 (s, 6 H), 4.58 (d, 2 H, $J = 5.56$ Hz), 6.86 (s, 1 H), 7.46 (s, 2 H), 7.84 (d, 1 H, $J = 1.52$ Hz), 8.72 (s, 1 H), 9.25 (t, 1 H, $J = 5.56$ Hz); ^{13}C -NMR (75 MHz): (DMSO- d_6) δ in ppm: 46.40, 56.11, 60.26, 107.41, 108.06, 124.77, 127.96, 143.25, 145.05, 149.11, 152.90, 165.90, 189.23, 189.45; IR (cm^{-1}): 3257, 1695, 1672, 1642, 1585, 1560, 1502, 1462, 1416, 1337, 1234, 1163, 1123, 1052, 998, 907, 871, 930, 752, 733. LC-MS: 6.7 min, m/z 347.8 $[\text{MH}]^+$ $\text{C}_{17}\text{H}_{17}\text{NO}_7$ (M_r 347.32). MP: 128 °C. Yield: 350 mg (81 %).

5-(3-Furyl)-3-(3,4,5-trimethoxyphenyl)-1*H*-pyrazin-2-one (**26**). ^1H -NMR (300 MHz): (DMSO- d_6) δ in ppm: 3.73 (s, 3 H), 3.84 (s, 6 H), 7.00 (s, 1 H), 7.74 (m, 2 H), 7.87 (s, 2 H), 8.13 (s, 1 H), 12.59 (bs, 1 H); ^{13}C -NMR (75 MHz): (DMSO- d_6) δ in ppm: 55.86, 60.07, 106.223, 107.97, 122.35, 123.55, 126.84, 131.20, 139.26, 139.39, 144.11, 148.97, 152.22, 154.63; IR (cm^{-1}): 1638, 1619, 1578, 1504, 1464, 1454, 1413, 1365, 1337, 1225, 1125, 1062, 1012, 994, 975, 872, 853, 813, 773, 732. LC-MS: 6.7 min, m/z 329.1 $[\text{MH}]^+$ $\text{C}_{17}\text{H}_{16}\text{N}_2\text{O}_5$ (M_r 328.32) HRMS: m/z calculated 328.1059; found 328.1069. MP: 204 °C. Yield: 70 mg (74 %).

2-Oxo-N-[2-oxo-2-(3-thienyl)ethyl]-2-(3,4,5-trimethoxyphenyl)acetamide (**27a**). $^1\text{H-NMR}$ (300 MHz): (DMSO- d_6) δ in ppm: 4.66 (d, 2 H, $J = 5.81$ Hz), 7.27 (m, 2 H), 7.56 (m, 2 H), 7.68 (dd, 1 H, $J = 4.67, 2.91$ Hz), 8.26 (m, 1 H), 8.66 (d, 1 H, $J = 1.26$ Hz), 8.78 (d, 1 H, $J = 3.03$ Hz), 8.96 (t, 1 H, $J = 5.81$ Hz), 12.25 (s, 1 H); $^{13}\text{C-NMR}$ (75 MHz): (DMSO- d_6) δ in ppm: 46.40, 112.19, 112.55, 121.26, 122.57, 123.46, 126.10, 126.36, 127.65, 133.85, 136.25, 138.54, 139.47, 163.77, 181.51, 188.91; IR (cm^{-1}): 3337, 1693, 1673, 1600, 1533, 1489, 1428, 1386, 1345, 1282, 1233, 1158, 1133, 1103, 1016, 902, 878, 832, 808, 784, 750. LC-MS: 7.4 min, m/z 335.1 [MNa] $^+$ $\text{C}_{16}\text{H}_{12}\text{N}_2\text{O}_3\text{S}$ (M_r 312.34). MP: 227 °C. Yield: 260 mg (79 %).

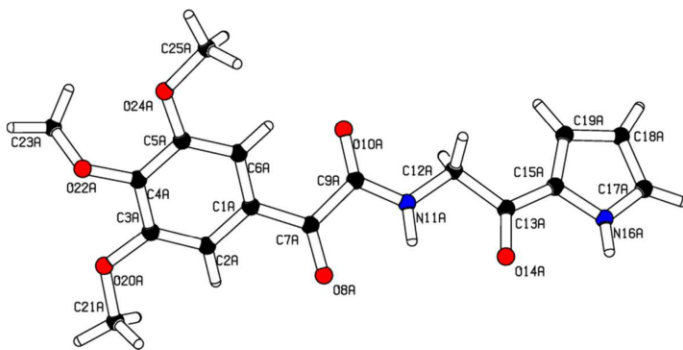
5-(3-Thienyl)-3-(3,4,5-trimethoxyphenyl)-1*H*-pyrazin-2-one (**27**). $^1\text{H-NMR}$ (300 MHz): (DMSO- d_6) δ in ppm: 3.73 (s, 3 H), 3.85 (s, 6 H), 7.61 (m, 1 H), 7.66 (d, 1 H, $J = 4.80$ Hz), 7.88–7.97 (m, 4 H), 12.65 (bs, 1 H); $^{13}\text{C-NMR}$ (75 MHz): (DMSO- d_6) δ in ppm: 55.86, 60.08, 106.23, 120.35, 122.85, 125.15, 126.96, 129.33, 131.31, 138.49, 139.25, 148.71, 152.23, 154.59; IR (cm^{-1}): 2937, 2835, 1637, 1582, 1506, 1466, 1415, 1347, 1328, 1241, 1228, 1124, 1093, 998, 863, 850, 843, 781, 769, 670, 623. HRMS: m/z calculated 344.0831; found 344.0812 $\text{C}_{17}\text{H}_{16}\text{N}_2\text{O}_4\text{S}$ (M_r 344.38). MP: 186 °C. Yield: 67 mg (71 %).

2-Oxo-N-[2-oxo-2-(3-pyridyl)ethyl]-2-(3,4,5-trimethoxyphenyl)acetamide (**28a**). $^1\text{H-NMR}$ (300 MHz): (DMSO- d_6) δ in ppm: 3.799 (s, 3 H), 3.91 (s, 6 H), 4.88 (d, 2 H, $J = 5.56$ Hz), 7.46 (s, 2 H), 7.60 (m, 1 H), 8.38 (m, 1 H), 8.84 (m, 1 H), 9.22 (s, 1 H), 9.32 (t, 1 H, $J = 5.56$ Hz); $^{13}\text{C-NMR}$ (75 MHz): (DMSO- d_6) δ in ppm: 46.00, 56.11, 60.25, 107.42, 123.93, 127.95, 130.19, 135.45, 143.26, 149.09, 152.90, 153.86, 165.98, 189.15, 194.21; IR (cm^{-1}): 3520, 1705, 1677,

1639, 1582, 1503, 1456, 1417, 1350, 1314, 1233, 1166, 1123, 986, 972, 857, 757, 725, 699. LC-MS: 6.1 min, m/z 358.9 $[MH]^+$ $C_{18}H_{18}N_2O_6$ (M_r 358.35). MP: 124 °C. Yield: 260 mg (62 %).

5-(3-Pyridyl)-3-(3,4,5-trimethoxyphenyl)-1*H*-pyrazin-2-one (**28**). 1H -NMR (300 MHz): (DMSO- d_6) δ in ppm: 3.73 (s, 3 H), 3.85 (s, 6 H), 7.46 (m, 1 H), 7.90 (m, 2 H), 8.14 (d, 1 H, $J = 2.78$ Hz), 8.32 (m, 1 H), 8.52 (m, 1 H), 9.17 (s, 1 H), 12.75 (bs, 1 H); ^{13}C -NMR (75 MHz): (DMSO- d_6) δ in ppm: 55.89, 60.12, 106.28, 123.66, 124.08, 128.83, 131.22, 131.67, 131.93, 139.39, 146.04, 148.24, 149.35, 152.29, 154.81; IR (cm^{-1}): 1648, 1579, 1533, 1500, 1487, 1452, 1433, 1408, 1364, 1340, 1252, 1233, 1222, 1191, 1174, 1122, 998, 876, 857, 807, 778, 736, 703. HRMS: m/z calculated 339.1219; found 339.1202 $C_{18}H_{17}N_3O_4$ (M_r 339.35) MP: 238 °C. Yield: 60 mg (63 %).

2-Oxo-N-[2-oxo-2-(1*H*-pyrrol-2-yl)ethyl]-2-(3,4,5-trimethoxyphenyl)acetamide (**29a**). 1H -NMR (300 MHz): ($CDCl_3$) δ in ppm: 3.91 (s, 6 H), 3.95 (s, 3 H), 4.68 (d, 2 H, $J = 4.80$ Hz), 6.33 (m, 1 H), 7.04 (m, 1 H), 7.10 (m, 1 H), 7.72 (s, 2 H), 7.93 (bs, 1 H), 9.58 (bs, 1 H); ^{13}C -NMR (75 MHz): ($CDCl_3$) δ in ppm: 44.77, 56.26, 61.00, 108.77, 111.38, 116.74, 125.63, 128.11, 129.20, 152.85, 162.30, 182.75, 185.26; IR (cm^{-1}): 1668, 1629, 1578, 1502, 1409, 1332, 1229, 1123, 1050, 991. LC-MS: 6.8 min, m/z 369.1 $[MNa]^+$ $C_{17}H_{18}N_2O_6$ (M_r 346,34). MP: 153 °C. Yield: 260 mg (20 %).



ORTEP of molecular structure of compound **29a** determined by Xray crystallography showing the atom numbering scheme. CCDC number: 986159

5-(1H-Pyrrol-2-yl)-3-(3,4,5-trimethoxyphenyl)-1*H*-pyrazin-2-one (**29**). $^1\text{H-NMR}$ (300 MHz): (CDCl_3) δ in ppm: 3.92 (s, 3 H), 3.96 (s, 6 H), 6.29 (m, 1 H), 6.45 (m, 1 H), 6.90 (m, 1 H), 7.49 (s, 1 H), 7.67 (s, 2 H), 9.22 (bs, 1 H); $^{13}\text{C-NMR}$ (75 MHz): (CDCl_3) δ in ppm: 56.43, 60.95, 104.16, 106.83, 110.40, 118.84, 127.96, 130.01, 130.93, 140.33, 150.98, 152.91, 156.16; IR (cm^{-1}): 3276, 2935, 2833, 1632, 1610, 1582, 1497, 1408, 1333, 1222, 1122, 999, 833, 722. LC-MS: 7.8 min, m/z 328.3 $[\text{MH}]^+$ $\text{C}_{17}\text{H}_{17}\text{N}_3\text{O}_4$ (M_r 327.33). MP: 201 °C. Yield: 20 mg (26 %).

N-[2-(4-Methoxyphenyl)-2-oxo-ethyl]-2-oxo-2-(3,4,5-trimethoxyphenyl)acetamide (**30a**).

$^1\text{H-NMR}$ (300 MHz): (DMSO-d_6) δ in ppm: 3.78 (s, 3 H), 3.85 (s, 3 H), 3.90 (s, 6 H), 4.78 (d, 2 H, $J = 5.68$ Hz), 7.07 (m, 2 H), 7.49 (s, 2 H), 8.02 (m, 2 H), 9.23 (t, 1 H); $^{13}\text{C-NMR}$ (75 MHz): (DMSO-d_6) δ in ppm: 45.80, 55.96, 56.50, 60.67, 107.79, 114.44, 127.98, 128.44, 130.68, 143.54, 153.31, 163.92, 166.48, 189.84, 193.05; IR (cm^{-1}): 3373, 1691, 1654, 1603, 1577, 1504, 1412, 1337, 1322, 1245, 1229, 1131, 1037, 999, 985, 830, 772, 727. LC-MS: 7.3 min, m/z 388.0 $[\text{MH}]^+$ $\text{C}_{20}\text{H}_{21}\text{NO}_7$ (M_r 387.38). MP: 128 °C. Yield: 300 mg (93 %).

5-(4-Methoxyphenyl)-3-(3,4,5-trimethoxyphenyl)-1*H*-pyrazin-2-one (**30**). ¹H-NMR (300 MHz): (DMSO-d₆) δ in ppm: 3.74 (s, 3 H), 3.79 (s, 3 H), 3.84 (s, 6 H), 7.01 (d, 2 H, J = 7.83 Hz), 7.90 (m, 5 H), 12.62 (bs, 1 H); ¹³C-NMR (75 MHz): (DMSO-d₆) δ in ppm: 55.12, 55.86, 60.10, 106.19, 114.13, 122.28, 125.95, 128.53, 131.54, 131.67, 139.17, 148.32, 152.25, 154.56, 158.85; IR (cm⁻¹): 1641, 1613, 1579, 1505, 1413, 1335, 1286, 1238, 1226, 1176, 1126, 1104, 864, 859, 831, 802, 770, 705, 662. LC-MS: 7.2 min, m/z 369.6 [MH]⁺ C₂₀H₂₀N₂O₅ (M_r 368.38). MP: 211 °C. Yield: 20 mg (12 %).

N-[2-(4-Chlorophenyl)-2-oxo-ethyl]-2-oxo-2-(3,4,5-trimethoxyphenyl)acetamide (**32a**). ¹H-NMR (300 MHz): (DMSO-d₆) δ in ppm: 3.78 (s, 3 H), 3.89 (s, 6 H), 4.83 (d, 2 H, J = 5.58 Hz), 7.48 (s, 2 H), 7.64, 8.06 (m, 2 H), (m, 2 H), 9.31 (t, 1 H, J = 5.58 Hz); ¹³C NMR (75 MHz): (DMSO-d₆) δ in ppm: 45.87, 56.14, 60.32, 107.41, 128.04, 129.02, 129.93, 133.40, 138.73, 143.23, 152.96, 166.13, 189.36, 193.64; IR (cm⁻¹): 3369, 1698, 1674, 1647, 1574, 1498, 1412, 1336, 1322, 1232, 1128, 1090, 993, 986. LC-MS: 8.4 min, m/z 392.0 [MH]⁺ C₁₉H₁₈ClNO₆ (M_r 391.80). MP: 148 °C. Yield: 210 mg (40 %).

5-(4-Chlorophenyl)-3-(3,4,5-trimethoxyphenyl)-1*H*-pyrazin-2-one (**32**). ¹H-NMR (300 MHz): (DMSO-d₆) δ in ppm: 3.74 (s, 3 H), 3.84 (s, 6 H), 7.47 (d, 2 H, J = 8.08 Hz), 7.87 (s, 2 H), 7.99 (d, 2 H, J = 8.08 Hz), 8.06 (s, 1 H), 12.76 (s, 1 H); ¹³C-NMR (75 MHz): (DMSO-d₆) δ in ppm: 55.89, 60.09, 106.30, 123.60, 126.30, 128.63, 130.13, 131.29, 131.93, 134.88, 139.36, 148.88, 152.26, 154.67; IR (cm⁻¹): 1654, 1613, 1585, 1504, 1489, 1439, 1410, 1337, 1229, 1219, 1178,

1126, 1087, 1010, 983, 867, 824, 775, 754, 733. HRMS: m/z calculated 372.0877; found 372.0865 $C_{19}H_{17}ClN_2O_4$ (M_r 372.80). MP: 238 °C. Yield: 61 mg (64 %).

N-[2-(3-Chlorophenyl)-2-oxo-ethyl]-2-oxo-2-(3,4,5-trimethoxyphenyl)acetamide (**33a**). 1H -NMR (300 MHz): (DMSO- d_6) δ in ppm: 3.79 (s, 3 H), 3.89 (s, 6 H), 4.84 (d, 2 H, $J = 5.56$ Hz), 7.47 (s, 2 H), 7.61 (dd, 1 H, $J = 8.08, 7.58$ Hz), 7.77 (d, 1 H, $J = 8.08$ Hz), 8.01 (d, 1 H, $J = 7.58$ Hz), 8.06 (s, 1 H), 9.31 (t, 1 H, $J = 5.56$ Hz); ^{13}C -NMR (75 MHz): (DMSO- d_6) δ in ppm: 45.98, 56.12, 60.28, 107.36, 126.65, 127.63, 127.99, 130.86, 133.46, 133.79, 136.51, 143.21, 152.92, 166.06, 189.28, 193.65; IR (cm^{-1}): 3256, 1704, 1683, 1638, 1586, 1505, 1461, 1417, 1338, 1219, 1197, 1165, 1125, 995, 978, 810, 759, 740. LC-MS: 8.4 min, m/z 392.0 $[MH]^+$ $C_{19}H_{18}ClNO_6$ (M_r 391.80). MP: 136 °C. Yield: 228 mg (70 %).

5-(3-Chlorophenyl)-3-(3,4,5-trimethoxyphenyl)-1*H*-pyrazin-2-one (**33**). 1H -NMR (300 MHz): (DMSO- d_6) δ in ppm: 3.73 (s, 3 H), 3.85 (s, 6 H), 7.36 (d, 1 H, $J = 7.83$ Hz), 7.46 (m, 1 H), 7.86 (s, 2 H), 7.95 (d, 1 H, $J = 7.83$ Hz), 8.02 (s, 1 H), 8.13 (s, 1 H), 12.82 (s, 1 H); ^{13}C -NMR (75 MHz): (DMSO- d_6) δ in ppm: 55.87, 60.10, 106.28, 123.11, 124.19, 127.03, 129.64, 130.55, 131.25, 133.67, 138.19, 139.37, 149.02, 152.27, 154.76; IR (cm^{-1}): 1640, 1592, 1579, 1505, 1462, 1411, 1333, 1232, 1186, 1124, 997, 859, 834, 799, 786. HRMS: m/z calculated 372.0877; found 372.0872 $C_{19}H_{17}ClN_2O_4$ (M_r 372.80). MP: 201 °C. Yield: 57 mg (60 %).

N-[2-(2-Chlorophenyl)-2-oxo-ethyl]-2-oxo-2-(3,4,5-trimethoxyphenyl)acetamide (**34a**). 1H -NMR (300 MHz): (DMSO- d_6) δ in ppm: 3.79 (s, 3 H), 3.88 (s, 6 H), 4.67 (d, 2 H, $J = 5.56$ Hz), 7.42–7.61 (m, 5 H), 7.82 (d, 1 H, $J = 7.83$ Hz), 9.39 (t, 1 H, $J = 5.56$ Hz); ^{13}C -NMR (75 MHz):

(DMSO- d_6) δ in ppm: 48.25, 56.10, 60.28, 107.35, 127.43, 127.93, 129.66, 130.18, 130.69, 132.96, 135.95, 143.22, 152.90, 165.96, 189.11, 196.83; IR (cm^{-1}): 3267, 1712, 1683, 1632, 1580, 1566, 1505, 1416, 1338, 1216, 1168, 1128, 1066, 990, 965, 755. LC-MS: 8.1 min, m/z 392.1 $[\text{MH}]^+$ $\text{C}_{19}\text{H}_{18}\text{ClNO}_6$ (M_r 391.80). MP: 108 °C. Yield: 178 mg (55 %).

5-(2-Chlorophenyl)-3-(3,4,5-trimethoxyphenyl)-1*H*-pyrazin-2-one (**34**). $^1\text{H-NMR}$ (300 MHz): (DMSO- d_6) δ in ppm: 3.72 (s, 3 H), 3.81 (s, 6 H), 7.42 (m, 2 H), 7.56 (d, 1 H, $J = 7.58$ Hz), 7.70 (d, 1 H, $J = 7.33$ Hz), 7.75 (s, 1 H), 7.84 (s, 2 H), 12.73 (bs, 1 H); $^{13}\text{C-NMR}$ (75 MHz): (DMSO- d_6) δ in ppm: 55.83, 60.08, 106.22, 126.88, 127.44, 129.47, 130.16, 131.09, 131.23, 131.35, 135.16, 139.25, 148.80, 152.23, 154.30; IR (cm^{-1}): 1652, 1616, 1587, 1506, 1477, 1466, 1440, 1414, 1363, 1334, 1232, 1187, 1130, 1034, 1004, 852, 749. HRMS: m/z calculated 372.0877; found 372.0867 $\text{C}_{19}\text{H}_{17}\text{ClN}_2\text{O}_4$ (M_r 372.80). MP: 192 °C. Yield: 28 mg (29 %).

N-[2-(4-Hydroxyphenyl)-2-oxo-ethyl]-2-oxo-2-(3,4,5-trimethoxyphenyl)acetamide (**35a**). $^1\text{H-NMR}$ (300 MHz): (DMSO- d_6) δ in ppm: 3.79 (s, 3 H), 3.92 (s, 6 H), 4.72 (d, 2 H, $J = 4.72$ Hz), 6.88 (d, 2 H, $J = 7.83$ Hz), 7.50 (s, 2 H), 7.92 (d, 2 H, $J = 7.83$ Hz), 9.18 (t, 1 H, $J = 4.80$ Hz), 10.45 (s, 1 H); $^{13}\text{C-NMR}$ (75 MHz): (DMSO- d_6) δ in ppm: 45.21, 56.11, 60.27, 107.43, 115.37, 126.26, 128.07, 130.50, 143.16, 152.91, 162.50, 166.06, 189.47, 192.31; IR (cm^{-1}): 3368, 1686, 1651, 1607, 1581, 1519, 1499, 1411, 1323, 1234, 1166, 1123, 992, 840. LC-MS: 6.9 min, m/z 374.1 $[\text{MH}]^+$ $\text{C}_{19}\text{H}_{19}\text{NO}_7$ (M_r 373.36). Yield: 70 mg (13 %).

5-(4-Hydroxyphenyl)-3-(3,4,5-trimethoxyphenyl)-1*H*-pyrazin-2-one (**35**). $^1\text{H-NMR}$ (300 MHz): (DMSO- d_6) δ in ppm: 3.73 (s, 3 H), 3.84 (s, 6 H), 6.83 (m, 2 H), 7.77 (m, 2 H), 7.83 (s, 1 H),

7.88 (s, 2 H), 9.52 (s, 1 H), 12.58 (bs, 1 H); ^{13}C -NMR (75 MHz): (DMSO- d_6) δ in ppm: 55.89, 60.11, 106.22, 115.50, 121.84, 126.04, 126.96, 131.61, 132.29, 139.16, 148.21, 152.26, 154.51, 157.12; IR (cm^{-1}): 3498, 2938, 1637, 1610, 1586, 1498, 1410, 1335, 1275, 1221, 1170, 1121, 1001, 859, 830, 773, 710. LC-MS: 6.6 min, m/z 355.3 $[\text{MH}]^+$ $\text{C}_{19}\text{H}_{18}\text{N}_2\text{O}_5$ (M_r 354.36). MP: 229 °C. Yield: 42 mg (54 %).

N-[2-(2-Hydroxyphenyl)-2-oxo-ethyl]-2-oxo-2-(3,4,5-trimethoxyphenyl)acetamide (**36a**). ^1H -NMR (300 MHz): (DMSO- d_6) δ in ppm: 3.79 (s, 3 H), 3.88 (s, 6 H), 4.79 (d, 2 H, $J = 5.68$ Hz), 6.99 (m, 2 H), 7.52 (m, 3 H), 7.88 (dd, 1 H, $J = 7.96, 1.52$ Hz), 11.25 (s, 1 H); ^{13}C -NMR (75 MHz): (DMSO- d_6) δ in ppm: 56.10, 60.32, 107.40, 117.57, 119.40, 120.53, 128.07, 130.14, 135.84, 143.19, 152.94, 159.57, 166.01, 189.35, 197.43; IR (cm^{-1}): 3354, 2943, 1665, 1634, 1586, 1543, 1505, 1456, 1418, 1342, 1282, 1242, 1169, 1160, 1126, 998, 743, 729. MS (EI): m/z 373.0 $[\text{M}]^+$ $\text{C}_{19}\text{H}_{19}\text{NO}_7$ (M_r 373.36). MP: 158 °C. Yield: 140 mg (27 %).

5-(2-Hydroxyphenyl)-3-(3,4,5-trimethoxyphenyl)-1*H*-pyrazin-2-one (**36**). ^1H -NMR (300 MHz): (DMSO- d_6) δ in ppm: 3.74 (s, 3 H), 3.83 (s, 6 H), 6.92 (m, 2 H), 7.16 (m, 1 H), 7.81 (s, 2 H), 7.96 (d, 1 H, $J = 7.58$ Hz), 8.17 (s, 1 H), 10.68 (s, 1 H), 12.65 (bs, 1 H); ^{13}C -NMR (75 MHz): (DMSO- d_6) δ in ppm: 55.89, 60.11, 106.11, 116.52, 119.45, 121.03, 126.16, 127.28, 128.60, 130.13, 131.23, 139.28, 148.08, 152.34, 154.25, 154.71; IR (cm^{-1}): 1639, 1607, 1576, 1505, 1447, 1413, 1337, 1243, 1129, 999, 843, 832, 741, 715. HRMS: m/z calculated 354.1215; found 354.1208 $\text{C}_{19}\text{H}_{18}\text{N}_2\text{O}_5$ (M_r 354.36). MP: 239 °C. Yield: 54 mg (57 %).

N-[2-(2-Fluoro-4-methoxy-phenyl)-2-oxo-ethyl]-2-oxo-2-(3,4,5-trimethoxyphenyl)acetamide

(**37a**). $^1\text{H-NMR}$ (300 MHz): (DMSO- d_6) δ in ppm: 3.79 (s, 3 H), 3.87 (s, 3 H), 3.89 (s, 6 H), 4.62 (dd, 2 H, $J = 5.47$, $^5J_{\text{HF}} 3.22$ Hz), 6.97 (m, 2 H), 7.48 (s, 2 H), 7.90 (m, 1 H), 9.27 (t, 1 H, $J = 5.46$ Hz); $^{13}\text{C-NMR}$ (75 MHz): (DMSO- d_6) δ in ppm: 48.58 ($^4J_{\text{CF}} = 10.2$ Hz), 56.14, 56.28, 60.32, 101.99 ($^2J_{\text{CF}} = 27.4$ Hz), 107.44, 111.63 ($^4J_{\text{CF}} = 2.7$ Hz), 115.74 ($^2J_{\text{CF}} = 13.7$ Hz), 128.08, 131.75 ($^3J_{\text{CF}} = 4.6$ Hz), 143.21, 152.95, 163.27 ($^1J_{\text{CF}} = 255.3$ Hz), 165.14 ($^3J_{\text{CF}} = 12.1$ Hz), 189.35, 190.76 ($^3J_{\text{CF}} = 5.3$ Hz); IR (cm^{-1}): 3406, 2843, 1672, 1652, 1611, 1572, 1505, 1448, 1417, 1325, 1244, 1234, 1128, 1100, 1026, 995, 987, 951, 869, 853, 819, 777. LC-MS: 8.0 min, m/z 406.1 $[\text{MH}]^+$ $\text{C}_{20}\text{H}_{20}\text{FNO}_7$ (M_r 405.37). MP: 144 $^\circ\text{C}$. Yield: 320 mg (61 %).

5-(2-Fluoro-4-methoxy-phenyl)-3-(3,4,5-trimethoxyphenyl)-1*H*-pyrazin-2-one (**37**). $^1\text{H-NMR}$ (300 MHz): (DMSO- d_6) δ in ppm: 3.73 (s, 3 H), 3.81 (s, 3 H), 3.83 (s, 6 H), 6.92 (m, 2 H), 7.67 (s, 1 H), 7.85 (s, 2 H), 7.95 (m, 1 H), 12.60 (bs, 1 H); $^{13}\text{C-NMR}$ (75 MHz): (DMSO- d_6) δ in ppm: 55.69, 55.86, 60.10, 102.00 ($^2J_{\text{CF}} = 26.0$ Hz), 106.24, 110.92 ($^4J_{\text{CF}} = 3.0$ Hz), 116.01 ($^2J_{\text{CF}} = 11.0$ Hz), 125.44, 126.98, 129.54 ($^3J_{\text{CF}} = 6.0$ Hz), 131.27, 139.31, 149.26, 152.26, 154.25, 159.72 ($^1J_{\text{CF}} = 245.0$ Hz), 159.99 ($^3J_{\text{CF}} = 11.0$ Hz); IR (cm^{-1}): 1643, 1623, 1576, 1500, 1464, 1445, 1409, 1335, 1287, 1278, 1226, 1125, 1117, 1061, 1000, 865, 846, 815, 775. HRMS: m/z calculated 386.1278; found 386.1272 $\text{C}_{20}\text{H}_{19}\text{FN}_2\text{O}_5$ (M_r 386.37). MP: 221 $^\circ\text{C}$. MP: Yield: 53 mg (56 %).

N-[2-(4-Hydroxy-3-methoxy-phenyl)-2-oxo-ethyl]-2-oxo-2-(3,4,5-trimethoxyphenyl)acetamide

(**38a**). $^1\text{H-NMR}$ (300 MHz): (DMSO- d_6) δ in ppm: 3.79 (s, 3 H), 3.85 (s, 3 H), 3.89 (s, 6 H), 4.76 (d, 2 H, $J = 5.68$ Hz), 6.90 (d, 1 H, $J = 8.34$ Hz), 7.49 (s, 2 H), 7.52 (d, 1 H, $J = 1.80$ Hz), 7.60 (dd, 1 H, $J = 8.34$, 1.80 Hz), 9.21 (t, 1 H, $J = 5.68$ Hz), 10.12 (s, 1 H); $^{13}\text{C-NMR}$ (75 MHz):

(DMSO- d_6) δ in ppm: 45.38, 55.71, 56.15, 60.32, 107.46, 111.28, 115.15, 122.89, 126.51, 128.11, 143.20, 147.61, 152.23, 152.95, 166.02, 189.46, 192.42; IR (cm^{-1}): 3308, 1677, 1651, 1585, 1506, 1414, 1342, 1270, 1169, 1129, 997, 816, 773, 682. MS (EI): m/z 403.0 $[\text{M}]^+$ $\text{C}_{20}\text{H}_{21}\text{NO}_8$ (M_r 403.38). MP: 160 °C. Yield: 260 mg (50 %).

5-(4-Hydroxy-3-methoxy-phenyl)-3-(3,4,5-trimethoxyphenyl)-1*H*-pyrazin-2-one (**38**). ^1H -NMR (300 MHz): (DMSO- d_6) δ in ppm: 3.73 (s, 3 H), 3.85 (s, 9 H), 6.82 (d, 1 H, $J = 7.83$ Hz), 7.38 (m, 1 H), 7.56 (s, 1 H), 7.94 (s, 3 H), 9.11 (s, 1 H), 12.59 (bs, 1 H); ^{13}C -NMR (75 MHz): (DMSO- d_6) δ in ppm: 55.42, 55.78, 60.12, 106.07, 108.74, 115.71, 117.27, 122.07, 127.40, 131.59, 132.05, 139.11, 146.33, 147.85, 152.27, 154.58; IR (cm^{-1}): 3502, 2998, 1642, 1608, 1582, 1500, 1412, 1338, 1236, 1219, 1132, 1122, 1035, 994, 860, 841, 788, 768, 701. HRMS: m/z calculated 384.1321; found 384.1328 $\text{C}_{20}\text{H}_{20}\text{N}_2\text{O}_6$ (M_r 384.38). MP: 211 °C. Yield: 31 mg (33 %).

2-Oxo-*N*-phenacyl-2-(3,4,5-trimethoxyphenyl)acetamide (**39a**). ^1H -NMR (300 MHz): (DMSO- d_6) δ in ppm: 3.79 (s, 3 H), 3.89 (s, 6 H), 4.84 (d, 2 H, $J = 5.56$ Hz), 7.46–7.75 (m, 5 H), 8.05 (m, 2 H), 9.29 (t, 1 H, $J = 5.56$ Hz); ^{13}C -NMR (75 MHz): (DMSO- d_6) δ in ppm: 45.83, 56.13, 60.30, 107.42, 127.96, 128.05, 128.87, 133.79, 134.73, 143.21, 152.94, 166.10, 189.38, 194.46; IR (cm^{-1}): 3268, 1704, 1686, 1635, 1585, 1506, 1451, 1418, 1339, 1228, 1164, 1126, 994, 861, 750, 687. MS (EI): m/z 357.0 $[\text{M}]^+$ $\text{C}_{19}\text{H}_{19}\text{NO}_6$ (M_r 357.36). MP: 113 °C. Yield: 250 mg (84 %).

5-Phenyl-3-(3,4,5-trimethoxyphenyl)-1*H*-pyrazin-2-one (**39**). ^1H -NMR (300 MHz): (DMSO- d_6) δ in ppm: 3.74 (s, 3 H), 3.84 (s, 6 H), 7.32 (t, 1 H, $J = 7.33$ Hz), 7.44 (dd, 2 H, $J = 7.83, 7.33$ Hz),

7.90 (s, 2 H), 7.97 (d, 2 H, J = 7.83 Hz), 8.01 (s, 1 H), 12.72 (bs, 1 H); ^{13}C -NMR (75 MHz): (DMSO- d_6) δ in ppm: 55.90, 60.11, 106.27, 123.26, 124.59, 127.38, 128.71, 131.45, 135.95, 139.29, 148.75, 152.28, 154.71; IR (cm^{-1}): 2992, 1633, 1579, 1499, 1449, 1412, 1333, 1238, 1225, 1127, 997, 855, 847, 777, 766, 726, 695. HRMS: m/z calculated 338.1266; found 338.1252 $\text{C}_{19}\text{H}_{18}\text{N}_2\text{O}_4$ (M_r 338.36). MP: 201 °C. Yield: 70 mg (74 %).

Profiling of compound 38 at a concentration of 1 μM against 300 wild-type protein kinases

(duplicate measurement, data represented as residual activities in % of control)

Kinase Name	Kinase Family*	Compound 38 at 1,0E-06 residual activities in % of control
PDGFR-beta	TK	1
RET	TK	5
HIPK4	CMGC	5
CLK4	CMGC	5
RIPK2	TKL	9
DYRK2	CMGC	9
ACV-R2B	TKL	11
LRRK2	TKL	12
CLK2	CMGC	12
ACV-R1	TKL	13
DAPK1	CAMK	15
MELK	CAMK	15
RPS6KA6	AGC	16
ACV-RL1	TKL	16
DYRK1B	CMGC	16
FLT3	TK	16
DYRK3	CMGC	20
VEGF-R2	TK	21
DAPK3	CAMK	21
PIM3	CAMK	22
CLK1	CMGC	24
DAPK2	CAMK	25
RPS6KA3	AGC	27
CSF1-R	TK	28
TGFB-R2	TKL	28
RPS6KA2	AGC	33

HIPK2	CMGC	34
TRK-C	TK	36
MST2	STE	36
FGR	TK	36
MST1	STE	38
FGF-R2	TK	39
ARK5	CAMK	41
VEGF-R3	TK	41
KIT	TK	42
RPS6KA1	AGC	42
HIPK1	CMGC	42
BLK	TK	43
DYRK1A	CMGC	43
IRAK4 (untagged)	TKL	43
SNF1LK2	CAMK	43
TRK-A	TK	44
MERTK	TK	44
ITK	TK	46
CDK5/p35NCK	CMGC	49
SRC (GST-HIS-tag)	TK	49
DYRK4	CMGC	50
TRK-B	TK	50
HIPK3	CMGC	51
VEGF-R1	TK	52
FYN	TK	53
LCK	TK	53
LYN	TK	54
YES	TK	54
HCK	TK	56
MEK2	STE	57
AXL	TK	57
MAP4K4	STE	57
SAK	OTHER	58
PDGFR-alpha	TK	59
MAP3K7/MAP3K7IP1	STE	59
ABL2	TK	61
BMPR1A	TKL	61
MINK1	STE	63
CDK2/CycA2	CMGC	64
CAMKK2	OTHER	64
ABL1	TK	64
PRKX	AGC	64
MKNK1	CAMK	65
ACV-R2A	TKL	65
FRK	TK	65
GSK3-alpha	CMGC	66
FER	TK	66
IKK-alpha	OTHER	66

GSK3-beta	CMGC	67
MAP3K11	STE	68
FGF-R3	TK	69
MEK1	STE	69
MYLK	CAMK	70
TTK	OTHER	70
MKNK2	CAMK	70
SGK1	AGC	71
FES	TK	71
CDK5/p25NCK	CMGC	71
TXK	TK	71
ERK7	CMGC	71
ZAK	TKL	72
PHKG1	CAMK	72
PAK7	STE	72
MAPKAPK2	CAMK	72
TYK2	TK	73
PASK	CAMK	73
TBK1	OTHER	73
TLK1	AGC	74
JNK3	CMGC	74
GSG2	OTHER	74
MYLK3	CAMK	74
MAP4K2	STE	74
DNA-PK	ATYP	74
NLK	CMGC	75
LIMK1	TKL	75
CK1-gamma2	CK1	75
CDK9/CycK	CMGC	75
MEKK2	STE	75
CAMK2A	CAMK	75
PIM1	CAMK	77
MUSK	TK	78
PIM2	CAMK	78
MAP4K5	STE	78
STK17A	CAMK	78
CK1-gamma3	CK1	78
TSF1	OTHER	79
MEKK3	STE	79
CDK1/CycB1	CMGC	79
GRK5	AGC	79
CDK8/CycC	CMGC	79
Aurora-A	OTHER	79
CAMK2B	CAMK	79
CK1-delta	CK1	79
CDK4/CycD1	CMGC	79
CLK3	CMGC	80
IKK-epsilon	OTHER	80

EPHB4	TK	80
STK33	CAMK	81
NEK7	OTHER	82
DDR2	TK	82
MAPKAPK5	CAMK	82
FGF-R1	TK	83
MYLK2	CAMK	83
CK2-alpha1	OTHER	84
TSSK1	CAMK	84
Aurora-B	OTHER	84
ACK1	TK	84
EIF2AK2	OTHER	84
IGF1-R	TK	85
GRK4	AGC	85
CDC42BPA	AGC	85
SLK	STE	85
CK1-epsilon	CK1	85
ALK (GST-HIS-tag)	TK	85
GRK6	AGC	85
CDK2/CycE1	CMGC	85
PYK2	TK	86
CDK1/CycA2	CMGC	86
CK1-gamma1	CK1	86
EPHB2	TK	86
SNARK	CAMK	86
CAMK2D	CAMK	86
NEK3	OTHER	87
GRK3	AGC	87
CK2-alpha2	OTHER	87
CHK2	CAMK	88
ERBB4	TK	88
CDK6/CycD1	CMGC	88
PCTAIRE1/CycY	CMGC	88
PRKG2	AGC	88
GRK7	AGC	88
PDK1	AGC	89
MAP3K9	STE	89
ERK2	CMGC	89
FGF-R4	TK	90
ACV-R1B	TKL	90
TAOK2	STE	91
PAK6	STE	91
IRAK1	TKL	91
JAK3	TK	91
ERK1	CMGC	91
PRK2	AGC	91
WNK2	OTHER	91
ROS	TK	91

CDK1/CycE1	CMGC	92
TIE2	TK	92
BRK	TK	92
EPHA7	TK	92
TAOK3	STE	92
LTK	TK	92
ROCK2	AGC	92
p38-delta	CMGC	93
PHKG2	CAMK	93
NEK2	OTHER	93
STK25	STE	93
PBK	OTHER	93
Aurora-C	OTHER	93
AMPK-alpha1 aa1-550	CAMK	93
ROCK1	AGC	94
p38-alpha	CMGC	94
MARK2	CAMK	95
INS-R	TK	95
MAP3K1	STE	95
MST3	STE	95
PKC-beta1	AGC	96
PKC-nu	AGC	96
S6K	AGC	96
MARK4	CAMK	96
CAMKK1	OTHER	96
AKT1	AGC	96
TYRO3	TK	96
ERBB2	TK	96
PRK1	AGC	97
CDK9/CycT1	CMGC	97
EGF-R	TK	97
FAK aa2-1052	TK	97
JAK2	TK	97
EPHA5	TK	97
SNK	OTHER	97
PAK3	STE	97
WNK3	OTHER	97
GRK2	AGC	97
EPHB1	TK	97
PKC-beta2	AGC	97
DMPK	AGC	98
TLK2	AGC	98
BTK	TK	98
PLK3	OTHER	98
RIPK5	TKL	99
JNK2	CMGC	99
MARK3	CAMK	99
EEF2K	ATYPICAL	99

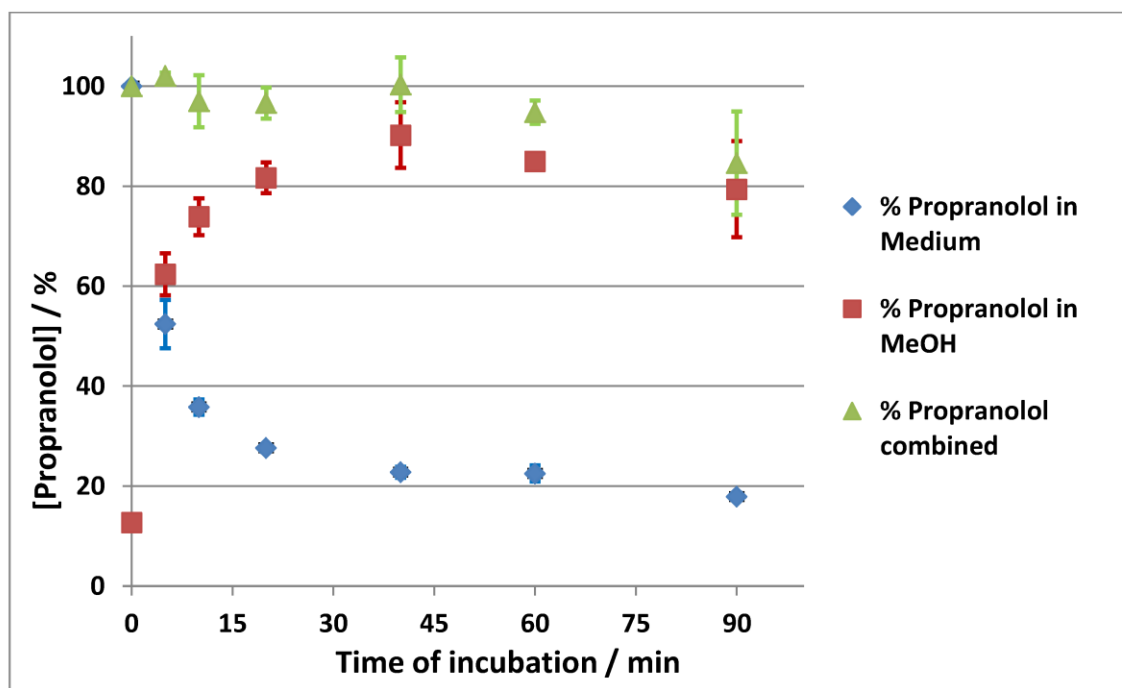
p38-gamma	CMGC	99
CSK	TK	99
PAK4	STE	99
JNK1	CMGC	99
NEK1	OTHER	99
SRMS	TK	99
B-RAF	TKL	100
PKC-theta	AGC	100
PKC-zeta	AGC	100
PRKG1	AGC	100
BRSK1	CAMK	100
STK39	STE	100
PKC-gamma	AGC	101
PKC-mu	AGC	101
CDC42BPB	AGC	101
MET	TK	101
mTOR	ATYPICAL	101
TEC	TK	101
AKT3	AGC	101
RPS6KA4	AGC	101
MKK6 S207D/T211D**	STE	102
CK1-alpha1	CK1	102
MAPKAPK3	CAMK	103
JAK1	TK	103
EPHA2	TK	103
PKC-eta	AGC	103
HRI	OTHER	103
PKC-alpha	AGC	103
PKA	AGC	103
PRKD2	CAMK	103
PKC-epsilon	AGC	103
PAK1	STE	103
BMX	TK	103
WNK1	OTHER	103
AKT2	AGC	103
TGFB-R1	TKL	104
EPHA8	TK	104
TSK2	CAMK	104
NEK11	OTHER	104
IKK-beta	OTHER	104
CDK7/CycH/MAT1	CMGC	104
EPHA4	TK	104
WEE1	OTHER	104
EPHA3	TK	104
ZAP70	TK	104
RPS6KA5	AGC	104
NIK	STE	105
NEK4	OTHER	105

NEK9	OTHER	105
ASK1	STE	106
PKC-iota	AGC	106
EPHA1	TK	106
CDK4/CycD3	CMGC	106
VRK1	CK1	106
STK23	CAMK	106
p38-beta	CMGC	106
EIF2AK3	OTHER	107
EPHB3	TK	107
PKC-delta	AGC	108
COT	STE	108
MATK	TK	108
CAMK1D	CAMK	108
SGK2	AGC	109
INSR-R	TK	109
PLK1	OTHER	109
CHK1	CAMK	110
SYK aa1-635	TK	110
RON	TK	110
NEK6	OTHER	111
MST4	STE	112
RAF1 Y340D/Y341D (untagged)**	TKL	112
SRPK1	CMGC	112
S6K-beta	AGC	113
SGK3	AGC	113
MAP3K10	STE	114
CDK3/CycE1	CMGC	114
MARK1	CAMK	115
CAMK4	CAMK	116
LIMK2	TKL	119
SRPK2	CMGC	120
DCAMKL2	CAMK	122
PAK2	STE	152

A radiometric protein kinase assay ($^{33}\text{PanQinase}^{\text{®}}$ Activity Assay) was used for measuring the kinase activity of the 300 protein kinases. All kinase assays were performed in 96-well FlashPlates[™] from Perkin Elmer (Boston, MA, USA) in a 50 μl reaction volume. For details see www.proqinase.com

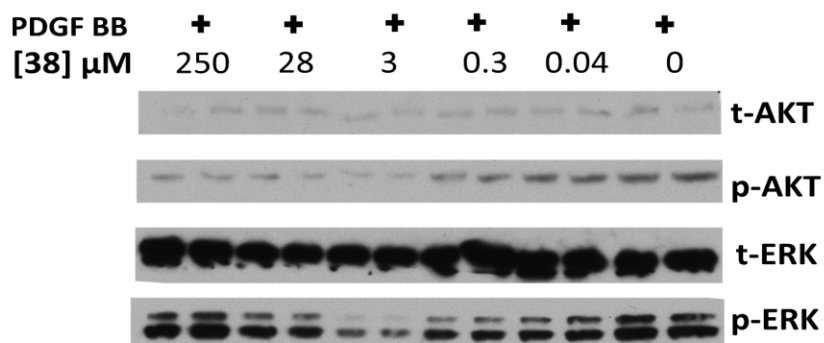
Measurement of intracellular uptake (Figure 8)

The measurement of the cellular uptake of **38** was determined using a Caco-2 cellular model. A control experiment was performed using the readily bioavailable β -blocker propranolol. The Caco-2 cells were grown in DMEM with Glutamax, 5 g/l Glucose and 10 % FCS and incubated in a 5 % CO₂ humidified atmosphere at 37 °C. For compound uptake experiments, cells were seeded in 1 mL per well into 12-well Cellstar[®] Culture Plates (Greiner Bio-One I. AG, Kremsmünster, AT). The cell number was 10⁶ cells per well. The plates were incubated for 10 days at 37 °C in a humidified atmosphere with 5 % CO₂ until the cells reached 100 % confluence. Consequently, the cell medium was removed and the cells were washed twice with Dulbecco's PBS and fresh DMEM without FCS. Test compound **38** and propranolol as standard (propranolol hydrochloride, P0884, Sigma Life Science, USA) were dissolved in FCS-free DMEM with 0.5 % DMSO (v/v). The final compound concentration in each experiment was 50 μ M. To every well in the cell plates 500 μ L of each solution were added. The cells with the compounds were incubated for the following periods: 5, 10, 20, 40, 60, and 90 minutes. After each period the medium was removed from the wells and the remaining compound concentration was measured by HPLC. The intracellular amount of the compound was determined by incubating the cells with cold methanol for 10 minutes. The methanol extractions were also determined by HPLC analysis. An Eclipse[®] XDB-C8 column with 5 μ m particle size (Agilent Technologies, USA) was used. The amount of **38** was determined at 254 nm, the amount of propranolol was determined at 286 nm based on a standard calibration curve for each compound. All experiments were determined in duplicate.



Measurement of the cellular uptake of reference compound **propranolol** using a Caco-2 model. The concentration of **propranolol** in the medium and intracellular was determined by HPLC analysis.

Western Blot analysis of **38** on the signal transduction in U87 cells



Effect of **38** on the signaling in U87 cells. The cells were treated with the indicated concentrations of **38** for 60 min at 37 °C and stimulated with 10 ng/ml PDGF BB for 10 min. Cells were lysed and lysates immunoblotted with the indicated antibodies. Similar results were obtained in duplicate experiments.

Primary antibodies:

- p44/42 MAPK (Erk1/2) (137F5) rabbit m-ab (t-Erk) Ref: #4695S Cell signalling technology
- P-p44/42 MAPK (T202/Y204) (197G2) rabbit m-ab (p-Erk) Ref: #4377S Cell signalling technology
- P-Akt (T308) (244F9) rabbit mAb #4056S von Cell signalling technology Ref: 09/2013
- Anti-PKB alpha S742B 1st Bleed (t-Akt), 1 x 0,05 mg; 0,28 mg/ml (courtesy by the lab of Prof. Dario Alessi, MRC, Dundee, Scotland)

Secondary antibodies:

- goat anti-rabbit (courtesy by the lab of Prof. Dario Alessi, MRC, Dundee, Scotland)
- anti-sheep (courtesy by the lab of Prof. Dario Alessi, MRC, Dundee, Scotland)

3.7 From Type I to Type II: Design, Synthesis, and Characterization of Potent Pyrazin-2-ones as DFG-Out Inhibitors of PDGFR β

Eugen Bethke, Boris Pinchuk, Christian Renn, Lydia Witt, Joachim Schlosser, and Christian Peifer

ChemMedChem **2016**, *11*, 1 – 12.

DOI: 10.1002/cmdc.201600494

The following publication deals with development and characterization of potent DFG-out inhibitors of PDGFR β .²⁰³ The inhibitors were based on the pyrazine-2-one scaffold which was successfully utilized for the DFG-in inhibitors described previously.^{201, 202} This scaffold was expanded toward the deep pocket (compare chapter “Kinase domain structure”). Molecular modeling studies were used to predict appropriate residues for addressing the deep pocket in PDGFR β . Thereby, moieties of known DFG-out inhibitors such as imatinib were combined with the pyrazine-2-one core. The designed hybrid inhibitors were accessed by a straightforward flexible synthetic route. That way developed compounds were evaluated in cellular proliferation assays on PDGFR β dependent cancer cells. Herein, the DFG-out inhibitor **3** showed a potent cytotoxic activity comparable to positive control imatinib.²⁰³ Molecular docking studies predicted DFG-out binding mode for compound **3** (Figure 23). Similar to the DFG-in inhibitor **2**, compound **3** builds two H-bonds to the hinge region and occupies the HR II by the trimethoxyphenyl residue. However, compound **3** additionally targets the deep pocket in the DFG-out kinase conformation (Figure 23B).

Both PDGFR β inhibitors **2** and **3** possess the same pyrazine-2-one core. This was a valid basis for comparison of DFG-in and DFG-out inhibitors possessing the same chemotype and biological target *in vitro*. Extensive biological characterization of these compounds was performed. Inhibitors **2** and **3** showed comparable IC₅₀ values in PDGFR β kinase activity assay: 20 nM and 19 nM, respectively. However, the inhibitory activity of compound **3** was determined to be time dependent and was shifted to lower IC₅₀ values over incubation

period. The slow on/off kinetics of compound **3** was a further evidence for the DFG-out binding mode of the kinase inhibitor.²³⁵ Cellular proliferation assays revealed that the DFG-out inhibitor **3** showed stronger cytotoxic activity on PDGFR β dependent cells than its DFG-in counterpart **2**. TGI values were measured as 55 μ M and 552 μ M, respectively. Moreover, the strong inhibitory activity of compound **3** could be proved in western blot analysis.²⁰³

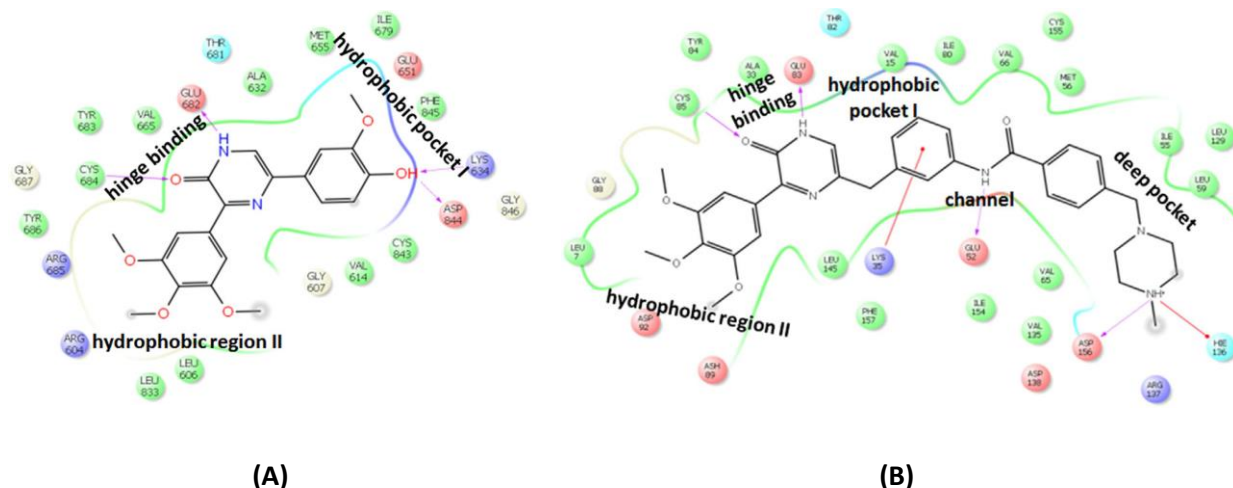


Figure 23: Modeled binding modes of developed PDGFR β inhibitors.^{203, 205} (A) Ligand interaction diagram of the DFG-in inhibitor **2** in the active site of a PDGFR β DFG-in homology model.²⁰² (B) Ligand interaction diagram of the DFG-out inhibitor **3** in the active site of a PDGFR β DFG-out homology model.²⁰³ Inhibitors **2** and **3** correspond to the compounds **1** and **5** in the paper “From Type I to Type II: Design, Synthesis, and Characterization of Potent Pyrazin-2-ones as DFG-Out Inhibitors of PDGFR β ”, respectively.

Inhibitors **2** and **3** were submitted for extensive kinase selectivity profiling in both activity-based (ProQinase, Freiburg, Germany) and affinity-based assays (DiscoverX, San Diego, CA, USA). The DFG-out inhibitor **3** was significantly more selective in both assay formats compared to the DFG-in inhibitor **2**. This finding was in line with the hypothesis about enhanced selectivity of DFG-out inhibitors (compare the chapter 1.2.3 “Comparison of DFG-in and DFG-out inhibitors”).

Dr. Eugen Bethke (born Johannes) and Dr. Joachim Schlosser performed the synthesis of the reported compounds. Christian Renn²³⁶ and I performed the biological characterization of all compounds *in vitro*.

From Type I to Type II: Design, Synthesis, and Characterization of Potent Pyrazin-2-ones as DFG-Out Inhibitors of PDGFR β

Eugen Bethke, Boris Pinchuk, Christian Renn, Lydia Witt, Joachim Schlosser, and Christian Peifer*^[a]

Reversible protein kinase inhibitors that bind in the ATP cleft can be classified as type I or type II binders. Of these, type I inhibitors address the active form, whereas type II inhibitors typically lock the kinase in an inactive form. At the molecular level, the conformation of the flexible activation loop holding the key DFG motif controls access to the ATP site, thereby determining an active or inactive kinase state. Accordingly, type I and type II kinase inhibitors bind to so-called DFG-in or DFG-out conformations, respectively. Based on our former study on highly selective platelet-derived growth factor receptor β (PDGFR β) pyrazin-2-one type I inhibitors, we expanded this

scaffold toward the deep pocket, yielding the highly potent and effective type II inhibitor **5** (4-[(4-methylpiperazin-1-yl)methyl]-*N*-[3-[[6-oxo-5-(3,4,5-trimethoxyphenyl)-1*H*-pyrazin-3-yl]methyl]phenyl]benzamide). In vitro characterization, including selectivity panel data from activity-based assays (300 kinases) and affinity-based assays (97 kinases) of these PDGFR β type I (**1**; 5-(4-hydroxy-3-methoxy-phenyl)-3-(3,4,5-trimethoxyphenyl)-1*H*-pyrazin-2-one) and II (**5**) inhibitors showing the same pyrazin-2-one chemotype are compared. Implications are discussed regarding the data for selectivity and efficacy of type I and type II ligands.

Introduction

Protein kinase inhibitors are established mainly in targeted anticancer therapies, and currently more than 30 drugs of this class have been approved for clinical use.^[1] Although there is actually no uniform agreement, the majority of kinase inhibitors can be categorized into type I–IV binders according to their variable binding modes in kinase proteins (Table 1).^[2–4] In

kinome of 518 human kinases, most reversible type I/II ligands, and in particular receptor tyrosine kinase (RTK) inhibitors, address the conserved hinge region and the greater ATP/substrate binding pocket area.^[11] This comprehensive active site is located between the β -sheet-rich N-terminal lobe and the C-terminal lobe mainly composed of α -helices.^[12]

Table 1. Classification of kinase inhibitors.

Type	Predominant features
I	hinge binder, DFG-in, active kinase conformation, ATP competitive
II	hinge binder, DFG-out, inactive kinase conformation, deep pocket, mixed ATP competitive
III	DFG-out, inactive kinase conformation, address only deep pocket
IV	covalent inhibitors

As a common control mechanism in many (but not all) kinases, access to this ATP active site is determined by the so-called activation loop which typically starts with an Asp-Phe-Gly (DFG) sequence.^[13–15] In a catalytically active kinase form, this rather flexible loop sequesters the DFG motif in a hydrophobic *back pocket* attached to the α -helix of the N-lobe, thereby providing access for the cofactor ATP to its binding site. Therefore, ATP-competitive type I inhibitors bind to this so-called *DFG-in* kinase conformation in an ATP-like manner.^[16] In opposition to the active enzyme, the DFG loop can move out of the *back pocket* toward the front entrance of the ATP site. Consequently, to some extent, access to the ATP/substrate area is blocked, leaving the kinase in a catalytically inactive form. In turn, as the DFG motif has moved out, the formerly occupied *back pocket* becomes accessible for type II inhibitors, which address this allosteric site (*deep pocket*, *switch-pocket*).^[17,18] Besides these extreme DFG-in/out conformations coding for type I and type II inhibitors, respectively, some intermediate forms of the DFG loop have been described that can be addressed by type I $\frac{1}{2}$ binders, for example.^[19,20]

terms of type I/II, this standardization of inhibitors corresponds to a respective active/inactive conformational state of the target kinase.^[5–7] In general, for the regulation of kinase activity, different conformations and various mechanisms are known, which include cellular translocation, allosteric modulators, or substrate complexation.^[4,8–10] However, regarding the

It is still under discussion whether type I or type II inhibitors are more effective in vitro and in vivo.^[21,22] Due to the highly conserved hinge/ATP pocket among the kinome and their predominant ATP-competitive nature, type I binders tend to inhibit

[a] E. Bethke, B. Pinchuk, C. Renn, L. Witt, Dr. J. Schlosser, Prof. Dr. C. Peifer
Christian Albrechts University of Kiel, Institute of Pharmacy,
Gutenbergstr. 76, 24118 Kiel (Germany)
E-mail: cpeifer@pharmazie.uni-kiel.de

Supporting information and the ORCID identification number(s) for the author(s) of this article can be found under <http://dx.doi.org/10.1002/cmdc.201600494>.

it multiple kinases^[23,24] which seems to translate into significant therapeutic efficacy.^[25] Despite this general notion, some highly selective type I inhibitors have been successfully developed.^[26–28] However, all inhibitors of active kinases (type I, DFG-in) must compete with high intracellular levels of ATP, which may contribute to an unfavorable in vitro/in vivo discrepancy.^[29] Another question in comparing DFG-in/out binders comes with on/off-target dynamics: type II inhibitors were reported to have extended target residence time, thus providing enhanced pharmacological benefit.^[3,30] Moreover, type II inhibitors are typically more selective for a particular kinase.^[3,31] This narrowed selectivity issue comes from the fact that not all kinases show a DFG flip, so that the enlarged and thus sterically demanding DFG-out/type II inhibitors only bind to those kinases that actually provide access to the *deep pocket*.^[32] Secondly, compared with the ATP site, the *deep pocket* is far less conserved among the kinome, offering highly specific interaction points for inhibitor design.^[18] Therefore, we became interested in determining if the DFG-in/out approaches could be compared in detail by using type I/II inhibitors based on the same chemical scaffold.

From type I to type II inhibitors

Having developed the potent and relatively selective pyrazin-2-one type I inhibitor **1** (Figure 1) against platelet-derived growth factor receptor β (PDGFR β),^[33] we aimed to expand this scaffold^[34] toward type II binders. Furthermore, we wanted to compare potent compounds of each type showing the same pyrazin-2-one core^[35] (“head hinge-binding moiety”) regarding parameters including kinase selectivity, on/off kinetics, and cellular efficacy.

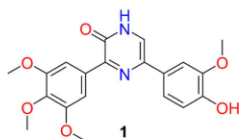


Figure 1. Potent and selective PDGFR β type I inhibitor **1**.

PDGFR β is a prominent member of the receptor tyrosine kinases (RTKs), a family that often adopts both DFG-in and DFG-out conformations.^[36,37] In this context, type I and type II inhibitors have been described for various RTKs including PDGFR β ,^[38] and a wealth of Protein Data Bank (PDB) structures provides structural evidence for the above-described active and inactive conformational kinase states.^[13] As no X-ray structure was available for the important drug target PDGFR β , we developed a DFG-in homology model and used it successfully for structure-based type I inhibitor design of compound **1** in our former study (Figure 2).^[33]

Accordingly, in the present study we built a DFG-out model for PDGFR β to develop type II binders by expanding the pyrazin-2-one core hinge binding moiety to address the *deep pocket*. As a starting point we docked our DFG-in inhibitor

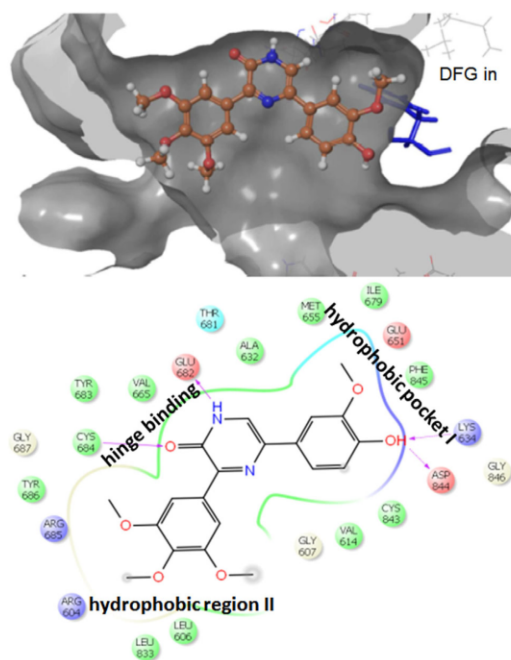


Figure 2. Modeled binding mode (top) and ligand interaction diagram (bottom) of type I binder **1** in the active site of our PDGFR β DFG-in homology model. Key ligand–protein interactions and binding pocket areas are shown.

1 into the PDGFR β DFG-out homology model (not shown).^[39] Consistent with the DFG-in pose of our optimized inhibitor **1** (see Figures 2 and 3) the pyrazin-2-one core forms key hydrogen bonds toward the hinge region. Furthermore, the trimethoxyphenyl system occupies the solvent-exposed *hydrophobic region II* (HRII). However, due to the significant DFG loop rearrangement the second aryl system fits suboptimally into the enlarged hydrophobic pocket I (HPI), and the *deep pocket* is completely unoccupied. Moreover, the DFG-out conformation opens a channel between HPI and the *deep pocket*, enabling further possibilities for ligand–protein interactions. Therefore, we aimed to design type II binders by maintaining the key pyrazin-2-one core of **1**, but adapting the aryl system that addresses the enlarged HPI. During our creative modeling approach, it turned out that: 1) a methylene bridge and 2) the aryl *meta*-position substituted by an amide were optimal to reach out through the narrow channel into the *deep pocket* (Scheme 1).

To identify an optimal moiety for exploiting *deep pocket* interactions (via attachment at the amine *meta* position of the pyrazin-2-one core) we contemplated known type II inhibitors possessing PDGFR β affinity such as imatinib (PDGFR β IC₅₀ = 0.1 μ M).^[40,41] Thus, from the pose of imatinib in related RTKs (e.g., PDB IDs: 3G0E,^[42] 1XBB,^[43] and 1T46^[44]) and the corresponding docking solution of imatinib in our PDGFR β DFG-out homology model, we decided to copy its benzamide side

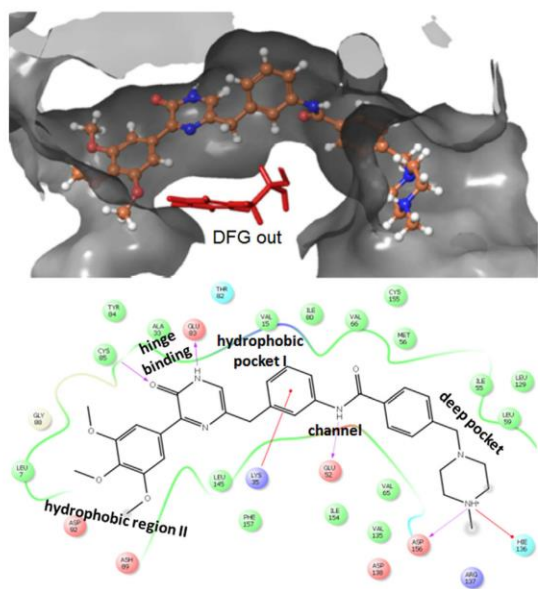
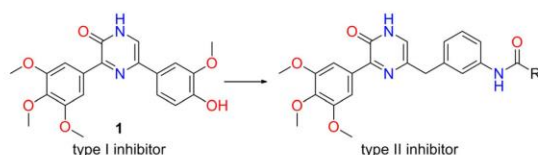


Figure 3. Modeled binding mode (top) and ligand interaction diagram (bottom) of the newly designed type II inhibitor **5** in the active site of our PDGFR β homology model in the DFG-out conformation. Key ligand-protein interactions are shown. In the DFG-out status adjacent to the HPI lined by Val15/Ile80/Lys35, a narrow channel (Val66/Glu52) opens toward the *deep pocket* (Met65/Val65/Ile55/Leu59). This cavity, which is absent in the DFG-in conformation, can be explored by a type II binder.



Scheme 1. Concept for type II inhibitor design guided by molecular modeling, starting from the type I binder **1**. The pyrazin-2-one core and the trimethoxyphenyl moiety were maintained, whereas the second aryl system was modified. A methylene bridge was introduced to position the aryl system in the enlarged HPI. At this aryl moiety a *meta*-amide substitution was found to be optimal to address the *deep pocket*.

chain to address the *deep pocket*, resulting in the hybrid inhibitor **5** (Figure 3). Additionally, further reported *deep pocket* binding moieties were chosen.^[45] Therefore, similar to **5** we designed hybrid inhibitors essentially consisting of the substituted arylamide moiety attached to the modified pyrazin-2-one core and also introduced a urea bridge at the former benzamide position (Scheme 2). These compounds were docked into the active site, yielding **5** as the top-ranked compound. Notably, in **5** the 4-[(4-methylpiperazin-1-yl)methyl]-*N*-phenylbenzamide moiety adopted from prototypical type II inhibitor imatinib^[46] revealed optimal ligand-protein interactions (Figure 3). These were actually highly similar to the binding mode of imatinib in c-kit (PDB ID: 1T46).^[44]

Results and Discussion

Chemistry

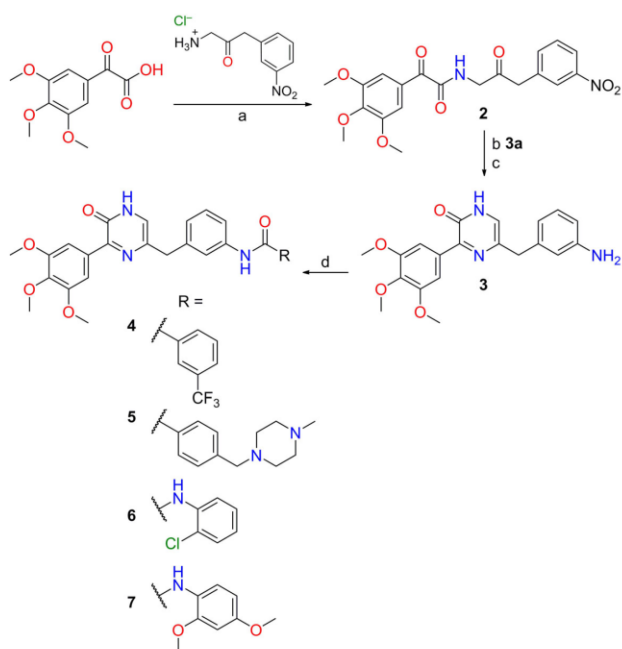
Motivated by the results of our modeling studies we developed a straightforward flexible synthetic route which was convergent at the last step via key building block **3** (Scheme 2). By this procedure we were able to generate variability regarding the substituted arylamide (**4**, **5**) and arylurea moieties (**6**, **7**), respectively, which were particularly designed to address the *deep pocket*.

The amide coupling of building block **3** with 3-(trifluoromethyl)benzoic acid by 1,1'-carbonyldiimidazole (CDI) catalysis in DMF to yield **4** was a standard reaction. However, when we applied these conditions for the coupling of **3** with 4-[(4-methylpiperazin-1-yl)methyl]benzoic acid, the reaction failed despite various modifications and attempts. The disappointing result was probably due to the ampholytic character of this moiety. The acid intramolecularly protonates the tertiary piperazine amine, thus leaving a nonreactive carboxylic anion. By screening different coupling methods, however, it turned out that using a modified *O*-(7-azabenzotriazol-1-yl)-*N,N,N'*-tetramethyluronium hexafluorophosphate (HATU) method under microwave irradiation successfully gave **5** in 43% yield. For the production of urea derivatives, building block **3** was treated with respective isocyanates and *N,N*-diisopropylethylamine (DIPEA) in absolute DMF under nitrogen at ambient temperature. Having the designed test compounds **4–7** in hand, we set out for their biological characterization.

Biological evaluation

In drug discovery, isolated enzymatic and cell-based *in vitro* assays serve as initial models to test inhibitors for their biological activity and efficacy.^[47] Accordingly, in an isolated enzyme assay a ligand's affinity for a target of interest can be studied under highly focused conditions. Although still providing an artificial test situation and therefore far away from the complexity of a living organism, the 96-well cell-based *in vitro* assay is considered to at least reflect key parameters of a hit compound such as beneficial ADME features and biological efficacy.^[48,49] Thus, to directly identify effective inhibitors, our key test compounds (DFG-in inhibitor **1**, designed DFG-out inhibitors **4–7**) as well as the PDGFR β DFG-in reference inhibitor CP-673451^[50] and imatinib as DFG-out ligand^[40] (Figure 4) were evaluated in a cell proliferation assay using PDGFR β -dependent U87-MG cells. In this U87-MG cell assay we identified CP-673451, imatinib, and compound **5** as the most potent compounds, whereas **1** showed moderate efficacy, and the urea derivative **7** the weakest efficacy (Table 2 and Figure 5).

To provide further evidence of a targeted impact in cells, we investigated the effect of compound **5** on PDGFR β signaling in NIH3T3 cells by western blot analysis using imatinib as reference compound (Figure 6).^[51] Herein, compound **5** significantly blocks the phosphorylation of PDGFR β at a concentration of 1 μM , whereas imatinib is already effective at 0.1 μM . In contrast, phosphorylation of the downstream kinases AKT and ERK



Scheme 2. Synthesis of pyrazin-2-one type II inhibitors via building block **3**. *Reagents and general conditions:* a) CDI-mediated amide coupling, NMP, 20 °C; b) NH_4Ac , microwave irradiation; c) Pd/C reduction; d) 1. amide coupling by CDI or HATU, 2. urea obtained by coupling with isocyanates. See the Experimental Section for details.

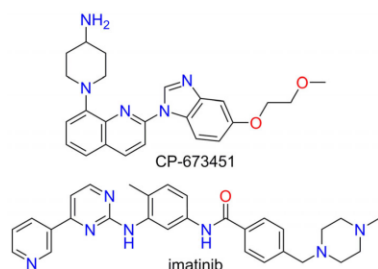


Figure 4. Reference compounds: PDGFR β DFG-in ligand CP-673451 and DFG-out inhibitor imatinib.

Test compound	TGI [μM]
1	552
4	177
5	55
6	190
7	1000
CP-673451	20
imatinib	75
imatinib mesylate	45

were more potently inhibited by **5** than by imatinib. An explanation would be that compound **5**, in addition to PDGFR β , inhibits further upstream RTKs of AKT and ERK, which were not blocked by imatinib, and this is in line with profiling data for **5** in kinase panels (see below and imatinib profile in the Supporting Information). Taken together, compound **5** has been proven to potently inhibit PDGFR β signaling in NIH3T3 cells at concentrations above 1 μM .

Based on these results, we aimed to further elucidate mechanistic aspects of ligand–protein binding for selected compounds. First, we compared **1**, PDGFR β DFG-in reference inhibitor CP-673451, as well as DFG-out binders imatinib and **5** by using our in-house standard enzymatic PDGFR β assay against an ATP concentration of 10 μM . Herein, CP-673451 revealed an IC_{50} value of 1 nM, which is similar to that given in the literature,^[50] indicating valid assay performance. In contrast to the relatively weak cellular efficacy, compound **1** showed a PDGFR β IC_{50} value of 20 nM. Furthermore, comparable to published data, imatinib^[52] was found to have a PDGFR β IC_{50} value of 58 nM,^[53] and compound **5** showed a PDGFR β IC_{50} value of 19 nM (Table 3 and Figure 7). Thus, in line with our molecular modeling approach and of **5** being an effective inhibitor of PDGFR β signaling in cells, these data provide strong evidence for the proposed ligand–target interaction design concept (see Figure 3).

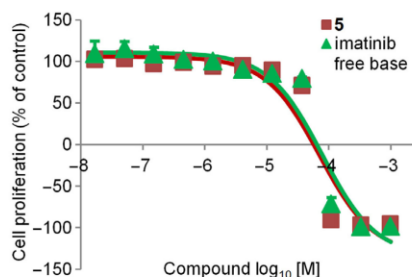


Figure 5. Determination of the antiproliferative profiles of compound **5** and imatinib in a cell proliferation assay using the U87-MG cell line. For clarity of presentation only the most effective DFG-out ligand **5** and imatinib as DFG-out reference are shown. Data are the mean \pm SD of $n=3$ experiments performed in duplicate. More details can be found in Supporting Information.

Having identified compound **5** as a highly potent inhibitor of PDGFR β , we next investigated ligand–protein binding in greater detail. In the applied enzymatic activity assay a phosphorylated and hence (over)activated PDGFR β kinase was deployed. As a consequence, the majority of the PDGFR β kinase should be present in the DFG-in conformation (probably in dynamic equilibrium with the DFG-out conformation). However, if our concept of **5** being a type II inhibitor is correct, this ligand should only be able to bind to the PDGFR β DFG-out conforma-

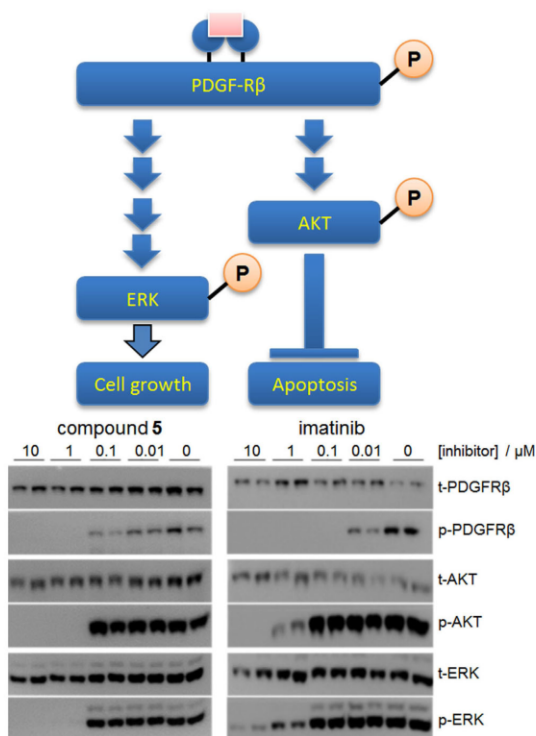


Figure 6. Simplified schematic representation of PDGFR β signaling (top) and the effects of compound **5** (lower left) and imatinib (lower right) on signaling in NIH3T3 cells. The cells were treated with the indicated compound concentrations for 60 min at 37 °C and stimulated with 10 ng mL⁻¹ PDGF-BB for 10 min. Cells were then lysed, and lysates were immunoblotted with the indicated antibodies. Similar results were obtained in duplicate experiments.

Table 3. Affinity of key compounds in an enzymatic PDGFR β assay determined as IC ₅₀ values.	
Compound	IC ₅₀ [nM]
1	20
5	19
CP-673451	1
imatinib	58

tion. Accordingly, in adding compound **5** to the kinase assay with increasing incubation time, the equilibrium state of active DFG-in and inactive DFG-out kinase form should be shifted toward the latter (this effect had also been described earlier for the DFG-out inhibitor TAK-593).^[54] Therefore, we next investigated the effect of varying incubation time for type I inhibitor CP-673451 and type II inhibitor **5** in a modified PDGFR β assay using an ATP concentration of 1 mM (Figure 8). The significantly increased ATP concentration was chosen in order to avoid limited substrate phosphorylation in the presence of a DFG-out inhibitor, and thus a diminished amount of active kinase.

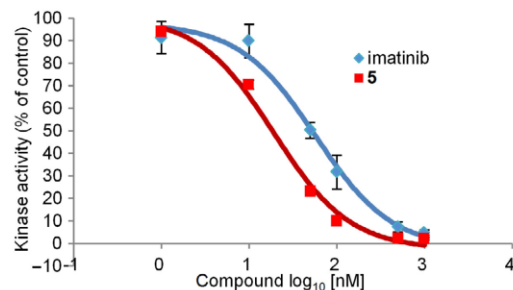


Figure 7. Ligand activity determination of imatinib (IC₅₀ = 58 nM) and compound **5** (IC₅₀ = 19 nM) in a PDGFR β kinase assay against an ATP concentration of 10 μ M. Data are the mean \pm SD of $n=3$ experiments performed in duplicate.

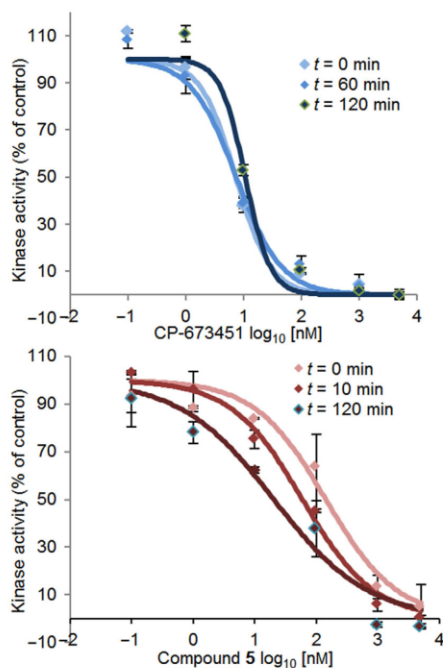


Figure 8. Effect of varying incubation time for type I inhibitor CP-673451 (top) and type II inhibitor **5** (bottom) in a PDGFR β assay using 1 mM ATP. Data are the mean \pm SD of $n=3$ experiments performed in duplicate.

According to the proposed type I binding mode for CP-673451, different incubation times had no significant effect on PDGFR β kinase activity (IC₅₀ values: 0 min = 7 nM, 60 min = 8 nM, 120 min = 11 nM). Thus, in line with earlier reports, these data provide further evidence for CP-673451 being a type I inhibitor.^[55] In contrast, compound **5** blocking PDGFR β activity was determined to be considerably time dependent (IC₅₀ values: 0 min = 143 nM, 10 min = 60 nM, 120 min = 20 nM). In fact, over a period of 120 min, the IC₅₀ values of **5** were shifted by a factor of seven toward higher PDGFR β affinity. These re-



sults strongly suggest a type II binding mode and slower on/off kinetics for **5** in the active site of PDGFR β relative to CP-673451.

Selectivity profiling in activity-based (ProQinase) and affinity-based assays (Discover_x)

In an activity-based biochemical ATP competition assay, activated (i.e., over-phosphorylated) enzymes were used in which kinases are thought to be present mainly in the DFG-in conformation. As typical read-out in an activity-based assay, the amount of substrate phosphorylation is measured, for example, by incorporating radioactive ³³P from labeled ATP within the reaction mixture. Despite being reduced to key biochemical parameters, in the kinase drug discovery field this type of activity assay is considered to represent the most true-to-life situation in living cells.^[49] In contrast, other assay systems determine a test compound's affinity^[56] by a ligand competition kinase fragment assay, for example, by using the displacement of the pan-kinase inhibitor staurosporine as readout. Notably, this assay setup is a long way from the actual biological function of kinases. However, in an affinity assay, a kinase fragment does not necessarily need to be over-activated because the readout is not ATP dependent. As a consequence, ligands that bind to the kinase by any manner, including active-site-directed but also allosteric inhibitors, can be identified. On the other hand, staurosporine represents a type I binder, suggesting that the kinase fragments used were initially present mainly in the DFG-in conformation.

In this regard, for type II ligand **5** the clear dependence of biological activity on incubation time used in our PDGFR β kinase activity assay raised the question: how comparable are the results obtained from different assay systems for type I and type II kinase inhibitors? We therefore submitted key compounds **1** and **5**, sharing the same pyrazin-2-one core, for standard profiling at a concentration of 1 μ M both over 300 kinases in activity-based assays (ProQinase, Freiburg, Germany, Figure 9A) and for profiling over 97 kinases in an affinity-based assay system (Discover_x, Figure 9B). Although not fully congruent in terms of the kinases used and readout technique, the revealed selectivity data were expected to provide a solid basis to discuss the question raised above.

The results showed differentiated selectivity profiles. In both assay formats type I binder **1** was significantly less selective than type II inhibitor **5**, which is in line with our hypothesis regarding DFG-in/out ligands. On the other hand, compound **5** was found to be more selective by measurements in activity assays when compared with affinity assays. These findings also correspond to our type I/II hypothesis and the assay-related facts discussed above.

When the profiling data are examined in greater detail, in the activity-based assay system DFG-in inhibitor **1** potently blocks PDGFR β , but in total addressing 47 out of 300 kinases with < 50% residual activity (S_{50} =0.16). In the same assay system DFG-out inhibitor **5** appears to be significantly more selective. Only four highly related RTKs, namely PDGFR β (18%),

PDGFR α (46%), RET (10%), and VEGFR2 (5%) were inhibited with < 50% residual activity (S_{50} =0.013).

In the affinity-based assay (readout: staurosporine residual binding) DFG-in ligand **1** strongly inhibits 21 out of 97 kinases (< 50% residual binding, S_{50} =0.22). As reported earlier, PDGFR β (0.7%) is potently blocked by compound **1**. On the other hand, DFG-out ligand **5** significantly binds to nine out of 97 kinases (S_{50} =0.11). Notably, those nine blocked kinases are all members of the TK family. Similar to the activity-based data discussed above, compound **5** binds to PDGFR β , PDGFR α , RET, and VEGFR2 (for all 0%, Figure 9A), indicating very high affinity for those kinases. Furthermore, in the affinity-based assay additional TKs were inhibited, namely CSF1R, FLT3, KIT, ABL1(-P), and AXL (Figure 9B; for concise comparison, see Table 4).

Table 4. Comparison of selected assay hits from activity assay system (ProQinase) and affinity assay system (Discover_x) for compound **5**.^[a]

Kinase	ProQinase [% residual activity]	Discover _x [% test compd signal]
ABL1(+P)	96	67
ABL1(-P)	_ ^[b]	0.6
AXL	112	33
CSF1R	92	0
FLT3	100	8.2
KIT	93	0
PDGFR β	18	0
PDGFR α	46	0
RET	10	0
VEGFR2	5	0.35

[a] See the Supporting Information for full details. [b] Non-phosphorylated ABL1(-P) was not used in the ProQinase panel.

Interestingly, phosphorylated (activated, DFG-in) as well as non-phosphorylated ABL1 (inactive, DFG-out) were used in the affinity assay panel. Herein, both ABL1(+P) and ABL1(-P) were addressed by DFG-in binder **1** to the same extent (60%). In contrast and in line with the notion of being a DFG-out ligand, compound **5** only weakly binds to ABL1(+P) (67%) but totally blocks ABL1(-P) (0.6%). When compared with the activity-based assay data, ABL1(+P) was not inhibited at all by **5** (96% residual activity; ABL1(-P) was not employed), which is consistent with our earlier assumption regarding phosphorylated/activated/DFG-in kinases and vice versa.

Taken together, both assay types reported to some extent similar and highly interesting selectivity profiles toward RTKs for potent and effective DFG-out inhibitor **5**. However, these results raise important questions: which assay setup more accurately reflects the real biochemical situation for type II ligands? Had DFG-out binders such as **5** been discriminated as false negatives when screened in activity-based assays, in particular against TK? Or had DFG-out binders been more likely to be identified as false positive hits in affinity-based assays? Probably both statements could be true, and we believe there is no easy answer to this. Further investigations including X-ray structure determination of **5** in PDGFR β (or in one of the closely related TKs blocked by **5**) and measurement of on/off kinet-

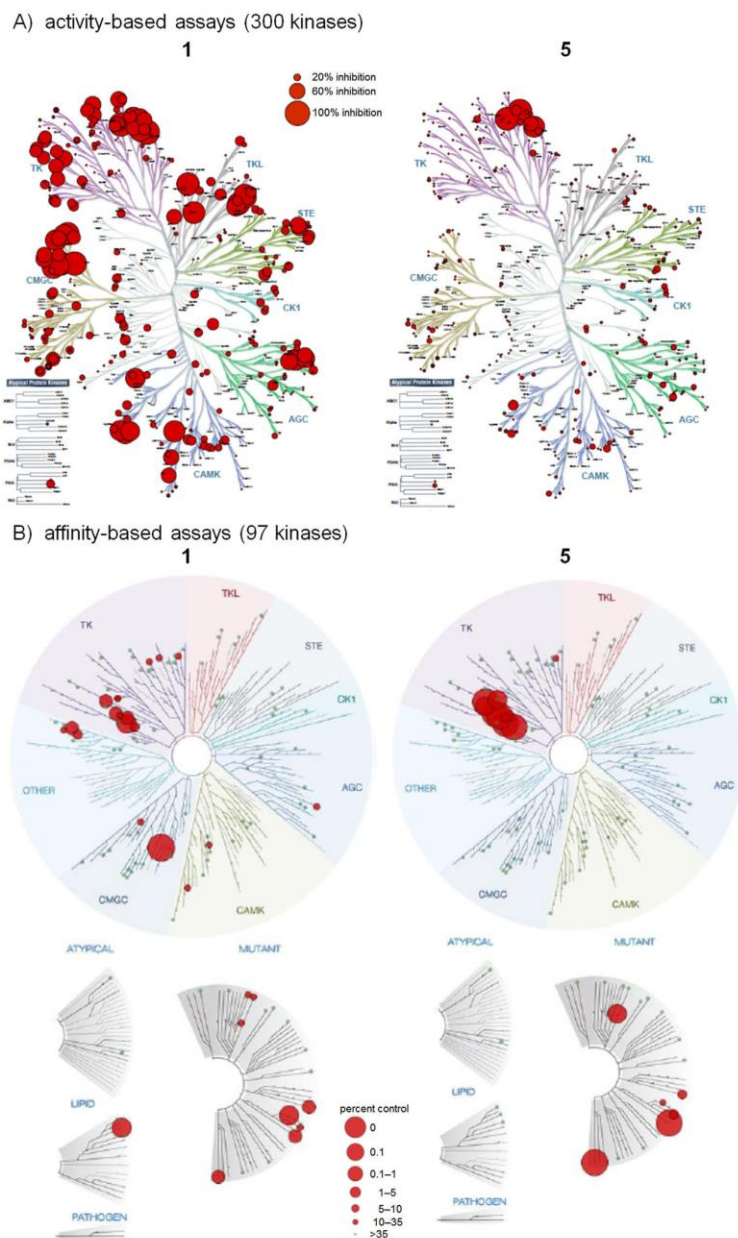


Figure 9. Graphical representation of the selectivity profile of compounds **1** (left)^[33] and **5** (right) at a concentration of 1 μM against 300 protein kinases in an activity-based assay system (A) and of 1 μM against 96 protein kinases in an affinity-based binding assay system (B). For clarity of representation, red circles indicate kinase inhibition relative to DMSO control (A, kinome render: bcb.med.usherbrooke.ca/kinomerender.php; illustration reproduced courtesy of Cell Signaling Technology Inc. www.cellsignal.com) or residual binding of staurosporine (B, treespot software: treespot.discover.com/). The size of the circle refers to the compound's affinity. See the Supporting Information for full details and selectivity profile representation of imatinib.

ics by surface plasmon resonance for **5** could be envisioned to provide further evidence for **5** being a type II inhibitor. One feasible option could be not to over-interpret information

from kinase selectivity panels determined at a single test compound concentration and to further prove hit compounds for their efficacy in cells (as shown above).^[57] However, as com-

plexity typically grows when it comes to different cell types or even in vivo situations, it remains to be seen in various assays if a hit really turns into an effective lead compound.^[58]

Conclusions

To summarize, based on type I inhibitor **1** from our former study, we successfully developed the present type II binder **5** by a structure-based modeling approach using a PDGFR β homology model. We demonstrated compound **5** to be a highly potent and effective type II PDGFR β inhibitor additionally targeting related TKs including CSF1R, KIT, FLT3, RET, and VEGFR2. This selectivity profile suggests **5** to be of significant interest in cancer research. Our biological data demonstrate compound **5** to be useful as a pharmacological tool for further development into a promising lead compound.

Experimental Section

Molecular modeling

All modeling was performed on a DELL 8 core system. For preparation, visualization, and building the 3D structures Maestro (version 10.3) from Schrödinger (Schrödinger, LLC, New York, NY, USA) was used. The primary sequence of PDGFR β consisting of 354 amino acids was taken from www.kinase.com. Homology modeling for PDGFR β was based on an X-ray structure of highly related c-kit (PDB ID: 1T46).

Chemistry

¹H NMR (300 MHz) and ¹³C NMR (75 MHz) were recorded on a Bruker Avance III 300 spectrometer (Rheinstetten, Germany) at 300 K with a multinuclear probe head using the manufacturer's pulse programs. The data are reported as follows: chemical shifts in ppm from Me₄Si (TMS) as external standard, multiplicity and coupling constant (Hz). NMR spectra were referenced either to TMS or to internal [D₆]DMSO (¹H NMR δ = 2.50) and internal [D₆]DMSO (¹³C NMR δ = 39.5) or internal CHCl₃ (¹H NMR δ = 7.26) and internal CDCl₃ (¹³C NMR δ = 77.0). All coupling constants (*J* values) are quoted in Hz. The following NMR abbreviations are used: br (broad), s (singlet), d (doublet), t (triplet), m (unresolved multiplet).

Mass spectra of the compounds were recorded after chromatographic separation. Mixtures were separated with an Agilent 1100 HPLC system (Waldbronn, Germany) consisting of a thermostated autosampler, diode array detection and an Agilent Zorbax Eclipse XDB C₈ column (150 × 4.6 mm, 5 μ m particle size). Elution was achieved with a solvent gradient system of water and acetonitrile, with 0.1% acetic acid and a flow rate of 1 mL min⁻¹. The eluent flow was diverted to the mass spectrometer. Mass spectra with nominal resolution were recorded with an Esquire LC mass spectrometer (Bruker Daltonik, Bremen, Germany), with electrospray ionization operating in the positive ion mode, with the following parameters: drying gas nitrogen 8 L min⁻¹, nebulizer 35 psi, dry gas heating 350 °C, HV capillary 4000 V, HV EndPlate offset -500 V. GC-MS was performed on an HP6890 Series System. EI mass spectra were recorded on a Varian MAT 311A (70 eV). HRMS data were recorded on a MAT-95 instrument (Finnigan). Infrared spectra were recorded with a Spectrum 100 FTIR spectrometer (PerkinElmer, USA).

Where appropriate, column chromatography was performed for crude precursors with Merck silica gel 60 (0.063–0.200 mm) or Acros Organics silica gel (0.060–0.200 mm; pore diameter ~ 60 nm). Column chromatography for test compounds was performed using a LaFlash system (VWR) with Merck silica gel 60 (0.015–0.040 mm) or RP8 columns. The progress of the reactions was monitored by thin-layer chromatography (TLC) performed with Merck silica gel 60 F₂₄₅ plates. Where necessary, reactions were carried out under nitrogen atmosphere using 4 Å molecular sieves. All reagents and solvents were obtained from commercial sources and used as received (THF was used after distillation over K/benzophenone). Reagents were purchased from Sigma–Aldrich Chemie, Steinheim, Germany; Lancaster Synthesis, Mülheim, Germany; or Acros, Nidderau, Germany. HPLC analysis was performed on a Hewlett–Packard HP 1090 Series II using a Thermo Betasil C₈ (150 × 4.6 mm 5 μ m) column (mobile phase flow rate 1.5 mL min⁻¹, gradient KH₂PO₄ buffer pH 2.3/methanol, UV detection λ = 230/254 nm). All key compounds submitted to biological assays were proven by this method to show \geq 98% purity.

Synthesis procedures and analytical data

Compound 1 (5-(4-hydroxy-3-methoxyphenyl)-3-(3,4,5-trimethoxyphenyl)-1*H*-pyrazin-2-one) was prepared as described by Horbert et al.^[33]

Compound 2 (*N*-[3-(3-nitrophenyl)-2-oxopropyl]-2-oxo-2-(3,4,5-trimethoxyphenyl)glyoxyacid): 400 mg (1.73 mmol, 1.1 equiv) of 2-(3,4,5-trimethoxyphenyl)glyoxyacid and 337 mg (2.08 mmol, 1.2 equiv) of CDI were dissolved in 15 mL absolute NMP and stirred for 3 h at 20 °C. Then 1 equiv α -ketoamine dissolved in 5 mL absolute NMP was added dropwise to the reaction mixture, which was stirred for 15 h at 20 °C. Ice was then added to produce a precipitate which was filtered and washed with water, cold methanol, and diethyl ether. Yield: 500 mg (1.20 mmol, 69%); ¹H NMR (300 MHz, [D₆]DMSO): δ = 3.78 (s, 3H, OCH₃), 3.84 (s, 6H, OCH₃), 4.12 (s, 2H, CH₂), 4.34 (d, ³*J* = 5.82 Hz, 2H, CH₂), 7.41 (s, 2H), 7.64 (td, ³*J* = 7.58 Hz, ⁴*J* = 0.88 Hz, 1H), 7.70 (dt, ³*J* = 7.61 Hz, ⁴*J* = 1.5 Hz, 1H), 8.12–8.16 (m, 2H), 9.21 ppm (t, ³*J* = 5.76 Hz, 1H, NH); ¹³C NMR (75.5 MHz, [D₆]DMSO): δ = 45.3 (CH₂), 48.7 (CH₂), 56.5 (OCH₃), 60.8 (OCH₃), 107.9, 122.2, 124.9, 128.4, 130.1, 137.0, 137.2, 143.7, 148.1, 153.4, 166.2, 189.5, 203.1 ppm; IR: 3286, 3078, 1727, 1664, 1632, 1603, 1578, 1535, 1457, 1415, 1349, 1234, 1167, 1131, 992, 859, 808, 765, 703 cm⁻¹; LC-MS (EI, 70 eV): *m/z* 417.2 [M + H]⁺ (calcd *m/z* = 416.4 for C₂₀H₂₀N₂O₈).

Compound 3a (5-[(3-nitrophenyl)methyl]-3-(3,4,5-trimethoxyphenyl)-1*H*-pyrazin-2-one): 244 mg (0.59 mmol, 1 equiv) of **2** and 452 mg (5.86 mmol, 10 equiv) NH₄Ac were dissolved in 3 mL concentrated acetic acid. This mixture was heated for 20 min at 90 °C in a microwave reactor (CEM Discover). Water was added to precipitate a light-brown solid which was filtered and washed with diethyl ether. Yield 200 mg (0.503 mmol, 86%); ¹H NMR (300 MHz, [D₆]DMSO): δ = 3.70 (s, 3H, CH₃), 3.79 (s, 6H, CH₃), 4.04 (s, 2H, CH₂), 7.44 (s, 1H), 7.61 (t, ³*J* = 7.92 Hz, 1H), 7.76 (s, 2H), 7.83 (d, ³*J* = 7.68 Hz, 1H), 8.07 (m, 1H), 8.27 (m, 1H), 12.35 ppm (s, 1H, NH); ¹³C NMR (75.5 MHz, [D₆]DMSO): δ = 37.9, 55.6, 60.0, 105.9, 121.2, 123.4, 124.4, 129.7, 131.2, 132.6, 135.8, 139.1, 142.2, 147.7, 149.0, 152.1, 154.4 ppm; IR: 2837, 1639, 1610, 1584, 1518, 1456, 1414, 1351, 1338, 1325, 1236, 1225, 1128, 995, 862, 765, 702 cm⁻¹; LC-MS (EI, 70 eV): *m/z* = 398.1 [M + H]⁺ (calcd *m/z* = 397.4 for C₂₀H₁₉N₃O₆).

Compound 3 (5-[(3-aminophenyl)methyl]-3-(3,4,5-trimethoxyphenyl)-1*H*-pyrazin-2-one): 80 mg (0.20 mmol) of **3a**, 100 μ L (0.101 mmol, 5 equiv) cyclohexene, one small spoon of Pd/C 10%

and 5 mL methanol were mixed in a 5 mL sealed vessel and heated in a microwave reactor (CEM Discover) for 10 min at 85 °C (max. 100 W). After cooling to 20 °C, the mixture was filtered and evaporated at reduced pressure. The product was crystallized from methanol as yellow crystals which were washed with diethyl ether. Yield: 48 mg (0.13 mmol, 65%); ¹H NMR (300 MHz, [D₆]DMSO): δ = 3.70 (s, 3H, OCH₃), 3.72 (s, 2H, CH₂), 3.79 (s, 6H, OCH₃), 4.95 (brs, 2H, NH₂), 6.37–6.41 (m, 1H), 6.45–6.48 (m, 2H), 6.93 (t, ³J = 7.56 Hz, 1H), 7.24 (s, 1H), 7.77 (s, 2H), 12.28 ppm (brs, 1H, NH); ¹³C NMR (75.5 MHz, [D₆]DMSO): δ = 39.2 (CH₂), 55.8 (OCH₃), 60.1 (OCH₃), 106.0, 111.8, 114.3, 116.4, 124.9, 128.7, 131.4, 134.5, 139.0, 140.3, 148.6, 152.2, 154.5 ppm; IR: 2934, 2836, 1641, 1584, 1518, 1504, 1456, 1414, 1350, 1338, 1223, 1126, 995, 862, 702, 522 cm⁻¹; LC-MS (EI, 70 eV): *m/z* = 368.3 [M + H]⁺ (calcd *m/z* = 367.4 for C₂₀H₂₁N₃O₄).

General method for amide coupling: Benzoic acid derivative (1.1 equiv) and 1.2 equiv of CDI were stirred for 3 h at 20 °C in absolute DMF. Then a solution of building block **3** in absolute DMF was added dropwise and the mixture was stirred for 15 h at 20 °C. Water was added and the reaction was extracted three times with ethyl acetate. The solvent was removed under reduced pressure and the product purified by flash chromatography.

Compound 4 (N-[3-[[6-oxo-5-(3,4,5-trimethoxyphenyl)-1H-pyrazin-3-yl]methyl]phenyl]-3-(trifluoromethyl)benzamide): Yield: 48 mg (0.13 mmol, 65%); ¹H NMR (300 MHz, [D₆]DMSO): δ = 3.70 (s, 3H, OCH₃), 3.77 (s, 6H, OCH₃), 3.79 (s, 2H, CH₂), 7.14 (d, ³J = 7.77 Hz, 1H), 7.31 (t, ³J = 7.85 Hz, 1H), 7.36 (s, 1H), 7.61 (d, ³J = 8.10 Hz, 1H), 7.75–7.80 (m, 2H), 7.77 (s, 2H), 7.96 (d, ³J = 8.01 Hz, 1H), 8.24 (d, ³J = 8.01 Hz, 1H), 8.28 (s, 1H), 10.43 (s, 1H, NH), 12.33 ppm (brs, 1H, NH); ¹³C NMR (75.5 MHz, [D₆]DMSO): δ = 38.9 (CH₂), 55.7 (OCH₃), 60.0 (OCH₃), 106.0, 118.5, 121.0, 123.9 (q, ¹JCF = 273.2 Hz), 124.1, 124.2, 124.7, 128.1, 128.6, 129.1 (q, ²JCF = 31.9 Hz), 129.7, 131.4, 131.8, 133.9, 135.7, 138.8, 139.0, 140.5, 149.0, 152.1, 154.5, 163.9 ppm; IR: 1670, 1634, 1603, 1578, 1521, 1506, 1489, 1472, 1456, 1413, 1338, 1325, 1201, 1188, 1169, 1109, 1072, 1007, 866 cm⁻¹; HRMS (EI, 70 eV): *m/z* = 539.1656 [M + H]⁺ (calcd *m/z* = 539.1668 for C₂₈H₂₄F₃N₃O₅).

Compound 5 (4-[[4-methylpiperazin-1-yl]methyl]-N-[3-[[6-oxo-5-(3,4,5-trimethoxyphenyl)-1H-pyrazin-3-yl]methyl]phenyl]benzamide): 4-[[4-methylpiperazin-1-yl]methyl]benzoic acid (1.5 equiv), 1 equiv of **3**, and 1.6 equiv of HATU were dissolved in absolute DMF and stirred for 30 min at 20 °C. Then 5 equiv of DIPEA were added dropwise and the mixture was heated in a microwave reactor for 30 min at 90 °C (max. 100 W). To this mixture 50 mL of 1 M NaOH solution was added and then extracted three times with ethyl acetate. The solvent was removed under reduced pressure and the product was purified by flash chromatography. Yield: 88 mg (0.15 mmol, 43%); ¹H NMR (300 MHz, [D₆]DMSO): δ = 2.15 (s, 3H, CH₃), 2.25–2.42 (m, 8H, CH₂), 3.52 (s, 2H, CH₂), 3.69 (s, 3H, OCH₃), 3.77 (s, 6H, OCH₃), 3.89 (s, 2H, CH₂), 7.09 (d, ³J = 7.62 Hz, 1H), 7.28 (t, ³J = 7.85 Hz, 1H), 7.35 (s, 1H), 7.43 (d, ³J = 8.37 Hz, 1H), 7.58 (d, 1H, ³J = 9.18 Hz), 7.77 (s, 2H), 7.80 (s, 1H), 7.88 (d, ³J = 8.31 Hz, 2H), 10.15 (s, 1H, NH), 12.34 ppm (brs, 1H, NH); ¹³C NMR (75.5 MHz, [D₆]DMSO): δ = 38.9 (CH₂), 45.7 (CH₃), 52.6 (CH₂), 54.7 (CH₂), 55.7 (OCH₃), 60.1 (OCH₃), 61.6 (CH₂), 106.0, 118.2, 120.8, 124.1, 124.3, 127.5, 128.5, 128.6, 131.4, 133.6, 134.0, 139.0, 139.2, 140.4, 142.2, 149.0, 152.1, 154.5, 165.3 ppm; IR: 2836, 1641, 1583, 1517, 1504, 1456, 1414, 1350, 1339, 1223, 1126, 995, 862, 702, 522 cm⁻¹; LC-MS (EI, 70 eV): *m/z* = 584.4 [M + H]⁺ (calcd *m/z* = 583.3 for C₃₃H₃₇N₅O₅).

Compound 6 (1-(2-chlorophenyl)-3-[[6-oxo-5-(3,4,5-trimethoxyphenyl)-1H-pyrazin-3-yl]methyl]phenyl]urea): 1-Chloro-2-isocya-

nato-benzene (1.1 equiv), 1 equiv of building block **3** and 1.6 equiv of DIPEA were dissolved in absolute DMF and stirred for 16 h at 20 °C. In this reaction it is very important to avoid any trace of water, as otherwise isocyanates generate carbamic acid, which easily decarboxylates toward amines. After 16 h, water was added and the mixture was extracted three times with ethyl acetate. The solvent was removed under reduced pressure and the product was purified by flash chromatography. Yield: 30 mg (0.06 mmol, 30%); ¹H NMR (300 MHz, [D₆]DMSO): δ = 3.70 (s, 3H, OCH₃), 3.78 (s, 6H, OCH₃), 3.87 (s, 2H, CH₂), 6.98–7.05 (m, 2H), 7.26–7.34 (m, 4H), 7.45 (dd, ³J = 7.97 Hz, ⁴J = 1.30 Hz, 1H), 7.52 (s, 1H), 7.79 (s, 2H), 8.14 (dd, ³J = 8.27 Hz, ⁴J = 1.22 Hz, 1H), 8.26 (s, 1H), 9.38 (s, 1H, NH), 12.33 ppm (brs, 1H, NH); ¹³C NMR (75.5 MHz, [D₆]DMSO): δ = 38.9 (CH₂), 55.7 (OCH₃), 60.1 (OCH₃), 106.0, 116.1, 118.6, 121.2, 121.8, 122.8, 123.2, 124.1, 127.5, 128.8, 129.2, 131.4, 135.9, 139.0 (q-C), 139.4 (q-C), 140.7, 152.0, 152.1, 154.5 ppm; IR: 2940, 1647, 1558, 1539, 1506, 1497, 1489, 1472, 1457, 1436, 1339, 1298, 1123, 1033, 999, 748 cm⁻¹; LC-MS (EI, 70 eV): *m/z* = 523 [M + H]⁺ (calcd *m/z* = 522.5 for C₂₇H₂₇ClN₄O₅).

Compound 7 (1-(2,4-dimethoxyphenyl)-3-[[6-oxo-5-(3,4,5-trimethoxyphenyl)-1H-pyrazin-3-yl]methyl]phenyl]urea): 1-Isocyanato-2,4-dimethoxybenzene (1.1 equiv), 1 equiv of building block **3** and 1.6 equiv of DIPEA were dissolved in absolute DMF and stirred for 16 h at 20 °C. Water was added and the mixture extracted three times with ethyl acetate. The solvent was removed under reduced pressure and the product was purified by flash chromatography. Yield: 35 mg (0.06 mmol, 34%); ¹H NMR (300 MHz, [D₆]DMSO): δ = 3.71 (s, 3H, OCH₃), 3.73 (s, 3H, OCH₃), 3.79 (s, 6H, OCH₃), 3.85 (s, 3H, OCH₃), 3.86 (s, 2H, CH₂), 6.47 (dd, ³J = 8.88 Hz, ⁴J = 2.68 Hz, 1H), 6.61 (d, ⁴J = 2.70 Hz, 1H), 6.93 (d, ³J = 7.10 Hz, 1H), 7.17–7.23 (m, 2H), 7.33 (s, 1H), 7.50 (s, 1H), 7.79 (s, 2H), 7.91 (d, ³J = 8.80 Hz, 1H), 7.96 (s, 1H, NH), 9.16 (s, 1H, NH), 12.34 ppm (brs, 1H, NH); ¹³C NMR (75.5 MHz, [D₆]DMSO): δ = 39.4 (CH₂), 55.7 (OCH₃), 56.2 (OCH₃), 56.3 (OCH₃), 60.5 (OCH₃), 99.2, 104.6, 106.5, 116.2, 118.8, 120.1, 122.2, 122.7, 123.9, 129.2, 131.9, 134.3, 139.5, 140.5 (q-C), 141.0 (q-C), 149.6, 152.6, 153.0, 155.0, 155.4 ppm; IR: 2920, 1647, 1636, 1558, 1541, 1506, 1497, 1489, 1472, 1456, 1437, 1339, 1207, 1157, 1126, 1036, 862, 831, 785, 701 cm⁻¹; LC-MS (EI, 70 eV): *m/z* = 547 [M + H]⁺ (calcd *m/z* = 546.5 for C₂₉H₃₀N₄O₇).

Biochemistry

All inhibitor solutions were prepared freshly in DMSO prior to each experiment and used immediately.

Kinase assays: The ADP-Glo™ kinase assay from Promega was used. The assay was performed according to the manufacturer's standard protocol.

Cellular assays: Cells were grown in DMEM with 10% FCS, 2 mM L-glutamine, and 1 mM sodium pyruvate and incubated in a 5% CO₂ humidified atmosphere at 37 °C. Cells were grown in cell flasks until ~90% confluence and then seeded to give 21 000 cells in 100 μL per well into 96-well CulturePlates™ (PerkinElmer). In addition to the test plates, one plate was prepared for reference measurement at day zero. All plates were incubated for 24 h at 37 °C in a humidified atmosphere with 5% CO₂. Compounds were dissolved in 100% DMSO (v/v) and added to the test plates. The final DMSO concentration in the assay was 0.5% (v/v). Viability of the cells in the day-zero control plates was determined on the same day without adding any compounds. For viability measurement the resazurin assay was used. The shift in the fluorescence signal was measured with an LS55 fluorescence spectrometer (PerkinElmer). Test plates were incubated for a further 48 h and cell viability was de-



fined as described above. Measured raw data were converted into percent of cell growth values by using the high control (0.5% DMSO (v/v) without compound) and the day-zero control. For dose-response studies, 11 different concentrations of compounds were tested in duplicates. IC₅₀ values were calculated using the four-parameter logarithmic fit option of GraphPad Prism 5.

Western blot analysis: Cells were treated with the indicated concentrations of test compounds for 1 h at 37 °C 30 min after addition to the cells. Cells were lysed, and lysates were immunoblotted with the indicated antibodies. The lysis buffer contained both phosphatase and protease inhibitors. Similar results were obtained in duplicate experiments. Further experimental details can be found in the Supporting Information.

Acknowledgements

This research project was supported by the Deutsche Forschungsgemeinschaft (DFG) grant PE 1605/2-1. We thank Dr. Ulrich Girreser and Martin Schütt (Institute of Pharmacy, Kiel, Germany) for excellent technical and analytical assistance.

Keywords: DFG-in/-out · kinase inhibitors · kinase selectivity · PDGFRβ inhibition · structure-based drug design

- [1] P. Wu, T. E. Nielsen, M. H. Clausen, *Drug Discovery Today* **2016**, *21*, 5–10.
- [2] R. Roskoski, Jr., *Pharmacol Res.* **2016**, *103*, 26–48.
- [3] Z. Zhao, H. Wu, L. Wang, Y. Liu, S. Knapp, Q. Liu, N. S. Gray, *ACS Chem. Biol.* **2014**, *9*, 1230–1241.
- [4] Z. Fang, C. Grutter, D. Rauh, *ACS Chem. Biol.* **2013**, *8*, 58–70.
- [5] A. Richters, J. Ketzer, M. Getlik, C. Grutter, R. Schneider, J. M. Heuckmann, S. Heynck, M. L. Sos, A. Gupta, A. Unger, C. Schultz-Fademrecht, R. K. Thomas, S. Bauer, D. Rauh, *J. Med. Chem.* **2013**, *56*, 5757–5772.
- [6] J. Zhang, P. L. Yang, N. S. Gray, *Nat. Rev. Cancer* **2009**, *9*, 28–39.
- [7] L. M. Wodicka, P. Ciceri, M. I. Davis, J. P. Hunt, M. Floyd, S. Salerno, X. H. Hua, J. M. Ford, R. C. Armstrong, P. P. Zarrinkar, D. K. Treiber, *Chem. Biol.* **2010**, *17*, 1241–1249.
- [8] R. A. Engh, D. Bossemeyer, *Adv. Enzyme Regul.* **2001**, *41*, 121–149.
- [9] L. N. Johnson, M. E. Noble, D. J. Owen, *Cell* **1996**, *85*, 149–158.
- [10] J. Weisner, R. Gontla, L. van der Westhuizen, S. Oeck, J. Ketzer, P. Janing, A. Richters, T. Muhlenberg, Z. Fang, A. Taher, V. Jendrosseck, S. C. Pelly, S. Bauer, W. A. van Otterlo, D. Rauh, *Angew. Chem. Int. Ed.* **2015**, *54*, 10313–10316; *Angew. Chem.* **2015**, *127*, 10452–10456.
- [11] M. W. Karaman, S. Herrgard, D. K. Treiber, P. Gallant, C. E. Atteridge, B. T. Campbell, K. W. Chan, P. Ciceri, M. I. Davis, P. T. Edeen, R. Faraoni, M. Floyd, J. P. Hunt, D. J. Lockhart, Z. V. Milanov, M. J. Morrison, G. Pallares, H. K. Patel, S. Pritchard, L. M. Wodicka, P. P. Zarrinkar, *Nat. Biotechnol.* **2008**, *26*, 127–132.
- [12] C. L. McClendon, A. P. Kornev, M. K. Gilson, S. S. Taylor, *Proc. Natl. Acad. Sci. USA* **2014**, *111*, E4623–4631.
- [13] R. S. Vijayan, P. He, V. Modi, K. C. Duong-Ly, H. Ma, J. R. Peterson, R. L. Dunbrack, Jr., R. M. Levy, *J. Med. Chem.* **2015**, *58*, 466–479.
- [14] Y. Shan, M. A. Seeliger, M. P. Eastwood, F. Frank, H. Xu, M. O. Jensen, R. O. Dror, J. Kuriyan, D. E. Shaw, *Proc. Natl. Acad. Sci. USA* **2009**, *106*, 139–144.
- [15] S. B. Hari, E. A. Merritt, D. J. Maly, *Chem. Biol.* **2013**, *20*, 806–815.
- [16] M. J. Meyers, M. Pelc, S. Kamtekar, J. Day, G. I. Poda, M. K. Hall, M. L. Michener, B. A. Reitz, K. J. Mathis, B. S. Pierce, M. D. Parikh, D. A. Mischke, S. A. Long, J. J. Parlow, D. R. Anderson, A. Thorarensen, *Bioorg. Med. Chem. Lett.* **2010**, *20*, 1543–1547.
- [17] E. V. Schneider, J. Bottcher, M. Blaesse, L. Neumann, R. Huber, K. Maskos, *J. Mol. Biol.* **2011**, *412*, 251–266.
- [18] I. Kufareva, R. Abagyan, *J. Med. Chem.* **2008**, *51*, 7921–7932.
- [19] H. Vashisth, L. Maragliano, C. F. Abrams, *Biophys. J.* **2012**, *102*, 1979–1987.
- [20] S. Müller, A. Chaikvad, N. S. Gray, S. Knapp, *Nat. Chem. Biol.* **2015**, *11*, 818–821.
- [21] M. Angiolini, *Future Med. Chem.* **2011**, *3*, 309–337.
- [22] A. K. Gaumann, F. Kiefer, J. Alfer, S. A. Lang, E. K. Geissler, G. Breier, *Int. J. Cancer* **2016**, *138*, 540–554.
- [23] M. A. Fabian, W. H. Biggs III, D. K. Treiber, C. E. Atteridge, M. D. Azimioara, M. G. Benedetti, T. A. Carter, P. Ciceri, P. T. Edeen, M. Floyd, J. M. Ford, M. Galvin, J. L. Gerlach, R. M. Grotzfeld, S. Herrgard, D. E. Insko, M. A. Insko, A. G. Lai, J. M. Lelias, S. A. Mehta, Z. V. Milanov, A. M. Velasco, L. M. Wodicka, H. K. Patel, P. P. Zarrinkar, D. J. Lockhart, *Nat. Biotechnol.* **2005**, *23*, 329–336.
- [24] Y. Gao, S. P. Davies, M. Augustin, A. Woodward, U. A. Patel, R. Kovelman, K. J. Harvey, *Biochem. J.* **2013**, *451*, 313–328.
- [25] L. Peng, Z. G. Song, S. C. Jiao, *Sci. Rep.* **2014**, *4*, 6104.
- [26] F. Zhao, J. Zhang, L. Zhang, Y. Hao, C. Shi, G. Xia, J. Yu, Y. Liu, *Bioorg. Med. Chem.* **2016**, *24*, 4281–4290.
- [27] X. Wang, D. M. Berger, E. J. Salaski, N. Torres, Y. Hu, J. I. Levin, D. Powell, D. Wojciechowicz, K. Collins, E. Frommer, *Bioorg. Med. Chem. Lett.* **2009**, *19*, 6571–6574.
- [28] H. Zhao, M. D. Serby, Z. Xin, B. G. Szczepankiewicz, M. Liu, C. Kosogof, B. Liu, L. T. Nelson, E. F. Johnson, S. Wang, T. Pederson, R. J. Gum, J. E. Clampit, D. L. Haasch, C. Abad-Zapatero, E. H. Fry, C. Rondinone, J. M. Trevillyan, H. L. Sham, G. Liu, *J. Med. Chem.* **2006**, *49*, 4455–4458.
- [29] B. Frantz, T. Klatt, M. Pang, J. Parsons, A. Rolando, H. Williams, M. J. Tocci, S. J. O'Keefe, E. A. O'Neill, *Biochemistry* **1998**, *37*, 13846–13853.
- [30] M. I. Davis, J. P. Hunt, S. Herrgard, P. Ciceri, L. M. Wodicka, G. Pallares, M. Hocker, D. K. Treiber, P. P. Zarrinkar, *Nat. Biotechnol.* **2011**, *29*, 1046–1051.
- [31] R. A. Norman, D. Toader, A. D. Ferguson, *Trends Pharmacol. Sci.* **2012**, *33*, 273–278.
- [32] H. Iwata, S. Imamura, A. Hori, M. S. Hixon, H. Kimura, H. Miki, *Bioorg. Med. Chem.* **2011**, *19*, 5342–5351.
- [33] R. Horbert, B. Pinchuk, E. Johannes, J. Schlosser, D. Schmidt, D. Cappel, F. Totzke, C. Schachtele, C. Peifer, *J. Med. Chem.* **2015**, *58*, 170–182.
- [34] B. Pinchuk, E. Johannes, S. Gul, J. Schlosser, C. Schachtele, F. Totzke, C. Peifer, *Mar. Drugs* **2013**, *11*, 3209–3223.
- [35] E. Johannes, R. Horbert, J. Schlosser, D. Schmidt, C. Peifer, *Tetrahedron Lett.* **2013**, *54*, 4067–4072.
- [36] G. V. Sharonov, E. V. Bocharov, P. M. Kolosov, M. V. Astapova, A. S. Arseniev, A. V. Feofanov, *J. Biol. Chem.* **2014**, *289*, 14955–14964.
- [37] M. Xu, L. Yu, B. Wan, L. Yu, Q. Huang, *PLoS One* **2011**, *6*, e22644.
- [38] D. E. Shaw, F. Baig, I. Bruce, S. Chamoin, S. P. Collingwood, S. Cross, S. Dayal, P. Druckes, P. Furet, V. Furminger, D. Haggart, M. Hussey, I. Konstantinova, J. C. Loren, V. Molteni, S. Roberts, J. Reilly, A. M. Saunders, R. Stringer, L. Sviridenko, M. Thomas, C. G. Thomson, C. Tomlins, B. Wen, Y. Yeh, A. C. Pearce, *J. Med. Chem.* **2016**, *59*, 7901–7914.
- [39] M. Zindler, B. Pinchuk, C. Renn, R. Horbert, A. Dobber, C. Peifer, *ChemMedChem* **2015**, *10*, 1335–1338.
- [40] M. Cristofanilli, P. Morandi, S. Krishnamurthy, J. M. Reuben, B. N. Lee, D. Francis, D. J. Booser, M. C. Green, B. K. Arun, L. Pusztai, A. Lopez, R. Islam, V. Valero, G. N. Hortobagyi, *Ann. Oncol.* **2008**, *19*, 1713–1719.
- [41] J. Dietrich, C. Hulme, L. H. Hurley, *Bioorg. Med. Chem.* **2010**, *18*, 5738–5748.
- [42] K. S. Gajiwala, J. C. Wu, J. Christensen, G. D. Deshmukh, W. Diehl, J. P. DiNitto, J. M. English, M. J. Greig, Y. A. He, S. L. Jacques, E. A. Lunney, M. McTigue, D. Molina, T. Quenzer, P. A. Wells, X. Yu, Y. Zhang, A. Zou, M. R. Emmett, A. G. Marshall, H. M. Zhang, G. D. Demetri, *Proc. Natl. Acad. Sci. USA* **2009**, *106*, 1542–1547.
- [43] S. Atwell, J. M. Adams, J. Badger, M. D. Buchanan, I. K. Feil, K. J. Froning, X. Gao, J. Hendle, K. Keegan, B. C. Leon, H. J. Muller-Dieckmann, V. L. Nienaber, B. W. Noland, K. Post, K. R. Rajashankar, A. Ramos, M. Russell, S. K. Burley, S. G. Buchanan, *J. Biol. Chem.* **2004**, *279*, 55827–55832.
- [44] C. D. Mol, D. R. Dougan, T. R. Schneider, R. J. Skene, M. L. Kraus, D. N. Scheibe, G. P. Snell, H. Zou, B. C. Sang, K. P. Wilson, *J. Biol. Chem.* **2004**, *279*, 31655–31663.
- [45] B. J. Druker, *Nat. Med.* **2009**, *15*, 1149–1152.
- [46] Y. Liu, N. S. Gray, *Nat. Chem. Biol.* **2006**, *2*, 358–364.
- [47] C. E. Thomas, Y. Will, *Expert Opin. Drug Discovery* **2012**, *7*, 109–122.
- [48] M. Bajpai, J. D. Esmay, *Drug Metab. Rev.* **2002**, *34*, 679–689.
- [49] M. Schirle, J. L. Jenkins, *Drug Discovery Today* **2016**, *21*, 82–89.



- [50] Y. Xi, M. Chen, X. Liu, Z. Lu, Y. Ding, D. Li, *Onco Targets Ther.* **2014**, *7*, 1215–1221.
- [51] M. Ohshima, Y. Yamaguchi, K. Kappert, P. Micke, K. Otsuka, *Biochem. Biophys. Res. Commun.* **2009**, *381*, 165–170.
- [52] N. Le Jeune, F. Dubois, V. Bin, N. Perek, *Eur. J. Cancer* **2006**, *42*, 1004–1013.
- [53] E. Y. Moawad, *J. Gastrointest. Cancer* **2015**, *46*, 272–283.
- [54] H. Iwata, S. Imamura, A. Hori, M. S. Hixon, H. Kimura, H. Miki, *Biochemistry* **2011**, *50*, 738–751.
- [55] J. Hye Kim, S. G. Park, W. K. Kim, S. U. Song, J. H. Sung, *Stem Cells* **2015**, *33*, 542–556.
- [56] P. Ranjitkar, A. M. Brock, D. J. Maly, *Chem. Biol.* **2010**, *17*, 195–206.
- [57] M. P. Patricelli, T. K. Nomanbhoy, J. Wu, H. Brown, D. Zhou, J. Zhang, S. Jagannathan, A. Aban, E. Okerberg, C. Herring, B. Nordin, H. Weissig, Q. Yang, J. D. Lee, N. S. Gray, J. W. Kozarich, *Chem. Biol.* **2011**, *18*, 699–710.
- [58] T. Wunberg, M. Hendrix, A. Hillisch, M. Lobell, H. Meier, C. Schmeck, H. Wild, B. Hinzen, *Drug Discovery Today* **2006**, *11*, 175–180.

Manuscript received: September 28, 2016

Revised: October 30, 2016

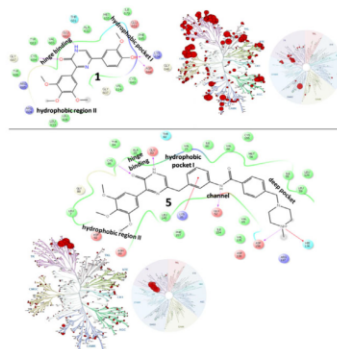
Final Article published: ■ ■ ■ ■ 0000

FULL PAPERS

E. Bethke, B. Pinchuk, C. Renn, L. Witt,
J. Schlosser, C. Peifer*



**From Type I to Type II: Design,
Synthesis, and Characterization of
Potent Pyrazin-2-ones as DFG-Out
Inhibitors of PDGFR β**



In with the out! Platelet-derived growth factor receptor β (PDGFR β) type II inhibitor **5** was designed, synthesized, characterized, and compared with a type I inhibitor. Differences regarding in vitro biological activity in a PDGFR β kinase assay, selectivity profiling in activity- and affinity-based assays, and cellular efficacy were demonstrated.



Supporting Information

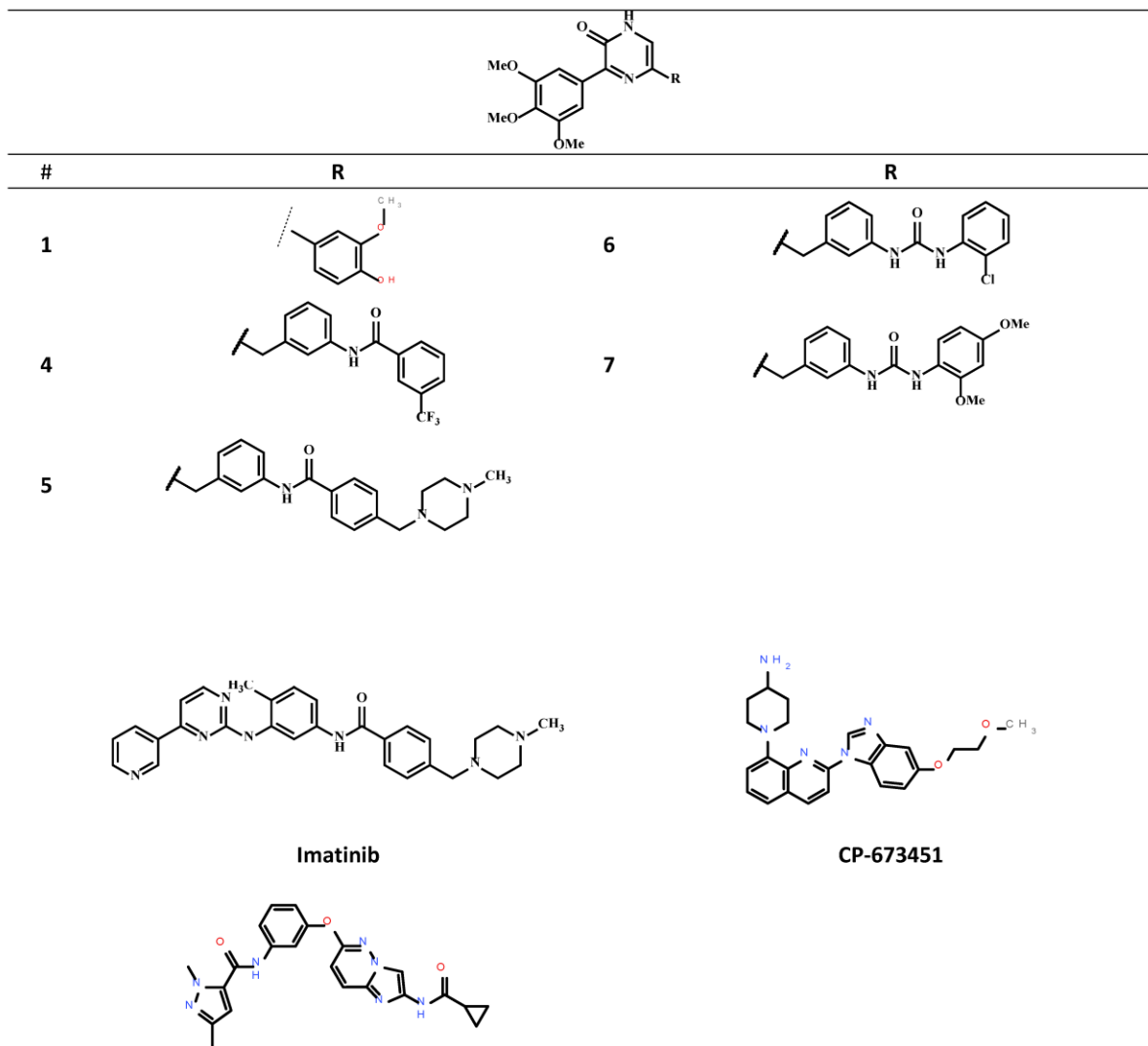
From Type I to Type II: Design, Synthesis, and Characterization of Potent Pyrazin-2-ones as DFG-Out Inhibitors of PDGFR β

Eugen Bethke, Boris Pinchuk, Christian Renn, Lydia Witt, Joachim Schlosser, and Christian Peifer^{*[a]}

cmdc_201600494_sm_miscellaneous_information.pdf

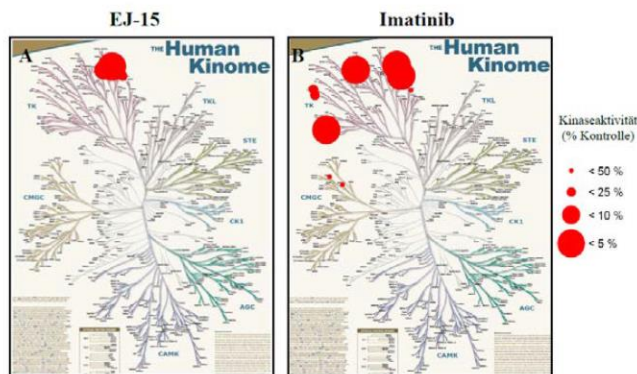
Supporting Information

1) Overview of key inhibitors

**DFG-out-Inhibitor TAK-593**

H. Iwata, S. Imamura, A. Hori, M. S. Hixon, H. Kimura and H. Miki,
Biochemistry 2011, 50, 738-751

2) Selectivity profiles of compound **5** over 300 kinases (present study) and imatinib over 310 kinases (Activity-based kinase profiling of approved tyrosine kinase inhibitors. Kitagawa et al., 2013, *Genes to Cells*, 18, 110-122). For clarity the results were illustrated by using “The Human Kinome poster” from Manning et al. *Science* (New York, N.Y.) 298, 1912–1934, 2002.



3) Data from affinity based assays (Scan EDGE) by DiscoverRX KINOMEScan™ Profiling Service, San Diego, USA. For all details please visit: <https://www.discoverx.com/services/drug-discovery-development-services/kinase-profiling/kinomescan>

Gene Symbol	compound	
	5	1
	%Ctrl @ 1000nM	%Ctrl @ 1000nM
ABL1(E255K)-phosphorylated	85	20
ABL1(T315I)-phosphorylated	99	53
ABL1-nonphosphorylated	0.6	30
ABL1-phosphorylated	67	30
ACVR1B	96	89
ADCK3	96	98
AKT1	98	100
AKT2	100	100
ALK	100	100
AURKA	75	7

AURKB	100	17
AXL	33	13
BMPR2	100	96
BRAF	100	100
BRAF(V600E)	100	100
BTK	93	100
CDK11	63	77
CDK2	94	93
CDK3	93	94
CDK7	100	25
CDK9	94	92
CHEK1	77	87
CSF1R	0	22
CSNK1D	93	81
CSNK1G2	100	61
DCAMKL1	94	97
DYRK1B	53	0
EGFR	73	90
EGFR(L858R)	69	81
EPHA2	100	95
ERBB2	79	97
ERBB4	100	88
ERK1	100	100
FAK	94	89
FGFR2	83	83
FGFR3	100	100
FLT3	8.2	1.3
GSK3B	100	100
IGF1R	100	99
IKK-alpha	100	90
IKK-beta	100	89
INSR	88	81

JAK2(JH1domain-catalytic)	96	90
JAK3(JH1domain-catalytic)	100	35
JNK1	85	39
JNK2	85	57
JNK3	100	46
KIT	0	2.6
KIT(D816V)	30	0.45
KIT(V559D,T670I)	6.2	34
LKB1	100	89
MAP3K4	89	86
MAPKAPK2	100	100
MARK3	91	99
MEK1	100	100
MEK2	100	100
MET	100	100
MKNK1	93	100
MKNK2	100	59
MLK1	100	100
p38-alpha	85	100
p38-beta	75	75
PAK1	100	70
PAK2	96	46
PAK4	95	56
PCTK1	100	100
PDGFRA	0	6.3
PDGFRB	0	0.7
PDPK1	99	99
PIK3C2B	73	48
PIK3CA	90	43
PIK3CG	48	0.7
PIM1	100	67
PIM2	100	54

PIM3	100	18
PKAC-alpha	100	100
PLK1	89	88
PLK3	100	100
PLK4	98	4.5
PRKCE	100	95
RAF1	97	100
RET	0	2
RIOK2	100	100
ROCK2	100	89
RSK2(Kin.Dom.1-N-terminal)	100	35
SNARK	100	26
SRC	100	43
SRPK3	100	100
TGFBR1	86	92
TIE2	81	68
TRKA	59	10
TSSK1B	100	100
TYK2(JH1domain-catalytic)	100	43
ULK2	95	97
VEGFR2	0.35	55
YANK3	100	100
ZAP70	100	100

KGS ▲	Kinase Name	Entrez Gene Symbol
ABL1(E255K)-phosphorylated	c-abl oncogene 1, receptor tyrosine kinase	ABL1
ABL1(T315I)-phosphorylated	c-abl oncogene 1, receptor tyrosine kinase	ABL1
ABL1-nonphosphorylated	c-abl oncogene 1, receptor tyrosine kinase	ABL1
ABL1-phosphorylated	c-abl oncogene 1, receptor tyrosine kinase	ABL1

ACVR1B	activin A receptor, type IB	ACVR1B
ADCK3	chaperone, ABC1 activity of bc1 complex homolog (S. pombe)	CABC1
AKT1	v-akt murine thymoma viral oncogene homolog 1	AKT1
AKT2	v-akt murine thymoma viral oncogene homolog 2	AKT2
ALK	anaplastic lymphoma receptor tyrosine kinase	ALK
AURKA	aurora kinase A	AURKA
AURKB	aurora kinase B	AURKB
AXL	AXL receptor tyrosine kinase	AXL
BMPR2	bone morphogenetic protein receptor, type II (serine/threonine kinase)	BMPR2
BRAF	v-raf murine sarcoma viral oncogene homolog B1	BRAF
BRAF(V600E)	v-raf murine sarcoma viral oncogene homolog B1	BRAF
BTK	Bruton agammaglobulinemia tyrosine kinase	BTK
CDK11	cyclin-dependent kinase 19	CDK19
CDK2	cyclin-dependent kinase 2	CDK2
CDK3	cyclin-dependent kinase 3	CDK3
CDK7	cyclin-dependent kinase 7	CDK7
CDK9	cyclin-dependent kinase 9	CDK9
CHEK1	CHK1 checkpoint homolog (S. pombe)	CHEK1
CSF1R	colony stimulating factor 1 receptor	CSF1R
CSNK1D	casein kinase 1, delta	CSNK1D
CSNK1G2	casein kinase 1, gamma 2	CSNK1G2
DCAMKL1	doublecortin-like kinase 1	DCLK1
DYRK1B	dual-specificity tyrosine-(Y)-phosphorylation regulated kinase 1B	DYRK1B
EGFR	epidermal growth factor receptor (erythroblastic leukemia viral (v-erb-b) oncogene homolog, avian)	EGFR
EGFR(L858R)	epidermal growth factor receptor (erythroblastic leukemia viral (v-erb-b) oncogene homolog, avian)	EGFR
EPHA2	EPH receptor A2	EPHA2
ERBB2	v-erb-b2 erythroblastic leukemia viral oncogene homolog 2, neuro/glioblastoma derived oncogene homolog (avian)	ERBB2
ERBB4	v-erb-a erythroblastic leukemia viral oncogene homolog 4 (avian)	ERBB4
ERK1	mitogen-activated protein kinase 3	MAPK3
FAK	PTK2 protein tyrosine kinase 2	PTK2
FGFR2	fibroblast growth factor receptor 2	FGFR2

FGFR3	fibroblast growth factor receptor 3	FGFR3
FLT3	fms-related tyrosine kinase 3	FLT3
GSK3B	glycogen synthase kinase 3 beta	GSK3B
IGF1R	insulin-like growth factor 1 receptor	IGF1R
IKK-alpha	conserved helix-loop-helix ubiquitous kinase	CHUK
IKK-beta	inhibitor of kappa light polypeptide gene enhancer in B-cells, kinase beta	IKBKB
INSR	insulin receptor	INSR
JAK2(JH1 domain-catalytic)	Janus kinase 2	JAK2
JAK3(JH1 domain-catalytic)	Janus kinase 3	JAK3
JNK1	mitogen-activated protein kinase 8	MAPK8
JNK2	mitogen-activated protein kinase 9	MAPK9
JNK3	mitogen-activated protein kinase 10	MAPK10
KIT	v-kit Hardy-Zuckerman 4 feline sarcoma viral oncogene homolog	KIT
KIT(D816V)	v-kit Hardy-Zuckerman 4 feline sarcoma viral oncogene homolog	KIT
KIT(V559D,T670I)	v-kit Hardy-Zuckerman 4 feline sarcoma viral oncogene homolog	KIT
LKB1	serine/threonine kinase 11	STK11
MAP3K4	mitogen-activated protein kinase kinase kinase 4	MAP3K4
MAPKAPK2	mitogen-activated protein kinase-activated protein kinase 2	MAPKAPK2
MARK3	MAP/microtubule affinity-regulating kinase 3	MARK3
MEK1	mitogen-activated protein kinase kinase 1	MAP2K1
MEK2	mitogen-activated protein kinase kinase 2	MAP2K2
MET	met proto-oncogene (hepatocyte growth factor receptor)	MET
MKNK1	MAP kinase interacting serine/threonine kinase 1	MKNK1
MKNK2	MAP kinase interacting serine/threonine kinase 2	MKNK2
MLK1	mitogen-activated protein kinase kinase kinase 9	MAP3K9
p38-alpha	mitogen-activated protein kinase 14	MAPK14
p38-beta	mitogen-activated protein kinase 11	MAPK11
PAK1	p21 protein (Cdc42/Rac)-activated kinase 1	PAK1
PAK2	p21 protein (Cdc42/Rac)-activated kinase 2	PAK2
PAK4	p21 protein (Cdc42/Rac)-activated kinase 4	PAK4
PCTK1	cyclin-dependent kinase 16	CDK16

PDGFRA	platelet-derived growth factor receptor, alpha polypeptide	PDGFRA
PDGFRB	platelet-derived growth factor receptor, beta polypeptide	PDGFRB
PDPK1	3-phosphoinositide dependent protein kinase-1	PDPK1
PIK3C2B	phosphoinositide-3-kinase, class 2, beta polypeptide	PIK3C2B
PIK3CA	phosphoinositide-3-kinase, catalytic, alpha polypeptide	PIK3CA
PIK3CG	phosphoinositide-3-kinase, catalytic, gamma polypeptide	PIK3CG
PIM1	pim-1 oncogene	PIM1
PIM2	pim-2 oncogene	PIM2
PIM3	pim-3 oncogene	PIM3
PKAC-alpha	protein kinase, cAMP-dependent, catalytic, alpha	PRKACA
PLK1	polo-like kinase 1 (Drosophila)	PLK1
PLK3	polo-like kinase 3 (Drosophila)	PLK3
PLK4	polo-like kinase 4 (Drosophila)	PLK4
PRKCE	protein kinase C, epsilon	PRKCE
RAF1	v-raf-1 murine leukemia viral oncogene homolog 1	RAF1
RET	ret proto-oncogene	RET
RIOK2	RIO kinase 2 (yeast)	RIOK2
ROCK2	Rho-associated, coiled-coil containing protein kinase 2	ROCK2
RSK2(Kin.Dom.1-N-terminal)	ribosomal protein S6 kinase, 90kDa, polypeptide 3	RPS6KA3
SNARK	NUAK family, SNF1-like kinase, 2	NUAK2
SRC	v-src sarcoma (Schmidt-Ruppin A-2) viral oncogene homolog (avian)	SRC
SRPK3	SFRS protein kinase 3	SRPK3
TGFBR1	transforming growth factor, beta receptor 1	TGFBR1
TIE2	TEK tyrosine kinase, endothelial	TEK
TRKA	neurotrophic tyrosine kinase, receptor, type 1	NTRK1
TSSK1B	testis-specific serine kinase 1B	TSSK1B
TYK2(JH1domain-catalytic)	tyrosine kinase 2	TYK2
ULK2	unc-51-like kinase 2 (C. elegans)	ULK2
VEGFR2	kinase insert domain receptor (a type III receptor tyrosine kinase)	KDR
YANK3	serine/threonine kinase 32C	STK32C
ZAP70	zeta-chain (TCR) associated protein kinase 70kDa	ZAP70

4) Data from activity based assays by ProQinase GmbH, Freiburg, Germany

Profiling of compound **5** at a concentration of 1 μ M against 300 wild-type protein kinases (duplicate measurement, data represented as residual activities in % of control). A radiometric protein kinase assay (33PanQinase® Activity Assay) was used for measuring the kinase activity of the 300 protein kinases. All kinase assays were performed in 96-well FlashPlates™ from Perkin Elmer (Boston, MA, USA) in a 50 μ l reaction volume. For further details please visit <http://proqinase.com/content/view/133>

#	Kinase	Kinase	5
	Name	Family	
			1 μM
1	ABL1	TK	96
2	ABL2	TK	108
3	ACK1	TK	82
4	ACV-R1	TKL	97
5	ACV-R1B	TKL	107
6	ACV-R2A	TKL	105
7	ACV-R2B	TKL	94
8	ACV-RL1	TKL	107
9	AKT1	AGC	103
10	AKT2	AGC	104
11	AKT3	AGC	104
12	ALK (GST-HIS-tag)	TK	95
13	AMPK-alpha1 aa1-550	CAMK	101
14	ARK5	CAMK	125
15	ASK1	STE	96
16	Aurora-A	OTHER	92
17	Aurora-B	OTHER	100
18	Aurora-C	OTHER	95
19	AXL	TK	112
20	BLK	TK	133
21	BMPR1A	TKL	108
22	BMX	TK	110
23	B-RAF	TKL	112
24	BRK	TK	149
29	CAMK2B	CAMK	79
30	CAMK2D	CAMK	101
31	CAMK4	CAMK	118
32	CAMKK1	OTHER	108
33	CAMKK2	OTHER	101
34	CDC42BPA	AGC	104
35	CDC42BPB	AGC	100
36	CDK1/CycA2	CMGC	94
37	CDK1/CycB1	CMGC	104
38	CDK1/CycE1	CMGC	99
39	CDK2/CycA2	CMGC	115

40	CDK2/CycE1	CMGC	98
41	CDK3/CycE1	CMGC	140
42	CDK4/CycD1	CMGC	105
43	CDK4/CycD3	CMGC	115
44	CDK5/p25NCK	CMGC	105
45	CDK5/p35NCK	CMGC	94
46	CDK6/CycD1	CMGC	88
47	CDK7/CycH/MAT1	CMGC	107
48	CDK8/CycC	CMGC	97
49	CDK9/CycK	CMGC	108
50	CDK9/CycT1	CMGC	101
51	CHK1	CAMK	134
52	CHK2	CAMK	100
53	CK1-alpha1	CK1	88
54	CK1-delta	CK1	85
55	CK1-epsilon	CK1	90
56	CK1-gamma1	CK1	102
57	CK1-gamma2	CK1	95
58	CK1-gamma3	CK1	98
59	CK2-alpha1	OTHER	95
60	CK2-alpha2	OTHER	100
61	CLK1	CMGC	99
62	CLK2	CMGC	99
63	CLK3	CMGC	96
64	CLK4	CMGC	94
65	COT	STE	105
66	CSF1-R	TK	92
67	CSK	TK	101
68	DAPK1	CAMK	78
69	DAPK2	CAMK	97
70	DAPK3	CAMK	94
71	DCAMKL2	CAMK	93
72	DDR2	TK	79
73	DMPK	AGC	103
74	DNA-PK	ATYP	92
75	DYRK1A	CMGC	110
76	DYRK1B	CMGC	100
77	DYRK2	CMGC	102
78	DYRK3	CMGC	93
79	DYRK4	CMGC	115
80	EEF2K	ATYPICAL	105
81	EGF-R	TK	78
82	EIF2AK2	OTHER	95
83	EIF2AK3	OTHER	99
84	EPHA1	TK	120

85	EPHA2	TK	123
86	EPHA3	TK	124
87	EPHA4	TK	107
88	EPHA5	TK	98
89	EPHA7	TK	111
90	EPHA8	TK	110
91	EPHB1	TK	127
92	EPHB2	TK	112
93	EPHB3	TK	121
94	EPHB4	TK	142
95	ERBB2	TK	103
96	ERBB4	TK	112
97	ERK1	CMGC	98
98	ERK2	CMGC	90
99	ERK7	CMGC	102
100	FAK aa2-1052	TK	96
101	FER	TK	116
102	FES	TK	119
103	FGF-R1	TK	115
104	FGF-R2	TK	110
105	FGF-R3	TK	135
106	FGF-R4	TK	110
107	FGR	TK	105
108	FLT3	TK	100
109	FRK	TK	108
110	FYN	TK	130
111	GRK2	AGC	98
112	GRK3	AGC	91
113	GRK4	AGC	100
114	GRK5	AGC	95
115	GRK6	AGC	86
116	GRK7	AGC	89
117	GSG2	OTHER	106
118	GSK3-alpha	CMGC	99
119	GSK3-beta	CMGC	98
120	HCK	TK	133
121	HIPK1	CMGC	101
122	HIPK2	CMGC	112
123	HIPK3	CMGC	129
124	HIPK4	CMGC	94
125	HRI	OTHER	106
126	IGF1-R	TK	121
127	IKK-alpha	OTHER	99
128	IKK-beta	OTHER	133
129	IKK-epsilon	OTHER	104

130	INS-R	TK	113
131	INSR-R	TK	111
132	IRAK1	TKL	97
133	IRAK4 (untagged)	TKL	110
134	ITK	TK	106
135	JAK1	TK	100
136	JAK2	TK	95
137	JAK3	TK	101
138	JNK1	CMGC	96
139	JNK2	CMGC	104
140	JNK3	CMGC	88
141	KIT	TK	93
142	LCK	TK	128
143	LIMK1	TKL	108
144	LIMK2	TKL	122
145	LRRK2	TKL	97
146	LTK	TK	113
147	LYN	TK	100
148	MAP3K1	STE	103
149	MAP3K10	STE	91
150	MAP3K11	STE	105
151	MAP3K7/MAP3K7IP1	STE	110
152	MAP3K9	STE	97
153	MAP4K2	STE	99
154	MAP4K4	STE	96
155	MAP4K5	STE	101
156	MAPKAPK2	CAMK	86
157	MAPKAPK3	CAMK	106
158	MAPKAPK5	CAMK	122
159	MARK1	CAMK	87
160	MARK2	CAMK	111
161	MARK3	CAMK	98
162	MARK4	CAMK	109
163	MATK	TK	144
164	MEK1	STE	80
165	MEK2	STE	92
166	MEKK2	STE	96
167	MEKK3	STE	90
168	MELK	CAMK	97
169	MERTK	TK	143
170	MET	TK	106
171	MINK1	STE	103
172	MKK6 S207D/T211D**	STE	97
173	MKNK1	CAMK	88
174	MKNK2	CAMK	92

175	MST1	STE	110
176	MST2	STE	104
177	MST3	STE	106
178	MST4	STE	115
179	mTOR	ATYPICAL	101
180	MUSK	TK	103
181	MYLK	CAMK	67
182	MYLK2	CAMK	97
183	MYLK3	CAMK	96
184	NEK1	OTHER	107
185	NEK11	OTHER	119
186	NEK2	OTHER	103
187	NEK3	OTHER	97
188	NEK4	OTHER	98
189	NEK6	OTHER	104
190	NEK7	OTHER	112
191	NEK9	OTHER	106
192	NIK	STE	123
193	NLK	CMGC	97
194	p38-alpha	CMGC	109
195	p38-beta	CMGC	103
196	p38-delta	CMGC	128
197	p38-gamma	CMGC	91
198	PAK1	STE	97
199	PAK2	STE	97
200	PAK3	STE	95
201	PAK4	STE	106
202	PAK6	STE	91
203	PAK7	STE	113
204	PASK	CAMK	121
205	PBK	OTHER	121
206	PCTAIRE1/CycY	CMGC	97
207	PDGFR-alpha	TK	46
208	PDGFR-beta	TK	18
209	PDK1	AGC	99
210	PHKG1	CAMK	98
211	PHKG2	CAMK	91
212	PIM1	CAMK	103
213	PIM2	CAMK	94
214	PIM3	CAMK	93
215	PKA	AGC	79
216	PKC-alpha	AGC	115
217	PKC-beta1	AGC	102
218	PKC-beta2	AGC	110
219	PKC-delta	AGC	98

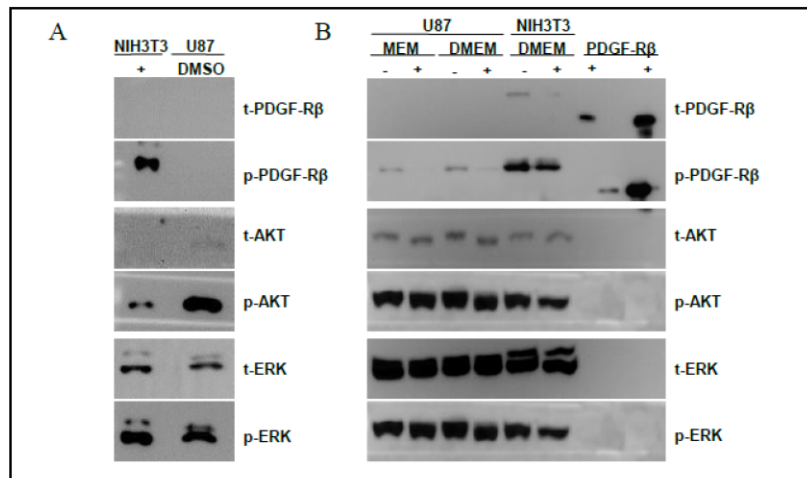
220	PKC-epsilon	AGC	115
221	PKC-eta	AGC	88
222	PKC-gamma	AGC	101
223	PKC-iota	AGC	104
224	PKC-mu	AGC	132
225	PKC-nu	AGC	119
226	PKC-theta	AGC	108
227	PKC-zeta	AGC	99
228	PLK1	OTHER	107
229	PLK3	OTHER	111
230	PRK1	AGC	104
231	PRK2	AGC	99
232	PRKD2	CAMK	98
233	PRKG1	AGC	94
234	PRKG2	AGC	93
235	PRKX	AGC	84
236	PYK2	TK	118
237	RAF1 Y340D/Y341D	TKL	97
238	RET	TK	10
239	RIPK2	TKL	99
240	RIPK5	TKL	103
241	ROCK1	AGC	96
242	ROCK2	AGC	98
243	RON	TK	126
244	ROS	TK	101
245	RPS6KA1	AGC	104
246	RPS6KA2	AGC	99
247	RPS6KA3	AGC	99
248	RPS6KA4	AGC	109
249	RPS6KA5	AGC	116
250	RPS6KA6	AGC	99
251	S6K	AGC	117
252	S6K-beta	AGC	99
253	SAK	OTHER	99
254	SGK1	AGC	104
255	SGK2	AGC	96
256	SGK3	AGC	131
257	SLK	STE	103
258	SNARK	CAMK	100
259	SNF1LK2	CAMK	97
260	SNK	OTHER	112
261	SRC (GST-HIS-tag)	TK	99
262	SRMS	TK	110
263	SRPK1	CMGC	113
264	SRPK2	CMGC	111

265	STK17A	CAMK	116
266	STK23	CAMK	107
267	STK25	STE	94
268	STK33	CAMK	90
269	STK39	STE	95
270	SYK aa1-635	TK	114
271	TAOK2	STE	97
272	TAOK3	STE	105
273	TBK1	OTHER	107
274	TEC	TK	106
275	TGFB-R1	TKL	100
276	TGFB-R2	TKL	89
277	TIE2	TK	115
278	TLK1	AGC	93
279	TLK2	AGC	88
280	TRK-A	TK	104
281	TRK-B	TK	142
282	TRK-C	TK	111
283	TSF1	OTHER	112
284	TSK2	CAMK	92
285	TSSK1	CAMK	130
286	TTK	OTHER	132
287	TXK	TK	95
288	TYK2	TK	105
289	TYRO3	TK	118
290	VEGF-R1	TK	65
291	VEGF-R2	TK	5
292	VEGF-R3	TK	82
293	VRK1	CK1	106
294	WEE1	OTHER	89
295	WNK1	OTHER	105
296	WNK2	OTHER	96
297	WNK3	OTHER	116
298	YES	TK	109
299	ZAK	TKL	123
300	ZAP70	TK	116
			$S_{50} = 0.013$



Activity based inhibition profile for **5** over 300 kinases. Color code: from red (strong inhibition) to green (no inhibition).

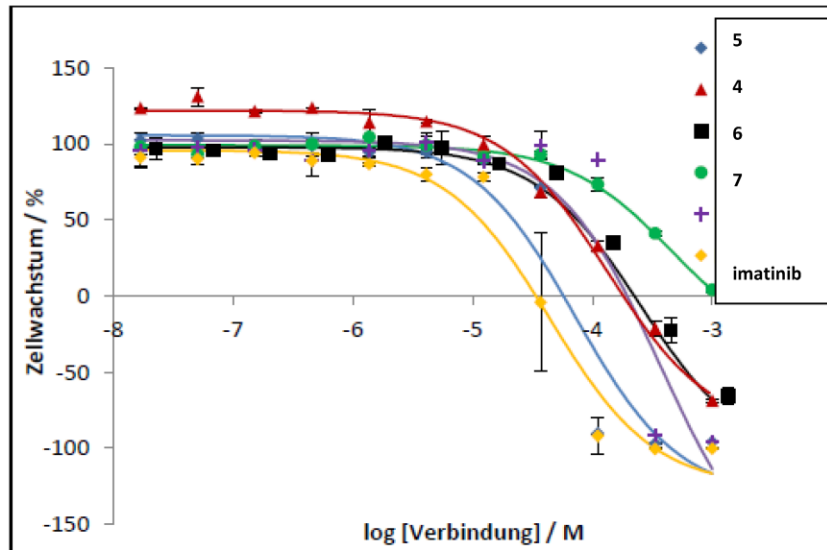
5) Method development for Western Blot



A) Detection of t-/p-AKT, t-/p-ERK in cell lysate of U87-MG cells. Detection of PDGFR β was not possible (NIH3T3 positive control)

B) Detection of t-/p-AKT, t-/p-ERK in cell lysate of U87-MG and NIH3T3 cells with positive control PDGFR β +/+. The signal in NIH3T3 cells was higher compared to U87-MG cells.

6) Determination of antiproliferative profiles of compounds in a cell proliferation assay using the U87-MG cell line.



4 Summary

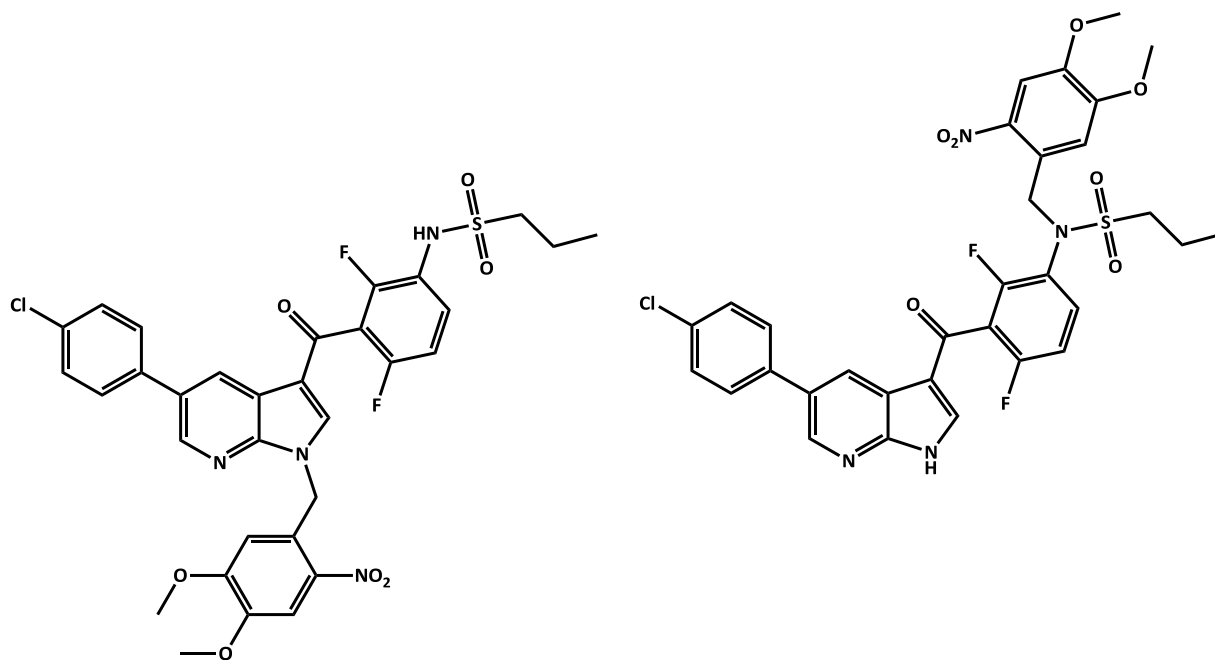
4.1 Photoactivatable prodrugs of kinase inhibitors

The main focus of the present thesis was on the biological characterization of novel photoactivatable prodrugs of smKIs. Aside from the fact that protein kinase inhibitors have effectively been applied in the therapy for the last 15 years and the caging technique has been utilized in different cellular applications, only very few caged smKIs have been described so far.^{165, 166} Moreover, photoactivatable prodrugs of approved smKIs have not been reported yet.

To the best of my knowledge, our research group developed the first photoactivatable prodrugs of an approved smKI.¹⁷⁶ The caging concept has successfully been applied on the antimelanoma agent vemurafenib.¹⁹³ A specifically acquired workflow for the caging of kinase inhibitors (Figure 12) could be effectively utilized up to animal models. Herein, basic hypotheses about the caging concept could be successfully corroborated *in vitro*: The synthesized photoactivatable prodrugs were proved to be inactive in several assays. Light-induced release of the active inhibitor could be impressively demonstrated *in vitro*. Recovery of activity was proved to be precisely controlled both temporally and spatially. The development of photoactivatable prodrugs of vemurafenib was the first proof-of-principle for the applicability of caging concept on an approved protein kinase inhibitor.

Furthermore, in the course of the work on photoactivatable prodrugs of vemurafenib, several conclusions could be drawn. Comparison of *in vitro* data for caged vemurafenib derivatives revealed that the caging of the hinge binding site of the inhibitor diminishes the inhibitory potency more effectively than the caging of other inhibitor moieties. The azaindole moiety in vemurafenib was previously identified to address the hinge region of the target BRAF^{V600E} kinase. Thus, the azaindole caged derivative of vemurafenib, compound **4**, exhibits significantly lower residual activity both in kinase and cellular assays than its sulfonamide caged counterpart, compound **13** (Figure 24).²³⁷ Moreover, blocking the hinge binder in

vemurafenib successfully prevented the affinity to off-target kinases as shown in kinase selectivity profiling.¹⁹³



azaindole caged derivative of vemurafenib **4**

sulfonamide caged derivative of vemurafenib **13**

Figure 24: Chemical structures of photoactivatable prodrugs of vemurafenib.¹⁹³ The azaindole caged compound **4** and the sulfonamide caged derivative **13** correspond to the compounds **2** and **4** in the published article,¹⁹³ respectively.

The cellular toxicity of the photo-cleaved DMNB group could be assessed by usage of two model compounds: Boc-protected L-alanine, compound **14**, and its DMNB photoactivatable derivative, compound **15** (Figure 25). The cleaved DMNB group exhibited moderate antiproliferative effects at concentrations above 10 μM , as demonstrated on different cell lines.^{193, 194} Potent kinase inhibitors show strong cytotoxic effects at much lower concentrations. Vemurafenib, for instance, already inhibits cellular growth *in vitro* at concentrations around 0.1 μM . Therefore, the toxicity of the cleaved DMNB group might not be critical and a wide therapeutic window is feasible. Furthermore, synergistic cytotoxic effects of the released active kinase inhibitor and the cleaved PPG toward cancer cells might be very interesting for medicinal applications as discussed in the article about caged VEGFR-2 kinase inhibitors.¹⁹⁴

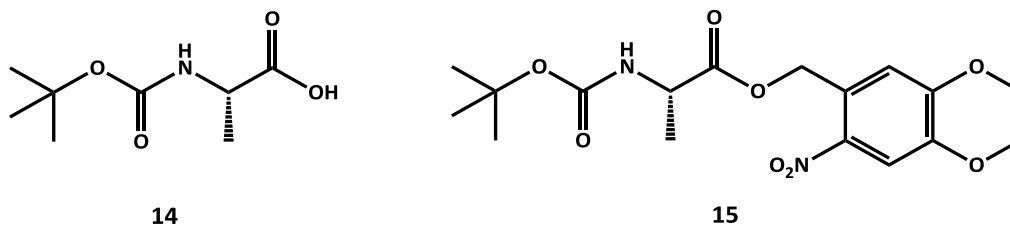


Figure 25: Chemical structures of the used model compounds.¹⁹³ Compound **14** is Boc-protected L-alanine and corresponds to “Boc-Ala” in the published article. Compound **15** is photoactivatable DMNB-protected derivative of the compound **14** and corresponds to “Boc-Ala-DMNB”.¹⁹³

Motivated by the success of photoactivatable vemurafenib prodrugs *in vitro*, we set out to develop caged prodrugs of other approved smKIs. In the course of our work, we designed photoactivatable derivatives of imatinib (Figures 6 and 17).¹⁹⁵ Our initial attempts toward direct caging of the amide function failed, as only the piperazine caged imatinib derivative, compound **16**, could be isolated (Figure 26).

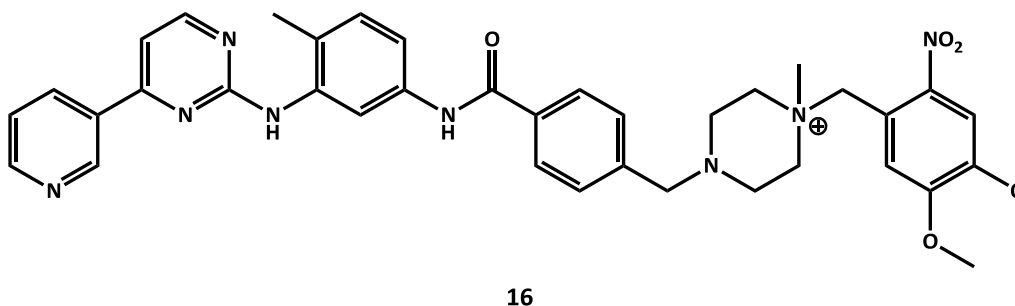


Figure 26: Chemical structure of compound 16, the piperazine DMNB-protected imatinib derivative.¹⁹⁵

Compound **16** was stable under UV-irradiation and no photoinduced release of imatinib could be achieved.¹⁹⁵ Only a circuitous synthetic route yielded the desired amide photoprotected derivatives of imatinib (Figure 17). Herein, two different PPGs were compared. It was found that the DMNB group exhibited more preferable characteristics for photoinduced cleavage than the coumarinyl group when attached to imatinib.

The findings described above underline the influence of both partners on the photoinduced reactivation: the inhibitor to be caged and the PPG to be bound to the inhibitor. Rapid and clean release of an active inhibitor is a prerequisite for successful usage of caged compounds.

Therefore, prior to biological applications, an appropriate PPG should be found for the distinct molecular moiety to be caged.

Interestingly, the reported amide caged derivative of imatinib (compound **5**, Figure 17) still showed measurable inhibition of PDGFR β in a kinase assay.¹⁹⁵ This finding is in line with the hypothesis that PPG cannot completely eradicate the activity of the caged compound when bound to an inhibitor site that is not the hinge binder. However, it is noteworthy to mention that even minor impurities or unwanted release of uncaged active inhibitor in the sample can cause residual biological activity. These minimal impurities are not always detectable by standard chemical analytics but could be sufficient to induce measurable responses in sensitive enzyme assays. Therefore, extensive chemical analysis is needed prior to application of caged compounds.

In the course of the work on development of photoactivatable protein kinase inhibitors, another significant discovery was made. A lot of kinase inhibitors are not stable to UV irradiation used for the cleavage of utilized PPGs. The PDGFR β inhibitors possessing the pyrazine-2-one core, for instance, underwent a rapid radical degradation when irradiated at 365 nm.²⁰⁵ Irradiation of VEGFR-2 inhibitors with a 3,4-diarylmaleimid core and of approved antimelanoma agent dabrafenib induced in both cases 1,6- π -electrocyclization followed by oxidation.^{194, 196} The revealed instability strongly restricts the applicability of affected inhibitors for caging. Due to these findings, all dabrafenib solutions should be carefully protected from light exposure when handled. Strikingly, to the best of my knowledge, the demonstrated photoinduced degradation of dabrafenib in solution (Figure 20) has previously not been described. Furthermore, the CHMP assessment report states "...the drug substance manufactured by the proposed supplier is sufficiently stable...".²³⁸ From my point of view, as consequence of demonstrated results the assessment report should be revised.

The photoinduced 1,6- π -electrocyclization mentioned above yielded novel compounds with interesting characteristics. For example, the autofluorescence of both carbazole compound **8** (Figure 18) and its DMNB-protected derivative **10** (Figure 19) could be used for proving the membrane permeability of DMNB-caged compounds in cellular assays.¹⁹⁴

Another aspect of the present work was the design and implementation of custom-made light sources for biological characterization of novel photoactivatable compounds. In cooperation with “Sahlmann Photochemical Solutions” (Bad Segeberg, Germany)²³⁹ novel purpose-built LED sources were developed. These UV sources were successfully utilized for different *in vitro* assays.

In summary, the present PhD thesis provided evidence for the applicability of photoactivatable prodrugs of approved smKIs at least *in vitro*. However, several preconditions should be fulfilled for successful caging of protein kinase inhibitors. First, the compound to be caged has to show distinct stability to the irradiation used for the photoinduced PPG-cleavage. Second, the biological target of the inhibitor should be known and the inhibitory potency should be precisely measurable. Third, the introduction of PPG should completely eradicate the activity of the inhibitor. Herein, the hinge binding moiety of the inhibitor should be protected. Fourthly, yielded caged compound should exhibit sufficient solubility and membrane permeability for cellular applications. Fifthly, the photoinduced release of parent compound should be quantitative, rapid and clean. The irradiation used for the deprotection should be delivered to the site of action. Therefore, special light emitting sources and light delivery systems have to be used. Furthermore, different PPGs can be applied for adjusting the wavelength of photoinduced deprotection and for improving bioavailability of caged compounds. The latter two points will be discussed in more details in the following chapter “Prospects”. The toxicity of the cleavage products of the PPG is not necessarily a problem, as was demonstrated on the example of the DMNB group.

The present work demonstrated that photoactivatable “caged” prodrugs of kinase inhibitors enable a precise temporal and spatial control of kinase activity. The caged smKIs might be a valuable research tool for investigating the kinase signaling *in vitro*.

4.2 Novel PDGFR β inhibitors

The second focus of the present work was on the characterization of novel PDGFR β inhibitors. Potent DFG-in and DFG-out inhibitors possessing the same chemotype were developed and compared *in vitro*. Pyrazine-2-one scaffold from hamacanthin B served as a lead structure. Extensive SAR studies were performed. Therefore, a novel synthetic route based on microwave-mediated ring closure strategy was used.²³⁰ Molecular modeling techniques such as WaterMap technology were successfully applied for the prediction of improved potency and selectivity of designed compounds. This rational approach led to the development of novel DFG-in inhibitors **1** and **2** (Figure 13) with IC₅₀ values in nanomolar range.^{201, 202}

Homology model of PDGFR β tyrosine kinase was used for molecular modeling.²⁰⁵ The modeling studies were applied to predict appropriate residues for addressing the deep pocket in PDGFR β . For design of novel DFG-out inhibitors the pyrazine-2-one scaffold was combined with moieties of known DFG-out inhibitors. These designed hybrid inhibitors were accessed by a flexible synthetic route.²⁰³ Extensive biological characterization *in vitro* identified compound **3** (Figure 13) as a potent and selective DFG-out inhibitor of PDFGR β .

The most potent agents of DFG-in and DFG-out series, compounds **2** and **3**, were extensively characterized *in vitro*. Besides comparable IC₅₀ values in low nanomolar range, several differences between the DFG-in inhibitor **2** and its DFG-out counterpart **3** were demonstrated. Compound **3** showed a time dependent binding kinetics to the target kinase. Moreover, the DFG-out inhibitor **3** was determined to be more potent than **2** both in cellular proliferation and western blot assays.²⁰³ Furthermore, compound **3** was shown to be more selective in different kinase profiling assays than the DFG-in inhibitor **2**. This finding was in line with the hypothesis about improved selectivity of DFG-out inhibitors.

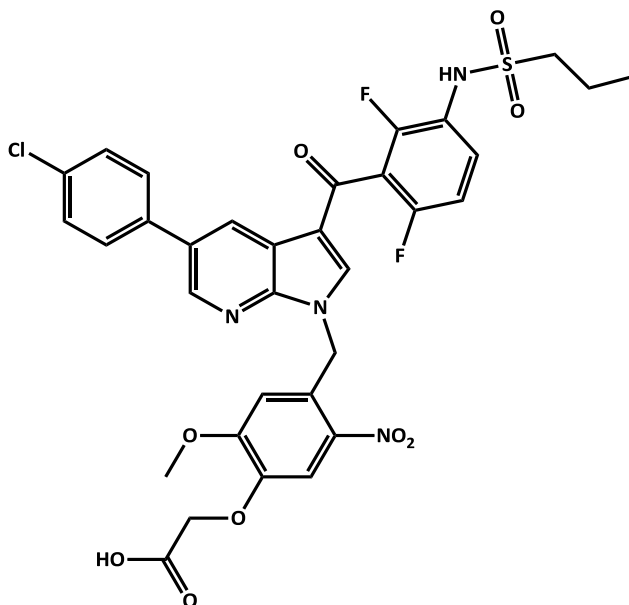
To summarize, our rational approach combining molecular modeling studies, novel synthetic routes, SAR investigations, and biological characterization led to the development of novel PDFGR β inhibitors. Especially, the DFG-out inhibitor **3** showed promising *in vitro* potency and selectivity and should be used for further lead optimization.

5 Prospects

5.1 Photoactivatable prodrugs of smKIs

5.1.1 *In vivo* testing of photoactivatable prodrugs of vemurafenib

After having proved the applicability of caging concept *in vitro*, the photoactivatable prodrugs of smKIs should be validated in animal models. Therefore, collaboration between our research group and the group of Prof. Dr. Knippschild in Ulm, Germany, was established. Together we have planned an extensive animal testing. Caged prodrugs of vemurafenib will be tested in a human melanoma xenograft model on CrI:NU(NCr)-*Foxn1*^{nu} nude mice.²⁴⁰ The design of the experiment is based on previously reported preclinical studies of vemurafenib.²⁴¹ Effects of vemurafenib and its caged derivative **4** (Figure 14) on melanoma growth will be tested both with and without UV irradiation. Furthermore, another photoactivatable prodrug of vemurafenib, compound **17** (Figure 27), will be evaluated *in vivo*.



azaindole caged derivative of vemurafenib **17**

Figure 27: Photoactivatable prodrug of vemurafenib **17.**²⁴² The azaindole moiety of vemurafenib was protected by a carboxylic acid analog of the DMNB PPG.¹⁶⁶

Prodrug **17** is an azaindole caged derivative of vemurafenib similar to compound **4**.²⁴² However, the DMNB protecting group is modified by introduction of a carboxylic acid (Figure 27). This modified PPG has previously been utilized to improve the solubility of caged compounds.^{166, 243} Compound **17** has recently been synthesized in our research group and showed similar photokinetic characteristics and at the same time highly enhanced solubility when compared to prodrug **4**.²⁴²

Following questions should be addressed by the projected animal experiments:

1. Are the caged prodrugs **4** and **17** bioavailable in the xenograft melanoma model?
2. What dosage of irradiation at 365 nm can be tolerated by animals without side effects?
3. Are the caged prodrugs **4** and **17** completely pharmacologically inactive when not irradiated?
4. Is it possible to restore the inhibitory activity of vemurafenib toward malignant melanoma by directed irradiation of photoactivatable prodrugs in the affected skin sites?

To reduce the number of test animals, several preliminary experiments are planned. The first two questions mentioned above should be answered by these preliminary tests. If the prodrugs are bioavailable and the irradiation is tolerable, the main experiment will be launched. Otherwise the animal testing will be cancelled. In preliminary experiments different methods for oral administration of caged compounds should be compared. Herein, administration of compounds emulsified in honey should be evaluated.²⁴⁴

Two appliances were specifically designed and custom-made for the proposed animal experiments. First, a mouse restrainer was developed for simultaneous fixing of the mouse and irradiation of posterior flanks of the test animal (Figure 28). Secondly, a LED pen for controlled irradiation at 365 nm (Figure 29) was custom-made by Sahlmann Photochemical Solutions.²³⁹



Figure 28: Custom-made mouse restrainer with a fixed test mouse. The posterior flank of the animal is accessible for irradiation.

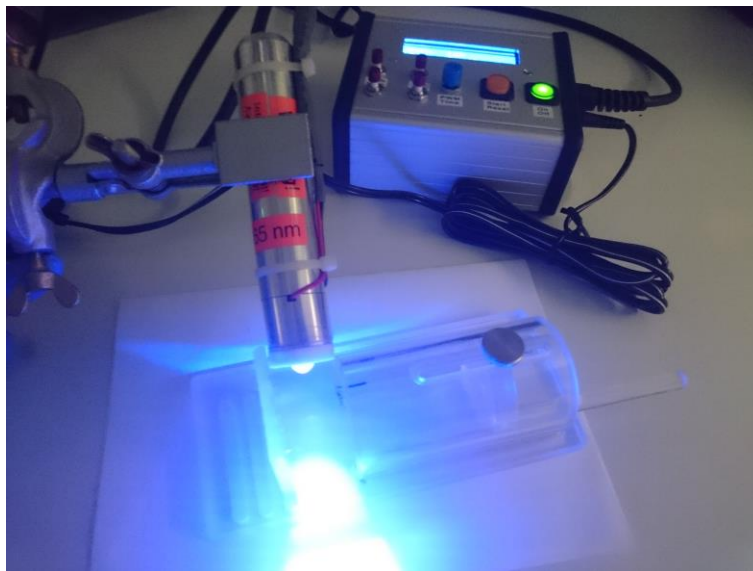


Figure 29: Custom-made LED pen for irradiation of test animals in the mouse restrainer.²³⁹ The illumination device was designed for the cleavage of the DMNB PPG by irradiation at 365 nm. Irradiation power and time can be adjusted by the control module at the top of the picture.

5.1.2 Approaches to overcome the limited penetration depth of light

One of the main challenges of the caging concept is the delivery of light to the target tissue. As previously described, the penetration depth of UV/visible light through biological tissues is limited and heavily depends on the applied wavelength (Figure 10). Moreover, intense UV irradiation can cause damage to biological tissue which may lead to novel malignancies.^{245, 246} Therefore, novel PPGs which are cleavable by visible light have been developed. Compounds caged by the BODIPY group (Table 1), for instance, can be released with green light irradiation at 500 nm.¹⁷⁷ However, even light with wavelengths close to 500 nm still has limited biological penetration. The maximum tissue permeability can be achieved by light irradiation within the so-called “phototherapeutic” or bio-optical window with wavelengths ranging from 650 to 850 nm.^{130, 247, 248} On the other hand, the energy provided by these wavelengths is typically not sufficient for breaking a chemical bound.²⁴⁹ Several possible solutions for increasing the depth of photoactivation have been proposed.²⁵⁰ Below, some of these ideas are named and shortly discussed. The approaches originate from the field of the PDT.¹³⁰ In my opinion, these developments might be transferable to applications of caged compounds.

Novel light-delivery systems

Delivery of light to the target tissue can be achieved by a technical combination of a powerful light source and a suitable fiberoptic delivery system.²⁴⁸ Enormous progress has been made in the field of light sources over the last decades.¹³⁰ Several novel laser and LED sources have been developed. Fiberoptic delivery devices compatible with clinical instrumentation such as injection needles (Figure 30) or endoscopes have been utilized. A successful combination of a diode laser and light delivery through an endoscope has recently been reported in a phase II clinical study of PDT of esophageal cancer.²⁵¹

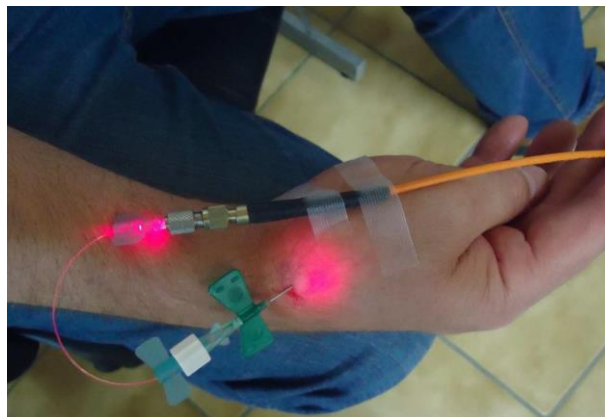


Figure 30: Example of red laser light delivery under the skin by an optical fiber and a needle.²⁵²

However, the application of fiber optic systems is limited to near-superficial or endoscopically accessible targets. The penetration depth of visible light achieved by direct delivery was reported to be about 3 mm underneath the skin.^{250, 253} Another way for targeted delivery of light is irradiation of designated tissue amenable during surgery. Illumination of deeper targets that are not operable still remains a great challenge.^{248, 250}

Two-photon excitation

Two-photon excitation (TPE) is a simultaneous absorption of two photons that leads to an excited energy state.^{250, 254} It can be used for release of a caged compound. Herein, irradiation with a doubled wavelength in comparison to standard photoactivation is used.^{140, 160} For instance, the DMNB PPG with a maximum absorption at 365 nm might be cleaved at 730 nm by TPE. One advantage of two-photon uncaging is the possible application of near-infrared (NIR) lasers for photoactivation.¹⁴⁰ The NIR irradiation has an increased tissue permeability compared to UV/visible light. TPE is a nonlinear optical process and requires high light intensities. Therefore, tightly focused femtosecond lasers are used as light sources.²⁵⁵ Two-photon absorption is limited to the area of highest light intensity, thus providing a possibility of 3D-control of action.²⁵⁶ This method has been successfully applied for PDT in xenograft models, where penetration depths about 2 cm could be achieved.^{257, 258}

Despite the advantages of deeper penetration and better spatial control, TPE exhibits the following key limitation: most described PPGs are not well-suited for two-photon

uncaging.^{140, 160} The quantum yield of TPE can be quantified by the two-photon action cross-section (TPACS) measured in Goeppert-Mayer units (GM). It is assumed that a TPACS of at least 0.1 GM is needed for biological application. The DMNB PPG, for instance, has a TPACS of 0.035 GM¹⁶⁰ and is therefore rather unsuitable for TPE applications. Further development of suitable PPGs with increased values of TPACS is required for an effective application of TPE *in vivo*. Another inherent disadvantage of TPE is the requirement of elaborate and expensive equipment such as pulsed femtosecond lasers for photoactivation.

Upconversion systems

Upconversion (UC) is a process of sequential absorption of several photons that causes emission of light with a shorter wavelength than the excitation irradiation.^{259–261} The process leads to an anti-Stokes luminescence.^{259, 262} Thereby, NIR illumination can be converted to higher energy irradiation such as UV or visible light. Absorption of low energy photons is comparable to that of TPE described above. However, several significant differences between UC and TPE should be highlighted. Real and long life energy levels of lanthanide ions absorb the excitation energy during the UC.²⁶³ The lanthanide ions are thereby embedded in an appropriate dielectric inorganic lattice. These guest-host systems are called upconversion nanoparticles (UCNPs) when their size is less than 100 nm.²⁶³ On the contrary, TPE utilizes organic molecules and involves virtual energy levels. As mentioned above, this explains the need of simultaneous absorption of two photons and therefore the requirement of high energetic pulsed femtosecond lasers for PTE.²⁵⁴ However, due to sequential absorption, no pulsed lasers are needed for UC, low-cost continuous-wave diode lasers are sufficient. Another advantage of UC is a much higher efficiency compared to TPE.²⁶³

UCNPs exhibit several advantageous optical characteristics such as high signal-to-noise ratio of emitted radiation, large anti-Stokes shifts, narrow emission bandwidths, no blinking, and no photobleaching.^{250, 263} Moreover, the upconverting range of UCNPs can be easily modulated by directed chemical design. Due to the fact that NIR radiation is within the phototherapeutic window, UCNPs can be used for converting NIR into local UV radiation in deeper tissues.²⁵⁰ These unique properties of UCNPs make them highly interesting for

biological applications. Meanwhile, several studies have been reported where UCNPs have been utilized for PDT, photothermal therapy or drug delivery. Moreover, UC has also been used for the cleavage of PPGs. Several examples of applied UC for photoactivation of caged compounds in deeper tissue have been described.^{263–266} Herein, the caged compounds were either loaded in the pores of silica coated UCNPs²⁶⁴ or covalently bound to thiolated silanes on the surface of coated UCNPs.²⁶⁶ The latter concept was successfully proved using the photocaged luciferin (Figure 31).

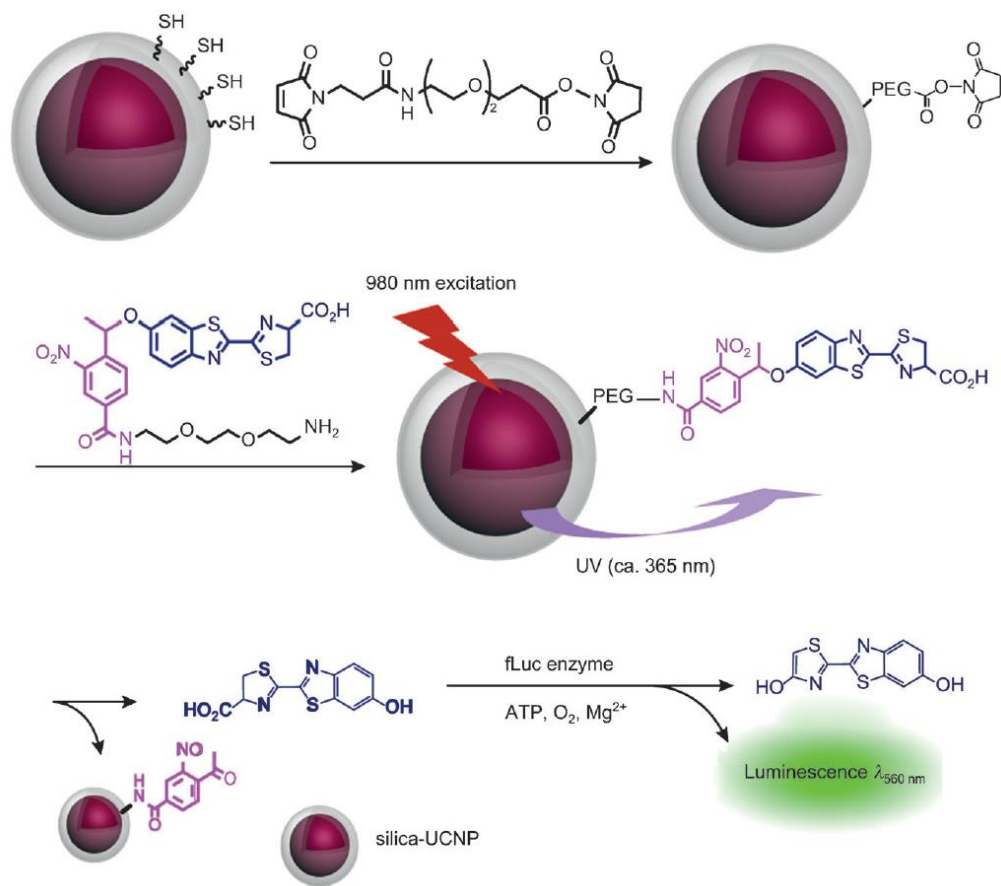


Figure 31: Proof-of-principle for the photolysis of caged D-luciferin by utilizing UCNPs coated with thiolated silane.²⁶⁶ 1-(2-nitrophenyl)ethyl caged luciferin was covalently bound to the UCNP by a linker. The excitation NIR radiation was upconverted by UCNPs to UV light that cleaved the PPG. The released luciferin was recognized by a luciferase (fLuc enzyme) and caused measurable bioluminescence.

The proof-of-principle study demonstrated that utilized UCNPs were cell-penetrating and exhibited no significant cytotoxicity in cellular assays.²⁶⁶ NIR irradiation was also well

tolerated. Furthermore, UCNPs might be conjugated with a tumor-targeting agent achieving enhanced tumor selectivity.^{267–269}

Despite all favorable characteristics of UC described above, several challenges have to be met prior possible medical application of UCNPs. The conversion efficiency of UCNPs still remains rather insufficient.²⁷⁰ This poor efficacy causes prolonged irradiation times needed for complete uncaging.²⁶⁶ Moreover, the loading capacity of UCNPs also remains limited.²⁶³ Development of highly efficient NIR-to-UV converting nanoparticles with enhanced quantum yield is therefore necessary.

Another very important issue to be addressed is the biocompatibility of UCNPs.²⁷¹ The used lanthanides are not found in biological systems under physiological conditions. UCNPs are not biodegradable *in vivo*. Therefore, an efficient clearance of UCNPs is a precondition for clinical applications of these particles.²⁶³ To date, only few investigations regarding possible toxicity of lanthanide doped nanoparticles have been performed so far. The *in vivo* toxicity of UCNPs has been systematically examined only in mouse, worms and zebrafish.²⁷² Herein, evidence for possible dose-dependent toxicity was provided.²⁷² Further *in vivo* investigations of possible UCNPs toxicity are highly required.^{263, 270, 272}

X-ray excitation

The NIR radiation permeates deeper into biological tissue than UV/visible light, however the penetration depth of NIR is limited too. Usually, maximum depths about one or two centimeters can be achieved.¹⁷¹ The highest reported NIR penetration was 3 cm *in vivo*.²⁷³ To address targets noninvasively deeper than that, application of high-energy X-rays is feasible.²⁷⁴ Since their discovery in 1895, X-rays have widely been used for medical imaging and radiotherapy. Besides great biological permeability, X-rays offer a possibility of distinguished spatial resolution up to 10 nm.²⁷⁵

X-ray irradiation cannot directly cleave a photoremovable protecting group. Therefore, scintillator materials that convert the X-rays to UV/visible light are necessary for photoactivation of caged compounds. Progress in nanotechnology led to the development of nanoparticles that can be used for this purpose.²⁷⁴ Several examples of scintillating

nanoparticles (ScNPs) have already been utilized as energy mediators for down conversion of X-ray to UV/visible light.²⁷⁴ ScNPs are materials with a wide band gap such as lanthanide doped nanoparticles.^{276, 277} Meanwhile, there are several reports where scintillators have successfully been utilized for PDT,^{278–280} optical imaging²⁸¹ or PUVA.²⁸² An overview of UVA (UV in the range of 315 – 400 nm) emitting ScNPs can be found in literature.²⁸² Furthermore, besides lanthanide doped nanoparticles other scintillating materials have been reported, for instance: zinc oxide nanoparticles,^{283, 284} copper doped zinc sulfide nanoparticles,²⁸⁵ and quantum dots.^{286, 287} ScNPs conjugated with targeting molecules have been developed to selectively address tumor cells.^{274, 279}

Similar to UCNPs, ScNPs might be loaded or conjugated with a caged prodrug. Different loading strategies for photosensitizers used in PDT have recently been described.²⁷⁴ Thus, the concept of coated UCNPs conjugated to a photoactivatable compound (Figure 31) might be transferred to ScNPs. Herein, X-ray irradiation might be converted to UV/visible light by scintillating nanoparticles. The emitted UV might cleave a PPG from the conjugated caged prodrug. As consequence, an active pharmaceutical ingredient might be released. X-ray excitation would enable addressing deeper targets with higher spatiotemporal resolution than irradiation by NIR. Compared to X-ray induced PDT, this concept would be advantageous in respect to enhanced selectivity of utilized kinase inhibitors. Furthermore, the hypoxic tumor environment as a typical challenge for PDT should not be a problem for the released smKIs.

To the best of my knowledge, the concept of using ScNPs to convert X-rays into UV/visible irradiation for reactivating photoactivatable prodrugs has not been evaluated yet. From my point of view, this approach would enable a smart possibility for combination of radiotherapy and precisely regulated release of active antitumor agents such as smKIs. Due to synergistic antitumor efficacy of X-rays and released smKIs, better therapeutic outcome might be possible. Moreover, lower dosage of harmful X-rays might be utilized. Of course, the concept of utilizing ScNPs for photoactivation of caged compounds is only an idea at this time. Several preconditions have to be met prior to biological applications of this approach: ScNPs with high scintillating efficacy and emission matching the wavelengths for PPG cleavage should be

evaluated. Caged prodrugs have to be effectively loaded or conjugated to scintillating materials. The successful release of active compounds upon X-ray irradiation should be proved under biological conditions. Last but not least, pharmacokinetic properties and toxicity profiles of utilized ScNPs should be extensively investigated prior to potential medical applications.

Cerenkov radiation

Cerenkov radiation (CR) occurs when a charged particle (β^- or β^+ - particle) travels through a dielectric medium at a speed faster than light in this medium.^{250, 288} Medium molecules become thereby polarized into excited energy states. When medium molecules relax back to the ground state they emit the so called Cerenkov luminescence.^{288, 289} CR is emission of light within a broad and continuous wavelength range (200 – 1000 nm).²⁵⁰ The intensity of CR is proportional to the frequency of emitted light. Therefore, the major part of luminescence occurs in UV and blue spectrum. Cerenkov radiation was first described in 1934.²⁹⁰ This physical phenomenon is responsible for the known blue glowing in nuclear reactors (Figure 32).

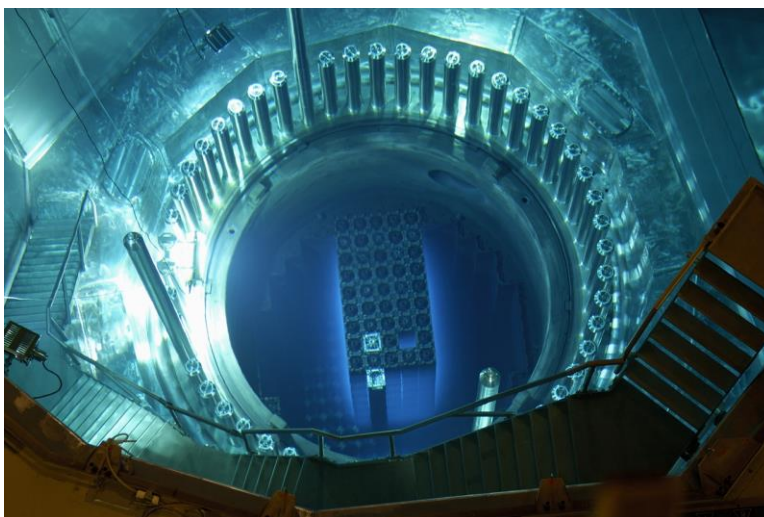


Figure 32: Cerenkov radiation in a reactor core.²⁹¹

Cerenkov radiation has been used in physics for particle identification²⁹² or in astrophysics for detection of high-energy gamma-rays.²⁹³ More recently, CR has been successfully applied in

several studies for optical imaging *in vivo*.^{270, 288, 294–297} For instance, CR could be utilized for imaging of thyroid gland of a patient who was treated with ^{131}I (Figure 33).²⁹⁸ Furthermore, Cerenkov radiation has recently been utilized in combination with titanium dioxide as a nanophotosensitizer for PDT in a mouse xenograft model of fibroblastic sarcoma.²⁹⁹ Herein, fluorodeoxyglucose ^{18}F FDG was used as a β^+ source. By coating the nanoparticles with transferrin, tumor specific accumulation could be achieved.²⁹⁹

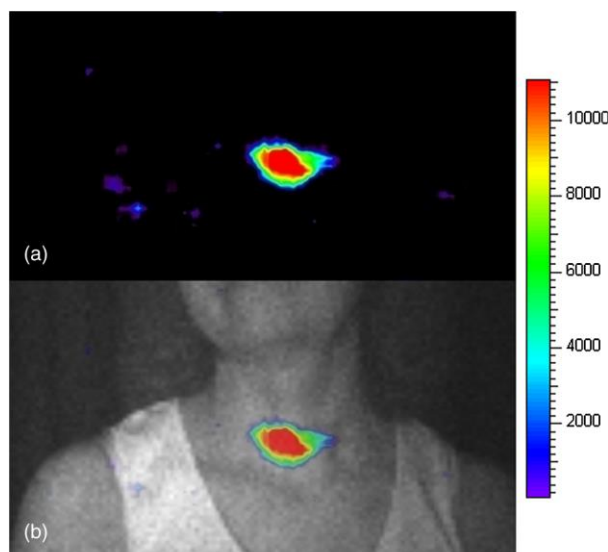


Figure 33: Proof-of-principle for applicability of CR for *in vivo* imaging in human.²⁹⁸ (a) CR of a thyroid gland of a patient treated with ^{131}I . (b) The overlay between the photographic image and the CR image of the patient.²⁹⁸

Successful usage of radioisotopes for biological imaging and induced PDT proved the applicability of Cerenkov radiation *in vivo*. A very interesting approach might be the application of CR for uncaging of photoactivatable prodrugs. The CR-induced release of caged compounds has already been impressively proved in 2012.³⁰⁰ Herein, a photoactivatable derivative of luciferin (Figure 34) was uncaged by administration of ^{18}F FDG in a mouse breast cancer model expressing luciferase.³⁰⁰

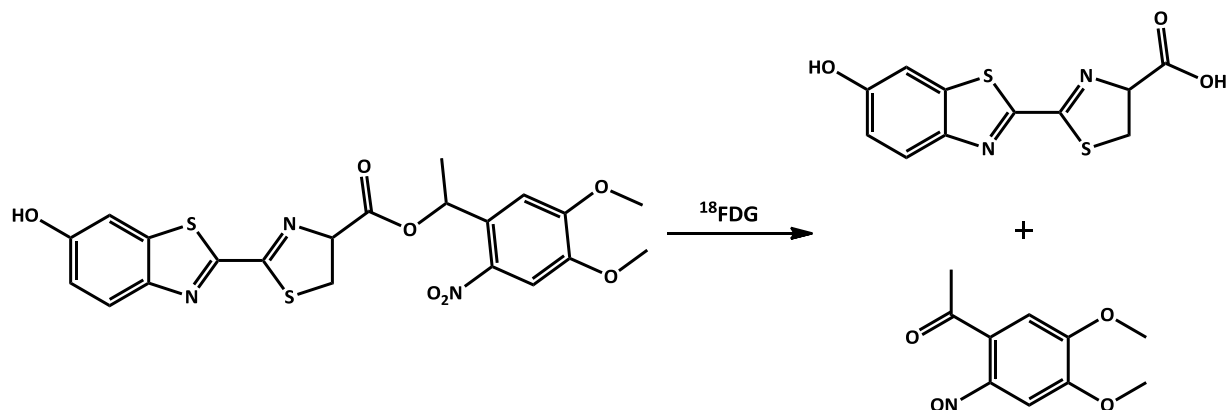


Figure 34: Uncaging of photoactivatable derivative of luciferin with Cerenkov radiation induced by ^{18}F FDG. Adapted and modified from the original publication.³⁰⁰

In this proof-of-concept study, the CR-induced release of luciferin could be monitored in real-time. *In vivo* experiments impressively demonstrated that the CR-induced uncaging is much more efficient in deeper tissue than the photoactivation by UV irradiation due to limited penetration of UV.³⁰⁰ This study produced a strong evidence for applicability of CR for reactivation of caged compounds *in vivo*. However, to the best of my knowledge, there are no studies utilizing CR for uncaging of photoactivatable prodrugs.

Application of CR for uncaging of photoactivatable smKIs might offer some advantage in therapy because many radiotracers that emit CR have already been approved for clinical usage.²⁷⁴ Tissue specific release of active inhibitors might be possible by usage of specific or modified tracers.^{299, 300} However, the approach might be limited by low intensity of CR.^{250, 274, 288} A possible solution might be the utilization of more efficient β -emitters such as ^{90}Y and ^{89}Zr .²⁷⁴

Another possibility for increasing the efficiency of CR for targeted uncaging of smKIs might be the application of linear accelerators (LINACs). LINACs are already used in cancer therapy.^{301, 302} Several studies provided evidence that irradiation with LINACs produce CR.^{303, 304} Herein, Cerenkov luminescent emission from LINACs is much greater than CR from beta radionuclides.²⁸⁸ An interesting approach might be the application of particle accelerators that are currently being used for proton therapy. Particle beams can reach deeper tissues and can be better focused on tumors than X-ray beams.³⁰⁵ Furthermore, CR

from the proton beams has already been demonstrated.³⁰⁶ This Cerenkov luminescence might be potentially used for cleavage of PPGs from caged compounds. However, to the best of my knowledge, no studies utilizing this approach have been performed yet.

From my point of view, the application of highly-focused particle beams for controlled activation of caged smKIs might be a unique possibility to combine radiotherapy with targeted pharmacological therapy of cancer. Due to possible synergistic effects, the applied radiation dose might be decreased. Of course, I am well aware that this idea is speculative. Many experiments regarding the cleavage efficacy of emitted CR and possible toxicities have to be carried out. Currently, our research group is working on investigation of applicability of CR-induced release of caged compounds. Herein, CR emitted both by radionuclides such as ^{18}F and by ionizing beams should be evaluated. Therefore, collaboration with the department for radiation therapy at university hospital in Kiel, Germany, has been established.

5.1.3 Concluding remarks

Photoactivatable prodrugs of smKIs represent an exciting option for basic research in the kinase inhibitors field. Spatiotemporal control of kinase action by irradiation of caged inhibitors *in vitro* has been demonstrated in the course of the present PhD work. The described prodrugs might be a powerful tool for studying the regulation and kinetics of protein phosphorylation. Furthermore, photoactivatable prodrugs of smKIs might find usage in clinical applications. Novel approaches to release the active compounds in deeper tissues described above might enable novel therapeutic possibilities. For instance, an abrupt rise of active inhibitor concentration in targeted tumor might be feasible due to controlled irradiation. As a consequence, systemic side effects and resistance development should be minimized. A combination of radiotherapy and induced release of active smKIs might be another promising option.

However, a lot of profound basic research is required prior to clinical applications of photoactivatable prodrugs of smKIs. Pharmacokinetic and toxicological characteristics of caged compounds should be surveyed in greater detail. Moreover, physicochemical properties such as aqueous solubility of caged prodrugs should be improved prior to *in vivo* applications. Herein, utilization of novel PPGs with enhanced solubility such as the BODIPY PPG might be useful. Furthermore, the biological effects of the cleaved PPG should be examined in more detail. A further aspect that should be investigated prior to clinical applications is the metabolic stability of caged compounds.

To summarize, caged prodrugs of smKIs might enable novel opportunities both in basic research and in therapeutic applications. However, multidisciplinary research and development in a collaboration of pharmacists, chemists, biochemists, physicians and biomedical engineers is needed for future implementation of photoactivatable prodrugs in therapy. Nevertheless, novel developments both in chemistry and nanotechnology allow a reasonable optimistic look into the future.

5.2 PDGFR β inhibitors

In the course of the present work novel potent PDGFR β inhibitors were developed and characterized *in vitro*. It was demonstrated that the DFG-out inhibitor **3** was both more selective and more potent in cellular assays than the DFG-in inhibitor **2** (Figure 13). Further development is needed to translate the promising *in vitro* potency in useful activity *in vivo*. Due to its enhanced selectivity, the DFG-out inhibitor **3** should be considered for further lead optimization. Therefore, improvement of physicochemical and pharmacokinetic properties should be pursued. Thus, water solubility and bioavailability of the compound **3** should be increased prior to *in vivo* testing. Extensive profiling in a cancer cell line panel, like the NCI60 panel, might be performed for identifying promising tumor targets. Usage of xenograft animal models should assess the applicability of novel inhibitors for possible treatment options. Furthermore, the results of *in vivo* validation should be compared with hitherto approved PDGFR β inhibitors.

The *in vitro* characterization of herein developed PDGFR β inhibitors led to the assumption that DFG-out inhibitors have more preferable pharmacological characteristics than the DFG-in inhibitors. This hypothesis should be critically evaluated by comparing inhibitors with similar chemotype for other kinase targets. Furthermore, it should be examined whether preferable *in vitro* properties of DFG-out inhibitors can be transferred into improved *in vivo* characteristics.

Methodology applied in the course of the present work, such as utilizing the WaterMap technology for molecular docking experiments and novel developed synthetic routes might be used for the development of further protein kinase inhibitors.

6 References

1. Lipmann, F. A.; Levene P.A. Serinephosphoric acid obtained on hydrolysis of vitellinic acid. *J. Biol. Chem. [Online]* **1932**, 109–114.
2. Burnett, G.; Kennedy, E. P. The enzymatic phosphorylation of proteins. *The Journal of biological chemistry* **1954**, *211* (2), 969–980.
3. Fisher, E. H.; Krebs, E. G. Conversion of phosphorylase b to phosphorylase a in muscle extracts. *The Journal of biological chemistry* **1955**, *216* (1), 121–132.
4. Fischer, E. H. Cellular regulation by protein phosphorylation. *Biochemical and Biophysical Research Communications* **2013**, *430* (2), 865–867. DOI: 10.1016/j.bbrc.2012.10.024.
5. Cohen, P. Protein kinases--the major drug targets of the twenty-first century? *Nature reviews. Drug discovery* **2002**, *1* (4), 309–315. DOI: 10.1038/nrd773.
6. Barford, D.; Johnson, L. N. The allosteric transition of glycogen phosphorylase. *Nature* **1989**, *340* (6235), 609–616. DOI: 10.1038/340609a0.
7. Latzer, J.; Shen, T.; Wolynes, P. G. Conformational switching upon phosphorylation: a predictive framework based on energy landscape principles. *Biochemistry* **2008**, *47* (7), 2110–2122. DOI: 10.1021/bi701350v.
8. Nishi, H.; Shaytan, A.; Panchenko, A. R. Physicochemical mechanisms of protein regulation by phosphorylation. *Frontiers in genetics* **2014**, *5*, 270. DOI: 10.3389/fgene.2014.00270.
9. Olsen, J. V.; Blagoev, B.; Gnäd, F.; Macek, B.; Kumar, C.; Mortensen, P.; Mann, M. Global, in vivo, and site-specific phosphorylation dynamics in signaling networks. *Cell* **2006**, *127* (3), 635–648. DOI: 10.1016/j.cell.2006.09.026.
10. Pawson, T.; Scott, J. D. Protein phosphorylation in signaling--50 years and counting. *Trends in biochemical sciences* **2005**, *30* (6), 286–290. DOI: 10.1016/j.tibs.2005.04.013.
11. Sadowski, I.; Stone, J. C.; Pawson, T. A noncatalytic domain conserved among cytoplasmic protein-tyrosine kinases modifies the kinase function and transforming activity of Fujinami sarcoma virus P130gag-fps. *Mol. Cell. Biol.* **1986**, *6* (12), 4396–4408. DOI: 10.1128/MCB.6.12.4396.
12. Pawson, T.; Gish, G. D.; Nash, P. SH2 domains, interaction modules and cellular wiring. *Trends in cell biology* **2001**, *11* (12), 504–511.
13. Rittinger, K.; Budman, J.; Xu, J.; Volinia, S.; Cantley, L. C.; Smerdon, S. J.; Gambelin, S. J.; Yaffe, M. B. Structural analysis of 14-3-3 phosphopeptide complexes identifies a dual role

- for the nuclear export signal of 14-3-3 in ligand binding. *Molecular cell* **1999**, *4* (2), 153–166.
14. Yaffe, M. B.; Rittinger, K.; Volinia, S.; Caron, P. R.; Aitken, A.; Leffers, H.; Gamblin, S. J.; Smerdon, S. J.; Cantley, L. C. The structural basis for 14-3-3:phosphopeptide binding specificity. *Cell* **1997**, *91* (7), 961–971.
15. Durocher, D.; Jackson, S. P. The FHA domain. *FEBS Letters* **2002**, *513* (1), 58–66. DOI: 10.1016/S0014-5793(01)03294-X.
16. Olsen, J. V.; Vermeulen, M.; Santamaria, A.; Kumar, C.; Miller, M. L.; Jensen, L. J.; Gnad, F.; Cox, J.; Jensen, T. S.; Nigg, E. A.; Brunak, S.; Mann, M. Quantitative phosphoproteomics reveals widespread full phosphorylation site occupancy during mitosis. *Science signaling* **2010**, *3* (104), ra3. DOI: 10.1126/scisignal.2000475.
17. Johnson, L. N. The regulation of protein phosphorylation. *Biochemical Society transactions* **2009**, *37* (Pt 4), 627–641. DOI: 10.1042/BST0370627.
18. Manning, G.; Whyte, D. B.; Martinez, R.; Hunter, T.; Sudarsanam, S. The protein kinase complement of the human genome. *Science (New York, N.Y.)* **2002**, *298* (5600), 1912–1934. DOI: 10.1126/science.1075762.
19. Lander, E. S.; Linton, L. M.; Birren, B.; Nusbaum, C.; Zody, M. C.; Baldwin, J.; Devon, K.; Dewar, K.; Doyle, M.; FitzHugh, W.; Funke, R.; Gage, D.; Harris, K.; Heaford, A.; Howland, J.; Kann, L.; Lehoczy, J.; LeVine, R.; McEwan, P.; McKernan, K.; Meldrim, J.; Mesirov, J. P.; Miranda, C.; Morris, W.; Naylor, J.; Raymond, C.; Rosetti, M.; Santos, R.; Sheridan, A.; Sougnez, C.; Stange-Thomann, Y.; Stojanovic, N.; Subramanian, A.; Wyman, D.; Rogers, J.; Sulston, J.; Ainscough, R.; Beck, S.; Bentley, D.; Burton, J.; Clee, C.; Carter, N.; Coulson, A.; Deadman, R.; Deloukas, P.; Dunham, A.; Dunham, I.; Durbin, R.; French, L.; Grafham, D.; Gregory, S.; Hubbard, T.; Humphray, S.; Hunt, A.; Jones, M.; Lloyd, C.; McMurray, A.; Matthews, L.; Mercer, S.; Milne, S.; Mullikin, J. C.; Mungall, A.; Plumb, R.; Ross, M.; Shownkeen, R.; Sims, S.; Waterston, R. H.; Wilson, R. K.; Hillier, L. W.; McPherson, J. D.; Marra, M. A.; Mardis, E. R.; Fulton, L. A.; Chinwalla, A. T.; Pepin, K. H.; Gish, W. R.; Chissoe, S. L.; Wendl, M. C.; Delehaunty, K. D.; Miner, T. L.; Delehaunty, A.; Kramer, J. B.; Cook, L. L.; Fulton, R. S.; Johnson, D. L.; Minx, P. J.; Clifton, S. W.; Hawkins, T.; Branscomb, E.; Predki, P.; Richardson, P.; Wenning, S.; Slezak, T.; Doggett, N.; Cheng, J. F.; Olsen, A.; Lucas, S.; Elkin, C.; Uberbacher, E.; Frazier, M.; Gibbs, R. A.; Muzny, D. M.; Scherer, S. E.; Bouck, J. B.; Sodergren, E. J.; Worley, K. C.; Rives, C. M.; Gorrell, J. H.; Metzker, M. L.; Naylor, S. L.; Kucherlapati, R. S.; Nelson, D. L.; Weinstock, G. M.; Sakaki, Y.; Fujiyama, A.; Hattori, M.; Yada, T.; Toyoda, A.; Itoh, T.; Kawagoe, C.; Watanabe, H.; Totoki, Y.; Taylor, T.; Weissenbach, J.; Heilig, R.; Saurin, W.; Artiguenave, F.; Brottier, P.; Bruls, T.; Pelletier, E.; Robert, C.; Wincker, P.; Smith, D. R.; Doucette-Stamm, L.; Rubenfield, M.; Weinstock, K.

- Lee, H. M.; Dubois, J.; Rosenthal, A.; Platzer, M.; Nyakatura, G.; Taudien, S.; Rump, A.; Yang, H.; Yu, J.; Wang, J.; Huang, G.; Gu, J.; Hood, L.; Rowen, L.; Madan, A.; Qin, S.; Davis, R. W.; Federspiel, N. A.; Abola, A. P.; Proctor, M. J.; Myers, R. M.; Schmutz, J.; Dickson, M.; Grimwood, J.; Cox, D. R.; Olson, M. V.; Kaul, R.; Shimizu, N.; Kawasaki, K.; Minoshima, S.; Evans, G. A.; Athanasiou, M.; Schultz, R.; Roe, B. A.; Chen, F.; Pan, H.; Ramser, J.; Lehrach, H.; Reinhardt, R.; McCombie, W. R.; La Bastide, M. de; Dedhia, N.; Blocker, H.; Hornischer, K.; Nordsiek, G.; Agarwala, R.; Aravind, L.; Bailey, J. A.; Bateman, A.; Batzoglou, S.; Birney, E.; Bork, P.; Brown, D. G.; Burge, C. B.; Cerutti, L.; Chen, H. C.; Church, D.; Clamp, M.; Copley, R. R.; Doerks, T.; Eddy, S. R.; Eichler, E. E.; Furey, T. S.; Galagan, J.; Gilbert, J. G.; Harmon, C.; Hayashizaki, Y.; Haussler, D.; Hermjakob, H.; Hokamp, K.; Jang, W.; Johnson, L. S.; Jones, T. A.; Kasif, S.; Kasprzyk, A.; Kennedy, S.; Kent, W. J.; Kitts, P.; Koonin, E. V.; Korf, I.; Kulp, D.; Lancet, D.; Lowe, T. M.; McLysaght, A.; Mikkelsen, T.; Moran, J. V.; Mulder, N.; Pollara, V. J.; Ponting, C. P.; Schuler, G.; Schultz, J.; Slater, G.; Smit, A. F.; Stupka, E.; Szustakowki, J.; Thierry-Mieg, D.; Thierry-Mieg, J.; Wagner, L.; Wallis, J.; Wheeler, R.; Williams, A.; Wolf, Y. I.; Wolfe, K. H.; Yang, S. P.; Yeh, R. F.; Collins, F.; Guyer, M. S.; Peterson, J.; Felsenfeld, A.; Wetterstrand, K. A.; Patrinos, A.; Morgan, M. J.; Jong, P. de; Catanese, J. J.; Osoegawa, K.; Shizuya, H.; Choi, S.; Chen, Y. J. Initial sequencing and analysis of the human genome. *Nature* **2001**, *409* (6822), 860–921. DOI: 10.1038/35057062.
20. Manning, G. Genomic overview of protein kinases. *WormBook : the online review of C. elegans biology [Online]* **2005**, 1–19.
21. Hanks, S. K.; Hunter, T. Protein kinases 6. The eukaryotic protein kinase superfamily: kinase (catalytic) domain structure and classification. *FASEB journal : official publication of the Federation of American Societies for Experimental Biology* **1995**, *9* (8), 576–596.
22. Hunter, T. Protein kinase classification. *Methods in enzymology* **1991**, *200*, 3–37.
23. Lindberg, R. A.; Quinn, A. M.; Hunter, T. Dual-specificity protein kinases: will any hydroxyl do? *Trends in biochemical sciences* **1992**, *17* (3), 114–119.
24. Walte, A.; Ruben, K.; Birner-Gruenberger, R.; Preisinger, C.; Bamberg-Lemper, S.; Hilz, N.; Bracher, F.; Becker, W. Mechanism of dual specificity kinase activity of DYRK1A. *The FEBS journal* **2013**, *280* (18), 4495–4511. DOI: 10.1111/febs.12411.
25. <http://kinase.com/human/kinome/phylogeny.html>.
26. <https://www.cellsignal.com/common/content/content.jsp?id=kinases-human-protein>.
27. Cohen, P.; Alessi, D. R. Kinase drug discovery--what's next in the field? *ACS chemical biology* **2013**, *8* (1), 96–104. DOI: 10.1021/cb300610s.

28. Wang, Q.; Zorn, J. A.; Kuriyan, J. A structural atlas of kinases inhibited by clinically approved drugs. *Methods in enzymology* **2014**, *548*, 23–67. DOI: 10.1016/B978-0-12-397918-6.00002-1.
29. Agafonov, R. V.; Wilson, C.; Kern, D. Evolution and intelligent design in drug development. *Frontiers in molecular biosciences* **2015**, *2*, 27. DOI: 10.3389/fmolb.2015.00027.
30. Hopkins, A. L.; Groom, C. R. The druggable genome. *Nature reviews. Drug discovery* **2002**, *1* (9), 727–730. DOI: 10.1038/nrd892.
31. Collett, M. S.; Erikson, R. L. Protein kinase activity associated with the avian sarcoma virus src gene product. *Proceedings of the National Academy of Sciences of the United States of America* **1978**, *75* (4), 2021–2024.
32. Eckhart, W.; Hutchinson, M. A.; Hunter, T. An activity phosphorylating tyrosine in polyoma T antigen immunoprecipitates. *Cell* **1979**, *18* (4), 925–933.
33. Blume-Jensen, P.; Hunter, T. Oncogenic kinase signalling. *Nature* **2001**, *411* (6835), 355–365. DOI: 10.1038/35077225.
34. Xu, J.; Wang, P.; Yang, H.; Zhou, J.; Li, Y.; Li, X.; Xue, W.; Yu, C.; Tian, Y.; Zhu, F. Comparison of FDA Approved Kinase Targets to Clinical Trial Ones: Insights from Their System Profiles and Drug-Target Interaction Networks. *BioMed research international* **2016**, *2016*, 2509385. DOI: 10.1155/2016/2509385.
35. Fischer, P. M. Approved and Experimental Small-Molecule Oncology Kinase Inhibitor Drugs: A Mid-2016 Overview. *Medicinal research reviews [Online]* **2016**.
36. Weinstein, I. B. Cancer. Addiction to oncogenes--the Achilles heel of cancer. *Science (New York, N.Y.)* **2002**, *297* (5578), 63–64. DOI: 10.1126/science.1073096.
37. Maurer, G.; Tarkowski, B.; Baccarini, M. Raf kinases in cancer-roles and therapeutic opportunities. *Oncogene* **2011**, *30* (32), 3477–3488. DOI: 10.1038/onc.2011.160.
38. Witsch, E.; Sela, M.; Yarden, Y. Roles for growth factors in cancer progression. *Physiology (Bethesda, Md.)* **2010**, *25* (2), 85–101. DOI: 10.1152/physiol.00045.2009.
39. Levitzki, A. Tyrosine kinase inhibitors: views of selectivity, sensitivity, and clinical performance. *Annual review of pharmacology and toxicology* **2013**, *53*, 161–185. DOI: 10.1146/annurev-pharmtox-011112-140341.
40. <https://www.drugs.com/newdrugs/fda-approves-xeljanz-rheumatoid-arthritis-3558.html>.
41. Hirosumi, J.; Tuncman, G.; Chang, L.; Gorgun, C. Z.; Uysal, K. T.; Maeda, K.; Karin, M.; Hotamisligil, G. S. A central role for JNK in obesity and insulin resistance. *Nature* **2002**, *420* (6913), 333–336. DOI: 10.1038/nature01137.

42. Nandipati, K. C.; Subramanian, S.; Agrawal, D. K. Protein kinases: mechanisms and downstream targets in inflammation-mediated obesity and insulin resistance. *Molecular and cellular biochemistry [Online]* **2016**.
43. Vulpetti, A.; Bosotti, R. Sequence and structural analysis of kinase ATP pocket residues. *Farmaco (Societa chimica italiana : 1989)* **2004**, *59* (10), 759–765. DOI: 10.1016/j.farmac.2004.05.010.
44. Knighton, D. R. *Crystal structure of the catalytic subunit of cyclic adenosine monophosphate-dependent protein kinase*; American Association for the Advancement of Science: Washington, D.C., 1991.
45. Weiss, M. M.; Harmange, J.-C.; Polverino, A. J.; Bauer, D.; Berry, L.; Berry, V.; Borg, G.; Bready, J.; Chen, D.; Choquette, D.; Coxon, A.; DeMelfi, T.; Doerr, N.; Estrada, J.; Flynn, J.; Graceffa, R. F.; Harriman, S. P.; Kaufman, S.; La, D. S.; Long, A.; Neervannan, S.; Patel, V. F.; Potashman, M.; Regal, K.; Roveto, P. M.; Schrag, M. L.; Starnes, C.; Tasker, A.; Teffera, Y.; Whittington, D. A.; Zanon, R. Evaluation of a series of naphthamides as potent, orally active vascular endothelial growth factor receptor-2 tyrosine kinase inhibitors. *Journal of medicinal chemistry* **2008**, *51* (6), 1668–1680. DOI: 10.1021/jm701098w.
46. Schrödinger Release 2015-4: Maestro, Schrödinger, LLC, New York, NY, 2015.
47. Tong, M.; Seeliger, M. A. Targeting conformational plasticity of protein kinases. *ACS chemical biology* **2015**, *10* (1), 190–200. DOI: 10.1021/cb500870a.
48. Wu, P.; Nielsen, T. E.; Clausen, M. H. FDA-approved small-molecule kinase inhibitors. *Trends in pharmacological sciences* **2015**, *36* (7), 422–439. DOI: 10.1016/j.tips.2015.04.005.
49. Lahiry, P.; Torkamani, A.; Schork, N. J.; Hegele, R. A. Kinase mutations in human disease: interpreting genotype-phenotype relationships. *Nature reviews. Genetics* **2010**, *11* (1), 60–74. DOI: 10.1038/nrg2707.
50. Traxler, P.; Furet, P. Strategies toward the design of novel and selective protein tyrosine kinase inhibitors. *Pharmacology & therapeutics* **1999**, *82* (2-3), 195–206.
51. Liao, J. J.-L. Molecular recognition of protein kinase binding pockets for design of potent and selective kinase inhibitors. *Journal of medicinal chemistry* **2007**, *50* (3), 409–424. DOI: 10.1021/jm0608107.
52. Azam, M.; Seeliger, M. A.; Gray, N. S.; Kuriyan, J.; Daley, G. Q. Activation of tyrosine kinases by mutation of the gatekeeper threonine. *Nature structural & molecular biology* **2008**, *15* (10), 1109–1118. DOI: 10.1038/nsmb.1486.

53. Godin-Heymann, N.; Ulkus, L.; Brannigan, B. W.; McDermott, U.; Lamb, J.; Maheswaran, S.; Settleman, J.; Haber, D. A. The T790M "gatekeeper" mutation in EGFR mediates resistance to low concentrations of an irreversible EGFR inhibitor. *Molecular cancer therapeutics* **2008**, *7* (4), 874–879. DOI: 10.1158/1535-7163.MCT-07-2387.
54. Zhang, J.; Shapiro, P.; Pozharski, E. Structure of extracellular signal-regulated kinase 2 in complex with ATP and ADP. *Acta crystallographica. Section F, Structural biology and crystallization communications* **2012**, *68* (Pt 12), 1434–1439. DOI: 10.1107/S1744309112042972.
55. Emrick, M. A.; Lee, T.; Starkey, P. J.; Mumby, M. C.; Resing, K. A.; Ahn, N. G. The gatekeeper residue controls autoactivation of ERK2 via a pathway of intramolecular connectivity. *Proceedings of the National Academy of Sciences of the United States of America* **2006**, *103* (48), 18101–18106. DOI: 10.1073/pnas.0608849103.
56. Schwartz, P. A.; Murray, B. W. Protein kinase biochemistry and drug discovery. *Bioorganic chemistry* **2011**, *39* (5-6), 192–210. DOI: 10.1016/j.bioorg.2011.07.004.
57. Zhang, J.; Yang, P. L.; Gray, N. S. Targeting cancer with small molecule kinase inhibitors. *Nature reviews. Cancer* **2009**, *9* (1), 28–39. DOI: 10.1038/nrc2559.
58. Rabiller, M.; Getlik, M.; Kluter, S.; Richters, A.; Tuckmantel, S.; Simard, J. R.; Rauh, D. Proteus in the world of proteins: conformational changes in protein kinases. *Archiv der Pharmazie* **2010**, *343* (4), 193–206. DOI: 10.1002/ardp.201000028.
59. Sanphanya, K.; Wattanapitayakul, S. K.; Phowichit, S.; Fokin, V. V.; Vajragupta, O. Novel VEGFR-2 kinase inhibitors identified by the back-to-front approach. *Bioorganic & medicinal chemistry letters* **2013**, *23* (10), 2962–2967. DOI: 10.1016/j.bmcl.2013.03.042.
60. Whittington, D. A.; Long, A. M.; Rose, P.; Gu, Y.; Zhao, H. *Crystal structure of the VEGFR2 kinase domain in complex with a pyridyl-pyrimidine benzimidazole inhibitor*, 2009.
61. Kornev, A. P.; Haste, N. M.; Taylor, S. S.; Eyck, L. F. T. Surface comparison of active and inactive protein kinases identifies a conserved activation mechanism. *Proceedings of the National Academy of Sciences of the United States of America* **2006**, *103* (47), 17783–17788. DOI: 10.1073/pnas.0607656103.
62. Kornev, A. P.; Taylor, S. S.; Eyck, L. F. T. A helix scaffold for the assembly of active protein kinases. *Proceedings of the National Academy of Sciences of the United States of America* **2008**, *105* (38), 14377–14382. DOI: 10.1073/pnas.0807988105.
63. Zheng, J.; Trafny, E. A.; Knighton, D. R.; Xuong, N.-H.; Taylor, S. S.; Teneyck, L. F.; Sowadski, J. M. 2.2 ANGSTROM REFINED CRYSTAL STRUCTURE OF THE CATALYTIC SUBUNIT OF CAMP-DEPENDENT PROTEIN KINASE COMPLEXED WITH MNATP AND A PEPTIDE INHIBITOR, 1993.

64. Hidaka, H.; Inagaki, M.; Kawamoto, S.; Sasaki, Y. Isoquinolinesulfonamides, novel and potent inhibitors of cyclic nucleotide-dependent protein kinase and protein kinase C. *Biochemistry* **1984**, *23* (21), 5036–5041. DOI: 10.1021/bi00316a032.
65. Tamaoki, T.; Nomoto, H.; Takahashi, I.; Kato, Y.; Morimoto, M.; Tomita, F. Staurosporine, a potent inhibitor of phospholipidCa⁺⁺-dependent protein kinase. *Biochemical and Biophysical Research Communications* **1986**, *135* (2), 397–402. DOI: 10.1016/0006-291X(86)90008-2.
66. Davis, P. D.; Hill, C. H.; Keech, E.; Lawton, G.; Nixon, J. S.; Sedgwick, A. D.; Wadsworth, J.; Westmacott, D.; Wilkinson, S. E. Potent selective inhibitors of protein kinase C. *FEBS Letters* **1989**, *259* (1), 61–63. DOI: 10.1016/0014-5793(89)81494-2.
67. Yaish, P.; Gazit, A.; Gilon, C.; Levitzki, A. Blocking of EGF-dependent cell proliferation by EGF receptor kinase inhibitors. *Science (New York, N.Y.)* **1988**, *242* (4880), 933–935.
68. Davies, S. P.; Reddy, H.; Caivano, M.; Cohen, P. Specificity and mechanism of action of some commonly used protein kinase inhibitors. *The Biochemical journal* **2000**, *351* (Pt 1), 95–105.
69. Garber, K. Rapamycin's Resurrection: A New Way to Target the Cancer Cell Cycle. *JNCI Journal of the National Cancer Institute* **2001**, *93* (20), 1517–1519. DOI: 10.1093/jnci/93.20.1517.
70. Heitman, J.; Movva, N. R.; Hall, M. N. Targets for cell cycle arrest by the immunosuppressant rapamycin in yeast. *Science (New York, N.Y.)* **1991**, *253* (5022), 905–909.
71. Rapamune prescribing information <http://labeling.pfizer.com/ShowLabeling.aspx?id=139>.
72. Buchdunger, E.; Zimmermann, J.; Mett, H.; Meyer, T.; Muller, M.; Druker, B. J.; Lydon, N. B. Inhibition of the Abl protein-tyrosine kinase in vitro and in vivo by a 2-phenylaminopyrimidine derivative. *Cancer research* **1996**, *56* (1), 100–104.
73. Druker, B. J.; Tamura, S.; Buchdunger, E.; Ohno, S.; Segal, G. M.; Fanning, S.; Zimmermann, J.; Lydon, N. B. Effects of a selective inhibitor of the Abl tyrosine kinase on the growth of Bcr-Abl positive cells. *Nature medicine* **1996**, *2* (5), 561–566.
74. <https://www.drugs.com/pro/imatinib.html> Revised: 10/2016.
75. Sasaki, Y.; Suzuki, M.; Hidaka, H. The novel and specific Rho-kinase inhibitor (S)-(+)-2-methyl-1-(4-methyl-5-isoquinoline)sulfonyl-homopiperazine as a probing molecule for Rho-kinase-involved pathway. *Pharmacology & therapeutics* **2002**, *93* (2-3), 225–232.
76. Fleischmann, R. Novel small-molecular therapeutics for rheumatoid arthritis. *Current opinion in rheumatology* **2012**, *24* (3), 335–341. DOI: 10.1097/BOR.0b013e32835190ef.

77. Mazzei, M. E.; Richeldi, L.; Collard, H. R. Nintedanib in the treatment of idiopathic pulmonary fibrosis. *Therapeutic advances in respiratory disease* **2015**, *9* (3), 121–129. DOI: 10.1177/1753465815579365.
78. Patterson, H.; Nibbs, R.; McInnes, I.; Siebert, S. Protein kinase inhibitors in the treatment of inflammatory and autoimmune diseases. *Clinical and experimental immunology* **2014**, *176* (1), 1–10. DOI: 10.1111/cei.12248.
79. Reichert, J. M.; Wenger, J. B. Development trends for new cancer therapeutics and vaccines. *Drug discovery today* **2008**, *13* (1-2), 30–37. DOI: 10.1016/j.drudis.2007.09.003.
80. Dar, A. C.; Shokat, K. M. The evolution of protein kinase inhibitors from antagonists to agonists of cellular signaling. *Annual review of biochemistry* **2011**, *80*, 769–795. DOI: 10.1146/annurev-biochem-090308-173656.
81. Muller, S.; Chaikuad, A.; Gray, N. S.; Knapp, S. The ins and outs of selective kinase inhibitor development. *Nature chemical biology* **2015**, *11* (11), 818–821. DOI: 10.1038/nchembio.1938.
82. Roskoski, R., JR. Classification of small molecule protein kinase inhibitors based upon the structures of their drug-enzyme complexes. *Pharmacological research* **2016**, *103*, 26–48. DOI: 10.1016/j.phrs.2015.10.021.
83. Davis, M. I.; Hunt, J. P.; Herrgard, S.; Ciceri, P.; Wodicka, L. M.; Pallares, G.; Hocker, M.; Treiber, D. K.; Zarrinkar, P. P. Comprehensive analysis of kinase inhibitor selectivity. *Nature biotechnology* **2011**, *29* (11), 1046–1051. DOI: 10.1038/nbt.1990.
84. Zhao, Z.; Wu, H.; Wang, L.; Liu, Y.; Knapp, S.; Liu, Q.; Gray, N. S. Exploration of type II binding mode: A privileged approach for kinase inhibitor focused drug discovery? *ACS chemical biology* **2014**, *9* (6), 1230–1241. DOI: 10.1021/cb500129t.
85. Kufareva, I.; Abagyan, R. Type-II kinase inhibitor docking, screening, and profiling using modified structures of active kinase states. *Journal of medicinal chemistry* **2008**, *51* (24), 7921–7932. DOI: 10.1021/jm8010299.
86. Fang, Z.; Grutter, C.; Rauh, D. Strategies for the selective regulation of kinases with allosteric modulators: exploiting exclusive structural features. *ACS chemical biology* **2013**, *8* (1), 58–70. DOI: 10.1021/cb300663j.
87. Garuti, L.; Roberti, M.; Bottegoni, G. Non-ATP Competitive Protein Kinase Inhibitors. *CMC* **2010**, *17* (25), 2804–2821. DOI: 10.2174/092986710791859333.
88. Iwata, H.; Oki, H.; Okada, K.; Takagi, T.; Tawada, M.; Miyazaki, Y.; Imamura, S.; Hori, A.; Lawson, J. D.; Hixon, M. S.; Kimura, H.; Miki, H. A Back-to-Front Fragment-Based Drug

- Design Search Strategy Targeting the DFG-Out Pocket of Protein Tyrosine Kinases. *ACS medicinal chemistry letters* **2012**, *3* (4), 342–346. DOI: 10.1021/ml3000403.
89. Norman, R. A.; Toader, D.; Ferguson, A. D. Structural approaches to obtain kinase selectivity. *Trends in pharmacological sciences* **2012**, *33* (5), 273–278. DOI: 10.1016/j.tips.2012.03.005.
90. Uitdehaag, J. C. M.; Zaman, G. J. R. A theoretical entropy score as a single value to express inhibitor selectivity. *BMC bioinformatics* **2011**, *12*, 94. DOI: 10.1186/1471-2105-12-94.
91. Debreczeni, J. E.; Bullock, A. N.; Atilla, G. E.; Williams, D. S.; Bregman, H.; Knapp, S.; Meggers, E. Ruthenium half-sandwich complexes bound to protein kinase Pim-1. *Angewandte Chemie (International ed. in English)* **2006**, *45* (10), 1580–1585. DOI: 10.1002/anie.200503468.
92. Koeberle, S. C.; Romir, J.; Fischer, S.; Koeberle, A.; Schattel, V.; Albrecht, W.; Grutter, C.; Werz, O.; Rauh, D.; Stehle, T.; Laufer, S. A. Skepinone-L is a selective p38 mitogen-activated protein kinase inhibitor. *Nature chemical biology* **2011**, *8* (2), 141–143. DOI: 10.1038/nchembio.761.
93. Gammons, M. V.; Fedorov, O.; Ivson, D.; Du, C.; Clark, T.; Hopkins, C.; Hagiwara, M.; Dick, A. D.; Cox, R.; Harper, S. J.; Hancox, J. C.; Knapp, S.; Bates, D. O. Topical antiangiogenic SRPK1 inhibitors reduce choroidal neovascularization in rodent models of exudative AMD. *Investigative ophthalmology & visual science* **2013**, *54* (9), 6052–6062. DOI: 10.1167/iovs.13-12422.
94. Knight, Z. A.; Shokat, K. M. Features of selective kinase inhibitors. *Chemistry & biology* **2005**, *12* (6), 621–637. DOI: 10.1016/j.chembiol.2005.04.011.
95. Ranjitkar, P.; Brock, A. M.; Maly, D. J. Affinity reagents that target a specific inactive form of protein kinases. *Chemistry & biology* **2010**, *17* (2), 195–206. DOI: 10.1016/j.chembiol.2010.01.008.
96. Davies, H.; Bignell, G. R.; Cox, C.; Stephens, P.; Edkins, S.; Clegg, S.; Teague, J.; Woffendin, H.; Garnett, M. J.; Bottomley, W.; Davis, N.; Dicks, E.; Ewing, R.; Floyd, Y.; Gray, K.; Hall, S.; Hawes, R.; Hughes, J.; Kosmidou, V.; Menzies, A.; Mould, C.; Parker, A.; Stevens, C.; Watt, S.; Hooper, S.; Wilson, R.; Jayatilake, H.; Gusterson, B. A.; Cooper, C.; Shipley, J.; Hargrave, D.; Pritchard-Jones, K.; Maitland, N.; Chenevix-Trench, G.; Riggins, G. J.; Bigner, D. D.; Palmieri, G.; Cossu, A.; Flanagan, A.; Nicholson, A.; Ho, J. W. C.; Leung, S. Y.; Yuen, S. T.; Weber, B. L.; Seigler, H. F.; Darrow, T. L.; Paterson, H.; Marais, R.; Marshall, C. J.; Wooster, R.; Stratton, M. R.; Futreal, P. A. Mutations of the BRAF gene in human cancer. *Nature* **2002**, *417* (6892), 949–954. DOI: 10.1038/nature00766.

97. Cantwell-Dorris, E. R.; O'Leary, J. J.; Sheils, O. M. BRAFV600E: implications for carcinogenesis and molecular therapy. *Molecular cancer therapeutics* **2011**, *10* (3), 385–394. DOI: 10.1158/1535-7163.MCT-10-0799.
98. Bollag, G.; Tsai, J.; Zhang, J.; Zhang, C.; Ibrahim, P.; Nolop, K.; Hirth, P. Vemurafenib: the first drug approved for BRAF-mutant cancer. *Nature reviews. Drug discovery* **2012**, *11* (11), 873–886. DOI: 10.1038/nrd3847.
99. Tsai, J.; Lee, J. T.; Wang, W.; Zhang, J.; Cho, H.; Mamo, S.; Bremer, R.; Gillette, S.; Kong, J.; Haass, N. K.; Sproesser, K.; Li, L.; Smalley, K. S. M.; Fong, D.; Zhu, Y.-L.; Marimuthu, A.; Nguyen, H.; Lam, B.; Liu, J.; Cheung, I.; Rice, J.; Suzuki, Y.; Luu, C.; Settachatgul, C.; Shellooe, R.; Cantwell, J.; Kim, S.-H.; Schlessinger, J.; Zhang, K. Y. J.; West, B. L.; Powell, B.; Habets, G.; Zhang, C.; Ibrahim, P. N.; Hirth, P.; Artis, D. R.; Herlyn, M.; Bollag, G. Discovery of a selective inhibitor of oncogenic B-Raf kinase with potent antimelanoma activity. *Proceedings of the National Academy of Sciences of the United States of America* **2008**, *105* (8), 3041–3046. DOI: 10.1073/pnas.0711741105.
100. Bollag, G.; Hirth, P.; Tsai, J.; Zhang, J.; Ibrahim, P. N.; Cho, H.; Spevak, W.; Zhang, C.; Zhang, Y.; Habets, G.; Burton, E. A.; Wong, B.; Tsang, G.; West, B. L.; Powell, B.; Shellooe, R.; Marimuthu, A.; Nguyen, H.; Zhang, K. Y. J.; Artis, D. R.; Schlessinger, J.; Su, F.; Higgins, B.; Iyer, R.; D'Andrea, K.; Koehler, A.; Stumm, M.; Lin, P. S.; Lee, R. J.; Grippo, J.; Puzanov, I.; Kim, K. B.; Ribas, A.; McArthur, G. A.; Sosman, J. A.; Chapman, P. B.; Flaherty, K. T.; Xu, X.; Nathanson, K. L.; Nolop, K. Clinical efficacy of a RAF inhibitor needs broad target blockade in BRAF-mutant melanoma. *Nature* **2010**, *467* (7315), 596–599. DOI: 10.1038/nature09454.
101. Rheault, T. R.; Stellwagen, J. C.; Adjabeng, G. M.; Hornberger, K. R.; Petrov, K. G.; Waterson, A. G.; Dickerson, S. H.; Mook, R. A., JR; Laquerre, S. G.; King, A. J.; Rossanese, O. W.; Arnone, M. R.; Smitheman, K. N.; Kane-Carson, L. S.; Han, C.; Moorthy, G. S.; Moss, K. G.; Uehling, D. E. Discovery of Dabrafenib: A Selective Inhibitor of Raf Kinases with Antitumor Activity against B-Raf-Driven Tumors. *ACS medicinal chemistry letters* **2013**, *4* (3), 358–362. DOI: 10.1021/ml4000063.
102. Wan, P. T. C.; Garnett, M. J.; Roe, S. M.; Lee, S.; Niculescu-Duvaz, D.; Good, V. M.; Jones, C. M.; Marshall, C. J.; Springer, C. J.; Barford, D.; Marais, R. Mechanism of activation of the RAF-ERK signaling pathway by oncogenic mutations of B-RAF. *Cell* **2004**, *116* (6), 855–867.
103. Brown, C. Targeted therapy: An elusive cancer target. *Nature* **2016**, *537* (7620), S106–8. DOI: 10.1038/537S106a.
104. Baker, S. J.; Reddy, E. P. Targeted inhibition of kinases in cancer therapy. *The Mount Sinai journal of medicine, New York* **2010**, *77* (6), 573–586. DOI: 10.1002/msj.20220.

105. Gross, S.; Rahal, R.; Stransky, N.; Lengauer, C.; Hoeflich, K. P. Targeting cancer with kinase inhibitors. *The Journal of clinical investigation* **2015**, *125* (5), 1780–1789. DOI: 10.1172/JCI76094.
106. Hughes, T. P.; Hochhaus, A.; Branford, S.; Muller, M. C.; Kaeda, J. S.; Foroni, L.; Druker, B. J.; Guilhot, F.; Larson, R. A.; O'Brien, S. G.; Rudoltz, M. S.; Mone, M.; Wehrle, E.; Modur, V.; Goldman, J. M.; Radich, J. P. Long-term prognostic significance of early molecular response to imatinib in newly diagnosed chronic myeloid leukemia: an analysis from the International Randomized Study of Interferon and STI571 (IRIS). *Blood* **2010**, *116* (19), 3758–3765. DOI: 10.1182/blood-2010-03-273979.
107. Hartmann, J. T.; Haap, M.; Kopp, H.-G.; Lipp, H.-P. Tyrosine kinase inhibitors - a review on pharmacology, metabolism and side effects. *Current drug metabolism* **2009**, *10* (5), 470–481.
108. Jabbour, E.; Deininger, M.; Hochhaus, A. Management of adverse events associated with tyrosine kinase inhibitors in the treatment of chronic myeloid leukemia. *Leukemia* **2011**, *25* (2), 201–210. DOI: 10.1038/leu.2010.215.
109. Hagen, B.; van Trinh, A. Managing Side Effects of Vemurafenib Therapy for Advanced Melanoma. *Journal of the advanced practitioner in oncology* **2014**, *5* (6), 400–410.
110. Kerkela, R.; Grazette, L.; Yacobi, R.; Iliescu, C.; Patten, R.; Beahm, C.; Walters, B.; Shevtsov, S.; Pesant, S.; Clubb, F. J.; Rosenzweig, A.; Salomon, R. N.; van Etten, R. A.; Alroy, J.; Durand, J.-B.; Force, T. Cardiotoxicity of the cancer therapeutic agent imatinib mesylate. *Nature medicine* **2006**, *12* (8), 908–916. DOI: 10.1038/nm1446.
111. Chapman, P. B.; Hauschild, A.; Robert, C.; Haanen, J. B.; Ascierto, P.; Larkin, J.; Dummer, R.; Garbe, C.; Testori, A.; Maio, M.; Hogg, D.; Lorigan, P.; Lebbe, C.; Jouary, T.; Schadendorf, D.; Ribas, A.; O'Day, S. J.; Sosman, J. A.; Kirkwood, J. M.; Eggermont, A. M. M.; Dreno, B.; Nolop, K.; Li, J.; Nelson, B.; Hou, J.; Lee, R. J.; Flaherty, K. T.; McArthur, G. A. Improved survival with vemurafenib in melanoma with BRAF V600E mutation. *The New England journal of medicine* **2011**, *364* (26), 2507–2516. DOI: 10.1056/NEJMoa1103782.
112. Flaherty, K. T.; Puzanov, I.; Kim, K. B.; Ribas, A.; McArthur, G. A.; Sosman, J. A.; O'Dwyer, P. J.; Lee, R. J.; Grippo, J. F.; Nolop, K.; Chapman, P. B. Inhibition of mutated, activated BRAF in metastatic melanoma. *The New England journal of medicine* **2010**, *363* (9), 809–819. DOI: 10.1056/NEJMoa1002011.
113. Barouch-Bentov, R.; Sauer, K. Mechanisms of drug resistance in kinases. *Expert opinion on investigational drugs* **2011**, *20* (2), 153–208. DOI: 10.1517/13543784.2011.546344.

114. Camidge, D. R.; Pao, W.; Sequist, L. V. Acquired resistance to TKIs in solid tumours: learning from lung cancer. *Nature reviews. Clinical oncology* **2014**, *11* (8), 473–481. DOI: 10.1038/nrclinonc.2014.104.
115. Mondal, J.; Tiwary, P.; Berne, B. J. How a Kinase Inhibitor Withstands Gatekeeper Residue Mutations. *Journal of the American Chemical Society* **2016**, *138* (13), 4608–4615. DOI: 10.1021/jacs.6b01232.
116. Lengauer, C.; Kinzler, K. W.; Vogelstein, B. Genetic instabilities in human cancers. *Nature* **1998**, *396* (6712), 643–649. DOI: 10.1038/25292.
117. Hanahan, D.; Weinberg, R. A. Hallmarks of Cancer: The Next Generation. *Cell* **2011**, *144* (5), 646–674. DOI: 10.1016/j.cell.2011.02.013.
118. Soverini, S.; Rosti, G.; Iacobucci, I.; Baccarani, M.; Martinelli, G. Choosing the best second-line tyrosine kinase inhibitor in imatinib-resistant chronic myeloid leukemia patients harboring Bcr-Abl kinase domain mutations: how reliable is the IC(50)? *The oncologist* **2011**, *16* (6), 868–876. DOI: 10.1634/theoncologist.2010-0388.
119. Eroglu, Z.; Ribas, A. Combination therapy with BRAF and MEK inhibitors for melanoma: Latest evidence and place in therapy. *Therapeutic Advances in Medical Oncology [Online]* **2015**.
120. Long, G. V.; Fung, C.; Menzies, A. M.; Pupo, G. M.; Carlino, M. S.; Hyman, J.; Shahheydari, H.; Tembe, V.; Thompson, J. F.; Saw, R. P.; Howle, J.; Hayward, N. K.; Johansson, P.; Scolyer, R. A.; Kefford, R. F.; Rizos, H. Increased MAPK reactivation in early resistance to dabrafenib/trametinib combination therapy of BRAF-mutant metastatic melanoma. *Nature communications* **2014**, *5*, 5694. DOI: 10.1038/ncomms6694.
121. Holderfield, M.; Deuker, M. M.; McCormick, F.; McMahon, M. Targeting RAF kinases for cancer therapy: BRAF-mutated melanoma and beyond. *Nature reviews. Cancer* **2014**, *14* (7), 455–467. DOI: 10.1038/nrc3760.
122. Das Thakur, M.; Salangsang, F.; Landman, A. S.; Sellers, W. R.; Pryer, N. K.; Levesque, M. P.; Dummer, R.; McMahon, M.; Stuart, D. D. Modelling vemurafenib resistance in melanoma reveals a strategy to forestall drug resistance. *Nature* **2013**, *494* (7436), 251–255. DOI: 10.1038/nature11814.
123. Rovithi, M.; Haas, R. R. de; Honeywell, R. J.; Poel, D.; Peters, G. J.; Griffioen, A. W.; Verheul, H. M. W. Alternative scheduling of pulsatile, high dose sunitinib efficiently suppresses tumor growth. *Journal of experimental & clinical cancer research : CR* **2016**, *35* (1), 138. DOI: 10.1186/s13046-016-0411-2.
124. <https://clinicaltrials.gov/ct2/show/NCT02712112>.

125. Lee, S. J.; Wang, J. Y. J. Exploiting the promiscuity of imatinib. *Journal of biology* **2009**, *8* (3), 30. DOI: 10.1186/jbiol134.
126. Mayer, G.; Heckel, A. Biologically active molecules with a "light switch". *Angewandte Chemie (International ed. in English)* **2006**, *45* (30), 4900–4921. DOI: 10.1002/anie.200600387.
127. Velema, W. A.; Szymanski, W.; Feringa, B. L. Photopharmacology: beyond proof of principle. *Journal of the American Chemical Society* **2014**, *136* (6), 2178–2191. DOI: 10.1021/ja413063e.
128. Ellis-Davies, G. C. R. Caged compounds: photorelease technology for control of cellular chemistry and physiology. *Nature methods* **2007**, *4* (8), 619–628. DOI: 10.1038/nmeth1072.
129. Deiters, A. Principles and applications of the photochemical control of cellular processes. *Chembiochem : a European journal of chemical biology* **2010**, *11* (1), 47–53. DOI: 10.1002/cbic.200900529.
130. Lerch, M. M.; Hansen, M. J.; van Dam, G. M.; Szymanski, W.; Feringa, B. L. Emerging Targets in Photopharmacology. *Angewandte Chemie (International ed. in English)* **2016**, *55* (37), 10978–10999. DOI: 10.1002/anie.201601931.
131. Morison, W. L.; Parrish, J. A.; Fitzpatrick, T. B. Controlled study of PUVA and adjunctive topical therapy in the management of psoriasis. *The British journal of dermatology* **1978**, *98* (2), 125–132.
132. Stern, R. S. Psoralen and ultraviolet a light therapy for psoriasis. *The New England journal of medicine* **2007**, *357* (7), 682–690. DOI: 10.1056/NEJMct072317.
133. Dougherty, T. J.; Gomer, C. J.; Henderson, B. W.; Jori, G.; Kessel, D.; Korbek, M.; Moan, J.; Peng, Q. Photodynamic therapy. *Journal of the National Cancer Institute* **1998**, *90* (12), 889–905.
134. Huang, Z. A review of progress in clinical photodynamic therapy. *Technology in cancer research & treatment* **2005**, *4* (3), 283–293.
135. Agostinis, P.; Berg, K.; Cengel, K. A.; Foster, T. H.; Girotti, A. W.; Gollnick, S. O.; Hahn, S. M.; Hamblin, M. R.; Juzeniene, A.; Kessel, D.; Korbek, M.; Moan, J.; Mroz, P.; Nowis, D.; Piette, J.; Wilson, B. C.; Golab, J. Photodynamic therapy of cancer: an update. *CA: a cancer journal for clinicians* **2011**, *61* (4), 250–281. DOI: 10.3322/caac.20114.
136. Sharman; Allen; van Lier, J. E. Photodynamic therapeutics: basic principles and clinical applications. *Drug discovery today* **1999**, *4* (11), 507–517.

137. Saini, R.; Lee, N. V.; Liu, K. Y. P.; Poh, C. F. Prospects in the Application of Photodynamic Therapy in Oral Cancer and Premalignant Lesions. *Cancers* **2016**, *8* (9). DOI: 10.3390/cancers8090083.
138. Hamblin, M. R.; Hasan, T. Photodynamic therapy: a new antimicrobial approach to infectious disease? *Photochemical & photobiological sciences : Official journal of the European Photochemistry Association and the European Society for Photobiology* **2004**, *3* (5), 436–450. DOI: 10.1039/b311900a.
139. Kharkwal, G. B.; Sharma, S. K.; Huang, Y.-Y.; Dai, T.; Hamblin, M. R. Photodynamic therapy for infections: clinical applications. *Lasers in surgery and medicine* **2011**, *43* (7), 755–767. DOI: 10.1002/lsm.21080.
140. Brieke, C.; Rohrbach, F.; Gottschalk, A.; Mayer, G.; Heckel, A. Light-controlled tools. *Angewandte Chemie (International ed. in English)* **2012**, *51* (34), 8446–8476. DOI: 10.1002/anie.201202134.
141. Kaplan, J. H.; Forbush, B.; Hoffman, J. F. Rapid photolytic release of adenosine 5'-triphosphate from a protected analog: Utilization by the sodium:potassium pump of human red blood cell ghosts. *Biochemistry* **1978**, *17* (10), 1929–1935. DOI: 10.1021/bi00603a020.
142. <http://www.servier.com/slidekit/?item=5>. licensed under a Creative Commons Attribution 3.0 Unported License.
143. *Photochromism. Molecules and systems*; Dürr, H., Bouas-Laurent, H., Eds., Rev. ed.; Elsevier: Amsterdam, 2003.
144. Broichhagen, J.; Frank, J. A.; Trauner, D. A roadmap to success in photopharmacology. *Accounts of chemical research* **2015**, *48* (7), 1947–1960. DOI: 10.1021/acs.accounts.5b00129.
145. Falencyk, C.; Schiedel, M.; Karaman, B.; Rumpf, T.; Kuzmanovic, N.; Grötli, M.; Sippl, W.; Jung, M.; König, B. Chromo-pharmacophores: Photochromic diarylmaleimide inhibitors for sirtuins. *Chem. Sci.* **2014**, *5* (12), 4794–4799. DOI: 10.1039/C4SC01346H.
146. Ferreira, R.; Nilsson, J. R.; Solano, C.; Andreasson, J.; Grotli, M. Design, Synthesis and Inhibitory Activity of Photoswitchable RET Kinase Inhibitors. *Scientific reports* **2015**, *5*, 9769. DOI: 10.1038/srep09769.
147. Weston, C. E.; Kramer, A.; Colin, F.; Yildiz, O.; Baud, M. G. J.; Meyer-Almes, F.-J.; Fuchter, M. J. Toward Photopharmacological Antimicrobial Chemotherapy Using Photoswitchable Amidohydrolase Inhibitors. *ACS infectious diseases [Online]* **2016**.

148. Deisseroth, K. Optogenetics. *Nature methods* **2011**, *8* (1), 26–29. DOI: 10.1038/nmeth.f.324.
149. Williams, S. C. P.; Deisseroth, K. Optogenetics. *Proceedings of the National Academy of Sciences of the United States of America* **2013**, *110* (41), 16287. DOI: 10.1073/pnas.1317033110.
150. Nagel, G.; Szellas, T.; Huhn, W.; Kateriya, S.; Adeishvili, N.; Berthold, P.; Ollig, D.; Hegemann, P.; Bamberg, E. Channelrhodopsin-2, a directly light-gated cation-selective membrane channel. *Proceedings of the National Academy of Sciences of the United States of America* **2003**, *100* (24), 13940–13945. DOI: 10.1073/pnas.1936192100.
151. Deisseroth, K.; Feng, G.; Majewska, A. K.; Miesenbock, G.; Ting, A.; Schnitzer, M. J. Next-generation optical technologies for illuminating genetically targeted brain circuits. *The Journal of neuroscience : the official journal of the Society for Neuroscience* **2006**, *26* (41), 10380–10386. DOI: 10.1523/JNEUROSCI.3863-06.2006.
152. Adamantidis, A. R.; Zhang, F.; Aravanis, A. M.; Deisseroth, K.; Lecea, L. de. Neural substrates of awakening probed with optogenetic control of hypocretin neurons. *Nature* **2007**, *450* (7168), 420–424. DOI: 10.1038/nature06310.
153. Method of the Year 2010. *Nat Meth* **2010**, *8* (1), 1. DOI: 10.1038/nmeth.f.321.
154. Mart, R. J.; Allemann, R. K. Azobenzene photocontrol of peptides and proteins. *Chemical communications (Cambridge, England)* **2016**, *52* (83), 12262–12277. DOI: 10.1039/c6cc04004g.
155. Shah, N. P.; Kasap, C.; Weier, C.; Balbas, M.; Nicoll, J. M.; Bleickardt, E.; Nicaise, C.; Sawyers, C. L. Transient potent BCR-ABL inhibition is sufficient to commit chronic myeloid leukemia cells irreversibly to apoptosis. *Cancer cell* **2008**, *14* (6), 485–493. DOI: 10.1016/j.ccr.2008.11.001.
156. Callaway, E. M.; Yuste, R. Stimulating neurons with light. *Current opinion in neurobiology* **2002**, *12* (5), 587–592.
157. Corrie, J. E.; DeSantis, A.; Katayama, Y.; Khodakhah, K.; Messenger, J. B.; Ogden, D. C.; Trentham, D. R. Postsynaptic activation at the squid giant synapse by photolytic release of L-glutamate from a 'caged' L-glutamate. *The Journal of physiology* **1993**, *465*, 1–8.
158. McCray, J. A.; Trentham, D. R. Properties and uses of photoreactive caged compounds. *Annual review of biophysics and biophysical chemistry* **1989**, *18*, 239–270. DOI: 10.1146/annurev.bb.18.060189.001323.

159. Mentel, M.; Laketa, V.; Subramanian, D.; Gillandt, H.; Schultz, C. Photoactivatable and cell-membrane-permeable phosphatidylinositol 3,4,5-trisphosphate. *Angewandte Chemie (International ed. in English)* **2011**, *50* (16), 3811–3814. DOI: 10.1002/anie.201007796.
160. Klan, P.; Solomek, T.; Bochet, C. G.; Blanc, A.; Givens, R.; Rubina, M.; Popik, V.; Kostikov, A.; Wirz, J. Photoremovable protecting groups in chemistry and biology: reaction mechanisms and efficacy. *Chemical reviews* **2013**, *113* (1), 119–191. DOI: 10.1021/cr300177k.
161. Adams, S. R.; Tsien, R. Y. Controlling cell chemistry with caged compounds. *Annual review of physiology* **1993**, *55*, 755–784. DOI: 10.1146/annurev.ph.55.030193.003543.
162. Curley, K.; Lawrence, D. S. Caged regulators of signaling pathways. *Pharmacology & therapeutics* **1999**, *82* (2-3), 347–354.
163. Deiters, A.; Garner, R. A.; Lusic, H.; Govan, J. M.; Dush, M.; Nascone-Yoder, N. M.; Yoder, J. A. Photocaged morpholino oligomers for the light-regulation of gene function in zebrafish and *Xenopus* embryos. *Journal of the American Chemical Society* **2010**, *132* (44), 15644–15650. DOI: 10.1021/ja1053863.
164. Shestopalov, I. A.; Sinha, S.; Chen, J. K. Light-controlled gene silencing in zebrafish embryos. *Nature chemical biology* **2007**, *3* (10), 650–651. DOI: 10.1038/nchembio.2007.30.
165. Morckel, A. R.; Lusic, H.; Farzana, L.; Yoder, J. A.; Deiters, A.; Nascone-Yoder, N. M. A photoactivatable small-molecule inhibitor for light-controlled spatiotemporal regulation of Rho kinase in live embryos. *Development (Cambridge, England)* **2012**, *139* (2), 437–442. DOI: 10.1242/dev.072165.
166. Bliman, D.; Nilsson, J. R.; Kettunen, P.; Andreasson, J.; Grotli, M. A Caged Ret Kinase Inhibitor and its Effect on Motoneuron Development in Zebrafish Embryos. *Scientific reports* **2015**, *5*, 13109. DOI: 10.1038/srep13109.
167. Jason S. Wood , Mary Koszelak , Judy Liu , and David S. Lawrence. A Caged Protein Kinase Inhibitor. *J. Am. Chem. Soc [Online]* **1998**, *120* (28), 7145–7146.
168. Pelliccioli, A. P.; Wirz, J. Photoremovable protecting groups: Reaction mechanisms and applications. *Photochem. Photobiol. Sci.* **2002**, *1* (7), 441–458. DOI: 10.1039/b200777k.
169. Weissleder, R. A clearer vision for in vivo imaging. *Nature biotechnology* **2001**, *19* (4), 316–317. DOI: 10.1038/86684.
170. Frangioni, J. In vivo near-infrared fluorescence imaging. *Current Opinion in Chemical Biology* **2003**, *7* (5), 626–634. DOI: 10.1016/j.cbpa.2003.08.007.

171. Smith, A. M.; Mancini, M. C.; Nie, S. Bioimaging: second window for in vivo imaging. *Nature nanotechnology* **2009**, *4* (11), 710–711. DOI: 10.1038/nnano.2009.326.
172. Sternberg, E. D.; Dolphin, D.; Brückner, C. Porphyrin-based photosensitizers for use in photodynamic therapy. *Tetrahedron* **1998**, *54* (17), 4151–4202. DOI: 10.1016/S0040-4020(98)00015-5.
173. Dommaschk, M.; Herges, R. Design of Photoswitchable Contrast Agents for Magnetic Resonance Imaging. Dissertation; Christian-Albrechts-Universität; Christian-Albrechts-Universität zu Kiel, Kiel, 2016.
174. Smith, N. A.; Sadler, P. J. Photoactivatable metal complexes: from theory to applications in biotechnology and medicine. *Philosophical transactions. Series A, Mathematical, physical, and engineering sciences* **2013**, *371* (1995), 20120519. DOI: 10.1098/rsta.2012.0519.
175. Huisman, M.; White, J. K.; Lewalski, V. G.; Podgorski, I.; Turro, C.; Kodanko, J. J. Caging the uncageable: using metal complex release for photochemical control over irreversible inhibition. *Chemical communications (Cambridge, England)* **2016**, *52* (85), 12590–12593. DOI: 10.1039/c6cc07083c.
176. Horbert, R. *Photoactivatable Kinase Inhibitors*; Universitätsbibliothek Kiel: Kiel, 2015.
177. Goswami, P. P.; Syed, A.; Beck, C. L.; Albright, T. R.; Mahoney, K. M.; Unash, R.; Smith, E. A.; Winter, A. H. BODIPY-derived photoremovable protecting groups unmasked with green light. *Journal of the American Chemical Society* **2015**, *137* (11), 3783–3786. DOI: 10.1021/jacs.5b01297.
178. Solomek, T.; Mercier, S.; Bally, T.; Bochet, C. G. Photolysis of ortho-nitrobenzylic derivatives: the importance of the leaving group. *Photochemical & photobiological sciences : Official journal of the European Photochemistry Association and the European Society for Photobiology* **2012**, *11* (3), 548–555. DOI: 10.1039/c1pp05308f.
179. Rajasekharan Pillai, V. N. Photoremovable Protecting Groups in Organic Synthesis. *Synthesis* **1980**, *1980* (01), 1–26. DOI: 10.1055/s-1980-28908.
180. Voelker, T.; Ewell, T.; Joo, J.; Edstrom, E. D. o-Nitrobenzyl as a photocleavable nitrogen protecting group for indoles, benzimidazole, and 6-chlorouracil. *Tetrahedron Letters* **1998**, *39* (5-6), 359–362. DOI: 10.1016/S0040-4039(97)10600-1.
181. Aujard, I.; Benbrahim, C.; Gouget, M.; Ruel, O.; Baudin, J.-B.; Neveu, P.; Jullien, L. o-nitrobenzyl photolabile protecting groups with red-shifted absorption: syntheses and uncaging cross-sections for one- and two-photon excitation. *Chemistry (Weinheim an der Bergstrasse, Germany)* **2006**, *12* (26), 6865–6879. DOI: 10.1002/chem.200501393.

182. Klink, B. U.; Goody, R. S.; Scheidig, A. J. A newly designed microspectrofluorometer for kinetic studies on protein crystals in combination with x-ray diffraction. *Biophysical journal* **2006**, *91* (3), 981–992. DOI: 10.1529/biophysj.105.078931.
183. Li, W.-h.; Zheng, G. Photoactivatable fluorophores and techniques for biological imaging applications. *Photochemical & photobiological sciences : Official journal of the European Photochemistry Association and the European Society for Photobiology* **2012**, *11* (3), 460–471. DOI: 10.1039/c2pp05342j.
184. <https://www.thermofisher.com/de/de/home/references/molecular-probes-the-handbook/crosslinking-and-photoactivatable-reagents/photoactivatable-reagents-including-photoreactive-crosslinkers-and-caged-probes.html#head3>.
185. Yip, R. W.; Sharma, D. K.; Giasson, R.; Gravel, D. Photochemistry of the o-nitrobenzyl system in solution: Evidence for singlet-state intramolecular hydrogen abstraction. *J. Phys. Chem.* **1985**, *89* (25), 5328–5330. DOI: 10.1021/j100271a002.
186. Il'ichev, Y. V.; Schworer, M. A.; Wirz, J. Photochemical reaction mechanisms of 2-nitrobenzyl compounds: methyl ethers and caged ATP. *Journal of the American Chemical Society* **2004**, *126* (14), 4581–4595. DOI: 10.1021/ja039071z.
187. Adams, S. R.; Kao, J. P. Y.; Tsien, R. Y. Biologically useful chelators that take up calcium(2+) upon illumination. *J. Am. Chem. Soc.* **1989**, *111* (20), 7957–7968. DOI: 10.1021/ja00202a042.
188. Cohen, M. H.; Williams, G.; Johnson, J. R.; Duan, J.; Gobburu, J.; Rahman, A.; Benson, K.; Leighton, J.; Kim, S. K.; Wood, R.; Rothmann, M.; Chen, G.; U, K. M.; Staten, A. M.; Pazdur, R. Approval summary for imatinib mesylate capsules in the treatment of chronic myelogenous leukemia. *Clinical cancer research : an official journal of the American Association for Cancer Research* **2002**, *8* (5), 935–942.
189. Parmar, K. K.; King, R. S. Imatinib Mesylate. *Cancer Practice* **2001**, *9* (5), 263–265. DOI: 10.1111/j.1523-5394.2001.95003.pp.x.
190. Peifer, C.; Stoiber, T.; Unger, E.; Totzke, F.; Schachtele, C.; Marme, D.; Brenk, R.; Klebe, G.; Schollmeyer, D.; Dannhardt, G. Design, synthesis, and biological evaluation of 3,4-diarylmaleimides as angiogenesis inhibitors. *Journal of medicinal chemistry* **2006**, *49* (4), 1271–1281. DOI: 10.1021/jm0580297.
191. Peifer, C.; Krasowski, A.; Hammerle, N.; Kohlbacher, O.; Dannhardt, G.; Totzke, F.; Schachtele, C.; Laufer, S. Profile and molecular modeling of 3-(indole-3-yl)-4-(3,4,5-trimethoxyphenyl)-1 H-pyrrole-2,5-dione (1) as a highly selective VEGF-R2/3 inhibitor. *Journal of medicinal chemistry* **2006**, *49* (25), 7549–7553. DOI: 10.1021/jm0609871.

192. Ferrara, N.; Gerber, H.-P.; LeCouter, J. The biology of VEGF and its receptors. *Nature medicine* **2003**, *9* (6), 669–676. DOI: 10.1038/nm0603-669.
193. Horbert, R.; Pinchuk, B.; Davies, P.; Alessi, D.; Peifer, C. Photoactivatable Prodrugs of Antimelanoma Agent Vemurafenib. *ACS chemical biology* **2015**, *10* (9), 2099–2107. DOI: 10.1021/acscchembio.5b00174.
194. Pinchuk, B.; Horbert, R.; Dobber, A.; Kuhl, L.; Peifer, C. Photoactivatable Caged Prodrugs of VEGFR-2 Kinase Inhibitors. *Molecules (Basel, Switzerland)* **2016**, *21* (5). DOI: 10.3390/molecules21050570.
195. Zindler, M.; Pinchuk, B.; Renn, C.; Horbert, R.; Dobber, A.; Peifer, C. Design, Synthesis, and Characterization of a Photoactivatable Caged Prodrug of Imatinib. *ChemMedChem* **2015**, *10* (8), 1335–1338. DOI: 10.1002/cmdc.201500163.
196. Pinchuk, B.; Drathen, T. von; Opel, V.; Peifer, C. Photoinduced Conversion of Antimelanoma Agent Dabrafenib to a Novel Fluorescent BRAFV600E Inhibitor. *ACS medicinal chemistry letters* **2016**, *7* (10), 962–966. DOI: 10.1021/acsmchemlett.6b00340.
197. Drathen, T. von. *Photoaktivierbare Prodrugs von Dabrafenib*. Bachelor Thesis, 2014.
198. Williams, L. Signal transduction by the platelet-derived growth factor receptor. *Science* **1989**, *243* (4898), 1564–1570. DOI: 10.1126/science.2538922.
199. Soskic, V.; Gorlach, M.; Poznanovic, S.; Boehmer, F. D.; Godovac-Zimmermann, J. Functional proteomics analysis of signal transduction pathways of the platelet-derived growth factor beta receptor. *Biochemistry* **1999**, *38* (6), 1757–1764. DOI: 10.1021/bi982093r.
200. Ibrahim, N.; Yu, Y.; Walsh, W. R.; Yang, J.-L. Molecular targeted therapies for cancer: sorafenib mono-therapy and its combination with other therapies (review). *Oncology reports* **2012**, *27* (5), 1303–1311. DOI: 10.3892/or.2012.1675.
201. Pinchuk, B.; Johannes, E.; Gul, S.; Schlosser, J.; Schachtele, C.; Totzke, F.; Peifer, C. Marine derived hamacanthins as lead for the development of novel PDGFRbeta protein kinase inhibitors. *Marine drugs* **2013**, *11* (9), 3209–3223. DOI: 10.3390/md11093209.
202. Horbert, R.; Pinchuk, B.; Johannes, E.; Schlosser, J.; Schmidt, D.; Cappel, D.; Totzke, F.; Schachtele, C.; Peifer, C. Optimization of potent DFG-in inhibitors of platelet derived growth factor receptorbeta (PDGF-Rbeta) guided by water thermodynamics. *Journal of medicinal chemistry* **2015**, *58* (1), 170–182. DOI: 10.1021/jm500373x.

203. Bethke, E.; Pinchuk, B.; Renn, C.; Witt, L.; Schlosser, J.; Peifer, C. From Type I to Type II: Design, Synthesis, and Characterization of Potent Pyrazin-2-ones as DFG-Out Inhibitors of PDGFRbeta. *ChemMedChem* **2016**, *11* (24), 2664–2674. DOI: 10.1002/cmdc.201600494.
204. Schlosser, J. *Design, Synthese und biologische Evaluierung von 3,5-disubstituierten (1H)-Pyrazinonen als Tyrosinkinaseinhibitoren*; s.n.]: [S.l., 2011.
205. Johannes, E.; Peifer, C. *Design, Synthese, Optimierung und Vergleich von Pyrazin-2-on DFGin- und DFGout-Inhibitoren*. @Kiel, Univ., Diss., 2015, 2015.
206. Sosman, J. A.; Kim, K. B.; Schuchter, L.; Gonzalez, R.; Pavlick, A. C.; Weber, J. S.; McArthur, G. A.; Hutson, T. E.; Moschos, S. J.; Flaherty, K. T.; Hersey, P.; Kefford, R.; Lawrence, D.; Puzanov, I.; Lewis, K. D.; Amaravadi, R. K.; Chmielowski, B.; Lawrence, H. J.; Shyr, Y.; Ye, F.; Li, J.; Nolop, K. B.; Lee, R. J.; Joe, A. K.; Ribas, A. Survival in BRAF V600-mutant advanced melanoma treated with vemurafenib. *The New England journal of medicine* **2012**, *366* (8), 707–714. DOI: 10.1056/NEJMoa1112302.
207. Poulikakos, P. I.; Persaud, Y.; Janakiraman, M.; Kong, X.; Ng, C.; Moriceau, G.; Shi, H.; Atefi, M.; Titz, B.; Gabay, M. T.; Salton, M.; Dahlman, K. B.; Tadi, M.; Wargo, J. A.; Flaherty, K. T.; Kelley, M. C.; Misteli, T.; Chapman, P. B.; Sosman, J. A.; Graeber, T. G.; Ribas, A.; Lo, R. S.; Rosen, N.; Solit, D. B. RAF inhibitor resistance is mediated by dimerization of aberrantly spliced BRAF(V600E). *Nature* **2011**, *480* (7377), 387–390. DOI: 10.1038/nature10662.
208. Shi, H.; Moriceau, G.; Kong, X.; Lee, M.-K.; Lee, H.; Koya, R. C.; Ng, C.; Chodon, T.; Scolyer, R. A.; Dahlman, K. B.; Sosman, J. A.; Kefford, R. F.; Long, G. V.; Nelson, S. F.; Ribas, A.; Lo, R. S. Melanoma whole-exome sequencing identifies (V600E)B-RAF amplification-mediated acquired B-RAF inhibitor resistance. *Nature communications* **2012**, *3*, 724. DOI: 10.1038/ncomms1727.
209. Johannessen, C. M.; Boehm, J. S.; Kim, S. Y.; Thomas, S. R.; Wardwell, L.; Johnson, L. A.; Emery, C. M.; Stransky, N.; Cogdill, A. P.; Barretina, J.; Caponigro, G.; Hieronymus, H.; Murray, R. R.; Salehi-Ashtiani, K.; Hill, D. E.; Vidal, M.; Zhao, J. J.; Yang, X.; Alkan, O.; Kim, S.; Harris, J. L.; Wilson, C. J.; Myer, V. E.; Finan, P. M.; Root, D. E.; Roberts, T. M.; Golub, T.; Flaherty, K. T.; Dummer, R.; Weber, B. L.; Sellers, W. R.; Schlegel, R.; Wargo, J. A.; Hahn, W. C.; Garraway, L. A. COT drives resistance to RAF inhibition through MAP kinase pathway reactivation. *Nature* **2010**, *468* (7326), 968–972. DOI: 10.1038/nature09627.
210. Jang, S.; Atkins, M. B. Treatment of BRAF-mutant melanoma: the role of vemurafenib and other therapies. *Clinical pharmacology and therapeutics* **2014**, *95* (1), 24–31. DOI: 10.1038/clpt.2013.197.

211. Swaika, A.; Crozier, J. A.; Joseph, R. W. Vemurafenib: an evidence-based review of its clinical utility in the treatment of metastatic melanoma. *Drug design, development and therapy* **2014**, *8*, 775–787. DOI: 10.2147/DDDT.S31143.
212. Dissanayake, K.; Toth, R.; Blakey, J.; Olsson, O.; Campbell, D. G.; Prescott, A. R.; MacKintosh, C. ERK/p90(RSK)/14-3-3 signalling has an impact on expression of PEA3 Ets transcription factors via the transcriptional repressor capicua. *The Biochemical journal* **2011**, *433* (3), 515–525. DOI: 10.1042/BJ20101562.
213. Baccarani, M.; Cilloni, D.; Rondoni, M.; Ottaviani, E.; Messa, F.; Merante, S.; Tiribelli, M.; Buccisano, F.; Testoni, N.; Gottardi, E.; Vivo, A. de; Giugliano, E.; Iacobucci, I.; Paolini, S.; Soverini, S.; Rosti, G.; Rancati, F.; Astolfi, C.; Pane, F.; Saglio, G.; Martinelli, G. The efficacy of imatinib mesylate in patients with FIP1L1-PDGFR -positive hypereosinophilic syndrome. Results of a multicenter prospective study. *Haematologica* **2007**, *92* (9), 1173–1179. DOI: 10.3324/haematol.11420.
214. Schultz, K. R.; Carroll, A.; Heerema, N. A.; Bowman, W. P.; Aledo, A.; Slayton, W. B.; Sather, H.; Devidas, M.; Zheng, H. W.; Davies, S. M.; Gaynon, P. S.; Trigg, M.; Rutledge, R.; Jorstad, D.; Winick, N.; Borowitz, M. J.; Hunger, S. P.; Carroll, W. L.; Camitta, B. Long-term follow-up of imatinib in pediatric Philadelphia chromosome-positive acute lymphoblastic leukemia: Children's Oncology Group study AALL0031. *Leukemia* **2014**, *28* (7), 1467–1471. DOI: 10.1038/leu.2014.30.
215. Adekola, K.; Agulnik, M. Advances in adjuvant therapy of gastrointestinal stromal tumors. *Current oncology reports* **2012**, *14* (4), 327–332. DOI: 10.1007/s11912-012-0241-0.
216. Hall, R. D.; Le, T. M.; Haggstrom, D. E.; Gentzler, R. D. Angiogenesis inhibition as a therapeutic strategy in non-small cell lung cancer (NSCLC). *Translational lung cancer research* **2015**, *4* (5), 515–523. DOI: 10.3978/j.issn.2218-6751.2015.06.09.
217. Huang, H.; Shen, J.; Vinos, S. A. Blockade of VEGFR1 and 2 suppresses pathological angiogenesis and vascular leakage in the eye. *PLoS one* **2011**, *6* (6), e21411. DOI: 10.1371/journal.pone.0021411.
218. Lee, S. H.; Jeong, D.; Han, Y.-S.; Baek, M. J. Pivotal role of vascular endothelial growth factor pathway in tumor angiogenesis. *Annals of surgical treatment and research* **2015**, *89* (1), 1–8. DOI: 10.4174/astr.2015.89.1.1.
219. https://www.drugs.com/drug-class/vegf-vegfr-inhibitors.html?condition_id=&generic=1&sort=rating&order=desc.

220. Banzi, M.; Blasio, S. de; Lallas, A.; Longo, C.; Moscarella, E.; Alfano, R.; Argenziano, G. Dabrafenib: a new opportunity for the treatment of BRAF V600-positive melanoma. *OncoTargets and therapy* **2016**, *9*, 2725–2733. DOI: 10.2147/OTT.S75104.
221. Hauschild, A.; Grob, J.-J.; Demidov, L. V.; Jouary, T.; Gutzmer, R.; Millward, M.; Rutkowski, P.; Blank, C. U.; Miller, W. H.; Kaempgen, E.; Martín-Algarra, S.; Karaszewska, B.; Mauch, C.; Chiarion-Sileni, V.; Martin, A.-M.; Swann, S.; Haney, P.; Mirakhur, B.; Guckert, M. E.; Goodman, V.; Chapman, P. B. Dabrafenib in BRAF-mutated metastatic melanoma: A multicentre, open-label, phase 3 randomised controlled trial. *The Lancet* **2012**, *380* (9839), 358–365. DOI: 10.1016/S0140-6736(12)60868-X.
222. Sullivan, R. J.; Flaherty, K. T. Resistance to BRAF-targeted therapy in melanoma. *European journal of cancer (Oxford, England : 1990)* **2013**, *49* (6), 1297–1304. DOI: 10.1016/j.ejca.2012.11.019.
223. Long, G. V.; Stroyakovskiy, D.; Gogas, H.; Levchenko, E.; Braud, F. de; Larkin, J.; Garbe, C.; Jouary, T.; Hauschild, A.; Grob, J. J.; Chiarion Sileni, V.; Lebbe, C.; Mandala, M.; Millward, M.; Arance, A.; Bondarenko, I.; Haanen, J. B. A. G.; Hansson, J.; Utikal, J.; Ferraresi, V.; Kovalenko, N.; Mohr, P.; Probachai, V.; Schadendorf, D.; Nathan, P.; Robert, C.; Ribas, A.; DeMarini, D. J.; Irani, J. G.; Casey, M.; Ouellet, D.; Martin, A.-M.; Le, N.; Patel, K.; Flaherty, K. Combined BRAF and MEK inhibition versus BRAF inhibition alone in melanoma. *The New England journal of medicine* **2014**, *371* (20), 1877–1888. DOI: 10.1056/NEJMoa1406037.
224. Zhu, Z.; Liu, W.; Gotlieb, V. The rapidly evolving therapies for advanced melanoma--Towards immunotherapy, molecular targeted therapy, and beyond. *Critical reviews in oncology/hematology* **2016**, *99*, 91–99. DOI: 10.1016/j.critrevonc.2015.12.002.
225. Shoemaker, R. H. The NCI60 human tumour cell line anticancer drug screen. *Nature reviews. Cancer* **2006**, *6* (10), 813–823. DOI: 10.1038/nrc1951.
226. Gunasekera, S. P.; McCarthy, P. J.; Kelly-Borges, M. Hamacanthins A and B, New Antifungal Bis Indole Alkaloids from the Deep-Water Marine Sponge, Hamacantha Sp. *J. Nat. Prod.* **1994**, *57* (10), 1437–1441. DOI: 10.1021/np50112a014.
227. Bao, B.; Sun, Q.; Yao, X.; Hong, J.; Lee, C.-O.; Cho, H. Y.; Jung, J. H. Bisindole alkaloids of the topsentin and hamacanthin classes from a marine sponge Spongosorites sp. *Journal of natural products* **2007**, *70* (1), 2–8. DOI: 10.1021/np060206z.
228. Zoraghi, R.; Worrall, L.; See, R. H.; Strangman, W.; Popplewell, W. L.; Gong, H.; Samaai, T.; Swayze, R. D.; Kaur, S.; Vuckovic, M.; Finlay, B. B.; Brunham, R. C.; McMaster, W. R.; Davies-Coleman, M. T.; Strynadka, N. C.; Andersen, R. J.; Reiner, N. E. Methicillin-resistant *Staphylococcus aureus* (MRSA) pyruvate kinase as a target for bis-indole alkaloids with

- antibacterial activities. *The Journal of biological chemistry* **2011**, *286* (52), 44716–44725. DOI: 10.1074/jbc.M111.289033.
229. Caldwell, J. J.; Veillard, N.; Collins, I. Design and synthesis of 2(1H)-pyrazinones as inhibitors of protein kinases. *Tetrahedron* **2012**, *68* (47), 9713–9728. DOI: 10.1016/j.tet.2012.09.039.
230. Johannes, E.; Horbert, R.; Schlosser, J.; Schmidt, D.; Peifer, C. Effective synthesis of 3,5-diaryl-(1H)-pyrazin-2-ones via microwave mediated ring closure. *Tetrahedron Letters* **2013**, *54* (31), 4067–4072. DOI: 10.1016/j.tetlet.2013.05.095.
231. Breiten, B.; Lockett, M. R.; Sherman, W.; Fujita, S.; Al-Sayah, M.; Lange, H.; Bowers, C. M.; Heroux, A.; Krilov, G.; Whitesides, G. M. Water networks contribute to enthalpy/entropy compensation in protein-ligand binding. *Journal of the American Chemical Society* **2013**, *135* (41), 15579–15584. DOI: 10.1021/ja4075776.
232. Abel, R.; Young, T.; Farid, R.; Berne, B. J.; Friesner, R. A. Role of the active-site solvent in the thermodynamics of factor Xa ligand binding. *Journal of the American Chemical Society* **2008**, *130* (9), 2817–2831. DOI: 10.1021/ja0771033.
233. Friesner, R. A.; Banks, J. L.; Murphy, R. B.; Halgren, T. A.; Klicic, J. J.; Mainz, D. T.; Repasky, M. P.; Knoll, E. H.; Shelley, M.; Perry, J. K.; Shaw, D. E.; Francis, P.; Shenkin, P. S. Glide: a new approach for rapid, accurate docking and scoring. 1. Method and assessment of docking accuracy. *Journal of medicinal chemistry* **2004**, *47* (7), 1739–1749. DOI: 10.1021/jm0306430.
234. Robinson, D. D.; Sherman, W.; Farid, R. Understanding kinase selectivity through energetic analysis of binding site waters. *ChemMedChem* **2010**, *5* (4), 618–627. DOI: 10.1002/cmdc.200900501.
235. Iwata, H.; Imamura, S.; Hori, A.; Hixon, M. S.; Kimura, H.; Miki, H. Biochemical characterization of TAK-593, a novel VEGFR/PDGFR inhibitor with a two-step slow binding mechanism. *Biochemistry* **2011**, *50* (5), 738–751. DOI: 10.1021/bi101777f.
236. Renn, C. *Biochemische Charakterisierung von DFGin/out-Kinaseinhibitoren*. Master Thesis, 2015.
237. Zhang, Y.; Zhang, K. Y.; Zhang, C. *B-Raf Kinase V600E oncogenic mutant in complex with PLX4032*, 2010.
238. Committee for Medicinal Products for Human Use (CHMP). CHMP assessment report Tafinlar.
239. http://www.sahlmann-ps.de/pages_en/index.html.

240. Charles River Laboratories International, Inc. Oncology Animal Models: www.criver.com/files/pdfs/rms/rm_rm_d_oncology_models.aspx.
241. Yang, H.; Higgins, B.; Kolinsky, K.; Packman, K.; Go, Z.; Iyer, R.; Kolis, S.; Zhao, S.; Lee, R.; Grippo, J. F.; Schostack, K.; Simcox, M. E.; Heimbrook, D.; Bollag, G.; Su, F. RG7204 (PLX4032), a selective BRAFV600E inhibitor, displays potent antitumor activity in preclinical melanoma models. *Cancer research* **2010**, *70* (13), 5518–5527. DOI: 10.1158/0008-5472.CAN-10-0646.
242. Neck, M. *Opimierung der Löslichkeit von photoaktivierbaren Proteinkinaseinhibitoren. Masterarbeit*, 2016.
243. Ni, J.; Auston, D. A.; Freilich, D. A.; Muralidharan, S.; Sobie, E. A.; Kao, J. P. Y. Photochemical gating of intracellular Ca²⁺ release channels. *Journal of the American Chemical Society* **2007**, *129* (17), 5316–5317. DOI: 10.1021/ja069361q.
244. Kuster, T.; Zumkehr, B.; Hermann, C.; Theurillat, R.; Thormann, W.; Gottstein, B.; Hemphill, A. Voluntary ingestion of antiparasitic drugs emulsified in honey represents an alternative to gavage in mice. *Journal of the American Association for Laboratory Animal Science : JAALAS* **2012**, *51* (2), 219–223.
245. D'Orazio, J.; Jarrett, S.; Amaro-Ortiz, A.; Scott, T. UV radiation and the skin. *International journal of molecular sciences* **2013**, *14* (6), 12222–12248. DOI: 10.3390/ijms140612222.
246. Viros, A.; Sanchez-Laorden, B.; Pedersen, M.; Furney, S. J.; Rae, J.; Hogan, K.; Ejiama, S.; Girotti, M. R.; Cook, M.; Dhomen, N.; Marais, R. Ultraviolet radiation accelerates BRAF-driven melanomagenesis by targeting TP53. *Nature* **2014**, *511* (7510), 478–482. DOI: 10.1038/nature13298.
247. Szacilowski, K.; Macyk, W.; Drzewiecka-Matuszek, A.; Brindell, M.; Stochel, G. Bioinorganic photochemistry: frontiers and mechanisms. *Chemical reviews* **2005**, *105* (6), 2647–2694. DOI: 10.1021/cr030707e.
248. Yoon, I.; Li, J. Z.; Shim, Y. K. Advance in photosensitizers and light delivery for photodynamic therapy. *Clinical endoscopy* **2013**, *46* (1), 7–23. DOI: 10.5946/ce.2013.46.1.7.
249. Chatani, S.; Kloxin, C. J.; Bowman, C. N. The power of light in polymer science: Photochemical processes to manipulate polymer formation, structure, and properties. *Polym. Chem.* **2014**, *5* (7), 2187–2201. DOI: 10.1039/C3PY01334K.
250. Zhou, Z.; Song, J.; Nie, L.; Chen, X. Reactive oxygen species generating systems meeting challenges of photodynamic cancer therapy. *Chemical Society reviews* **2016**, *45* (23), 6597–6626. DOI: 10.1039/c6cs00271d.

251. Yano, T.; Kasai, H.; Horimatsu, T.; Yoshimura, K.; Teramukai, S.; Morita, S.; Tada, H.; Yamamoto, Y.; Kataoka, H.; Kakushima, N.; Ishihara, R.; Isomoto, H.; Muto, M. A multicenter phase II study of salvage photodynamic therapy using talaporfin sodium (ME2906) and a diode laser (PNL6405EPG) for local failure after chemoradiotherapy or radiotherapy for esophageal cancer. *Oncotarget [Online]* **2016**.
252. Weber, M. *Clinical Applications of Biological Lasertherapy*: Lauenfoerde, 2013.
253. Hong, G.; Diao, S.; Chang, J.; Antaris, A. L.; Chen, C.; Zhang, B.; Zhao, S.; Atochin, D. N.; Huang, P. L.; Andreasson, K. I.; Kuo, C. J.; Dai, H. Through-skull fluorescence imaging of the brain in a new near-infrared window. *Nature photonics* **2014**, *8* (9), 723–730. DOI: 10.1038/nphoton.2014.166.
254. Pawlicki, M.; Collins, H. A.; Denning, R. G.; Anderson, H. L. Zweiphotonenabsorption und das Design von Zweiphotonenfarbstoffen. *Angew. Chem.* **2009**, *121* (18), 3292–3316. DOI: 10.1002/ange.200805257.
255. Park, Y. I.; Lee, K. T.; Suh, Y. D.; Hyeon, T. Upconverting nanoparticles: a versatile platform for wide-field two-photon microscopy and multi-modal in vivo imaging. *Chemical Society reviews* **2015**, *44* (6), 1302–1317. DOI: 10.1039/c4cs00173g.
256. LaFratta, C. N.; Fourkas, J. T.; Baldacchini, T.; Farrer, R. A. Mehrphotonen-Mikrofabrikation. *Angew. Chem.* **2007**, *119* (33), 6352–6374. DOI: 10.1002/ange.200603995.
257. Collins, H. A.; Khurana, M.; Moriyama, E. H.; Mariampillai, A.; Dahlstedt, E.; Balaz, M.; Kuimova, M. K.; Drobizhev, M.; Yang, V. X. D.; Phillips, D.; Rebane, A.; Wilson, B. C.; Anderson, H. L. Blood-vessel closure using photosensitizers engineered for two-photon excitation. *Nature Photon* **2008**, *2* (7), 420–424. DOI: 10.1038/nphoton.2008.100.
258. Starkey, J. R.; Rebane, A. K.; Drobizhev, M. A.; Meng, F.; Gong, A.; Elliott, A.; McInerney, K.; Spangler, C. W. New two-photon activated photodynamic therapy sensitizers induce xenograft tumor regressions after near-IR laser treatment through the body of the host mouse. *Clinical cancer research : an official journal of the American Association for Cancer Research* **2008**, *14* (20), 6564–6573. DOI: 10.1158/1078-0432.CCR-07-4162.
259. Auzel, F. Upconversion and anti-Stokes processes with f and d ions in solids. *Chemical reviews* **2004**, *104* (1), 139–173. DOI: 10.1021/cr020357g.
260. Zhou, B.; Shi, B.; Jin, D.; Liu, X. Controlling upconversion nanocrystals for emerging applications. *Nature nanotechnology* **2015**, *10* (11), 924–936. DOI: 10.1038/nnano.2015.251.

261. Wang, M.; Abbineni, G.; Clevenger, A.; Mao, C.; Xu, S. Upconversion nanoparticles: synthesis, surface modification and biological applications. *Nanomedicine: Nanotechnology, Biology and Medicine* **2011**, *7* (6), 710–729. DOI: 10.1016/j.nano.2011.02.013.
262. Haase, M.; Schafer, H. Upconverting nanoparticles. *Angewandte Chemie (International ed. in English)* **2011**, *50* (26), 5808–5829. DOI: 10.1002/anie.201005159.
263. Chen, G.; Qiu, H.; Prasad, P. N.; Chen, X. Upconversion nanoparticles: design, nanochemistry, and applications in theranostics. *Chemical reviews* **2014**, *114* (10), 5161–5214. DOI: 10.1021/cr400425h.
264. Jayakumar, M. K. G.; Idris, N. M.; Zhang, Y. Remote activation of biomolecules in deep tissues using near-infrared-to-UV upconversion nanotransducers. *Proceedings of the National Academy of Sciences of the United States of America* **2012**, *109* (22), 8483–8488. DOI: 10.1073/pnas.1114551109.
265. Yang, Y.; Liu, F.; Liu, X.; Xing, B. NIR light controlled photorelease of siRNA and its targeted intracellular delivery based on upconversion nanoparticles. *Nanoscale* **2013**, *5* (1), 231–238. DOI: 10.1039/c2nr32835f.
266. Yang, Y.; Shao, Q.; Deng, R.; Wang, C.; Teng, X.; Cheng, K.; Cheng, Z.; Huang, L.; Liu, Z.; Liu, X.; Xing, B. In vitro and in vivo uncaging and bioluminescence imaging by using photocaged upconversion nanoparticles. *Angewandte Chemie (International ed. in English)* **2012**, *51* (13), 3125–3129. DOI: 10.1002/anie.201107919.
267. Idris, N. M.; Gnanasammandhan, M. K.; Zhang, J.; Ho, P. C.; Mahendran, R.; Zhang, Y. In vivo photodynamic therapy using upconversion nanoparticles as remote-controlled nanotransducers. *Nature medicine* **2012**, *18* (10), 1580–1585. DOI: 10.1038/nm.2933.
268. Cui, S.; Yin, D.; Chen, Y.; Di, Y.; Chen, H.; Ma, Y.; Achilefu, S.; Gu, Y. In vivo targeted deep-tissue photodynamic therapy based on near-infrared light triggered upconversion nanoconstruct. *ACS nano* **2013**, *7* (1), 676–688. DOI: 10.1021/nn304872n.
269. Zhang, P.; Steelant, W.; Kumar, M.; Scholfield, M. Versatile photosensitizers for photodynamic therapy at infrared excitation. *Journal of the American Chemical Society* **2007**, *129* (15), 4526–4527. DOI: 10.1021/ja0700707.
270. Yang, Y.; Mu, J.; Xing, B. Photoactivated drug delivery and bioimaging. *Wiley interdisciplinary reviews. Nanomedicine and nanobiotechnology* **2017**, *9* (2). DOI: 10.1002/wnan.1408.
271. Ai, X.; Lyu, L.; Zhang, Y.; Tang, Y.; Mu, J.; Liu, F.; Zhou, Y.; Zuo, Z.; Liu, G.; Xing, B. Remote Regulation of Membrane Channel Activity by Site-Specific Localization of

- Lanthanide-Doped Upconversion Nanocrystals. *Angewandte Chemie (International ed. in English) [Online]* **2017**.
272. Sun, Y.; Feng, W.; Yang, P.; Huang, C.; Li, F. The biosafety of lanthanide upconversion nanomaterials. *Chemical Society reviews* **2015**, *44* (6), 1509–1525. DOI: 10.1039/c4cs00175c.
273. Henderson, T. A.; Morries, L. D. Near-infrared photonic energy penetration: can infrared phototherapy effectively reach the human brain? *Neuropsychiatric disease and treatment* **2015**, *11*, 2191–2208. DOI: 10.2147/NDT.S78182.
274. Kamkaew, A.; Chen, F.; Zhan, Y.; Majewski, R. L.; Cai, W. Scintillating Nanoparticles as Energy Mediators for Enhanced Photodynamic Therapy. *ACS nano* **2016**, *10* (4), 3918–3935. DOI: 10.1021/acsnano.6b01401.
275. Sakdinawat, A.; Attwood, D. Nanoscale X-ray imaging. *Nature Photon* **2010**, *4* (12), 840–848. DOI: 10.1038/nphoton.2010.267.
276. Wojtowicz, A. J. Rare-earth-activated wide bandgap materials for scintillators. *Nuclear Instruments and Methods in Physics Research Section A: Accelerators, Spectrometers, Detectors and Associated Equipment* **2002**, *486* (1-2), 201–207. DOI: 10.1016/S0168-9002(02)00703-9.
277. Cooper, D. R.; Bekah, D.; Nadeau, J. L. Gold nanoparticles and their alternatives for radiation therapy enhancement. *Frontiers in chemistry* **2014**, *2*, 86. DOI: 10.3389/fchem.2014.00086.
278. Chen, W.; Zhang, J. Using Nanoparticles to Enable Simultaneous Radiation and Photodynamic Therapies for Cancer Treatment. *J. Nanosci. Nanotech.* **2006**, *6* (4), 1159–1166. DOI: 10.1166/jnn.2006.327.
279. Chen, W. Nanoparticle Self-Lighting Photodynamic Therapy for Cancer Treatment. *Journal of Biomedical Nanotechnology* **2008**, *4* (4), 369–376. DOI: 10.1166/jbn.2008.001.
280. Takahashi, J.; Misawa, M. Analysis of Potential Radiosensitizing Materials for X-Ray-Induced Photodynamic Therapy. *Nanobiotechnol* **2007**, *3* (2), 116–126. DOI: 10.1007/s12030-008-9009-x.
281. Sudheendra, L.; Das, G. K.; Li, C.; Stark, D.; Cena, J.; Cherry, S.; Kennedy, I. M. NaGdF₄:Eu³⁺ Nanoparticles for Enhanced X-ray Excited Optical Imaging. *Chemistry of materials : a publication of the American Chemical Society* **2014**, *26* (5), 1881–1888. DOI: 10.1021/cm404044n.

282. Scaffidi, J. P.; Gregas, M. K.; Lauly, B.; Zhang, Y.; Vo-Dinh, T. Activity of psoralen-functionalized nanoscintillators against cancer cells upon X-ray excitation. *ACS nano* **2011**, *5* (6), 4679–4687. DOI: 10.1021/nn200511m.
283. Armelao, L.; Heigl, F.; Jürgensen, A.; Blyth, R. I. R.; Regier, T.; Zhou, X.-T.; Sham, T. K. X-ray Excited Optical Luminescence Studies of ZnO and Eu-Doped ZnO Nanostructures. *J. Phys. Chem. C* **2007**, *111* (28), 10194–10200. DOI: 10.1021/jp071379f.
284. Liu, Y.; Zhang, Y.; Wang, S.; Pope, C.; Chen, W. Optical behaviors of ZnO-porphyrin conjugates and their potential applications for cancer treatment. *Appl. Phys. Lett.* **2008**, *92* (14), 143901. DOI: 10.1063/1.2908211.
285. Ma, L.; Zou, X.; Bui, B.; Chen, W.; Song, K. H.; Solberg, T. X-ray excited ZnS: Cu,Co afterglow nanoparticles for photodynamic activation. *Appl. Phys. Lett.* **2014**, *105* (1), 13702. DOI: 10.1063/1.4890105.
286. Yang, W.; Read, P. W.; Mi, J.; Baisden, J. M.; Reardon, K. A.; Lerner, J. M.; Helmke, B. P.; Sheng, K. Semiconductor nanoparticles as energy mediators for photosensitizer-enhanced radiotherapy. *International journal of radiation oncology, biology, physics* **2008**, *72* (3), 633–635. DOI: 10.1016/j.ijrobp.2008.06.1916.
287. Kang, Z.; Zhang, Y.; Menkara, H.; Wagner, B. K.; Summers, C. J.; Lawrence, W.; Nagarkar, V. CdTe quantum dots and polymer nanocomposites for x-ray scintillation and imaging. *Applied physics letters* **2011**, *98* (18), 181914. DOI: 10.1063/1.3589366.
288. Tanha, K.; Pashazadeh, A. M.; Pogue, B. W. Review of biomedical Cerenkov luminescence imaging applications. *Biomedical optics express* **2015**, *6* (8), 3053–3065. DOI: 10.1364/BOE.6.003053.
289. Xu, Y.; Liu, H.; Cheng, Z. Harnessing the power of radionuclides for optical imaging: Cerenkov luminescence imaging. *Journal of nuclear medicine : official publication, Society of Nuclear Medicine* **2011**, *52* (12), 2009–2018. DOI: 10.2967/jnumed.111.092965.
290. Cherenkov, P. A. *Visible emission of clean liquids by action of gamma radiation. Doklady Akademii Nauk SSSR. Vol 2*, 451, 1934.
291. <http://www.nuclear-power.net/nuclear-power/reactor-physics/atomic-nuclear-physics/fundamental-particles/beta-particle/cherenkov-radiation/>.
292. Seguinot, J.; Ypsilantis, T. Photo-ionization and Cherenkov ring imaging. *Nuclear Instruments and Methods* **1977**, *142* (3), 377–391. DOI: 10.1016/0029-554X(77)90671-1.
293. Bernlöhr, K. Simulation of imaging atmospheric Cherenkov telescopes with CORSIKA and sim_telarray. *Astroparticle Physics* **2008**, *30* (3), 149–158. DOI: 10.1016/j.astropartphys.2008.07.009.

294. Mitchell, G. S.; Gill, R. K.; Boucher, D. L.; Li, C.; Cherry, S. R. In vivo Cerenkov luminescence imaging: a new tool for molecular imaging. *Philosophical transactions. Series A, Mathematical, physical, and engineering sciences* **2011**, *369* (1955), 4605–4619. DOI: 10.1098/rsta.2011.0271.
295. Thorek, D. L.; Robertson, R.; Bacchus, W. A.; Hahn, J.; Rothberg, J.; Beattie, B. J.; Grimm, J. Cerenkov imaging - a new modality for molecular imaging. *American journal of nuclear medicine and molecular imaging* **2012**, *2* (2), 163–173.
296. Spinelli, A. E.; Boschi, F. Novel biomedical applications of Cerenkov radiation and radioluminescence imaging. *Physica medica : PM : an international journal devoted to the applications of physics to medicine and biology : official journal of the Italian Association of Biomedical Physics (AIFB)* **2015**, *31* (2), 120–129. DOI: 10.1016/j.ejmp.2014.12.003.
297. Sun, X.; Huang, X.; Guo, J.; Zhu, W.; Ding, Y.; Niu, G.; Wang, A.; Kiesewetter, D. O.; Wang, Z. L.; Sun, S.; Chen, X. Self-illuminating 64Cu-doped CdSe/ZnS nanocrystals for in vivo tumor imaging. *Journal of the American Chemical Society* **2014**, *136* (5), 1706–1709. DOI: 10.1021/ja410438n.
298. Spinelli, A. E.; Ferdeghini, M.; Cavedon, C.; Zivelonghi, E.; Calandrino, R.; Fenzi, A.; Sbarbati, A.; Boschi, F. First human Cerenkography. *Journal of biomedical optics* **2013**, *18* (2), 20502. DOI: 10.1117/1.JBO.18.2.020502.
299. Kotagiri, N.; Sudlow, G. P.; Akers, W. J.; Achilefu, S. Breaking the depth dependency of phototherapy with Cerenkov radiation and low-radiance-responsive nanophotosensitizers. *Nature nanotechnology* **2015**, *10* (4), 370–379. DOI: 10.1038/nnano.2015.17.
300. Ran, C.; Zhang, Z.; Hooker, J.; Moore, A. In vivo photoactivation without "light": use of Cerenkov radiation to overcome the penetration limit of light. *Molecular imaging and biology : MIB : the official publication of the Academy of Molecular Imaging* **2012**, *14* (2), 156–162. DOI: 10.1007/s11307-011-0489-z.
301. Peach, K.; Wilson, P.; Jones, B. Accelerator science in medical physics. *The British journal of radiology* **2011**, *84 Spec No 1*, S4–10. DOI: 10.1259/bjr/16022594.
302. Wilson, P.; Jones, B.; Yokoi, T.; Hill, M.; Vojnovic, B. Revisiting the ultra-high dose rate effect: implications for charged particle radiotherapy using protons and light ions. *The British journal of radiology* **2012**, *85* (1018), e933–9. DOI: 10.1259/bjr/17827549.
303. Axelsson, J.; Davis, S. C.; Gladstone, D. J.; Pogue, B. W. Cerenkov emission induced by external beam radiation stimulates molecular fluorescence. *Medical physics* **2011**, *38* (7), 4127–4132. DOI: 10.1118/1.3592646.

304. Glaser, A. K.; Davis, S. C.; McClatchy, D. M.; Zhang, R.; Pogue, B. W.; Gladstone, D. J. Projection imaging of photon beams by the Cerenkov effect. *Medical physics* **2013**, *40* (1), 12101. DOI: 10.1118/1.4770286.
305. Dinesh Mayani, D. Proton therapy for cancer treatment. *Journal of oncology pharmacy practice : official publication of the International Society of Oncology Pharmacy Practitioners* **2011**, *17* (3), 186–190. DOI: 10.1177/1078155210375858.
306. Jang, K. W.; Yoo, W. J.; Shin, S. H.; Shin, D.; Lee, B. Fiber-optic Cerenkov radiation sensor for proton therapy dosimetry. *Optics express* **2012**, *20* (13), 13907–13914. DOI: 10.1364/OE.20.013907.

7 Appendix

7.1 List of Abbreviations

¹⁸ FDG	2-deoxy-2-(¹⁸ F)fluoro-D-glucose
Ab	antibody
ABL	Abelson tyrosine kinase
ADME	absorption, distribution, metabolism, and excretion
AGC	family group of protein kinases A, G, and C
ALL	acute lymphoid leukemia
AP	adenine pocket
ATP	adenosine triphosphate
BCR	breakpoint cluster region
Boc	<i>tert</i> -butyloxycarbonyl protecting group
BSA	bovine serum albumin
<i>C. elegans</i>	<i>Caenorhabditis elegans</i>
CAMK	calcium/calmodulin-dependent protein kinase
CDK	cyclin-dependent kinase
CHMP	Committee for Medicinal Products for Human Use
CK1	casein kinase 1
c-Kit	mast/stem cell growth factor receptor
CLK	CDC2-like kinase
CMGC	protein kinase group containing CDK, MAPK, GSK3 and CLK families
CML	chronic myeloid leukemia

CR	Cerenkov radiation
DMNB	4,5-dimethoxy-2-nitrobenzyl
DMNP	1-(4,5-dimethoxy-2-nitrophenyl)
DMSO	dimethyl sulfoxide
DPBS	Dulbecco's phosphate-buffered saline
e.g.	exempli gratia, for example
EGFR	epidermal growth factor receptor
ERK	extracellular signal-regulated kinase
GIST	gastrointestinal stromal tumor
GSK3	glycogen synthase kinase 3
H-bond	hydrogen bond
HP I	hydrophobic pocket I,
HR II	hydrophobic region II
IC ₅₀	half maximal inhibitory concentration
JAK	janus kinase
LED	light emitting diode
LINACs	linear particle accelerators
mAb	monoclonal antibody
MAPK	mitogen-activated protein kinase
MEK	mitogen-activated protein kinase kinase
MRSA	methicillin-resistant Staphylococcus aureus
mTOR	mammalian target of rapamycin
NCI	national cancer institute, USA

NIR	near-infrared
PBR	phosphate binding region
PDGFR	platelet-derived growth factor receptor
PDT	photodynamic therapy
PKA	protein kinase A
PKC	protein kinase C
PPG	photoremovable or photocleavable protecting group
PUVA	psoralen and ultraviolet A
ROCK	rho-associated protein kinase
ROS	reactive oxygen species
RTK	receptor tyrosine kinase
SAR	structure-activity relationship
ScNPs	scintillating nanoparticles
SH2	Src Homology 2
SI	supplementary information for a paper
smKI	small molecule kinase inhibitors
SP	sugar pocket
STE	protein kinase group, homologs of yeast sterile 7, 11 and 20 kinases
TGI	total growth inhibition
TK	tyrosine kinases
TKL	tyrosine kinase-like
TPACS	two-photon action cross-section
TPE	two-photon excitation

UCNPs	upconversion nanoparticles
UP	upconversion
UV	ultraviolet
UVA	ultraviolet A
VEGFR	vascular endothelial growth factor receptor
<i>v-Src</i>	gene found in Rous sarcoma virus

7.2 List of Figures

Figure 1: Phylogenetic tree of the human kinome. Seven major protein kinase groups can be distinguished: TKL, STE, CK1, AGC, CAMK, CMGC and TK. Kinases discussed more in this work are labeled with bold red letters. The phylogenetic tree is adapted from cell signaling technology.²⁶ 4

Figure 2: Schematic presentation of the kinase domain of VEGFR-2 (PDB code: 3B8R).⁴⁵ This and subsequent figures showing 3D protein structures were visualized using Maestro 10.4.⁴⁶ The N-terminus is colored purple and the C-terminus is blue. The hinge region is depicted in green..... 6

Figure 3: Schematic model of the ATP-binding site in an active kinase. The representation is based on the crystallized structure of ERK2 kinase in complex with ATP (PDB code: 4GT3).⁵⁴ Amino acid residue glutamine 103 (Glu103) was indicated as the gatekeeper in accordance to previous studies.⁵⁵ The pharmacophore model by Traxler and Furet was applied.^{43, 50} Maestro 10.4 was used for visualization.⁴⁶ Only key residues are shown for better clarity. ATP is depicted with ball and sticks. The amino acid residues are represented as thin tubes. H-Bonds are indicated by yellow dashed lines. HR II = hydrophobic region II, AP = adenine pocket, HP I = hydrophobic pocket I, SP = sugar pocket, PBR = phosphate binding region. 8

Figure 4: Binding site in the VEGFR-2 kinase domain in different DFG conformations.⁵⁹ The representations were visualized using Maestro 10.4⁴⁶ and are according to the noted PDB codes. **(A)** DFG-in conformation is shown (PDB code: 3B8R).⁴⁵ The phenylalanine residue Phe1047 blocks the deep pocket. The adenine pocket is exposable for ATP (blue oval). **(B)** DFG-out conformation is depicted (PDB code: 3EWH).⁶⁰ The phenylalanine residue Phe1047 is now rearranged and blocks access to the adenine pocket for ATP. The deep pocket (red oval) can now be addressed by inhibitors. 9

Figure 5: The regulatory (purple) and catalytic (yellow) spines in the active PKA kinase.²⁸ The presentation is in accordance to Kornev *et al.*⁶² and is based on the PDB code: 1ATP.⁶³ Disruption of these spines drives the inactive kinase conformation..... 10

Figure 6: Chemical structure of imatinib, the first approved kinase inhibitor for cancer treatment...... 12

Figure7: Schematic representation of irreversible photoactivation (uncaging). A photoremovable protecting group (PPG, purple star in the figure) is covalently bound to a compound (blue triangle). As consequence, the compound is caged and inactive. After irradiation with light at appropriate wavelength the PPG is cleaved and the released active

compound can bind to its target. Thus, biological effects can be induced upon irradiation. The activation is irreversible. Some graphical elements used in the visualization such as membrane and receptor were adopted from Servier Medical Art.¹⁴² 20

Figure 8: Schematic representation of reversible photoswitching.¹³⁰ An inactive compound (blue square) can be reversibly switched to its active isomer (dark blue triangle) that can interact with its biological target. The activation is reversible. The backward reaction can be induced by irradiation at a different wavelength. Some graphical elements used in the visualization were adopted from Servier Medical Art.¹⁴² 21

Figure 9: Schematic representation of optogenetics.¹³⁰ A genetically modified, photoresponsive protein, mostly an ion channel can be activated by light to evoke a biological effect. Some graphical elements used in the visualization were adopted from Servier Medical Art.¹⁴² 22

Figure 10: The penetration depth of different light wavelengths into biological tissue.^{172, 173} 25

Figure 11: Schematic representation of release mechanism of *o*-nitrobenzyl caged compounds.^{176, 178, 185, 186} "X" stands for the released compound. 28

Figure 12: Workflow for the caging of protein kinase inhibitors.¹⁷⁶ 29

Figure 13: Hamacanthin B as lead for the development of PDGFR β inhibitors with pyrazine-2(1H)-one scaffold. Comparison between DFG-in inhibitors **1** and **2** and DFG out inhibitor **3** was one of the aims in the present thesis. 32

Figure 14: Chemical structures of vemurafenib and its photoactivatable prodrug **4.** The caged compound **4** corresponds to the caged prodrug **2** in the article "Photoactivatable Prodrugs of Antimelanoma Agent Vemurafenib"..... 84

Figure 15: Phospho-ERK staining of melanoma SKMel13 cells after incubation with vemurafenib and the photoactivatable prodrug **4.** The top four rows of a 96-well-plate with treated cells are shown. The phosphorylated ERK is immunostained with a combination of primary and secondary Ab. The latter one is conjugated to a red fluorescent dye. The experiment was performed in dark without UV irradiation. 85

Figure 16: Phospho-ERK staining of melanoma SKMel13 cells after incubation with DMSO and the photoactivatable prodrug **4 of vemurafenib.** The bottom four rows of the same 96-well-plate as in Figure 15 are shown. These rows were irradiated at 365 nm with 0.9 W for

five minutes. The phosphorylated ERK is immunostained with a combination of a primary and a secondary Ab. The latter one is conjugated to a red fluorescent dye.86

Figure 17: Chemical structures of photoactivatable prodrugs of imatinib.¹⁹³ DMNB- caged imatinib derivative **5** and coumarin-4-ylmethyl caged derivative **6** correspond to the compounds **2** and **3** in the article “Design, Synthesis, and Characterization of a Photoactivatable Caged Prodrug of Imatinib”, respectively.¹⁹³88

Figure 18: Chemical structures of examined VEGFR-2 inhibitors.^{190, 191, 194} 3,4-diarylmaleimide **7** and carbazole **8** correspond to the compounds **1** and **3** in the article “Photoactivatable Caged Prodrugs of VEGFR-2 Kinase Inhibitors”, respectively.¹⁹⁴113

Figure 19: Chemical structures of photoactivatable VEGFR-2 inhibitors.¹⁹⁴ Caged 3,4-diarylmaleimide **9** and caged carbazole **10** correspond to the compounds **4** and **5** in the article “Photoactivatable Caged Prodrugs of VEGFR-2 Kinase Inhibitors”, respectively.¹⁹⁴114

Figure 20: Photoinduced conversion of the approved smKI dabrafenib to the novel inhibitor 11.¹⁹⁶ Compound **11** corresponds to the derivative **2** in the article “Photoinduced Conversion of Antimelanoma Agent Dabrafenib to a Novel Fluorescent BRAF^{V600E} Inhibitor”140

Figure 21: Chemical structures of marine derived hamacanthin B²²⁷ and designed PDGFR β inhibitors with pyrazine-2(1*H*)-one core.²⁰¹ Compounds **1** and **12** correspond to the compounds **5** and **8** in the paper “Marine derived hamacanthins as lead for the development of novel PDGFR β protein kinase inhibitors”, respectively.171

Figure 22: Chemical structure of compound 2, a novel potent DFG-in inhibitor of PDGFR β . Compound **2** corresponds to compound **38** in the article “Optimization of potent DFG-in inhibitors of platelet derived growth factor receptor β (PDGF-R β) guided by water thermodynamics”.²⁰²190

Figure 23: Modeled binding modes of developed PDGFR β inhibitors.^{203, 205} (A) Ligand interaction diagram of the DFG-in inhibitor **2** in the active site of a PDGFR β DFG-in homology model.²⁰² (B) Ligand interaction diagram of the DFG-out inhibitor **3** in the active site of a PDGFR β DFG-out homology model.²⁰³ Inhibitors **2** and **3** correspond to the compounds **1** and **5** in the paper “From Type I to Type II: Design, Synthesis, and Characterization of Potent Pyrazin-2-ones as DFG-Out Inhibitors of PDGFR β ”, respectively.....246

Figure 24: Chemical structures of photoactivatable prodrugs of vemurafenib.¹⁹³ The azaindole caged compound **4** and the sulfonamide caged derivative **13** correspond to the compounds **2** and **4** in the published article,¹⁹³ respectively.278

- Figure 25: Chemical structures of the used model compounds.**¹⁹³ Compound **14** is Boc-protected L-alanine and corresponds to “Boc-Ala” in the published article. Compound **15** is photoactivatable DMNB-protected derivative of the compound **14** and corresponds to “Boc-Ala-DMNB”.¹⁹³279
- Figure 26: Chemical structure of compound 16, the piperazine DMNB-protected imatinib derivative.**¹⁹⁵279
- Figure 27: Photoactivatable prodrug of vemurafenib 17.**²⁴² The azaindole moiety of vemurafenib was protected by a carboxylic acid analog of the DMNB PPG.¹⁶⁶283
- Figure 28: Custom-made mouse restrainer with a fixed test mouse.** The posterior flank of the animal is accessible for irradiation.285
- Figure 29: Custom-made LED pen for irradiation of test animals in the mouse restrainer.**²³⁹ The illumination device was designed for the cleavage of the DMNB PPG by irradiation at 365 nm. Irradiation power and time can be adjusted by the control module at the top of the picture.285
- Figure 30: Example of red laser light delivery under the skin by an optical fiber and a needle.**²⁵²287
- Figure 31: Proof-of-principle for the photolysis of caged D-luciferin by utilizing UCNP coated with thiolated silane.**²⁶⁶ 1-(2-nitrophenyl)ethyl caged luciferin was covalently bound to the UCNP by a linker. The excitation NIR radiation was upconverted by UCNP to UV light that cleaved the PPG. The released luciferin was recognized by a luciferase (fLuc enzyme) and caused measurable bioluminescence.289
- Figure 32: Cerenkov radiation in a reactor core.**²⁹¹292
- Figure 33: Proof-of-principle for applicability of CR for *in vivo* imaging in human.**²⁹⁸ (a) CR of a thyroid gland of a patient treated with ¹³¹I. (b) The overlay between the photographic image and the CR image of the patient.²⁹⁸293
- Figure 34: Uncaging of photoactivatable derivative of luciferin with Cerenkov radiation induced by ¹⁸FDG.** Adapted and modified from the original publication.³⁰⁰294

Curriculum Vitae

PERSÖNLICHE DATEN

Name: Boris Pinchuk
Geburtsdatum: 21.10.1986
Geburtsort: Odessa, Ukraine
Staatsangehörigkeit: deutsch

SCHULAUSSILDUNG UND STUDIUM

09/2002 - 07/2007 Goethe-Gymnasium, Schwerin
07/2007 **Allgemeine Hochschulreife**
07/2007 - 10/2010 **Bachelor of Science Chemie**, Christian-Albrechts-Universität zu Kiel
10/2010 - 05/2013 **Master of Science Biochemie und Molekularbiologie**, Christian-Albrechts-Universität zu Kiel

BERUFLICHER WERDEGANG UND PROMOTION

03/2010 - 04/2010 **Wissenschaftliche Hilfskraft**, Zentrum Molekulare Biowissenschaften, Kiel
11/2011 - 01/2012 **Wissenschaftliche Hilfskraft**, Pharmazeutisches Institut, Kiel
03/2012 - 08/2012 **Betriebspraktikum**, Dräger Safety AG & Co. KGaA, Lübeck
10/2012 - 03/2013 **Masterarbeit**, European ScreeningPort, Hamburg
Seit 08/2013 **Wissenschaftlicher Mitarbeiter und Promotion**, Arbeitsgruppe von Prof. Dr. Peifer, Pharmazeutisches Institut, Christian-Albrechts-Universität zu Kiel
03/2014 - 04/2014 **Forschungsaufenthalt**, Medical Research Council Protein Phosphorylation and Ubiquitylation Unit (MRC PPU), Dundee, Schottland

Erklärung

Die vorliegende Arbeit wurde unter Anleitung von Herrn Prof. Dr. Christian Peifer im Fachbereich Pharmazeutische und Medizinische Chemie des Pharmazeutischen Instituts der Christian-Albrechts-Universität zu Kiel im Zeitraum von August 2013 bis März 2017 angefertigt.

Hiermit erkläre ich, Boris Pinchuk, dass der Inhalt und die Form dieser Abhandlung, abgesehen von der Beratung durch meinen Betreuer, selbstständig von mir erarbeitet wurden. Es wurden keine weiteren Quellen als angegeben herangezogen. Die Arbeit hat an keiner Stelle im Rahmen eines Prüfungsverfahrens vorgelegen und ist unter Einhaltung der Regeln guter wissenschaftlicher Praxis der Deutschen Forschungsgemeinschaft entstanden. Es handelt sich um meinen ersten Promotionsversuch.

Kiel, März 2017

Boris Pinchuk

Die Ergebnisse der vorliegenden Arbeit wurden bereits in folgenden Beiträgen veröffentlicht:

Fachzeitschriften

Pinchuk, B.; Johannes, E.; Gul, S.; Schlosser, J.; Schaechtele, C.; Totzke, F.; Peifer, C. Marine derived hamacanthins as lead for the development of novel PDGFRbeta protein kinase inhibitors. *Marine drugs* **2013**, *11* (9), 3209–3223. DOI: 10.3390/md11093209.

Horbert, R.; Pinchuk, B.; Johannes, E.; Schlosser, J.; Schmidt, D.; Cappel, D.; Totzke, F.; Schachtele, C.; Peifer, C. Optimization of potent DFG-in inhibitors of platelet derived growth factor receptorbeta (PDGF-Rbeta) guided by water thermodynamics. *Journal of medicinal chemistry* **2015**, *58* (1), 170–182. DOI: 10.1021/jm500373x.

Horbert, R.; Pinchuk, B.; Davies, P.; Alessi, D.; Peifer, C. Photoactivatable Prodrugs of Antimelanoma Agent Vemurafenib. *ACS chemical biology* **2015**, *10* (9), 2099–2107. DOI: 10.1021/acscchembio.5b00174.

Zindler, M.; Pinchuk, B.; Renn, C.; Horbert, R.; Dobber, A.; Peifer, C. Design, Synthesis, and Characterization of a Photoactivatable Caged Prodrug of Imatinib. *ChemMedChem* **2015**, *10* (8), 1335–1338. DOI: 10.1002/cmdc.201500163.

Pinchuk, B.; Horbert, R.; Dobber, A.; Kuhl, L.; Peifer, C. Photoactivatable Caged Prodrugs of VEGFR-2 Kinase Inhibitors. *Molecules (Basel, Switzerland)* **2016**, *21* (5). DOI: 10.3390/molecules21050570.

Pinchuk, B.; Drathen, T. von; Opel, V.; Peifer, C. Photoinduced Conversion of Antimelanoma Agent Dabrafenib to a Novel Fluorescent BRAFV600E Inhibitor. *ACS medicinal chemistry letters* **2016**, *7* (10), 962–966. DOI: 10.1021/acsmchemlett.6b00340.

Bethke, E.; Pinchuk, B.; Renn, C.; Witt, L.; Schlosser, J.; Peifer, C. From Type I to Type II: Design, Synthesis, and Characterization of Potent Pyrazin-2-ones as DFG-Out Inhibitors of PDGFRbeta. *ChemMedChem* **2016**, *11* (24), 2664–2674. DOI: 10.1002/cmdc.201600494.

Posterbeiträge

Horbert, R.; Pinchuk, B.; Rahlff, J.; Schaechtele, C.; Gul, S.; Peifer C. Design, Synthesis and Biological Evaluation of 3,4-Diarylmaleimides as Vascular Endothelial Growth Factor Receptor (VEGF-R) Inhibitors. *7th Polish-German Symposium on Pharmaceutical Sciences*, **2013**, Gdansk, Poland.

Horbert, R.; Pinchuk, B.; Gul, S.; Peifer C. Design, Staurosporine-Derived 3,4-Diarylmaleimides as Vascular Endothelial Growth Factor Receptor (VEGF-R) Inhibitors. *DPhG annual conference*, **2013**, Freiburg, Germany.

Pinchuk, B.; Horbert, R.; Johannes, E.; Schlosser, J.; Schmidt, D.; Peifer, C. Development of Novel PDGFR β Protein Kinase Inhibitors based on the Pyrazin-2(1H)-one Scaffold derived from marine Hamacanthins. *GEOMAR-Biotech Mini Symposium*, **2015**, Kiel, Germany.

Pinchuk, B.; Horbert, R.; Davies, P.; Alessi, D.; Peifer, C. Photoactivatable Prodrugs of Approved Kinase Inhibitor Vemurafenib, *250th ACS National Meeting*, **2015**, Boston (MA), USA.

Pinchuk, B.; Horbert, R.; Doebber, A.; Davies, P.; Alessi, D.; Peifer, C. Photoactivatable Prodrugs of Kinase Inhibitor Vemurafenib, *8th Summer School Medicinal Chemistry*, **2016**, Regensburg, Germany.

Danksagung

An erster Stelle möchte ich mich herzlich bei meinem Doktorvater, Prof. Dr. Christian Peifer, für das spannende Thema meiner Promotion bedanken. Danke für Dein ständiges Vertrauen, Deine Diskussionsbereitschaft und die Freiheit, die ich während meiner Promotionszeit genießen konnte. Ein besonderer Dank gilt Deiner menschlichen und verständnisvollen Umgangsart. Nicht zu vergessen sind natürlich auch die gemeinsamen Angelausflüge.

Prof. Dr. Axel Scheidig möchte ich für die Übernahme des Zweitgutachtens danken. Vielen Dank für die immer freundliche Beratung, die ich während meines Studiums aber auch danach bei Dir erfahren habe. Zusätzlich möchte ich mich für die Kristallisationsversuche bedanken, die ich bei Dir machen durfte, selbst wenn diese erfolglos waren.

Prof. Dr. Uwe Knippschild danke ich für die Übernahme meines dritten Gutachtens. Auch möchte ich mich für die enge Kooperation bei der Etablierung von Tierversuchen bedanken. Ein besonderes Dankeschön gilt dabei Dr. Joachim Bischoff. Danke Dir für die freundliche Aufnahme in Ulm und für die angenehme Zusammenarbeit.

Der analytischen Abteilung unter der Leitung von Dr. Ulrich Girreser danke ich für die Aufnahme von NMR- und Massenspektren. Bei Karl Willi Bock möchte ich mich für unverzügliche Reparaturen jeglicher elektrischer Geräte bedanken. Dirk Böhme danke ich für die Werkstatteleistungen und den schnellen Bau von speziellen Vorrichtungen.

Dem ganzen Arbeitskreis von Prof. Dr. Scheidig und insbesondere Christina Hopf möchte ich für die Unterstützung bei mehreren Versuchsreihen danken.

Sehr gerne möchte ich mich bei all meinen jetzigen und früheren Kollegen im Arbeitskreis von Prof. Dr. Peifer bedanken. Ein besonderer Dank gilt Dr. Rebecca Horbert. Du hast mit dem Thema der photoaktivierbaren Proteinkinaseinhibitoren angefangen und damit den wesentlichen Grundstein für meine Doktorarbeit gelegt. Danke Dir für die stets sehr angenehme und fruchtbare Zusammenarbeit. Dr. Eugen Bethke möchte ich für die Darstellung von zahlreichen PDGFR β Inhibitoren danken. Bei Alexander Döbber möchte ich mich für die zahlreichen Diskussionsstunden und Anregungen bedanken. Dr. Melanie Zindler

danke ich für die Bereitstellung von geschützten Imatinib-Derivaten. Dr. Jakob Halekotte, Lydia Witt, Dorian Schmidt und Miriam Schehr möchte ich unter anderem dafür danken, dass ihr zigmal meine Vorträge über photoaktivierbare Prodrugs ausgehalten habt, obwohl ihr selbst mit dem Thema nichts zu tun hattet. Ein großes Dankeschön gilt auch meinem Büronachbarn Martin Schütt. Du hast nicht nur Substanzen nachsynthetisiert, sondern auch immer für die gute Laune im Arbeitskreis gesorgt. Natürlich möchte ich mich auch bei den ehemaligen Studenten: Christian Renn, Thorsten von Drathen, Viktoria Opel, Jantje Weber, Melanie Neck, Linda Heintze und Theo Rodat bedanken. Jeder von euch hat etwas für meine Arbeit beigetragen.

Mein großer Dank gilt Christian, Alex, Jakob und Lydia für das Korrekturlesen dieser Arbeit.

Dem ganzen „AK ohne Hosen“ möchte ich herzlich für die tolle und entspannte Arbeitsatmosphäre danken, vor allem aber für all die tollen Momente, die wir gemeinsam außerhalb der Arbeitszeit erlebt haben. Die Hochzeiten, die wir gemeinsam gefeiert haben, die zahlreichen Spielabende und Partys werden mir immer in Erinnerung bleiben. Ihr habt dazu beigetragen, dass meine Promotion tatsächlich eine wunderbare Zeit war.

Beim Thema Freizeit angelangt, möchte ich meinen Freunden Stasik, Lera, Artur, Larisa, Sascha, Sveta und ein Paar mehr für die tollen Erlebnisse danken, die wir bereits hatten und noch gemeinsam vor uns haben. Meinen Studienkommilitonen und Freunden: Ben, Arne, Stephan, Smets, Baschi, Uta und Birk danke ich für die schöne gemeinsame Zeit, vor allem außerhalb der Vorlesungen.

Ein großer Dank gilt natürlich auch meiner Familie. Ihr habt mich immer unterstützt und meine Promotion in Deutschland erst überhaupt ermöglicht. Danke an meine Eltern, Samira und Oleg Pinchuk, ihr habt mich zu dem Menschen erzogen, der ich bin. Ich weiß, mein Vater wäre stolz auf mich.

Zum Schluss möchte ich mich vom ganzen Herzen bei meiner wunderbaren Frau, Lena, bedanken. Du begleitest mich auf meinem ganzen Weg, vom Abitur bis zur Promotion, und bist mir immer eine große Hilfe und noch eine größere Freude gewesen. Ich bin glücklich, Dich an meiner Seite zu haben und freue mich schon auf alles, was noch vor uns liegt.